THE DYNAMIC BEHAVIOUR OF A SURFACE HOSE ATTACHED TO A CALM BUOY

THOMAS O'DONOGHUE

B.E., M.ENG.SC.

Thesis submitted for the degree of

Doctor of Philosophy

Department of Offshore Engineering

Heriot-Watt University

Edinburgh

May 1987

CONTENTS Page N°

continued.....

ACKNOWLEDGEMENTS

I would like to thank the following people who helped ensure the successful completion of this thesis:

My supervisor, Professor A R Halliwell, Department of Offshore Engineering, Heriot-Watt University, for his constant kindness, interest and assistance in the course of this study.

Professor D G Owen, Head of the Department of Offshore Engineering, Heriot-Watt University, for allowing me full use of the departmental facilities.

Mr J Bree, Department of Mathematics, Heriot Watt University, for the major contribution made by him to solving the "snaking problem".

Mrs J Nicol, Secretary, Department of Offshore Engineering, for her expertise in typing and help in preparing the thesis for presentation.

The technical staff of the workshops and hydraulics laboratory at Heriot-Watt University for constructing the models and assisting in the model tests.

My friends and colleagues at Heriot-Watt University who were always willing to discuss matters of the study with me.

Dunlop Oil and Marine for supplying the hose models and some of the photographs.

I also gratefully acknowledge receipt of financial assistance from University College Cork, Éire, the Pfizer Chemical Corporation and Heriot-Watt University.

ABSTRACT

The objective of this study is a quantitative understanding of the mechanisms by which bending moments and axial loads are induced on a floating hose-string attached to a CALM buoy by the combined action of waves and buoy motions.

The study is based on physical model tests in which the CALM buoy with floating hose-string attached is modelled in a wave basin facility. Simultaneous measurements are recorded of the waves, buoy motions and bending moments or axial loads along the hose-string. Bending in two orthogonal planes is considered: vertical bending in the plane perpendicular to the water surface and horizontal bending in the plane of the water surface. The latter is due to the "snaking" of the hose-string. The analysis of the model test data is based, for the most part, on spectral analysis techniques.

The experimental work is augmented by theoretical analysis. Considering the heave, surge and pitch of the buoy as uncoupled s.d.o.f. systems leads to models for the prediction of the SBM's response in waves. Analytical models, based on engineer's bending theory, are developed for the prediction of the vertical and snake-induced horizontal bending moments along the hose-string.

Conclusions are reached regarding the response of the CALM buoy in waves and the dependence of vertical bending, horizontal bending and axial loads on the waves and buoy motions.

LIST OF PLATES

LIST OF TABLES

(Tables in appendices are not included in this list)

LIST OF FIGURES

(Figures in appendices are not included in this list)

Plate 1.1 A CALM SPM System (courtesy of Dunlop, Oil and Marine)

1. INTRODUCTION

1.1 The CALM Single Point Mooring

The exploitation of crude oil reserves from offshore sites has led to the development of large crude oil-transportation systems. The transportation of oil from an offshore oilfield to a land-based refinery is achieved in one of two ways. One solution is to lay a pipeline from the oilfield to shore. The second solution is to deploy a single point mooring (SPM) terminal system at the production location and, in the absence of adequate port facilities, at an offshore site close to the shore destination.

The concept of SPM terminals is an old one. The first was designed for installation off Sweden in 1958. The system was considered as a short-term answer to the then emerging problem of limited port facilities to accommodate the increasing growth in tanker size. By the early 1970s however, as a result of the four-fold increase in oil prices, the SPM concept had achieved widespread industry acceptance. SPMs often allow development of marginal fields which have insufficient recoverable reserves to justify a pipeline system. If the economics can support the cost of a pipeline an SPM may ensure income during the pipeline design and construction period and is often retained as a back-up system subsequent to pipeline completion.

Gruy (1982) summarises the applications of SPMs in offshore production operations and describes the many types of SPM concepts. The basic principle is always the same. The tanker moors to a single point which may rotate 360 degrees in the horizontal plane. The fluid transfer system used to convey the oil is also capable of 360 degrees rotation. The tanker may therefore load (or unload) as it weathervanes about the mooring

under the action of the prevailing wave, current and wind conditions.

The most common SPM is the catenary anchor leg mooring (CALM) (Plate 1.1). The distinctive feature of this system is a floating buoy moored by catenary chains which are anchored to the seafloor (Figure 1.1). Four, six or eight chains are used. The tanker is moored to the buoy at the bow. Oil is transported between the sea-bed pipeline and the buoy via flexible submarine hoses and between the buoy and tanker via one or more flexible floating hose-strings.

The CALM is a simple, proven system. It was originally conceived as primarily a shallow water system - less than 50m - but has been installed in much deeper waters. One of the most significant deeper water applications was the deployment of a CALM SPM terminal at BP's Buchan field in the North Sea (Lindner (1979)). The buoy is moored by six catenary chains in a water depth of 110m. Salmon (1982) discusses many of the improvements made to various components of the CALM SPM system which accompanied its introduction to the North Sea. The Shell UK buoy off the Isle of Anglesey, North Wales, is one of the world's largest and accommodates tankers up to 600,000 dwt. This buoy is over 17m in diameter and is moored by eight chains in about 40m of water.

1.2 Floating Hose-Strings Attached to a CALM Buoy

The floating hose link between the tanker and the mooring buoy of a CALM SPM consists of a number of individual hose lengths, each 10m long, bolted together by means of steel flanges built into the ends of the hose lengths.

The carcass of a hose consists of rubber strengthened with a number of textile fabric or textile cord or wire cord layers, together with at least

one helix of heavy steel wire. The flotation medium, consisting of sponge rubber, PVC foam or similar closed cell material, may be integrally built onto the basic hose. Alternatively individual flotation units may be fitted over the basic hose length with sufficient space between the floats to allow normal flexibility. The first-off-the-buoy hose experiences the greatest forces and bending moments in the ocean environment and its design differs from the mainline hoses. This hose is strengthened by the addition of extra reinforcement to the end which is connected to the buoy manifold. The reinforcement is continued into the body of the hose, tapering gradually along its length. Only half of this hose has flotation medium. It is usual practice to design the buoy manifold such that the first-off-the-buoy hose connects to it at an angle of 15 degrees to the horizontal and intersects the still water level at the point of connection (Figure 1.2).

The length of hose-string required is dictated by the maximum distance between the buoy and tanker manifold. The Buchan system, for example, incorporates 150m of floating hose while the hose-strings at Anglesey are 300m long.

Super-sized export tankers demand rapid loading and unloading of cargo to be cost effective. This has led to the development of large-bore hoses. The largest hoses available have a bore diameter of 24 inches (0.61m). Figure 1.3 shows the dimensions of a typical 24 inch mainline and first-off-the-buoy hose.

Plate 1.2 shows lengths of 24 inch floating hose.

When the conveying of cargo is completed at an SPM terminal the floating hose-strings are disconnected from the tanker manifold and left floating

full of sea-water with one end attached to the buoy.

1.3 Studies of Floating Hose-Strings

The complexities involved in the design of floating hoses for particular locations are twofold. Firstly, the single point mooring dynamics, coupled with the prevailing sea conditions, subject the hose-string to a complex system of motions and loads. Secondly, the nature of the materials used in hose construction make it difficult to predict the induced stresses under given loading conditions.

The solution used to overcome the latter problem is to study the performance of hoses in a dynamic test facility. Such a facility has been constructed at the Southwest Research Institute (SWRI), Texas to study different types of hose construction under similar loading conditions (Furness (1981)). This test rig was constructed through sponsorship from the Oil Companies International Marine Forum (OCIMF). The results of studies conducted at SWRI are used by the OCIMF to set down guidelines for the design and construction of offshore floating hoses (Tschoepe (1981)).

Plate 1.3 shows a length of hose under test in a dynamic test facility.

Various studies have been conducted which address the more fundamental problem of quantifying the forces and moments induced on floating hoses in the ocean environment. These studies have been carried out for the most part by hose manufacturers. However, much of their work has not been published and is documented only in internal reports (Bridgestone (1976), Dunlop (1973), Graham (1982)).

The author is aware of only four published papers which address the behaviour of floating hose-strings in the ocean environment and the contents of these are summarised in what follows:

(1) Brady (1974) reports on load measurements recorded at a CALM buoy off Nigeria. The strain-gauged load-measuring spool was fitted between the 24 inch first-off-the-buoy hose and the buoy manifold. Measurements of axial load, torsion and bending moments in two orthogonal planes were recorded. From the statistical analysis of the 60 second records and from visual records of the sea conditions, attempts were made to correlate the measured loads with the environmental data. Brady presents some of the general observations made. These include a dependency of vertical bending on the higher frequency sea state components and a dependency of axial load and torsion on the lower frequency swell conditions. The desired correlation is severely limited due to the lack of accurate wave records.

(2) Saito (1980) reports on load measurements recorded from a strain-gauged spool fitted between a CALM buoy manifold and a 20 inch first-off-the-buoy floating hose in Tokyo Bay. Axial load, torsion and two bending moments as well as wave height were recorded. No details of the analysis procedure is presented. A set of simple results relating the amplitudes of axial force variation, of torsional torque variation and of bending moment variation as linear functions of wave height are presented. There is no suggestion of a dependency on wave frequency. There is mention in the same publication of model tests conducted on floating hose-strings and of a simple dynamic analytical model relating surge motion of the buoy and axial load in the first hose. However, few details or results are presented.

(3) Young (1980) describes model tests conducted on floating hoses. However, this study is concerned with hoses attached to an articulated single point mooring tower and not to a CALM buoy.

Moreover Young is not concerned with quantitatively establishing the forces and moments on the hoses but with assessing qualitatively the performance of eight different hose-string configurations. Young presents his observations in full but his results have little application to the CALM problem. One observation emphasised by Young is worthy of mention here as it is given much consideration in later chapters of this thesis; that is, all hose configurations were subject to "snaking". Snaking is a phenomenon whereby the hose takes on a sinewave shape transverse to the direction of wave travel and in the plane of the water surface. This sinewave then travels down the length of the hose giving the appearance of a snake travelling through water.

(4) Brown (1984) presents a full account of the development of a static and a dynamic mathematical model of a marine hose-string attached to a CALM buoy. The hose-string is modelled as a beam and beam bending theory is used. The equation of motion for beam bending is applied in the vertical plane only. The loading on the beam in waves is given as the hose weight minus the buoyancy force. The boundary conditions include provision for buoy heave and buoy pitch motion. The equation of motion is solved using a finite-difference scheme, yielding results for hose displacement, slope, bending moment and shear along the length of hose.

1.4 Objective and Approach of Study

The floating hose link is a vital one in an SPM terminal system. Failure or damage to any part of a floating hose-string may cause oil spillage and terminal downtime with serious pollution and financial consequences. Ziccardi (1970) points out that the selection of a hose system for an SPM

terminal depends on both operational requirements and environmental conditions. Operational requirements such as working pressure, desired through-put, nature of products to be transported, are generally well-defined. However there is a serious lack of knowledge of the forces and moments induced on floating hose-strings in the ocean environment. This has meant that the design of floating hose-strings has, for the most part, been based on trial and error.

The objective of this study is a quantitative understanding of the mechanism by which forces and moments are induced on floating hose-strings attached to a CALM buoy by the combined action of waves and buoy motions. The results of the study can be applied in a test programme of hose constructions and thereby help to establish the design of floating hose-strings on a more scientific basis than heretofore.

The study is based primarily on physical model tests in which the buoy motions and the forces and moments along the hose-string are measured in various sea conditions. Chapter 2 describes the design and construction of the mooring and hose-string model and the methods of measuring and recording the buoy motions and hose-string loading. The experimental data processing and analysis techniques are presented in Chapter 3.

The analysis, presentation and discussion of the experimental results proceeds in two stages. Chapter 4 presents first the relationships established between buoy motions and incident wave conditions. Then, in Chapter 5, the loading along the hose-string is considered in relation to the incident waves as well as the buoy motions.

The experimental work is augmented by theoretical analysis. In Chapter 6 the heave, surge and pitch of the buoy are considered as uncoupled

s.d.o.f. systems; this leads to the development of models for the prediction of the SBM's response in waves. Chapter 7 presents analytical models for the vertical and horizontal bending of the hose-string in waves.

In Chapter 8 comparisons are made between the experimental results and those of the theoretical models. Chapter 9 completes the thesis with a summary of the conclusions reached throughout the study.

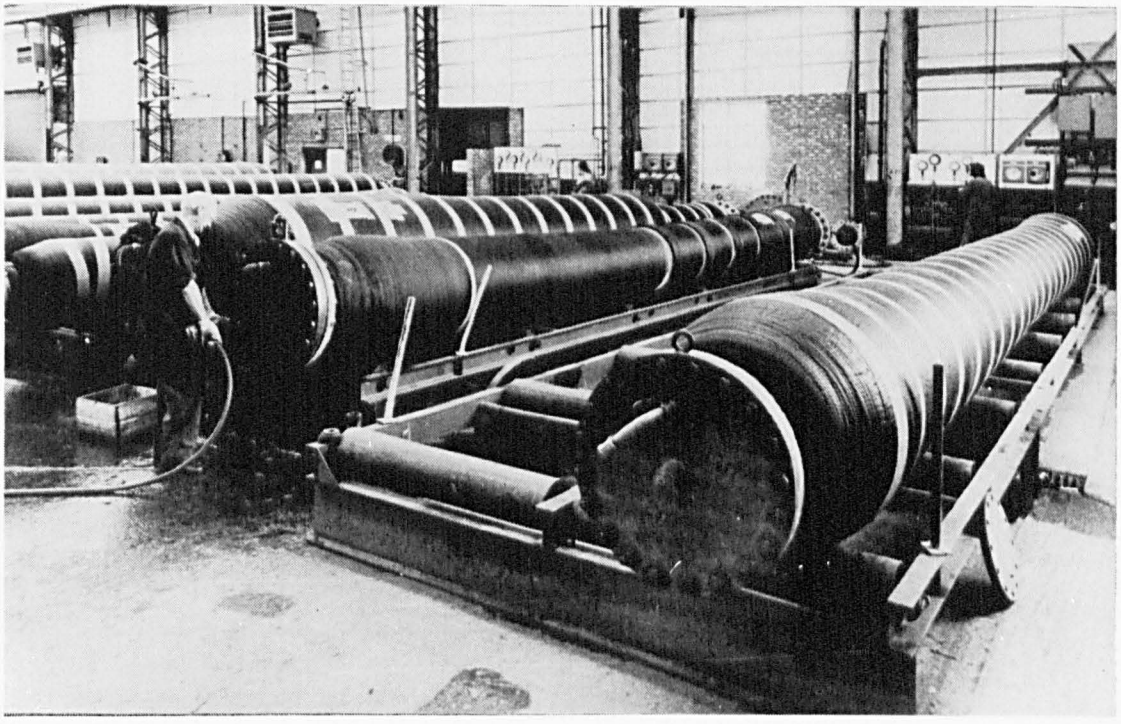

Plate 1.2 Lengths of 24in Floating Hose (courtesy of Dunlop, Oil and Marine)

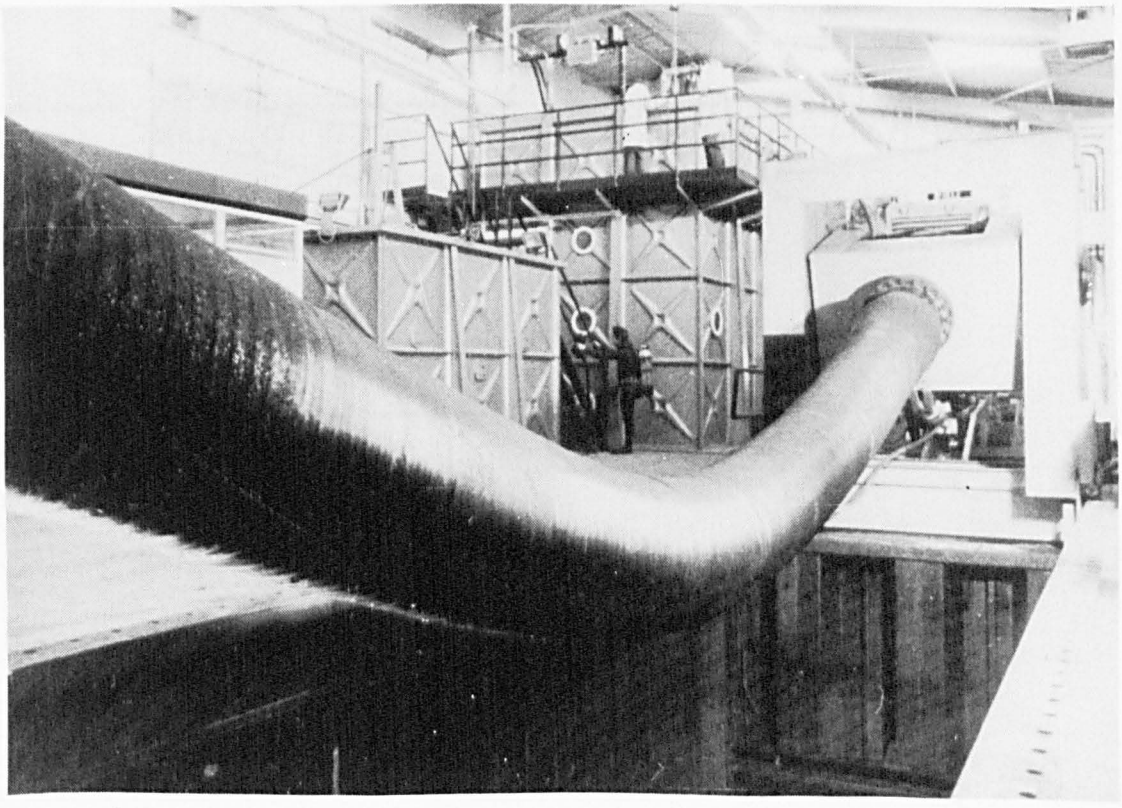

Plate 1.3 Hose Length under test in a Dynamic Test Facility (courtesy of Dunlop, Oil and Marine)

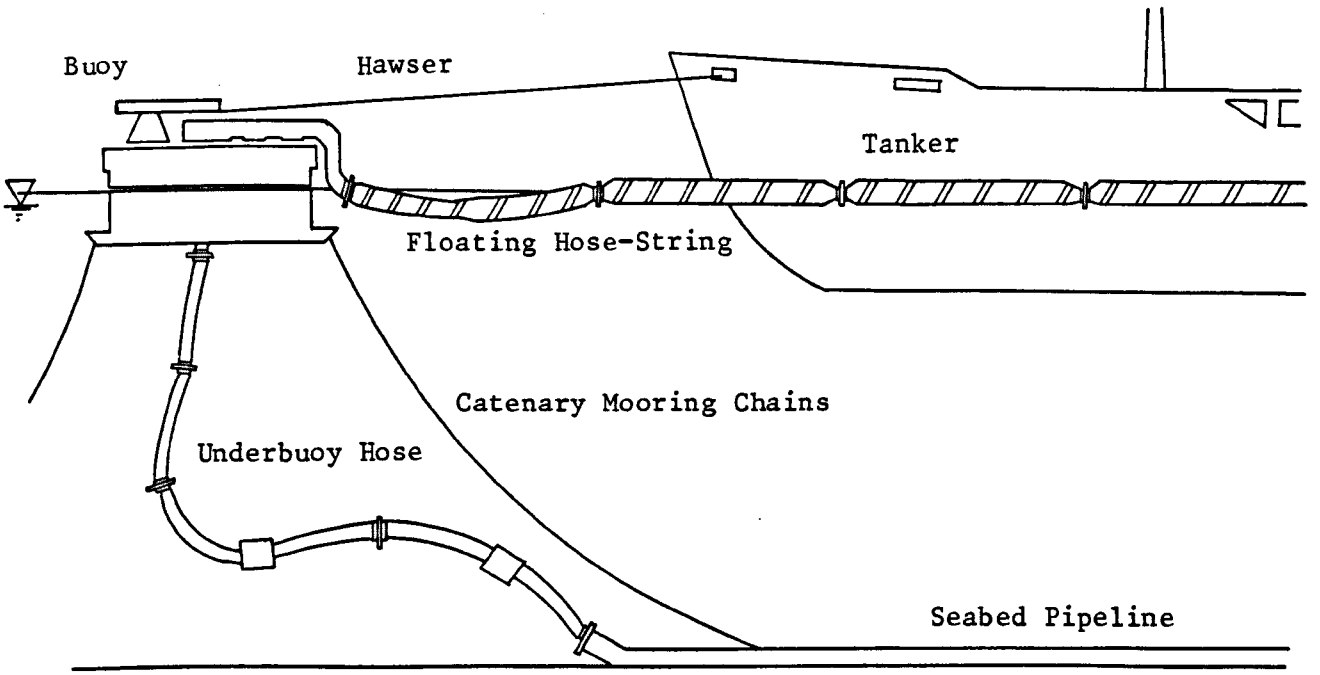

Figure 1.1 The components of a CALM SPM installation

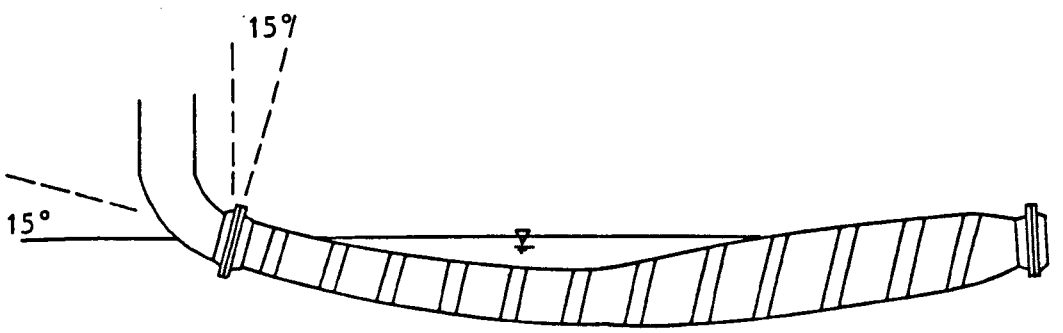

Figure 1.2 The first-off-the-buoy hose

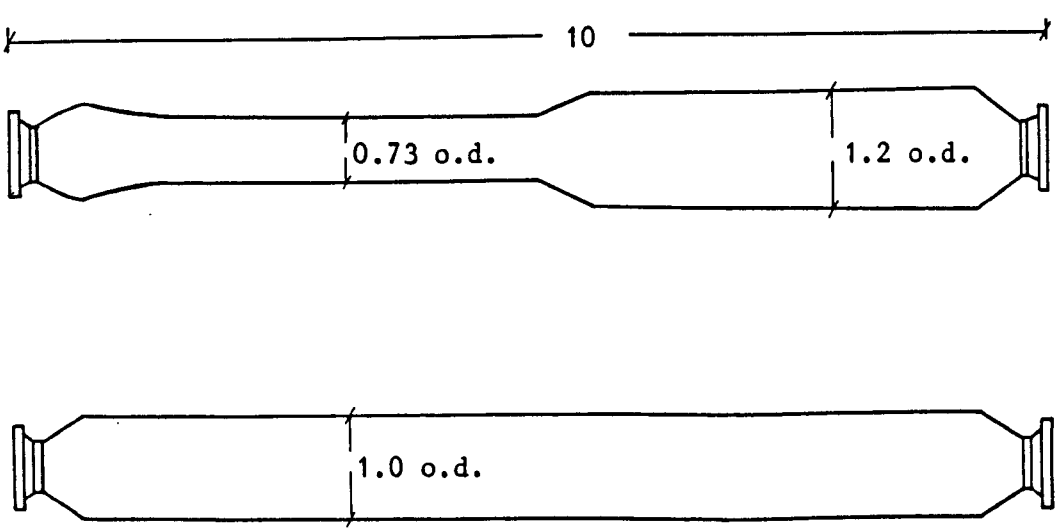

Figure 1.3 Dimensions of typical 24 inch first-off-the-buoy and mainline hoses (all dimensions in metres; scale 1:75)

2. MODEL TESTS: MODEL AND INSTRUMENTATION

2.1 Introduction

2.1.1 Overview

Floating hose-strings are likely to experience their most severe loading conditions when they are not connected to a tanker and lie in the sea surface full of sea-water with one end attached to the buoy and the other end free. These conditions are termed the "survival conditions" of the system. The model tests described in this thesis attempt to simulate the survival conditions for the hose-strings. The prototype environmental conditions have been simplified so that the main objective - an understanding of the mechanism by which loads are induced on the hose-string - can be realised. The waves are long-crested and travel in the same direction as the hose-string alignment, as shown in Figure 2.1. Moreover no attempt has been made to simulate current.

Within the Offshore Engineering Department at Heriot-Watt University, interest in the subject of floating hose-strings attached to a CALM buoy developed from an initial enquiry made by Shell UK Oil to the Department regarding a particular aspect of the performance of the hose-strings attached to their CALM buoy off Anglesey, North Wales. For this reason the Anglesey system was used as the prototype reference for the model tests.

The purpose of the model tests is to obtain measurements of buoy motions and forces and moments along the hose-string's length in various sea conditions. Figure 2.2 shows schematically how this data is acquired. The buoy motions are measured using a two-camera system focussed on light-emitting diodes attached to the buoy. The forces and moments along the

hose-string are measured using strain-gauged phosphor bronze units fitted between the hose lengths. The incident waves are measured using a conductance wave probe. The voltage outputs from the conditioning units and amplifiers associated with these transducers are stored on magnetic tape.

2.1.2 Test Facility

The model tests were conducted in the wave basin facility. The basin (Figure 2.3) is 9m x 9m, with a working water depth of 0.9m. The eighteen wave-making paddles, each 0.3m wide, are aligned along one side of the basin. Wave-absorbing beaches are positioned along the other three sides. The paddles are fitted with electronically-controlled wave-absorbing facilities which, together with the beaches, prevent wave reflections building up within the basin during a test period. The presence of the paddles and the beaches results in a working area of about 5.1m by 5.7m at the basin floor and a working area of about 8.0m by 7.6m at the water surface. The optimum frequency range of the paddles for wave generation is about 0.4 to 2.0Hz. Wave heights of up to 200mm may be produced though clearly this is a function of frequency, the maximum height at high frequencies being limited by wave-breaking and at low frequencies by limitations on the paddle stroke.

2.1.3 Model Scale

The criterion for the choice of scale for a physical model test depends on the particular characteristics of the study in question. It depends on the capabilities of the wave-making system, the dimensions of the test facility and the characteristics of the structure to be tested. The scale selected will certainly depend on the scaling laws applicable to the phenomenon of interest. For example, when viscous forces are important

and gravity forces are negligible Reynolds scaling laws should be applied. This requires that the fluid velocity in the model must equal the fluid velocity in the prototype multiplied by the model scale, where scale is defined as the ratio of length in the prototype to length in the model, i.e. $S = L_p/L_m$. Reynolds number-dependent phenomena are often required to be modelled at very low scales (small values of S) or in wind tunnels where very high fluid flow velocities can be achieved. Froude scaling is applicable when gravity forces are important and viscous effects are secondary or negligible. In cases where both viscous and gravity effects are important, such as the total resistance on a ship moving through water, special techniques need to be applied to evaluate separately the two effects.

In the case of wave action on structures Froude scaling is applicable and is therefore used in this study where floating hose-strings are attached to a CALM buoy and subjected to wave action. There may be some aspects of this problem where viscous effects are important and Reynolds scaling is appropriate, such as the longitudinal motion of the hose through the water, but the primary forces and motions are dependent on the gravity effects. Table 2.1 presents a list of Froude multipliers for a model with scale S.

Considering all the characteristics required to be modelled in relation to the available test facilities, a scale value of between 40 and 50 was deemed the most appropriate. The final scale value selected was 43, the limiting criterion being the ratio of the stiffness properties of the available hose model to those of the prototype.

2.2 Hose-String Model

An ideal model of a floating hose would model the geometry, density, bending stiffness, axial stiffness and torsional stiffness. This requires that all the material properties as well as the geometric properties are scaled appropriately. This is an extremely difficult if not impossible task and some compromise must therefore be reached. The most important properties of the floating hose which govern the loading and response in waves are its bending stiffness, its mass per unit length and its displacement or flotation. For this reason the specifications for the hose-string model were limited to accurately reproducing these properties only.

2.2.1 Hose Bending Stiffness

Unique bending stiffness values are not quoted for a hose type because of the nature of its construction and the properties of its constituent materials. Nevertheless hose manufacturers subject hose samples to so-called "bend tests" before supplying to the customer. A typical bend test arrangement is schematised in Figure 2.4. The flanges at the ends of the hose length sample are fitted with a rigid beam 6 feet (1.83m) long. The hose sample is laid on trolleys and a cable is attached between the free ends of the beams. The cable is tensioned resulting in a moment applied to the hose causing it to bend. When sufficient curvature has been achieved the lengths A and B are recorded as well as a number of values of y corresponding to values of x. The radius of curvature (R) of the hose and the applied moment (M_o) are obtained from the set of geometrical readings and the applied tension. The product of the moment and the radius of curvature is a measure of the bending stiffness of the hose sample.

A serious problem associated with the test is that it does not produce pure bending of the hose sample because the loading mechanism induces a compression component on the hose which itself exerts a moment as the sample bends. The bend test result can therefore only be considered as representative of the bending stiffness of hoses of similar construction. Besides this problem associated with the test set-up, there is a further problem associated with the hose's construction: the load within the cable which pulls the beam ends together decays from an initial value at a given radius to a fairly constant value over a period of about ten minutes.

To set a target for the bending stiffness of the hose model, two sets of data, recorded from bend tests conducted on a 24 inch floating hose to be used at the Anglesey SPM, were obtained. The results are presented in Table 2.2. The $M_o xR$ values are $130kNm^2$ and $91kNm^2$ and are considered representative for 24 inch floating hose. Based on these figures a target $M_o xR$ value of $100kNm^2$ was set for the prototype equivalent of the hose model.

In order that direct comparisons could be made between the bending characteristics of the model and prototype hoses, a test rig was constructed which enables simulation of the prototype bend tests. The test rig is shown in Plate 2.1. The hose sample is laid on supports which have PTFE studs fitted to their undersides. The table surface is also made from PTFE so that friction between the table and the hose supports is minimum. A known bending moment is applied to the hose sample by suspending weights as shown. The resulting curvature is recorded by photographing the deflected shape.

The selection of a hose model which possesses the target bending stiffness properties was a difficult task. Initially various commercially-available tubings were examined but were found to be unsuitable. PVC tubing was too stiff and tended to retain curvature after bending; rubber tubing coiled excessively when laid on the water surface. It was known that Dunlop Oil and Marine had supplied the hose models used in the tests conducted by Young (1980) using a scale of 48. A sample of these was requested from Dunlop. Tests conducted to examine the bending stiffness of the sample received showed that, based on a prototype $M_o xR$ value of $100kNm^2$, the sample fitted a model scale value of between 30 and 40. The sample was therefore too stiff for use in this study and an alternative was requested from Dunlop.

The second hose sample, constructed and supplied by Dunlop Oil and Marine specially for this study, consists of a low specific gravity rubber built onto a wire helix. Table 2.3 summarises the results obtained from bend tests carried out on this sample using the test rig. The results for $M_o xR$ are very consistent for the 18 tests. The average is $5.81 \times 10^{-4} Nm^2$ and the standard deviation is 7.5% of the mean. If the mean value is compared with the prototype target value of $100kNm^2$ then the appropriate scale value is 44.4. However, a model of the Anglesey buoy had been constructed at the initial stages of this project, before the Dunlop hose model was available. The scale used for the buoy model was 43. For this reason, and because a precise bending stiffness value for the model cannot be defined, it was decided to use a scale value of 43 for the model tests. Based on this figure the prototype equivalent of the model's $M_o xR$ value is about $85kNm^2$.

The hose model sample can be tensioned prior to bending using the bend

test rig by hanging a weight over each of the side pulleys (Plate 2.1). If this weight is equal to one half the weight applied to cause bending of the sample, then the compression effect associated with the standard bend test is removed. This enables measurement of the actual bending stiffness of the hose sample, that is its EI value. A number of results from these "pure bending" tests are presented in Table 2.4. The mean value of the results yields a prototype equivalent EI value of $152kNm^2$.

2.2.2 Hose Mass and Displacement

The reserve buoyancy of a body in a fluid is the displacement of the body in the fluid minus the body's mass in air. (Displacement is the mass of the fluid displaced when the body is totally submerged in the fluid.) If the reserve buoyancy of a floating body is correctly modelled in a hydraulic model test then the hydrostatic forces acting on the body due to a fluctuating water level will be correctly modelled. If the fluctuating water level is caused by surface waves, hydrodynamic forces also act on the floating body. These latter forces depend on the body's shape and size. Significant errors occur in the forces induced on the floating body due to waves if the distortion of the geometric properties of the body is large even though the reserve buoyancy is correctly modelled.

In the case of a floating hose-string it is required therefore to model the geometry and the mass per unit length. However the rubber tubing to be used as the base for the hose model has an outside diameter which is too small to correctly model the outside diameter of the prototype 24 inch floating hose at a 43 scale. Since it was not possible to increase the outside diameter of the hose without affecting its stiffness it was decided to fit flotation units along the length with sufficient space between them to avoid affecting the hose stiffness. In this way the hose

size (in terms of volume) and, therefore, its displacement could be correctly modelled though the hose shape was distorted.

Figure 2.5 presents details of the hose prototype and model. The prototype figures were obtained from data presented for 24 inch floating hoses in Dunlop's Offshore Hose Manual (1971). The flotation units were hand-bored from 12.5mm thick sheets of closed-cell foam rubber using two cork borers fitted together. The required mass per unit length was achieved by inserting a string with lead shot attached into the bore of the hose carcass. Plate 2.2 shows the individual components of a mainline hose model.

The steel flanges used for bolting two prototype hose lengths together were modelled as single units constructed from phosphor bronze. These units were also used for attaching strain gauges in the construction of transducers for the measurement of forces and moments along the hose-string's length (Section 2.4). The weight of the units was controlled in order to maintain the correct mass per unit length.

It was not possible to ballast the model sufficiently to achieve the correct model mass for the first-off-the-buoy hose. Only the reserve buoyancy is correctly modelled for this hose. (The discrepancy in the outer diameter of the model is about 10%, or about 1.5mm.)

A total of eighteen mainline hose models and two first-off-the-buoy hose models were constructed. This allowed the capability of attaching two hose-strings to the buoy simultaneously, each hose-string having an equivalent prototype length of 107m.

2.3 SBM Model

The moored buoy component of an SPM system is referred to as the SBM (single buoy mooring). This section deals with the design of the SBM model.

A common problem which arises when modelling a particular CALM SBM in a wave basin is that the working water depth in the basin is not geometrically similar to the water depth in which the prototype SBM lies. This problem has been addressed in the course of this study and a technique has been developed for the design of a CALM SBM model which retains the important properties of the prototype while allowing some modifications to individual characteristics of the SBM. In particular, the SBM's draft and heave and surge mass to stiffness ratios are accurately reproduced while the water depth, the weight and pretension angles of the mooring chains and the mass and submerged cross-sectional area of the SBM model may be dissimilar to the prototype values. (Mooring chain pretension angle is defined as the angle the line of the chain makes with the horizontal at the fairlead.) The technique is detailed in Appendix A1 and is outlined in the following.

When the moored buoy floats in still water with draft h, vertical equilibrium requires that

$$M = \rho A h - (\sum T_v^o)/g \qquad (2.1)$$

where M = buoy mass

A = mean submerged cross-sectional area

$\sum T_v^o$ = sum of the vertical components of tension in the eight mooring chains.

(Superscript "o" refers to equilibrium conditions)

The mass to stiffness ratio for heave is given by

$$r_H = M/[\rho g A + C_H] \tag{2.2}$$

where C_H = the stiffness of eight catenary chains in heave

= the increase in the sum of the vertical components of tension in the eight chains due to unit heave displacement.

The mass to stiffness ratio for surge is

$$r_s = M/C_s \tag{2.3}$$

where C_s = stiffness of eight catenary chains in surge.

Using equations (2.1), (2.2) and (2.3) as basis, Appendix A1 shows that for an eight-chain mooring with equal pretension angles, the equations governing the selection of the buoy model mass and the weight and pretension angle of the mooring model chains are

$$M_m = C_1 - (\sum T_v{}^o)_m/g \tag{2.4}$$

$$M_m = C_2C_5(\sum T_v{}^o)_m + C_3 \tag{2.5}$$

$$M_m = C_4C_6(\sum T_v{}^o)_m \tag{2.6}$$

(Subscript "m" refers to the model.)

For a solution to exist which satisfies all three equations simultaneously, Appendix A1 shows that C_5 and C_6 must be related as follows:

$$C_6 = C_7C_5 + C_8 \tag{2.7}$$

The values of the constants C_1, C_2, C_3, C_4, C_7 and C_8 depend on the properties of the prototype SBM, the model scale S and the mean submerged cross-sectional area of the buoy model, A_m. Expressions for these constants are presented in A1.

The values of C_5 and C_6 depend on the pretension angle selected for the mooring chains of the model and on the model's water depth. They are defined by

$$C_5 = (C_H)_m/(\sum T_v^o)_m \tag{2.8}$$

and

$$C_6 = (C_s)_m/(\sum T_v^o)_m \tag{2.9}$$

The procedure for the design of the SBM model in a particular wave basin with water depth d_m is to select a pretension angle ϕ_m for the chains such that equation (2.7) is satisfied. This requires the computation of heave and surge stiffness coefficients (C_{H_m} and C_{s_m}) for the eight-chain mooring for each trial ϕ_m. (The method is outlined in Chapter 6.) Once the correct ϕ_m has been obtained, thereby giving C_5 and C_6, equations (2.4), (2.5) and (2.6) can be solved for the required values of M_m and $(\sum T_v^o)_m$. The latter then determines the weight of chain required, w_m.

It should be noted that when using a distorted model the dynamic equations of motion of the SBM are also distorted even though the natural frequencies may be modelled correctly. This means that measured motions of the model cannot be scaled directly to give the equivalent prototype motions. If, for example, the prototype buoy mass is M and the equivalent prototype value of the mass of the model is aM, and the system is lightly

damped, then the measured displacements need to be multiplied by a to give the displacements of the prototype.

The SBM model used in this study is detailed in Figure 2.6. The buoy, Figure 2.7, was constructed from PVC. The top section of the buoy is capable of rotation relative to the bottom section by virtue of a ball-and-race bearing built onto the top of the bore of the bottom section. The hose-string is connected to the buoy at the pipe shown. One end of the pipe is fixed to the top section of the buoy and the other end has a slope of 15° to the horizontal when the buoy floats in still water. The buoy is fitted with pockets top and bottom into which ballast weight in the form of thin sheets of lead can be fitted to achieve the required total weight.

The buoy models the size and general shape of the Anglesey buoy. However, the mean submerged cross-sectional area of the buoy model is about 40% greater than the corresponding value of an exact scale model of the Anglesey buoy. The buoy mass and the chain weight and pretension angle have been selected using the technique outlined above, in order that the buoy's draft and heave and surge mass to stiffness ratios are similar to those of the Anglesey buoy. This required a buoy mass which is about 40% greater and a chain weight about 50% greater than the corresponding scaled Anglesey SBM values.

Plate 2.3 shows the SBM model.

Plate 2.4 shows the hose-string attached to the SBM in still water, ready for testing.

2.4 Force and Moment Measurement

The phosphor bronze units fitted between the hose lengths of the hose-string model and between the buoy and first-off-the-buoy hose model, were used for the fixing of strain gauges to measure forces and moments. Two sets of transducers were designed and constructed.

Transducer set #1 was designed to enable the simultaneous measurement of axial load and bending moment along the string, and of torsion and bending moment along the string. The transducers are illustrated in Figure 2.8. The size of the phosphor bronze units was dictated by the hose diameter, the low weight requirements and the sizes of the strain gauges used.

It was found that this particular design of transducer had two main problems associated with it. Firstly, it was not possible to construct the phosphor bronze unit as one piece because of the large difference in bore diameter between the arms and central section. This meant that the two arms and central cylinder had to be machined separately and then welded together. This proved a difficult task and led, in some cases, to units with arms attached obliquely to the central section. Secondly, the cylinder is structurally stiff in comparison with other shapes, resulting in small strains, low sensitivity and consequently very high amplification requirements.

To avoid using a cylinder as the structural element that is strained and thereby avoid the difficulties mentioned above, the requirement that axial load and bending moment, and torsion and bending moment be measured simultaneously was omitted from the design of tansducer set #2. Tests in which torsion along the hose-string was measured using transducer set #1 showed that torsion is very low and difficult to measure accurately at a

43 scale. Consequently the requirement to measure torsion was also omitted from the design of transducer set #2.

This thesis reports only on the measurements obtained using transducer set #2. Axial load along the hose-string was measured using the type of transducer detailed in Figure 2.9(a). This consists of a strain-gauged phosphor bronze proving-ring fitted between the two arms onto which the hoses are attached. The essence of the bending moment transducers, Figure 2.9(b), is a strain-gauged deep plate which responds to bending in one plane only. Vertical bending along the hose-string is measured by positioning each transducer with the plane of its strain-gauged plate parallel with the plane of the still water surface. Horizontal bending is then measured by rotating the hose-string 90° so that the plane of the strain-gauged plate of each bending transducer is perpendicular to the water surface.

The strain gauges were fixed to the phosphor bronze units using a superglue and waterproofed by a coating of a mixture of two epoxy compounds which form a tough rubber-like covering. SHOWA N11-FA-1-120 gauges were used. (BLH-FAED-06B gauges were used for the torsion transducers in transducer set #1).

Each transducer was designed as a full Wheatstone-bridge resistive transducer to maximise sensitivity and cancel differential temperature effects on the gauges. Bridge supply voltage, signal conditioning and signal amplification was controlled by a CIL strain gauge amplifier (SGA) unit. This allows a gain of up to 10,000 and a bridge supply of up to 10 volts.

Each transducer was calibrated by applying known loads to it and recording

the corresponding voltage outputs from the strain gauge amplifier unit. The calibration data is then used as input to a computer program which computes the calibration factor from the slope of the straight line fitted to the data using a least squares method.

2.5 Buoy Motion Measurement

The six degrees of freedom of buoy motion are illustrated in Figure 2.10. There is effectively no yaw motion of the SBM in long-crested waves because of the mooring but the top section is capable of rotation about the moored hull.

The SELSPOT system, manufactured by the Selective Electronic Company (1976), is used to measure the buoy motions in waves. The essence of the system is a photodetector with four electrodes. When the infra-red light from a light-emitting diode (LED) is focussed on the detector surface, a photocurrent, divided among the four electrodes, will occur. The current is used to obtain two voltage signals linearly related to the x and y co-ordinates of the LED. By turning the LEDs on and off at a high rate and in such a way that only one LED is on at a time, the detector can be used to measure the position of several LEDs simultaneously.

In order to measure the six buoy motions, two cameras and four LEDs positioned on the top surface of the buoy are required. For this system a total of sixteen voltages are recorded at any instant in time.

The system is calibrated by relating the LED voltages recorded at still conditions to the geometric positions of the camera lenses relative to the LED positions. The calibration values are applied to the voltages recorded from each LED at a particular time during a test to obtain the position of the LEDs at that time. The buoy motions are calculated from

the LED positions using three-dimensional geometry and vector analysis. The theoretical basis for the calibration of the SELSPOT system and for the calculation of the buoy motions is presented in Appendix A2.

2.6 Wave Generation and Wave Measurement

The floating hose model tests were conducted in both regular and irregular waves. For the former, the sinewave signal to the wave-making paddles was controlled using a signal generator.

The irregular (non-sinusoidal) voltage signal controlling the generation of the irregular waves was defined using a suite of computer programs available on a BBC Microcomputer with second processor. The programs can be used to generate waves with any wave spectrum in the wave basin. The voltage signal is defined by digitally filtering white noise, the filter shape being defined by the required wave spectrum and the transfer function between voltage to the paddles and wave height in the basin. This method of wave signal generation follows that described by Funke (1974).

The waves generated in the basin were measured using a Churchill wave probe and associated wave monitor module. The probe consists of a pair of stainless steel wires, 1.5mm in diameter and spaced 12.5mm apart. It operates on the principle of measuring the current flowing between the wires when the wires are immersed in water. This current is proportional to the depth of immersion. The current produced is sensed by an electronic circuit which produces an output voltage proportional to the instantaneous depth of immersion. The output voltage may be calibrated in terms of wave height by varying the immersion of the probe in still water by a measured amount and noting the change in output signal.

2.7 Data Recording

The hydraulic model tests conducted on the floating hose-string attached to the CALM buoy required up to 27 voltage signals to be recorded: 1 wave probe voltage signal, 16 SELSPOT LED voltage signals and 10 force/moment transducer voltage signals. These were recorded on an EMI SE3000 magnetic tape recording system. The SE3000 comprises 13 FM (frequency modulation) channels, 1 AM (amplitude modulation) channel and 1 voice channel.

The 16 voltage signals from the SELSPOT motion-monitoring system were multiplexed using a base ten data acquisition system. This system samples the 16 signals, converts to digital form and outputs the multiplexed signal as a pulse coded modulated (PCM) signal. The PCM signal is stored on the AM channel of the SE3000.

Eleven of the 13 FM channels were used to record the wave probe and force/moment transducer signals. The voice channel was used to record test titles and descriptions for test identification on playback.

Two 6-channel Gould chart recorders were used to obtain hard-copy records of the voltage signals during the tests. These records were not used in any subsequent analysis procedures other than as checks on the computer-processed magnetic tape recordings.

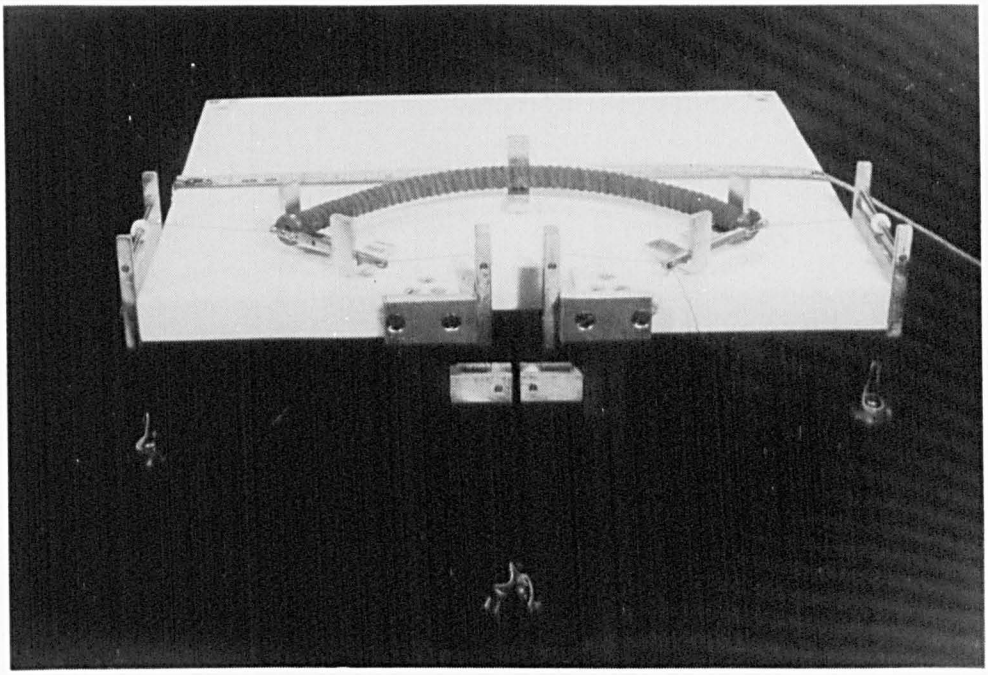

Plate 2.1 Test Rig for Bending Stiffness Measurement

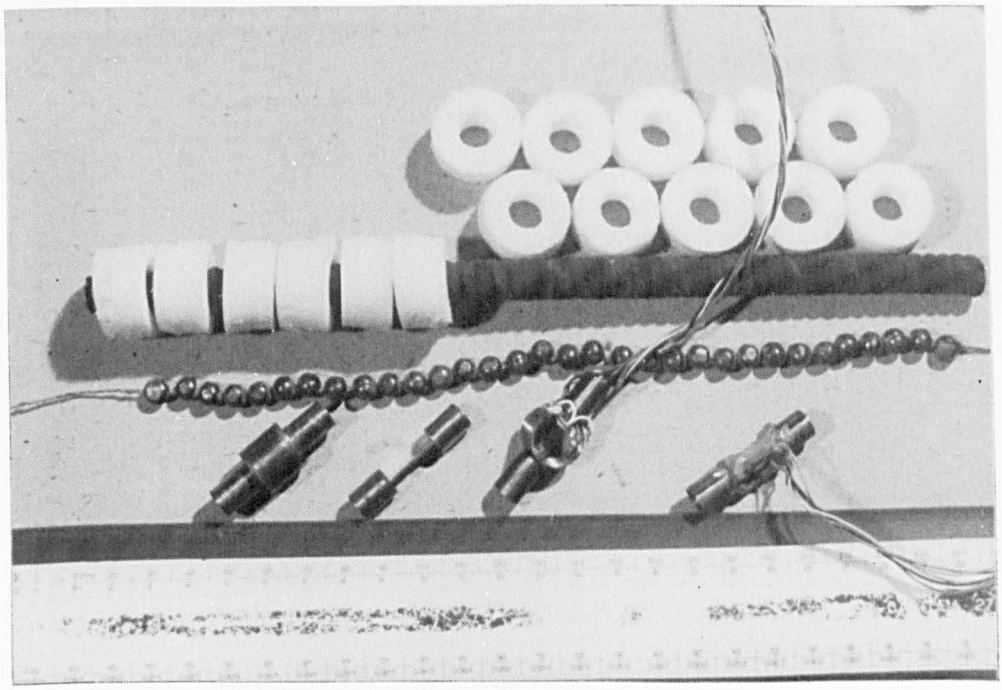

Plate 2.2 Components of Hose Model

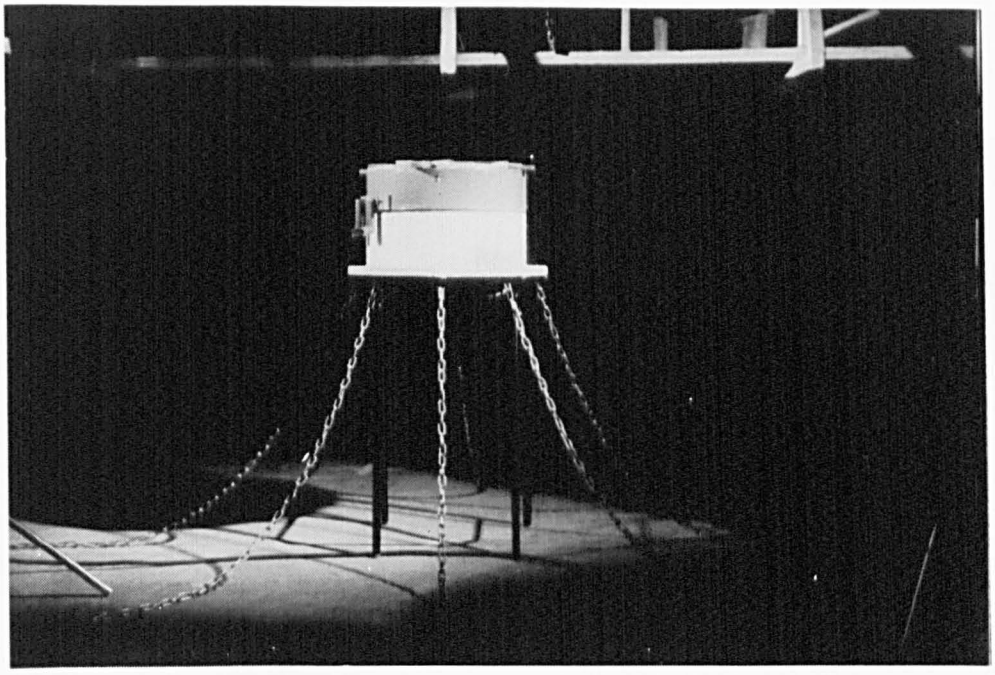

Plate 2.3 The SBM Model

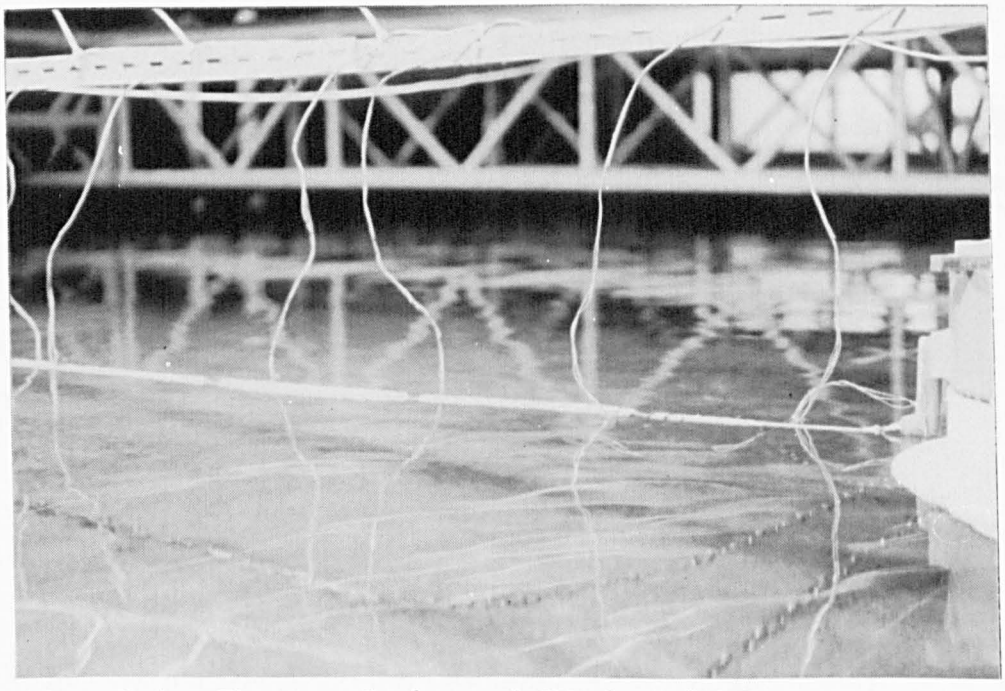

Plate 2.4 The Hose-String and SBM in Still Water

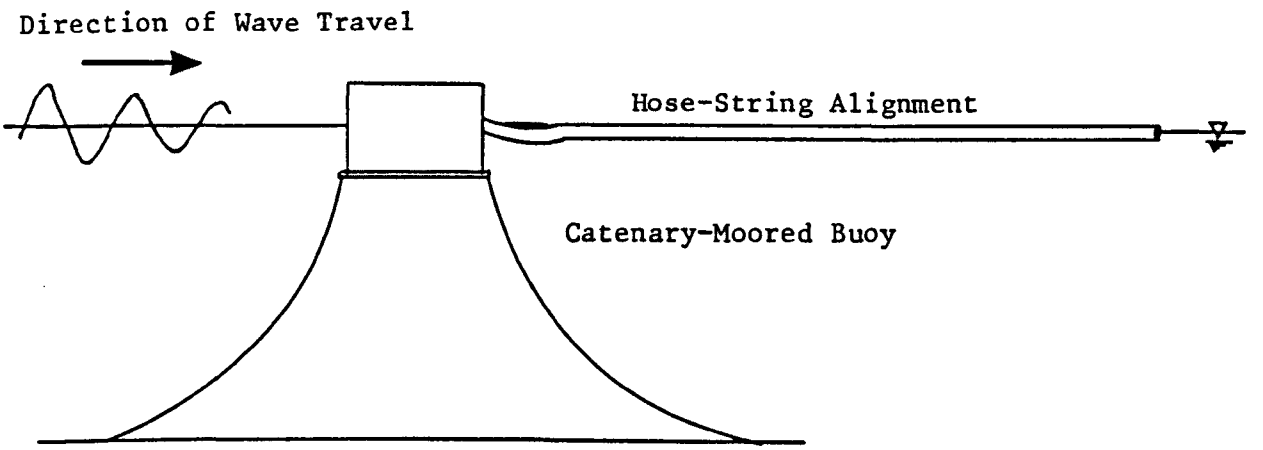

Figure 2.1 Test Condition

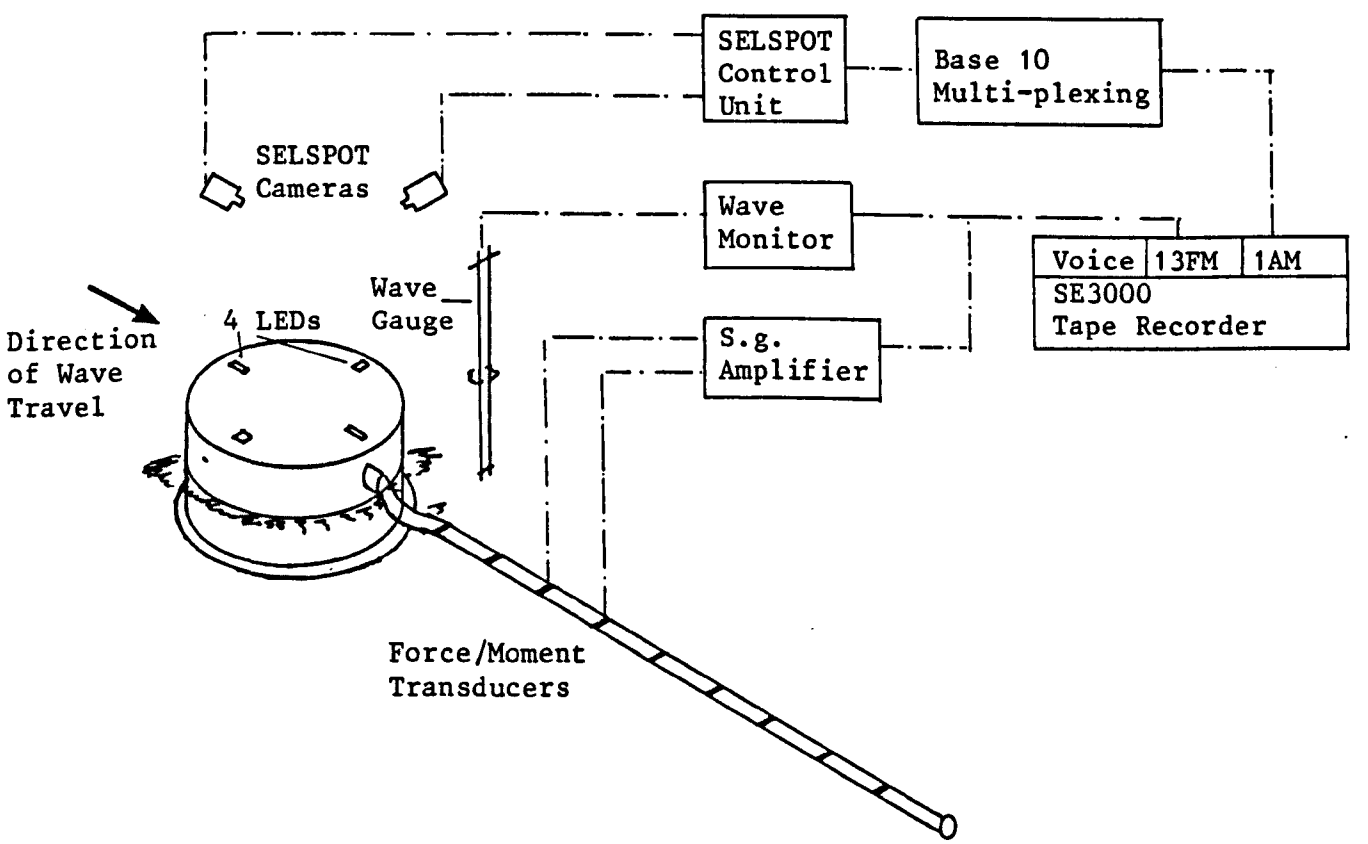

Figure 2.2 Data Acquisition From Model Tests

Model scale $S = l_p/l_m$ = length in prototype/length in model			
Property	(units)	multiplier =	$\frac{\text{value in prototype}}{\text{value in model}}$
time	(secs)		$S^{1/2}$
frequency	(Hz)		$S^{-1/2}$
velocity	(m/s)		$S^{1/2}$
acceleration	(m/s^2)		1.0
mass	(kg)		S^3
mass per unit length	(kg/m)		S^2
force	(N)		S^3
moment	(Nm)		S^4
bending stiffness	(Nm^2)		S^5

Table 2.1

List of Froude multipliers for linear scale S
e.g. time in prototype/time in model = $S^{1/2}$

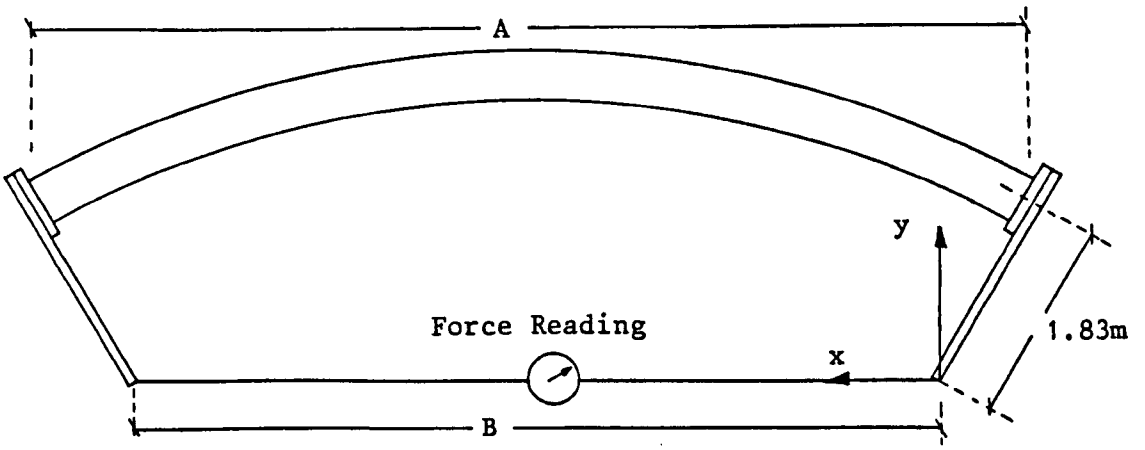

Figure 2.4 Schematic of manufacturer's bend test

Test #1

Applied Load (kg) 1400
Applied Moment (kNm) 25.1

Hose Curvature Data:

A = 9.81m B = 7.93m

x (m)	y (m)
2.1	2.44
2.4	2.53
2.7	2.6
3.0	2.67
3.3	2.7
3.6	2.71
3.9	2.71
4.2	2.7
4.5	2.67
4.8	2.6
5.1	2.54
5.4	2.48

Hose radius of curvature (m) 5.2

$M_oR = 130 kNm^2$

Test #2

Applied Load (kg) 1385
Applied Moment (kNm) 24.9

Hose Curvature Data:

A = 9.37m B = 7.05m

x (m)	y (m)
1.5	2.6
1.8	2.72
2.1	2.87
2.4	2.96
2.7	3.02
3.0	3.05
3.3	3.06
3.6	3.04
3.9	2.99
4.2	2.93
4.5	2.84
4.8	2.73
5.1	2.63

Hose radius of curvature (m) 3.66

$M_oR = 91 kNm^2$

Table 2.2 . Bend test results for 24 inch mainline floating hose

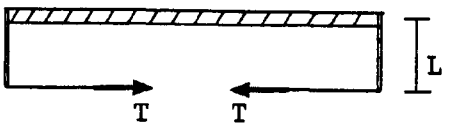

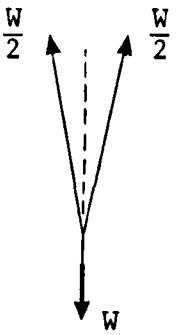

$M_oR = T.L.R$

$L = 50mm; \quad T = W/2$

$M_oR(Nm^2) = WR \times 245.25 \times 10^{-9}$, W in grams, R in mm

Test N°	Suspended Mass W (gr)	Measured Radius of Curvature R (mm)	$M_oR \times 10^4$ (Nm^2)
1.1	10	260	6.4
1.2	10	226	5.5
1.3	10	216	5.3
7.1	10	238	5.8
7.2	10	215	5.3
7.3	10	215	5.3
2.1	20	144	7.1
2.2	20	111	5.4
2.3	20	122	6.0
8.1	20	122	6.0
8.2	20	111	5.4
8.3	20	122	6.0
3.1	30	83	6.1
3.2	30	83	6.1
3.3	30	83	6.1
9.1	30	79	5.8
9.2	30	78	5.7
9.3	30	74	5.4
Total 18			Mean 5.81×10^{-4} SD 7.5% of mean

Table 2.3

Results of bend tests on hose model sample #2
(Tests simulate prototype bend tests)

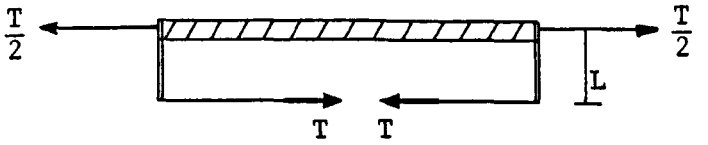

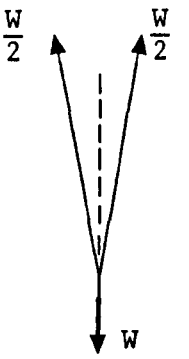

$M_oR = T.L.R$

$L = 50mm;\ T = W/2$

$M_oR(Nm^2) = WR \times 245.25 \times 10^{-9}$, W in grams, R in mm

Test N°	Suspended Mass W (gr)	Measured Radius of Curvature R (mm)	$M_oR \times 10^4$ (Nm^2)
5.1	20	226	11.1
5.2	20	181	8.9
5.3	20	204	10.0
5.4	20	183	9.0
6.1	30	158	11.6
6.2	30	158	11.6
Total 6			Mean 10.4×10^{-4} SD 11% of mean

Table 2.4

Results of bend tests on hose model sample #2 with compression component removed

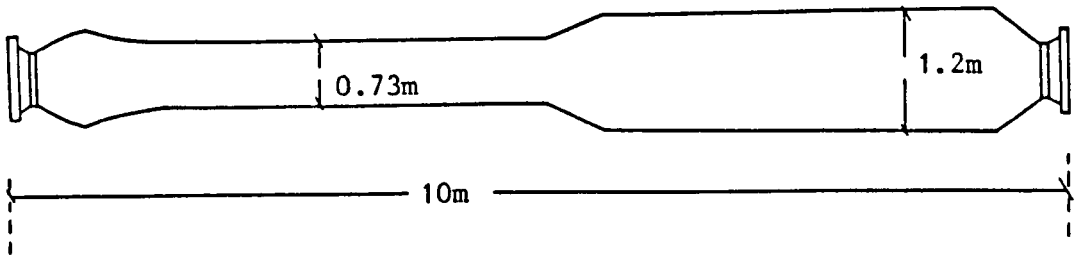

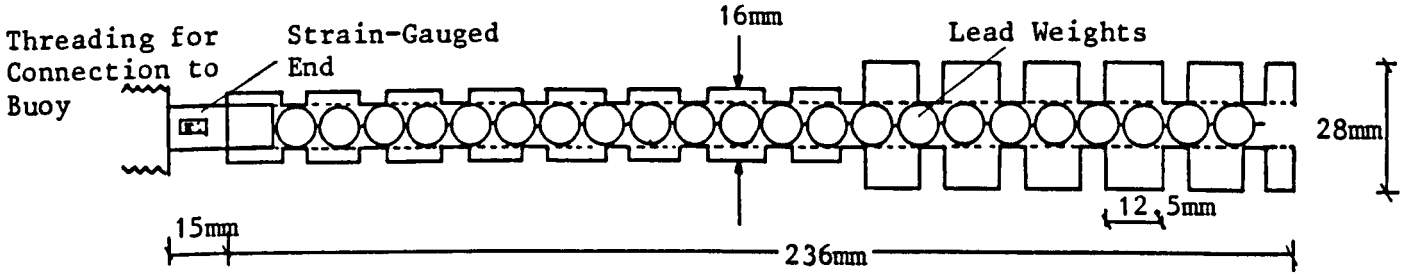

Prototype		Model	
Displacement in sea-water	7800kg	Displacement in water	74.5gr
Mass in air full of sea-water	7300kg	Mass in air full of water	68 gr
Reserve buoyancy	500kg	Reserve buoyancy	6.5gr

(a) First-off-the-buoy hose

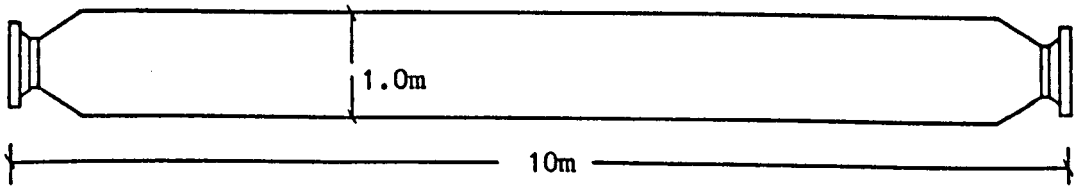

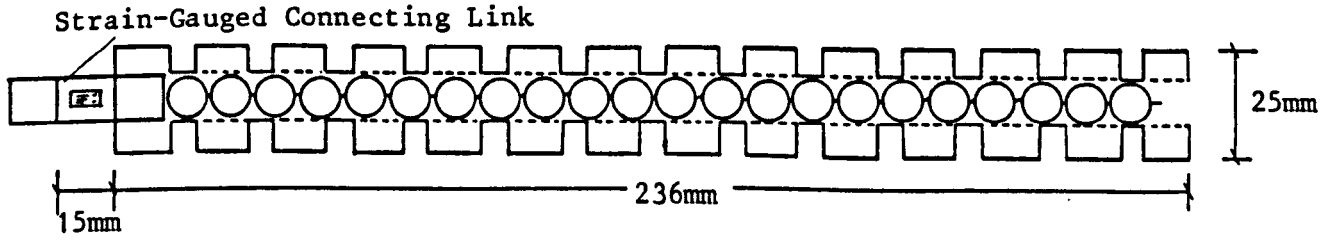

Prototype		Model	
Displacement in sea-water	7000kg	Displacement in water	87.5gr
Mass in air full of sea-water	5600kg	Mass in air full of water	70 gr
Reserve buoyancy	1400kg	Reserve buoyancy	17.5gr

(b) Mainline hose

Figure 2.5 Comparison of properties of prototype and model hoses

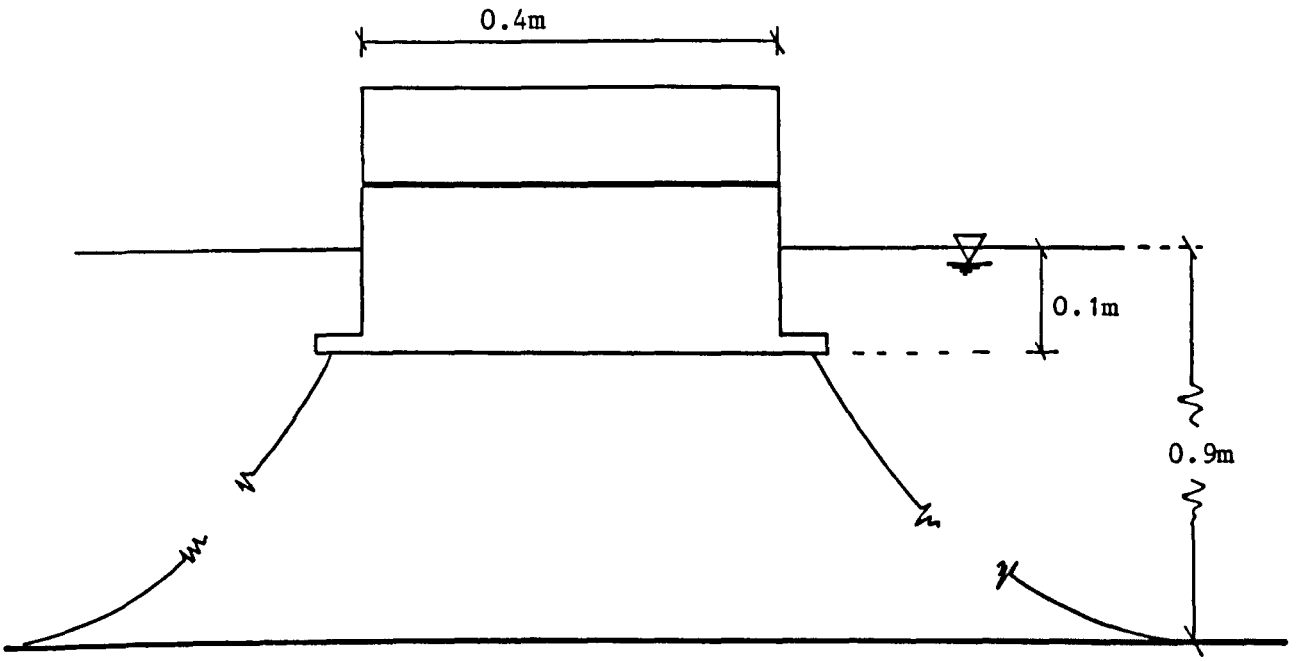

Buoy mass = 10.34kg;
Met.ht. = 0.035m; roll radius of gyration = 0.11m
8 chains: pret.angle = 64°; wt.in water = 2.5N/m

Figure 2.6 SBM model (scale 1:75)

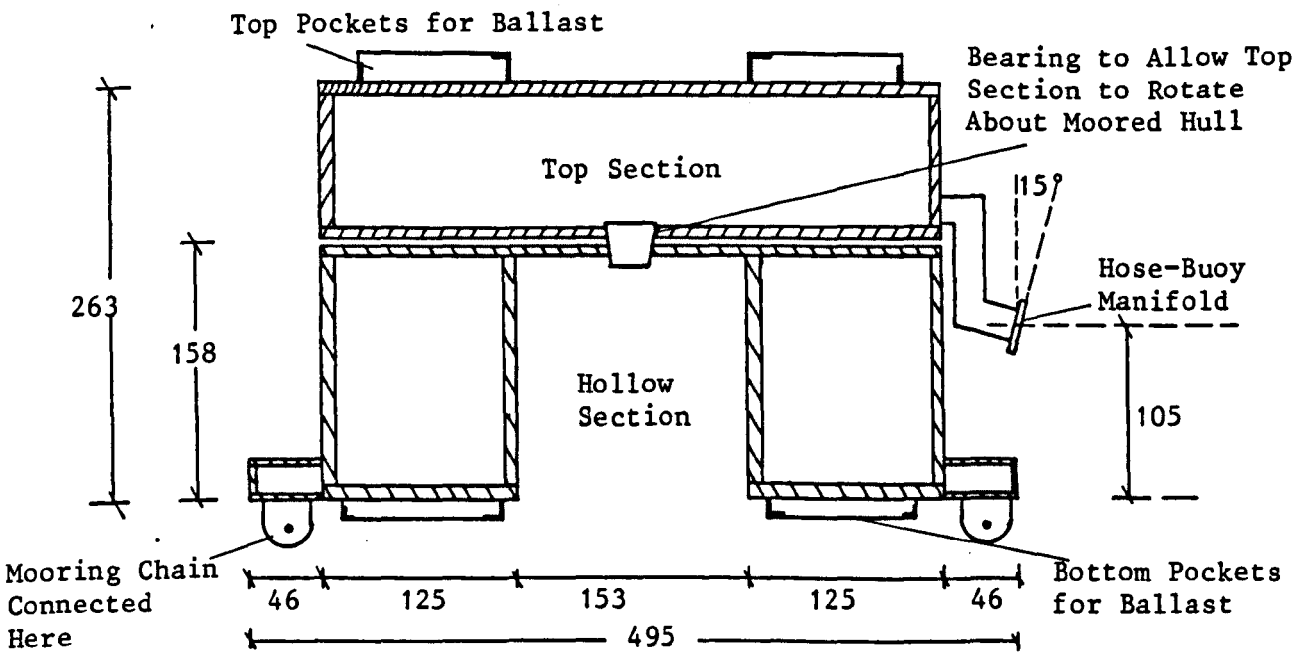

Material: PVC
Dimensions in mm
Scale 1:50

Figure 2.7 Section through buoy model

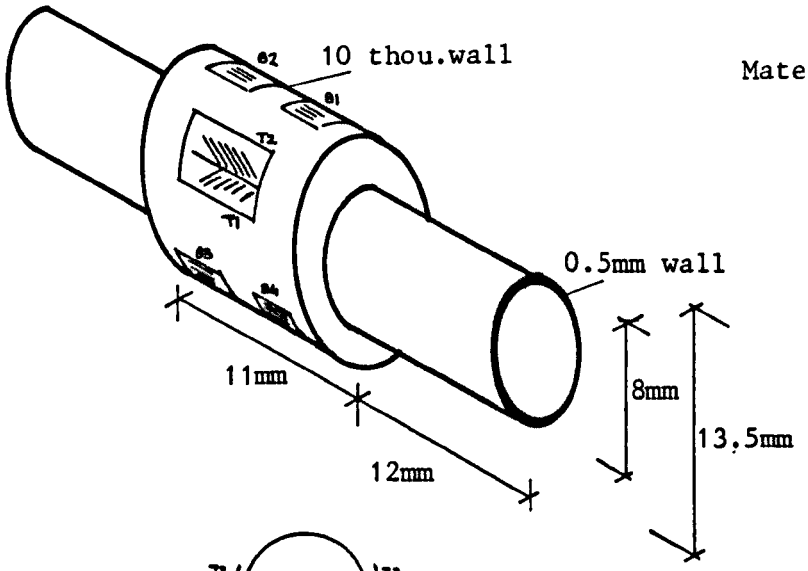

Positioning of Torsion Gauges

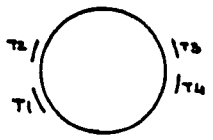

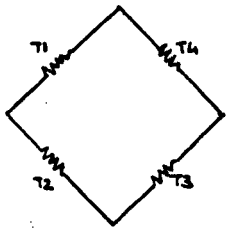

W.b. arrangement: Torsion

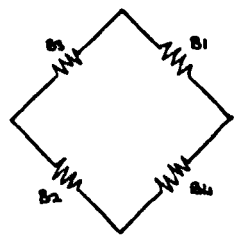

W.b. arrangement: Bending

(a) Bending and Torsion Transducer

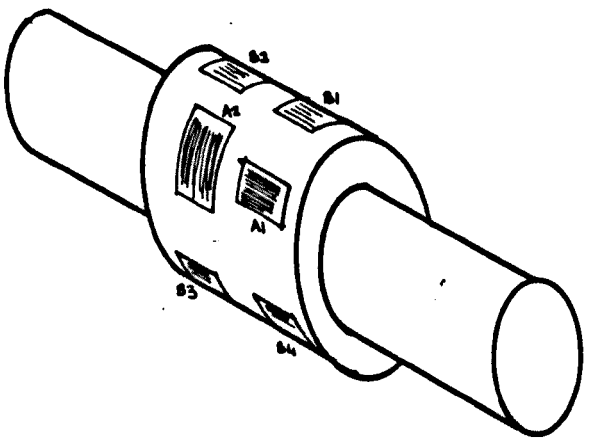

Positioning of Axial Load Gauges

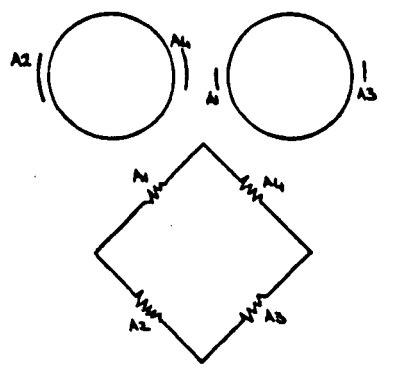

W.b. arrangement: Axial Load

(b) Bending and Axial Load Transducer

Figure 2.8 Transducer set #1

Material: Phosphor Bronze

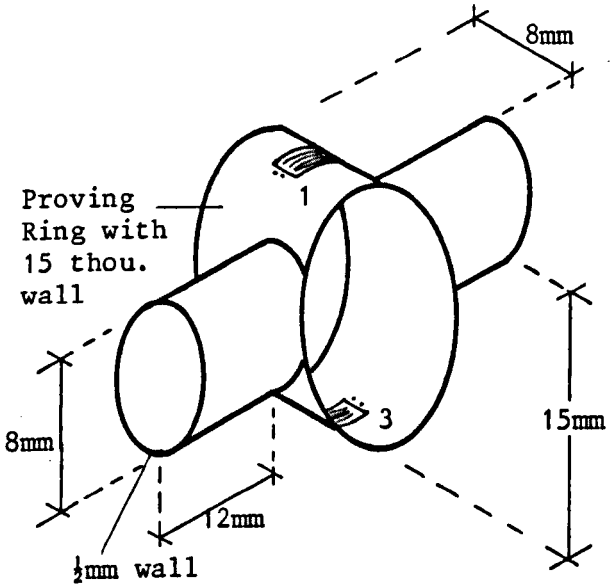

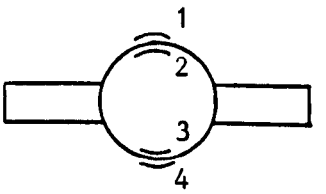

Plan Showing s.g. positions

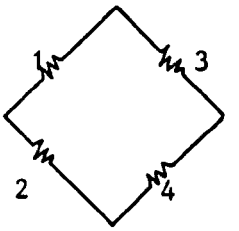

W.b. arrangement

(a) Axial load transducer: strain gauges on phosphor bronze proving ring

Material: Phosphor Bronze

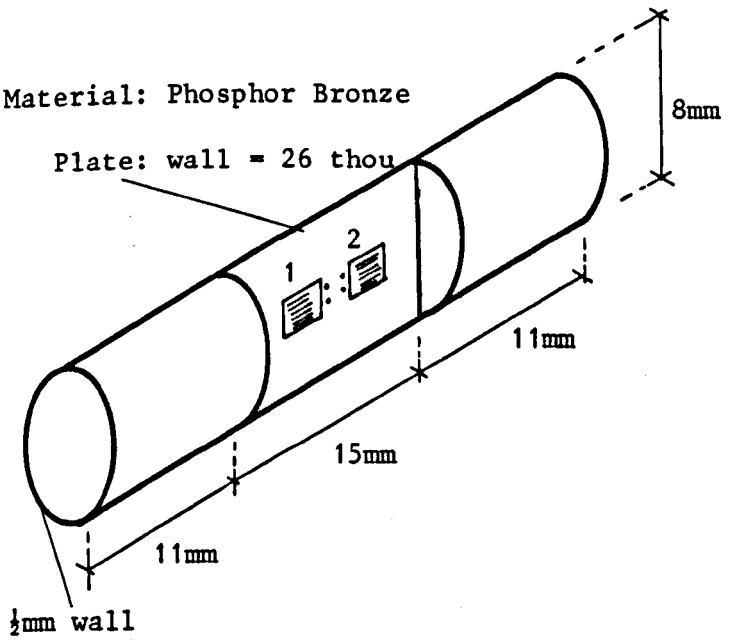

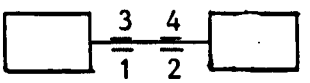

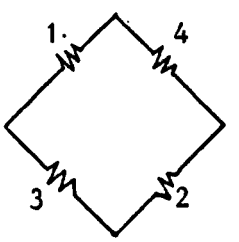

W.b. arrangement

(b) Bending moment transducer: strain gauges on deep plate

Figure 2.9 Transducer set #2

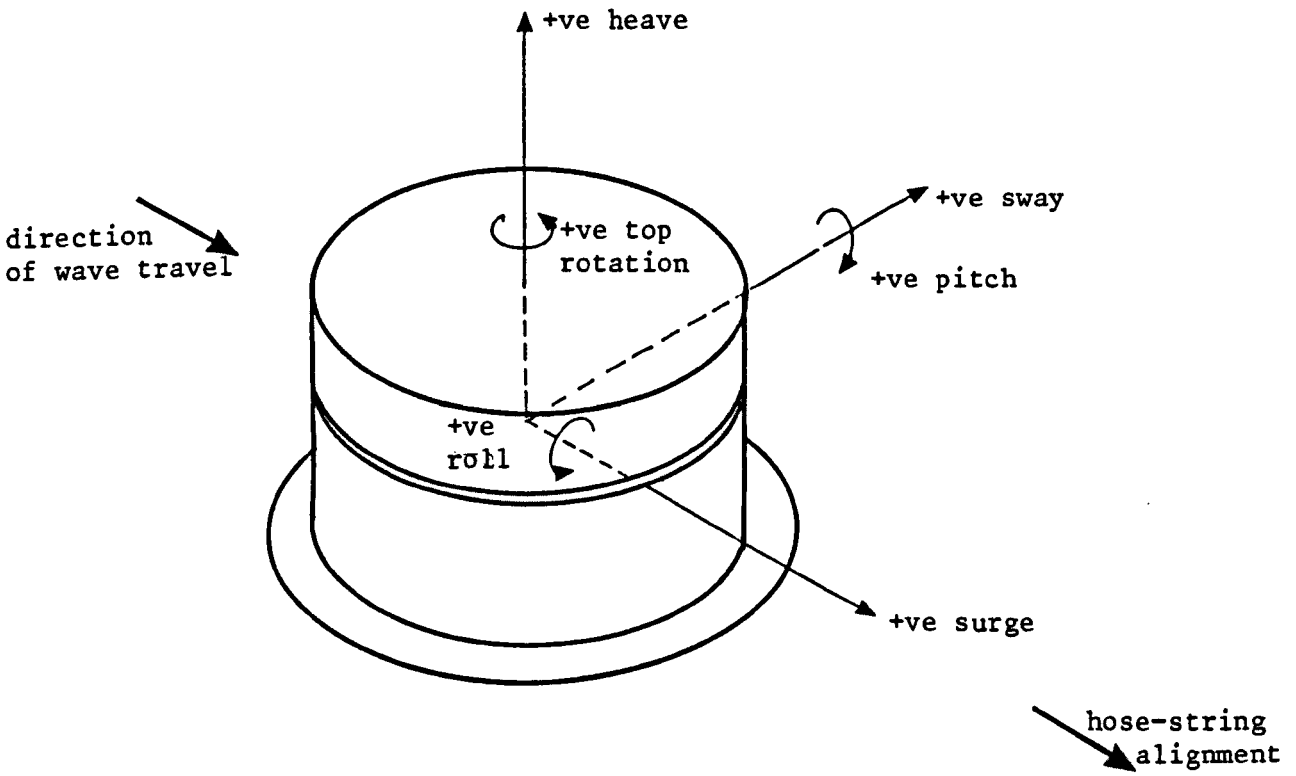

Figure 2.10 Six degrees of freedom of buoy motion

3. EXPERIMENTAL DATA PROCESSING AND ANALYSIS

3.1 Introduction

This chapter describes the methods used for the processing and analysis of the experimental data.

The procedure for processing the 27 voltage records of each floating hose model test using the ECLIPSE minicomputer to produce the corresponding 17 time series and the system for the transfer of these series to the GEC minicomputer for analysis are first described.

The time series are analysed using digital spectral analysis. Section 3.3 presents the background theory for the auto-spectral analysis program ANAL1 and the cross-spectral analysis program ANALX. The analyses are summarised by the flowcharts presented for each computer program.

Besides the model tests conducted on floating hoses attached to a CALM buoy, ancillary model tests were conducted to investigate certain hydrodynamic characteristics of the SBM. These are referred to as the SBM free- and forced-motion tests. Sections 3.4 and 3.5 present the theoretical basis for the analysis of the results obtained from these tests.

3.2 Data Processing

The hardware used for processing the experimental data is illustrated schematically in Figure 3.1. The system is based on the use of two minicomputers controlling two separate stages of the process: the Data General ECLIPSE minicomputer is used for data reduction and the GEC 4180 multi-user minicomputer is used for data analysis. Data is transferred between the two machines via a BBC microcomputer.

3.2.1 Data Reduction

Data reduction refers to the sampling of the 27 voltage records stored on magnetic tape and the processing of the sampled data to produce 17 time series. The procedure is based on the use of three computer programs operating on the ECLIPSE minicomputer, namely HOSES, SPOCAL (SELSPOT calibration) and GETHIST (get time histories). These programs are edited versions of programs which were available on the ECLIPSE prior to this study. For this reason they are not presented in detail here.

Figure 3.2 outlines the use of the computer programs in the data reduction procedure. Program HOSES is the data acquisition program and controls the sampling of the 27 voltage records via the analogue-digital convertor. The sampling rate is 10Hz and 1k samples are acquired from each record. The 27 by 1024 voltage samples are stored in the datafile BUOYDATAS.

Before any analysis of the data stored in BUOYDATAS can take place the two-camera/four LED SELSPOT system must be calibrated using program SPOCAL. This program samples the LED voltage signals recorded at still conditions and relates these voltages to the geometric positions of the camera lenses relative to the LED positions to produce the camera calibration factors. The SELSPOT calibration factors are stored in the datafile CALSPOT (calibration factors for SELSPOT). The theoretical basis for the calibration of the SELSPOT system is presented in Appendix A2.

Since the program SPOCAL was not written for this study its validity was checked by carrying out the following exercise. Using a hypothetical two-camera/four LED arrangement and hypothetical camera calibration factors, the 16 LED voltages corresponding to the buoy in its static (calibration) position were hand-calculated from the theory presented in Appendix A2.

Those voltages were then used as input to SPOCAL and the camera calibration factors computed. The values obtained were the same as the hypothetical calibration factors, thereby confirming the validity of the program SPOCAL.

The program GETHIST is used to analyse the data stored in BUOYDATAS to produce the time series of buoy motions in 6 degrees of freedom, the wave elevation time series and the 10 force/moment time series. The camera calibration factors are read from CALSPOT and the calibration factors for the wave probe and force/moment transducers are read from CALFACTOR. The reduced data is stored in four datafiles each containing 17 by 256 values.

The program SEPARATE separates the data stored in the four datafiles created by GETHIST into 17 individual datafiles, F1, F2, ..., F17, corresponding to the 17 time series. Each file contains 1024 values.

The validity of GETHIST and SEPARATE was checked as follows. Hypothetical CALSPOT and CALFACTOR files were created. The theoretical basis for the calculation of the buoy motions from the LED voltages recorded during a test is presented in Appendix A2. This theory was used to hand-calculate the 16 LED voltages corresponding to a hypothetical displacement of the buoy from its static position. The voltages corresponding to hypothetical variations in the wave and force records were calculated using the hypothetical CALFACTOR file. The hypothetical BUOYDATAS was created by combining the LED voltages and wave and force voltages. The 17 time series computed by GETHIST and SEPARATE, with the hypothetical BUOYDATAS, CALSPOT and CALFACTOR files as input, were the same as the time series corresponding to the hypothetical buoy displacement and variations in the wave and force/moment records. The validity of GETHIST and SEPARATE was

thereby confirmed.

3.2.2 Data Transfer

The transfer of the files F1, F2, ..., F17 to the GEC 4180 for analysis is achieved by first transferring the data to floppy disk and then transferring from floppy disk to the GEC (Figure 3.1).

The BBC UNITERM package (Byrne (1985)) was used for the transfer of files between the ECLIPSE and BBC floppy disks, the two computers communicating via the RS232 interface. UNITERM is primarily used for terminal emulation but it incorporates a file transfer protocol enabling file transfer.

A more powerful software package than UNITERM for file transfer between two computers, normally between a microcomputer and a minicomputer or mainframe, is the KERMIT system. This is an error-protected file transfer system designed by Columbia University Centre for Computing Activities (CUCCA), USA, to work over RS232 interfaces. KERMIT is used here for file transfer between BBC floppy disk and the GEC 4180 minicomputer. The system requires a BBC KERMIT 'chip in the BBC, a KERMIT program in the GEC and an RS232 interface cable linking the two machines. Lancaster University (1985) documents the use of KERMIT with the BBC while Loach (1985) documents its use with the GEC 4000 series of minicomputers. (KERMIT could not be used for file transfer between the ECLIPSE and BBC because no KERMIT program was available on the ECLIPSE.)

3.2.3 Data Analysis

The GEC 4180 minicomputer is a more powerful machine than the ECLIPSE. It has a number of software packages available to it and a range of peripheral devices which include a high quality plotter and a variety of terminal types. The GEC at Heriot-Watt is part of a network of computers

which can be accessed from a large number of locations within the university and elsewhere. For these reasons the GEC was preferred to the ECLIPSE for the data analysis.

All programs written on the GEC for this study use FORTRAN 77. Extensive use is made of the GINO library package of graphics subroutines available on the GEC. Plotfiles created using GINO may be displayed on graphics terminals prior to plotting. The plotter is a BENSON 1302 drum plotter with a resolution of 0.05mm.

3.3 Spectral Analysis

Spectral analysis is a powerful mathematical tool developed for the study of the fundamental nature of signals and systems which has many applications in engineering problems. It is especially useful in environmental problems where the excitation forces are often random.

Many textbooks deal with the theory of spectral analysis, some of which are listed in the textbook list accompanying this thesis. The summary presented in what follows forms the basis of the two spectral analysis programs ANAL1 and ANALX developed for the analysis of the experimental data time series.

3.3.1 Auto-Spectral Analysis

3.3.1.1 Fourier Representation of a Periodic Function

If x(t) is a periodic function of time t with period T, then it can always be expressed as an infinite trigonometric series, a Fourier series, of the form

$$x(t) = \tfrac{1}{2}a_o + 2 \sum_{k=1}^{\infty} a_k \cos 2\pi kt/T + b_k \sin 2\pi kt/T \qquad (3.1)$$

where a_o, a_k and b_k are Fourier coefficients given by

$$a_o = 2/T \int_o^T x(t)dt \qquad (3.2)$$

$$a_k = 1/T \int_o^T x(t)\cos 2\pi kt/T \, dt \qquad (3.3)$$

$$b_k = 1/T \int_o^T x(t)\sin 2\pi kt/T \, dt \qquad (3.4)$$

The Fourier series replaces the function x(t) by the sum of its mean value $\frac{1}{2}a_o$ and an infinite number of harmonics whose frequencies are

$$f_k = k/T \qquad k = 1,2,3,.... \qquad (3.5)$$

The amplitude of the k^{th} harmonic is

$$A_k = 2(a_k^2 + b_k^2)^{\frac{1}{2}} \qquad (3.6)$$

The variance of the k^{th} harmonic, which describes its energy content, is

$$V_k = \tfrac{1}{2}A_k^2 \qquad (3.7)$$

The quantity $S_k = \frac{1}{2}A_k^2 T$ is termed the auto-spectral density at frequency f_k. A plot of S_k against frequency is termed the auto-spectrum of x(t), or, simply, the spectrum of x(t).

3.3.1.2 The Discrete Fourier Transform (DFT)

Using complex notation equations (3.3) and (3.4) can be combined into a single equation by defining

$$X_k = a_k - ib_k \qquad (3.8)$$

Substituting for a_k and b_k gives the Finite Fourier Transform

$$X_k(k\geq 1) = 1/T \int_0^T x(t)\exp(-i2\pi kt/T)dt \qquad (3.9)$$

When analysing a waveform using digital computer the continuous record x(t) is not known. The digitised waveform consists of N samples equally spaced Δt seconds apart producing a discrete series x_r, r = 0,1,..,(N-1). The total time length of the sample is $N\Delta t$ seconds. The Finite Fourier Transform is then approximated by the Discrete Fourier Transform (DFT) given by

$$X_k = 1/N \sum_{r=0}^{N-1} x_r \exp(-i2\pi kr/N) \qquad (3.10)$$

It may be shown that $|X_{N+1}| = |X_1|$ and $|X_{-1}| = |X_1|$. That is, a graph of $|X_k|$ against frequency f_k repeats itself periodically and is symmetrical about the zero frequency position.

If the DFT of the series x_r is computed directly from equation (3.10) N multiplications of the form $x_r\exp(-i2\pi kr/N)$ would have to be made for each of the N values of X_k. The total work involved in calculating the full sequence of X_k would require N^2 multiplications. The Fast Fourier Transform (FFT) algorithm is a technique for computing the X_k sequence which reduces the work involved to a number of operations of the order of $N\log_2 N$. This represents an extremely large reduction in computer processing time. The FFT algorithm used in the analysis programs developed for this study has been taken from Newland (1984) which follows the method first described by Cooley and Tukey (1965). To use the FFT the series x_r must consist of N values where N is a positive integer power of 2, i.e. $N = 2^M$ where M is a positive integer.

3.3.1.3 Computing The Auto-Spectrum From the DFT

The spectral ordinates of the continuous one-sided spectrum of the discrete series x_r, in terms of linear frequency, are given by

$$S_{xx}(f_k = k/T) = 2TX_k^* X_k \qquad k = 0,1,\ldots,N/2 \qquad (3.11)$$

where X_k is the DFT of x_r and X_k^* is the complex conjugate of X_k. Equation (3.11) forms the basis of all contemporary digital spectral analysis.

There are four important considerations to be taken into account when using equation (3.11) to calculate the spectrum from a sample record of a process:

(1) If there are frequencies greater than $1/2\Delta t$ Hz present in the signal these are interpreted by the analysis as having a frequency less than $1/2\Delta t$ Hz because of the periodicity of the DFT. The result is a distortion of the spectrum known as "aliasing". The frequency $1/2\Delta t$ Hz is termed the Nyquist frequency.

Aliasing is avoided by passing the signal through a low-pass filter with a cut-off frequency of $1/2\Delta t$ Hz prior to analysis.

(2) If the mean of the series x_r is not zero the spectral ordinate becomes excessively large at zero frequency. For this reason the data must be de-meaned prior to spectral analysis. Furthermore, the spectrum is falsely distorted in the region of zero frequency if there is a slow drift on the sample time series, due perhaps to instrumentation drift. It is common practice therefore to remove this slow drift by de-trending the data prior to analysis.

The method used here to de-trend the data is to calculate the average of the first one third of the record and the average of the last one third, assume that the average varies linearly from one end of the record to the other and to normalise the raw data accordingly to remove this linearly-varying mean.

(3) If the measured waveform is not exactly periodic then the prime requirement of the Fourier transform is violated and this leads to possibly the greatest source of error in any digitally computed spectrum. The measured record is equivalent to multiplying the periodic function by a rectangular window function. The Fourier transform of the product is equal to the convolution of the Fourier transform of the periodic function with the Fourier transform of the window function. This leads to the problem known as "leakage": the true spectral estimate at a particular frequency is modified by power leaking from other frequency components. Leakage can erroneously introduce harmonic components which did not exist in the original signal.

Leakage can be significantly reduced by windowing the sampled time history record before analysis, i.e. by replacing the inherent rectangular window with a more periodic window function. One commonly used window shape is the cosine taper illustrated in Figure 3.3.

To correct for the loss of amplitude caused by applying the window function, the resulting spectral ordinates must be divided by

$$W = 1/N \sum_{r=0}^{N-1} \omega_r^2 \qquad (3.12)$$

where ω_r is the weighting applied to the data point x_r.

(4) If a measured sample is only one of an infinite number of possible samples from a random process, the spectrum computed using equation (3.11) will be statistically inaccurate. To improve the statistical accuracy the spectral estimates must be averaged or smoothed. There are a number of different smoothing techniques, the choice of any one being dependent on the process under study as well as on the maximum length of record that can be analysed.

The method used here is to smooth the spectral estimates in the frequency domain using the triangular weighting function illustrated in Figure 3.4. According to this smoothing process the spectral estimate at frequency f_i is replaced by the averaged estimate $\bar{S}_{xx}(f_i)$ given by

$$\bar{S}_{xx}(f_i) = 1/P \sum_{j=-p}^{j=p} S_{xx}(f_{i+j})[1.0 - |j|/P] \qquad (3.13)$$

where (2p+1) is the total number of estimates in the window.

The steps involved in the computation of the spectrum of a recorded measurement may now be summarised as follows.

(1) The signal is passed through a low-pass filter with cut-off frequency $1/2\Delta t$ Hz, where $1/\Delta t$ Hz is the sampling frequency. If N samples are acquired then the sample series is x_r, $r = 0,1,\ldots,(N-1)$ and the time length is $T = N\Delta t$ seconds.

(2) De-mean and de-trend the time series x_r.

(3) Apply the cosine taper to x_r (Figure 3.3).

(4) Compute the DFT X_k using the FFT algorithm to obtain

$$X_k = a_k - ib_k \qquad k = 0,1,....,N-1$$

corresponding to frequencies $f_k = k/T$ Hz.

(5) Estimates of the one-sided spectrum are obtained from

$$S_{xx_k} = 2TX_k^* X_k$$

corresponding to frequencies $f_k = 0,1/T,....,1/2\Delta t$ Hz.

(6) Correct the spectral estimates for the loss of amplitude caused by the cosine taper, i.e.

$$S_{xx_k} = S_{xx_k}/W$$

where W is given by equation (3.12).

(7) Smooth the estimates using the triangular weighting function defined by Figure 3.4 and equation (3.13) to give $\bar{S}_{xx_k}$, $k = 0,1,....,N/2$ corresponding with frequencies $f_k = 0,1/T,....,1/2\Delta t$ Hz.

The auto-spectral analysis program ANAL1 follows the steps listed above. The flowchart is shown in Figure 3.5 and a typical output is presented in Figure 3.6.

3.3.2 Cross-Spectral Analysis

The auto-spectrum is used to establish the characteristic frequency signature and amplitude levels of a random process, yielding information about the physical process being measured. In this study it is also required to establish the frequency dependence between a measured response y(t) of a system, e.g. SBM heave, and the measured input x(t), e.g. wave

height. This requires computing the cross-spectrum between the response and the input.

In terms of the DFTs X_k and Y_k of the time series x_r and y_r, the cross-spectral estimate at frequency f_k is given by

$$S_{xy_k} = 2TX_k^* Y_k \tag{3.14}$$

S_{xy_k} is complex and may be represented by

$$S_{xy_k} = C_{xy_k} - iQ_{xy_k} \tag{3.15}$$

where C_{xy_k} is termed the co-spectral estimate at f_k and Q_{xy_k} the quad-spectral estimate.

The cross-spectrum is of limited use but is an essential step in the calculation of more powerful functions such as the coherence function and the frequency response function.

The coherence function is defined by

$$\gamma_{xy_k}^2 = |\overline{S_{xy_k}}|^2 / \overline{S_{xx_k}}\ \overline{S_{yy_k}} \tag{3.16}$$

It is possible to show that $\gamma_{xy_k}^2$ is always between zero and unity. For statistical accuracy the coherence function must be calculated from the smoothed cross-spectral and auto-spectral estimates. If unsmoothed estimates are used a meaningless result of unity is obtained for γ_{xy}^2 at all frequencies.

The usefulness of the coherence function is that it expresses the fraction of the total power in y(t) which is linearly related to x(t). A coherence value of less than unity implies that the system relating x(t) and y(t) is

non-linear, and/or the signals have been contaminated by noise, and/or the output y(t) is due to other inputs besides x(t).

The frequency response function between the measured response y(t) and measured input x(t) at frequency f_k is given by

$$H_{xy_k} = \overline{S_{xy_k}}/\overline{S_{xx_k}} \tag{3.17}$$

The frequency response function, expressed in this way, may be used to obtain the amplitude ratio and phase difference between the input and the response. If, for example, the input at frequency f is $A_x \sin 2\pi ft$ and the response is $A_y \sin(2\pi ft + \phi_{xy})$ then

$$|H_{xy}| = A_y/A_x \tag{3.18}$$

and

$$\tan^{-1} Q_{xy}/C_{xy} = \phi_{xy} \tag{3.19}$$

where Q_{xy} and C_{xy} are the quad- and co-spectrum values respectively.

A graph of $|H_{xy}|$ against frequency is often termed the transfer function for the linear system. The phase function, or phase spectrum, is a graph of ϕ_{xy} against frequency.

If the transfer function between input and response is known then the response spectrum $S_{yy}(f)$ corresponding to a known input spectrum $S_{xx}(f)$ may be obtained from

$$S_{yy}(f) = |H_{xy}(f)|^2 S_{xx}(f) \tag{3.20}$$

The phase and transfer functions are relevant to linear systems only. Any estimates of these functions must be accompanied by an estimate of the

coherence function. For those frequencies for which the coherence is low, the phase and transfer function estimates cannot be applied in the context of a linear system.

Equations (3.14) to (3.19) form the basis of the cross-spectral analysis program ANALX. The program computes and plots the auto-spectra of the input and response time series and the coherence, transfer and phase functions. The flowchart for ANALX is presented in Figure 3.7 and a typical output is presented in Figure 3.8.

3.4 SBM Free-Motion Analysis

3.4.1 Free Vibration Theory

The equation of motion describing the free response of a single degree of freedom mechanical system consisting of a mass, spring and dashpot, as shown in Figure 3.9, is

$$M\ddot{x} + Q\dot{x} + Kx = 0 \tag{3.21}$$

The equation can be written as

$$\ddot{x} + 2\nu\omega_o\dot{x} + \omega_o^2 x = 0 \tag{3.22}$$

where

$$\omega_o = (K/M)^{\frac{1}{2}} \tag{3.23}$$

and

$$\nu = Q/2(KM)^{\frac{1}{2}} \tag{3.24}$$

ω_o is the undamped natural frequency of the system and ν is the damping factor.

The free-motion response is

$$x(t) = R\exp(-\nu\omega_o t)\sin(\Omega t + \phi) \tag{3.25}$$

where the magnitudes of R and ϕ depend on the initial conditions and Ω, the damped natural frequency, is given by

$$\Omega^2 = \omega_o{}^2(1 - \nu^2) \tag{3.26}$$

The free-motion response is illustrated in Figure 3.10. If two successive positive (or negative) maxima of the response are considered then the ratio of the first to the second is

$$r = \exp(2\pi\nu/(1 - \nu^2)^{\frac{1}{2}}) \tag{3.27}$$

The logarithmic decrement is defined as

$$\delta = \log_e r \tag{3.28}$$

and is related to the damping factor by

$$\nu = 1/(1 + (2\pi/\delta)^2)^{\frac{1}{2}} \tag{3.29}$$

3.4.2 Heave Free-Motion Analysis

Section 6.4 presents the equation of motion describing the free heave response of the SBM in water as

$$(M + M_{a_H})\ddot{y} + Q_H\dot{y} + K_H y = 0 \tag{3.30}$$

where $y(t)$ is the free heave response

M is the SBM's mass

M_{a_H} is the heave added mass

Q_H is the heave damping constant

K_H is the heave stiffness of the SBM.

The added mass term arises from the heave acceleration of the SBM in

water. The concept of added mass is discussed in Section 6.4. The concern here is to establish a basis for the calculation of the added mass at the heave natural frequency from a measure of the heave free-motion in water.

In the heave free-motion tests the buoy is given an initial heave displacement, is released and the resulting free-motion recorded. The heave damped natural frequency Ω_H and the logarithmic decrement are obtained from the record. The heave damping factor is obtained using equation (3.29) and the heave undamped natural frequency from equation (3.26).

If the SBM's mass M and heave stiffness K_H are known then, from equation (3.23), the heave added mass is obtained from

$$\omega_{o_H} = [K_H/(M + M_{a_H})]^{\frac{1}{2}} \tag{3.31}$$

The heave damping constant at the heave natural frequency is, following equation (3.24), obtained from

$$Q_H = 2\nu[K_H(M + M_{a_H})]^{\frac{1}{2}} \tag{3.32}$$

3.4.3 Pitch Free-Motion Analysis

The equation of motion for the free pitch response of the SBM in water is (Section 6.4)

$$(Mk_p^2 + M_{a_p} k_p^2)\ddot{\theta} + Q_p\dot{\theta} + K_p\theta = 0 \tag{3.33}$$

where $\theta(t)$ is the free pitch response

M_{a_p} is the pitch added mass

k_p is the pitch radius of gyration of the buoy.

The pitch free-motion test results are analysed in the same way as for heave, except that the heave mass term $(M + M_{a_H})$ is replaced by the pitch moment of inertia term $(M + M_{a_p})k_p^2$.

3.5 SBM Forced-Motion Analysis

As the SBM responds to waves its motion generates waves which radiate away from the buoy. The work done by the damping, often referred to as radiation damping, may be equated to the energy of the generated waves.

3.5.1 Heave Forced-Motion Analysis

In a heave forced-motion test the buoy is forced to oscillate in heave with known frequency ω and amplitude A_o, as illustrated in Figure 3.11. The SBM's displacement is then

$$y(t) = A_o \cos(\omega t) \tag{3.34}$$

The SBM's heave velocity is, therefore,

$$\dot{y}(t) = -A_o \omega \sin(\omega t) \tag{3.35}$$

The heave damping force is proportional to the velocity and is

$$F_{d_H} = Q_H \dot{y}(t) \tag{3.36}$$

where Q_H is the damping constant at frequency ω.

There are two inherent approximations in this representation of the damping force. Q_H is assumed constant with time and viscous damping is assumed, that is the force is linearly proportional to the velocity.

The total work done by damping in one period T of heave oscillation is

$$W_{d_H} = \int_o^T Q_H \dot{y}(t)\dot{y}(t)dt \tag{3.37}$$

where $T = 2\pi/\omega$.

Substituting for $\dot{y}(t)$ and integrating gives

$$W_{d_H} = Q_H A_o^2 \pi\omega \tag{3.38}$$

The amplitudes of the waves generated by the heave oscillations are the same at all points equidistant from the buoy's centre (Figure 3.11). The wave amplitude decays with distance away from the buoy as the circumference of the wave front increases. If the amplitude of the wave at radius r from the buoy is a_r (Figure 3.11) then, according to deep-water linear wave theory, the energy in the wave is

$$E = (\tfrac{1}{2}\rho g a_r^2)(2\pi g/\omega^2)(2\pi r) \tag{3.39}$$

where $2\pi g/\omega^2$ is the wavelength and $2\pi r$ is the circumference of the circular wave front.

Equating the energy in the wave E to the work done by damping W_{d_H} gives

$$Q_H = 2\pi\rho g^2 (a_r/A_o)^2 (r/\omega^3) \tag{3.40}$$

Equation (3.40) can be used to obtain the heave damping constant Q_H at frequency ω from a measure of the radiated wave amplitude a_r at a known distance r from the buoy's centre and a measure of the amplitude of the heave forced-motion A_o.

3.5.2 Pitch Forced-Motion Analysis

In a pitch forced-motion test the buoy is forced to pitch with frequency ω and amplitude θ_o, as illustrated in Figure 3.12, so that the pitch rotation is given by

$$\theta(t) = \theta_o \cos(\omega t) \tag{3.41}$$

The pitch velocity is, therefore,

$$\dot{\theta}(t) = -\theta_o \omega \sin(\omega t) \tag{3.42}$$

and the pitch damping moment is

$$T_{d_p} = Q_p \dot{\theta}(t) \tag{3.43}$$

where Q_p is the pitch damping constant.

The total work done by the damping moment in one period T of pitch oscillation is

$$W_{d_p} = \int_o^T Q_p \dot{\theta}(t) \dot{\theta}(t) dt \tag{3.44}$$

Substituting for $\dot{\theta}(t)$ and integrating gives

$$W_{d_p} = Q_p \theta_o^2 \pi \omega \tag{3.45}$$

The amplitudes of the waves generated by the pitch motion are a maximum along a line through the buoy's centre and perpendicular to the pitch axis and are zero along the pitch axis as illustrated in Figure 3.12. It is assumed here that the amplitude of a wave at radius r from the buoy's centre is linearly proportional to its perpendicular distance from the pitch axis. With reference to Figure 3.12 therefore

$$a(r,\phi) = a_r \cos\phi \tag{3.46}$$

The wave energy in the elemental length of wave dS is

$$dE = \tfrac{1}{2}\rho g (a_r \cos\phi)^2 (2\pi g/\omega^2) dS \tag{3.47}$$

Substituting $rd\phi$ for dS, then the total wave energy at radius r is

$$E = 4[\tfrac{1}{2}\rho g a_r^2 2\pi g/\omega^2 \int_0^{\pi/2} r\cos^2\phi d\phi] \qquad (3.48)$$

Integrating gives

$$E = \rho g^2 \pi^2 r a_r^2/\omega^2 \qquad (3.49)$$

Equating the wave energy E to the work done by the damping W_{d_p} gives the following expression for the pitch damping constant:

$$Q_p = \pi\rho g^2 (a_r/\theta_o)^2 (r/\omega^3) \qquad (3.50)$$

Equation (3.50) may be used to obtain the pitch damping constant Q_p at frequency ω from a measure of the amplitude of the pitch forced oscillation θ_o and of the radiated wave amplitude a_r at a distance r from the buoy's centre and perpendicular to the pitch axis.

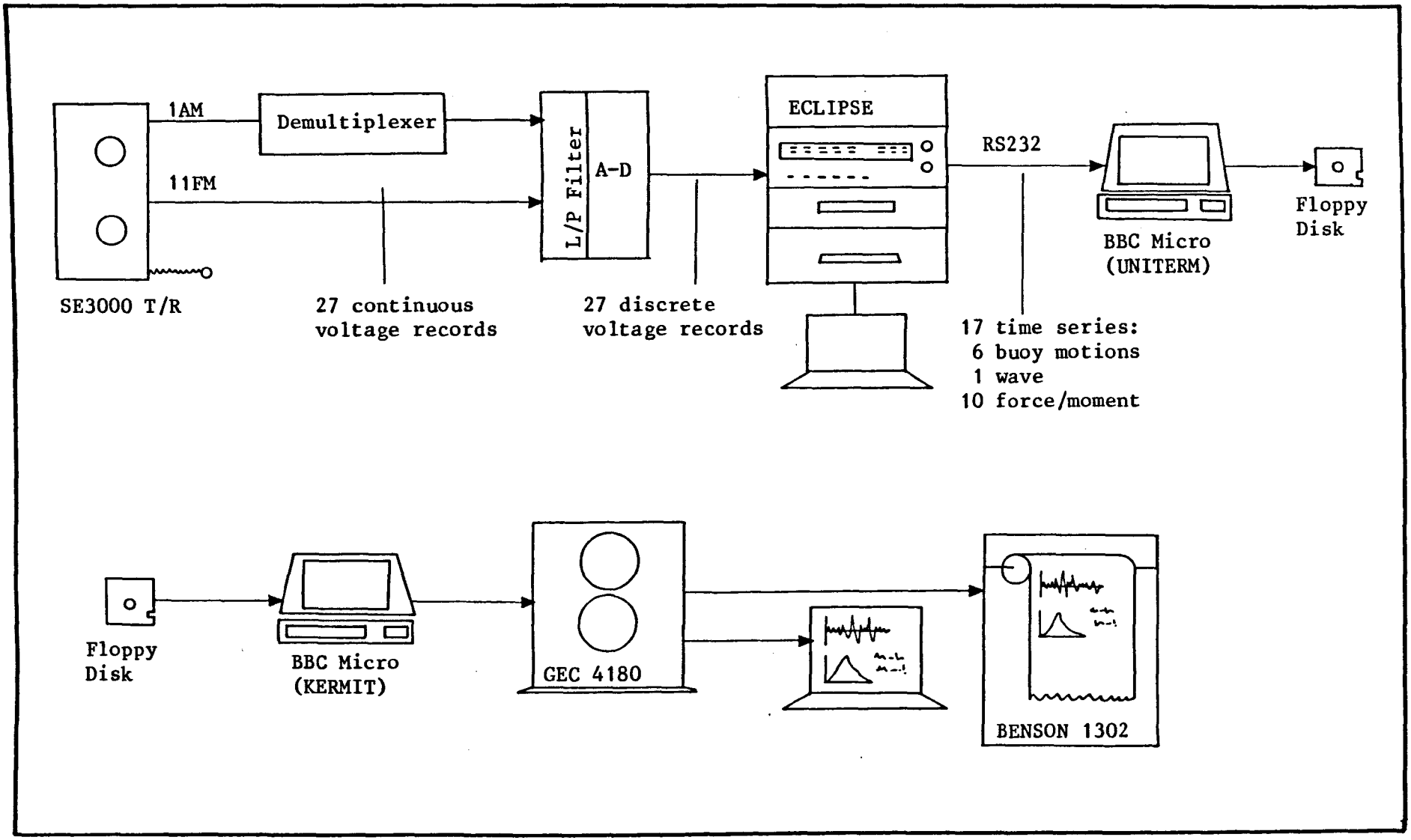

Figure 3.1 Data Processing

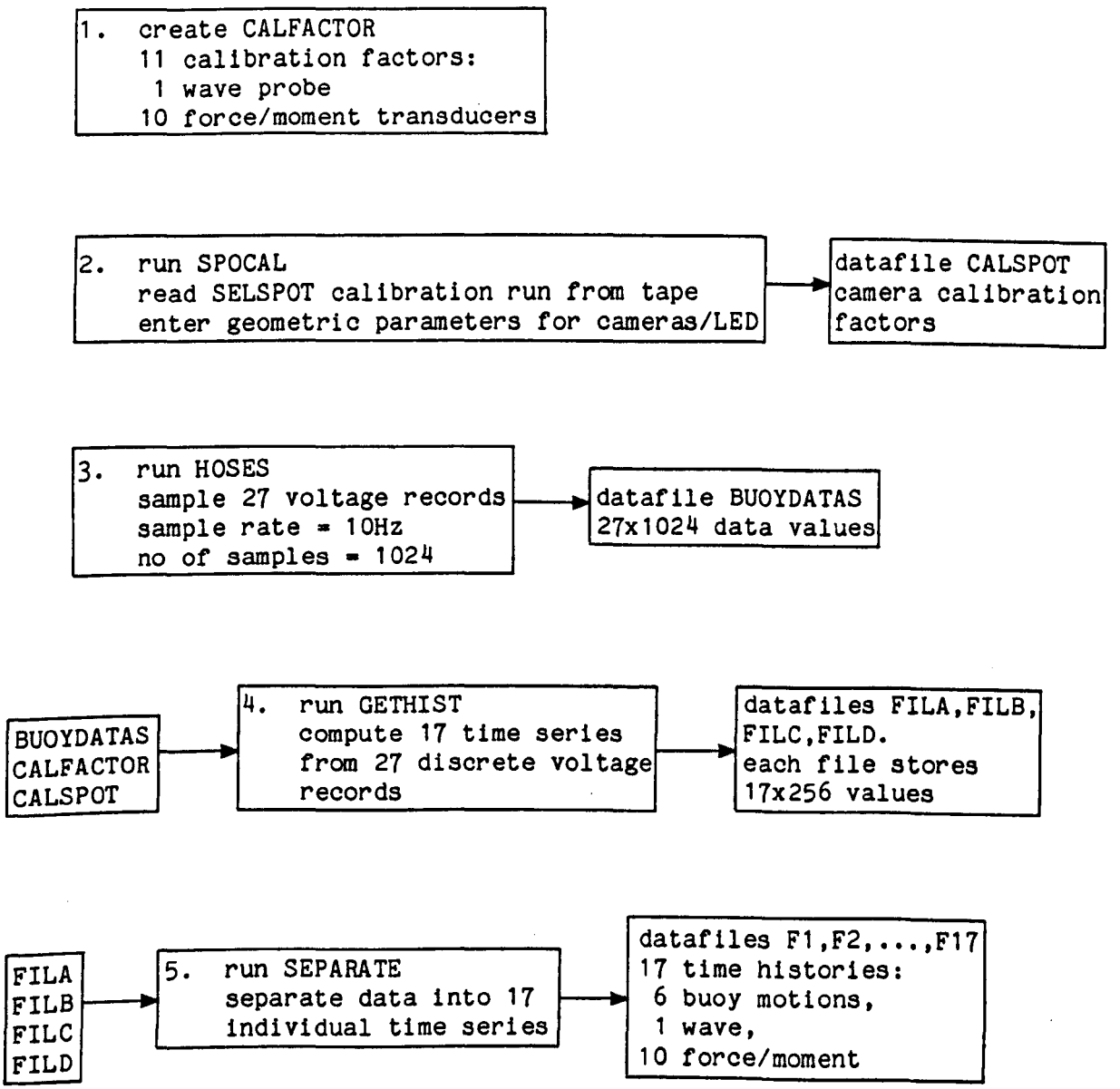

Figure 3.2

Data Reduction Procedure on the ECLIPSE Minicomputer

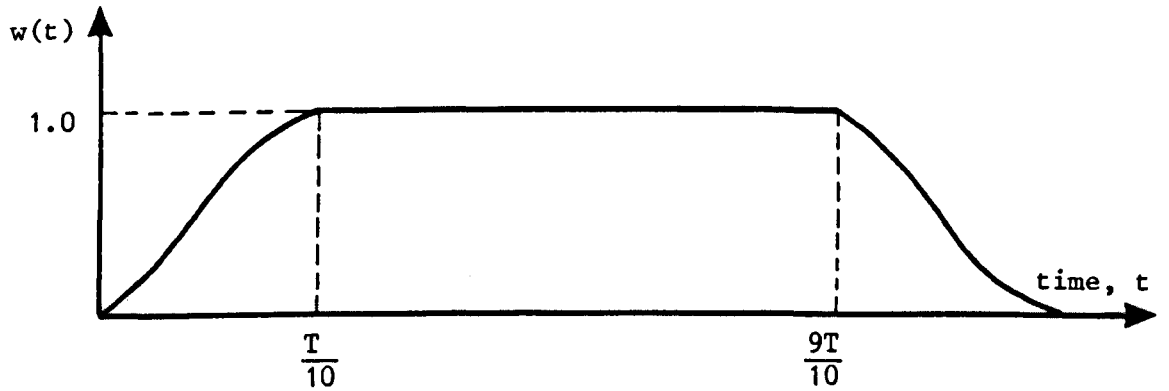

$$w(t) = \frac{1}{2}(1 - \cos 10\pi t/T) \qquad 0 \leq t \leq T/10$$

$$w(t) = 1.0 \qquad T/10 \leq t \leq 9T/10$$

$$w(t) = \frac{1}{2}[1 + \cos 10\pi(t - 9T/10)/T] \qquad 9T/10 \leq t \leq T$$

Figure 3.3 The Cosine Taper

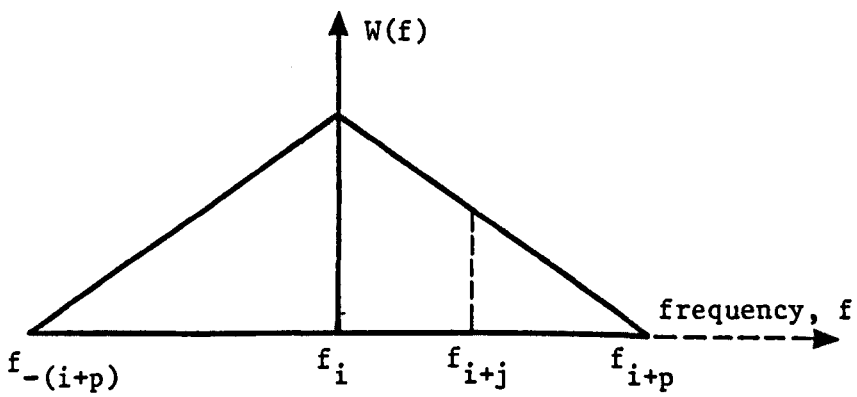

NE = no of estimates in window

P = (NE-1)/2

Weighting = $W(f_{i+j}) = 1.0 - |j/p| \qquad -p \leq j \leq p$

Figure 3.4 Frequency-domain triangular smoothing window

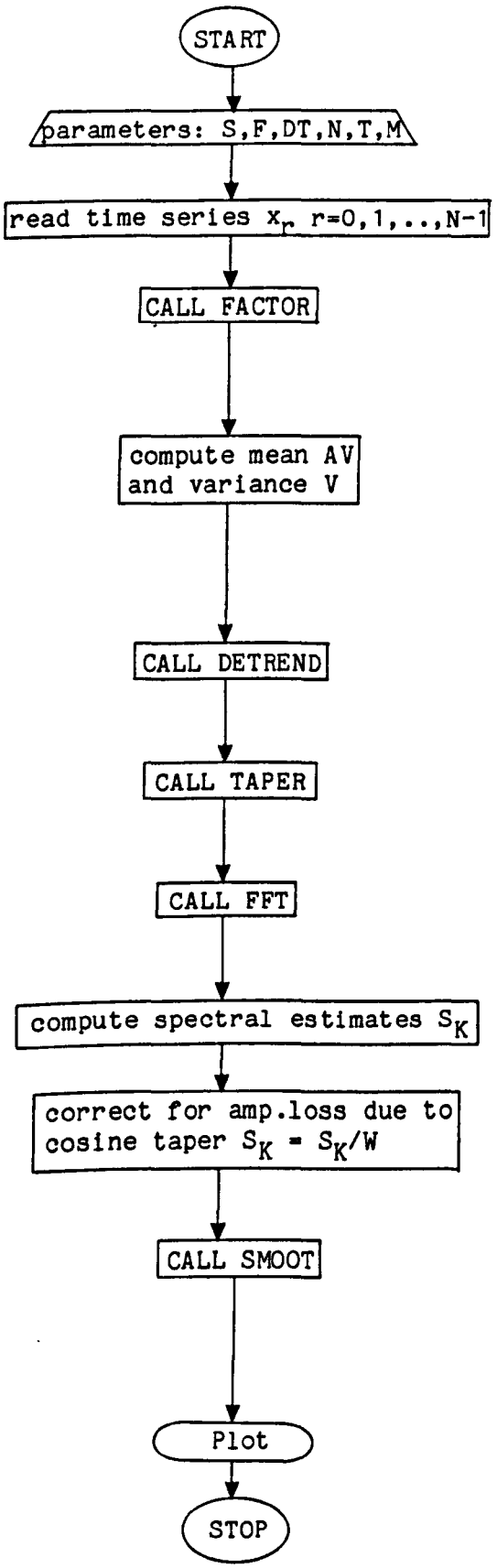

Notes

S = model scale
F = sampling frequency
DT = 1/F
N = no of samples
T = N.DT ; $N = 2^M$

subroutine FACTOR scales data to prototype values

$$AV = 1/N \sum_{r=0}^{N-1} x_r$$

$$V = 1/N \sum_{r=0}^{N-1} x_r^2 - (AV)^2$$

subroutine DETREND de-means and de-trends data

subroutine TAPER applies cosine taper: $x_r = x_r w_r$ (Figure 3.3)

subroutine FFT computes DFT of x_r to give $X_k = a_k - ib_k$ k=0,..,N-1

$$S_k = 2TX_k^* X_k \quad k=0,1,\ldots,N/2$$

$$W = 1/N \sum_{r=0}^{N-1} \omega_r^2 \qquad S_k = S_k/W$$

subroutine SMOOT smoothes spectral estimates as described by equation (3.13) and Figure 3.4 to give

S_k k=0,1,....,N/2

Figure 3.5

Flowchart for ANAL1

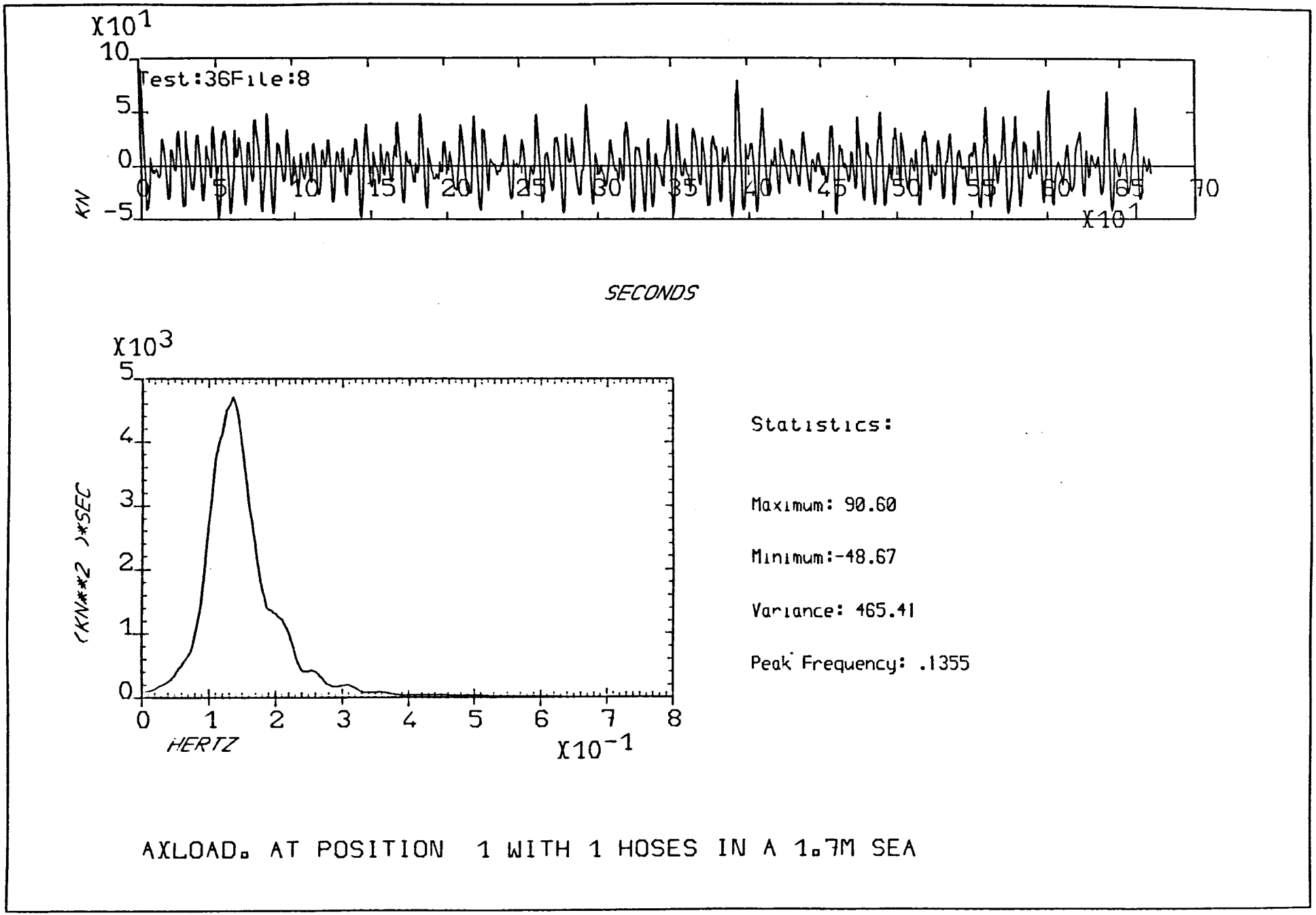

Figure 3.6 Sample output from ANAL1

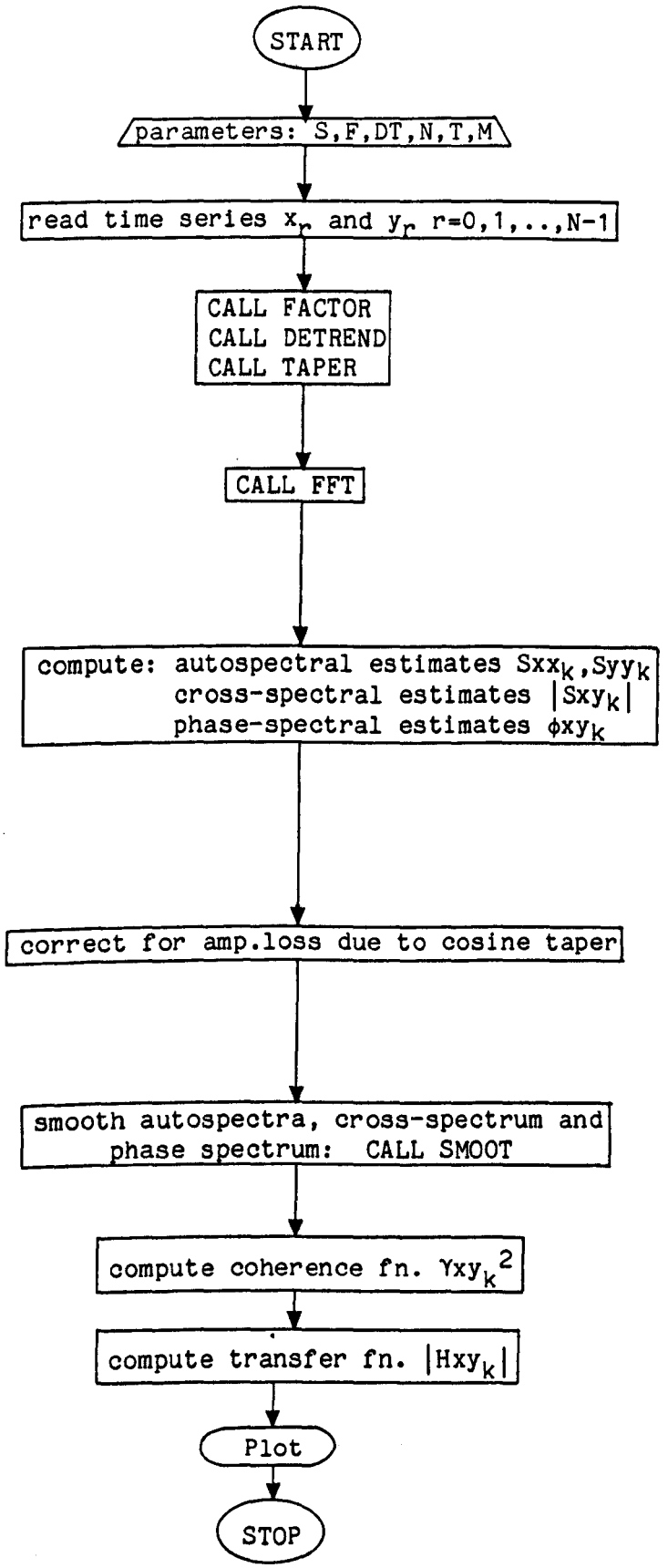

Notes

See Notes Figure 3.5

subroutine FFT: compute DFT of x_r and y_r to give

$X_k, Y_k = a_k - ib_k \quad k=0,1,..,N-1$

$Sxx_k = 2TX_k^* X_k$

$Syy_k = 2TY_k^* Y_k$

$Sxy_k = 2TX_k^* Y_k = Cxy_k - iQxy_k$

$\phi xy_k = \tan^{-1}[Qxy_k / Cxy_k]$

$$W = 1/N \sum_{r=0}^{N-1} \omega_r^2$$

$Sxx_k = Sxx_k / W$ etc

Smoothing gives $\bar{S}xx_k$, $\bar{S}yy_k$

$|\bar{S}xy_k|$ and $\bar{\phi}xy_k \quad k=0,1,..N/2$

$\gamma xy_k^2 = |\bar{S}xy_k|^2 / \bar{S}xx_k \bar{S}yy_k$

$Hxy_k = \bar{S}xy_k / \bar{S}xx_k$

Figure 3.7

Flowchart for ANALX

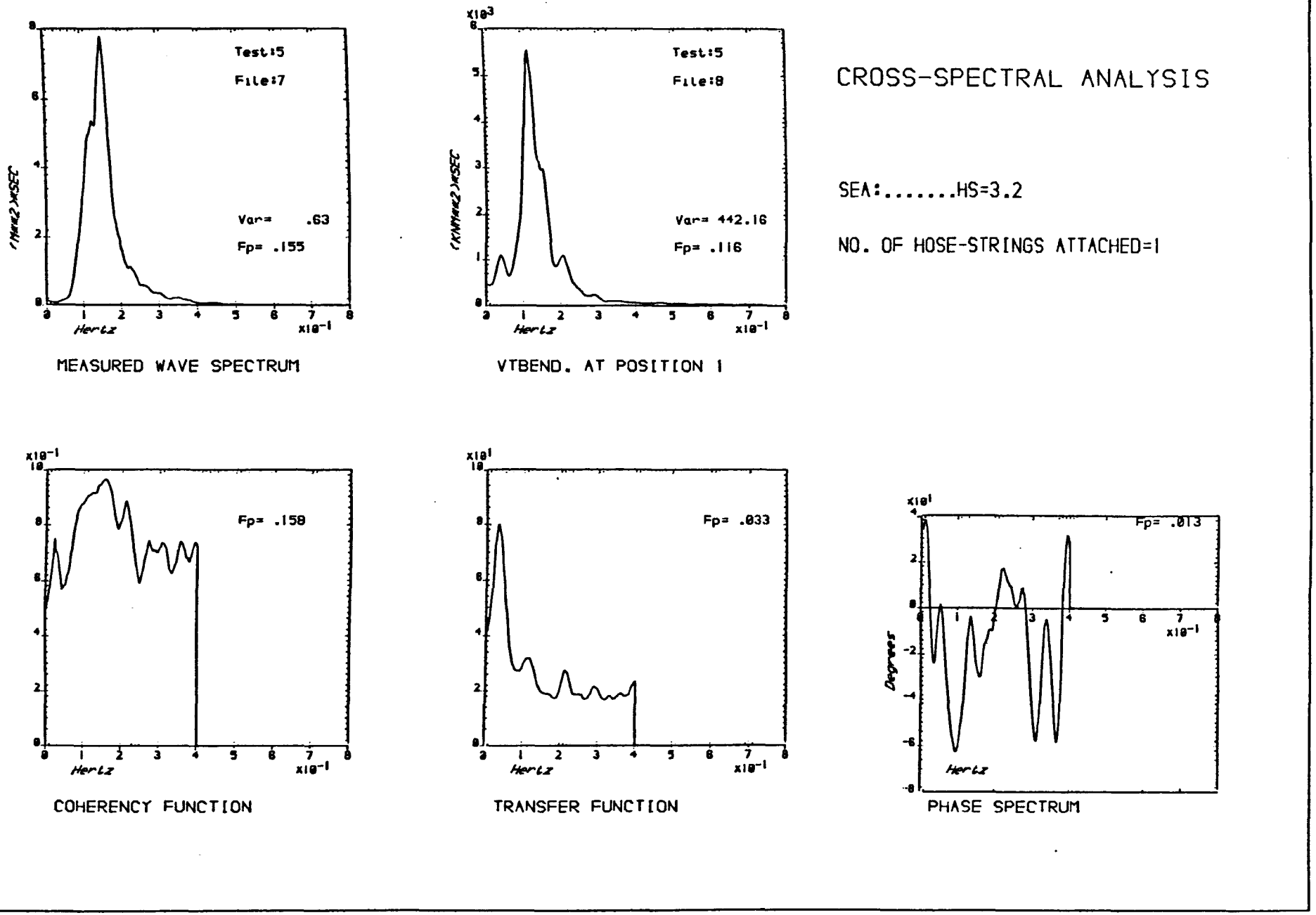

Figure 3.8 Sample output from ANALX

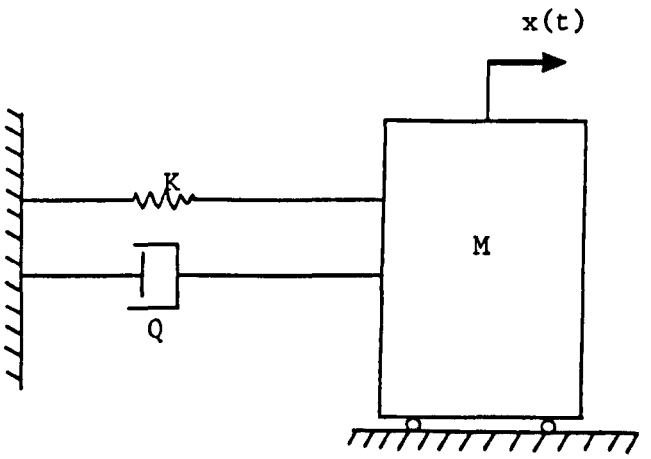

Figure 3.9 Representation of a single-degree-of-freedom mechanical system

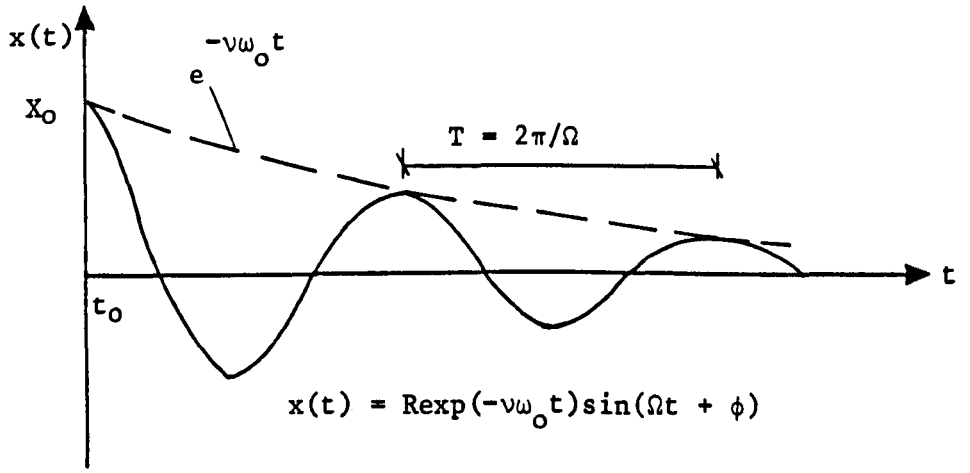

Figure 3.10 Free-motion response of a single-degree-of-freedom mechanical system

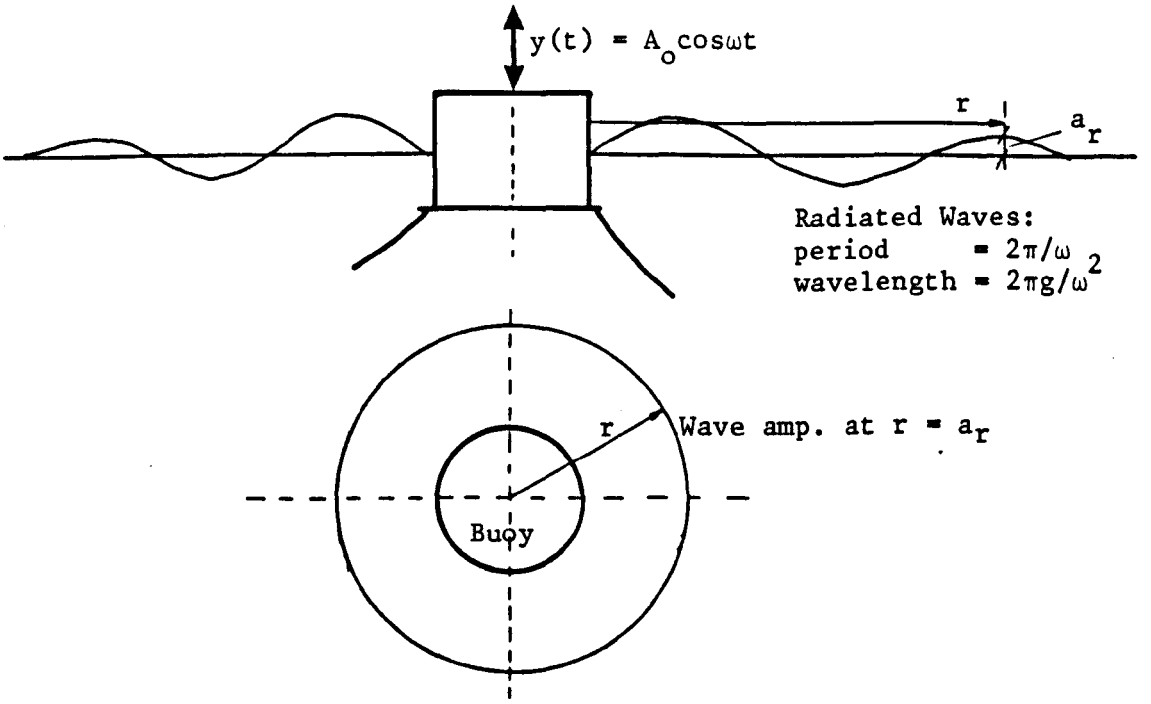

Figure 3.11 Radiated waves from heave forced-motion

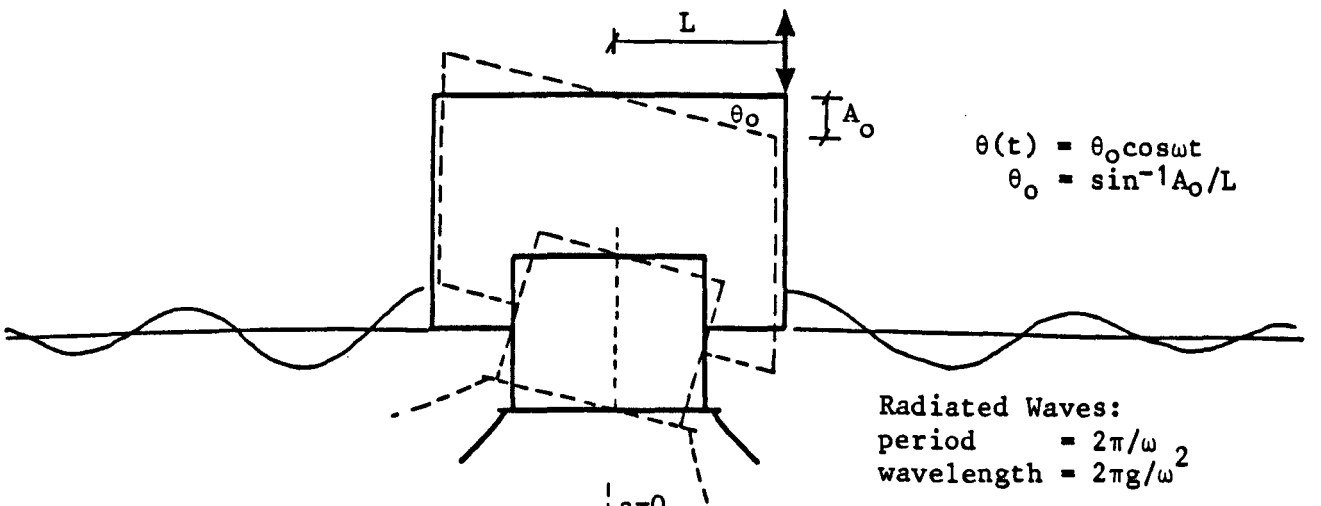

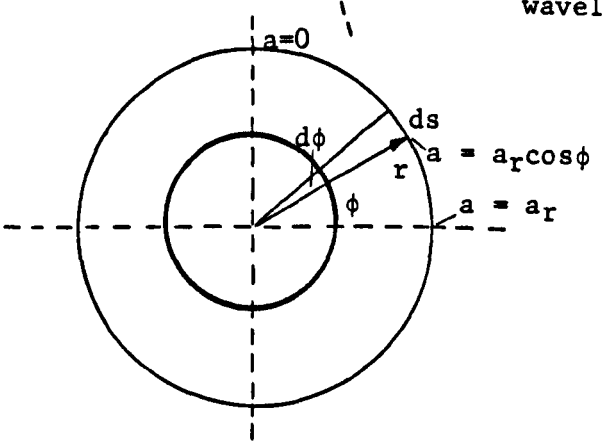

Figure 3.12 Radiated waves from pitch forced-motion

4. MODEL TEST RESULTS: SBM MOTIONS

4.1 Introduction

The loading on a floating hose-string attached to a CALM buoy depends on the response of the SBM to wave action. It is necessary therefore to understand the behaviour of the SBM in waves. The model test results presented in this chapter help towards that understanding.

The results of the analysis of the measured SBM motions in various sea conditions are presented in Section 4.2. The auto- and cross-spectral analysis programs presented in Chapter 3 are used to obtain the SBM motion spectra and the phase and transfer functions between the measured waves and the heave, surge and pitch of the buoy.

The results of the SBM free- and forced-motion tests are presented in Sections 4.3 and 4.4. Results are presented for the heave and pitch natural frequencies and for the heave and pitch damping as functions of frequency.

4.2 SBM Motions in Waves

The six degrees of freedom of SBM motion have been illustrated in Figure 2.10. Prior to the main test series a number of model tests were conducted in which the six motions were measured in different wave conditions, with and without hose-strings attached. The results showed that

(1) the SBM motions, other than top rotation, are not affected by the presence of hose-strings;

(2) top rotation occurs only when hose-strings are attached. The frequency of top rotation is the same as the snaking frequency of the hose-strings;

(3) sway and roll motions of the SBM are negligible.

Result (2) implies that the top rotation results from the horizontal bending induced on the hose at the buoy by the string's snaking. On the basis of these results it was decided to concentrate the analysis on the heave, surge and pitch motions only.

The main test series involved the simultaneous measurement of buoy motions and hose loading in three irregular and four regular wave conditions. The irregular seas are referred to as SEA1, SEA2 and SEA3. Table 4.1 summarises the spectral properties of these seas.

	SEA1	SEA2	SEA3
Spectrum Type	ISSC	ISSC	ISSC
Peak Spectral Frequency (Hz)	0.165	0.138	0.07
Significant Wave Height (m)	2.1	1.7	1.4

Table 4.1

Spectral properties of the irregular seas used in the model tests

The ISSC spectral shape was used because it is broad-banded. Transfer functions for linear responses can therefore be obtained which extend over a wider frequency range than those obtained from other, less broad wave spectra such as JONSWAP. By testing with three ISSC wave spectra with different peak frequencies, the transfer function result from each sea can be combined to produce a single transfer function result extending over a wide frequency range. A sample measurement of the wave record and spectrum of each of the three seas is shown in Figures 4.1, 4.2 and 4.3.

The regular wave tests were conducted with waves of frequency 0.25Hz, 0.167Hz, 0.125Hz and 0.1Hz. The wave height at each frequency was different for each test.

4.2.1 Auto-Spectral Analysis Results

The SBM motions were measured three times in each of the irregular seas SEA1, SEA2 and SEA3. (The three times correspond with the three different hose loading tests - axial load, vertical and horizontal bending.) The recorded measurements of wave height, heave, surge and pitch from every test were analysed using the auto-spectral analysis program ANAL1. A typical result for each of heave, surge and pitch in SEA2 is shown in Figures 4.4, 4.5 and 4.6. All of the spectra are presented in Figure 4.7. The results show good repeatability in that there is little difference between the results obtained from each test run.

The heave response is strongly selective in that there is no heave at frequencies greater than about 0.16Hz. Accordingly the heave spectra are characterised by being very much narrower than their corresponding wave spectra.

The surge spectra are characterised by a non-linear response at low frequencies as well as a response at the incident wave frequencies. The low frequency response is a measure of the slow drift of the SBM in waves resulting from its low surge stiffness. The slow drift is greater than the response at the wave frequencies in seas whose energy is concentrated at high frequencies (SEA1); for low frequency seas (SEA3) the slow drift is negligible compared to the response at the wave frequencies.

The pitch spectra are characterised by a dominant spectral peak at around 0.1Hz, irrespective of the position of the peak spectral frequency of the

sea. There is significant non-linear pitch response at low frequencies in SEA1; this may be a result of the mooring chains causing the buoy to pitch as it drifts.

The results in Figure 4.7 give strong indications of the natural frequencies of the SBM: the peak of the narrow-banded heave spectrum in SEA1 suggests a heave natural frequency of about 0.13Hz; the low frequency peaks of the surge spectra in SEA1 and SEA2 suggest a surge natural frequency between 0.025Hz and 0.03Hz; the pitch results suggest a pitch natural frequency of 0.1Hz.

The natural frequencies of the SBM motions, as well as the amplitude of response as a function of frequency, may be studied more efficiently using the results of cross-spectral analysis.

4.2.2 Cross-Spectral Analysis Results

The cross-spectral analysis program ANALX was used to establish the phase and transfer functions between the waves and SBM motions at those frequencies for which the measured response is linear. The waves were measured at a position in line with the sway axis of the SBM (Figure 2.10); the computed phase function is therefore the phase difference between the SBM response and the wave at the buoy's centre.

The cross-spectral analysis was carried out between the measured waves and measured heave, surge and pitch of the SBM for each of the three irregular seas. (Because of the repeatability of the results only one analysis was required for each response in each sea.) In this way three estimates were obtained for the phase and transfer function of each response. A typical complete cross-spectral analysis result for each of heave, surge and pitch is shown in Figures 4.8, 4.9 and 4.10 respectively.

The three measures of the phase and transfer functions have been combined to produce Figures 4.11, 4.12 and 4.13. Only phase and transfer function estimates at frequencies for which the coherency is greater than 0.8 and, therefore, for which the response is predominantly linear, are included. The upper limit on the frequency axis is set at 0.3Hz corresponding with the highest frequency waves of practical interest. Figures 4.11, 4.12 and 4.13 include results obtained from the regular wave tests.

4.2.2.1 SBM Heave

The three irregular wave test results for the heave phase and transfer functions are in good agreement (Figure 4.11). The transfer function obtained from SEA1 and SEA2 peaks at around 0.11Hz with a value of 3.2; the transfer function from SEA3 has a maximum of 3.5 at 0.12Hz. For frequencies greater than the peak frequencies the transfer function decays rapidly, reaching a value of about 0.3 at 0.16Hz. The regular wave results at 0.125Hz and 0.167Hz agree with the irregular wave results.

The irregular wave test results show a gradual reduction in the heave transfer function as the frequency decreases from the peak frequency: the transfer function is 3.0 at 0.1Hz and 2.0 at 0.06Hz. However, the regular wave result at 0.1Hz is 2.1, about 40% less than the irregular wave result, and reveals a much more rapid decay from the maximum value at the peak frequency to the expected value of 1.0 at low frequencies. This difference between the irregular and regular wave results first suggests non-linearity. However, linearity is indicated by the high coherency at all frequencies for which the transfer function has been produced (the coherency between waves and heave is 0.96 at 0.1Hz in Figure 4.8) and by the fact that the three irregular seas produce the same transfer function.

A possible explanation for the difference between the results may lie in the dilemma inherent in spectral analysis: the smoothing of spectral estimates to achieve greater statistical accuracy results in coarser frequency resolution, causing energy at sharp spectral peaks to be smeared out over a wide frequency range. This being the case, then the regular wave result is the better measure of the transfer function at 0.1Hz and the function decays from its maximum at the peak frequency to 1.0 at low frequencies more rapidly than indicated by the irregular wave results.

The heave phase function shows that for low frequencies, less than 0.1Hz, the SBM heave is almost in phase with the waves. There is a rapid increase in the magnitude of the phase difference between 0.1Hz and 0.13Hz; at 0.13Hz the SBM lags the wave by about 90°. The magnitude of the phase difference decreases again as the frequency increases from 0.13Hz.

4.2.2.2 SBM Surge

Figure 4.12 shows that the surge phase and transfer functions, obtained from the three irregular wave test results, agree very well over a wide frequency range of 0.06Hz to 0.3Hz. Moreover, the regular wave results are, in general, consistent with the irregular wave results.

The surge transfer function increases from about 0.24 at 0.3Hz to about 2.5 at 0.06Hz. The increasing value of the transfer function for lower frequencies is indicative of the low surge natural frequency of the SBM.

The phase difference between the SBM's surge and the wave tends to zero at very low frequencies. The magnitude of the phase difference increases gradually with increasing frequency so that by 0.1Hz the surge lags the wave by about 100°. Between 0.1Hz and 0.2Hz the phase lag is some value

between 100° and 140°. The regular and irregular wave results agree well within this frequency range. The magnitude of the phase difference appears to decrease for frequencies greater than 0.2Hz.

The surge phase and transfer functions established from the model tests may be used to predict the linear surge response of the SBM in waves. They do not, however, enable the prediction of the non-linear, low frequency drift. However it is the higher frequency linear surge response that is important in determining bending moments and axial loads induced on an attached hose-string and, in this context therefore, the slow drift is of little importance.

4.2.2.3 SBM Pitch

The pitch transfer functions, Figure 4.13, obtained from the irregular wave tests are in good agreement at those frequencies at which the results overlap. They show that for frequencies greater than 0.16Hz the pitch amplitude is small, between 1° and 2° per metre wave amplitude. There is a rapid rise in the transfer function as the frequency decreases from 0.16Hz. The regular wave results at 0.125Hz and 0.16Hz are consistent with the irregular wave results.

The peak in the transfer function at 0.1Hz corresponds to the pitch natural frequency of the SBM. In the same way as for heave, the definition of the sharp peak at the natural frequency is affected by the coarser frequency resolution inherent in the smoothing of the spectral estimates. This may explain the 16% difference between the irregular wave result of 6.0 deg/m and the regular wave result of 7.0 deg/m at 0.1Hz.

There is some scatter between the pitch phase function results. However, there is consistency in the sense that the phase difference is almost

always negative. The scatter results from difficulties in measuring the phase of very low responses.

4.3 SBM Free-Motion Test Results

This section presents the results of the heave and pitch free-motion tests. The tests were conducted to establish the heave and pitch natural frequencies of the SBM from measures of the SBM's free-motion in water.

The added masses for heave and pitch at the heave and pitch natural frequencies are obtained from the values of the natural frequencies. It is known that heave and pitch added mass remain fairly constant with frequency (Chapter 6). The added mass values obtained here can be used in a model for the prediction of the SBM's heave and pitch response in regular waves of different frequency (Chapter 6).

Because of the low surge stiffness of the SBM, the surge natural frequency is low and outside the wave frequency range. Since it is known that surge added mass is very dependent on the surge frequency (Chapter 6), the added mass at the surge natural frequency obtained from a surge free-motion test is of little use in a model predicting the surge response of the buoy in waves. For this reason no free-motion tests were conducted for surge.

4.3.1 Heave Free-Motion

Two accelerometers were fixed to the top of the moored buoy with their sensitive axes aligned with the vertical. The output from each accelerometer was set to zero at still conditions. The buoy was pushed vertically downwards and released, the oscillatory responses from the accelerometers being traced on the chart recorder. Two separate heave free-motion tests were carried out.

The recorded acceleration-time measurements were converted to the equivalent prototype displacement-time records. A typical result is shown in Figure 4.14.

Estimates of the heave damped natural period were obtained by dividing by n the time measured to complete n heave cycles. The average of the estimates is 7.4 seconds. The first result obtained from the heave free-motion tests is, therefore,

$$\Omega_H = 0.85 \text{ rads/sec} \qquad (4.1)$$

$$= 0.135\text{Hz}$$

where Ω_H is the damped heave natural frequency of the SBM in water.

The logarithmic decrement is calculated from the ratio of two successive maximum values, as follows

$$\delta_i = \log_e(y_i/y_{i+1}) \qquad (4.2)$$

where

$$y_i = y(t = i2\pi/\Omega_H)$$

$$y_{i+1} = y(t = (i+1)2\pi/\Omega_H)$$

Figure 4.15 shows the logarithmic decrement δ_i plotted against the mean of the heave maxima y_i and y_{i+1}. The results show that, in general, the measured δ_i at larger amplitudes of heave exceeds that at the smaller amplitudes. This means that the damping forces must increase with amplitude more rapidly than they would if they were governed by the viscous (linear) damping law. In order to maintain the linearity of the damping force in the equation of motion, the measured heave free-motion has been approximated by a motion governed by the viscous law, with

logarithmic decrement equal to the mean of the measured values of δ_i, i.e. with $\delta_i = \bar{\delta}_i = 0.45$. The envelope of the linear viscous approximation of the measured response is shown in Figure 4.14.

With $\delta = 0.45$ and $\Omega_H = 0.85$, the undamped heave natural frequency is obtained using equations 3.29 and 3.26 and is

$$\omega_{o_H} = 0.852 \text{ rads/sec} \tag{4.3}$$

The damped and undamped natural frequencies are almost equal because the damping is light.

The heave stiffness and mass of the SBM are 2.46×10^3kN/m and 1.025×10^6kg respectively (Section 6.2.2). The heave added mass, obtained using equation (3.31), is therefore

$$M_{a_H} = 2.34 \times 10^6 \text{kg} \tag{4.4}$$

A heave added mass coefficient C_{a_H} may be defined as follows

$$M_{a_H} = C_{a_H} \rho V \tag{4.5}$$

where $\rho = 1000\text{kg/m}^3$ = water density

$V = 1070\text{m}^3$ = immersed volume of the buoy.

The heave added mass coefficient, at the heave natural frequency, is 2.18.

A heave damping coefficient C_{d_H} may be defined as follows:

$$Q_H = C_{d_H} \rho V \omega \tag{4.6}$$

where the damping constant Q_H is obtained from equation (3.32). Substitution for the values in equation (3.32) and (4.6) gives $Q_H = 4.1$kg/sec and $C_{d_H} = 0.45$.

4.3.2 Pitch Free-Motion

Two accelerometers were placed on the edge of the top surface of the moored buoy and at opposite ends of a diameter. The sensitive axes were aligned with the vertical. The output from each accelerometer was set to zero at still conditions. The free-motion was initiated by pushing vertically downwards at the position of one of the accelerometers and releasing. Simultaneous measurements of the acceleration at opposite sides of the buoy were recorded using the chart recorder. A typical acceleration record is reproduced in Figure 4.16.

The measured accelerations do not take the form of exponentially decaying sine functions typical of damped free-motion. Moreover, there are instances when both sides of the buoy are moving in the same direction. The reason for these results is that the buoy heaves as well as pitches when it is released. However, the test observations showed that at the later stages of the tests the heave motion had died out and the predominant motion was pitch. The records showed that the time period for one complete cycle varies during the test, but differs little from about 10 seconds (prototype) during the later stages. The estimate obtained for the damped pitch natural frequency is, therefore, 0.6 rads/sec. Because the damping is light the undamped natural frequency is also estimated at 0.6 rads/sec.

The pitch natural frequency is related to the inertia and stiffness terms of the pitch equation of motion by

$$\omega_{o_p}^2 = K_p/(M + M_{a_p})k_p^2 \qquad (4.7)$$

where K_p is the pitch stiffness of the SBM

M is the SBM mass

M_{a_p} is the pitch added mass

k_p is the pitch radius of gyration.

The values of K_p, M and k_p are 27.5 x 10^3kNm/rad, 1.025 x 10^6kg and 4.7m respectively. The pitch added mass is, therefore, 2.25 x 10^6kg and the pitch added mass coefficient C_{a_p}, defined in the same way as the heave added mass coefficient (equation 4.5), is 2.1.

4.4 SBM Forced-Motion Test Results

The object of the buoy forced-motion tests is to obtain estimates of heave and pitch damping as functions of frequency. As the buoy is forced to oscillate, waves are generated which radiate away from the buoy. The damping, often referred to as radiation damping, is obtained by equating the measured energy of the radiated waves to the work done by the damping forces. Section 3.5 presents the equations relating the damping force to the wave amplitude at a known distance from the buoy and the amplitude and frequency of the forced oscillation. This section presents the results of processing the buoy forced-motion test measurements using the equations presented in Section 3.5.

The surge natural frequency is low and outside the wave frequency range. The surge response in waves is therefore little influenced by the damping. For this reason no forced-motion tests were carried out for surge.

4.4.1 Heave Forced-Motion

The experimental set-up for the heave forced-motion tests is shown in Figure 4.17. The hydraulic actuator was positioned with its ram aligned with the vertical and directly above the centre of the buoy. The

frequency of the forced oscillation was set from the signal generator. The measured amplitude of oscillation was obtained from the average of the outputs from the two accelerometers. Two tests with different amplitudes of oscillation were carried out for each frequency. The amplitudes of the generated waves were measured at four different distances from the buoy. In this way eight estimates of the damping were obtained at each frequency.

The heave damping Q_H (Ns/m) at frequency ω (rads/sec) is obtained from the measured amplitude of buoy oscillation A_o (m) and the measured wave amplitude a_r (m) at a distance r (m) from the buoy using the equation (equation 3.40)

$$Q_H = 2\pi\rho g^2(a_r/A_o)^2(r/\omega^3) \qquad (4.8)$$

The definition of the heave damping coefficient C_{d_H} is given by equation (4.6). The model test measurements were processed according to equations (4.8) and (4.6). The results are presented in Figure 4.18 as a graph of the heave damping coefficient against frequency.

The primary difficulty associated with the heave forced-motion tests is the measurement of the radiated waves, whose amplitudes range between 0.5 and 5.0mm. The order of accuracy of wave amplitude measurement is about 0.25mm. This means that the error in the wave measurement may be as much as 50% for the smaller waves resulting in an error in the C_{d_H} estimate of the same order of magnitude as the estimate itself.

The individual results at each frequency in Figure 4.18 reflect the difficulty in accurately measuring the radiated waves. An examination of the average values reveals the underlying trend of the results. Heave damping is greatest at around 0.5 rads/sec and decreases rapidly to a

minimum at around 1.1 rads/sec. The damping remains low for frequencies higher than 1.1 rads/sec.

To apply the results in a model predicting the heave response of the buoy in waves the variation of the heave damping coefficient with frequency is approximated by the broken line shown in Figure 4.18.

4.4.2 Pitch Forced-Motion

The experimental set-up for the pitch forced-motion tests is shown in Figure 4.19. The cradle arrangement fitted to the buoy is fixed to a rigid structure at f and has pivots at a, b, c, d and e as shown. Since the centre of gravity of the buoy lies along its centre-line and is close to the still water level, the cradle's construction ensures that the action of the ram causes the buoy to pitch only, with no component of surge (sway) or heave. The wave gauges are positioned along the line through the buoy's centre and perpendicular to the pitch axis. Measurements of the ram's acceleration from the two accelerometers and of the generated waves from the four wave gauges were recorded on the chart recorder. Two tests, each with a different amplitude of ram oscillation, were conducted at each frequency.

The pitch damping Q_p (Nms) at frequency ω (rads/sec) is obtained from the measured amplitude of ram oscillation A_o (m) and the measured wave amplitude a_r (m) at a distance r (m) from the buoy using the equations (equation 3.50)

$$Q_p = \pi\rho g^2 (a_r/\theta_o)^2 (r/\omega^3) \qquad (4.9)$$

and

$$\theta_o = \tan^{-1}(A_o/L) \qquad (4.10)$$

where L (m) is the prototype equivalent of the length L shown in Figure 4.19. The pitch damping coefficient C_{d_p} is defined by the equation

$$C_{d_p} = Q_p/(\rho V \omega k_p^2) \qquad (4.11)$$

where k_p is the pitch radius of gyration of the buoy.

The test measurements were processed according to equations (4.9), (4.10) and (4.11). The results are presented in Figure 4.20 as a graph of the pitch damping coefficient against frequency.

The difficulty of accurately measuring the waves generated by the forced-motion of the buoy applies to pitch as well as to heave. This difficulty is reflected in the scatter of results at each frequency in Figure 4.20. An average result has been obtained by plotting the mean values at each frequency. Pitch damping is a maximum at around 1.1 rads/sec. Damping decreases rapidly as the frequency decreases from 1.1 rads/sec and decreases less rapidly as the frequency increases from 1.1 rads/sec.

The approximate variation of the pitch damping coefficient with frequency is represented by the broken line shown in Figure 4.20.

4.5 Summary of Results

The results from the measurements of the SBM motions in waves and from the free- and forced-motion tests are summarised as follows.

The heave natural frequency of the SBM in water, established from the results of the heave free-motion tests, is 0.135Hz, giving a heave added mass coefficient of 2.18.

The buoy does not heave in high frequency waves resulting in the measured

heave spectra (Figure 4.7) being very much narrower than their corresponding wave spectra. The wave-heave transfer and phase functions are shown in Figure 4.11: at low frequencies the buoy heaves in phase with the waves and with approximately the same amplitude as the wave. Close to the buoy's heave natural frequency, the heave amplitude is up to 3.5 times that of the wave amplitude and the heave lags the wave by about 90°. There is effectively no heave for frequencies greater than 0.16Hz.

The heave forced-motion tests have yielded an approximate result for the heave damping coefficient of the SBM as a function of frequency (Figure 4.18).

The SBM drifts in waves because of its low surge stiffness. The surge spectra (Figure 4.7) are accordingly characterised by a non-linear surge response at low frequencies.

The surge transfer function (Figure 4.12) increases gradually from about 0.24 at 0.3Hz to about 2.5 at 0.06Hz. The surge lags the wave by about 120° for frequencies between 0.1 and 0.2Hz. For frequencies less than 0.1Hz the magnitude of the phase lag decreases.

The pitch natural frequency of the SBM in water, estimated from the pitch free-motion tests, is about 0.1Hz, giving a pitch added mass coefficient of about 2.1.

The pitch spectra (Figure 4.7) are characterised by a dominant spectral peak at 0.1Hz, irrespective of the peak spectral frequency of the sea. The pitch transfer function (Figure 4.13) shows that the pitch is small: for frequencies greater than 0.16Hz the pitch amplitude per metre wave amplitude is between 1° and 2°. At the pitch natural frequency of 0.1Hz

the pitch amplitude is about 7^{o} per metre wave amplitude.

The pitch forced-motion tests have yielded an approximate result for the pitch damping coefficient of the SBM as a function of frequency (Figure 4.20).

In general, the results for the SBM motion obtained from the regular wave tests agree with those obtained from the irregular wave tests.

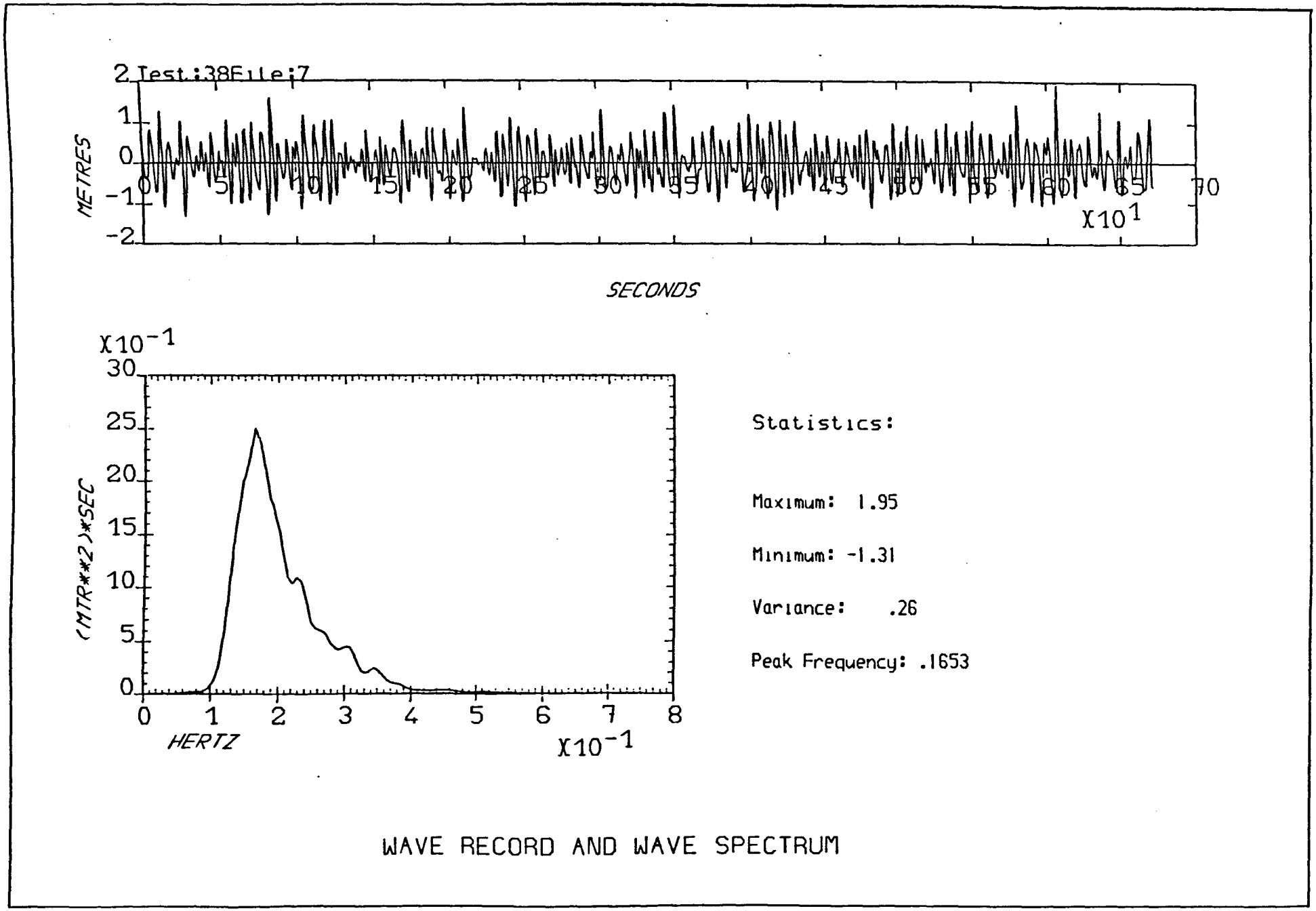

Figure 4.1 SEA1: wave record and spectrum

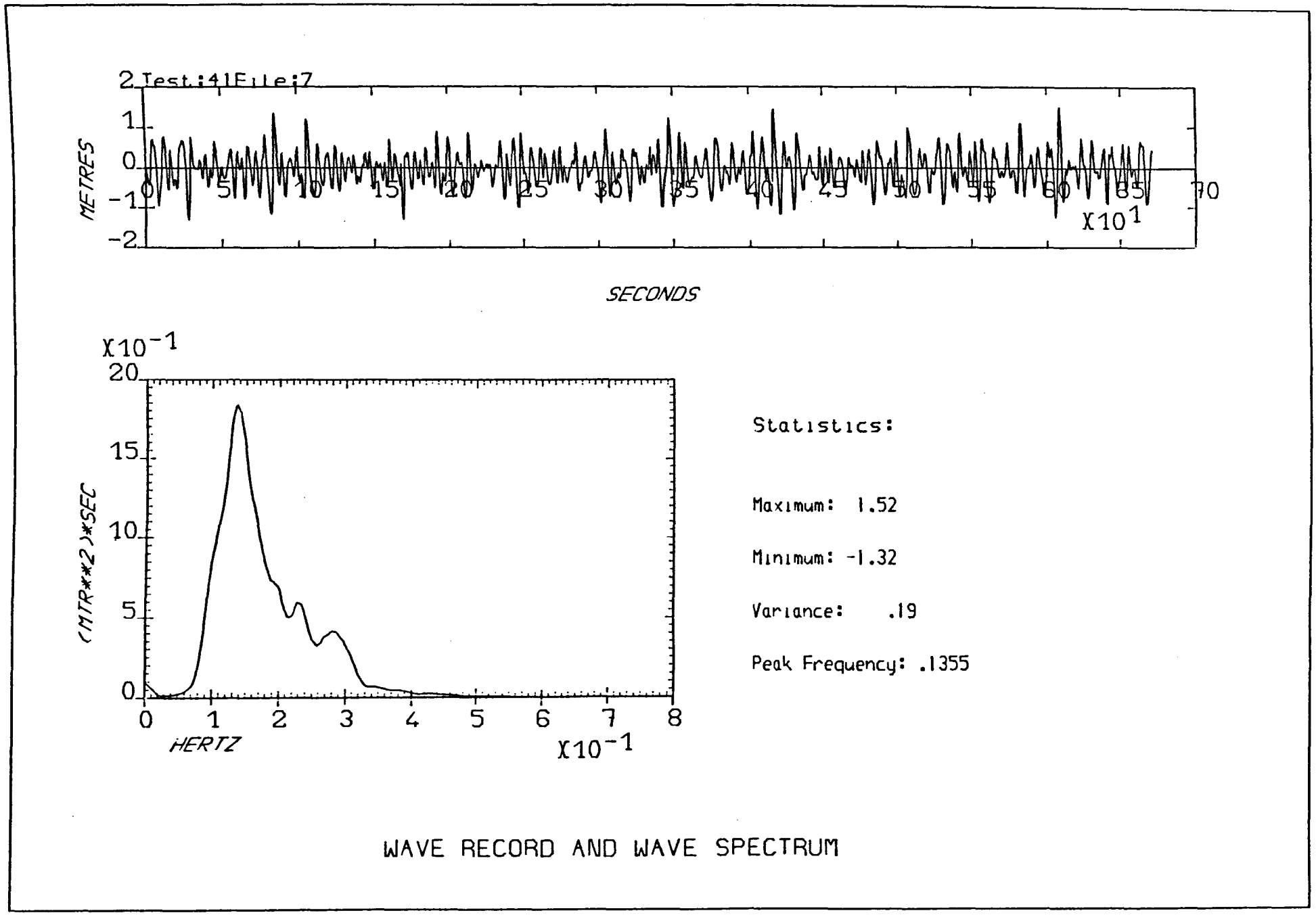

Figure 4.2 SEA2: wave record and spectrum

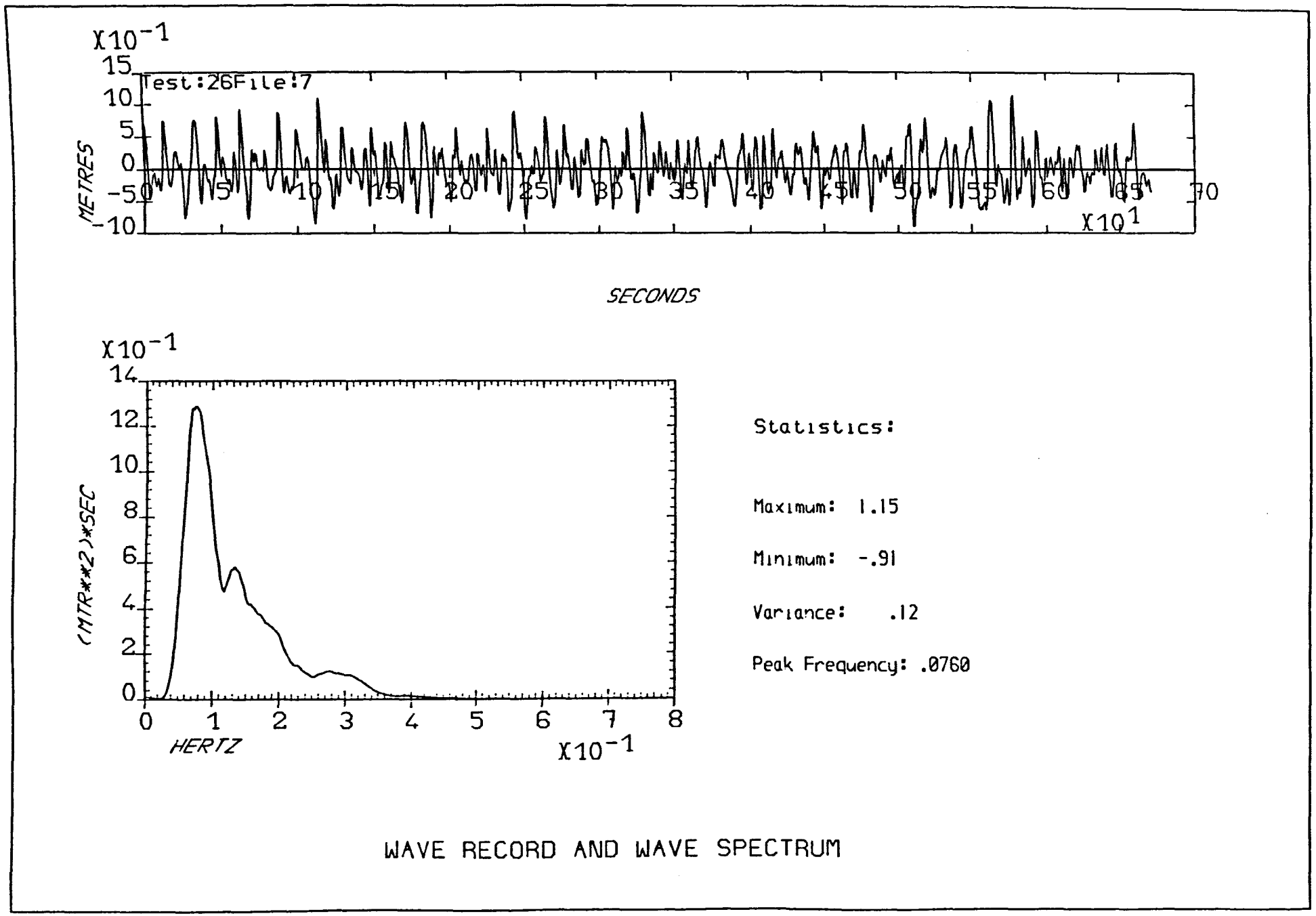

Figure 4.3 SEA3: wave record and spectrum

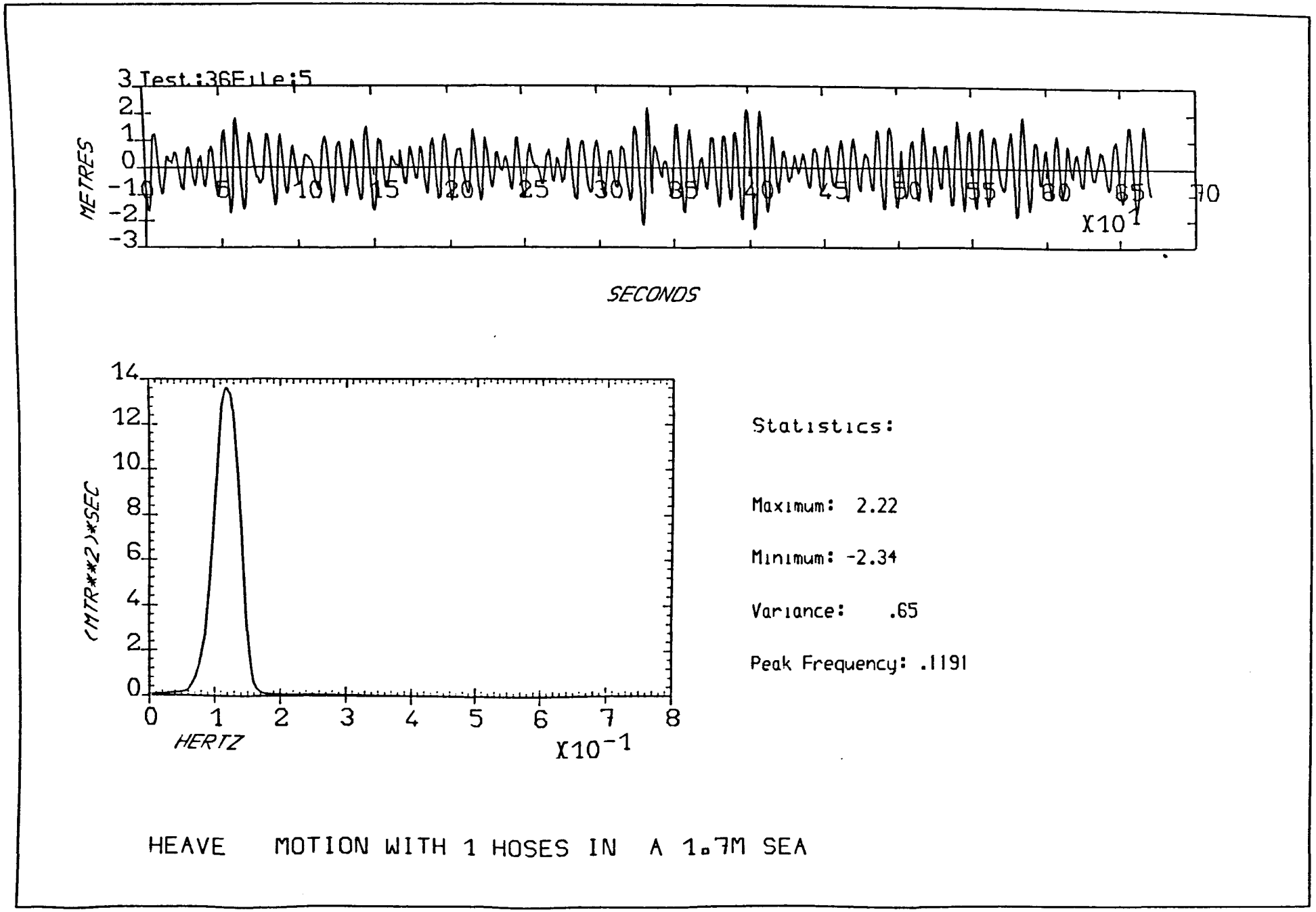

Figure 4.4 Measured heave in SEA2

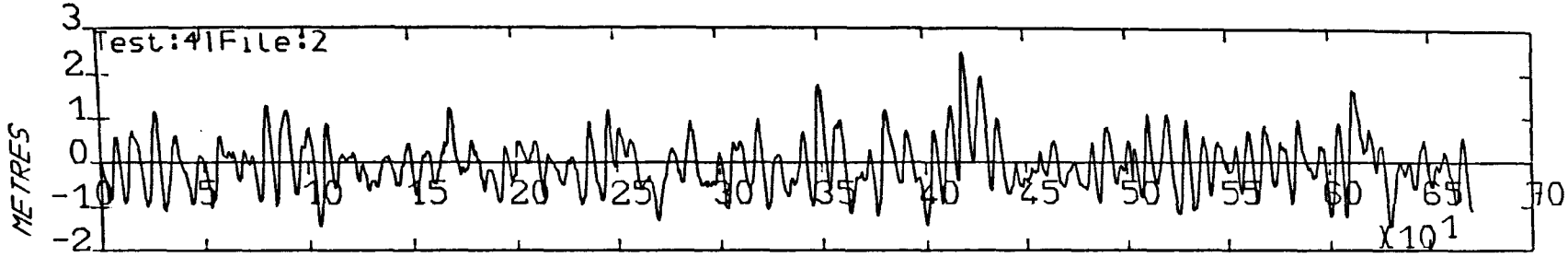

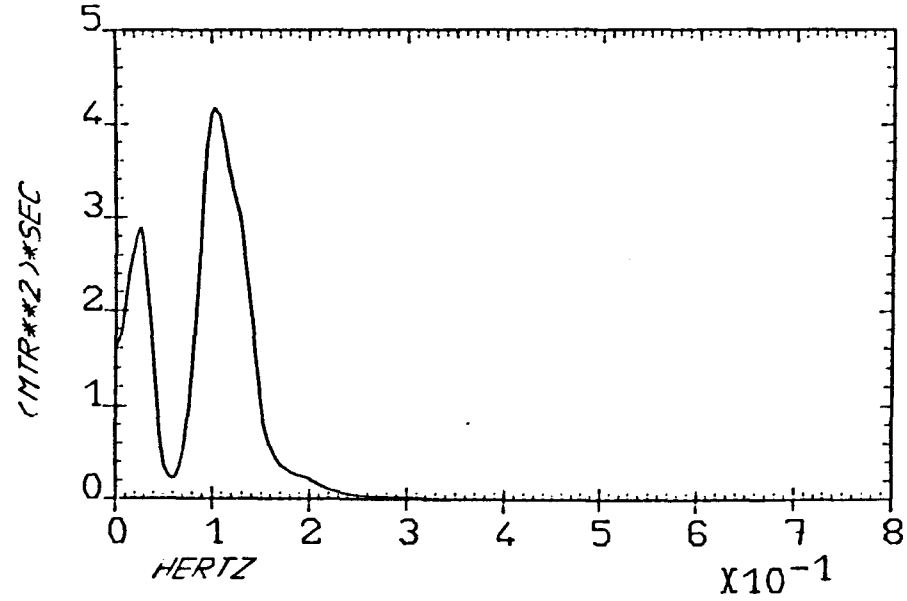

Statistics:

Maximum: 2.49

Minimum: -1.45

Variance: .35

Peak Frequency: .1028

SURGE MOTION WITH 1 HOSES IN A 1.8M SEA

Figure 4.5 Measured surge in SEA2

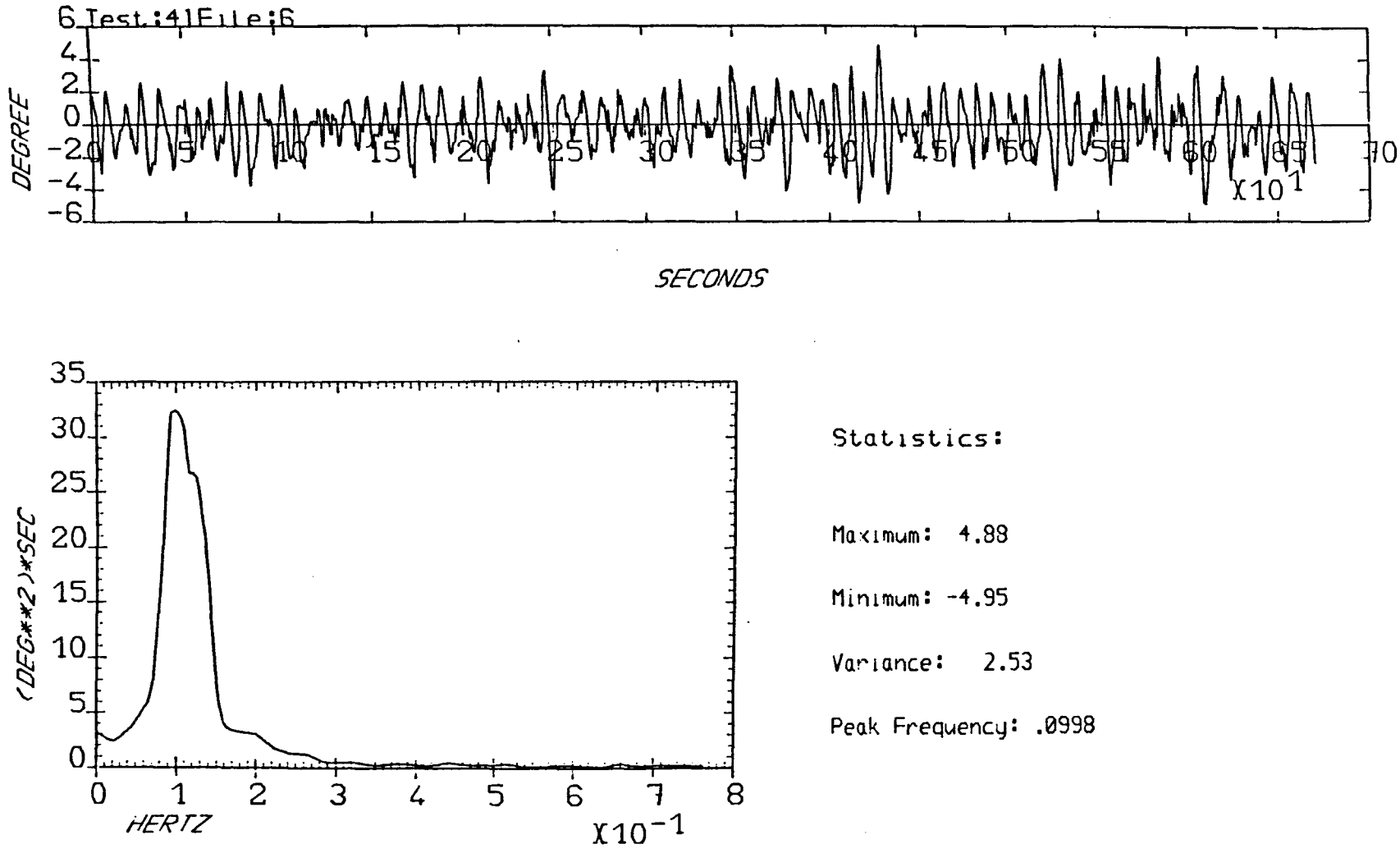

Figure 4.6 Measured pitch in SEA2

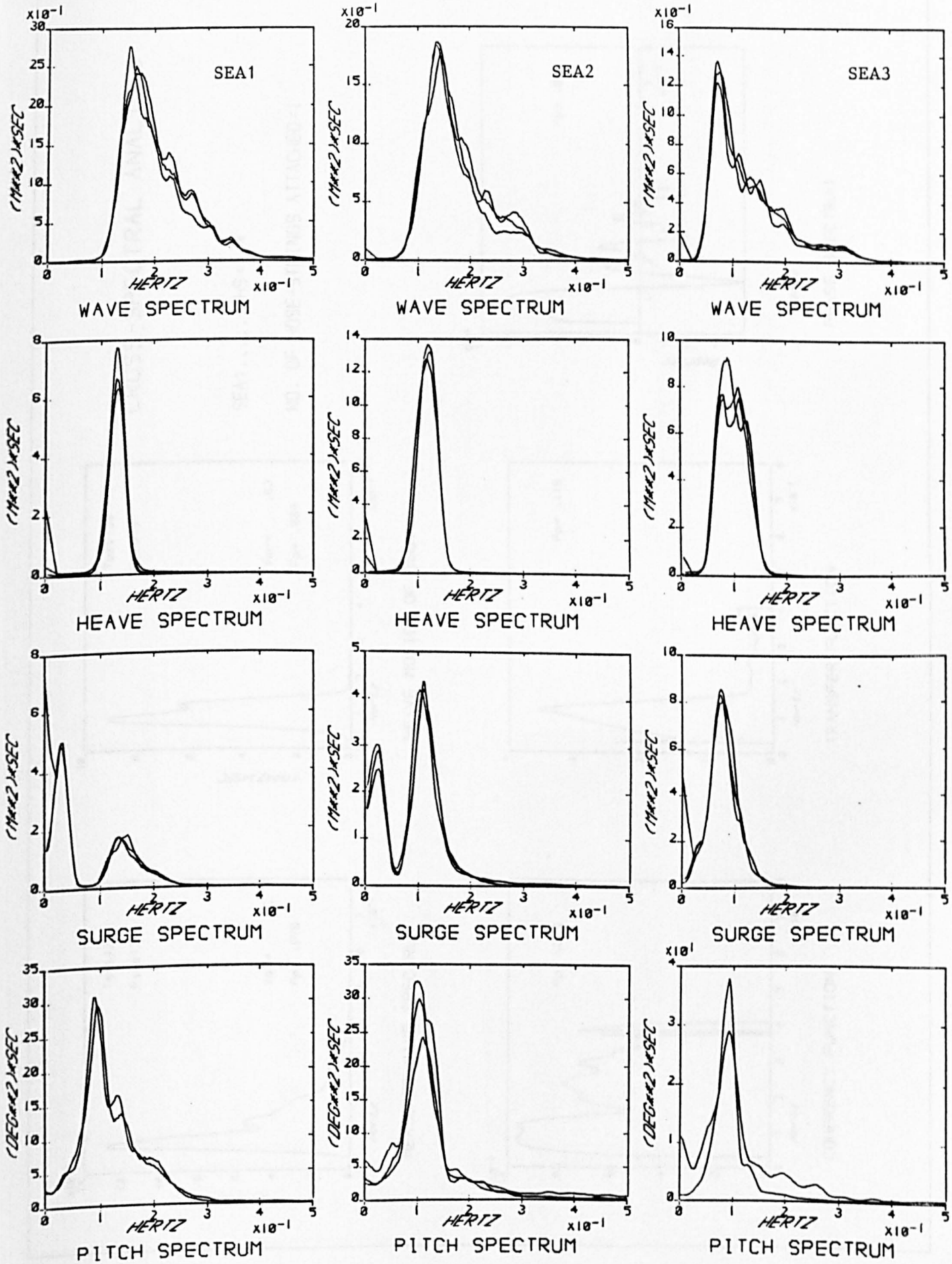

Figure 4.7 Measured wave, heave, surge and pitch spectra

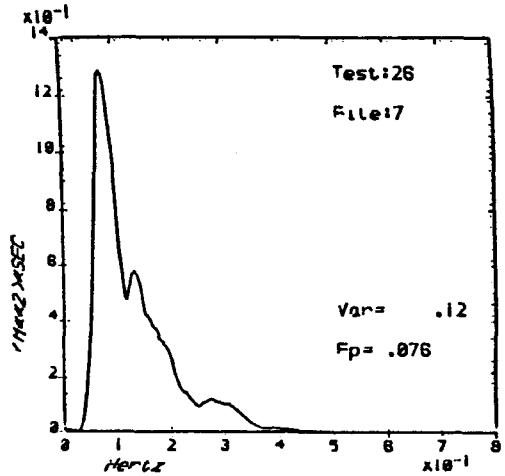

MEASURED WAVE SPECTRUM

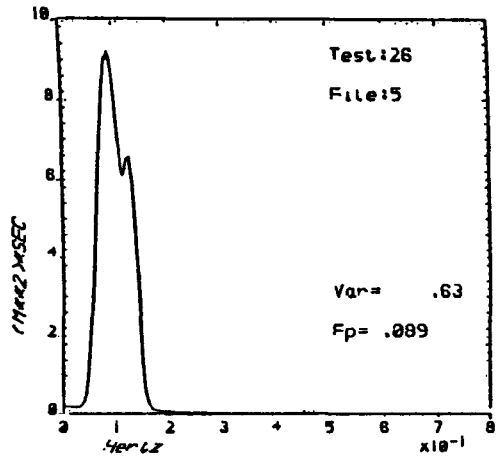

HEAVE MOTION OF BUOY

CROSS-SPECTRAL ANALYSIS

SEA:.....HS=1.4

NO. OF HOSE-STRINGS ATTACHED=1

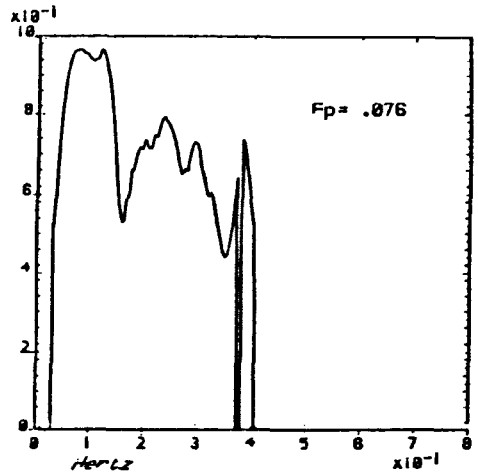

COHERENCY FUNCTION

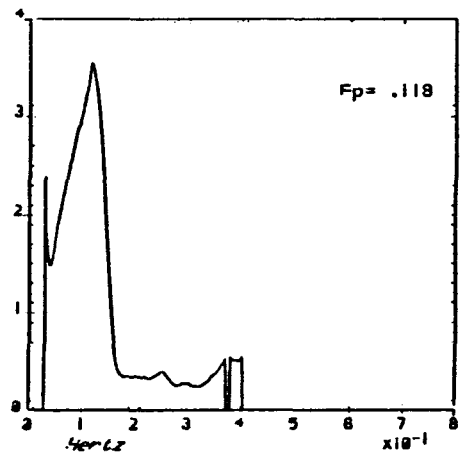

TRANSFER FUNCTION

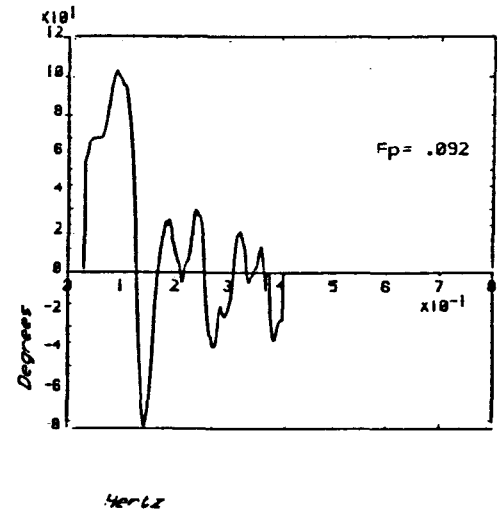

PHASE SPECTRUM

Figure 4.8 Cross-spectral analysis result: wave-heave in SEA3

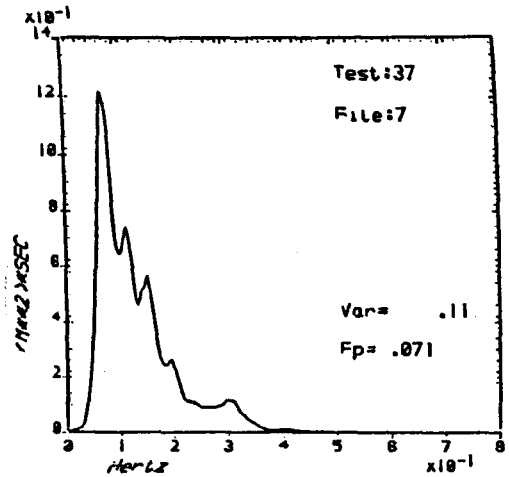

MEASURED WAVE SPECTRUM

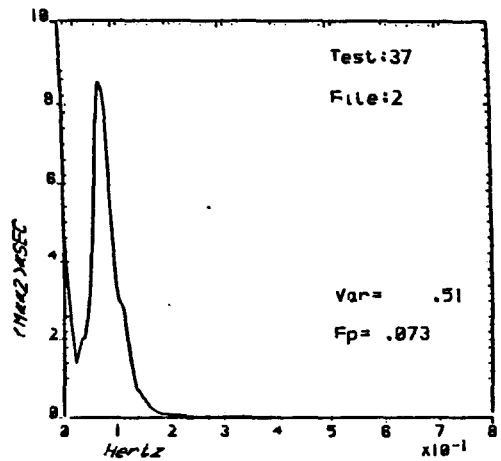

SURGE MOTION OF BUOY

CROSS-SPECTRAL ANALYSIS

SEA:.....HS=1.4

NO. OF HOSE-STRINGS ATTACHED=1

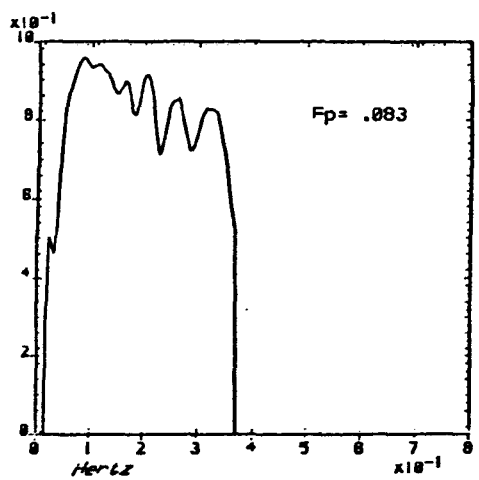

COHERENCY FUNCTION

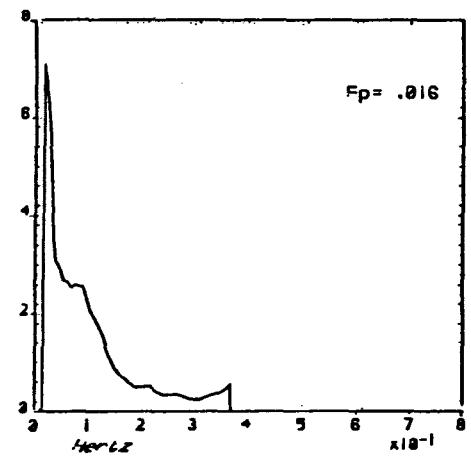

TRANSFER FUNCTION

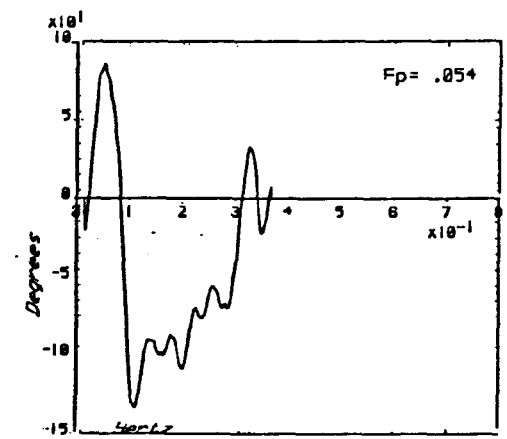

PHASE SPECTRUM

Figure 4.9 Cross-spectral analysis result: wave-surge in SEA3

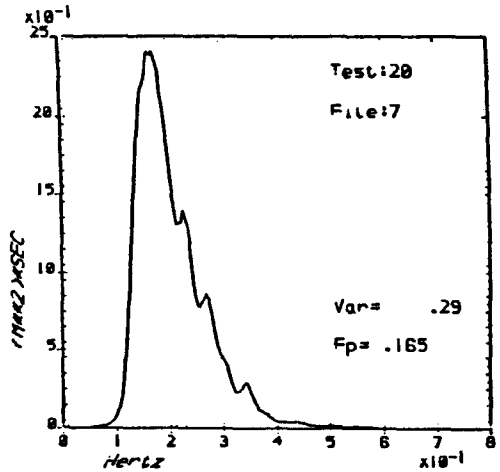

MEASURED WAVE SPECTRUM

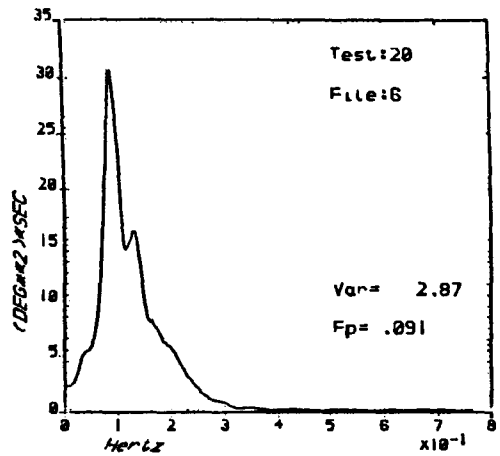

PITCH MOTION OF BUOY

CROSS-SPECTRAL ANALYSIS

SEA:.....HS=2.1

NO. OF HOSE-STRINGS ATTACHED=1

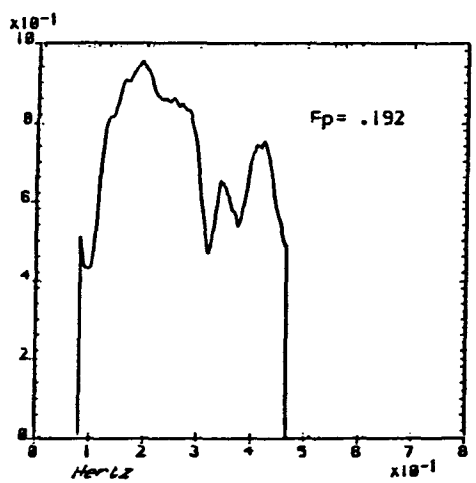

COHERENCY FUNCTION

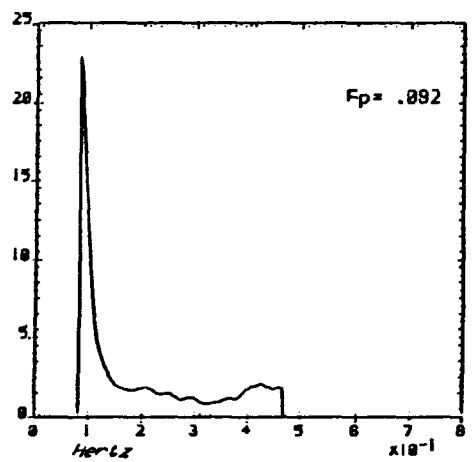

TRANSFER FUNCTION

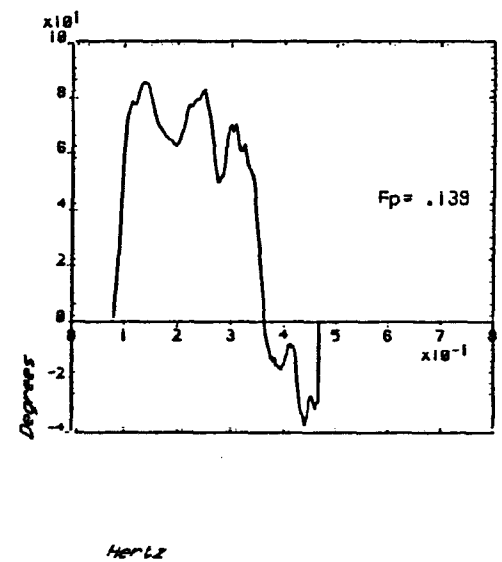

PHASE SPECTRUM

Figure 4.10 Cross-spectral analysis result: wave-pitch in SEA1

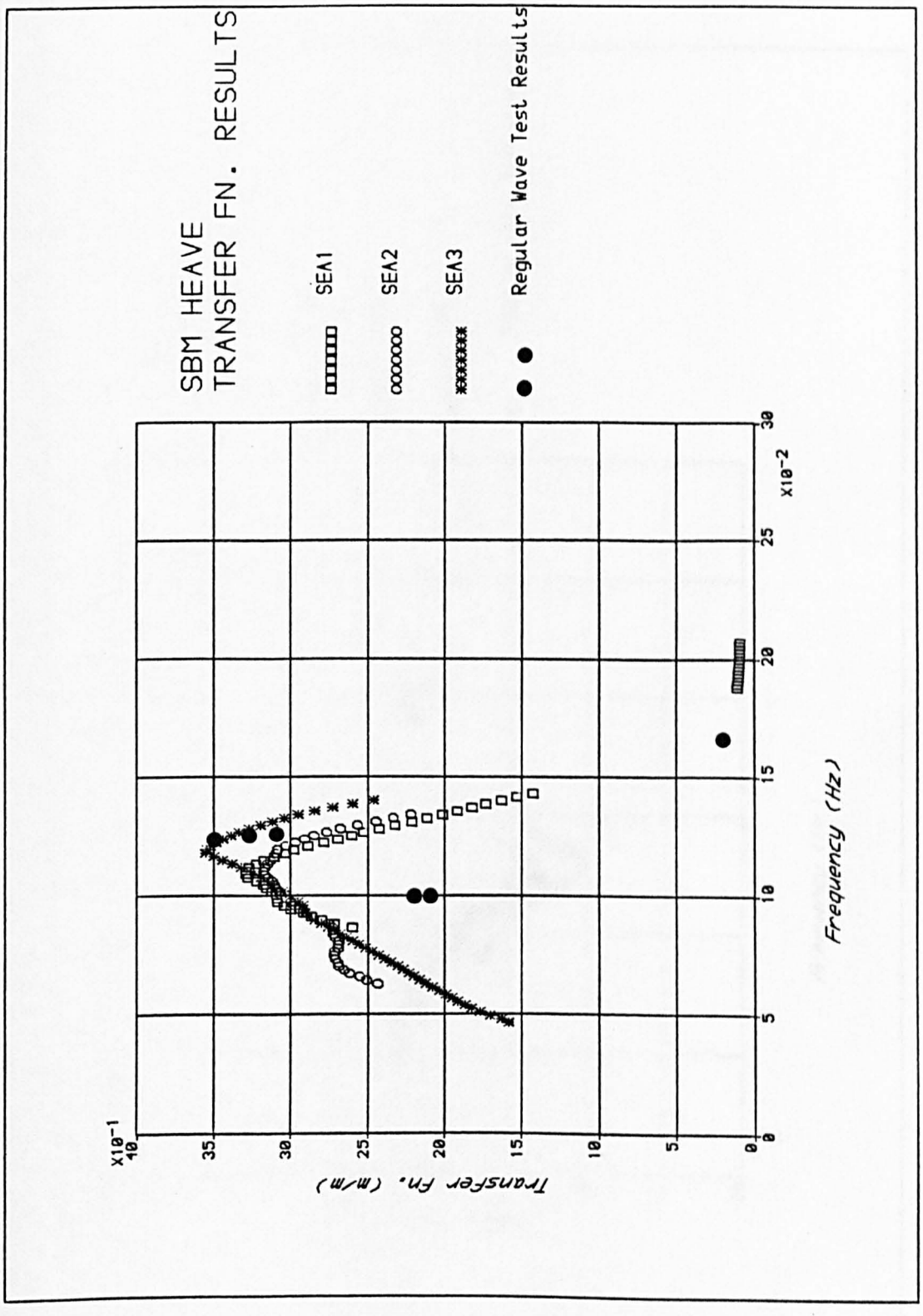

Figure 4.11(i) SBM heave transfer function from model tests

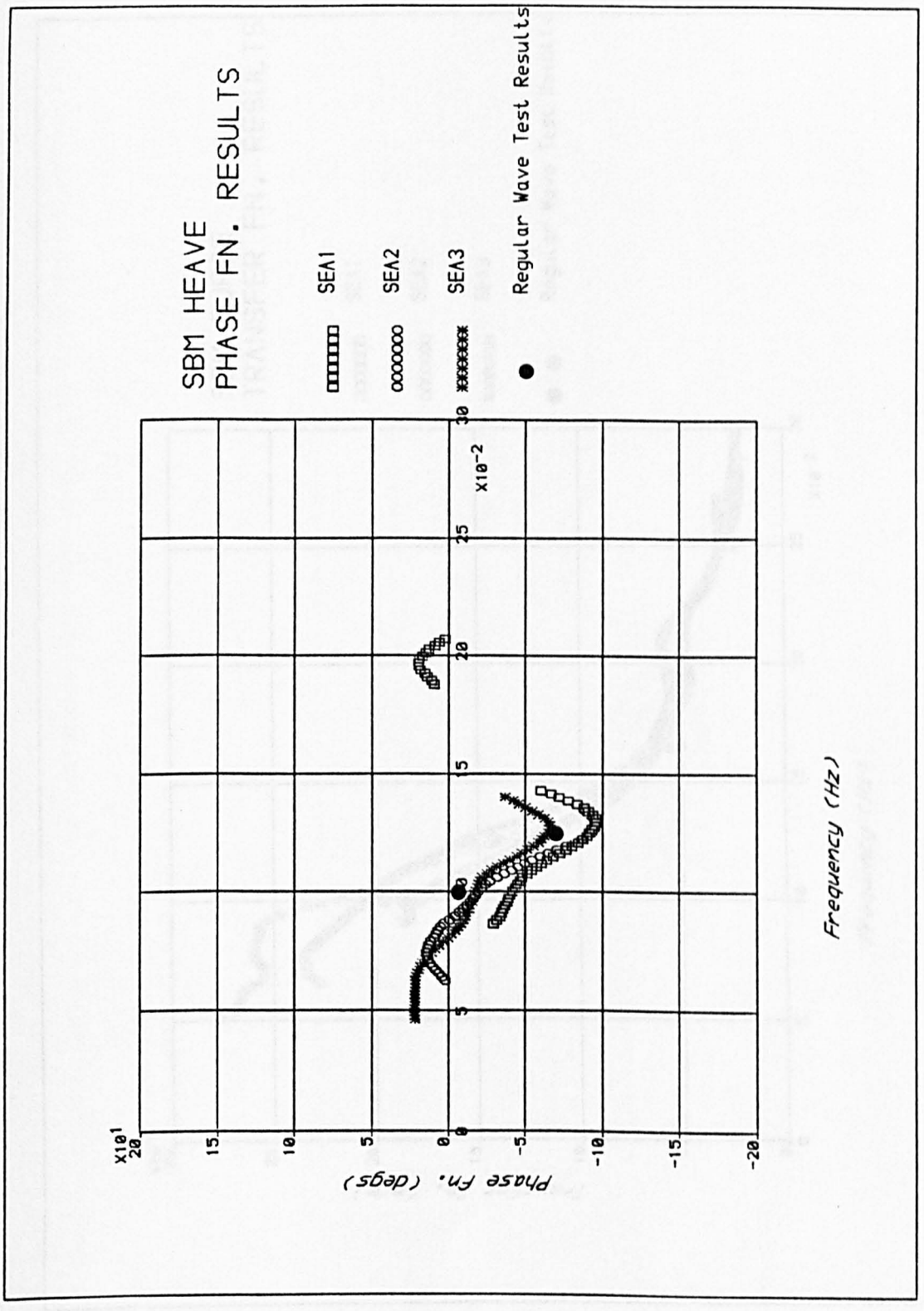

Figure 4.11(ii) SBM heave phase function from model tests

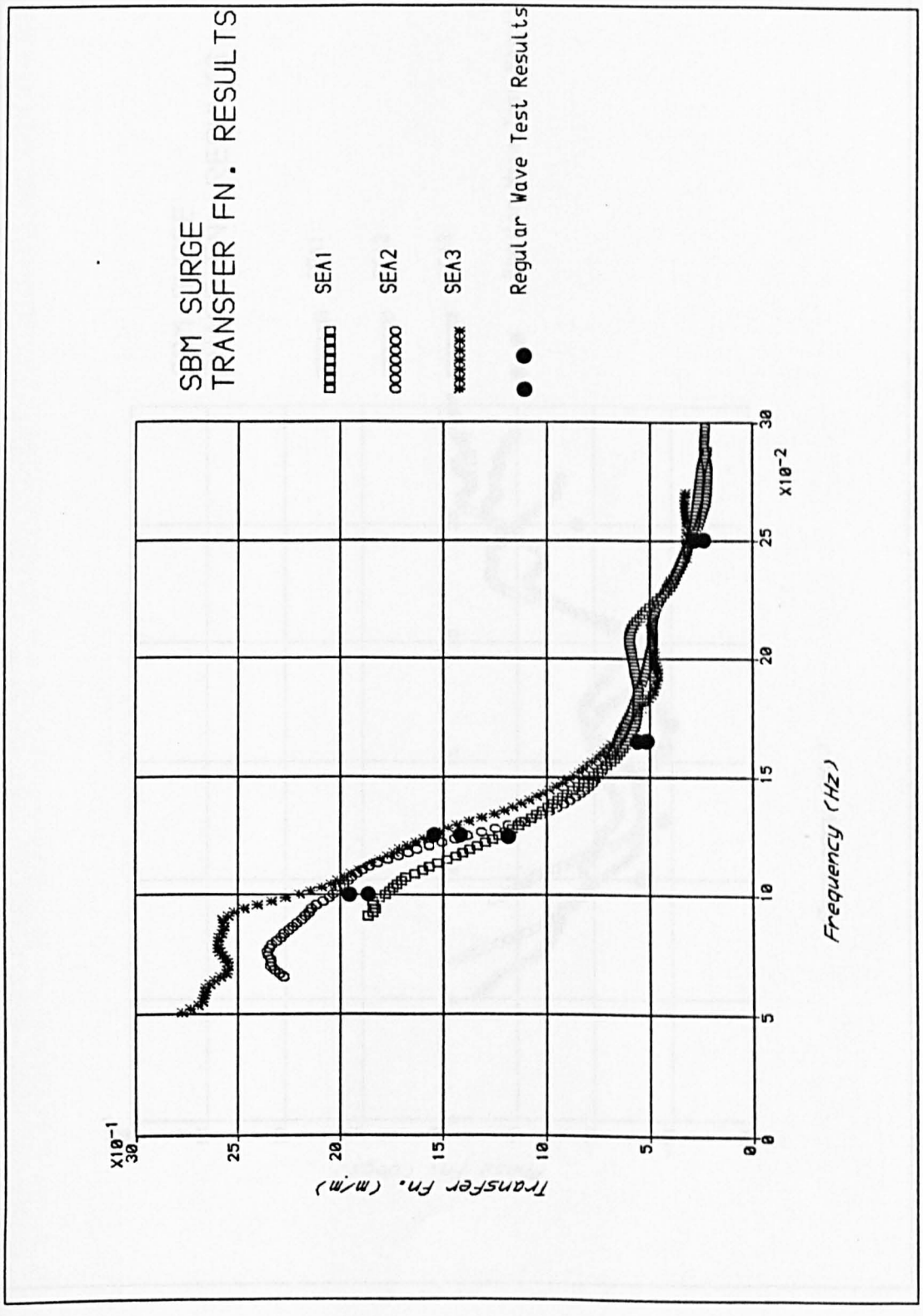

Figure 4.12(i) SBM surge transfer function from model tests

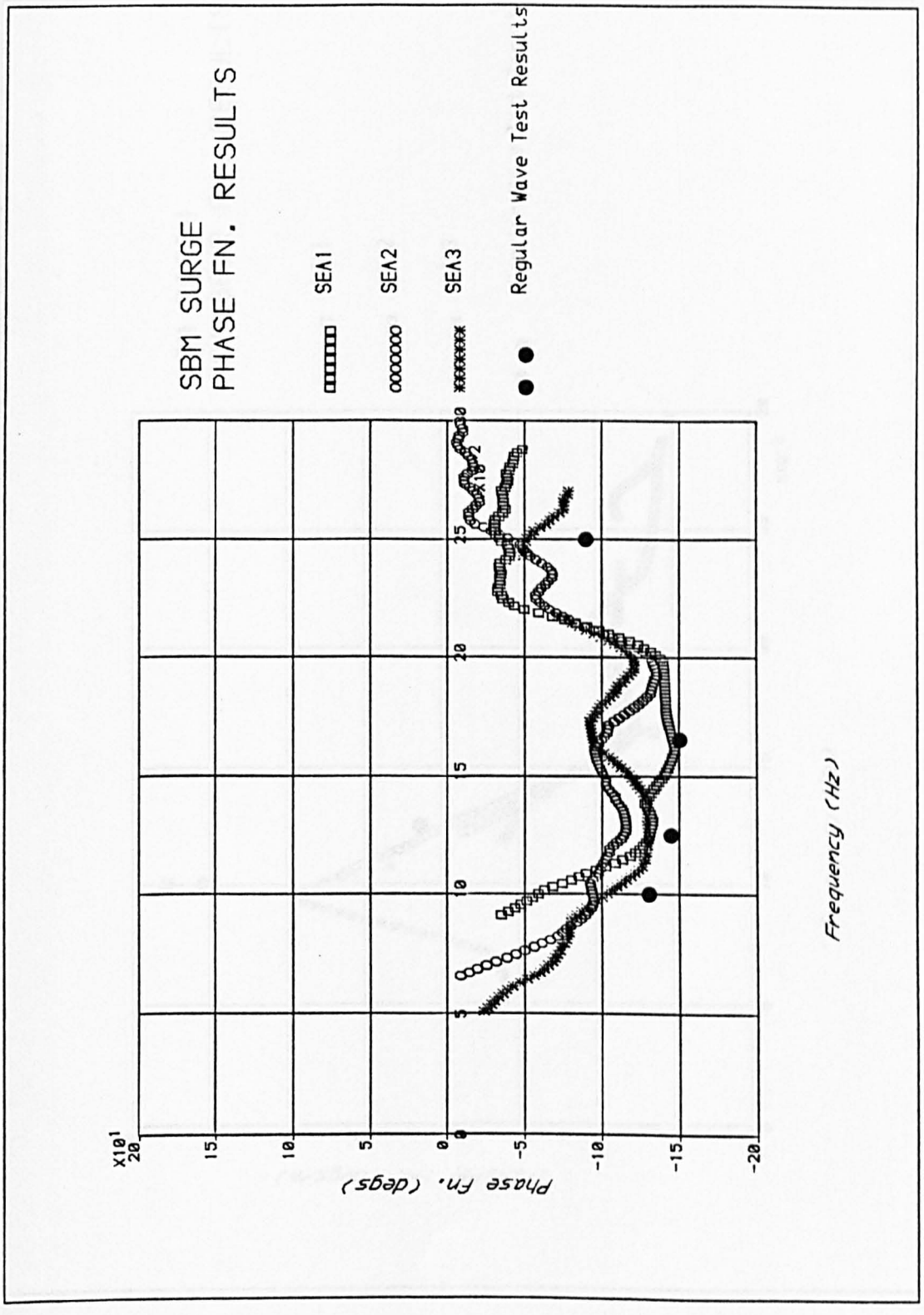

Figure 4.12(ii) SBM surge phase function from model tests

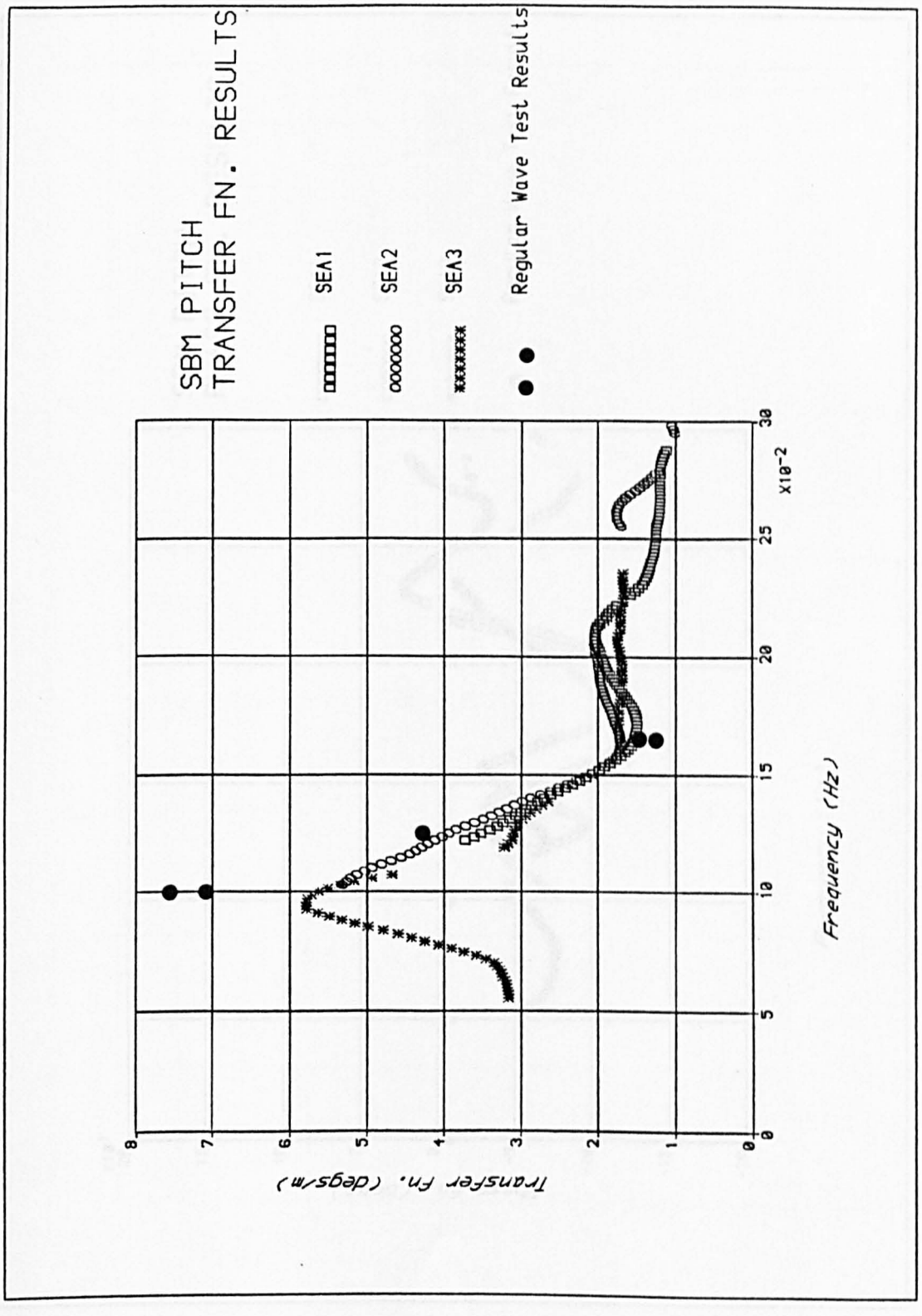

Figure 4.13(i) SBM pitch transfer function from model tests

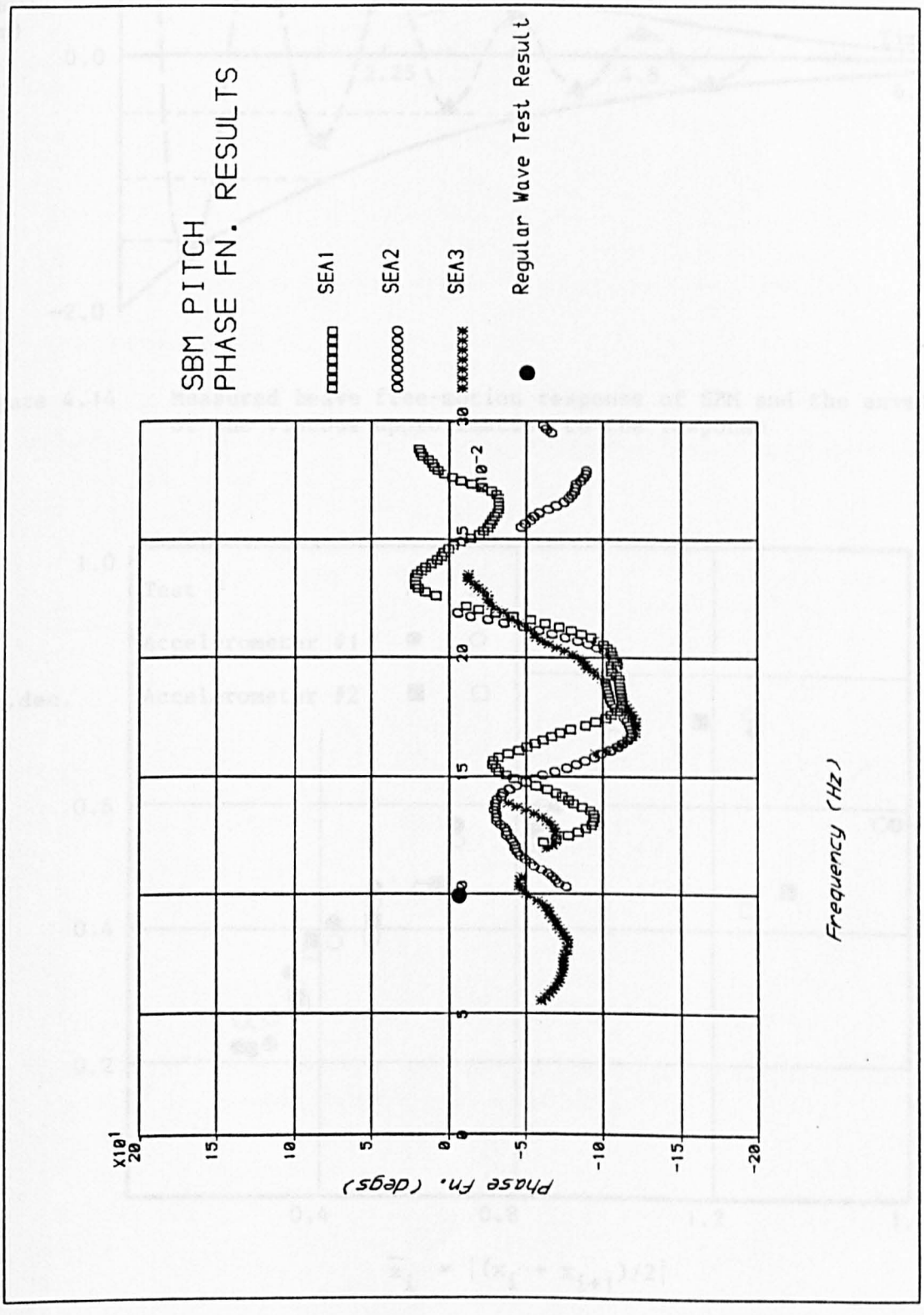

Figure 4.13(ii) SBM pitch phase function from model tests

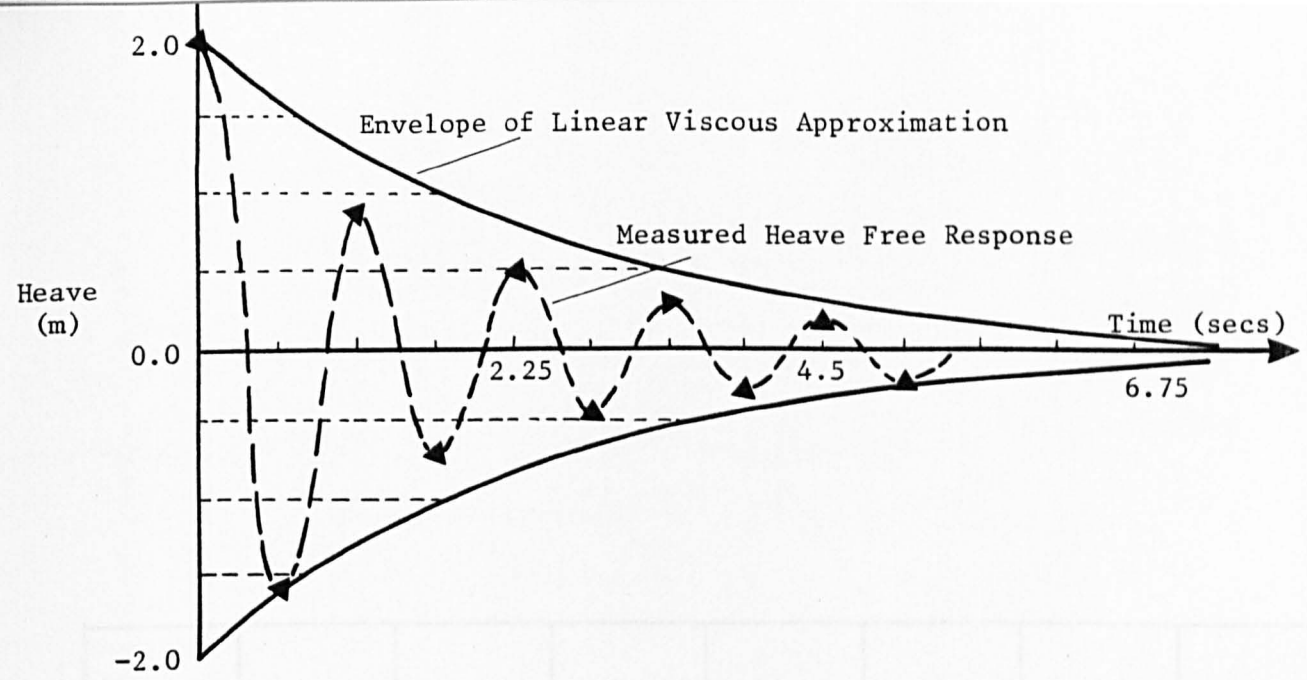

Figure 4.14 Measured heave free-motion response of SBM and the envelope of the viscous approximation to the response

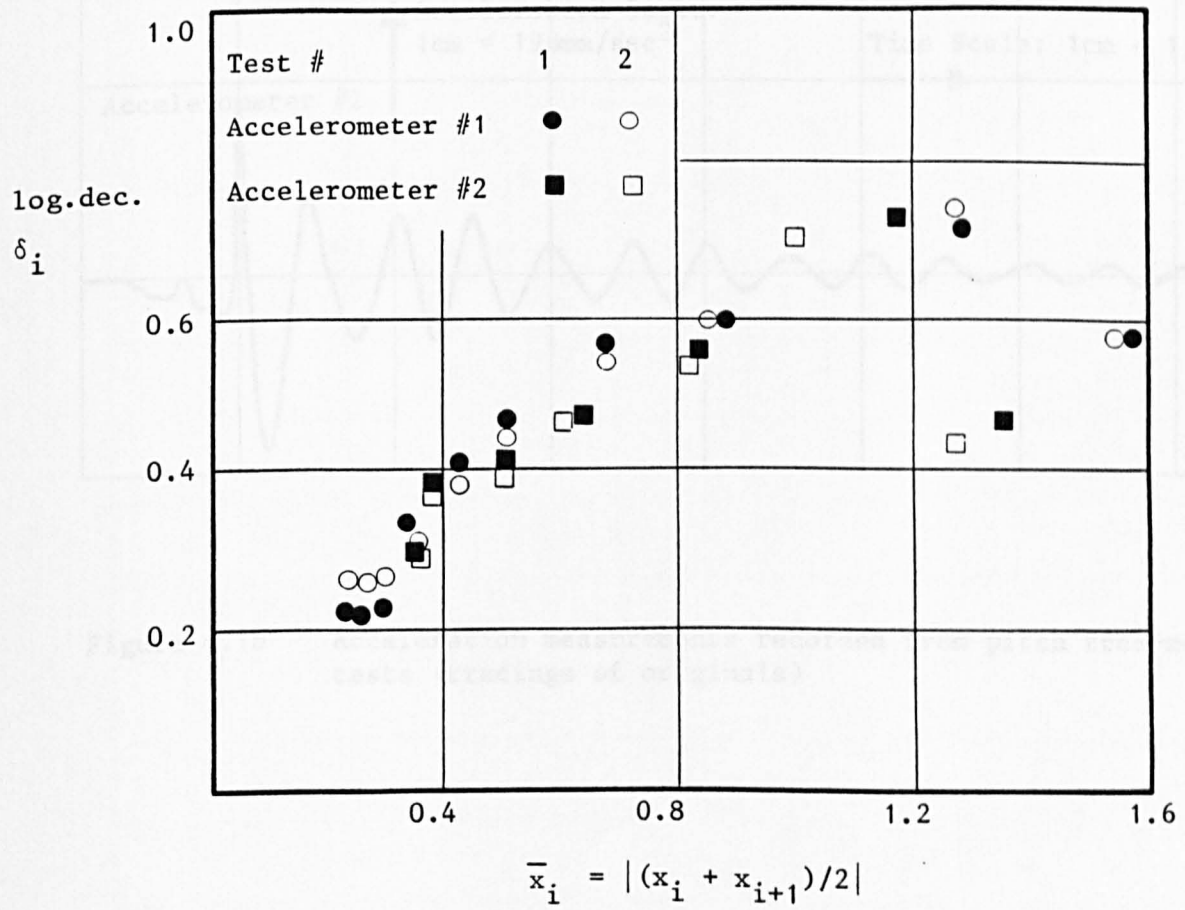

Figure 4.15 Logarithmic decrement versus mean of two successive maxima in heave free response

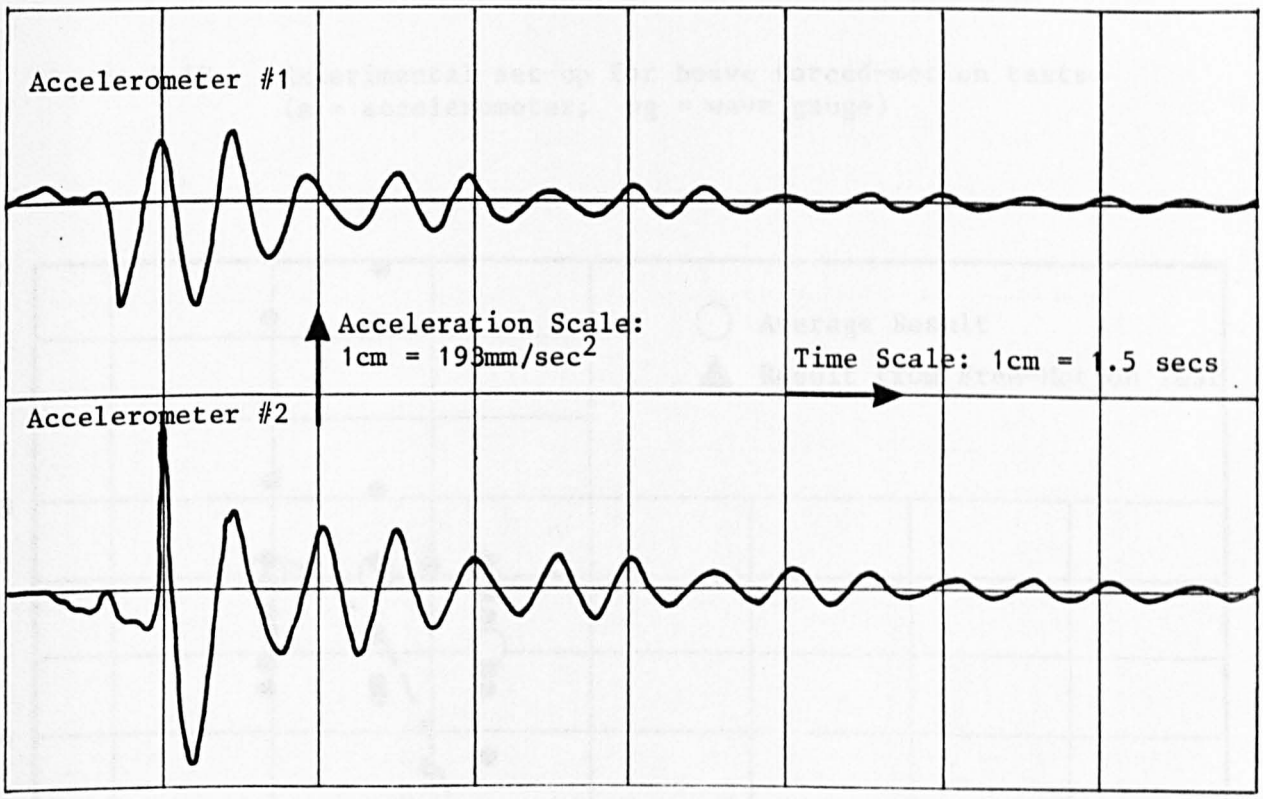

Figure 4.16 Acceleration measurements recorded from pitch free-motion tests (tracings of originals)

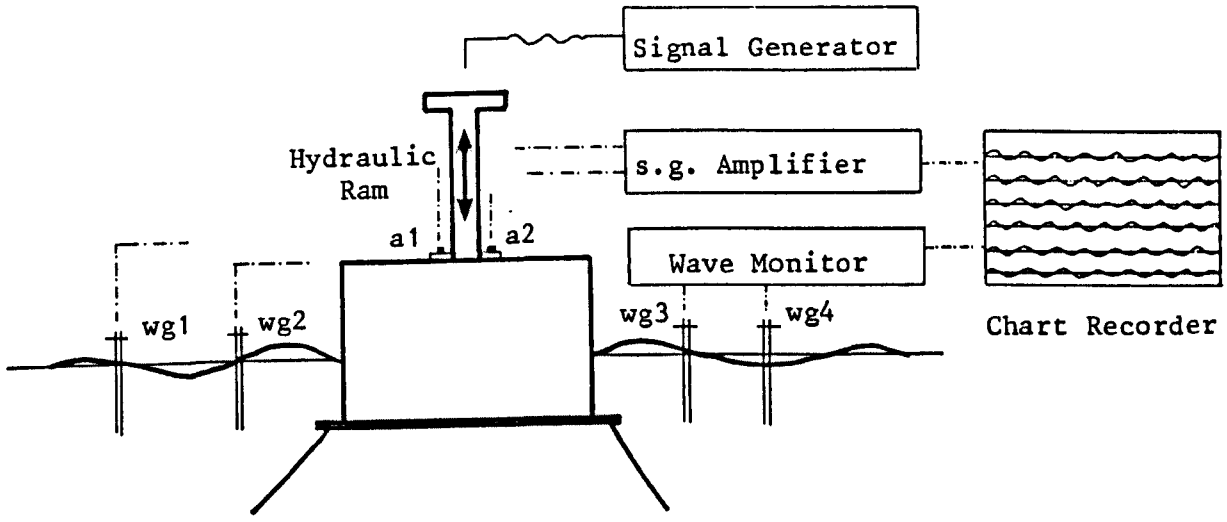

Figure 4.17 Experimental set-up for heave forced-motion tests (a = accelerometer; wg = wave gauge)

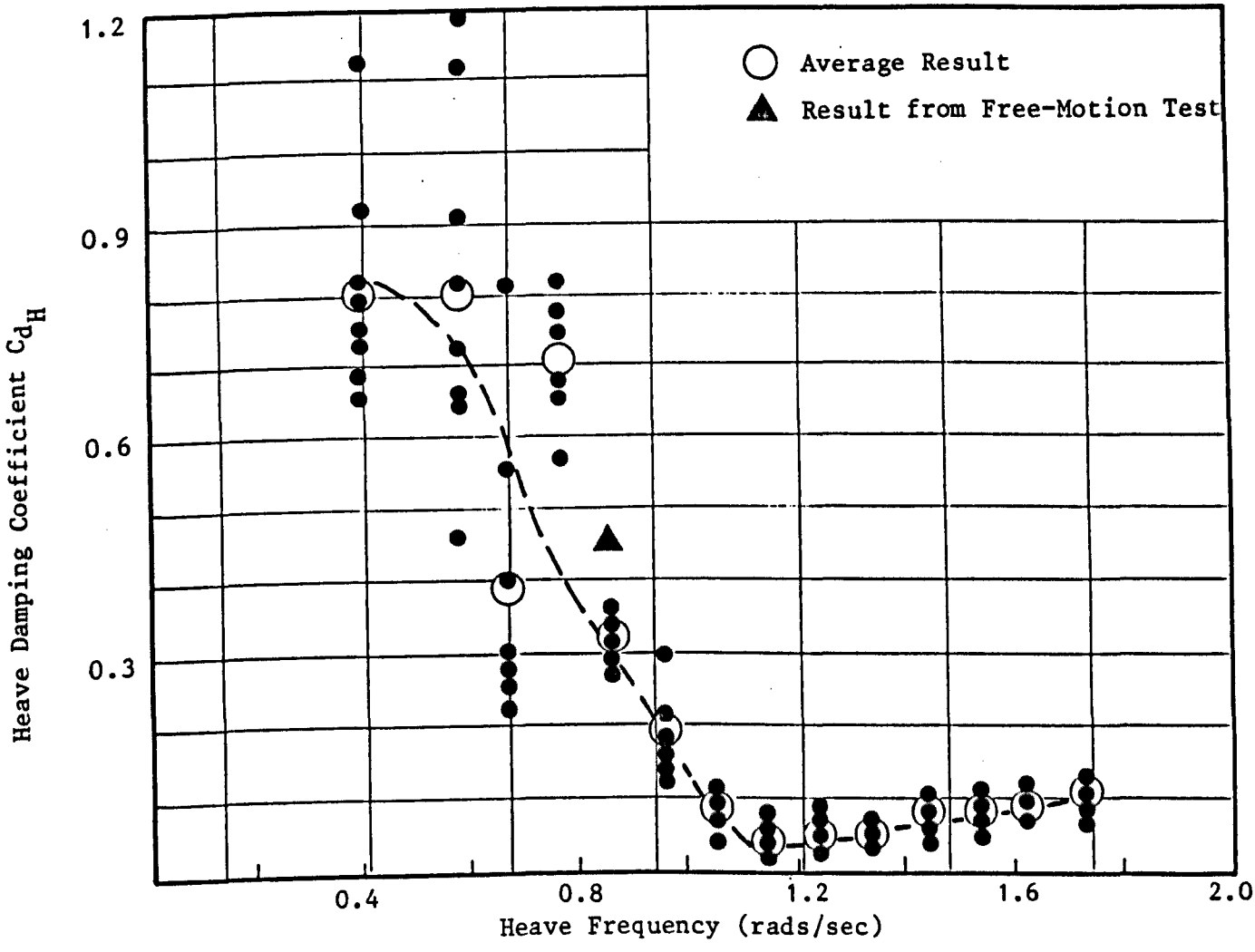

Figure 4.18 Heave damping coefficients from heave forced-motion tests

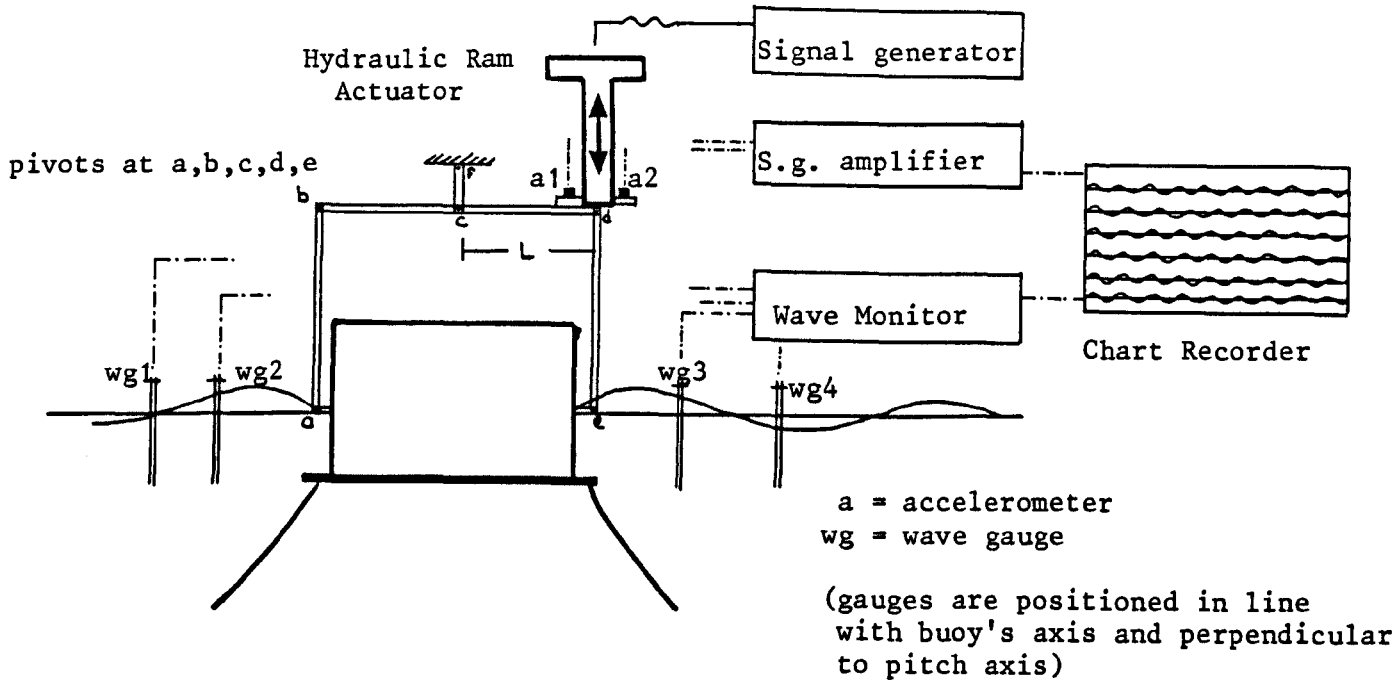

Figure 4.19 Experimental set-up for pitch forced-motion tests

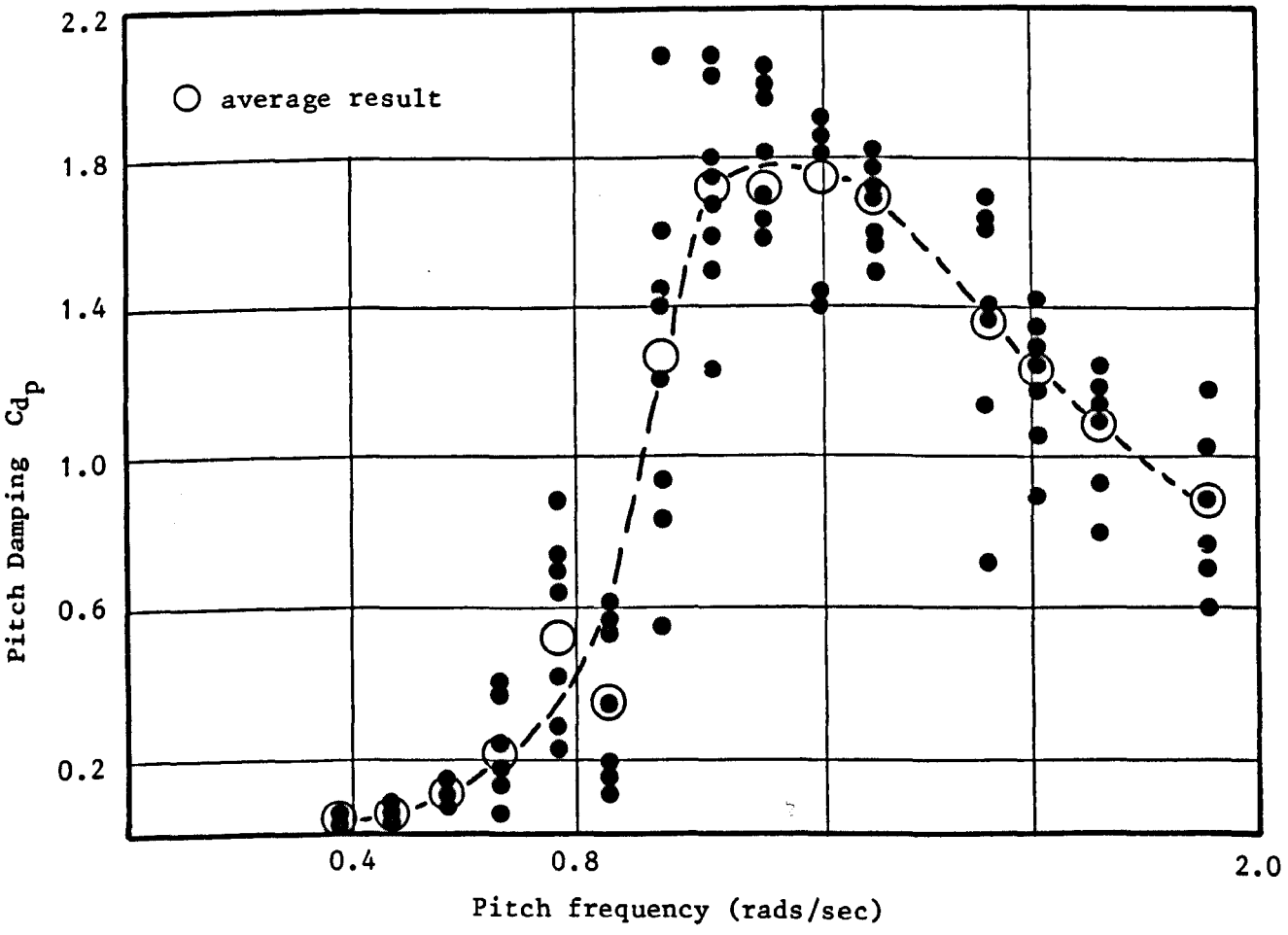

Figure 4.20 Pitch damping coefficients from pitch forced-motion tests

5. MODEL TEST RESULTS: BENDING MOMENTS AND AXIAL LOADS ALONG THE HOSE-STRING

The objective of this chapter is to establish from the model test measurements the magnitudes of the bending moments and axial loads along the hose-string in waves and their dependence on the SBM's motions and the waves.

5.1 Vertical Bending

Vertical bending has been measured at ten positions along the hose-string in the three irregular seas SEA1, SEA2 and SEA3 and in regular waves with f = 0.1, 0.125, 0.167 and 0.25Hz. Each of the 70 vertical bending moment records obtained has been analysed for its spectrum and basic statistical properties using the computer program ANAL1.

To accurately measure the vertical bending moment at a position on the hose-string, the transducer must be placed with its strain-gauged plate parallel to the water surface and must remain in that plane throughout the test. Since the alignment of a transducer can only be judged by eye there will always be some error in the measurement of vertical bending. If the hose-string snakes the magnitude of horizontal bending induced on the string is greater than the vertical bending and a poorly-aligned transducer will respond to a component of the horizontal bending. Snaking can cause the hose-string to twist so that a transducer accurately aligned in still water prior to a test may become poorly aligned during the test. The more accurate measurements of vertical bending are obtained in conditions when there is little or no snaking of the string. For this reason attention is focussed on the measurements of vertical bending obtained in the higher frequency wave conditions in which snaking is low, i.e. irregular waves SEA1 and regular waves with f = 0.25Hz and

f = 0.167Hz. Examples of the vertical bending moment measurements and their spectra obtained in these wave conditions are presented in Appendix A3.1.

Figure 5.1 presents the r.m.s. vertical bending measured along the hose-string in irregular waves SEA1, where r.m.s. is equal to the square root of the variance of the record. It is seen that the vertical bending is a maximum at the hose-buoy manifold and decays rapidly to reach a near-constant value at positions greater than 3. (Position #1 refers to the hose-buoy manifold; a unit increase in the position number corresponds to an increase in distance from the buoy of one hose length.) The vertical bending at the buoy depends on the buoy motions and the waves; the bending at positions away from the buoy is independent of the buoy motions and depends only on the waves. The same results may be observed in Figure 5.2 which shows the amplitude of vertical bending per metre wave amplitude measured along the string in regular waves with f = 0.25Hz.

Based on the results presented in Figures 5.1 and 5.2 it is proposed to consider separately (i) the relationship between the waves and vertical bending at positions away from the buoy and (ii) the relationship between vertical bending at the buoy and the waves and buoy motions.

5.1.1 Vertical Bending at Positions Away from the Buoy

The vertical bending at positions away from the buoy depends on the waves only. At these positions the wave-vertical bending mechanisms may be considered as a single input-single output mechanism with the waves as input and the vertical bending as output (response), as schematised in Figure 5.3. If the system is linear then the wave spectrum $S_{\eta\eta}(f)$ is related to the vertical bending spectrum $S_{MM}(f)$ by

$$S_{MM}(f) = |H_{\eta M}(f)|^2 S_{\eta\eta}(f) \qquad (5.1)$$

where $|H_{\eta M}(f)|$ is the wave-vertical bending transfer function for positions away from the buoy. The transfer function $|H_{\eta M}(f)|$ can, in principle, be obtained from a cross-spectral analysis between the measured waves and the vertical bending at any of the positions away from the buoy. However, because of the difficulties inherent in the measurement of vertical bending along the hose-string, estimates of the transfer function have been obtained from the cross-spectral analysis between the measured waves and vertical bending at each position on the hose-string greater than or equal to 3 measured in irregular waves SEA1. The complete cross-spectral analysis result for position 3 is shown in Figure 5.4 and the transfer function estimates obtained from each position are plotted in Figure 5.5. Only transfer function estimates obtained at frequencies for which the coherence is greater than 0.8 have been reproduced in Figure 5.5. Two regular wave results are included; these are the mean values of the vertical bending amplitude divided by the wave amplitude measured at positions greater than 3 in the regular wave tests with f = 0.1Hz and f = 0.167Hz.

The results presented in Figure 5.5 show a wide scatter, reflecting the difficulties inherent in measuring the vertical bending. The results do show a common underlying trend of increasing transfer function with increasing frequency. This is as expected since the hose-string is subject to greater curvature in the steeper, higher frequency waves. Figure 5.5 is incomplete in that no result is presented for frequencies less than 0.125Hz. This is due to SEA1 having no energy at frequencies less than 0.1Hz (Figure 4.7). However it is expected that the transfer

function will approach zero as the wave frequency decreases and the waves tend to low steepness.

The result given in Figure 5.5 is considered again in Chapter 8 when it is compared with the transfer function obtained from an analytical model for vertical bending.

5.1.2 Vertical Bending at the Hose-Buoy Manifold

The difficulties associated with measuring vertical bending along the hose-string do not apply at the hose-buoy manifold because the transducer can be positioned relatively accurately by screwing into the connecting piece on the buoy and is kept from twisting by the buoy's presence. Accordingly all of the vertical bending moment measurements recorded at the hose-buoy manifold in regular waves with f = 0.1, 0.125, 0.167 and 0.25Hz and in the irregular waves SEA1 and SEA3 are considered in what follows.

Vertical bending at the buoy depends on the frequency-dependent response of the buoy to the waves. It is the sum of components due to the heave, surge and pitch response of the buoy, i.e. $M(t) = M_y(t) + M_x(t) + M_\theta(t)$, and is therefore a single input-single output mechanism with multiple paths as schematised in Figure 5.6. (The function $H_{xy}(f)$ is the frequency response function between input x(t) and response y(t) and contains amplitude (transfer function) and phase (phase function) information.)

If the frequency response functions $H_{yM_y}(f)$, $H_{xM_x}(f)$ and $H_{\theta M_\theta}(f)$ (Figure 5.6) can be established then the separate contributions of the heave, surge and pitch of the buoy to the total vertical bending M(t) can be found and the vertical bending of the hose attached to any buoy with known response functions $H_{\eta y}(f)$, $H_{\eta x}(f)$ and $H_{\eta\theta}(f)$ can be predicted. However,

the following analysis shows that the response functions $H_{yM_y}(f)$, $H_{xM_x}(f)$ and $H_{\theta M_\theta}(f)$ cannot be obtained from an analysis of the measured buoy motions y(t), x(t) and θ(t) and the measured vertical bending M(t):

The cross-spectral analysis between the measured heave y(t) and the measured vertical bending M(t) yields the frequency response function $H_{yM}(f)$. Since heave, surge and pitch are coherent with the waves and therefore coherent with each other, we have

$$H_{yM} = H_{yM_y} + H_{yx}H_{xM_x} + H_{yx}H_{x\theta}H_{\theta M_\theta} \tag{5.2}$$

(where '(f)' has been eliminated for ease of presentation).

Similarly

$$H_{xM} = H_{yM_y}/H_{yx} + H_{xM_x} + H_{x\theta}H_{\theta M_\theta} \tag{5.3}$$

and

$$H_{\theta M} = H_{yM_y}/(H_{yx}H_{x\theta}) + H_{xM_x}/H_{x\theta} + H_{\theta M_\theta} \tag{5.4}$$

Writing equations (5.2) to (5.4) in matrix form gives

$$\begin{bmatrix} 1 & H_{yx} & H_{yx}H_{x\theta} \\ 1/H_{yx} & 1 & H_{x\theta} \\ 1/(H_{yx}H_{x\theta}) & 1/H_{x\theta} & 1 \end{bmatrix} \begin{Bmatrix} H_{yM_y} \\ H_{xM_x} \\ H_{\theta M_\theta} \end{Bmatrix} = \begin{Bmatrix} H_{yM} \\ H_{xM} \\ H_{\theta M} \end{Bmatrix} \tag{5.5}$$

or, simply,

$$[A]\{a\} = \{b\} \tag{5.6}$$

Each of the terms in [A] and {b} may be obtained from cross-spectral analysis between the measured responses; but det{a} = 0 and equations (5.6) cannot therefore be solved for H_{yM_y}, H_{xM_x} and $H_{\theta M_\theta}$.

The only way to establish the frequency response functions which quantify the separate contribution of each buoy motion to the total vertical bending at the buoy is to conduct separate model tests in which the buoy is constrained to move in heave only, surge only and pitch only.

The transfer function between the incident waves and vertical bending at the buoy, for the particular SBM used in the model tests, can be obtained from a cross-spectral analysis between the measured waves and vertical bending in the irregular waves SEA1 and SEA3. The results of the analyses are presented in Figures 5.7 and 5.8. The transfer function results at those frequencies for which the coherence is greater than 0.8 are reproduced in Figure 5.9, together with the transfer function results obtained from the regular wave tests.

The transfer function results obtained from the regular and irregular wave tests are in general good agreement. The transfer function peaks at around 0.12Hz, suggesting a strong dependence on the SBM's heave which also peaks at about 0.12Hz (Figure 4.11). As the frequency decreases from 0.12Hz the transfer function also decreases; this may be due to the increasing tendency of the buoy to heave in phase with and with the same amplitude as the waves, as frequency tends to low values. The response of the SBM in high frequency waves is low and the vertical bending at the buoy is then due to the wave loading on the hose-string.

It is emphasised that the transfer function presented in Figure 5.9

applies to the particular SBM considered in this study. The transfer function for a different SBM will differ from that presented in Figure 5.9 if its response functions $H_{\eta y}(f)$, $H_{\eta x}(f)$ and $H_{\eta\theta}(f)$ (Figure 5.6) are not the same as those of the SBM studied here.

5.2 Snaking and Horizontal Bending

Under certain conditions of waves and buoy motions the hose-string takes on a sinewave shape close to the buoy, transverse to the direction of wave travel and in the plane of the water surface. The sine wave travels the length of the hose-string decaying in amplitude as it does so. This phenomenon - already referred to as snaking - results in bending moments induced on the hose-string which are in the plane of the water surface. These moments are referred to as the horizontal bending moments.

Plates 5.1, 5.2 and 5.3 show snaking in regular waves. It was clear from the model tests that a snake originates when the buoy surges. Moreover, for one complete snake cycle - the hose is deflected to the side, returns to the mean position, deflects to the other side and returns again to the mean position - the buoy completes two surge cycles. This means that the snake frequency is half the surge frequency. The mechanism of wave-surge-horizontal bending is therefore non-linear and linear cross-spectral analysis does not apply.

Because snaking occurs when the buoy surges, only those horizontal bending moment measurements obtained in the lower frequency waves are considered in what follows (the buoy surges little in the higher frequency waves); i.e. attention is focussed on the horizontal bending moment measurements obtained in regular waves with f = 0.1Hz and f = 0.125Hz and in the irregular waves SEA2 and SEA3. Appendix A3.2 presents examples of the

horizontal bending moment measurements and their spectra obtained in these wave conditions.

Figure 5.10 shows the horizontal bending moment record and its spectrum for position 2 in regular waves with f = 0.125Hz. The record is almost sinusoidal with frequency 0.064Hz, that is almost exactly half the incident wave and surge frequency. Figure 5.11 shows the horizontal bending moment and its spectrum recorded at position 4 in SEA2. The peak in the spectrum occurs at 0.049Hz which is almost exactly half the peak frequency of the surge spectrum in SEA2 (0.11Hz, Figure 4.7). Figure 5.12 shows the horizontal bending for position 4 in SEA3; again the peak spectral frequency value of 0.035Hz is half the peak frequency of the surge spectrum in SEA3 (0.07Hz, Figure 4.7).

The fact that snaking and horizontal bending occurs with frequency that is half the surge frequency allows a poor measurement of horizontal bending, caused by poor transducer alignment, to be identified since the measurement will contain significant energy at the wave frequencies.

5.2.1 Measurements of Horizontal Bending

Figures 5.13 and 5.14 present the simultaneous measurements of the surge motion of the buoy and the horizontal bending at various positions on the hose-string recorded in the regular wave tests with f = 0.125Hz and f = 0.1Hz respectively. (The measurements of bending at positions 1, 3 and 10 are not shown as these were seen to contain significant energy at the wave frequencies.)

The measurements of horizontal bending in waves with f = 0.125Hz have a dominant frequency component at 0.064Hz, that is at half the wave and surge frequency, and has weak higher frequency components (for example,

Figure 5.10). The horizontal bending measurements recorded in waves with f = 0.1Hz exhibit the characteristics of beating: the snake response at 0.05Hz (half the surge frequency) waxes and wanes with a period of about 110 secs, that is with a beating frequency of about 0.009Hz. The beating results from the sum of two components with frequencies f_1 and f_2 which are close in value. The values of f_1 and f_2 may be obtained from the measured high frequency variation f_s = 0.05Hz and beating frequency f_b = 0.009Hz, since

$$(f_1 - f_2) = f_b$$
and
$$\frac{1}{2}(f_1 + f_2) = f_s \qquad (5.7)$$

Equations (5.7) give f_1 = 0.0545Hz and f_2 = 0.0455Hz. The frequency resolution of the spectral analysis is not sufficiently high for these frequency components to be recognised in the spectrum of the measured horizontal bending, as seen for example in Figure 5.15. The measured beating characteristics suggest that at least one natural mode of vibration of the hose-string is excited in regular waves with f = 0.1Hz.

The absolute maximum value of horizontal bending divided by the square root of the surge amplitude measured along the hose-string in the regular wave tests is presented in Figure 5.16. The square root of the surge amplitude is used for reasons that will become apparent later (Chapter 7). There are two distinct differences between the results for f = 0.125Hz and f = 0.1Hz.

Firstly, for equivalent surge amplitude, the bending of the hose-string at the end of the first-off-the-buoy hose (position 2) is greater when the surge frequency is 0.125Hz than when it is 0.1Hz. This is mainly due to

the higher surge frequency generating a snake of shorter wavelength, resulting in greater hose curvature.

Secondly, the horizontal bending in the case of f = 0.125Hz decays rapidly along the hose-string from a maximum at the end of the first-off-the-buoy hose; the decay is more gradual in the case of f = 0.1Hz. The forcing in the case of f = 0.125Hz generates a snake near to the buoy which decays in amplitude due to damping as it travels along the string. It is suggested that in the case of f = 0.1Hz natural modes of vibration of the hose-string are excited so that, though the bending due to snaking decays along the string, there remains the bending due to the natural vibration of the string.

The absolute maximum value of horizontal bending divided by the square root of the maximum surge amplitude measured along the hose-string in irregular waves SEA2 and SEA3 is presented in Figure 5.17. As for the regular wave test results the maximum bending of the hose-string occurs at the end of the first-off-the-buoy hose and is greater in the higher frequency waves SEA2. The wide frequency band of the forcing in the irregular wave conditions can excite a number of natural modes of vibration of the hose-string. This results in a decay of the bending moments measured along the hose-string that is similar to that obtained in the regular wave test with f = 0.1Hz. The simultaneous measurements of the surge motion of the buoy and the horizontal bending at locations along the hose-string obtained in the irregular waves SEA2 and SEA3 are presented in Figures 5.18 and 5.19. In each figure a major snake travelling along the string, caused by a large surge movement of the buoy, is indicated.

The model test results for the maximum horizontal bending of the hose-

string are summarised in Table 5.1. The maximum bending, occurring at the end of the first-off-the-buoy hose, depends on the amplitude and frequency of the buoy's surge and is independent of any excited natural modes of vibration. The surge frequency values given in Table 5.1 for the irregular wave test results are the peak frequency values of the surge spectra in the irregular waves. In the context of Table 5.1 therefore, the surge frequency values given for the irregular wave test results are nominal in the sense that the maximum surge and maximum bending may occur when the buoy surges with a frequency that is not equal to the peak frequency of the surge spectrum.

Surge Frequency f (hz)	Maximum Surge a_s (m)	Maximum Bending M (kNm)	$M/(a_s)^{1/2}$
Regular Wave Test Results:			
0.125	0.37	11.6	19.1
0.1	0.5	10.5	14.8
Irregular Wave Test Results:			
0.11 (SEA2)	2.44	26.0	16.6
0.07 (SEA3)	2.25	21.7	14.5

Table 5.1

Model test measurements of maximum horizontal bending; maximum bending occurs at the end of the first-off-the-buoy hose

5.2.2 Measurements of Snake Wavelength

The results presented in Table 5.1 show that the snake-induced horizontal bending of the hose-string depends on the surge frequency of the buoy. This results from a dependence of the snake wavelength on the surge frequency.

Estimates of snake wavelength can be obtained from the photographs of the snake shapes. The prototype-equivalent length of each hose length of the hose-string model is 10.7m. Accordingly, inspection of Plates 5.1 to 5.3 yields the estimates of snake wavelength presented in Table 5.2.

Surge Frequency f (Hz)	Snake Wavelength L_s (m)
0.06	43 (±2)
0.09	37 (±2)
0.125	32 (±2)

Table 5.2

Snake wavelengths estimated from Plates 5.1 to 5.3

The results presented in Table 5.2 show that the snake wavelength decreases as the surge frequency increases. This implies that the curvature and bending of the hose-string increase with increasing surge frequency.

5.3 Axial Load

Axial load along the hose-string has been measured in the irregular waves SEA1, SEA2 and SEA3 and in regular waves with f = 0.1, 0.125, 0.167 and 0.25Hz. Appendix A3.3 presents examples of the axial load measurements recorded in these wave conditions as well as the spectrum of each

measurement.

The spectra of axial load measurements in regular waves show that the axial load response is non-linear: the response in regular waves is the superposition of a response at the wave frequency and responses at higher harmonics, as seen, for example, in Figure 5.20. In most cases the responses at the higher harmonics are low compared to that at the incident wave frequency. The purpose of the presentation which follows is to highlight the main features of the axial load response. In this context therefore the low responses at the higher harmonics are neglected so that the system may be approximated as linear. For some measurements, notably for positions 6 to 10 in regular waves with f = 0.125Hz and f = 0.25Hz, the higher harmonic responses are significant relative to the response at the wave frequency. The reasons for these results are not known at the time of writing. However, such results are not representative of the general axial load response in regular waves and, furthermore, the irregular wave test measurements exhibit no such higher harmonic responses. For these reasons, measurements of axial load, whose spectra reveal significant higher harmonic responses, have not been included in the presentation which follows.

Figure 5.21 presents the first 400 seconds of the axial load measurements recorded in irregular waves SEA2. The results show that the variation of axial load at any position on the hose-string is in phase with the variation of axial load at every other position on the string. This means that the hose-string is compressed and tensioned by the push-pull action exerted on it by the movement of the buoy. Heave and pitch play little part in this push-pull action and the wave-axial load mechanism can, therefore, be represented as a single path, single input-single output

mechanism as illustrated in Figure 5.22. The spectrum of axial load at position i, $S_{F_iF_i}(f)$, is related to the incident wave spectrum $S_{\eta\eta}(f)$ by

$$S_{F_iF_i}(f) = |H_{\eta F_i}|^2 S_{\eta\eta}(f) \qquad (5.8)$$

where

$$|H_{\eta F_i}| = |H_{\eta x}(f)| . |H_{xF_i}(f)| \qquad (5.9)$$

$|H_{\eta x}(f)|$ is the wave-surge transfer function

$|H_{xF_i}(f)|$ is the surge-axial load transfer function

Equations (5.8) and (5.9) imply that if the transfer function between surge and axial load at position i is established then the spectrum of axial load at i can be predicted in any sea condition for any buoy whose wave-surge transfer function is known.

5.3.1 Transfer Functions for Surge-Axial Load

Estimates of the surge-axial load transfer functions for positions i between 1 and 6 have been obtained from the cross-spectral analysis of the surge and axial load at i measured in the irregular waves SEA1, SEA2 and SEA3. An example of a complete cross-spectral analysis result, that for position 1 in SEA3, is presented in Figure 5.23. Figures 5.24 to 5.29 present the surge-axial load transfer functions obtained for positions 1 to 6 respectively. Only transfer function values at frequencies for which the coherence is greater than 0.8 are presented. The transfer function values obtained from the regular wave tests are included in Figures 5.24 to 5.29. In general the transfer functions obtained for each position from the three irregular wave tests overlap and show good agreement. There is also good agreement between the regular and irregular wave test results.

Figures 5.24 to 5.29 reveal the main characteristic of the axial load response: axial load increases with increasing surge frequency. This is as expected since both the velocity and acceleration of the buoy's surge increase as the surge frequency increases, resulting in greater velocity and acceleration of the hose-string in the water surface and, therefore, greater hydrodynamic resistance to the imposed push-pull action on the string.

5.3.2 Dependence of Axial Load on Hose-String Length

The axial load at a position on the hose-string depends on the length of hose-string "ahead" of that position: in general, axial load increases with increasing proximity to the buoy due to the greater length of hose-string "ahead" of the hose positions closer to the buoy. This result may be observed from Figures 5.24 to 5.29 by the general increase in the slope of the transfer function for increasing proximity to the buoy. The result is more directly observed in Figure 5.30 which shows the r.m.s. (r.m.s. is equal to the square root of the variance) axial load divided by the r.m.s. surge measured along the hose-string in the irregular waves. Figure 5.30 shows that axial load generally increases with proximity to the buoy. There is, however, a drop in axial load at position 2; this may be due to the first-off-the-buoy hose being submerged. Since axial load depends on the length of hose-string, it is important to realise that 12 hose lengths, each 10.7m long (prototype) constituted the hose-string used in the model tests; the length of hose-string "ahead" of position i is therefore given by $L_i(m) = [12 - (i-1)]10.7$.

Figure 5.31 presents the amplitude of axial load per metre surge amplitude measured along the hose-string in the regular wave tests. Similar results to those of the irregular wave tests (Figure 5.30) may be observed.

5.3.3 A General Result for Axial Load

The model test results presented above refer to the particular hose-string length of 12 x 10.7m = 128m used in the model tests. The following treatment of the results leads to a general result for application to hose-strings of any length.

The axial load at the free end of the string is zero. From Figures 5.30 and 5.31 it is seen that the axial load increases approximately linearly with distance L from the free end to a maximum value at position 3 (L = 9 x 10.7m), the rate of increase S being dependent on the surge frequency. For the regular wave results (Figure 5.31), the rate of increase in the axial load per metre distance from the free end is approximately given by

$$S = \frac{\bar{F}_3/a_s}{9 \times 10.7} \qquad (5.10)$$

where $\bar{F}_3/a_s$ is the axial load amplitude at position 3 per metre surge amplitude.

The corresponding value of S from the irregular wave test results is

$$S = \frac{(F_3)_{rms}/(a_s)_{rms}}{9 \times 10.7} \qquad (5.11)$$

where $(F_3)_{rms}$ is the r.m.s. axial load at position 3 and $(a_s)_{rms}$ is the r.m.s. surge.

The values of S, defined by equations (5.10) and (5.11) have been obtained from Figures 5.31 and 5.30 and are presented in Table 5.3.

Regular Wave Test Results:

Wave Frequency (Hz)	Surge Frequency (Hz)	$\bar{F}_3/a_s$ (kN/m)	S (kN/m^2)
0.1	0.1	29.6	0.307
0.125	0.125	46.0	0.478
0.167	0.167	69.0	0.716

Irregular Wave Test Results:

Wave Peak Frequency	Surge Peak Frequency	$(F_3)_{rms}$ $(a_s)_{rms}$	S
0.07 (SEA3)	0.07	24.6	0.255
0.14 (SEA2)	0.11	37.7	0.391
0.165(SEA1)	0.14*	40.0	0.415

(* This choice of peak frequency for the surge in SEA1 is tentative; the spectrum has a more dominant peak at about 0.03Hz (Figure 4.7).)

Table 5.3

The values of S are plotted against surge frequency in Figure 5.32. The irregular wave result at 0.14Hz is inaccurate because of poor choice of the surge frequency signature in SEA1 (see * in Table 5.3). The value of S is seen therefore to be approximately linearly dependent on the surge frequency.

Figure 5.32 effectively summarises the results for axial load presented in Sections 5.3.1 and 5.3.2. It may be applied as a general result as follows:

In regular waves the axial load amplitude at L(m) from the free end is given by

$$\bar{F} = a_s L S_f \qquad (5.12)$$

where S_f (kN/m^2) is the value of S at the surge frequency and is obtained from Figure 5.32 and a_s(m) is the surge amplitude.

In irregular waves the r.m.s. axial load at L(m) from the free end is given by

$$F_{rms} = (a_s)_{rms} L S_f \qquad (5.13)$$

where S_f (kN/m^2) is the value of S at the surge peak frequency and is obtained from Figure 5.32 and $(a_s)_{rms}$ is the r.m.s. surge.

If the first-off-the-buoy hose is submerged (as is generally the case in practice) the magnitude of the axial load obtained for position 3 on the string using the above method should be used as the estimate of the axial load at positions 1 and 2.

This chapter has established from the model test results the magnitudes of the bending moments and axial loads along the hose-string in various wave conditions and their dependence on the SBM's motions and the waves. The results for vertical and horizontal bending are considered again in Chapter 8 when they are compared with the results of analytical models which predict the bending of the hose-string in waves.

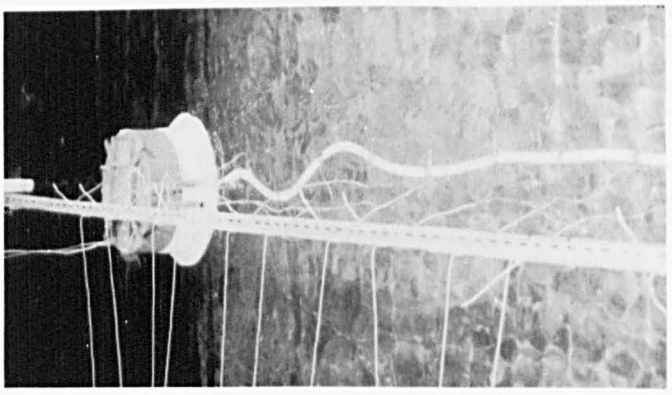

Plate 5.1 Snaking in Regular Waves with Frequency 0.125Hz

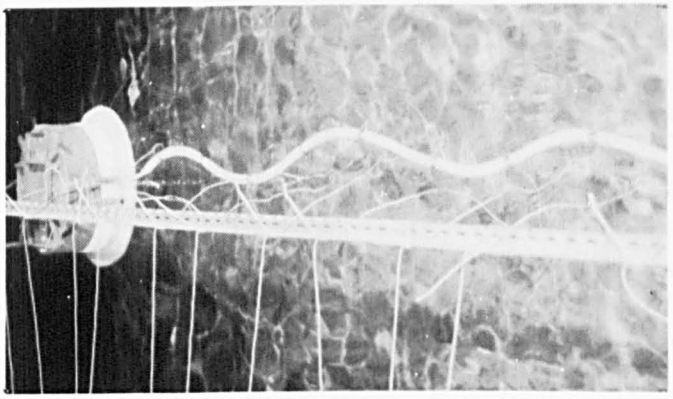

Plate 5.2 Snaking in Regular Waves with Frequency 0.09Hz

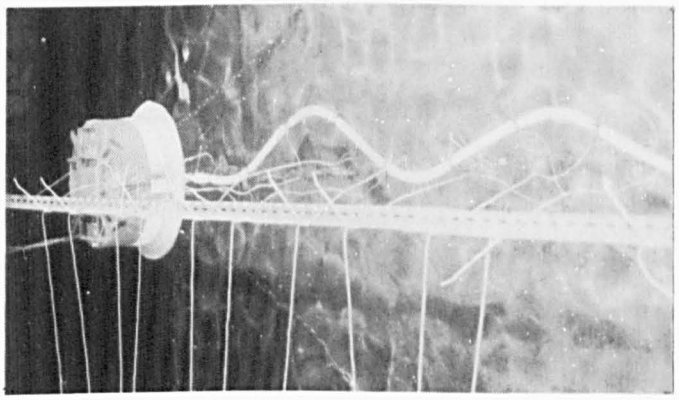

Plate 5.3 Snaking in Regular Waves with Frequency 0.06Hz

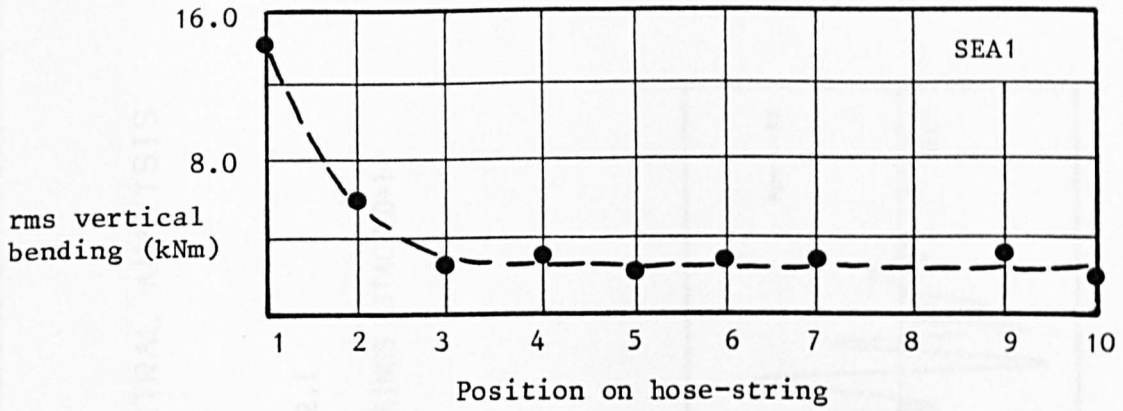

Figure 5.1 rms vertical bending measured along the hose-string in irregular waves SEA1

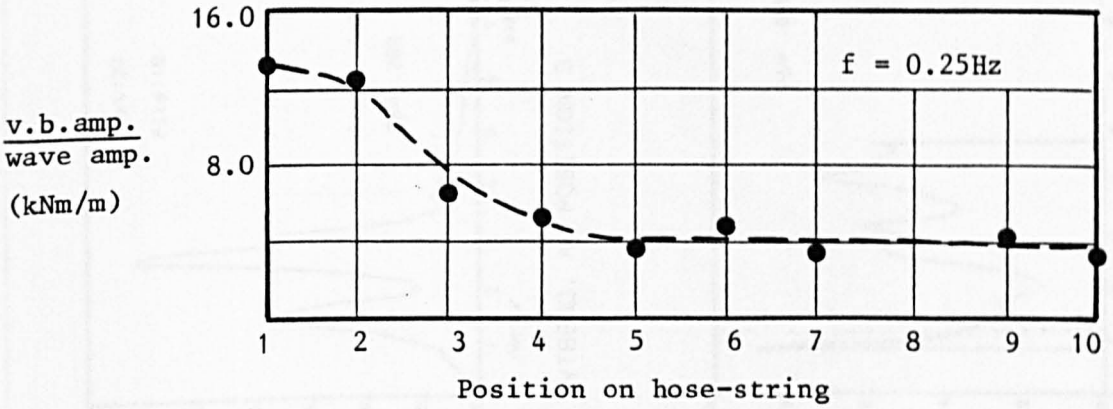

Figure 5.2 Vertical bending amplitude divided by the wave amplitude measured along the hose-string in regular waves with f = 0.25Hz

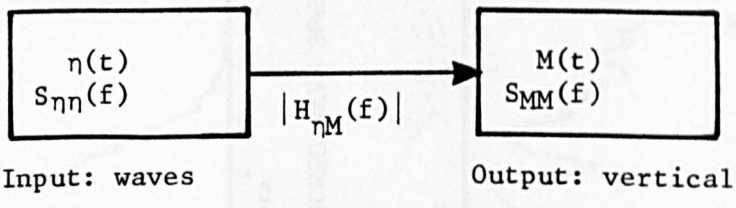

Figure 5.3 Single input-single output mechanism for waves - vertical bending at positions away from the buoy

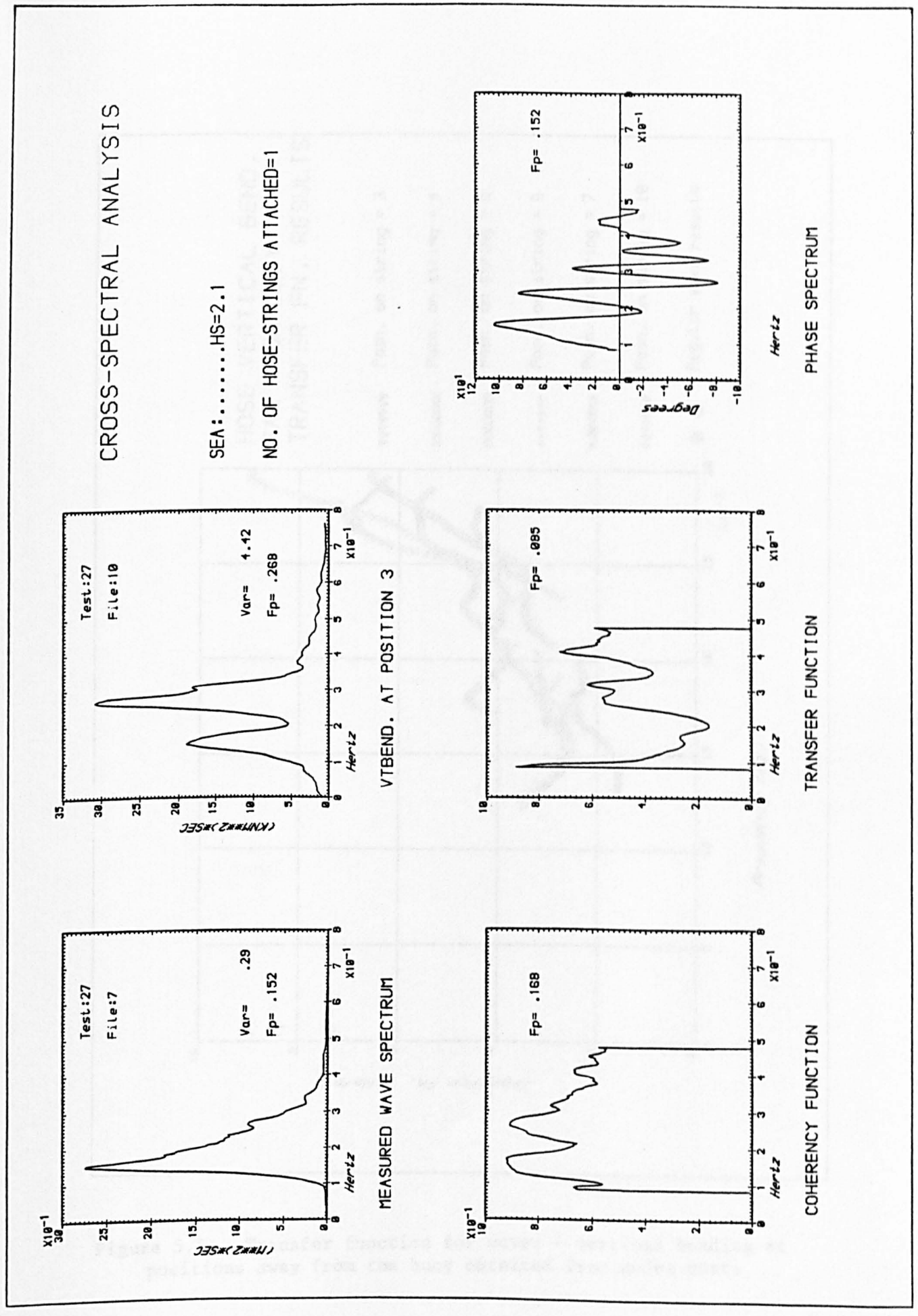

Figure 5.4 Cross-spectral analysis result for waves - vertical bending at position 3 in SEA1

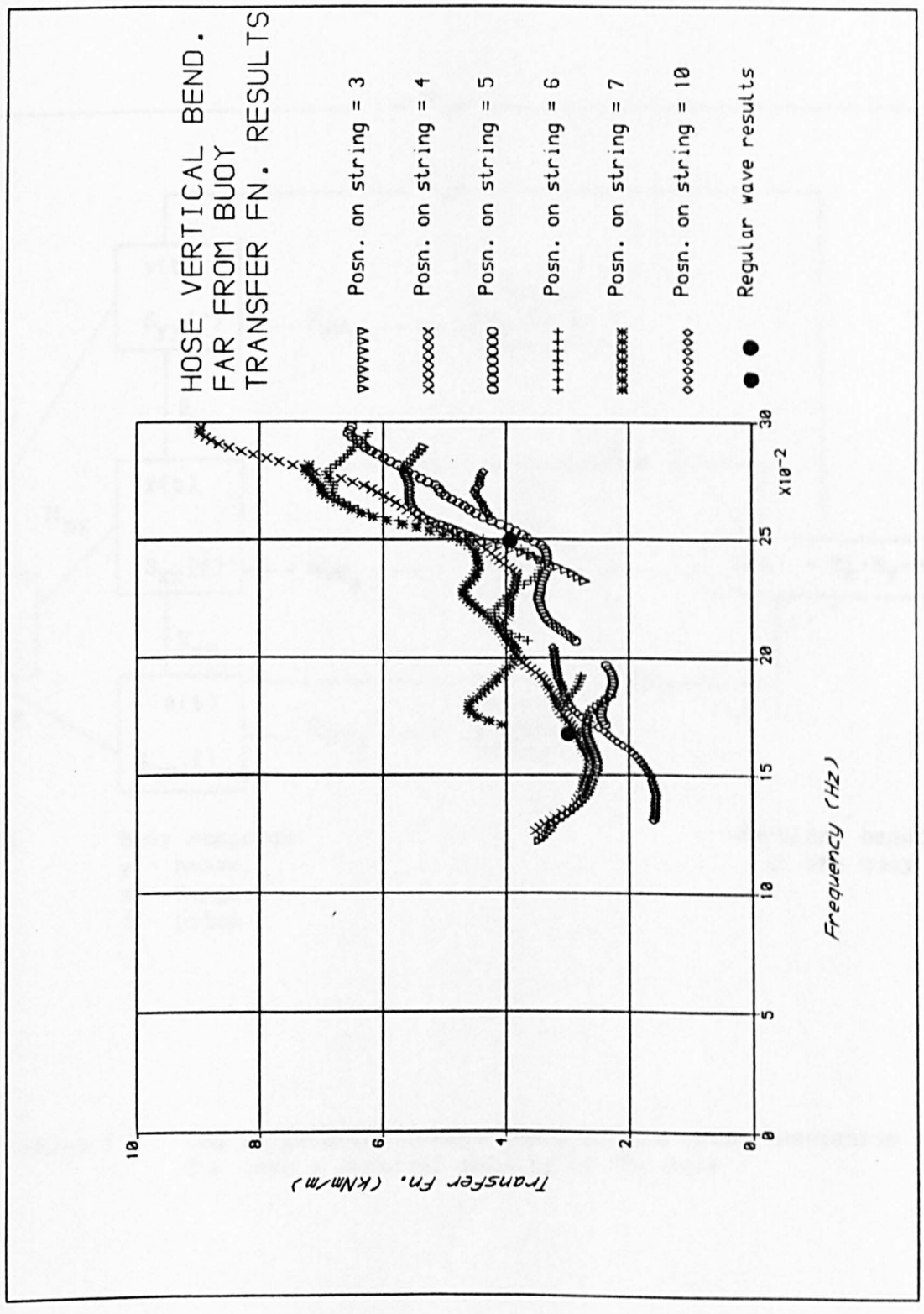

Figure 5.5 Transfer function for waves - vertical bending at positions away from the buoy obtained from model tests

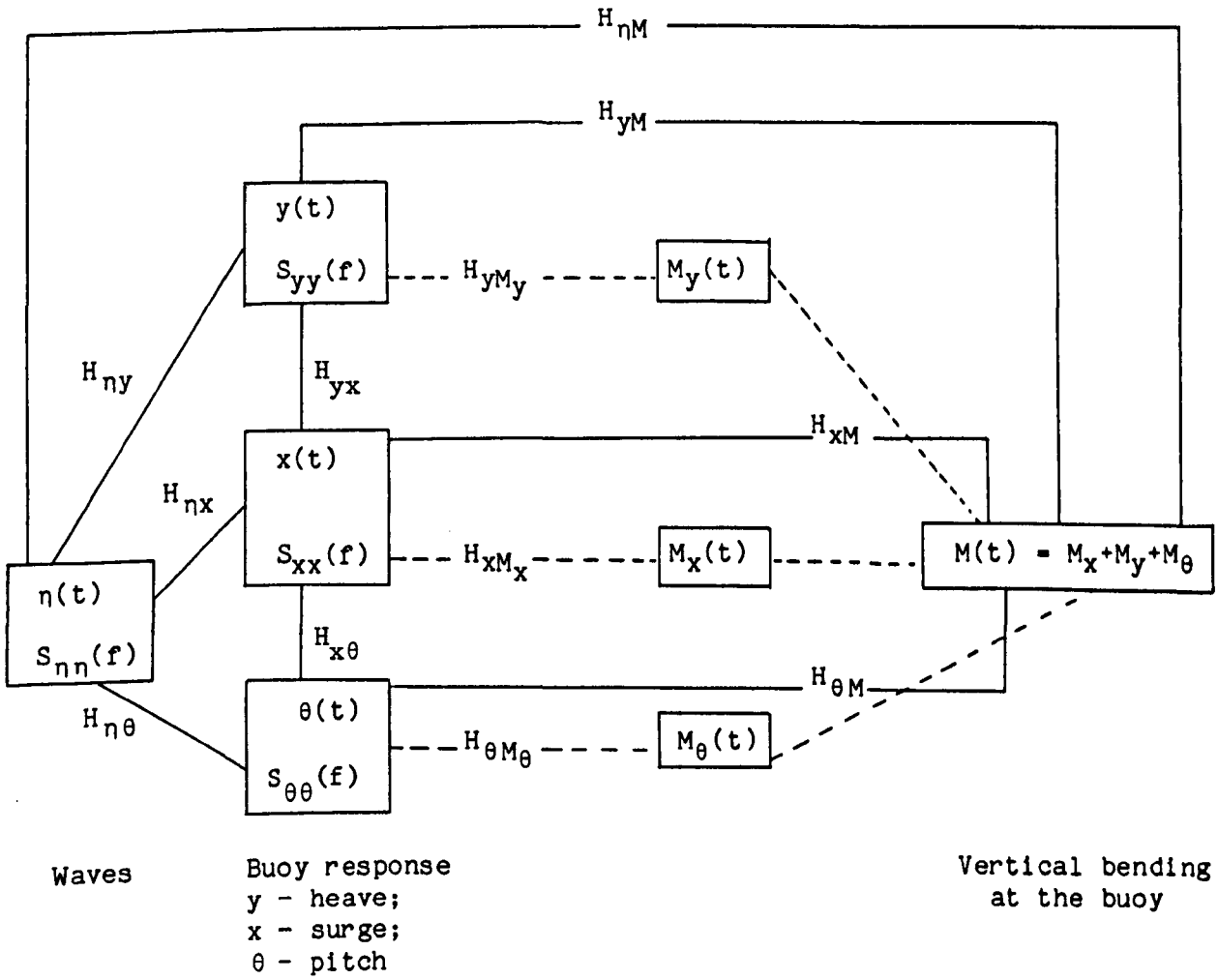

Figure 5.6 Multiple-path, single input-single output mechanism for wave - vertical bending at the buoy

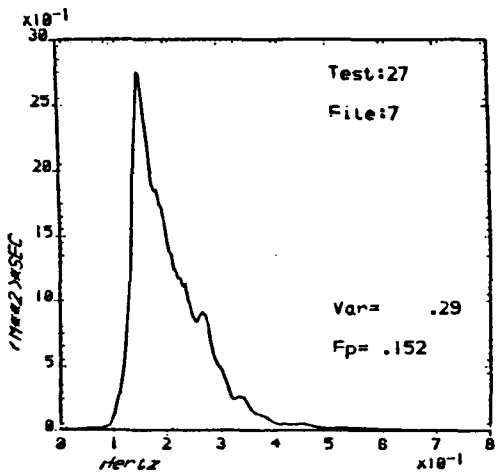

MEASURED WAVE SPECTRUM

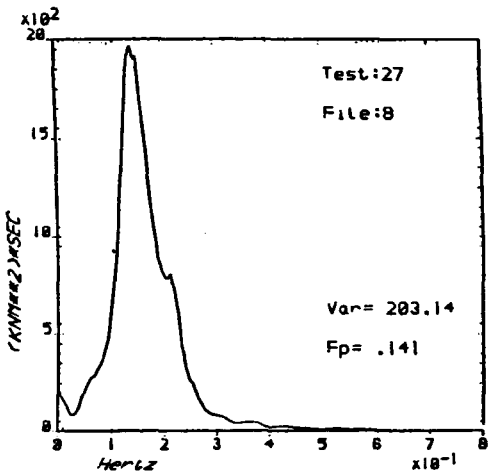

VTBEND. AT POSITION 1

CROSS-SPECTRAL ANALYSIS

SEA:.....HS=2.1

NO. OF HOSE-STRINGS ATTACHED=1

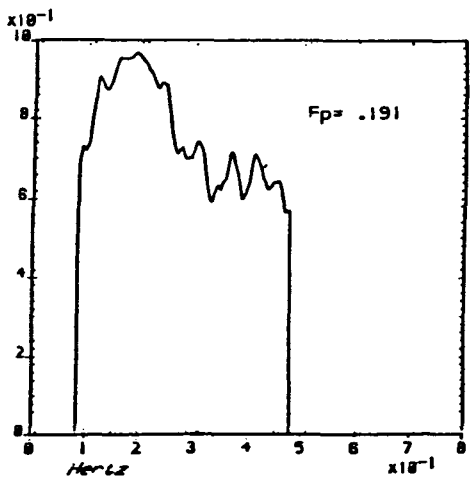

COHERENCY FUNCTION

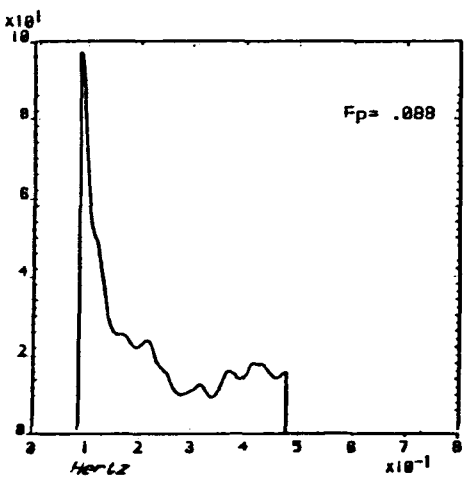

TRANSFER FUNCTION

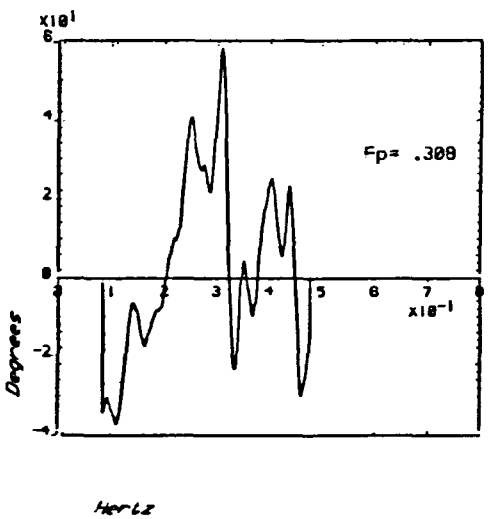

PHASE SPECTRUM

Figure 5.7 Cross-spectral analysis result for waves - vertical bending at the buoy in SEA1

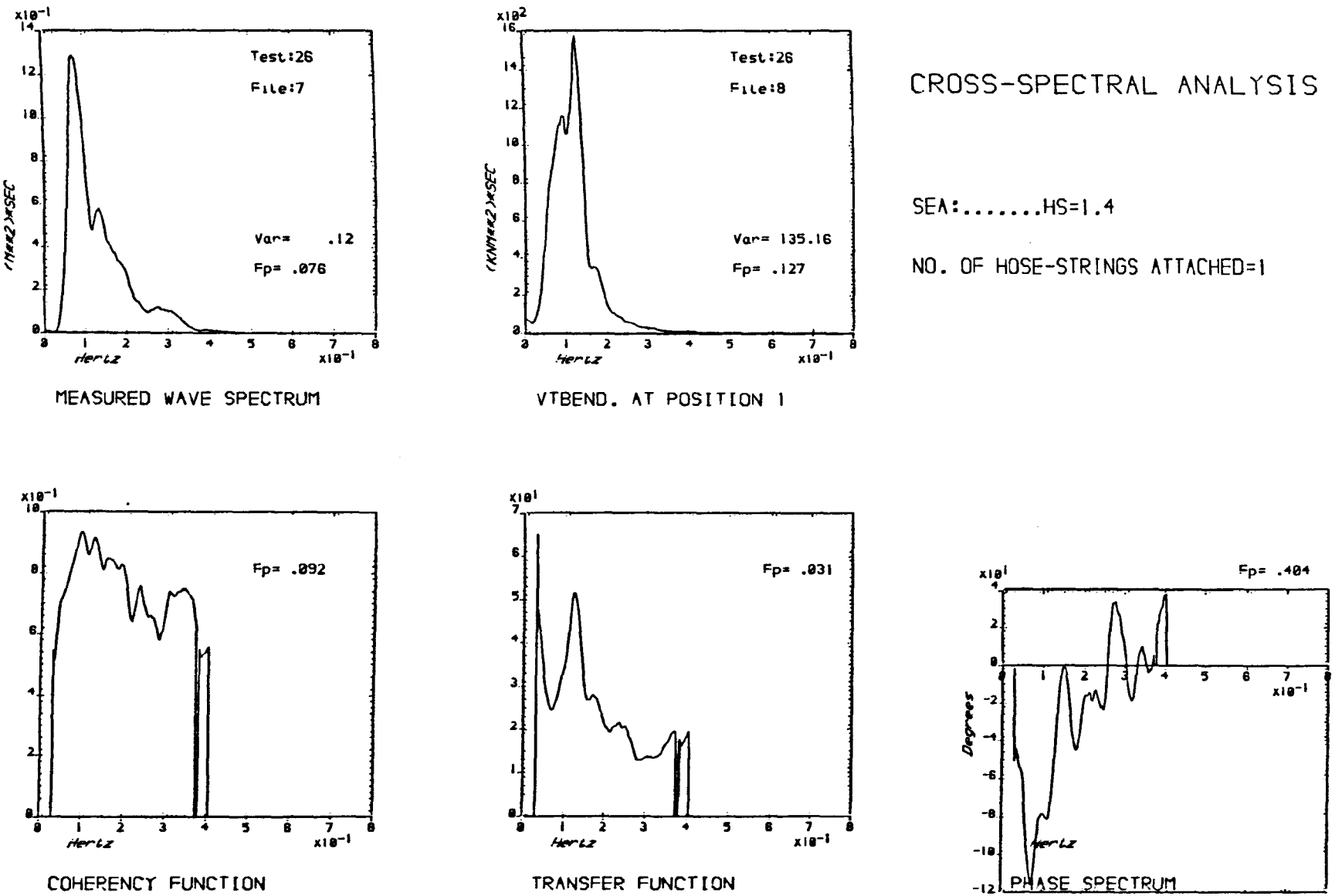

Figure 5.8 Cross-spectral analysis result for waves - vertical bending at the buoy in SEA3

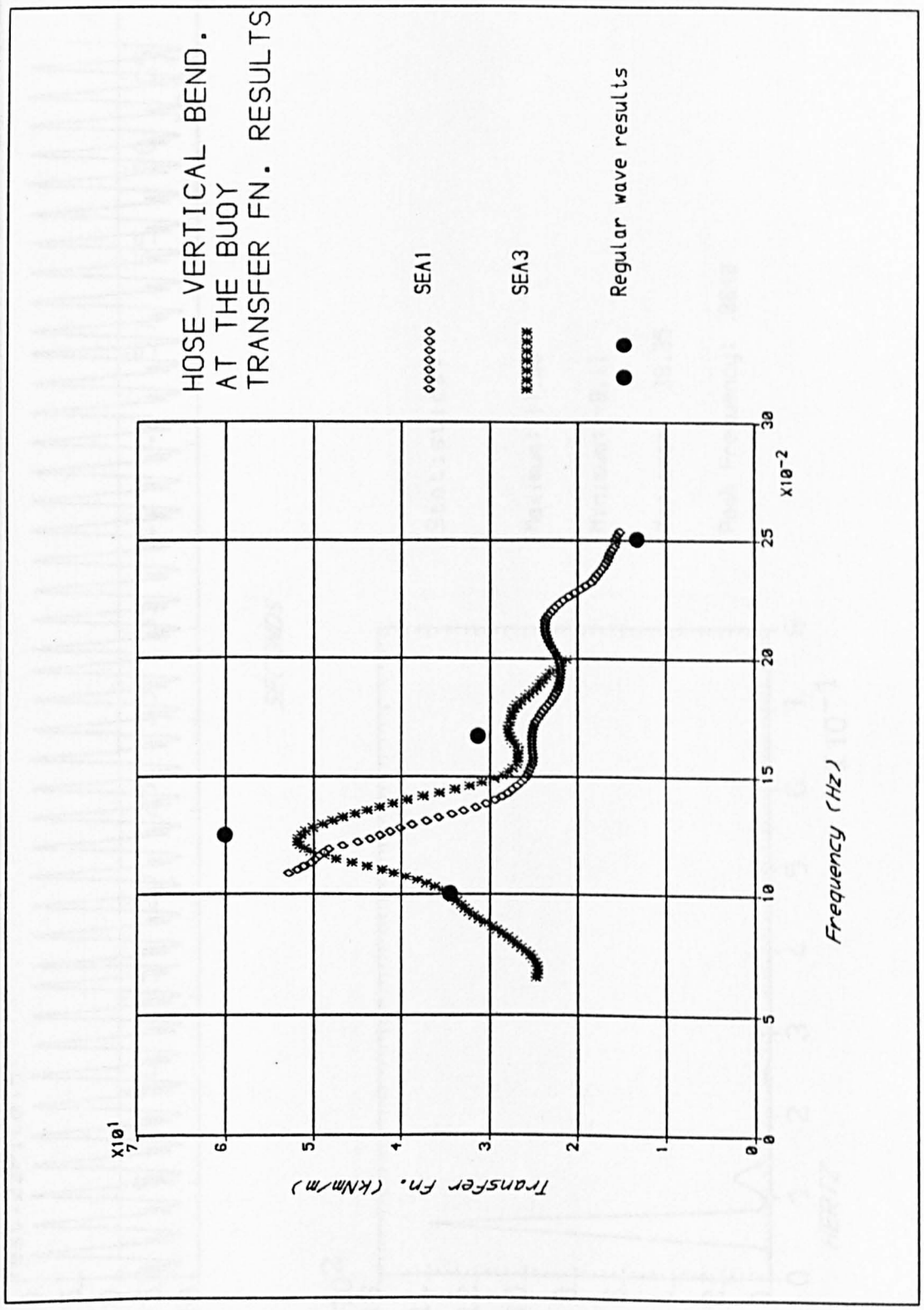

Figure 5.9 Transfer function for waves - vertical bending at the buoy obtained from model tests

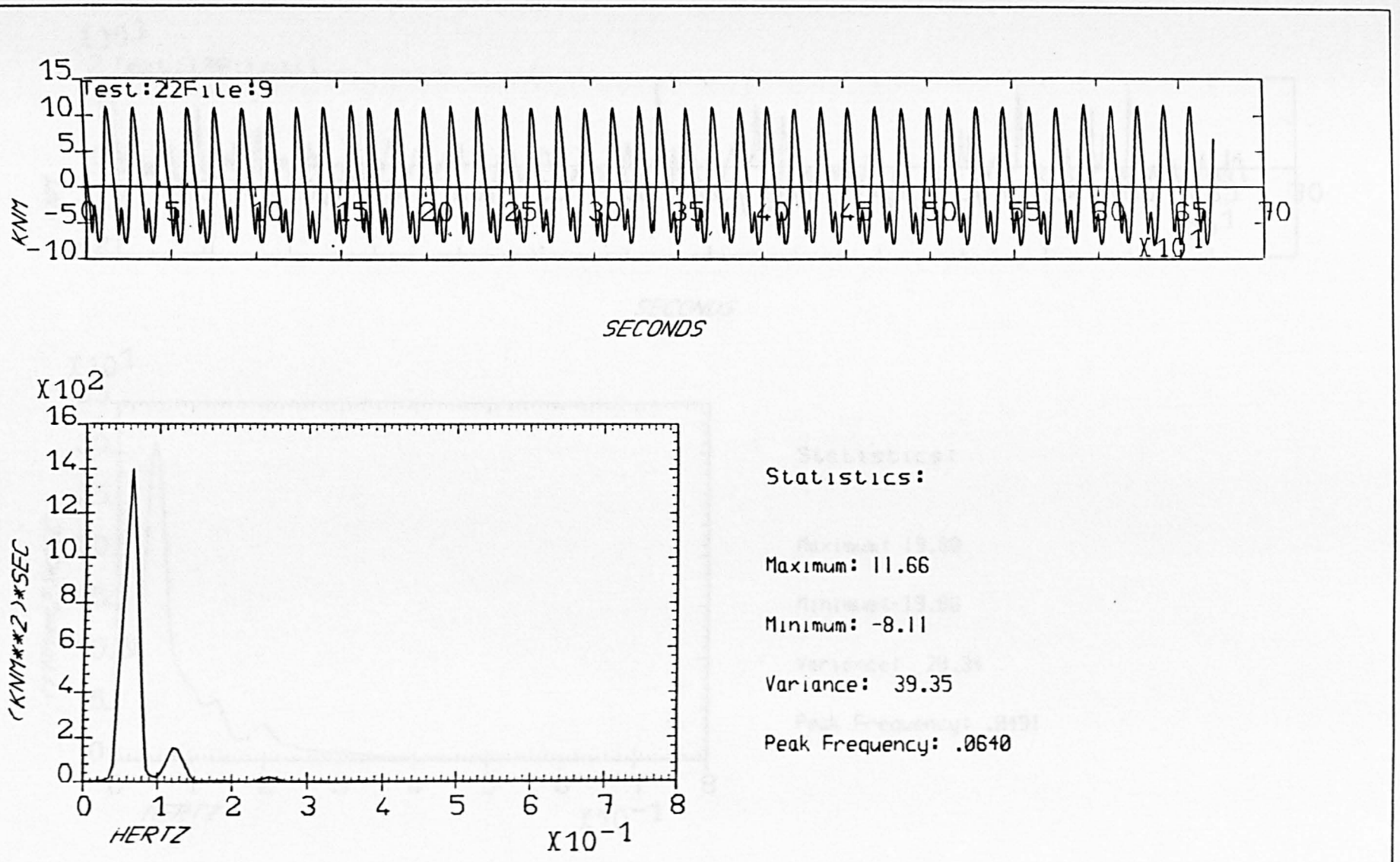

Figure 5.10 Horizontal bending at position 2 measured in regular waves with f = 0.125Hz

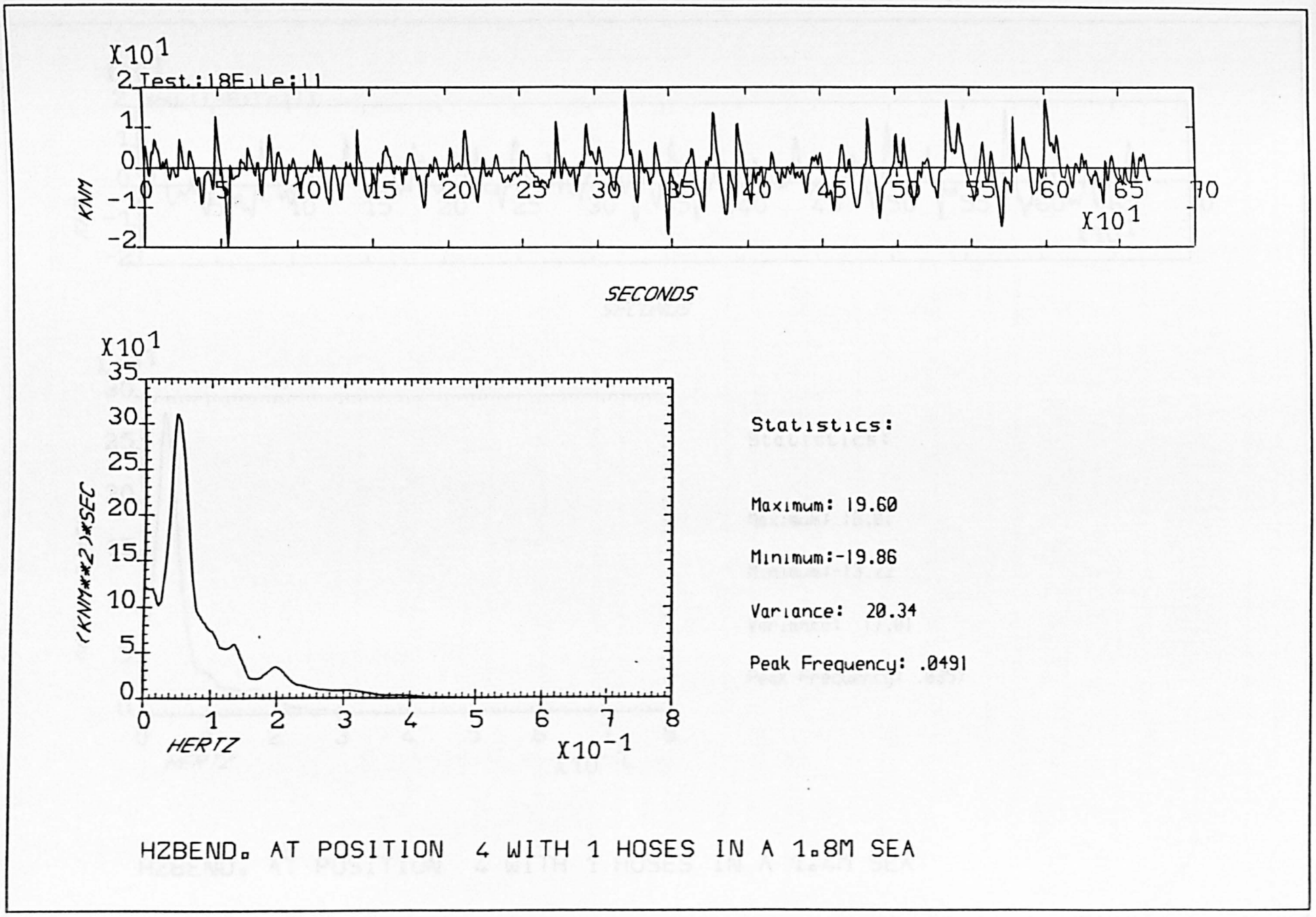

Figure 5.11 Horizontal bending at position 4 measured in SEA2

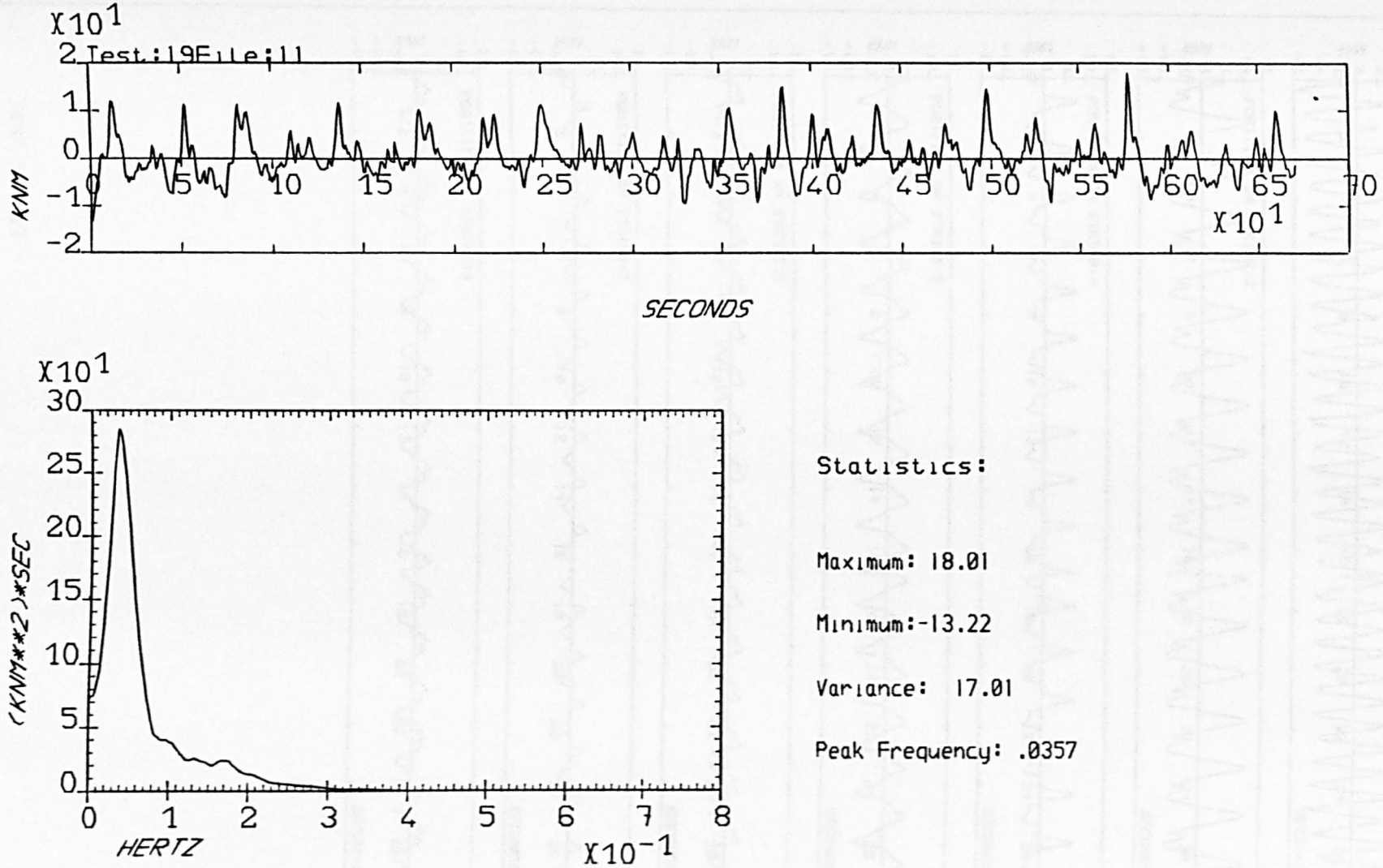

Figure 5.12 Horizontal bending at position 4 measured in SEA3

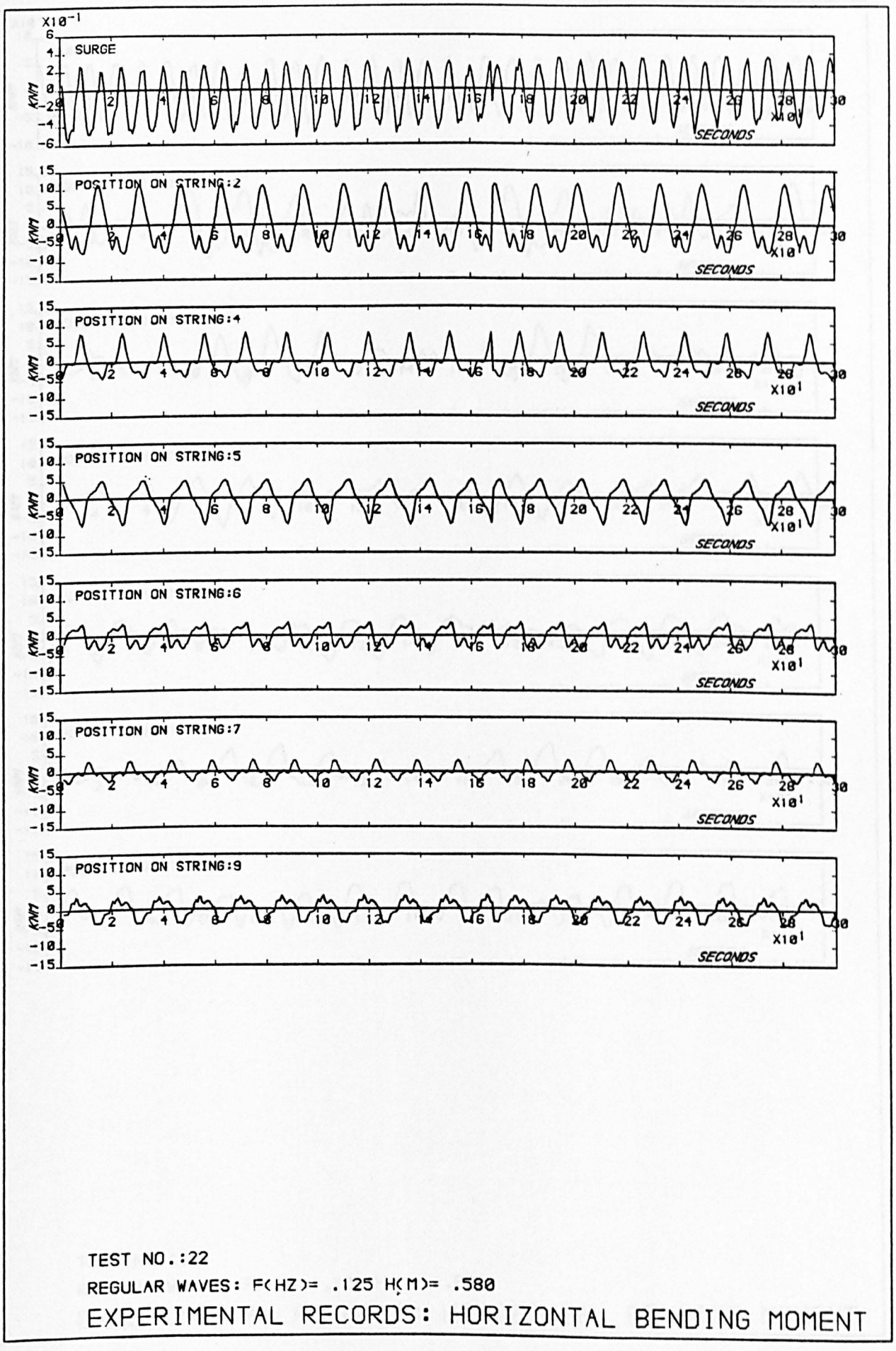

Figure 5.13 SBM surge motion and horizontal bending along the hose-string measured in regular waves with f = 0.125Hz

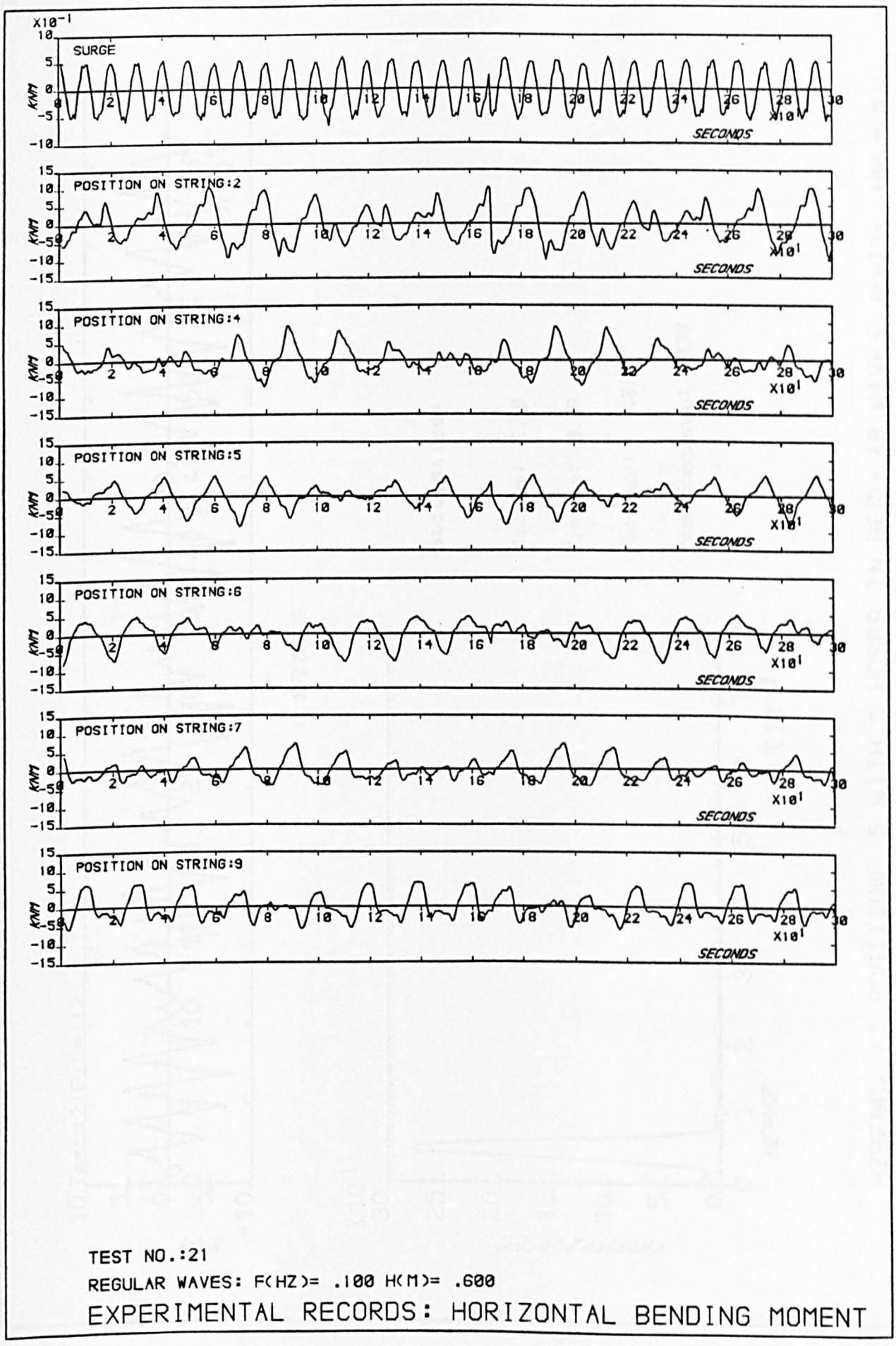

Figure 5.14 SBM surge motion and horizontal bending along the hose-string measured in regular waves with f = 0.1Hz

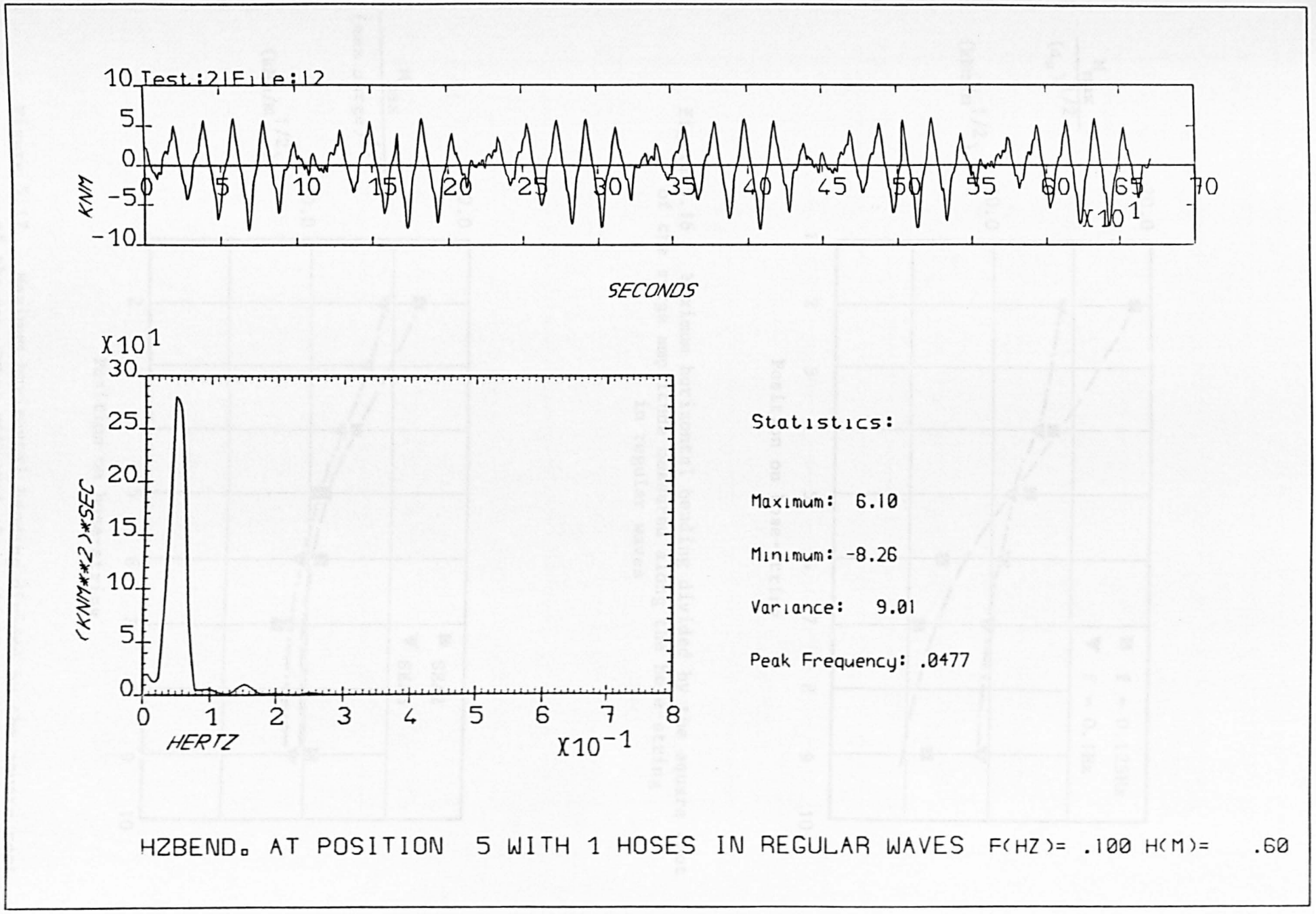

Figure 5.15 Horizontal bending at position 5 measured in regular waves with f = 0.1Hz

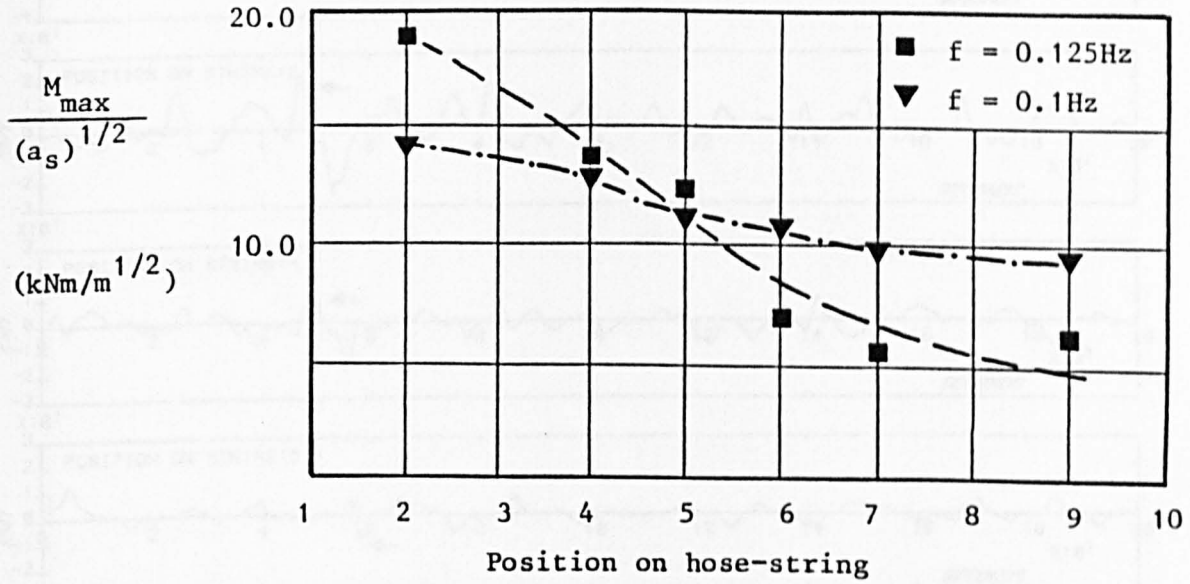

Figure 5.16 Maximum horizontal bending divided by the square root of the surge amplitude measured along the hose-string in regular waves

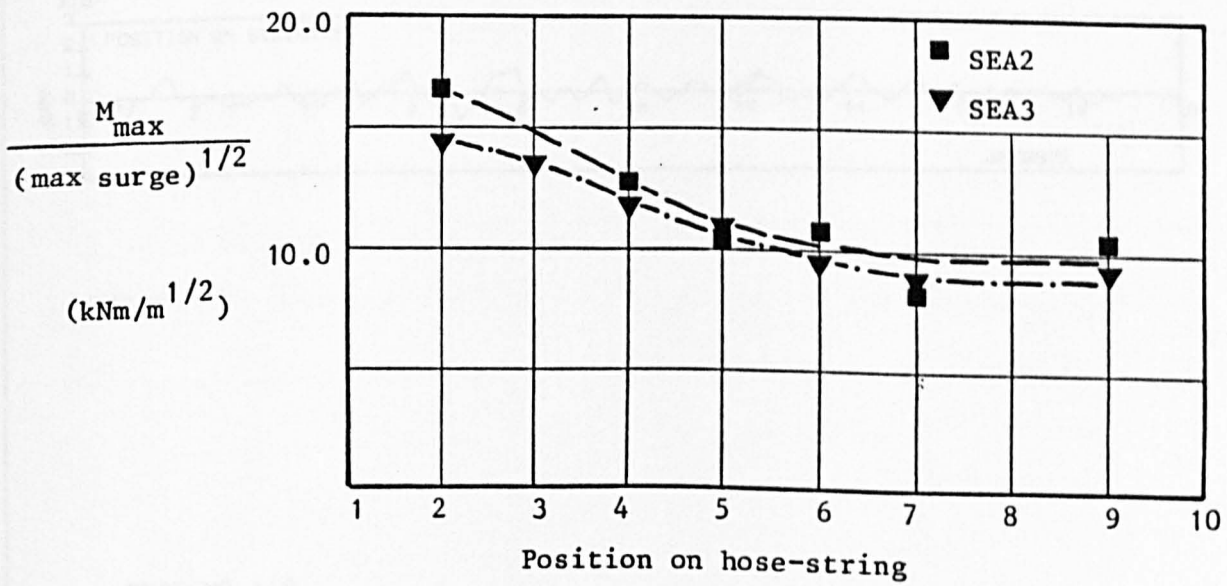

Figure 5.17 Maximum horizontal bending divided by the square root of the max surge measured along the hose-string in irregular waves

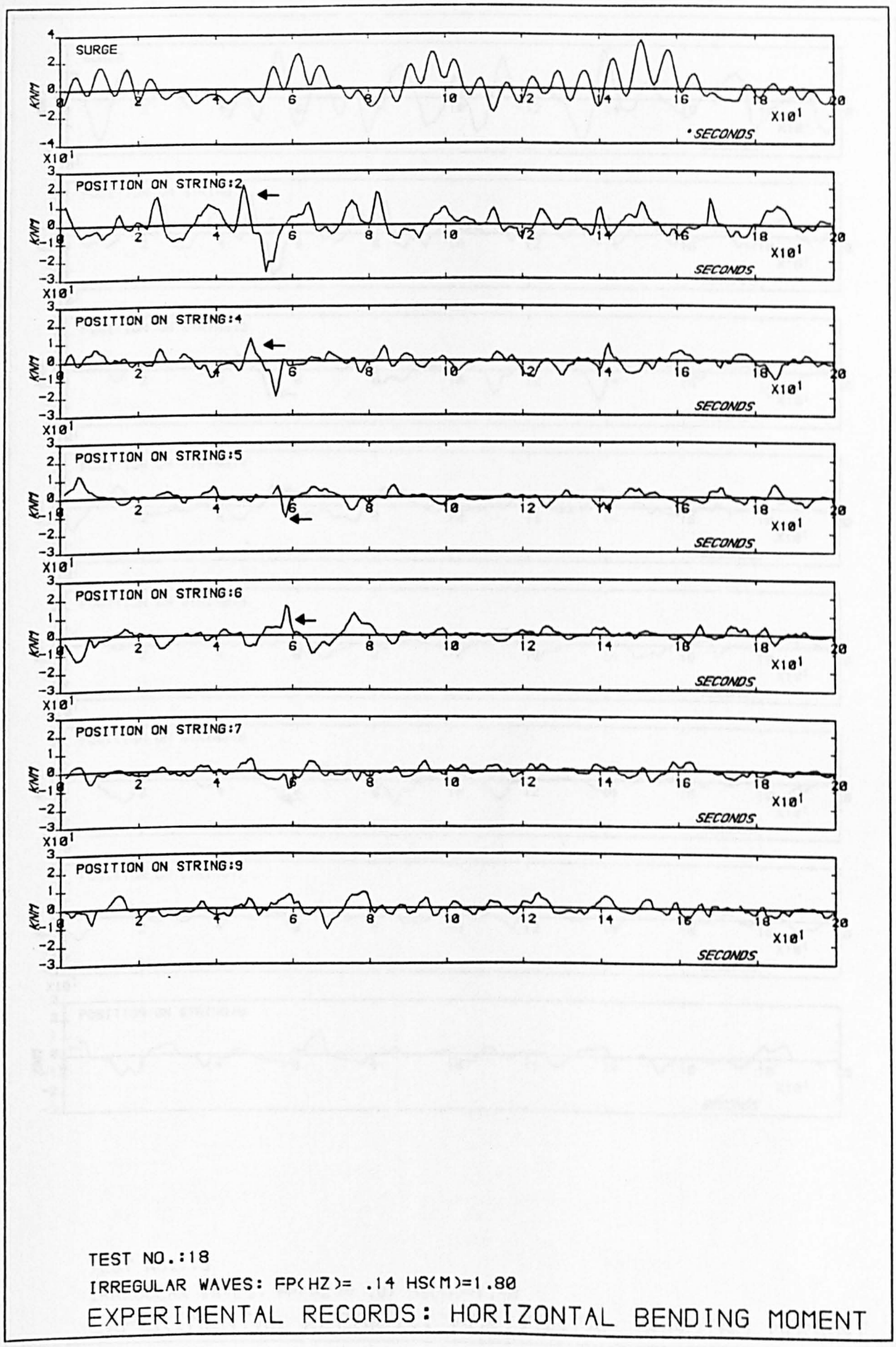

Figure 5.18 SBM surge motion and horizontal bending along the hose-string measured in SEA2

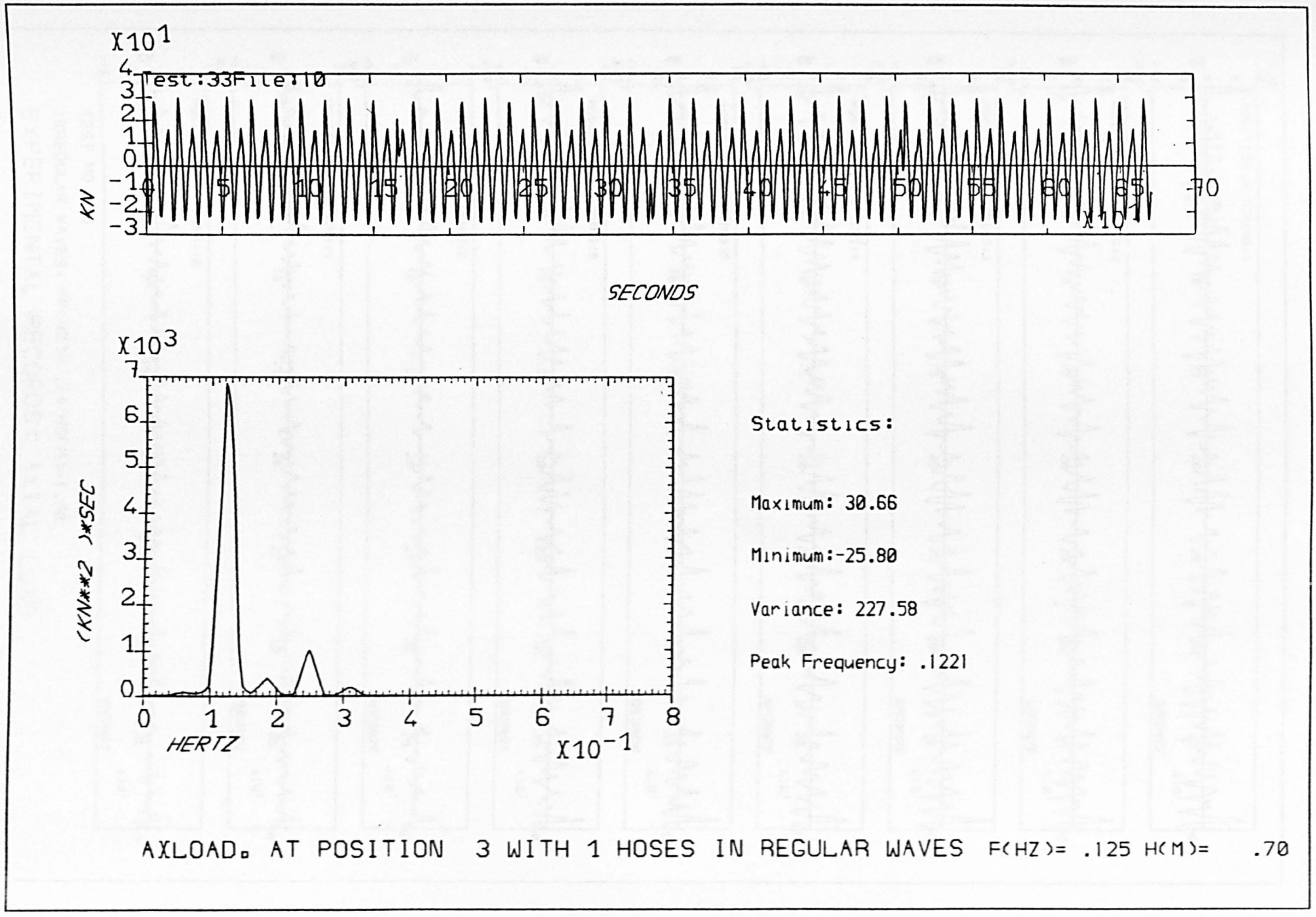

Figure 5.20 Axial load at position 3 measured in regular waves with f = 0.125Hz

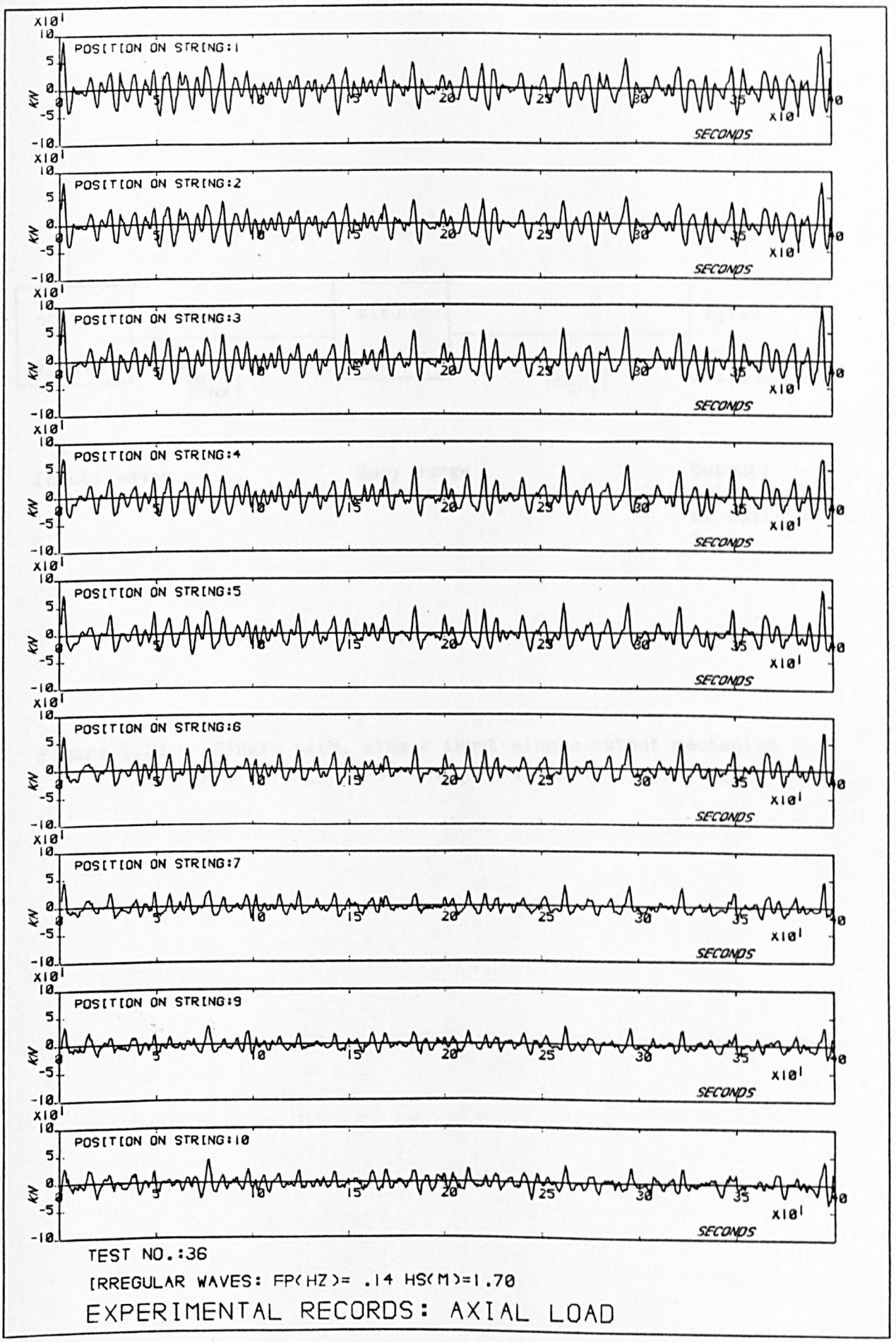

Figure 5.21 Axial load along the hose-string measured in SEA2

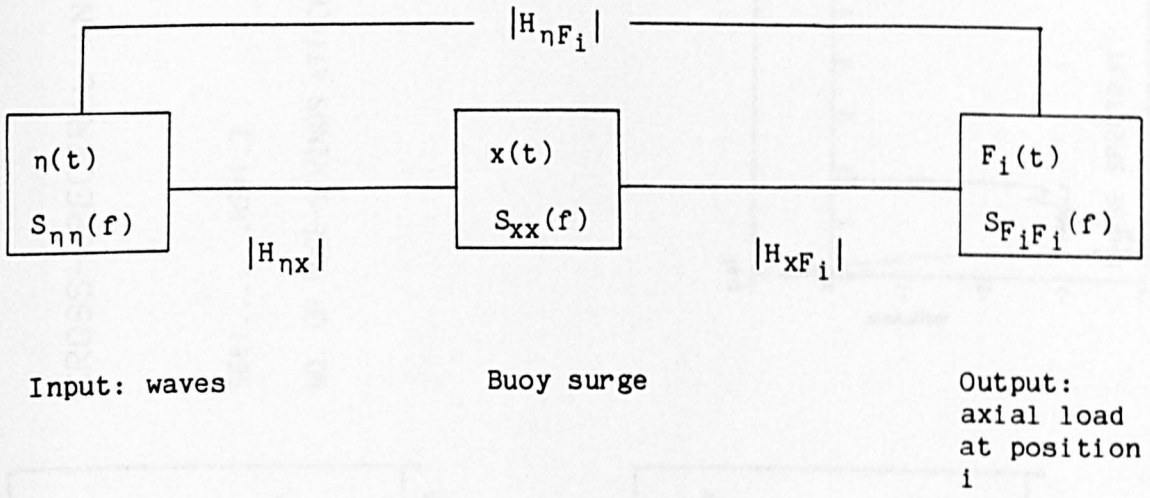

Figure 5.22 Single path, single input-single output mechanism for waves - axial load at position i

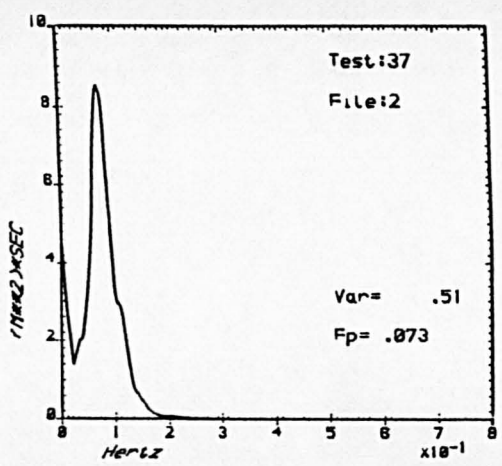

SURGE MOTION OF BUOY

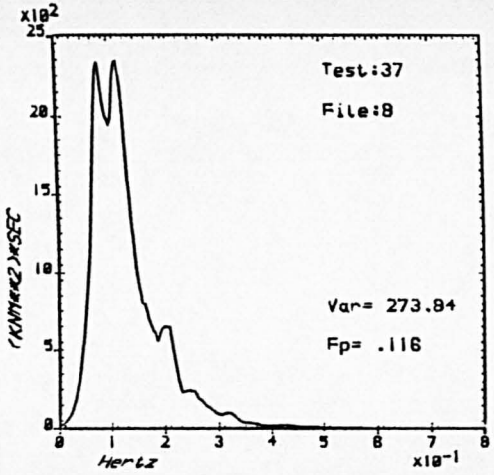

AXLOAD. AT POSITION 1

CROSS-SPECTRAL ANALYSIS

SEA:.....HS=1.3

NO. OF HOSE-STRINGS ATTACHED=1

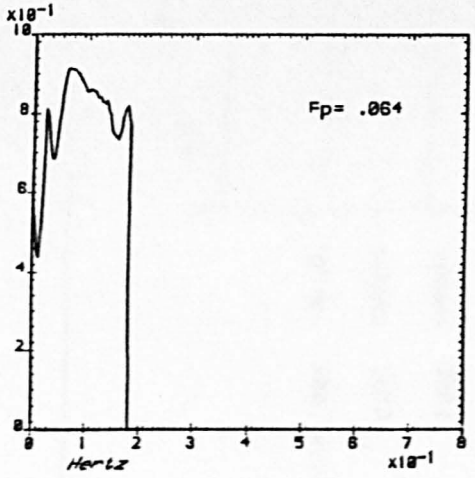

COHERENCY FUNCTION

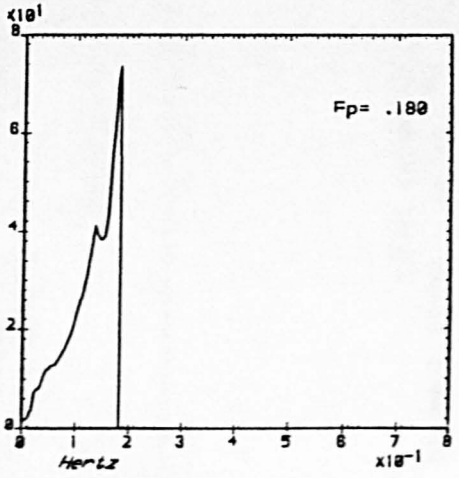

TRANSFER FUNCTION

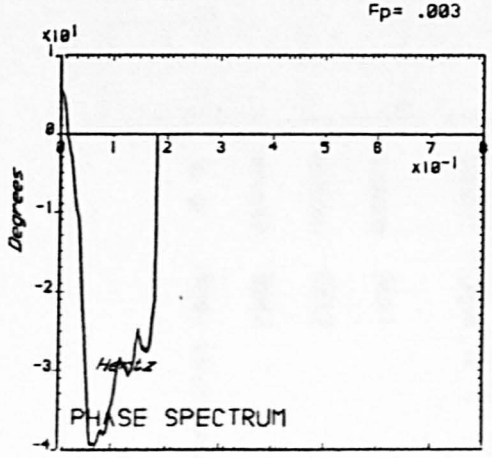

PHASE SPECTRUM

Figure 5.23 Cross-spectral analysis results for SBM surge - axial load at position 1 in SEA3

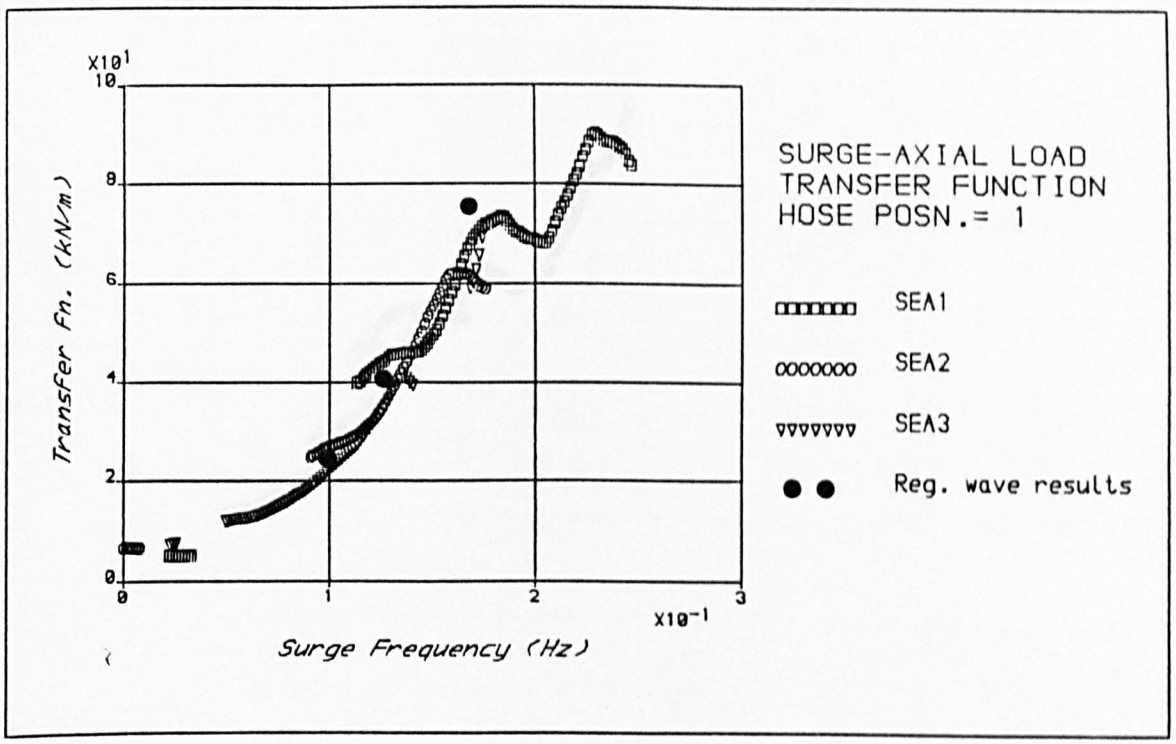

Figure 5.24 Transfer function for surge - axial load at position 1 obtained from model tests

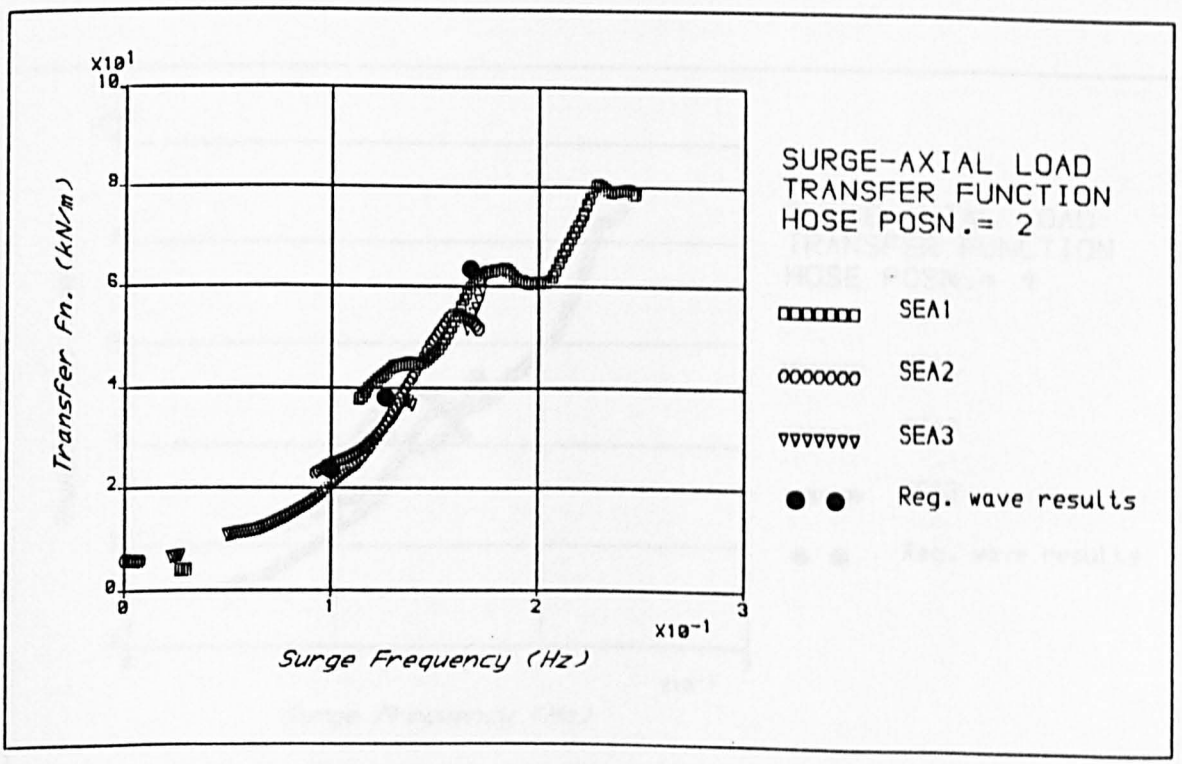

Figure 5.25 Transfer function for surge - axial load at position 2 obtained from model tests

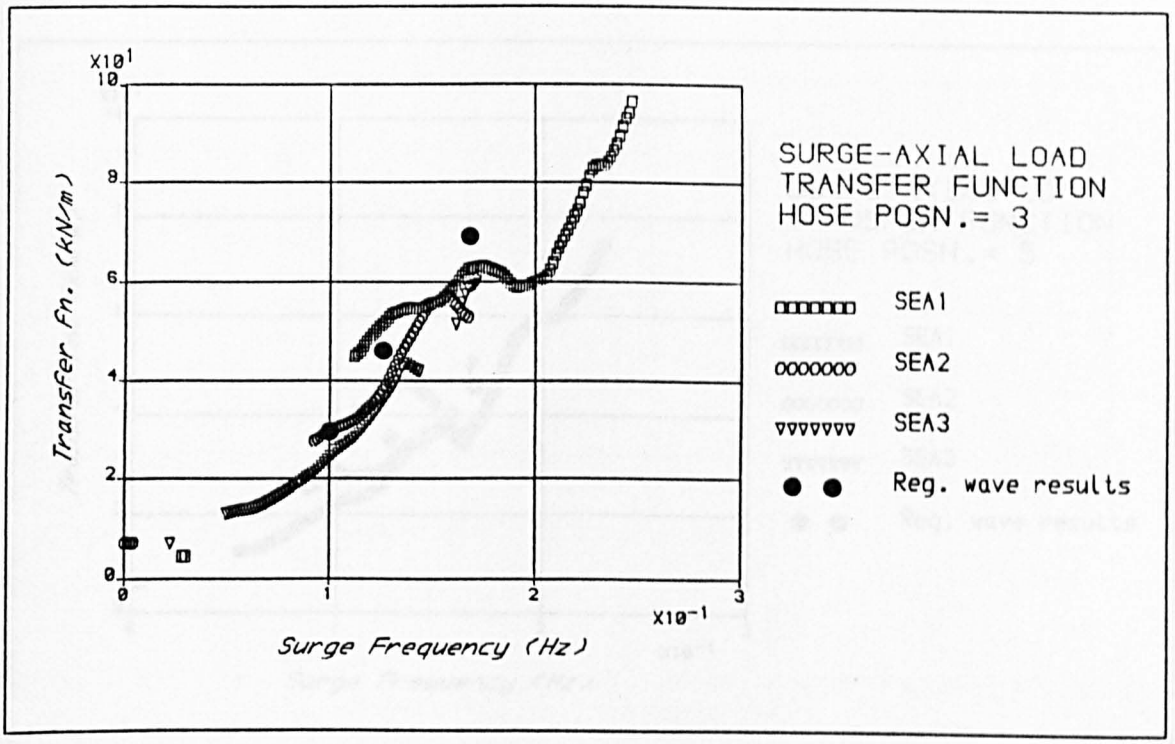

Figure 5.26 Transfer function for surge - axial load at position 3 obtained from model tests

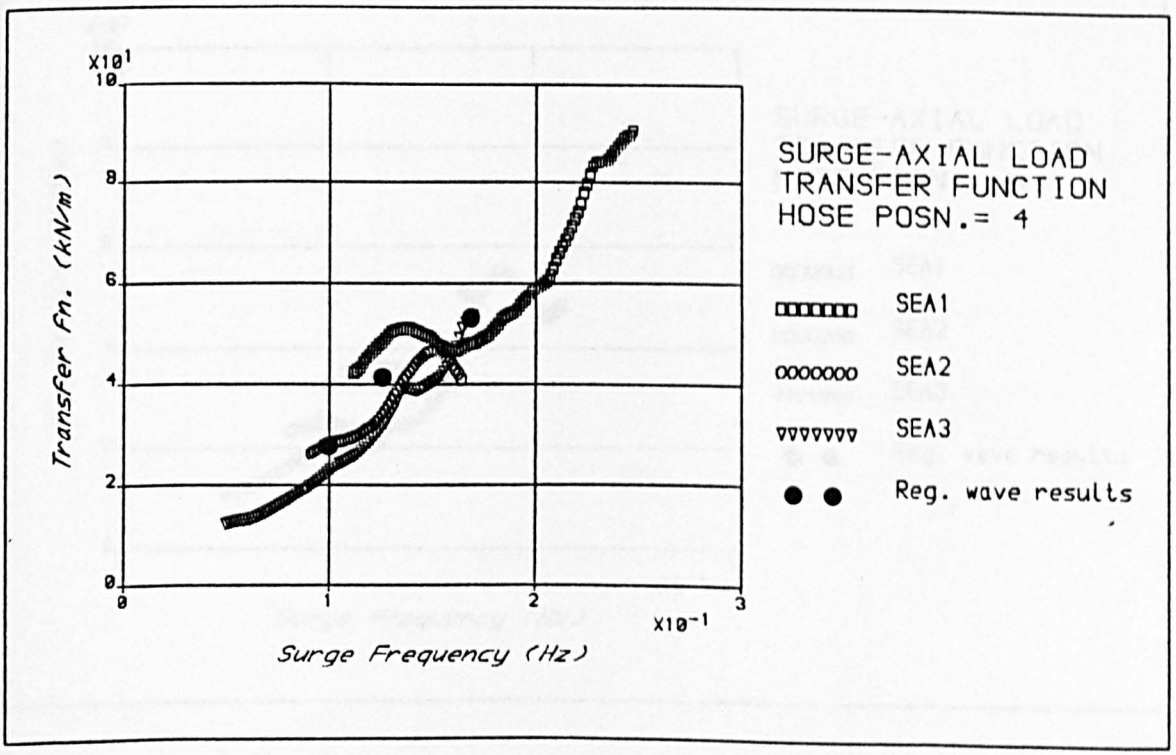

Figure 5.27 Transfer function for surge - axial load at position 4 obtained from model tests

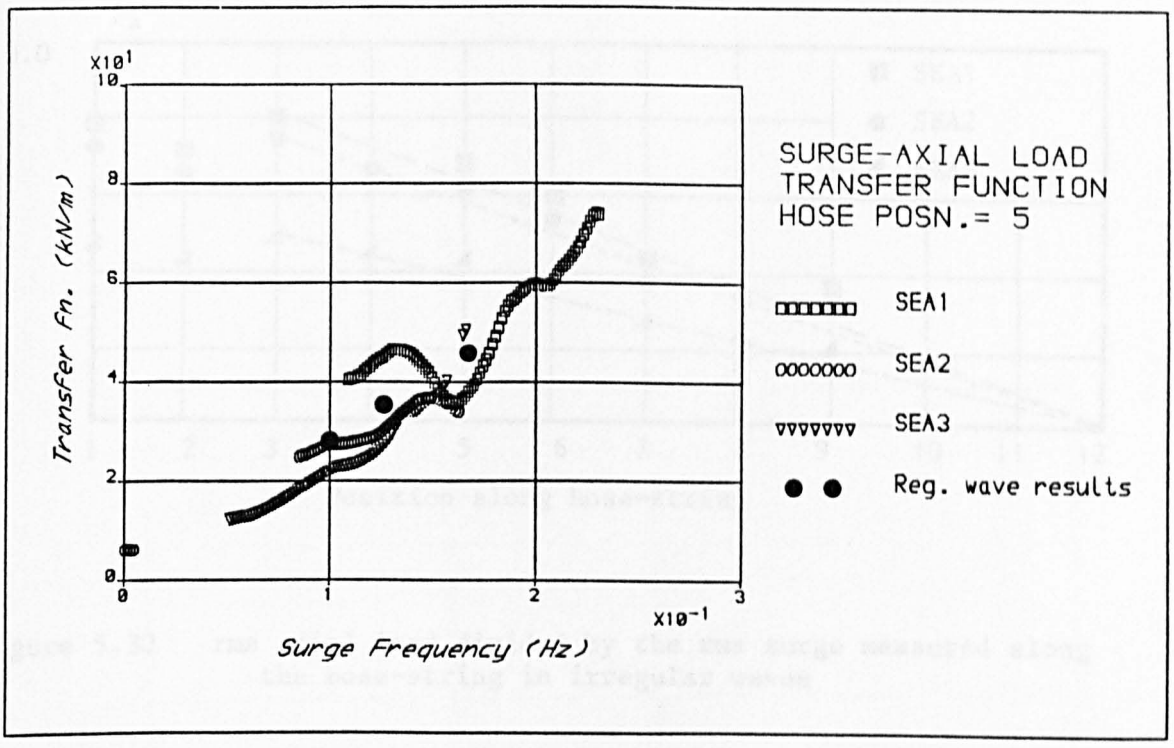

Figure 5.28 Transfer function for surge - axial load at position 5 obtained from model tests

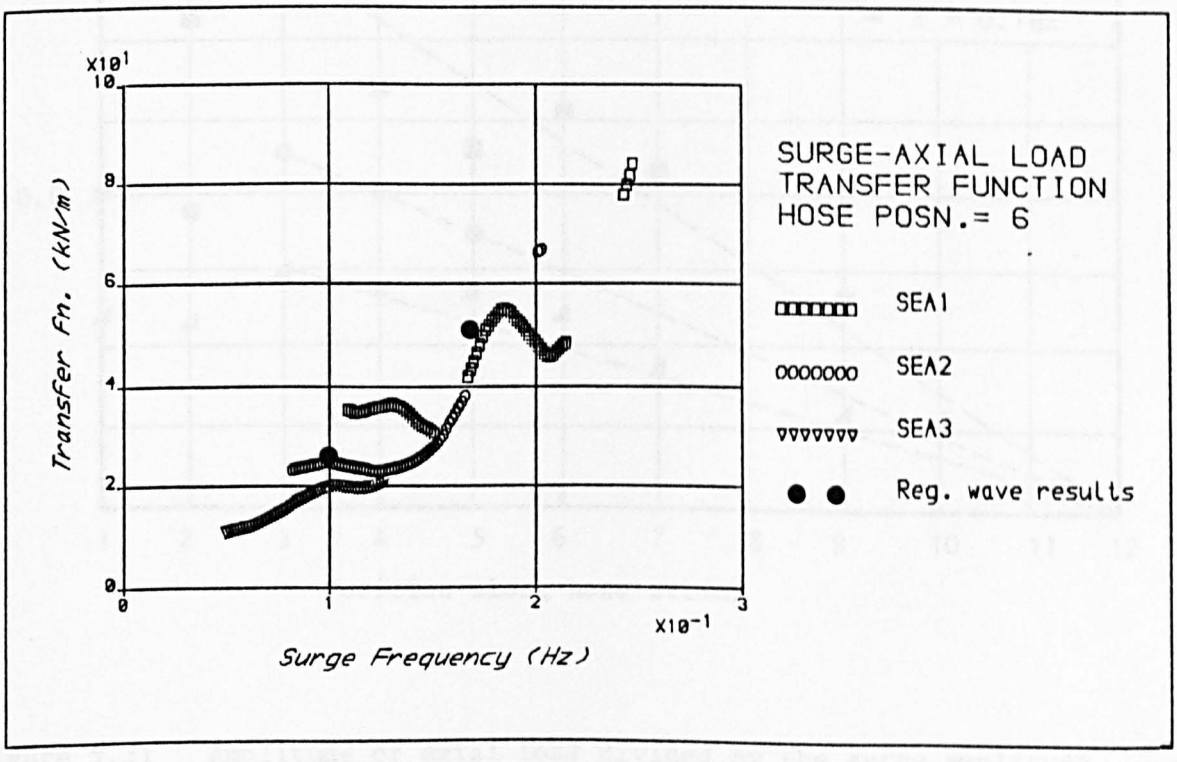

Figure 5.29 Transfer function for surge - axial load at position 6 obtained from model tests

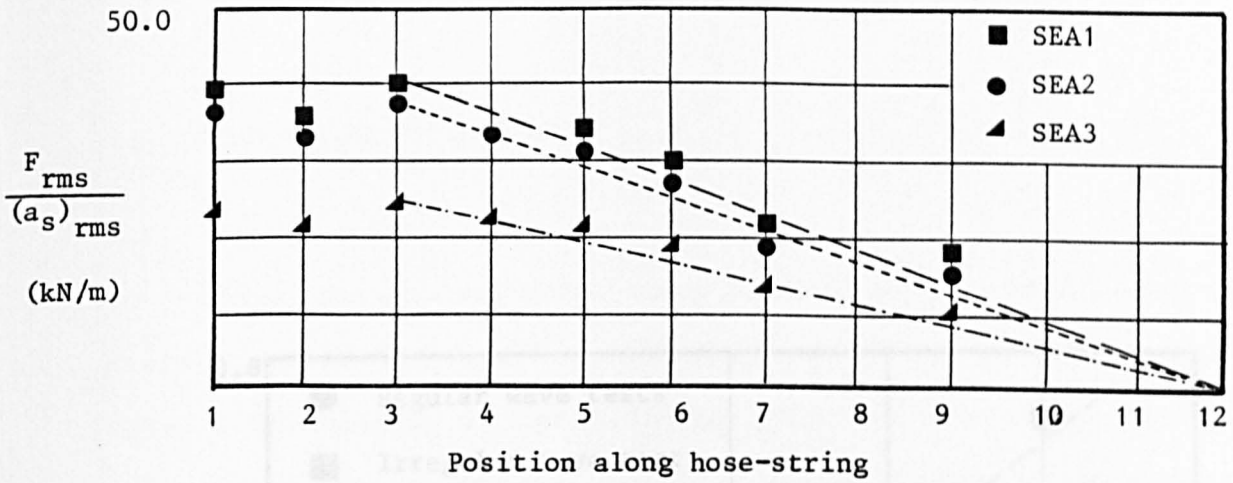

Figure 5.30 rms axial load divided by the rms surge measured along the hose-string in irregular waves

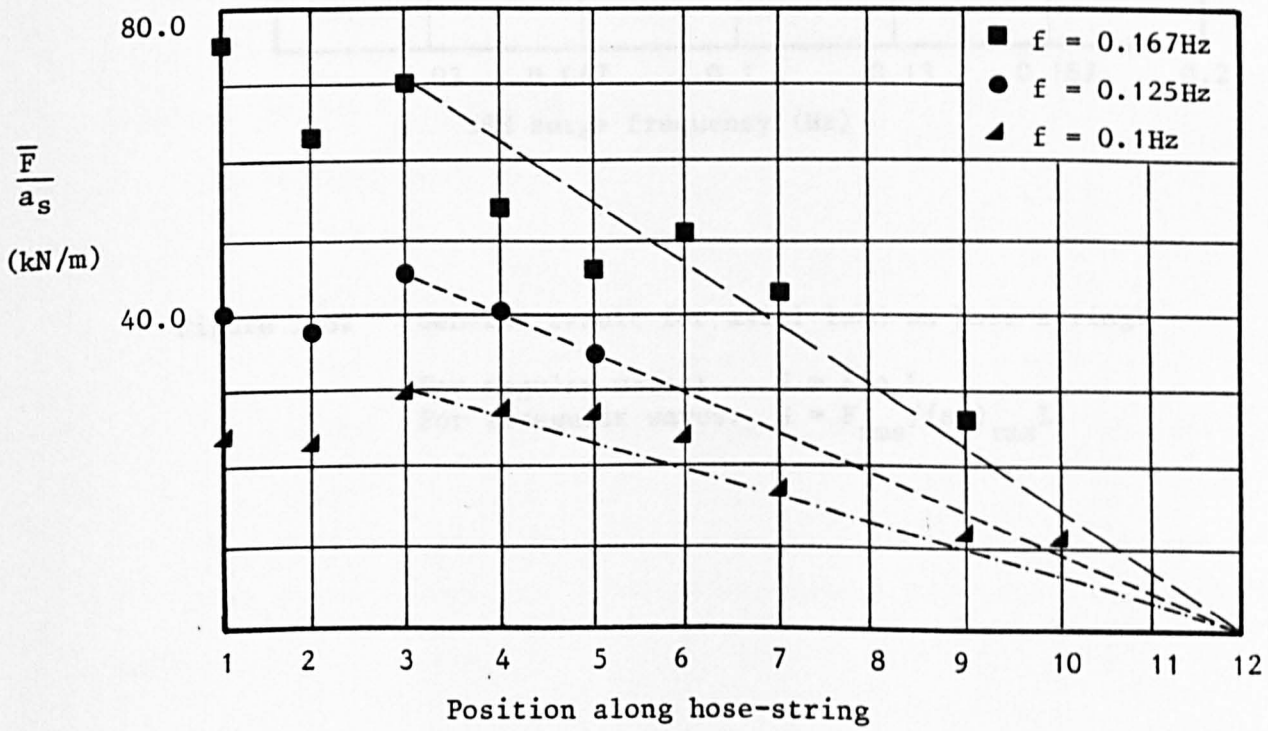

Figure 5.31 Amplitude of axial load divided by the surge amplitude measured along the hose-string in regular waves

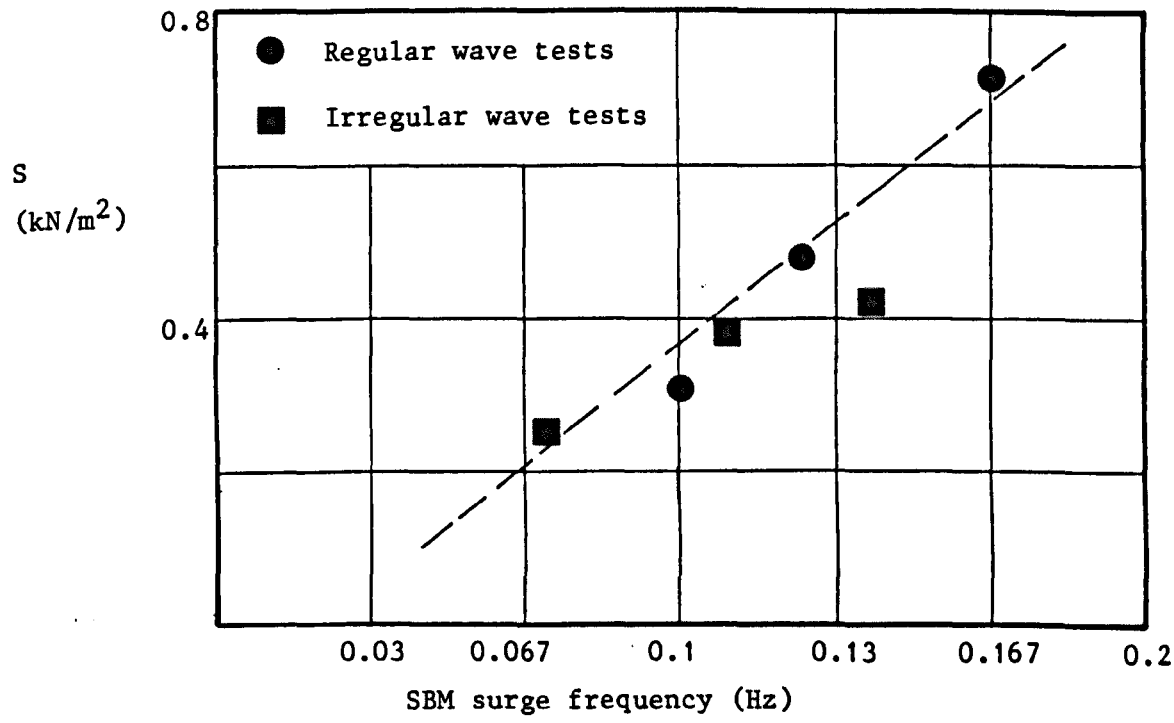

Figure 5.32 General result for axial load on hose-string:

For regular waves: $S = \overline{F}/a_s L$

For irregular waves: $S = F_{rms}/(a_s)_{rms} L$

6. SBM MOTION PREDICTION

6.1 Introduction

The bending moments and axial loads induced on a floating hose string attached to an SBM depend on the response of the SBM to the incident waves. The response of the particular CALM buoy used in the model tests has been studied in Chapter 4. This chapter addresses the problem of predicting the response of the CALM buoy in waves.

The problem is simplified by considering the buoy motions in regular waves with circular frequency σ as uncoupled, single degree-of-freedom systems, with harmonically-varying forcing functions. We therefore seek to establish equations of the form

$$M_T[d^2\xi/dt^2] + Q[d\xi/dt] + K\xi = F\sin(\sigma t+\beta) \qquad (6.1)$$

where ξ is the buoy displacement

M_T is total mass

Q is damping

K is stiffness

F is the amplitude of the excitation force

β is the phase difference between the waves and the excitation force.

For buoy heave, surge and pitch displacements y, x and θ respectively, equation (6.1) becomes

$$M_{TH}[d^2y/dt^2] + Q_H[dy/dt] + K_Hy = F_H\sin(\sigma t+\beta_H) \qquad (6.2)$$

$$M_{TS}[d^2x/dt^2] + Q_S[dx/dt] + K_Sx = F_S\sin(\sigma t+\beta_S) \qquad (6.3)$$

$$I_{TP}[d^2\theta/dt^2] + Q_P[d\theta/dt] + K_P\theta = T_P\sin(\sigma t+\beta_P) \qquad (6.4)$$

where subscripts H, S and P refer to heave, surge and pitch respectively. For pitch the total mass M_T and the excitation force F in equation (6.1) are replaced by the pitch total moment of inertia I_{TP} and the pitch excitation moment T_P.

Ideally, a study of the hydrodynamically-dependent inertia, damping and excitation terms in equations (6.2) to (6.4) would incorporate a detailed numerical model formulated from potential theory. Such a study could form the basis of a major research project in its own right. A much less formal approach is adopted in this chapter, the effectiveness of which can be assessed when the results are compared with the buoy motion results obtained from the physical model tests.

The stiffness terms in equations (6.2) to (6.4) are independent of the hydrodynamics and depend only on the properties of the buoy and the mooring chains. The method for evaluating these terms is presented prior to considering the hydrodynamic forces on the buoy.

6.2 Stiffness Characteristics of an 8-Chain CALM SBM

The stiffness characteristics of an 8-chain CALM SBM for a particular direction of motion are obtained by studying the total restoring force acting on the SBM when it is displaced in that direction of motion. In general the total restoring force will have a component due to the chains and a component due to the buoy properties.

6.2.1 Restoring Forces and Moments Due to the Chains

6.2.1.1 Heave

Appendix A4 details the load-displacement technique used to obtain the restoring force in heave due to the 8 chains. The method used follows that outlined by Langley (1982). It requires the computation of the

change in the vertical component of tension in each chain at the fairlead due to movement in heave. A summary of the method is presented in what follows.

With reference to Figure 6.1, the length of chain s_1 is related to the heave displacement y as follows.

$$s_1 - s_0 + x_0 = (1/2y_1)(s_1^2-y_1^2)\sinh^{-1}(2s_1y_1/(s_1^2-y_1^2)) \qquad (6.5)$$

where s is the length of chain off the ground and subscripts 0 and 1 refer to the equilibrium and displaced positions respectively, as shown in Figure 6.1.

By defining $r_1 = s_1/y_0$, $r_0 = s_0/y_0$ and $r_y = y_1/y_0 = 1 + (y/y_0)$, equation (6.5) can be rewritten as

$$f(r_1) = r_1-r_0+x_0/y_0-(1/2r_y)(r_1^2-r_y^2)\sinh^{-1}(2r_1r_y/(r_1^2-r_y^2)) = 0 \qquad (6.6)$$

For a known heave displacement y, equation (6.6) may be solved for r_1 using the Newton-Raphson method. The vertical component of tension in each chain T_{v_1} is then given by the catenary equation

$$T_{v_1} = \omega s_1 = \omega r_1 y_0 \qquad (6.7)$$

where ω is the submerged weight of chain per unit length.

The total heave restoring force due to the 8 chains R_H corresponding to the heave displacement y is

$$R_H = 8(T_{v_1} - T_{v_0}) \qquad (6.8)$$

where T_{v_0} is the vertical component of tension in each chain at the fairlead at equilibrium and is given by

$$T_{V_0} = \omega s_0 = \omega r_0 y_0 \qquad (6.9)$$

6.2.1.2 Surge

For a given surge displacement the net surge restoring force due to the 8 chains is obtained by resolving in the surge direction the horizontal component of tension in each chain at the fairlead. The method is detailed in Appendix A4 and is summarised in what follows.

With reference to Figure 6.2 it may be shown that for a surge displacement x

$$s_1 - s_0 + D + x_0 = [(s_1^2 - y_0^2)/2y_0]\sinh^{-1}(2s_1 y_0/(s_1^2 - y_0^2)) \qquad (6.10)$$

where D = x for chain #1

= -x for chain #2

= $x\cos 45^\circ$ for chains #3

= $-x\cos 45^\circ$ for chains #4.

(Chains #5 have no effect on the restoring force for relatively small displacements.)

By defining $r_1 = s_1/y_0$ and $r_0 = s_0/y_0$, equation (6.10) can be rewritten as

$$f(r_1) = r_1 - r_0 + D/y_0 + x_0/y_0 - \tfrac{1}{2}(r_1^2 - 1)\sinh^{-1}(2r_1/(r_1^2 - 1)) = 0 \qquad (6.11)$$

For a known surge displacement x and hence D, equation (6.11) may be solved to obtain r_1 for each chain using the Newton-Raphson method. The horizontal component of tension in each chain at the fairlead T_{H_1} is then obtained from the catenary equation

$$T_{H_1} = \tfrac{1}{2}\omega y_0 (r_1^2 - 1) \qquad (6.12)$$

The surge restoring force R_s due to the 8 chains corresponding to the surge displacement x is then given by

$$R_s = T_{H_1}{}^1 - T_{H_1}{}^2 + 2T_{H_1}{}^3\cos\alpha_3 - 2T_{H_1}{}^4\cos\alpha_4 \qquad (6.13)$$

where the superscripts 1, 2, 3 and 4 refer to the chain identification numbers shown in Figure 6.2 and the angles α_3 and α_4 are evaluated as shown in Appendix A4. (α_3 and α_4 are approximately equal to 45°.)

A computer program was developed which uses the above techniques to establish the restoring forces due to the 8 chains of a CALM SBM as the SBM moves in heave and surge. The input data is the chain weight per unit length in water (ω), the depth of water in which the chains lie (y_0) and the chains' pretension angle. The output includes a plot of the load-displacement curves. The program also fits polynomials of the form $F = c_1x + c_2x^3$ to the force-displacement data using a least squares polynomial fit. The result of each fit is also plotted and the equation of the polynomial printed.

Figure 6.3 shows the chain stiffness characteristics in surge and heave for the SBM used in the model tests conducted for this study. The restoring forces as functions of displacement are given by the equations of the fitted polynomials, i.e.

$$\begin{aligned} R_H(kN) &= 110y + 0.16y^3 \\ R_s(kN) &= 89.8x + 0.77x^3 \end{aligned} \qquad (6.14)$$

where y and x are the heave and surge displacements in metres respectively. Note that the cubic term is weak in comparison to the linear term in both relationships and can be neglected when considering

the CALM buoy's motions in waves. This means that the 8-chain system has linear stiffness coefficients of approximately 110kN/m in heave and 90kN/m in surge.

6.2.1.3 Pitch

Appendix A4 uses a moment-angular displacement method to show that for a small pitch angle θ (Figure 6.4) the restoring moment due to the 8 chains is approximately

$$R_P = (2T_{H_0} b + 6T_{v_0} h)\theta \qquad (6.15)$$

where T_{H_0} and T_{v_0} are the horizontal and vertical components of tension in the chains at the fairlead at equilibrium, b is the buoy diameter and h is the draft of the buoy.

6.2.2 SBM Heave Stiffness

The total heave restoring force acting on a CALM buoy when it is displaced in heave by an amount y is given by

$$R_{T_H} = \rho g A y + K_{H_C} y \qquad (6.16)$$

where ρ is the water density

g is the acceleration due to gravity

A is the cross sectional area of the buoy and is constant over the buoy's draft

K_{H_C} is the heave stiffness of the chain system.

The total heave stiffness of the SBM is

$$K_H = \rho g A + K_{H_C} \qquad (6.17)$$

For the SBM used in the model tests ρ = 1000kg/m^3, A = 240m^2 and K_{H_C} =

110kN/m; the heave stiffness of this SBM is therefore 2.46 x 10^3kN/m. Note that the chains contribute less than 5% to the total heave stiffness.

6.2.3 SBM Surge Stiffness

When a CALM SBM is displaced in surge from its equilibrium position the only surge restoring force acting on the SBM is that due to the chains. The surge stiffness of the CALM SBM is therefore equal to the surge stiffness of the chain system. For the SBM used in the model tests the surge stiffness K_S is equal to 90kN/m.

6.2.4 SBM Pitch Stiffness

When a CALM SBM is rotated in pitch through a small angle θ, the total restoring moment acting on the SBM (Figure 6.4) is given by

$$R_{T_P} = (B.GM + K_{P_C})\theta \qquad (6.18)$$

where B is the buoyancy force on the buoy at equilibrium

GM is the metacentric height of the floating buoy

K_{P_C} is the pitch stiffness of the chain system.

Substitution for K_{P_C} using equation (6.15) gives

$$K_P = B.GM + 2T_{H_0}b + 6T_{V_0}h \qquad (6.19)$$

For the SBM considered in the model tests B = 10 x 10^6N, b = 17.3m, GM = 1.53m and h = 4.5m; a catenary analysis for the mooring chains at equilibrium gives T_{H_0} = 130 x 10^3N and T_{V_0} = 280 x 10^3N. The pitch stiffness of the SBM used in the model tests is, therefore, 27.6 x 10^3kNm/radian. Note that the horizontal components of tension in the chains provide about 16% of the pitch stiffness and the vertical components provide about 27%. In total the mooring chains provide nearly as much pitch stiffness as the stability properties of the buoy.

6.3 Hydrodynamic Forces on a CALM SBM

6.3.1 Background Theory

If a floating body is small compared to the incident wavelength, since the body displaces its own weight of water, it is clear that the forces on the body are exactly those that would have occurred on the displaced fluid. The motions of such a body will therefore be the same as would have occurred for the displaced fluid. For bodies such as a CALM buoy that are restrained and/or large relative to the incident wavelength such that the kinematics change significantly over the body dimension, the situation becomes more complex because the body affects the waves. The wave force calculations for these bodies must take into account the scattering or diffraction of the incident waves by the body as well as the hydrodynamic forces resulting from the generation of waves which radiate from the body as it responds to the excitation forces.

The method by which wave forces on large floating bodies are computed is based on linear potential flow theory. This theory is based on the assumptions that flow separation does not occur, that viscous effects are confined to the boundary layers on the body surface, that the flow is irrotational and the incident wave height is sufficiently small for linear wave theory to apply. The problem reduces to the determination of the velocity potential Φ which satisfies the Laplace equation within the fluid region subject to the boundary conditions at the seabed, the water surface and the body surface.

A fundamental property of linear potential theory is that potentials can be superimposed. Accordingly the velocity potential for the wave-body interaction can be represented as the sum of the incident wave, the scattered wave and the radiated wave potentials, i.e.

$$\Phi = \Phi_w + \Phi_s + \Phi_r \qquad (6.20)$$

Pressure is given by $\rho(\partial\Phi/\partial t)$ and the integration of the pressures around the body surface gives the hydrodynamic forces. The forces due to the incident and scattered wave potentials are termed the "excitation" forces and are the same as when the body is held fixed. The forces arising from the body's motions and derived from the forced potential Φ_r, are conveniently separated into components in phase with the velocity and the acceleration of each mode of motion. These components are termed the "added mass" and "damping" forces respectively.

Sarpkaya (1981) outlines the general approach to linear potential theory as well as the specific techniques applicable to particular body configurations for the evaluation of the scattered and radiated wave potentials.

Within the context of the present study it is not appropriate to develop a detailed numerical model based on potential theory for the prediction of the hydrodynamic forces on a CALM buoy. Instead it is proposed to approximate the buoy as a floating vertical circular cylinder for which published results for the hydrodynamic forces obtained from linear potential theory are available.

6.3.2 Published Results for Floating Vertical Circular Cylinders

A number of published papers present results for the hydrodynamic forces on floating vertical circular cylinders obtained using linear potential theory. The forces are seen to depend on the radius and draft of the cylinder and on the water depth. Since the intention here is to apply the results to the SBM used in the model tests only those results available

for cylinders with similar properties as the idealised buoy will be considered.

The idealisation of the buoy is illustrated in Figure 6.5. The equivalent cylinder has non-dimensional properties $d/r = 4.62$ and $h/r = 0.52$ where d is the water depth, r is the cylinder radius and h the draft. The published results of Garrett (1971), Garrison (1974) and Yeung (1981) include data which is valid for cylinders with these non-dimensional properties.

Garrett (1971) obtained the magnitude and phase of the wave excitation forces and moments on a truncated cylinder extending down from the free surface. The results are presented as graphs of non-dimensional coefficients of horizontal force, vertical force and torque (pitch moment) against the non-dimensional frequency parameter $\sigma^2 r/g$, where σ is the incident wave circular frequency. Results are presented for d/r values of 0.75 and 1.5 with $(d-h)/r$ values of 0.0, 0.5 and 1.0.

Garrison (1974) outlines a method for computing the magnitude and phase of the wave excitation forces and moments as well as the added mass and damping forces for floating bodies of arbitrary shape. The method is applied to certain floating bodies including a vertical circular cylinder. The results presented include graphs of the coefficient of horizontal (surge) excitation force and of added mass and damping coefficients against the non-dimensional frequency parameter. The results are given for d/r values of 1.0, 1.5 and infinity, with the draft equal to half the radius in each case, i.e. $h/r = 0.5$. There is little difference between the results presented for the two cases $d/r = \infty$, $h/r = 0.5$ and $d/r = 1.5$, $h/r = 0.5$. This implies that the water depth has no influence on the forces beyond a certain value of d/r which may be taken as 1.5. This

means that Garrett's results for d/r = 1.5 and h/r = 0.5 can be applied to the circular cylinder idealisation of the SBM. Garrison presents no results for the vertical (heave) excitation force and pitch excitation moment but reports that these are the same as presented by Garrett.

Yeung (1981) uses a formulation which follows closely that used by Garrett but uses a different solution technique to study the added mass and damping of a vertical circular cylinder in finite-depth waters. An extensive range of results is presented which includes graphs of added mass and damping coefficients against the non-dimensional frequency parameter for d/r values between 0.2 and 5.0 and (d-h)/d values between 0.1 and 1.0. Of particular interest are the results for d/r = 5.0, (d-h)/d = 0.9 (i.e. h/r = 0.5) as these correspond closely to the properties of the idealised buoy.

In order to standardise the results of Garrett, Garrison and Yeung for presentation here, a set of non-dimensional force coefficients are defined as follows.

The non-dimensional heave excitation force coefficient C_{FH}, surge excitation force coefficient C_{FS} and pitch excitation moment coefficient C_{TP} are defined by

$$F_H = C_{FH}\rho g\pi r^2 a \qquad (6.21)$$

$$F_S = C_{FS}\rho g\pi r^2 a \qquad (6.22)$$

$$T_P = C_{TP}\rho g\pi r^2 ar \qquad (6.23)$$

where a is the incident wave amplitude and F_H, F_S and T_P are the amplitudes of the harmonically-varying heave, surge and pitch excitation forces and moments.

The added mass coefficients in heave (C_{aH}), surge (C_{aS}) and pitch (C_{aP}) are given by

$$M_{aH} = C_{aH}\rho V \tag{6.24}$$

$$M_{aS} = C_{aS}\rho V \tag{6.25}$$

$$M_{aP} = C_{aP}\rho V \tag{6.26}$$

where M_a is added mass and V is immersed volume.

The heave damping coefficient C_{dH} is given by

$$Q_H = C_{dH}\rho V\sigma \tag{6.27}$$

where $Q_H[dy/dt]$ is the heave damping force and σ is the circular frequency of the incident waves. The surge and pitch damping coefficients are similarly defined by

$$Q_S = C_{dS}\rho V\sigma \tag{6.28}$$

$$Q_P = C_{dP}\rho V\sigma k_P^2 \tag{6.29}$$

where k_P is the pitch radius of gyration of the cylinder.

The definitions of the coefficients, summarised in Table 6.1, have been applied to selected results from those of Garrett, Garrison and Yeung to produce Figures 6.6 and 6.7.

Figure 6.6 presents the results obtained for the excitation forces in heave and surge and the pitch excitation moment obtained by Garrett for the cylinder with $d/r = 1.5$, $h/r = 0.5$ and for the surge excitation force obtained by Garrison for the cylinder with $d/r = \infty$, $h/r = 0.5$. The two results for surge are the same indicating that the water depth has no influence on the forces beyond the value of $d/r = 1.5$ for the cylinder

Equations of motion:

Heave: $(M+M_{aH})d^2y/dt^2 + Q_H dy/dt + K_H y = F_H \sin(\sigma t+\beta_H)$

Surge: $(M+M_{aS})d^2x/dt^2 + Q_S dx/dt + K_S x = F_S \sin(\sigma t+\beta_S)$

Pitch: $(M+M_{aP})k_P^2(d^2\theta/dt^2) + Q_P d\theta/dt + K_P \theta = T_P \sin(\sigma t+\beta_P)$

	Force/Moment Coefficient	Added Mass Coefficient	Damping Coefficient
Heave	$C_{FH} = F_H/(\rho g\pi r^2 a)$	$C_{aH} = M_{aH}/\rho V$	$C_{dH} = Q_H/\rho V\sigma$
Surge	$C_{FS} = F_S/(\rho g\pi r^2 a)$	$C_{aS} = M_{aS}/\rho V$	$C_{dS} = Q_S/\rho V\sigma$
Pitch	$C_{TP} = T_P/(\rho g\pi r^2 ar)$	$C_{aP} = M_{aP}/\rho V$	$C_{dP} = Q_P/\rho V\sigma k_P^2$

Table 6.1

Definition of excitation force, excitation moment, added mass and damping coefficients for floating vertical circular cylinder

with $h/r = 0.5$. Garrett's results may therefore be applied to the cylinder approximating the buoy used in the model tests which has $d/r = 4.6$ (Figure 6.5). Some general points may be noted from Figure 6.6: the heave force tends to the buoyancy force and its phase tends to zero as $\sigma^2 r/g$ tends to zero; the surge force is in phase with minus the slope of the incident wave for small values of $\sigma^2 r/g$; the pitch moment behaves in much the same way as the surge force, having a maximum at a value of $\sigma^2 r/g$ close to 1 while its phase is always the same as that of the surge force.

Figure 6.7 presents the heave and surge added mass and damping coefficients obtained from the results of Garrison for the cylinder with $d/r = \infty$, $h/r = 0.5$ and from Yeung for the cyinder with $d/r = 5.0$, $h/r = 0.5$. There is very good agreement between the results from the two

sources. The heave added mass coefficient is approximately constant with a value of 1.0 over a wide range of $\sigma^2 r/g$; the surge added mass coefficient, on the other hand, is very much dependent on $\sigma^2 r/g$. The behaviour of the heave and surge damping coefficients is also dissimilar: heave damping decreases with increasing $\sigma^2 r/g$ while surge damping generally increases with increasing $\sigma^2 r/g$ (for the range of $\sigma^2 r/g$ shown). The significance of the results for damping is that at low frequencies forced heave motion of the cylinder will generate larger waves which radiate away from the cylinder than forced surge motion, while for higher frequencies the opposite is true.

The pitch added mass coefficient obtained from the results of Garrison ($d/r = \infty$, $h/r = 0.5$) is nearly independent of frequency and has a value of 2.01. Similarly the pitch added mass coefficient obtained from the results of Yeung ($d/r = 2.0$, $h/r = 0.5$) is also nearly independent of frequency and has a value of about 2.3. Garrison reports that the pitch damping is extremely small for the cylinder studied and, accordingly, presents no graph for the pitch damping coefficient. There is some doubt as to the definition of the pitch damping coefficient used by Yeung. For these reasons no results for the pitch damping coefficient have been obtained from the published papers.

It is of interest to note that Yeung reports that the behaviour of the pitch added mass and damping coefficients is complex, depending very much on the cylinder's geometric parameters. In particular Yeung reports that when the draft to radius ratio is 0.5 ($h/r = 0.5$) the pitch damping becomes extremely small (as reported by Garrison) with an associated constant value of added mass as a function of frequency and small pitch excitation moment which becomes zero at certain frequencies. This

phenomenon is apparently related to the possibility that the phasing and magnitude of the contributions from the bottom and sides of the cylinder to the total pitch moment cancel one another. It must be noted that these results are in apparent disagreement with the results of Garrett presented in Figure 6.6(c).

6.3.3 Hydrodynamic Forces From Free- and Forced-Motion Tests

The hydrodynamic coefficients in heave and pitch obtained from the free- and forced-motion tests carried out on the SBM used in the model tests (Sections 4.3 and 4.4) can now be compared with those of the floating vertical circular cylinder approximation of the SBM.

The heave natural frequency of the SBM, measured from the heave free-motion of the SBM in still water, is 0.85 rads/sec, yielding a heave added mass coefficient of 2.18 at a value of 0.64 of the non-dimensional frequency parameter $\sigma^2 r/g$. This value is approximately twice that shown in Figure 6.7(a) for the cylinder approximation of the SBM. The difference between the results highlights the effects the differences in shape can have on the hydrodynamic properties. The greater heave added mass for the SBM is due to the discontinuities in shape caused by the presence of the outer edge onto which the chains are attached on the underside of the buoy and by the open central section of the submerged part of the buoy (Figure 6.5).

The pitch natural frequency of the SBM, estimated from the pitch free-motion tests (and confirmed by the spectral analysis of the measured pitch motion in waves) is 0.628 rads/sec, yielding a pitch added mass coefficient of 2.1 at $\sigma^2 r/g = 0.35$. This is close to the pitch added mass coefficient obtained from the results of Garrison (2.01) and Yeung (2.3) for the cylinder approximation of the SBM. This suggests that the

discontinuities in the buoy's shape play a lesser role in the determination of pitch added mass than heave added mass.

The heave damping coefficients obtained for the SBM from the heave forced-motion tests (Figure 4.18) are plotted in Figure 6.8 against $\sigma^2 r/g$ together with the results obtained from Garrison (1974) for the cylinder approximation of the SBM. Again there are marked differences between the two sets of results, due primarily to the differences in shape between the buoy and the cylinder. The results are similar in that the greatest damping occurs at the lower frequencies.

The pitch damping coefficients obtained for the SBM from the pitch forced-motion tests (Figure 4.20) are plotted against $\sigma^2 r/g$ in Figure 6.9. (There are no corresponding results for the cylinder approximation of the SBM.) The shape of the graph is the same as for the surge damping coefficient. This is as might be expected since the variation with frequency of the surge excitation force is the same as that of the pitch excitation moment.

6.3.4 A Note on the Surge and Heave Excitation Forces

It is worth comparing the surge and heave excitation forces given in Figure 6.6 with simple first estimates of these forces.

Consider first the surge excitation force. Because the buoy is large the velocity-dependent drag forces are very small compared to the inertia forces. If the problem is simplified by neglecting the diffraction effects as well as the velocity drag forces then the estimate of the surge force is the force on a circular cylinder in ideal flow. The force is readily obtained from potential flow theory (e.g. Dean and Dalrymple (1984), Chapter 8) and is given by

$$dF = C_m \rho \pi r^2 \dot{u} dy \tag{6.30}$$

where dF = the force on an elemental length of the cylinder

r = is the cylinder radius

$\dot{u}$ = is the fluid particle acceleration

C_m = $1+k_m$, where $k_m \rho \pi r^2 \dot{u} dy$ is the force necessary to accelerate the fluid around the stationary cylinder and $k_m = 1.0$ for the circular cylinder.

Applying equation (6.30) to the calculation of the wave-induced force on the cylinder approximation of the buoy, as illustrated in Figure 6.10, the surge force is given by

$$F_S = C_m \rho \pi r^2 \int_{-h}^{0} \dot{u} dy \tag{6.31}$$

where h is the cylinder draft and, from linear wave theory,

$$\dot{u} = -\sigma^2 a e^{ky} \cos(kx-\sigma t) \tag{6.32}$$

where σ is the wave circular frequency

a is the wave amplitude

k is the wave number and, for deep water linear waves, is equal to σ^2/g.

Substituting for $\dot{u}$ in equation (6.31) and evaluating the integral gives

$$F_S = C_m \rho g \pi r^2 a(1-e^{-kh})[-\cos(kx-\sigma t)] \tag{6.33}$$

The surge force coefficient is, therefore,

$$C_{FS} = C_m(1-e^{-kh}) \tag{6.34}$$

and the surge force is in phase with minus the slope of the wave.

For the cylinder with h/r = 0.5 equation (6.34) becomes

$$C_{FS} = C_m[1 - (\exp(-\sigma^2 r/g))^{1/2}] \qquad (6.35)$$

Figure 6.11 presents the result given by equation (6.35) as a graph of C_{FS} against $\sigma^2 r/g$, together with the results obtained from Garrett (1970) shown in Figure 6.6(b). The differences between the two results shown in Figure 6.11 represent the effects of diffraction on the surge force. Clearly diffraction effects are greatest at high values of $\sigma^2 r/g$, that is for large values of diameter to wavelength ratios. For low values of $\sigma^2 r/g$, corresponding to smaller diameter cylinders in long waves, diffraction effects are negligible and the results tend to the same value. It should be noted that neither of the results presented in Figure 6.11 for the surge force takes account of the velocity-dependent drag forces.

For a vertical circular cylinder with shallow draft, a first estimate of the heave excitation force in waves is the force due to the dynamic pressure acting on the base of the cylinder, as illustrated in Figure 6.12. From deep-water, linear wave theory the dynamic pressure under a progressive wave, asin(kx-σt), is

$$P_{dyn} = \rho g a e^{-ky} \sin(kx-\sigma t) \qquad (6.36)$$

where y is depth below mean water level.

For the cylinder with radius r and draft h, the heave force estimate is the integration of the dynamic pressure over the base of the cylinder at depth y = -h, i.e.

$$F_H = \rho g a(\pi r^2) e^{-kh} \sin(kx-\sigma t) \qquad (6.37)$$

The heave force coefficient is, therefore,

$$C_{FH} = e^{-kh} \tag{6.38}$$

and for the cylinder with $h/r = 0.5$

$$C_{FH} = [\exp(-\sigma^2 r/g)]^{1/2} \tag{6.39}$$

Figure 6.13 presents the result given by equation (6.39) as a graph of C_{FH} against $\sigma^2 r/g$, together with the result obtained from Garrett (1970) shown in Figure 6.6(a). There are two reasons why the result from Garrett is always less than the first estimate result: firstly, Garrett includes the effects of diffraction which reduce the total forcing potential in the same way as for surge; secondly, Garrett includes the force due to the vertical acceleration of the water past the cylinder which is out of phase with the dynamic pressure force. As $\sigma^2 r/g$ tends to zero the heave excitation force tends to the buoyancy force caused by the fluctuating water level.

6.4 Empirical Models for SBM Motion Prediction

The equations of motion of the SBM in heave, surge and pitch are given by equations (6.2) to (6.4). The stiffness term for each degree-of-freedom of motion has been obtained using the procedures described in Section 6.2. It is proposed to apply the results for the hydrodynamic forces discussed in Section 6.3 to determine the excitation, added mass and damping forces in the equations of motion. The resulting models are "empirical" in the sense that coefficients are used to determine the quantities in the equations of motion.

The equation of motion for the general displacement ξ of the SBM is (equation 6.1)

$$(M+M_a)[d^2\xi/dt^2] + Q[d\xi/dt] + K\xi \cdot = F\sin(\sigma t+\beta) \qquad (6.40)$$

If equation (6.40) is rewritten in the form

$$\ddot{\xi} + 2\alpha\dot{\xi} + \omega_o^2\xi = G\sin(\sigma t+\beta) \qquad (6.41)$$

where

$$2\alpha = Q/(M+M_a)$$

$$\omega_o^2 = K/(M+M_a)$$

$$G = F/(M+M_a)$$

then the steady state response is given by

$$\xi(t) = R\sin(\sigma t+\beta-\gamma) \qquad (6.42)$$

where

$$R = G/[(\omega_o^2-\sigma^2)^2 + (2\alpha\sigma)^2]^{1/2} \qquad (6.43)$$

and

$$\gamma = \tan^{-1}[2\alpha\sigma/(\omega_o^2-\sigma^2)] \qquad (6.44)$$

The amplitude of the response per unit wave amplitude, i.e. the response transfer function, is

$$H = R/a \qquad (6.45)$$

The phase difference between the response and the waves is

$$\psi = \beta-\gamma \qquad (6.46)$$

The response of the SBM in heave, surge and pitch has been obtained for 30 values of $\sigma^2 r/g$ between 0.1 and 3.0 (corresponding to values of linear frequency between 0.054Hz and 0.294Hz). The hydrodynamic coefficients at

each frequency have been obtained from the data presented in Figures 6.6 to 6.9; the hydrodynamic forces have been obtained from the coefficients and the geometric properties of the buoy using the definitions given in Table 6.1.

6.4.1 SBM Heave

The heave added mass and damping coefficients used in the empirical model for SBM heave are those obtained from the heave free- and forced-motion model tests. The heave added mass value of 2.18 is assumed constant with frequency. The heave damping coefficients are given by the experimental result in Figure 6.8. The heave excitation force is approximated by the heave excitation force on the cylinder approximation of the SBM as obtained from the results of Garrett (1971) and presented in Figure 6.6(a). The SBM data and the coefficients corresponding to 10 values of frequency are presented in Table 6.2.

The SBM heave transfer and phase functions obtained from the empirical model are presented in Figures 6.14(a) and 6.14(b) respectively. The transfer function peak and rapid phase change at 0.135Hz corresponds to the heave natural frequency of the SBM. As the frequency decreases from the natural frequency the SBM tends to heave in phase with the waves and with the same amplitude as the waves. For frequencies greater than the natural frequency there is a rapid decay in the heave response of the SBM.

6.4.2 SBM Surge

No free- or forced-motion tests were carried out for surge. The coefficients of the surge excitation, added mass and damping forces have been obtained from the published results of Garrett (1971) and Garrison (1974) for the cylinder approximation of the buoy, as presented in Figures 6.6(b) and 6.7(b). The coefficients obtained for 10 values of frequency are presented in Table 6.3.

The SBM surge transfer and phase functions obtained from the empirical model are presented in Figures 6.15(a) and 6.15(b) respectively. The surge natural frequency is low, less than 0.05Hz, due to the low surge stiffness of the SBM. Accordingly the surge response increases with decreasing frequency. For frequencies less than 0.15Hz and greater than the natural frequency the surge is in phase with the slope of the wave. (For frequencies less than the natural frequency the surge will be in phase with minus the slope of the wave.)

6.4.3 SBM Pitch

The pitch added mass and damping coefficients used in the empirical model for SBM pitch are those established from the pitch free- and forced-motion tests. The pitch added mass value of 2.1 is assumed constant with frequency. The pitch damping coefficients are given in Figure 6.9. The estimate of the pitch excitation moment is the pitch excitation moment on the cylinder approximation of the buoy as obtained from the results of Garrett (1971) and presented in Figure 6.6(c). The coefficients corresponding to 10 values of frequency are presented in Table 6.4.

The SBM pitch transfer and phase functions predicted by the empirical model are presented in Figures 6.16(a) and 6.16(b) respectively. The peak in the transfer function and the 180° phase shift at around 0.1Hz corresponds to the pitch natural frequency of the SBM. For frequencies less than the natural frequency the SBM pitches in phase with minus the wave slope; for frequencies greater than the natural frequency and less than 0.2Hz the pitch is approximately in phase with the wave slope; at high frequencies the SBM tends to pitch in phase with the wave crest. The rapid phase change and very large response at the natural frequency results from the very low pitch damping close to the natural frequency

obtained from the pitch forced-motion tests, a result that is in agreement with the results of Garrison (1974) and Yeung (1981) discussed in Section 6.3.

The effectiveness of the empirical models presented in this chapter will be assessed when the predictions are compared with the heave, surge and pitch transfer and phase functions obtained for the SBM from the model tests. Of particular concern will be those force coefficients applied to the SBM which have been obtained from the published results for the floating vertical cylinder approximation to the buoy.

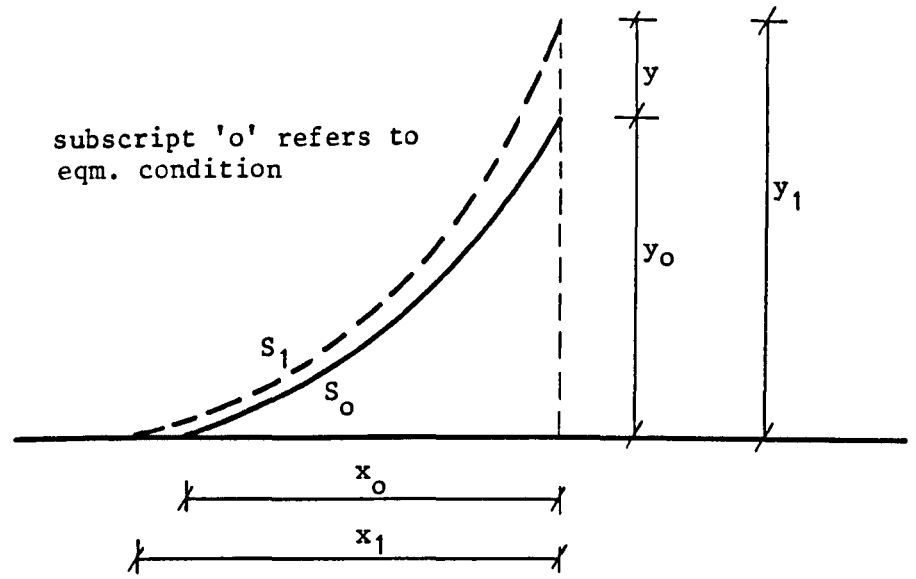

Figure 6.1 Definition sketch for the heave displacement y of a catenary mooring chain

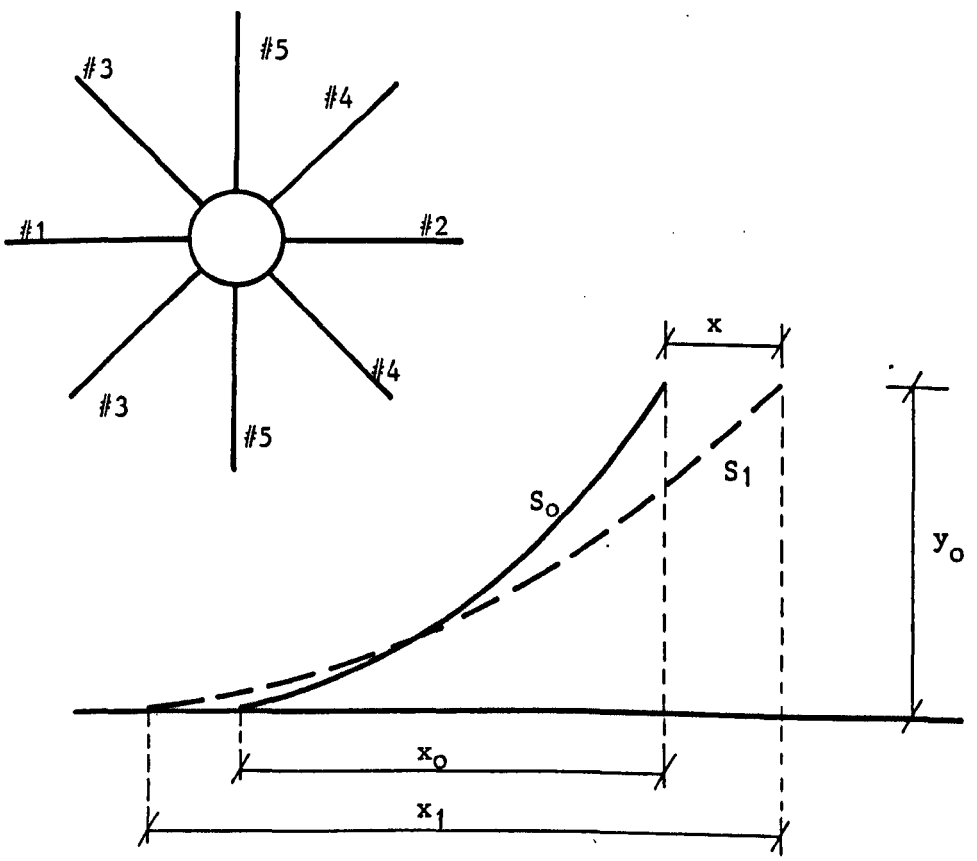

Figure 6.2 Definition sketch for the surge displacement x of a catenary mooring chain

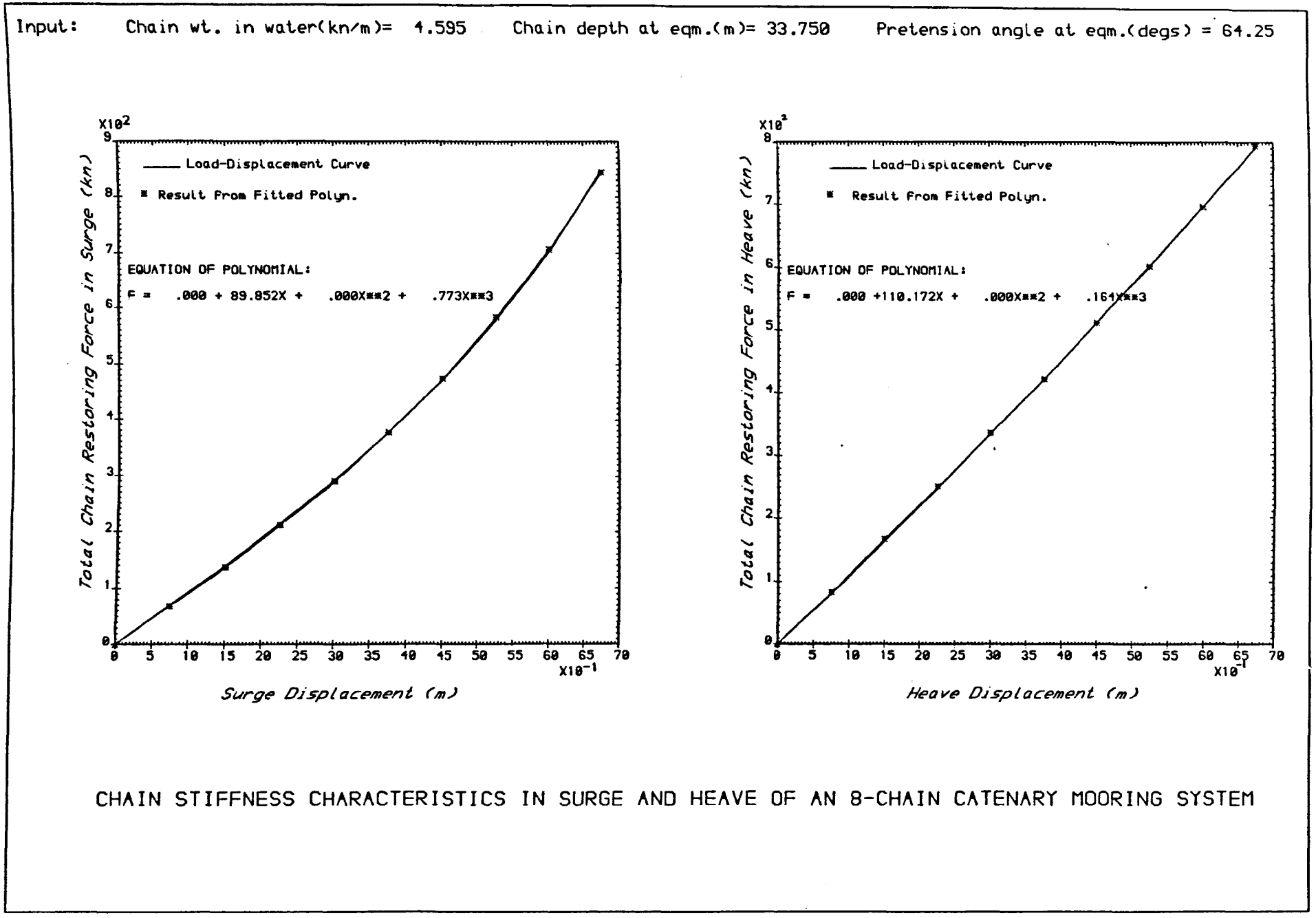

Figure 6.3 The heave and surge stiffness characteristics of the 8-chain catenary mooring modelled in the model tests

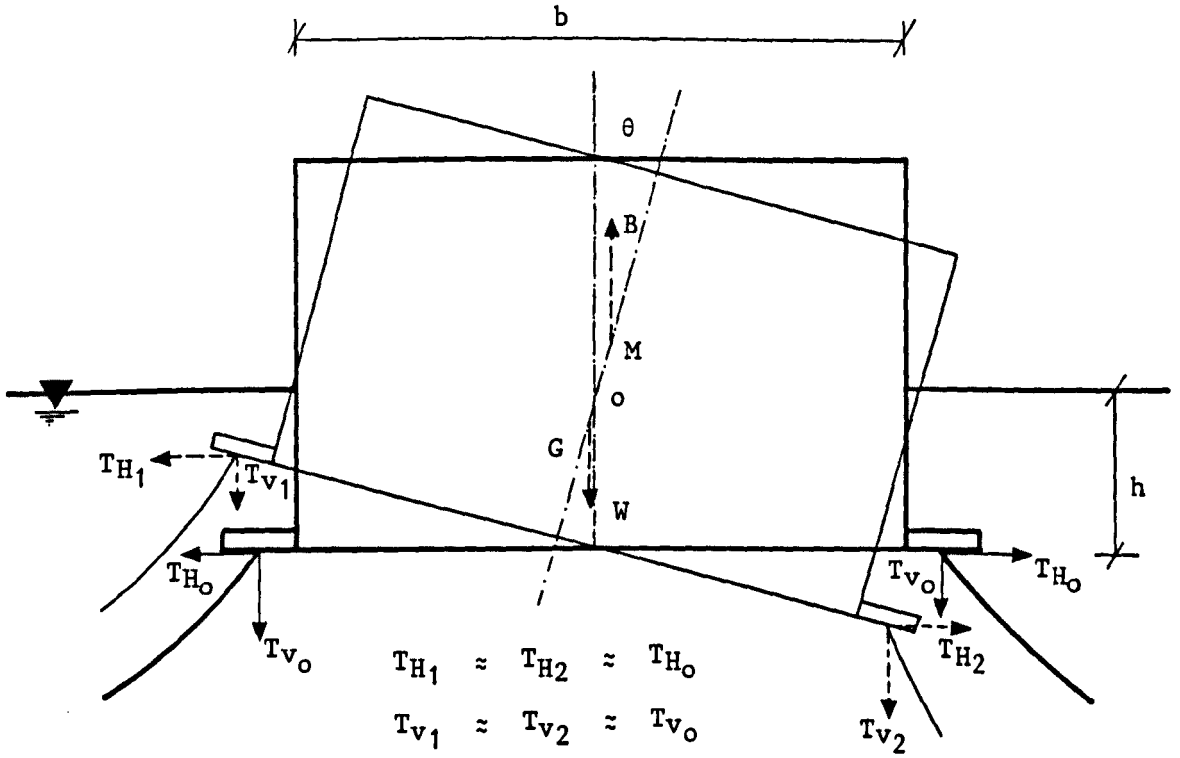

Total restoring moment = $(B.GM + 6T_{v_o}h + 2T_{H_o}b)\theta$

Figure 6.4 Illustration of SBM pitch

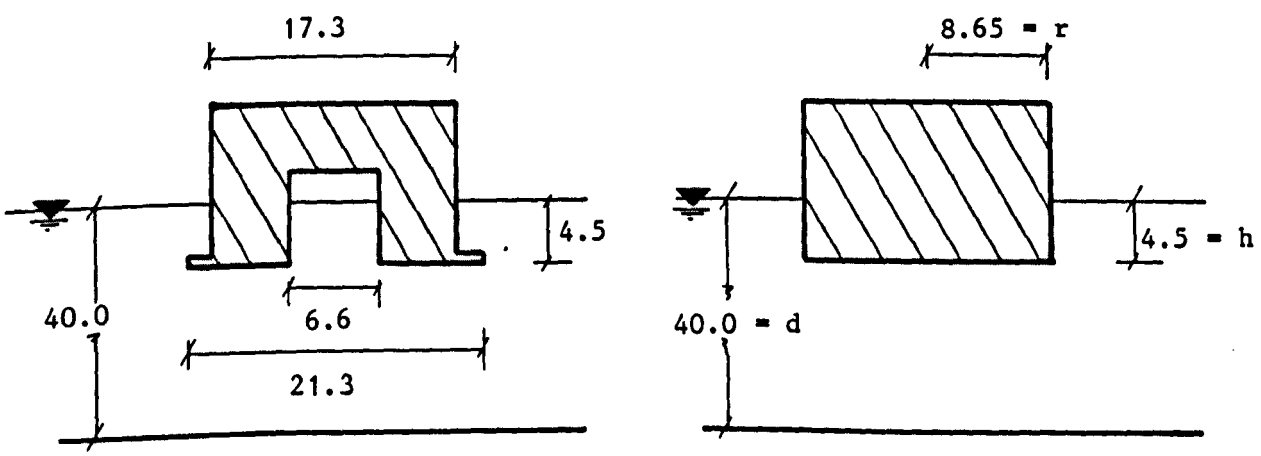

Section through buoy

Section through cylinder approx. of buoy

Figure 6.5 Approximation of buoy as a vertical circular cylinder (dimensions in metres)

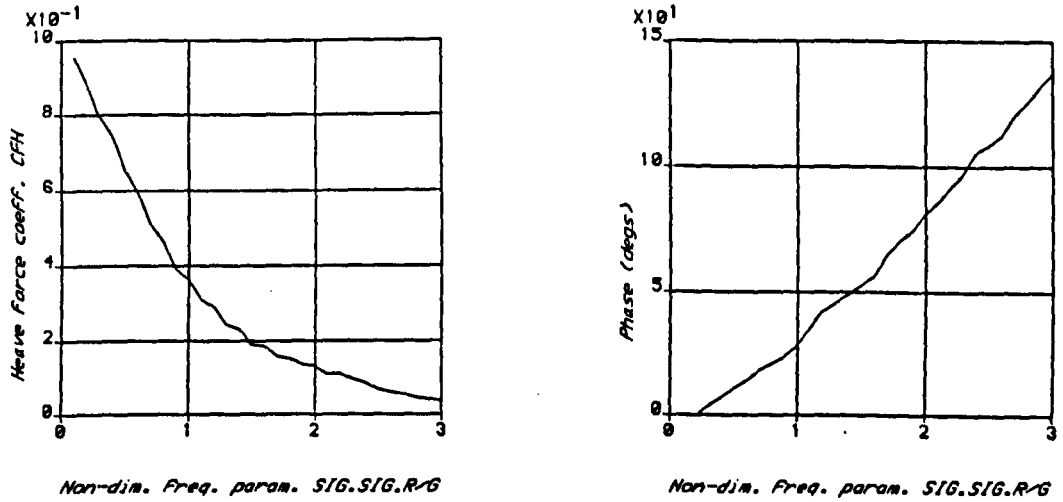

(a) Heave excitation force: from Garrett (1971) with d/r = 1.5, h/r = 0.5

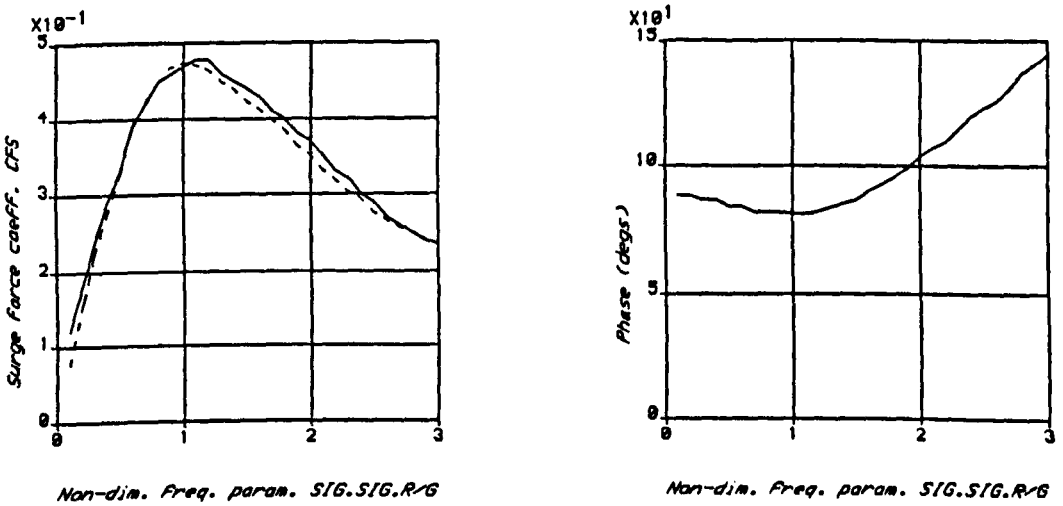

(b) Surge excitation force: Garrett (1971) with d/r = 1.5, h/r = 0.5 ——
Garrison (1974) with d/r = ∞, h/r = 0.5 -------

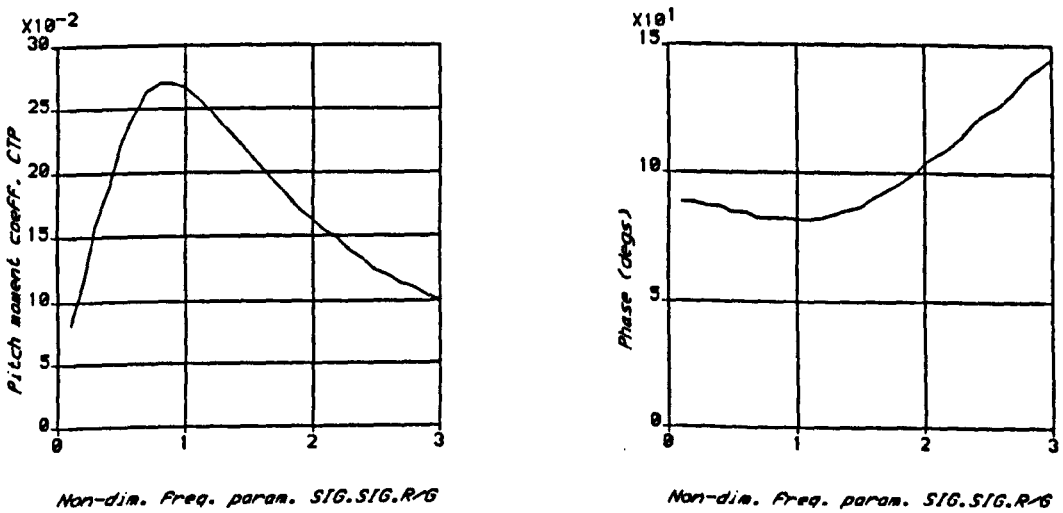

(c) Pitch excitation moment: from Garrett (1971) with d/r = 1.5, h/r = 0.5

Figure 6.6 Phases and magnitudes of the excitation forces and moments on a floating vertical circular cylinder

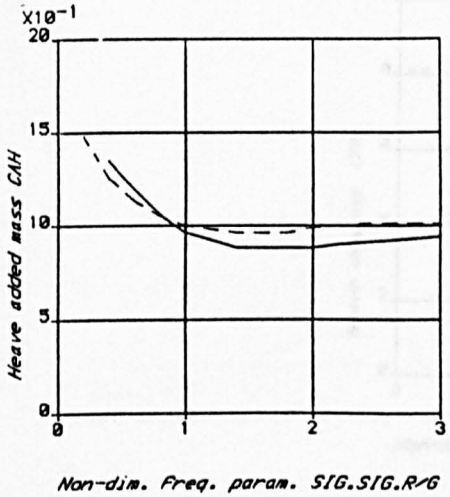

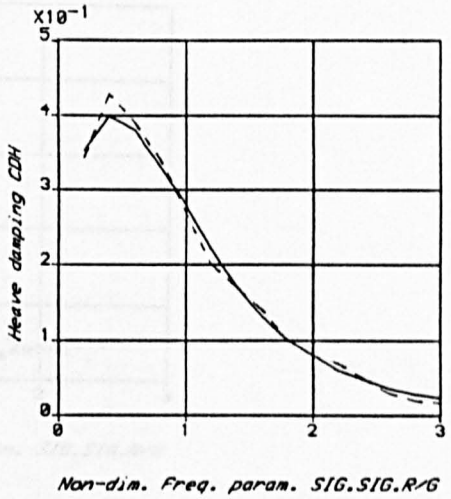

(a) Heave added mass and damping:
----- Garrison (1974) with d/r = ∞, h/r = 0.5
—— Yeung (1981) with d/r = 5.0, h/r = 0.5

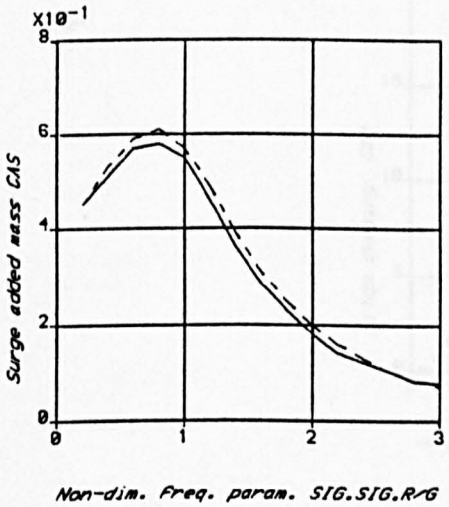

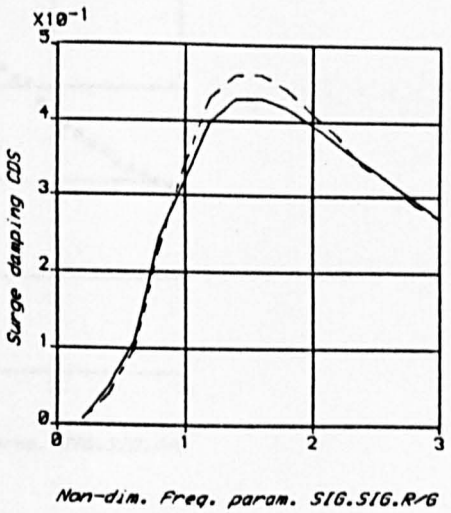

(b) Surge added mass and damping:
----- Garrison (1974) with d/r = ∞, h/r = 0.5
—— Yeung (1981) with d/r = 5.0, h/r = 0.5

Figure 6.7 Added mass and damping coefficients for a floating vertical circular cylinder

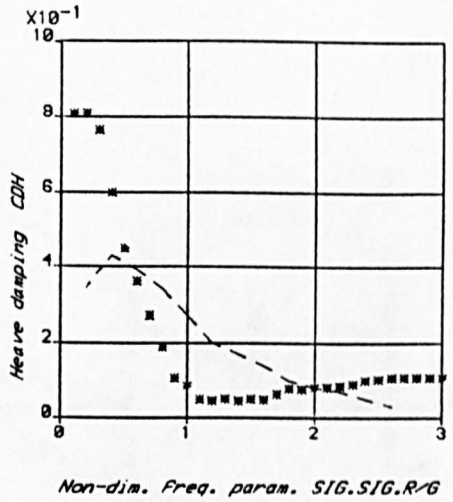

Figure 6.8 A comparison between the heave damping coefficients obtained for the SBM from the heave forced-motion tests (*Figure 4.18) and the heave damping coefficients for the vertical circular cylinder (Garrison, Figure 6.7)

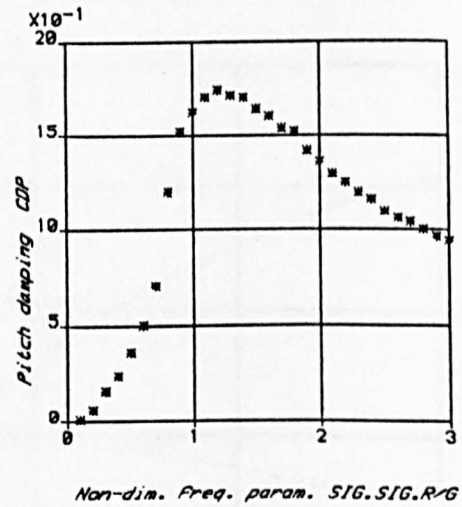

Figure 6.9 SBM pitch damping coefficients obtained from the pitch forced-motion tests (Figure 4.20)

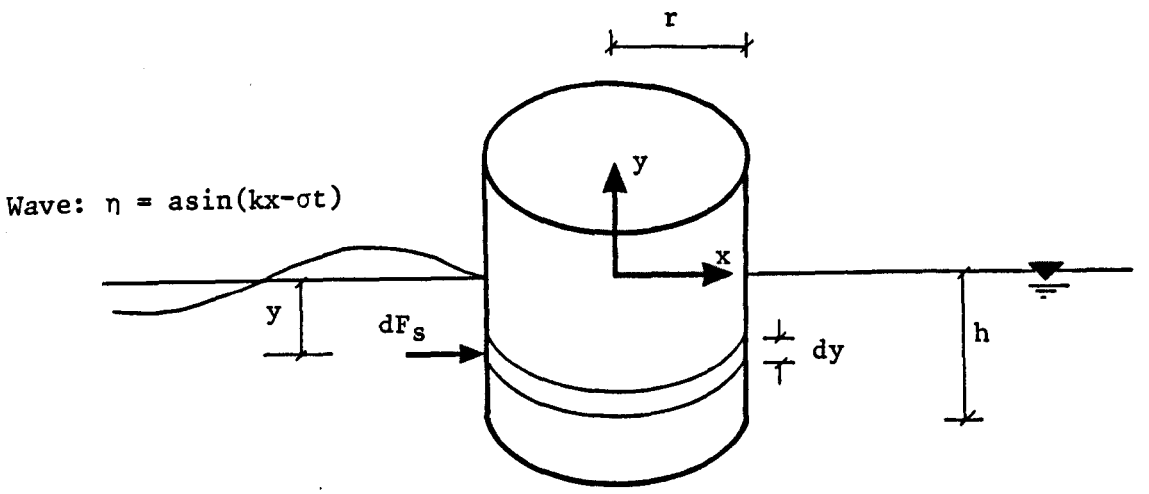

Figure 6.10 Definition sketch for the calculation of a first estimate of the surge excitation force on a cylinder

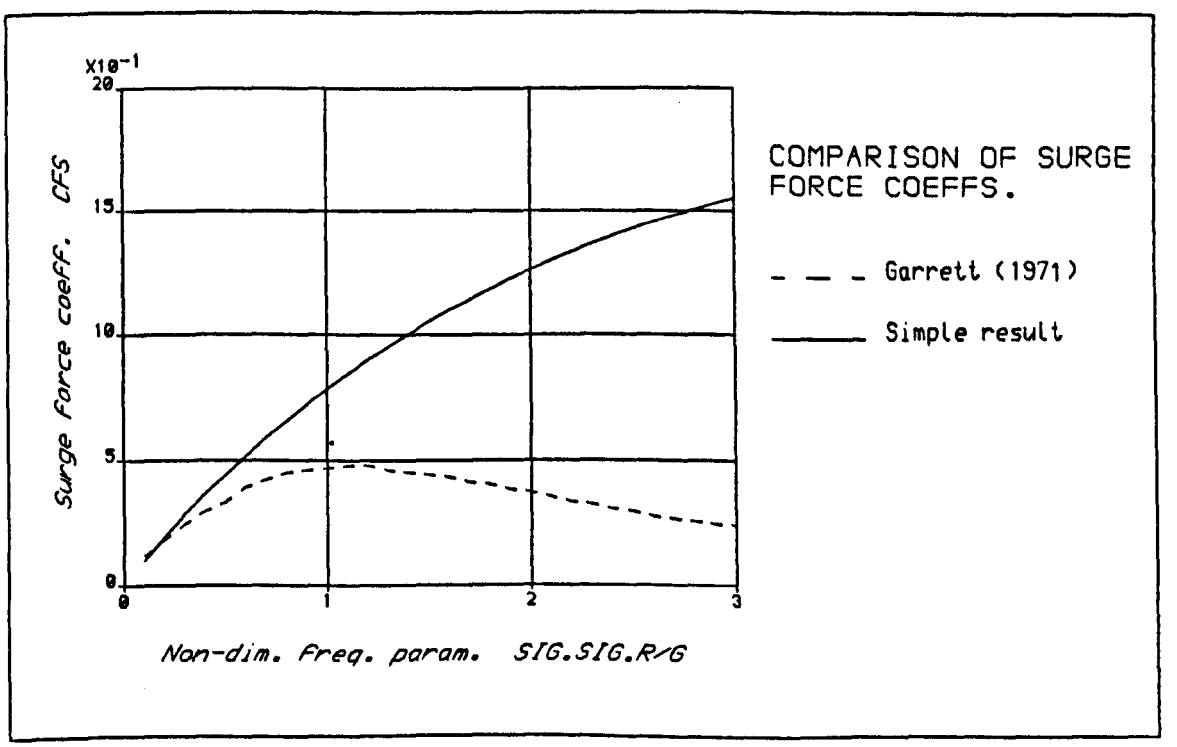

Figure 6.11 Comparison of the surge force coefficients obtained from Garrett (Figure 6.6) and from a first estimate of the surge force

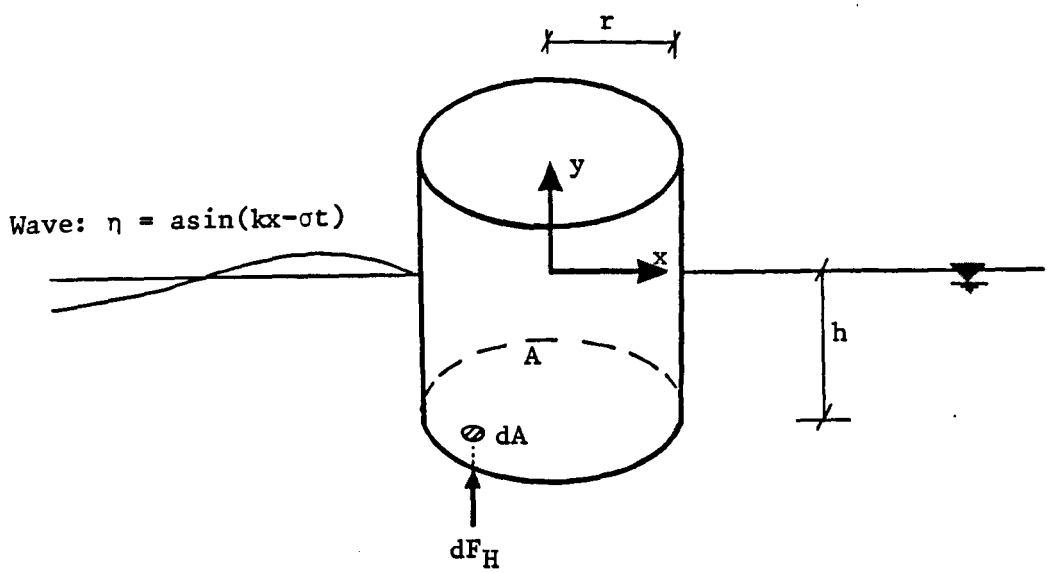

Figure 6.12 Definition sketch for the calculation of a first estimate of the heave excitation force on a circular cylinder

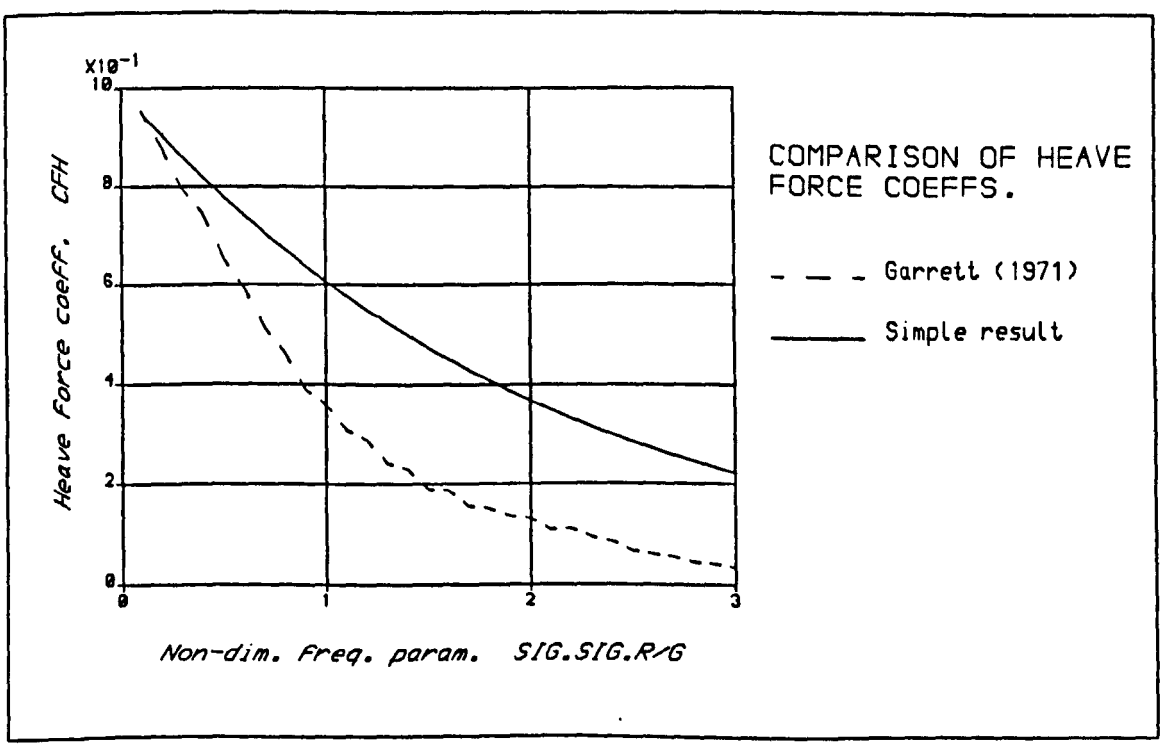

Figure 6.13 Comparison of the heave force coefficients obtained from Garrett (Figure 6.6) and from a first estimate of the heave force

Heave e.o.m. $(M+M_{aH})d^2y/dt^2 + Q_H dy/dt + K_H y = F_H \sin(\sigma t+\beta_H)$

SBM Data: $M = 1.025 \times 10^6 kg$ $V = 1060 m^3$ $r = 8.65m$

Heave stiffness $K_H = 2.445 \times 10^3 kN/m$

Frequency (Hz)	$\sigma^2 r/g$	C_{FH} (Fig 6.6(a))	β_H (rads) (Fig 6.6(a))	C_{aH} (Expt)	C_{dH} (Expt Fig 6.8)
0.054	0.1	0.95	0.0	2.18	0.81
0.107	0.4	0.74	0.12	2.18	0.6
0.142	0.7	0.51	0.32	2.18	0.27
0.169	1.0	0.36	0.5	2.18	0.08
0.193	1.3	0.24	0.8	2.18	0.05
0.214	1.6	0.19	0.98	2.18	0.05
0.234	1.9	0.13	1.3	2.18	0.08
0.251	2.2	0.11	1.6	2.18	0.08
0.268	2.5	0.07	1.9	2.18	0.10
0.284	2.8	0.04	2.2	2.18	0.11

Table 6.2

Sample of data used in the empirical model for the SBM's heave prediction

Surge e.o.m: $(M+M_{as})d^2x/dt^2 + Q_s dx/dt + K_s x = F_s \sin(\sigma t+\beta_s)$

SBM data: $M = 1.0256 \times 10^6 kg$ $r = 8.65m$ $V = 1060m^3$

Surge stiffness: $K_s = 90kN/m$

Frequency (Hz)	$\sigma^2 r/g$	C_{FS} (Fig 6.6(b))	β_S (rads) (Fig 6.6(b))	C_{as} (Fig 6.7(b))	C_{dH} (Fig 6.7(b))
0.054	0.1	0.08	1.54	0.41	0.005
0.107	0.4	0.28	1.51	0.53	0.04
0.142	0.7	0.42	1.43	0.60	0.15
0.169	1.0	0.47	1.42	0.57	0.34
0.193	1.3	0.45	1.46	0.43	0.45
0.214	1.6	0.41	1.57	0.31	0.46
0.234	1.9	0.36	1.73	0.22	0.42
0.251	2.2	0.32	1.92	0.16	0.38
0.268	2.5	0.28	2.2	0.11	0.33
0.284	2.8	0.25	2.4	0.08	0.29

Table 6.3

Sample of data used in the empirical model for the SBM's surge prediction

Pitch e.o.m. $(M+M_{aP})k_p^2(d^2\theta/dt^2) + Q_P d\theta/dt + K_P\theta = T_P\sin(\sigma t+\beta_P)$

SBM data: $M = 1.0256 \times 10^6$kg $r = 8.65$m $V = 1060$m^3 $k_P = 4.7$m

Pitch stiffness: 27.5×10^3kNm/radian

Frequency (Hz)	$\sigma^2 r/g$	C_{TP} (Fig 6.6(c))	βP (rads) (Fig 6.6(c))	C_{aP} (Expt)	C_{dP} (Expt Fig 6.9)
0.054	0.1	0.08	1.54	2.1	0.01
0.107	0.4	0.19	1.51	2.1	0.24
0.142	0.7	0.26	1.43	2.1	0.7
0.169	1.0	0.27	1.42	2.1	1.62
0.193	1.3	0.24	1.46	2.1	1.71
0.214	1.6	0.20	1.57	2.1	1.6
0.234	1.9	0.17	1.73	2.1	1.42
0.251	2.2	0.15	1.92	2.1	1.25
0.268	2.5	0.12	2.2	2.1	1.1
0.284	2.8	0.11	2.4	2.1	1.0

Table 6.4

Sample of data used in the empirical model for the SBM's pitch prediction

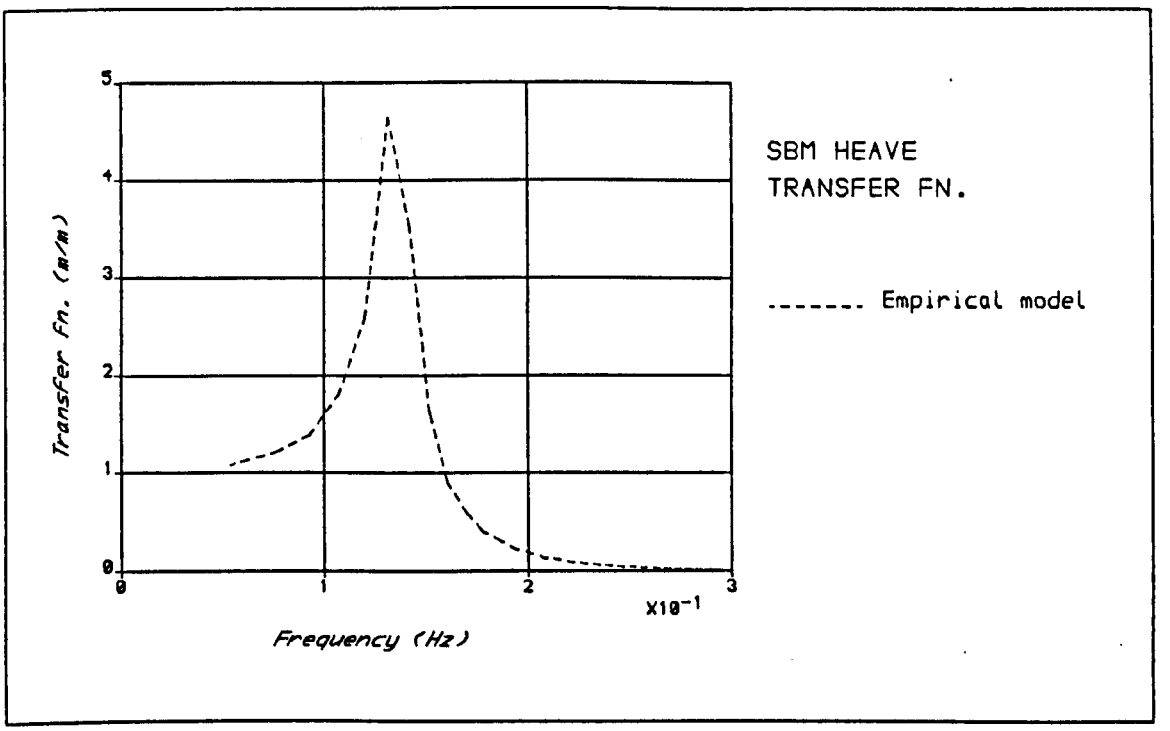

(a) Transfer function

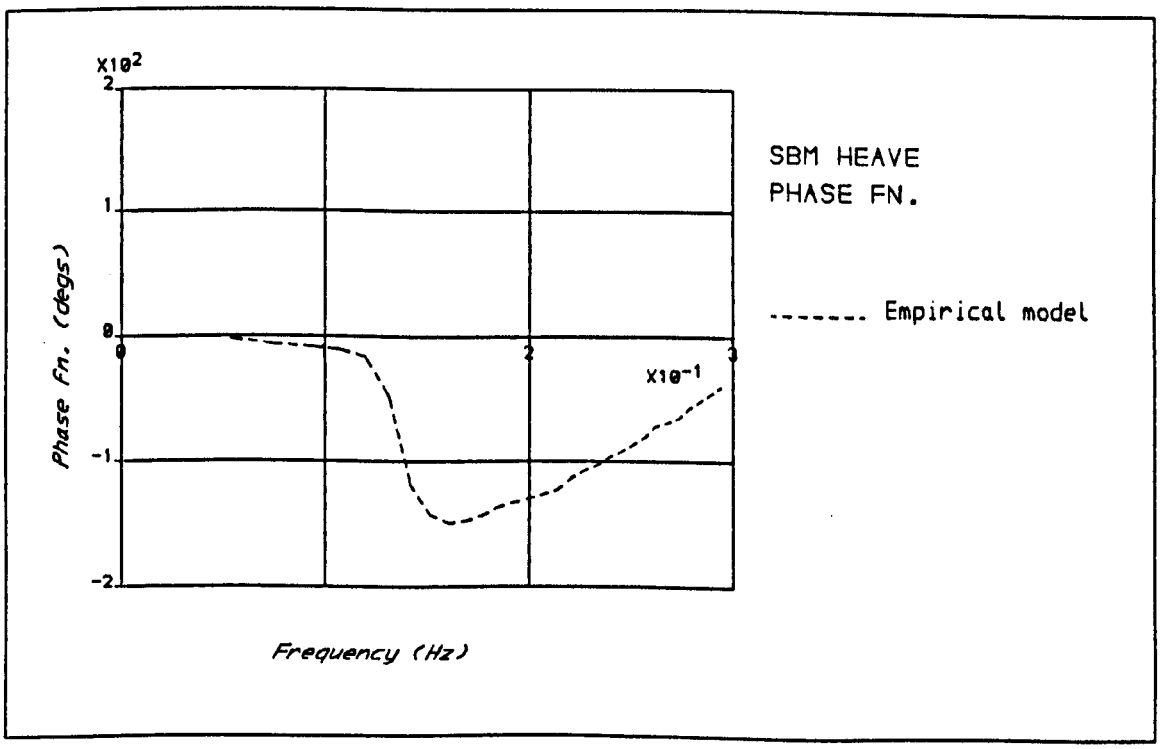

(b) Phase function

Figure 6.14 Empirical model prediction of SBM heave

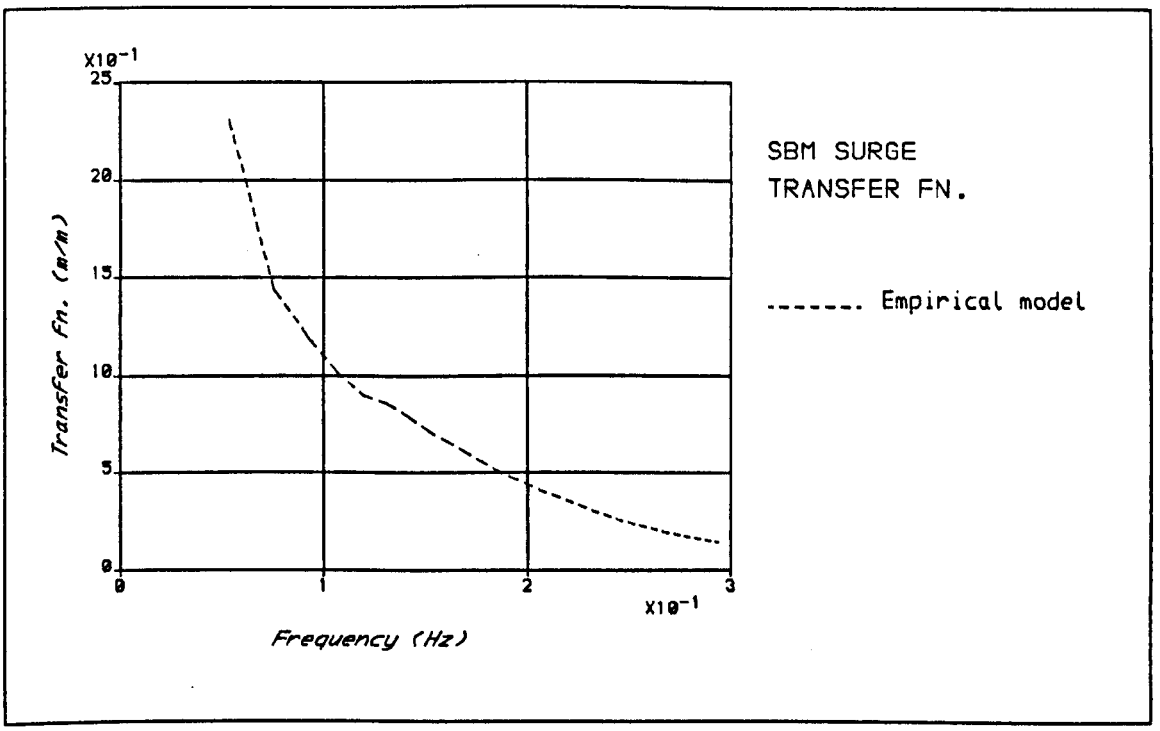

(a) Transfer function

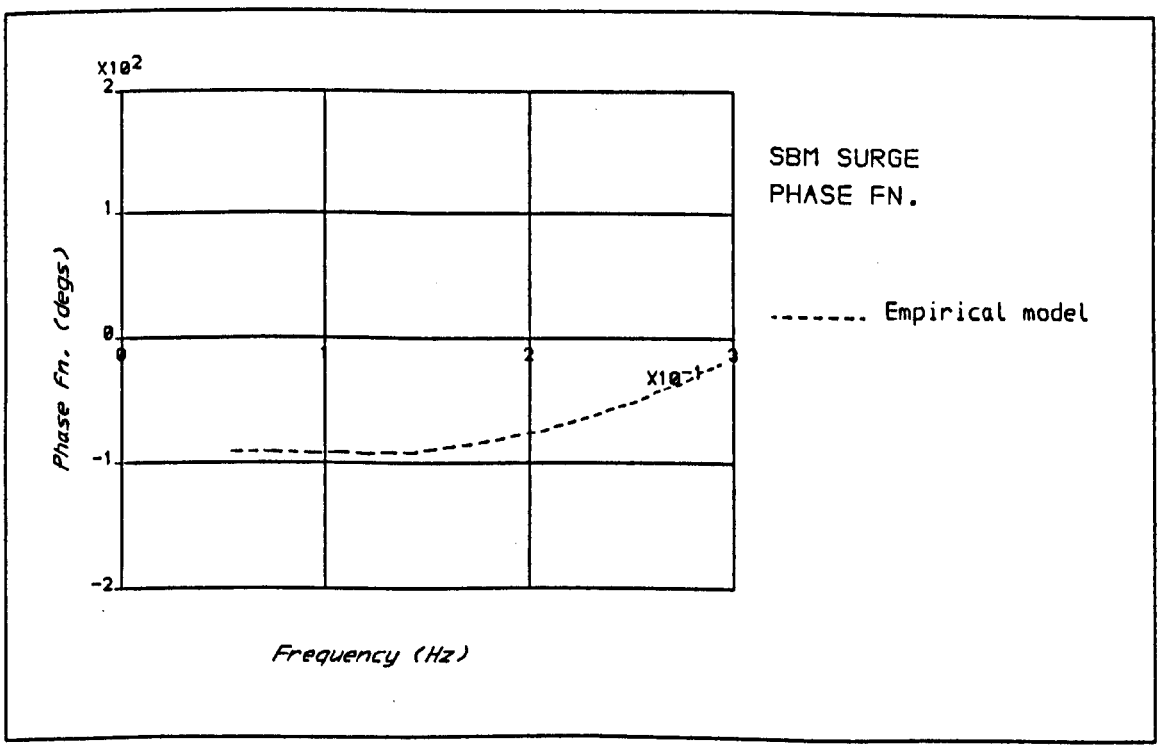

(b) Phase function

Figure 6.15 Empirical model prediction of SBM surge

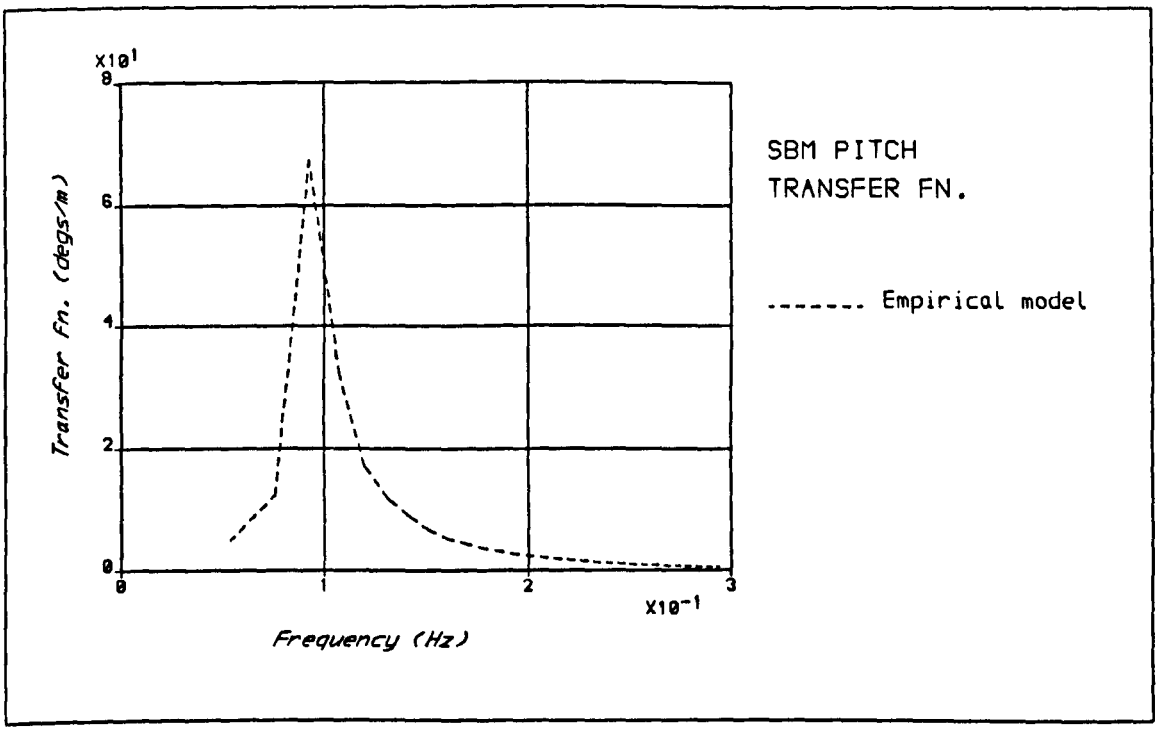

(a) Transfer function

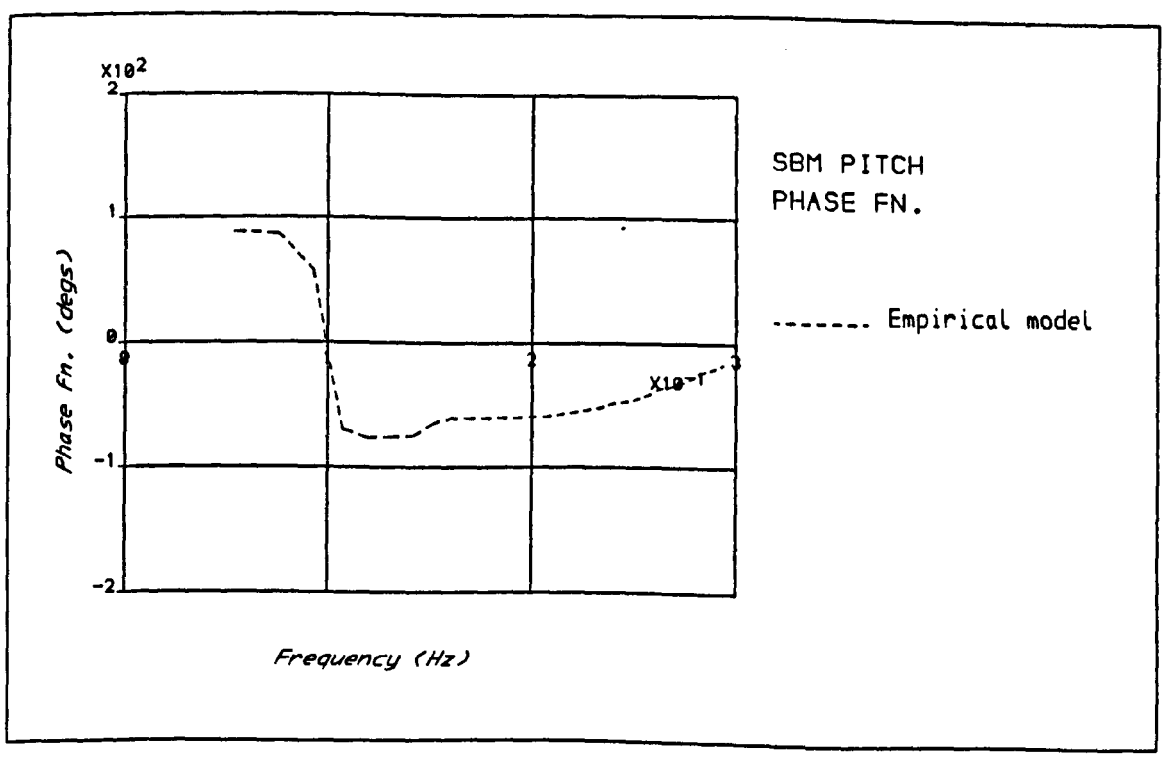

(b) Phase function

Figure 6.16 Empirical model prediction of SBM pitch

7. ANALYTICAL MODELS FOR HOSE-STRING BENDING

7.1 Introduction

This chapter presents analytical models for the vertical and horizontal bending of the hose-string in waves.

The behaviour of the hose-string in waves is complex. The string is subjected to axial loads while it simultaneously bends in a horizontal plane (snaking) and in a vertical plane as it attempts to follow the profile of the waves. It has been necessary to simplify this complex behaviour for the development of the analytical models presented here. The effectiveness of the models can be tested when predictions are compared with the results from the physical model tests.

The hose-string behaviour is first simplified by considering the vertical bending and the horizontal bending as independent of each other and neglecting any axial load effects. The solutions for the separate vertical and horizontal bending problems are based on the assumption that the bending of the hose-string can be described using engineer's bending theory.

7.2 Analytical Model for Vertical Displacement and Bending

7.2.1 Problem Definition

With reference to Figure 7.1 the problem of vertical bending is defined as follows.

A hose-string of length L, diameter 2r, bending stiffness EI and mass per unit length m, lies in still water with one end free and the other end attached to a CALM buoy such that its central axis intersects the still water at an angle θ_o to the horizontal.

Reference vertical and longitudinal axes, y and x, are set with y=0 corresponding to the still water level and x=0 corresponding to the point at which the hose connects to the buoy.

Regular waves travel in the direction of hose-string alignment such that the water level at x at time t is given by

$$\eta(x,t) = a_w \cos(\sigma t - kx) \tag{7.1}$$

where a_w is the wave amplitude

σ is the wave circular frequency

k is the wave number.

For linear, deep-water waves $k = \sigma^2/g$.

It is assumed that the waves cause the buoy to heave only, with amplitude a_h, frequency σ and a phase difference with the waves of ϕ. The free-end of the hose-string is assumed to follow the profile of the waves.

It is required to establish the displacement of the hose axis, and hence the vertical bending moment, along the hose-string at time t for given buoy heave and wave conditions.

Because the hose-string is modelled as a beam subject to bending, the solution requires solving the beam equation of motion

$$EI\, \partial^4 y/\partial x^4 + m\partial^2 y/\partial t^2 = p(x,t) \tag{7.2}$$

subject to the following boundary conditions:

(1) $$y(0,t) = a_h \cos(\sigma t + \phi) \tag{7.3}$$

(2) $$\partial y/\partial x(0,t) = \tan(\pi - \theta_o) \tag{7.4}$$

(3) $$y(L,t) = a_w \cos(\sigma t - kL) + Y_e \tag{7.5}$$

(4) $\partial y/\partial x(L,t) = ka_w \sin(\sigma t - kL)$ (7.6)

(An alternative boundary condition to (4) is that the bending moment at the free end is zero, i.e. $\partial^2 y/\partial x^2(L,t) = 0$. Replacing (4) with this makes no difference to the solution.)

$p(x,t)$ is the vertical loading per unit length and Y_e is the displacement of the hose-string axis at the free end in still water.

7.2.2 Vertical Loading

The net vertical force generated by waves on a partially-submerged floating hose-string is primarily due to the change in buoyancy force. If the instantaneous water level is d above the base of the hose, as shown in Figure 7.2, then the buoyancy force per unit length is given by

$$b = \rho g[(\pi-\gamma)r^2 + (d-r)^2 \tan\gamma] \quad (7.7)$$

where $\gamma = \cos^{-1}(d-r)/r$.

The net vertical force per unit length in the positive y direction is

$$p = b - mg \quad (7.8)$$

A graph of p against d is shown as the broken line in Figure 7.3. When d is less than zero the hose clears the water surface and $p = -mg$. For d greater than or equal to 2r the hose is totally submerged and the buoyancy force is maximum with $b = \pi r^2 \rho g$.

Consider approximating p by the linear function p' represented by the solid line in Figure 7.3. p' is a good approximation to p when $0 \leq d \leq 2r$, i.e. when the hose is partially submerged. If, however, the hose is totally submerged such that $d = (2+\alpha)r$, where α is positive, then it may be shown that

$$p'/p = 1 + \alpha/(2(1-m/\pi r^2\rho)) \qquad (7.9)$$

Similarly, if the hose clears the water surface by a distance αr so that $d = -\alpha r$ then

$$p'/p = 1 + \alpha(\pi r^2\rho/2m) \qquad (7.10)$$

The errors involved in approximating p by p' when the hose is not partially submerged depend on the reserve buoyancy (mass minus displacement) of the hose. For the hose-string considered in this study $r = 0.5m$ and $m = 500kg/m$ and equations (7.9) and (7.10) reduce to

$$p'/p = 1 + 1.37\alpha \quad , \quad \text{for } d = (2+\alpha)r \qquad (7.11)$$

$$p'/p = 1 + 0.785\alpha \quad , \quad \text{for } d = -\alpha r \qquad (7.12)$$

Therefore, for every radius that the hose is submerged the error in the approximation of the vertical load increases by 137% of the true value; for every radius that it is exposed the error increases by 78% of the true value.

The above results show clearly that p can only be approximated by p' as long as the hose-string remains partially submerged. Because of the low bending stiffness of the hose it is envisaged that this condition is met in a wide range of wave conditions. Indeed, observations during the model tests showed this to be the case. For this reason it was decided to proceed with the analysis using the linear approximation to p. Cases in which the hose-string does not remain partially submerged can be readily identified during the analysis of such cases.

If $y(x,t)$ is the displacement of the hose axis and $\eta(x,t)$ is the water level, then

$$d(x,t) = \eta(x,t) + r - y(x,t) \qquad (7.13)$$

The vertical load on the hose is

$$p(x,t) = p'(x,t) = (\pi r^2 \rho g/2r)[\eta(x,t) + r - y(x,t)] - mg \qquad (7.14)$$

If Y_e is the displacement of the hose-axis when the hose-string floats freely in still water, then

$$mg = (\pi r^2 \rho g/2r)(r-Y_e) \qquad (7.15)$$

Substituting for mg in equation (7.14) gives

$$p(x,t) = (\pi r^2 \rho g/2r)[\eta(x,t) - y(x,t) + Y_e] \qquad (7.16)$$

7.2.3 Solution of Equation of Motion

If p(x,t) in equation (7.2) is substituted by the expression given by equation (7.16) the resulting equation of motion can be arranged to give

$$\partial^4 y/\partial x^4 + (1/c^2)\partial^2 y/\partial t^2 + Fy = H\cos(\sigma t - kx) - G \qquad (7.17)$$

where $c^2 = EI/m$

$F = \pi r^2 \rho g/2rEI$

$H = a_w F$

$G = -Y_e F$.

The solution of the equation of motion is assumed to be of the form

$$y(x,t) = u_1(x)\cos\sigma t + u_2(x)\sin\sigma t + u_3(x) \qquad (7.18)$$

Substituting for y, $\partial^2 y/\partial t^2$ and $\partial^4 y/\partial x^4$ in equation (7.18) leads to the following three fourth order o.d.e.s:

$$d^4 u_1/dx^4 - (\sigma^2/c^2 - F)u_1 = H\cos kx \qquad (7.19)$$

$$d^4 u_2/dx^4 - (\sigma^2/c^2 - F)u_2 = H\sin kx \qquad (7.20)$$

$$d^4u_3/dx^4 + Fu_3 = -G \qquad (7.21)$$

The form of the solutions of equations (7.19) and (7.20) depends on the sign of (σ^2/c^2-F). For all cases considered in this study (σ^2/c^2-F) was less than zero. For ease of presentation therefore, only the solutions of equations (7.19) and (7.20) with (σ^2/c^2-F) less than zero are presented.

$$\text{Letting} \quad 4R^4 = F - \sigma^2/c^2$$
$$\text{and} \quad 4S^4 = F \qquad (7.22)$$

then the solutions of equations (7.19) to (7.21) are

$$u_1(x) = a_1e^R\cos Rx + b_1e^R\sin Rx + c_1e^{-R}\cos Rx + d_1e^{-R}\sin Rx + A\cos kx$$
$$u_2(x) = a_2e^R\cos Rx + b_2e^R\sin Rx + c_2e^{-R}\cos Rx + d_2e^{-R}\sin Rx + A\sin kx \qquad (7.23)$$
$$u_3(x) = a_3e^S\cos Sx + b_3e^S\sin Sx + c_3e^{-S}\sin Sx + d_3e^{-S}\sin Sx - G/F$$

where a_1, a_2, a_3, b_1, etc, are constants which depend on the boundary conditions and

$$A = H/(k^4+4R^4) \qquad (7.25)$$

For a finite solution at $x = \infty$

$$a_1 = b_1 = a_2 = b_2 = a_3 = b_3 = 0$$

The solution of the equation of motion reduces therefore to

$$\begin{aligned} y(x,t) = {} & [c_1e^{-Rx}\cos Rx + d_1e^{-Rx}\sin Rx + A\cos kx]\cos\sigma t \\ & + [c_2e^{-Rx}\cos Rx + d_2e^{-Rx}\sin Rx + A\sin kx]\sin\sigma t \\ & + [c_3e^{-Sx}\cos Sx + d_3e^{-Sx}\sin Sx - G/F] \end{aligned} \qquad (7.26)$$

where c_1, c_2, c_3, d_1, d_2 and d_3 are obtained from the boundary conditions given by equations (7.3) and (7.4) and are

$$\begin{aligned} c_1 &= d_1 = a_h\cos\phi - A \\ c_2 &= -a_h\sin\phi \\ d_2 &= -kA/R + c_2 \\ c_3 &= G/F = -Y_e \\ d_3 &= 1/S\ \tan(\pi-\theta_o) \end{aligned} \tag{7.27}$$

The vertical bending moment along the hose-string is given by

$$M = -EI\partial^2 y/\partial x^2 \tag{7.28}$$

Therefore

$$\begin{aligned} M(x,t) = &-EI[2R^2e^{-Rx}c_1(\sin Rx-\cos Rx) - Ak^2\cos kx]\cos\sigma t \\ &-EI[2R^2e^{-Rx}(c_2\sin Rx-d_2\cos Rx) - Ak^2\sin kx]\sin\sigma t \\ &-EI[2S^2e^{-Sx}(c_3\sin Sx-d_3\cos Sx)] \end{aligned} \tag{7.29}$$

According to the axis system used, positive bending moment implies compression on the underside of the hose-string.

7.2.4 Results for Vertical Displacement and Bending

7.2.4.1 Static Result

The vertical displacement of the hose-string in still water is given by the third term on the r.h.s. of equation (7.26), i.e.

$$y(x,0) = c_3e^{-Sx}\cos Sx + d_3e^{-Sx}\sin Sx + Y_e \tag{7.30}$$

It is clear that this solution satisfies the boundary conditions for static displacement: for positions far away from the buoy the first two

terms tend to zero and the hose floats with its axis at its equilibrium depth Y_e; at x=0, y=0 and the hose-string axis intersects the still water-line.

The vertical bending moment along the hose-string in still water is, from equation (7.29),

$$M(x,0) = -EI2S^2e^{-Sx}(c_3 \sin Sx - d_3 \cos Sx) \qquad (7.31)$$

For positions far away from the buoy where the string floats at its equilibrium depth, the bending moment is zero. The bending moment is a maximum at the hose-buoy connection and is

$$M(0,0) = EI2S \tan(\pi - \theta_o) \qquad (7.32)$$

Substituting for S (equations 7.22 and 7.17) gives

$$M(0,0) = 2EI^{3/4}(\pi r^2 \rho g/8r)^{1/4} \tan(\pi - \theta_o) \qquad (7.33)$$

Figure 7.4 shows the effects of varying the bending stiffness on the static displacement of the hose-string axis and on the vertical bending moment, with r = 0.5m, m = 500kg/m and $\theta_o = 15^o$. The stiffer hose-string requires a slightly longer length to reach equilibrium but its greater stiffness causes it to generate the larger bending moments.

Figure 7.5 shows the effects of varying the angle of the hose-buoy manifold on the static hose displacement and vertical bending moment. Clearly, the curvature and bending moment increase with increasing values of the angle. (It is usual practice to design the manifold with an angle of 15^o to the horizontal so that the first-off-the-buoy hose can absorb small surge movements of the buoy.)

It should be noted that the magnitude of the displacement of the hose axis is always less than the hose radius in the results presented in Figures 7.4 and 7.5. For these cases therefore the hose is always partially submerged and the linear approximation of the loading is applicable.

7.2.4.2 Dynamic Result

The dynamic component of the displacement of the hose-string axis in equation (7.26) is

$$y(x,t) = [c_1 e^{-Rx}\cos Rx + d_1 e^{-Rx}\sin Rx + A\cos kx]\cos\sigma t + [c_2 e^{-Rx}\cos Rx + d_2 e^{-Rx}\sin Rx + A\sin kx]\sin\sigma t \quad (7.34)$$

where A is given by equation (7.25) and c_1, d_1, c_2 and d_2 are given in equation (7.27).

The dynamic component of the bending moment along the hose-string in equation (7.29) is

$$M(x,t) = -EI[2R^2 e^{-Rx} c_1(\sin Rx-\cos Rx) - Ak^2\cos kx]\cos\sigma t - EI[2R^2 e^{-Rx}(c_2\sin Rx-d_2\cos Rx) - Ak^2\sin kx]\sin\sigma t \quad (7.35)$$

(a) Positions away from the buoy

Consider values of x greater than x_o where the hose at x_o is sufficiently far from the buoy to be unaffected by conditions at the buoy. The dynamic displacement at these positions is

$$y(x\geq x_o,t) = ha_w\cos(\sigma t-kx) \quad (7.36)$$

where

$$h = 1/[1 + (2rEI/\pi r^2\rho g)((\sigma^2/g)^4-\sigma^2/c^2)] \quad (7.37)$$

For positions away from the buoy, therefore, the hose moves in phase with the waves and with amplitude ha_w; that is, its displacement is linearly proportional to the wave amplitude a_w. ha_w may be less than, equal to or greater than the wave amplitude, depending on whether $[(\sigma^2/g)^4-\sigma^2/c^2]$ is greater than zero, zero or less than zero respectively.

The value of h has been plotted against wave frequency for two values of the bending stiffness of a hose-string with r = 0.5m and m = 500kg/m, as shown in Figure 7.6.

We are interested in determining for each wave frequency the maximum wave amplitude for which the hose-string remains partially submerged throughout the wave cycle, since this sets the limit on the wave amplitude for which the linear load approximation is valid. When h > 1, the amplitude of dynamic displacement of the hose is greater than the wave amplitude and the hose will not remain partially submerged throughout the wave cycle when

$$ha_w + |Y_e| > a_w + r \tag{7.38}$$

as illustrated in Figure 7.7(b).

When h < 1 the hose does not remain partially submerged when

$$ha_w - |Y_e| < a_w - r \tag{7.39}$$

as illustrated in Figure 7.7(c).

For the linear load approximation to be valid therefore, the wave amplitude must be less than a_{w_L} where a_{w_L} is given by

$$\begin{aligned} a_{w_L} &= (r-|Y_e|)/(h-1) \quad \text{for } h > 1 \\ a_{w_L} &= (r-|Y_e|)/(1-h) \quad \text{for } h < 1 \end{aligned} \tag{7.40}$$

Figure 7.8 shows the value of a_{w_L} plotted against wave frequency for the same hose properties used for Figure 7.6. At low wave frequencies the amplitude of hose displacement is slightly greater than the wave amplitude and the wave amplitude needs therefore to be very large before the hose becomes submerged under the wave trough. As frequency increases, h becomes increasingly greater than 1.0 and the limiting wave amplitude decreases accordingly. When h = 1.0, corresponding to when $[(\sigma^2/g)^4 - \sigma^2/c^2]$ is equal to zero, the hose follows the wave profile exactly and remains partially submerged irrespective of the wave amplitude. At higher frequencies h decreases rapidly from 1.0 resulting in a rapid decrease in the value of the limiting wave amplitude. At very high frequencies h tends to zero and the hose remains straight in the waves, with the result that the limit on the wave amplitude is $(r-|y_e|)$.

For the hose-string considered in this study, with EI = 150kNm^2, Figure 7.8 shows that the linear load approximation is valid for a very wide range of wave conditions.

The vertical bending moment amplitude at positions away from the buoy is given by

$$M(x \geq x_o, t) = EIk^2 h a_w \cos(\sigma t - kx) \qquad (7.41)$$

where h is given by equation (7.37).

Bending moment is linearly proportional to the wave amplitude. Figure 7.9 shows the amplitude of vertical bending per unit wave amplitude as a function of frequency, for the hose-string with r = 0.5m and m = 500kg/m. As the wave frequency increases the steepness increases, resulting in greater curvature and bending of the hose-string. The decreasing value of

the bending moment at the higher frequencies corresponds with the decreasing value of h below 1.0 and the increasing tendency of the hose-string to remain straight in the waves.

(b) At the buoy

The dynamic displacement of the hose axis at the hose-buoy connection is, from equation (7.34),

$$y(0,t) = (c_1+A)\cos\sigma t + c_2\sin\sigma t \qquad (7.42)$$

Substituting for c_1 and c_2 from equation (7.27) gives

$$y(0,t) = a_h\cos(\sigma t+\phi) \qquad (7.43)$$

This is, of course, in keeping with the boundary condition given by equation (7.3) and simply states that the hose displacement at x = 0 is equal to the buoy's displacement.

The hose at x = 0 remains partially submerged throughout the wave cycle if the following condition is met:

$$|a_h\cos(\sigma t+\phi) - a_w\cos\sigma t| < r, \quad 0 \le t \le 2\pi/\sigma \qquad (7.44)$$

If this condition is met then the dynamic vertical bending at x = 0 is, from equation (7.35),

$$M(0,t) = EI[(2c_1R^2+Ak^2)\cos\sigma t + 2d_2R^2\sin\sigma t] \qquad (7.45)$$

where $4R^4 = \pi r^2\rho g/2rEI - \sigma^2/c^2$

$c_1 = a_h\cos\phi - A$

$d_2 = -a_h\sin\phi - kA/R$

and

$A = ha_w$

where h is given by equation (7.37).

Writing equation (7.45) in the form

$$M(0,t) = EI[M_1 \cos\sigma t + M_2 \sin\sigma t] \tag{7.46}$$

then the amplitude of the dynamic bending moment variation at x = 0 is

$$\bar{M} = EI(M_1^2 + M_2^2)^{1/2} \tag{7.47}$$

where $M_1 = 2c_1R^2 + Ak^2$

$M_2 = 2d_2R^2$

It may be shown that $\bar{M}$ is approximately given by

$$\bar{M} = a_w s^{1/2} EI^{1/2} \psi \tag{7.48}$$

where s is the slope of the linear load approximation shown in Figure 7.3, i.e.

$$s = \pi r^2 \rho g / 2r \tag{7.49}$$

and ψ is a function of the heave transfer function value and phase value at frequency σ and is given by

$$\psi = [(a_h/a_w)^2 + 1.0 - 2(a_h/a_w)\cos\phi]^{1/2} \tag{7.50}$$

A comparison between results obtained using the "exact" solution given by equation (7.47) and the approximate solution given by equation (7.48), for typical hose properties and buoy heave responses, is shown in Table 7.1. The results show that the error involved in the approximation is of the order of 10% or less.

Frequency (rads/sec) σ	a_h/a_w	ϕ	Dynamic Vertical Bending Amplitude at x=0 (kNm/m)	
			"Exact" Soln.	Approx. Soln.
0.41	2.2	11°	35.1	35.3
0.628	3.05	-29°	59.8	63.4
0.72	3.3	-59°	75.3	80.8
1.04	0.16	0°	24.8	23.8
1.41	0.0	0°	26.9	28.4
Hose data: r = 0.35m EI = 150kNm^2 m = 500kg/m				

Table 7.1

A comparison of results obtained for the amplitude of dynamic vertical bending at x=0 using the "exact" solution (equation 7.47) and the approximate solution (equation 7.48)

The usefulness of the approximation given by equation (7.48) is that the dependance of the dynamic vertical bending at x=0 on the loading and the bending stiffness is immediately apparent. Note that the approximation is independent of wave frequency. The dependance of the bending on the heave response is shown in Figure 7.10 in which the value of ψ is plotted against a_h/a_w for a number of values of the phase ϕ. ψ is linearly proportional to a_h/a_w for a_h/a_w greater than 1.0. As the buoy tends to move in phase with the waves (ϕ tending to zero) and with the same amplitude as the waves (a_h/a_w tending to 1.0) the dynamic vertical bending at x=0 tends to zero. For a particular amplitude of heave response, maximum bending occurs when the heave is 180° out of phase with the waves.

To conclude this section, the displacement of the first 50m of a hose-string with r = 0.5m, m = 500kg/m and EI = 150kNm^2 in waves of amplitude

1.0m is shown in Figures 7.11 to 7.17. Each figure shows the displacement at five equally-spaced time intervals within one wave cycle. The broken line represents the instantaneous water level. For each of the cases considered in Figures 7.11 to 7.14 the buoy heave amplitude is equal to the wave amplitude and the heave phase is zero. In waves of period 2 seconds, Figure 7.14, the hose-string remains almost straight in the waves; this is in accordance with results presented in Figure 7.6 which showed that h tends to zero at high frequencies. Cases in which the heave amplitude is not equal to the wave amplitude and/or the heave is not in phase with the waves are shown in Figures 7.15 to 7.17. In each of these cases the hose at the buoy becomes submerged and exposed at instances during the cycle and the bending moments predicted using equation (7.45) will be higher than the actual values because of the over-estimate of the loading. Clearly the error involved will be small in the cases shown in Figures 7.15 and 7.17 and larger in the case shown in Figure 7.16.

The main limitation of the analytical model presented here for the vertical displacement and bending of the hose-string is that inherent in the linear approximation of the vertical loading. Other limitations include the requirement that the hose radius and bending stiffness be constant over the string's length. These limitations may be overcome by using a numerical model. Such a model, based on the use of a finite-difference scheme, has been presented by Brown (1984).

7.3 Analytical Model for Snaking and Horizontal Bending

7.3.1 Problem Definition

The phenomenon referred to as snaking has been described in the presentation and discussion of the model test results given in Chapter 5. The tests have shown that a snake originates at the buoy as a result of the SBM's surge motion and travels the length of the hose-string, decaying in magnitude as it does so. The objective of this section is to develop an analytical model which predicts the frequency, amplitude and wavelength of snaking, and thereby the induced horizontal bending, for given SBM surge conditions.

As was the case for the vertical bending model, it has been necessary to retain only the most significant features of the problem in order to develop an analytical model for the snaking phenomenon.

A hose-string of length L, diameter 2r, bending stiffness EI and mass per unit length m, lies in the water surface with one end free and the other end attached to a buoy which moves in surge only, Figure 7.18. Reference longitudinal and lateral axes, x and z, are set with the x axis coincident with the line of the undeflected hose-string and z=0 corresponds with zero lateral deflection. Displacements in the x and z directions are denoted u and w respectively.

Under steady conditions, the buoy is moving longitudinally with a sinusoidal motion and the hose-string is deflecting laterally. The problem is to define the lateral vibration of the hose-string subject to the condition that the end x=0 moves longitudinally with a motion given by

$$u(x=0) = a_s(1 - \cos\sigma t) \qquad (7.51)$$

where a_s = amplitude of buoy surge

σ = buoy surge circular frequency.

7.3.2 Formulation of Problem

(The formulation and solution of the snaking problem has been carried out in collaboration with Mr J Bree, Department of Mathematics, Heriot-Watt University.)

Axial load along the hose-string is assumed to be zero and the string is modelled as a beam governed by engineer's bending theory. The forces and moments acting on an element of the beam, whose longitudinal and lateral displacements are u and w respectively, are shown in Figure 7.19. The equation of motion in the x direction is

$$S\theta - [S+(\partial S/\partial\theta)d\theta](\theta+d\theta) = mRd\theta\partial^2u/\partial t^2 \qquad (7.52)$$

Therefore

$$-\partial/\partial\theta(S\theta) = mR\partial^2u/\partial t^2 \qquad (7.53)$$

The equation of motion in the z direction is

$$-S + [S+(\partial S/\partial\theta)d\theta] = mRd\theta\partial^2w/\partial t^2 \qquad (7.54)$$

Therefore

$$\partial S/\partial\theta = mR\partial^2w/\partial t^2 \qquad (7.55)$$

Taking moments about the left hand edge of the element gives

$$M - [M+(\partial M/\partial\theta)d\theta] + [S+(\partial S/\partial\theta)d\theta]Rd\theta = 0 \qquad (7.56)$$

Therefore

$$\partial M/\partial\theta = SR \qquad (7.57)$$

From beam bending theory

$$M/EI = 1/R = -\partial^2 z/\partial x^2 \tag{7.58}$$

By letting $\theta = \partial z/\partial x$, $Rd\theta = dx$ and $w = z$ and using equation (7.57) and (7.58), equations (7.53) and (7.55) become

$$EI\partial/\partial x(\partial^3 z/\partial x^3 . \partial z/\partial x) = m\partial^2 u/\partial t^2 \tag{7.59}$$

and

$$EI\partial^4 z/\partial x^4 + m\partial^2 z/\partial t^2 = 0 \tag{7.60}$$

respectively.

Equation (7.60) is the beam bending equation of motion for lateral deflection $z(x,t)$ and holds along the length of the beam. Equation (7.59) arises from the longitudinal motion of the beam and is assumed to hold only at end $x=0$. This assumption implies no longitudinal motion of the hose-string at positions far away from the moving buoy. In effect then, equation (7.59) applied at $x=0$ is a boundary condition for the free lateral vibration of the beam model.

The observed decay in magnitude of a snake as it travels the length of the hose-string results from the damping forces generated by the motion of the hose-string in water. To take account of these forces in the model it is necessary to incorporate a damping term in equation (7.60) as follows:

$$EI\partial^4 z/\partial x^4 + Q\partial z/\partial t + m\partial^2 z/\partial t^2 = 0 \tag{7.61}$$

where $Q\partial z/\partial t$ is the damping force per unit length.

Letting

$$c^2 = EI/m \tag{7.62}$$

and

$$K = Q/EI \tag{7.63}$$

then the problem reduces to solving the equation of motion

$$\partial^4 z/\partial x^4 + K\partial z/\partial t + (1/c^2)\partial^2 z/\partial t^2 = 0 \tag{7.64}$$

subject to the boundary condition

$$[\partial/\partial x(\partial^3 z/\partial x^3 . \partial z/\partial x)]_{x=0} = a_s(\sigma^2/c^2)\cos\sigma t \tag{7.65}$$

7.3.3 Solution of Equation of Motion

Appendix A5 presents in detail the method of solving equation (7.64) subject to the boundary condition given by equation (7.65). A summary of the method is presented in what follows.

Equation (7.64) is of fourth order and its solution consists therefore of four independent solutions. These solutions take the form of a travelling wave, so that

$$z(x,t) = \sum_{j=1}^{4} A_j(x)e^{i(k_j x-\omega t)} \tag{7.66}$$

Appendix A5 shows that the values of k_j are such that

$$z(x,t) = A_1 e^{-\beta x} e^{i(\alpha x-\omega t)} + A_2 e^{-\alpha x} e^{i(-\beta x-\omega t)} + A_3 e^{\beta x} e^{i(-\alpha x-\omega t)} + A_4 e^{\alpha x} e^{i(\beta x-\omega t)} \tag{7.67}$$

where $\alpha = H^{1/4}\cos\theta/4$

$\beta = H^{1/4}\sin\theta/4$

$H = [(\omega^2/c^2)2 + \omega^2 K^2]^{1/2}$

$\tan\theta = Kc^2/\omega$.

For a finite solution at $x = \infty$, $A_3 = A_4 = 0$ and so

$$z(x,t) = A_1 e^{-\beta x} e^{i(\alpha x - \omega t)} + A_2 e^{-\alpha x} e^{i(-\beta x - \omega t)} \tag{7.68}$$

Letting $A_1 = Ee^{i\gamma}$ and $A_2 = Fe^{i\delta}$ the solution is

$$z(x,t) = Ee^{-\beta x} e^{i(\alpha x - \omega t + \gamma)} + Fe^{-\alpha x} e^{i(-\beta x - \omega t + \delta)} \tag{7.69}$$

The values of E, γ, F and δ can be obtained from the boundary condition.

The real parts of the derivatives $\partial z/\partial x$, $\partial^2 z/\partial x^2$, $\partial^3 z/\partial x^3$ and $\partial^4 z/\partial x^4$ at x=0 are given by

$$[\partial z/\partial x]_{x=0} = EH^{1/4}\sin(\omega t - \theta/4 - \gamma) - FH^{1/4}\cos(\omega t - \theta/4 - \delta) \tag{7.70}$$

$$[\partial^2 z/\partial x^2]_{x=0} = -EH^{1/2}\cos(\omega t - \theta/2 - \gamma) + FH^{1/2}\cos(\omega t - \theta/2 - \delta) \tag{7.71}$$

$$[\partial^3 z/\partial x^3]_{x=0} = -EH^{3/4}\sin(\omega t - 3\theta/4 - \gamma) - FH^{3/4}\cos(\omega t - 3\theta/4 - \delta) \tag{7.72}$$

$$[\partial^4 z/\partial x^4]_{x=0} = EH\cos(\omega t - \theta - \gamma) + FH\cos(\omega t - \theta - \delta) \tag{7.73}$$

The boundary condition can be re-written in the form

$$[\partial^3 z/\partial x^3 . \partial^2 z/\partial x^2 + \partial^4 z/\partial x^4 . \partial z/\partial x]_{x=0} = a_s(\sigma^2/c^2)\cos\sigma t \tag{7.74}$$

If the derivatives in equation (7.74) are replaced by the expressions given by equations (7.70) to (7.73) then it may be shown (Appendix A5) that

$$E^2 H^{5/4}(1+\lambda^4)^{1/2}\cos(2\omega t - 5\theta/4 - 2\gamma + \phi) = a_s(\sigma^2/c^2)\cos\sigma t \tag{7.75}$$

where $\lambda = F/E$

$\phi = \tan^{-1} 1/\lambda^2$ and is in the third quadrant.

For the boundary condition to be satisfied, i.e. for equation (7.75) to be satisfied, we require

$$\gamma = \phi/2 - 5\theta/8 = \delta$$

$$\omega = \sigma/2$$

$$E^2H^{5/4}(1+\lambda^4)^{1/2} = a_s\sigma^2/c^2$$

The unknowns E, γ, F and δ in the solution given by equation (7.69) have therefore been established from the boundary condition. Taking real parts only, the solution can now be summarised as follows:

$$z(x,t) = Ee^{-\beta x}\cos(\alpha x-\omega t-\gamma) + Fe^{-\alpha x}\cos(-\beta x-\omega t-\gamma) \qquad (7.76)$$

where

(i) $\omega = \sigma/2$

(ii) $\theta = \tan^{-1}Kc^2/\omega$

(iii) λ is the positive root of the quadratic

$$(\cos\theta/4+\cos3\theta/4)\lambda^2 - (\sin\theta/4+\cos\theta/4+\sin3\theta/4-\cos3\theta/4)\lambda - (\sin3\theta/4-\sin\theta/4) = 0$$

(iv) $\phi = \tan^{-1}1/\lambda^2$, ϕ is in the third quadrant

(v) $\gamma = \phi/2 - 5\theta/8$

(vi) $H = [(\omega^2/c^2)^2 + \omega^2K^2]^{1/2} = (\sigma/2c)^2[1 + (2Kc^2/\sigma)^2]^{1/2}$

(vii) $E^2H^{5/4}(1+\lambda^4)^{1/2} = a_s\sigma^2/c^2$

(viii) $F = \lambda E$

(ix) $\alpha = H^{1/4}\cos\theta/4$

(x) $\beta = H^{1/4}\sin\theta/4$

The snake-induced horizontal bending moment is

$$M(x,t) = (EI)EH^{1/2}e^{-\beta x}\cos(\alpha x-\omega t+\gamma+\theta/2) - (EI)FH^{1/2}e^{-\alpha x}\cos(-\beta x-\omega t+\gamma+\theta/2) \qquad (7.77)$$

For zero damping, K=0, equations (7.76) and (7.77) reduce to

$$z(x,t)|_{K=0} = 2^{5/4} a_s^{1/2} (c/\sigma)^{1/4} \cos[(\sigma/2c)^{1/2} x - \sigma t/2 + 3\pi/4] \qquad (7.78)$$

and

$$M(x,t)|_{K=0} = (-EI)(\sigma/2c) 2^{5/4} a_s^{1/2} (c/\sigma)^{1/4} \cos[(\sigma/2c)^{1/2} x - \sigma t/2 + 3\pi/4] \qquad (7.79)$$

respectively.

7.3.4 Results

The magnitude of snake-induced horizontal bending depends on the wavelength and amplitude of the snake. The frequency of horizontal bending is the same as the snake frequency. To understand the dependence of horizontal bending on the buoy's surge motion, it is necessary to study the dependence of each of the snake properties - frequency, wavelength and amplitude - on the surge amplitude and frequency and on the damping in the system.

Two results are immediately apparent from the solution given by equation (7.76). These are:

(1) The snake frequency is equal to half the surge frequency, as shown by equation (7.76(i)).

(2) The snake amplitude is proportional to the square root of the surge amplitude. This result follows from equations (7.76(vii)) and (7.76(viii)).

The solution given by equation (7.76) consists of the sum of two exponentially-decaying travelling waves. The first of these travels in the positive x direction, has a wavelength of $2\pi/\alpha$ and its rate of decay is proportional to $\exp(-\beta x)$. The second wave travels in the negative x

direction, has wavelength $2\pi/\beta$ and decays in proportion to $\exp(-\alpha x)$. This latter wave represents a wave that is reflected back from the free end of the hose-string and results from the damping in the system. For realistic snake shapes the damping is such that $\alpha >> \beta$ and the damping wave decays rapidly to zero from a maximum at the buoy end. For hose-string positions $x \geq x_o$, where x_o is not close to the buoy, the snake shape is therefore defined by the first wave in the solution, i.e.

$$z(x \geq x_o, t) = Ee^{-\beta x}\cos(\alpha x - \omega t + \gamma) \tag{7.80}$$

The snake wavelength is

$$L_s = 2\pi/\alpha \tag{7.81}$$

and the snake amplitude at x is

$$Z = Ee^{-\beta x} \tag{7.82}$$

Consider first the dependency of the snake wavelength on the surge frequency and on the damping. Substitution for H and θ in equation (7.76(ix)) by the expressions given by equations (7.76(vi)) and (7.76(ii)) respectively, gives

$$\alpha = (\sigma/2c)^{1/2}[1 + (2Kc^2/\sigma)^2]^{1/8}\cos(\tfrac{1}{4}\tan^{-1}(2Kc^2/\sigma)) \tag{7.83}$$

A non-dimensional wavelength number Γ and a non-dimensional damping number Ω are defined as follows:

$$\Gamma = L_s(\sigma/2c)^{1/2} \tag{7.84}$$

$$\Omega = 2Kc^2/\sigma \tag{7.85}$$

Substitution in equation (7.83) gives

$$\alpha = \Gamma/L_s(1 + \Omega^2)^{1/8}\cos(\tfrac{1}{4}\tan^{-1}\Omega) \qquad (7.86)$$

From equation (7.81) we then have

$$\Gamma = 2\pi/[(1+\Omega^2)^{1/8}\cos(\tfrac{1}{4}\tan^{-1}\Omega)] \qquad (7.87)$$

The snake wavelength for any combination of σ, c^2 and K can be obtained from equation (7.87). A graph of Γ versus Ω is shown by the solid line in Figure 7.20. When $\Omega=0$, $\Gamma=2\pi$, so the wavelength for zero damping is

$$L_s\Big|_{K=0} = 2\pi/(\sigma/2c)^{1/2} \qquad (7.88)$$

The wavelength for zero damping is therefore inversely proportional to the square root of the surge frequency. (This result could, of course, have been obtained directly from equation (7.78).)

The gradual decay of the graph in Figure 7.20 shows a weak dependency of wavelength on damping: the wavelength decreases slowly as the damping increases. For example, for the hose-string with $c^2 = 300m^4/s^2$, the wavelengths corresponding to surge frequencies of 1.57 rads/sec (0.25Hz) and 0.62 rads/sec (0.1Hz), are 29.5m and 46.7m respectively when there is no damping present. With damping K = 0.002 (this represents a large degree of damping as will be seen from later figures) the wavelengths corresponding to the same frequencies are 28.0m and 41.3m respectively, the percentage decreases being about 5% and 11% respectively.

A useful approximation to the Γ-Ω relationship, shown by the broken line in Figure 7.20, is given by the linear relationship

$$\Gamma = 2\pi - 0.368\Omega \qquad (7.89)$$

Substitution for Γ and Ω gives

$$L_s = 2\pi/(\sigma/2c)^{1/2} - 1.04Kc^{5/2}/\sigma^{3/2} \qquad (7.90)$$

The dependence of the snake wavelength on the buoy's surge and on the damping may now be summarised and is presented as result (3):

(3) The snake wavelength is independent of the surge amplitude. A good estimate of the snake wavelength is obtained from the result for zero damping, i.e.

$$L_s = L_s\big|_{K=0} = 2\pi/(\sigma/2c)^{1/2} \qquad (7.91)$$

The wavelength is therefore approximately inversely proportional to the square root of the surge frequency. Damping reduces the wavelength from the zero damping value by an amount given by

$$\Delta L_s = 1.04Kc^{5/2}/\sigma^{3/2} \qquad (7.92)$$

For high frequencies ΔL_s tends to zero. For low frequencies and high damping, the difference between the damped and undamped wavelength is of the order of 10%.

Consider now the dependency of the snake amplitude on surge frequency and damping. The snake amplitude at x has been given by equation (7.76) as

$$Z = Ee^{-\beta x} \qquad (7.82)$$

E is the amplitude of the snake when it originates; β is a measure of the rate at which the value of E decays along the hose-string. Both E and β depend on the surge frequency and the damping.

Substituting for H in equation (7.76(vii)) and for H and θ in equation (7.76(x)), and using the definition of Ω given by equation (7.85), leads to

$$E/a_s^{1/2} = 2^{5/4}(c/\sigma)^{1/4}(1+\Omega^2)^{-5/16}(1+\lambda^4)^{-1/4} \qquad (7.97)$$

and

$$\beta = (\sigma/2c)^{1/2}(1+\Omega^2)^{1/8}\sin(\tfrac{1}{4}\tan^{-1}\Omega) \qquad (7.98)$$

Two non-dimensional numbers, N_1 and N_2, are defined as follows:

$$N_1 = (E/a_s^{1/2})2^{-5/4}(\sigma/c)^{1/4} = (1+\Omega^2)^{-5/16}(1+\lambda^4)^{-1/4} \qquad (7.99)$$

$$N_2 = \beta/(\sigma/2c)^{1/2} = (1+\Omega^2)^{1/8}\sin(\tfrac{1}{4}\tan^{-1}\Omega) \qquad (7.100)$$

A graph of N_1 versus Ω and of N_2 versus Ω is shown by the solid lines in Figures 7.21 and 7.22 respectively. The graphs show that the value of E decreases rapidly and the rate of decay of snake amplitude increases as the damping increases. Consider the following approximations to the N_1-Ω and N_2-Ω relationships:

$$N_1 = 0.636\Omega^{-1/2} \qquad (7.101)$$

and

$$N_2 = 0.21\Omega^{1/2} \qquad (7.102)$$

The approximation given by equation (7.101) is valid only for $\Omega \geq 0.5$, i.e. for values of Ω not close to zero. The approximations are represented by the broken lines in the respective graphs.

Substitution in equations (7.99) and (7.100) gives

$$E/a_s^{1/2} = 2^{5/4}(c/\sigma)^{1/4}0.636(2Kc^2/\sigma)^{-1/2} \qquad (7.103)$$

$$\beta = 0.21(\sigma/2c)^{1/2}(2Kc^2/\sigma)^{1/2} \qquad (7.104)$$

The following conclusions may now be made regarding the dependency of the snake amplitude on surge frequency and damping:

(4) The maximum amplitude of the snake is approximately proportional to the fourth root of the surge frequency (when $\Omega \geq 0.5$). The rate of decay of the snake as it travels the length of the hose-string is approximately independent of surge frequency. The snake amplitude is approximately inversely proportional to the square root of the damping. The decay rate increases approximately in proportion to the square root of the damping.

Figures 7.23 to 7.27 present the snake shapes (at arbitrarily taken time t=0) for five different surge frequencies. In each case the surge amplitude is 1.0m and the hose-string has $c^2 = 300m^4/s^2$. In each figure the snake shape is presented for five different values of the damping. The figures can be examined for the dependence of snake shape on surge frequency and damping; it may be seen that the dependence is in accordance with the results presented above. Note in particular the decrease in wavelength as the frequency increases; the slight decrease in wavelength as the damping increases; the rapid decrease in snake amplitude and the increase in the rate of decay of amplitude along the string as the damping increases; the increase in snake amplitude as frequency increases when $\Omega \geq 0.5$ and the damping is constant.

The snake-induced horizontal bending moment along the hose-string is given by (equation 7.77):

$$M(x,t) = M_1\cos(\theta_1-\omega t) - M_2\cos(\theta_2-\omega t) \qquad (7.105)$$

where $M_1 = (EI)EH^{1/2}e^{-\beta x}$

$\theta_1 = \alpha x + \gamma + \theta/2$

$M_2 = (EI)FH^{1/2}e^{-\alpha x}$

$\theta_2 = -\beta x + \gamma + \theta/2.$

From result (1) the bending moment frequency is half the surge frequency. From result (2) the bending moment is proportional to the square root of the surge amplitude. Since the bending moment is linearly proportional to the snake amplitude and inversely proportional to the square of the snake wavelength, the dependence of the bending on the surge frequency and the damping can be inferred from results (3) and (4).

Using trigonometry it may be shown that the amplitude of the horizontal bending moment variation at x is

$$\bar{M}(x) = (EI)H^{1/2}[E^2e^{-2\beta x} + F^2e^{-2\alpha x} - 2EFe^{(-\alpha-\beta)x}\cos(\alpha+\beta)x]^{1/2} \qquad (7.106)$$

Figures 7.28 to 7.31 present the amplitude of horizontal bending, divided by the square root of the surge amplitude, as a function of position along the hose-string for four different values of damping. In each figure the bending variation is presented for four different values of surge frequency. As before, the hose-string has $c^2 = 300m^4/s^2$.

For zero damping, Figure 7.28, the bending moment amplitude is constant along the hose-string's length. As damping increases the bending moment amplitude decreases and the rate of decay of bending moment along the string increases. Bending moment increases with increasing surge frequency; this follows from the decrease in snake wavelength as the frequency increases.

For positions close to the buoy the damping wave is not zero and increases in magnitude with proximity to the buoy. This wave reduces the curvature of the hose-string and, therefore, the bending moments.

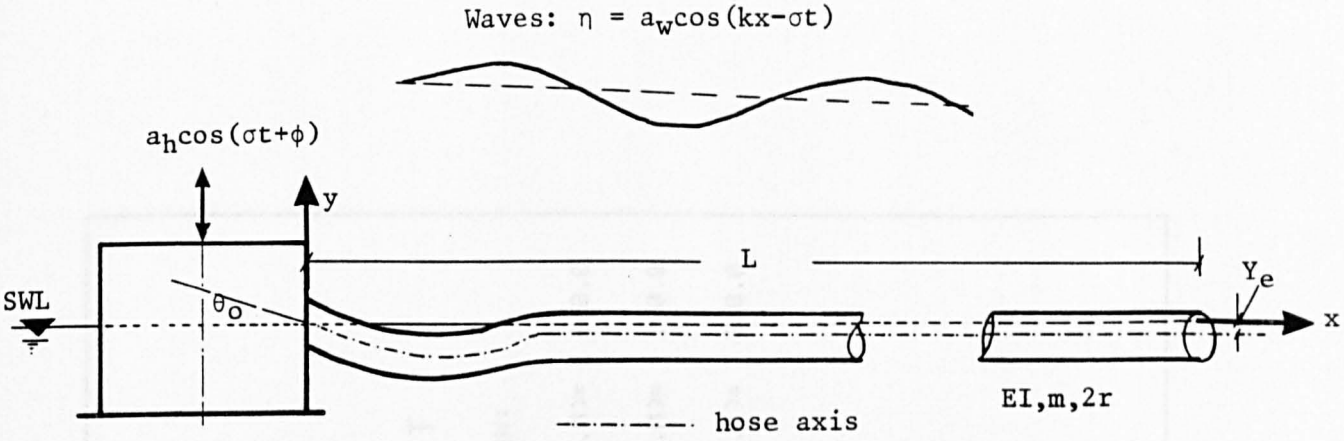

Figure 7.1 Definition sketch for vertical displacement and bending analytical model

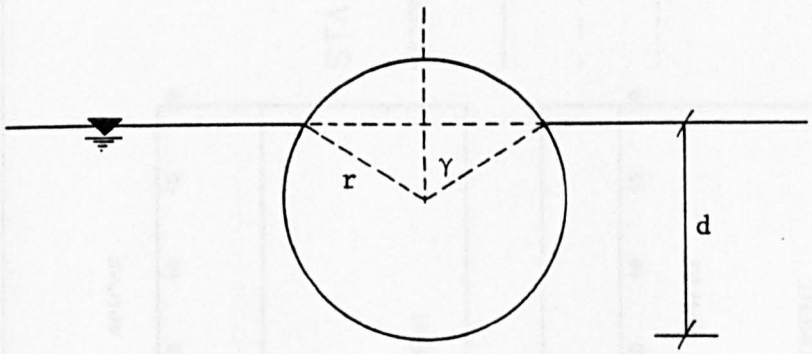

Figure 7.2 Base of hose is d below the instantaneous water level

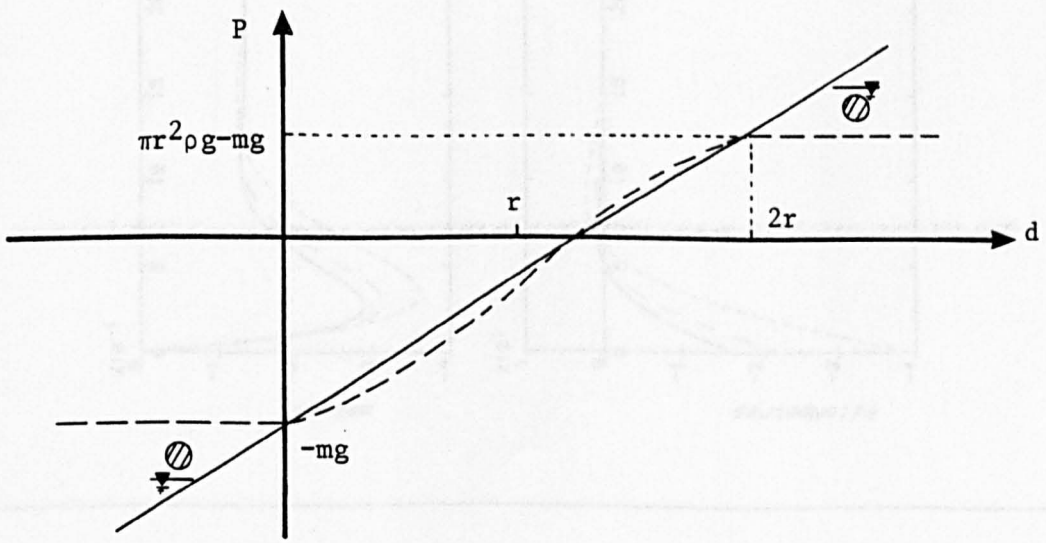

Figure 7.3 Vertical force on hose as a function of submerged depth d

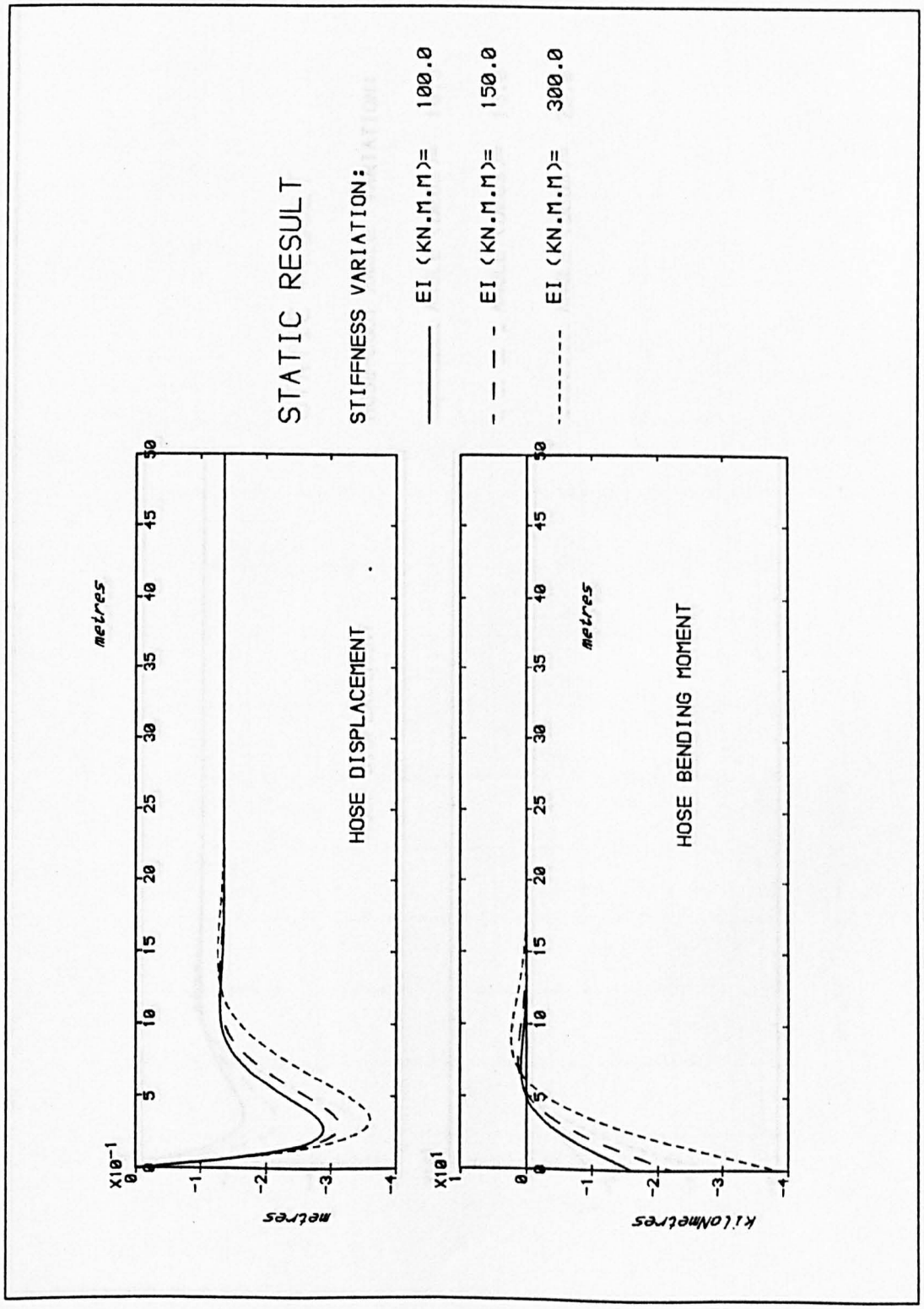

Figure 7.4 Effect of bending stiffness on hose-string static displacement and bending moment

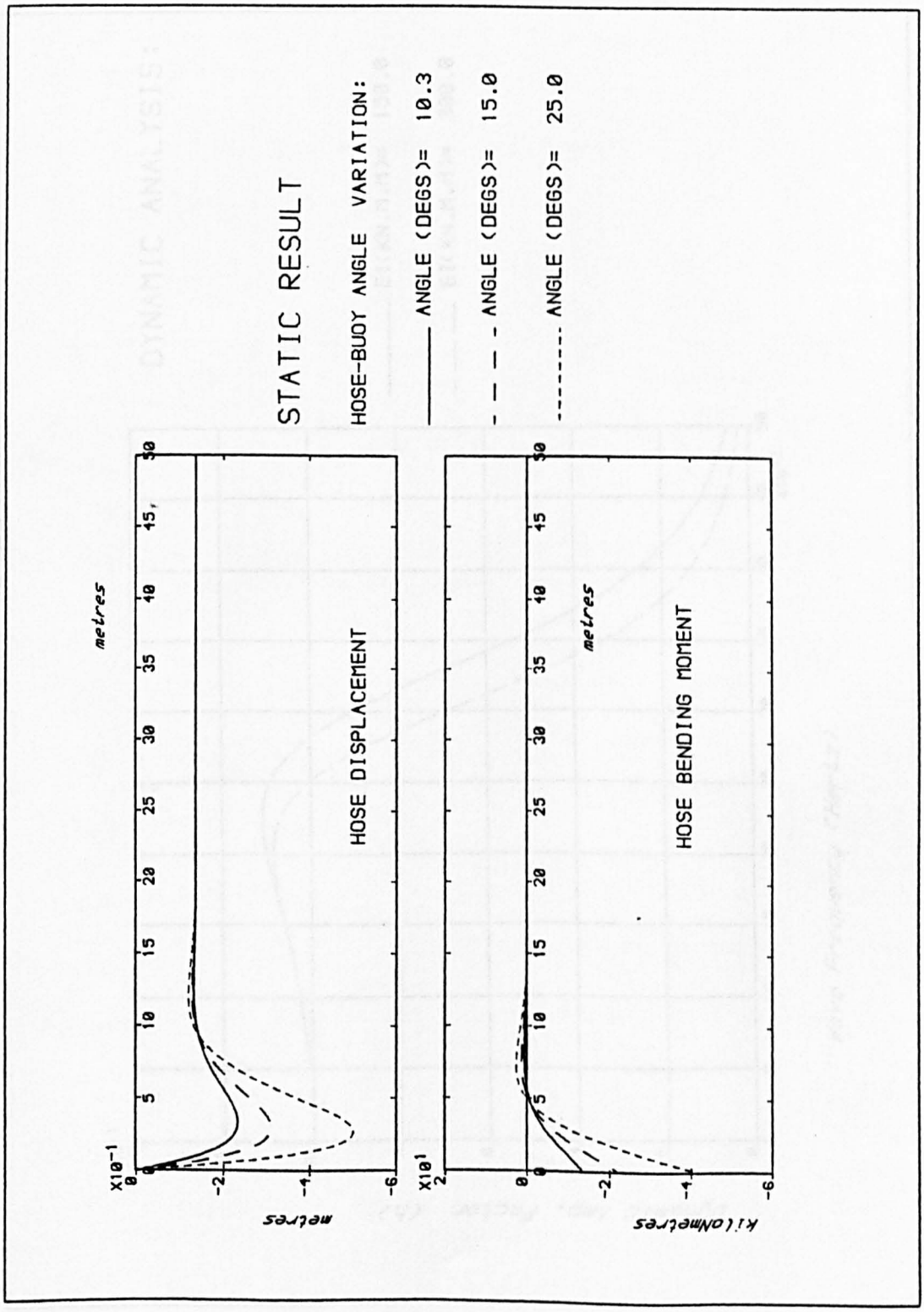

Figure 7.5 Effect of hose-buoy angle on the static displacement and bending of the hose-string

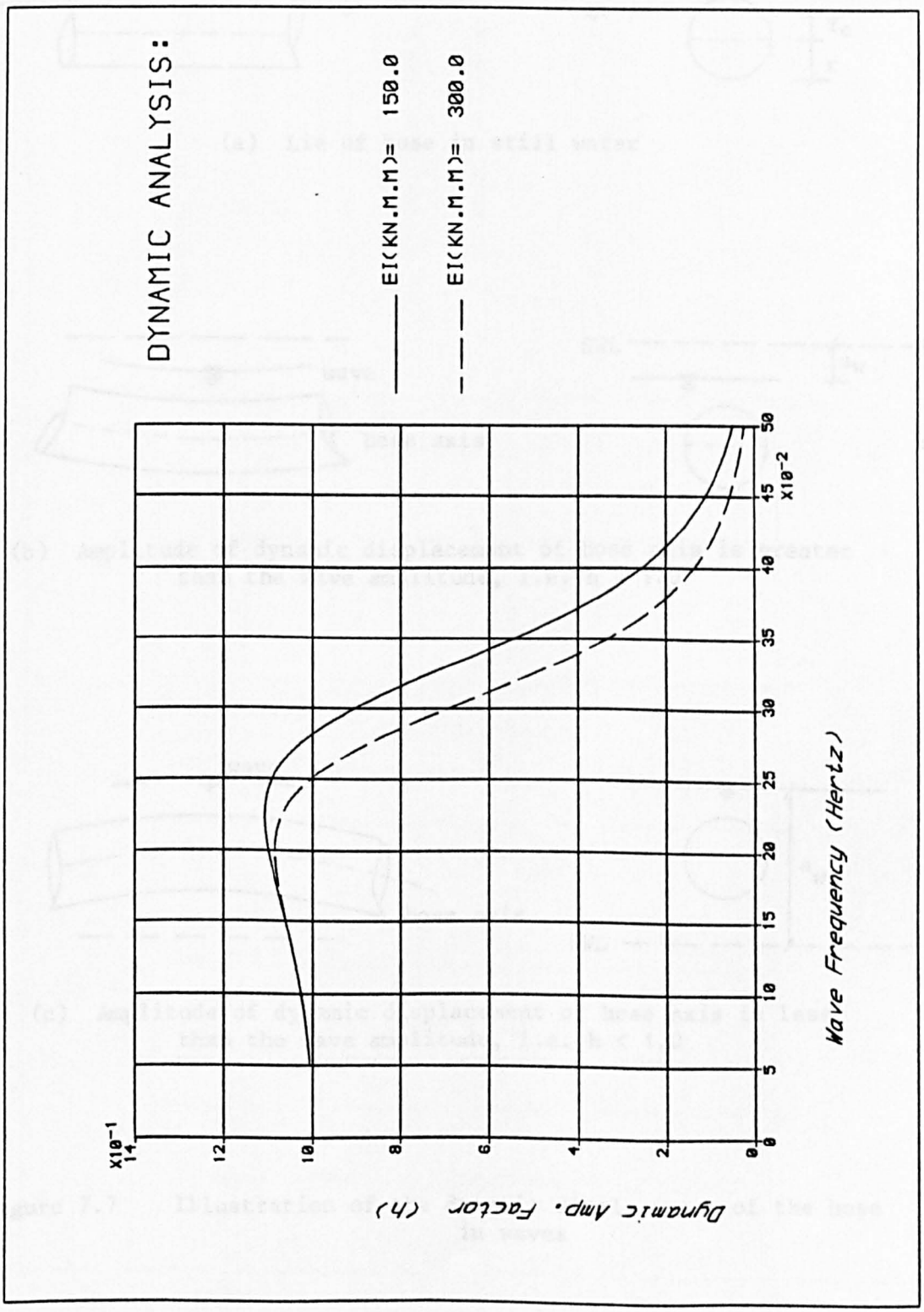

Figure 7.6 Hose-string dynamic amplification factor

(a) Lie of hose in still water

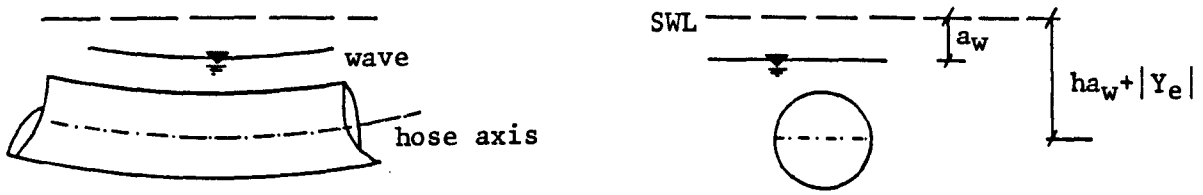

(b) Amplitude of dynamic displacement of hose axis is greater than the wave amplitude, i.e. h > 1.0

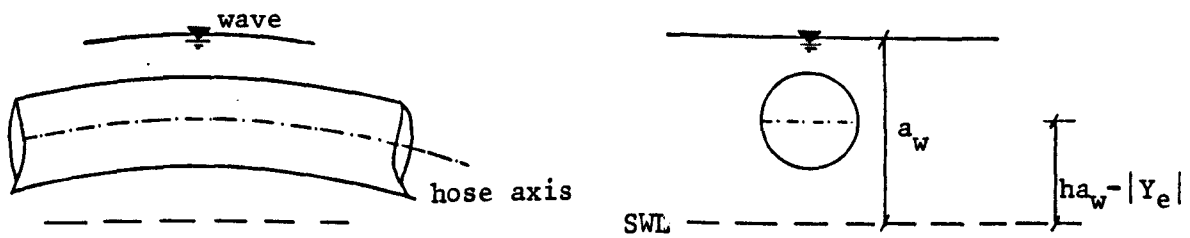

(c) Amplitude of dynamic displacement of hose axis is less than the wave amplitude, i.e. h < 1.0

Figure 7.7 Illustration of the dynamic displacement of the hose in waves

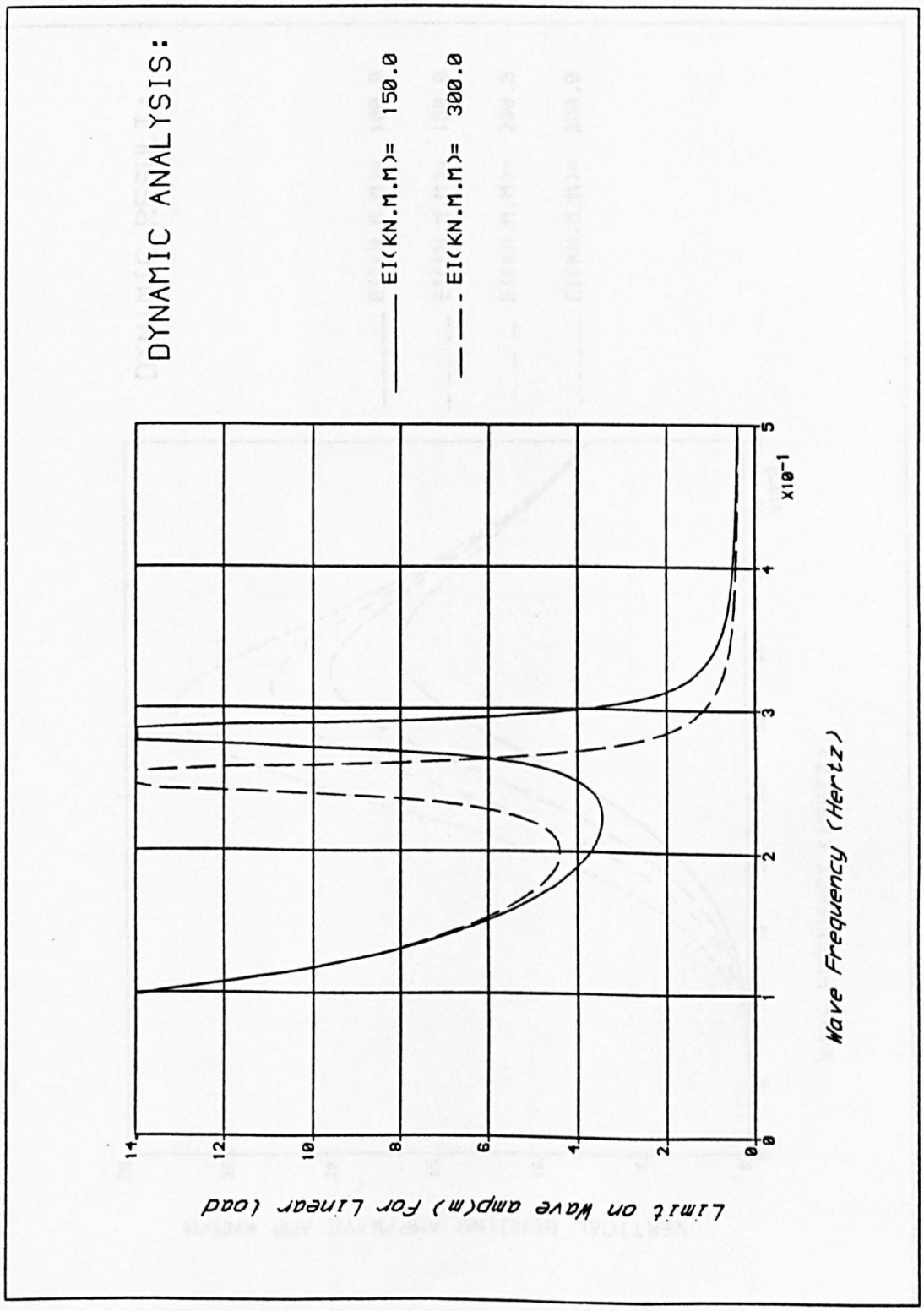

Figure 7.8 Limit on wave amplitude for hose to remain partially submerged throughout the wave cycle

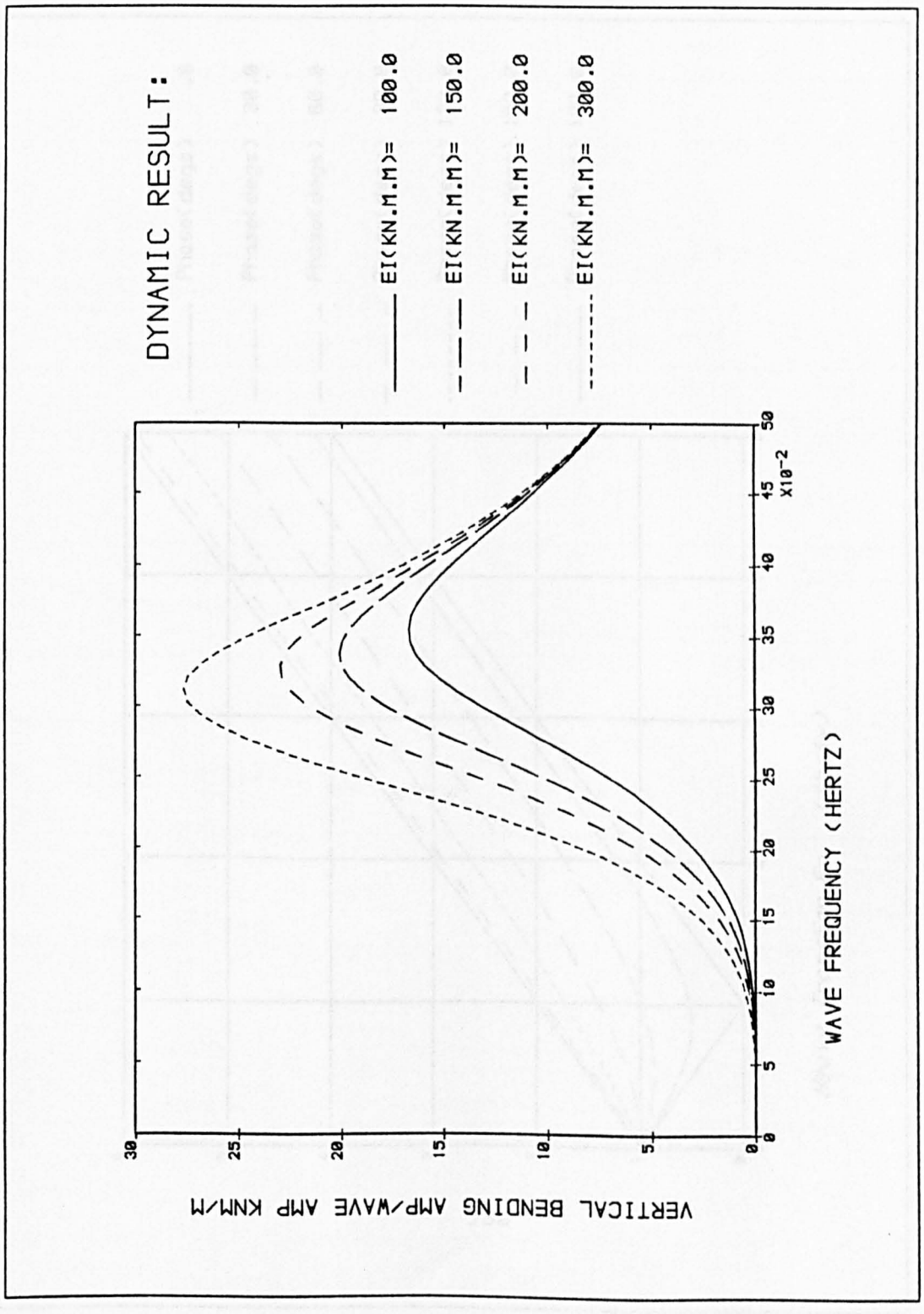

Figure 7.9 Dynamic vertical bending amplitude per unit wave amplitude for the hose with r = 0.5m and m = 500kg/m

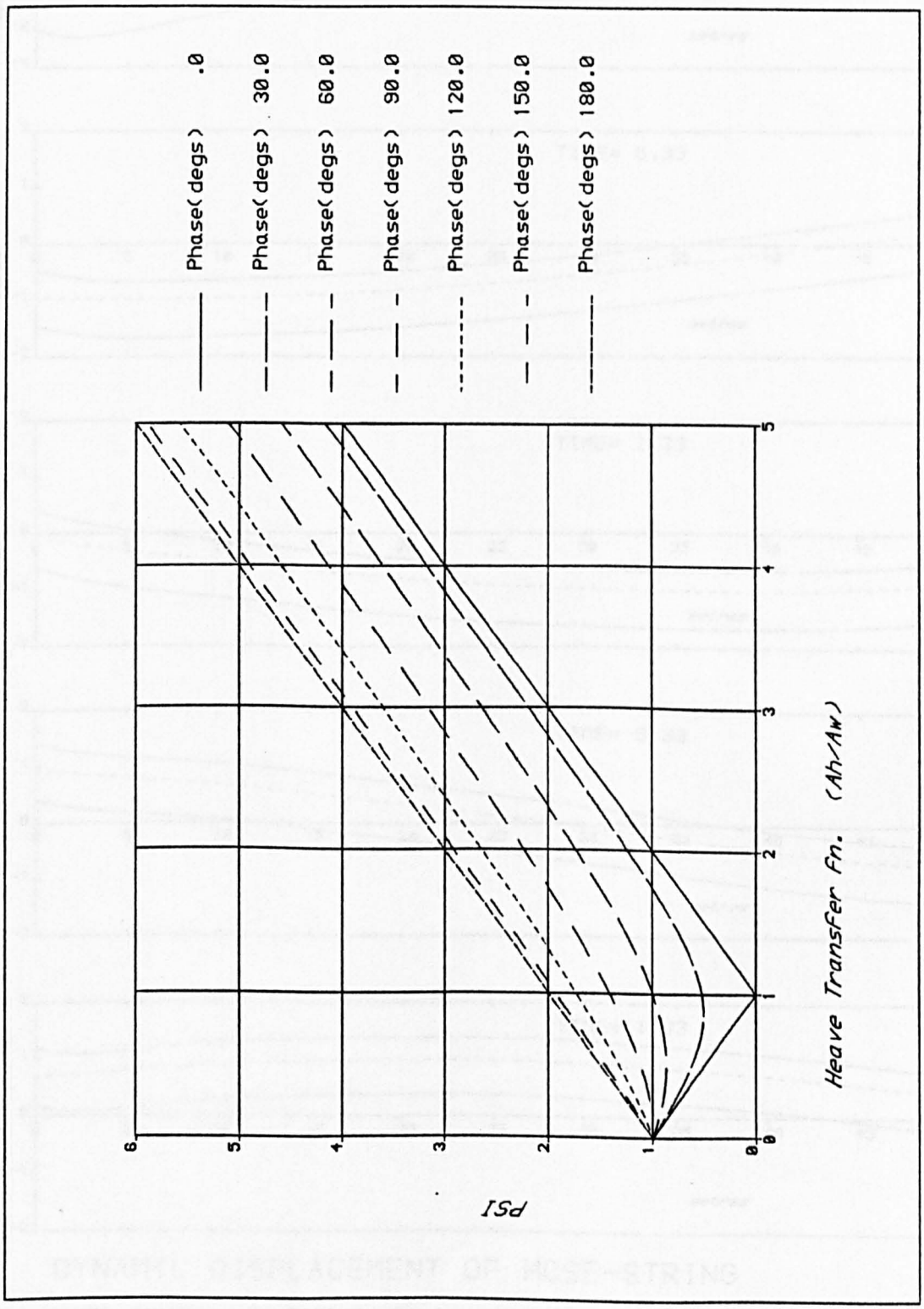

Figure 7.10 Dependence of ψ on the heave amplitude and phase

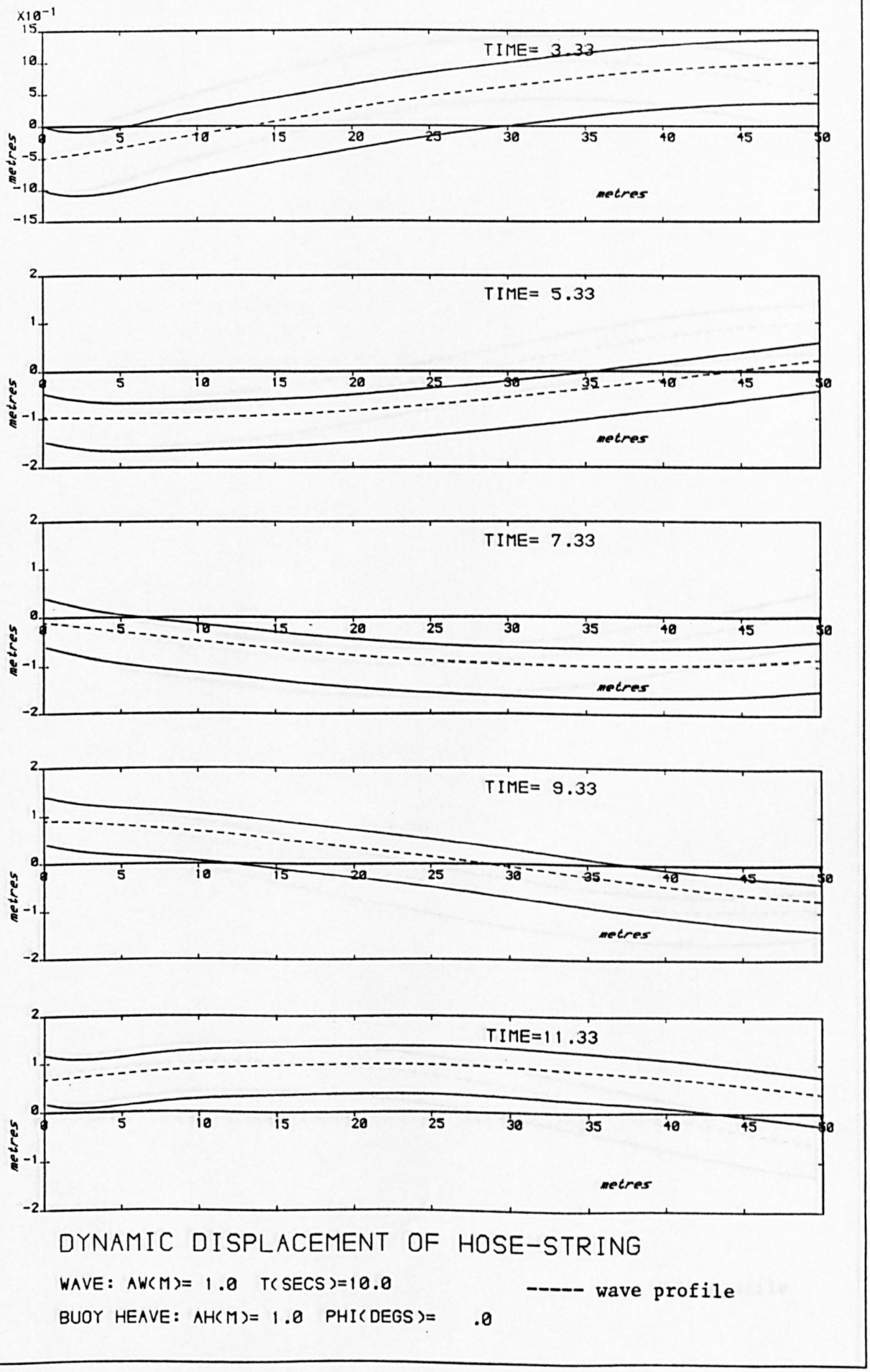

Figure 7.11 Dynamic displacement of first 50m of a hose-string in 10sec waves. (The SBM heaves with the same amplitude as the waves and in phase with the waves.)

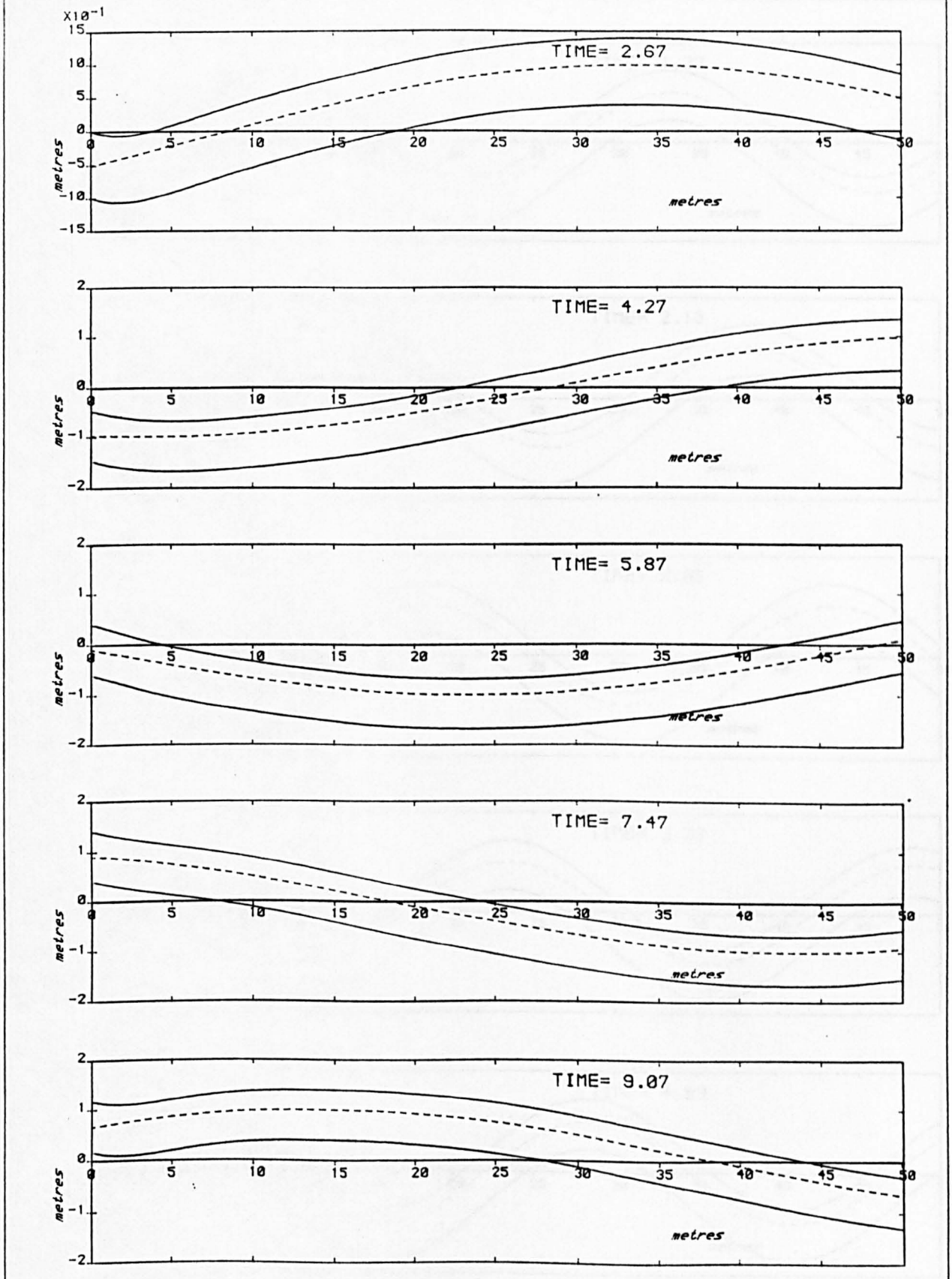

Figure 7.12 Dynamic displacement of first 50m of a hose-string in 8sec waves. (The SBM heaves with the same amplitude as the waves and in phase with the waves.)

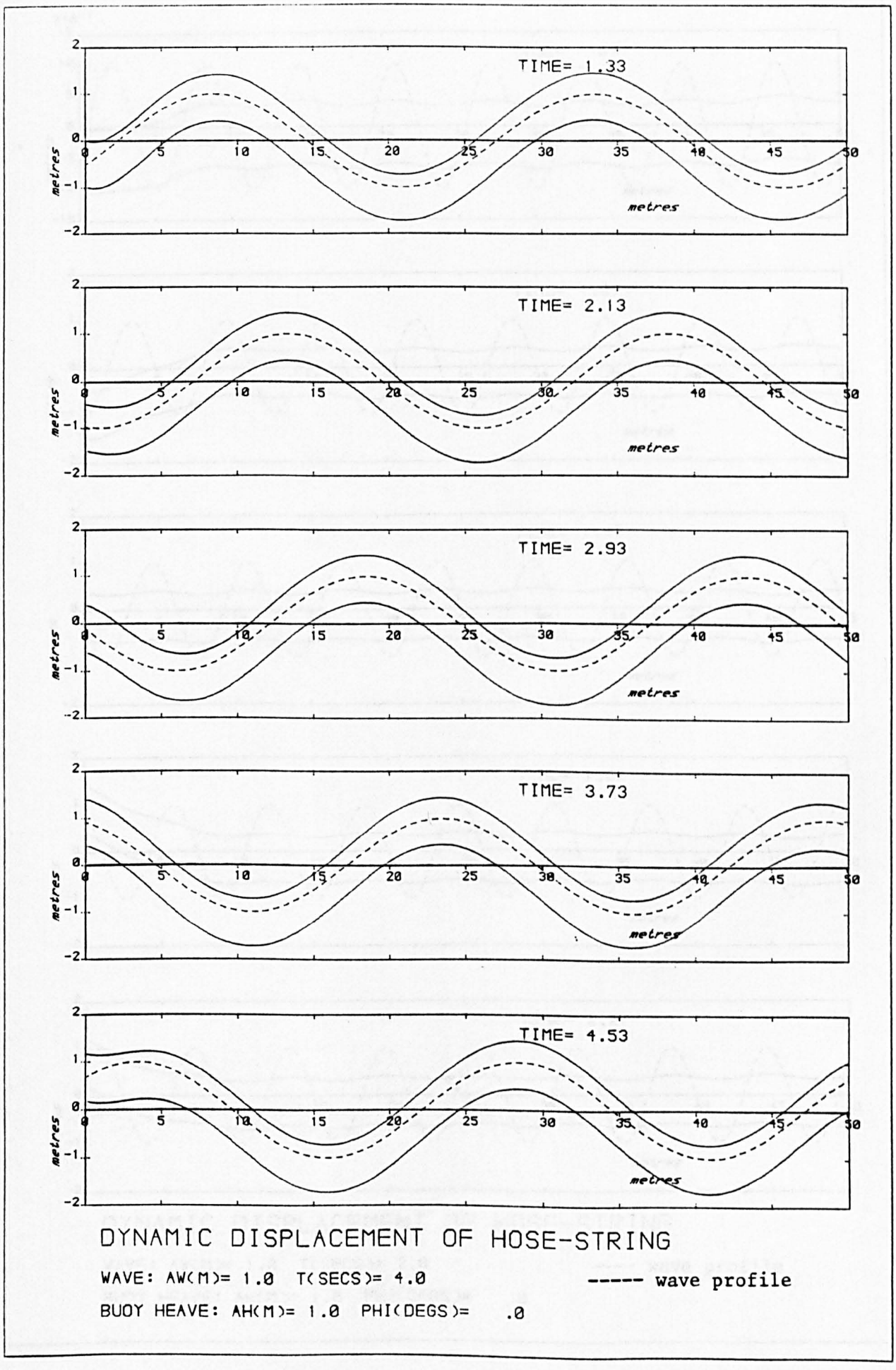

Figure 7.13 Dynamic displacement of first 50m of a hose-string in 4sec waves. (The SBM heaves with the same amplitude as the waves and in phase with the waves.)

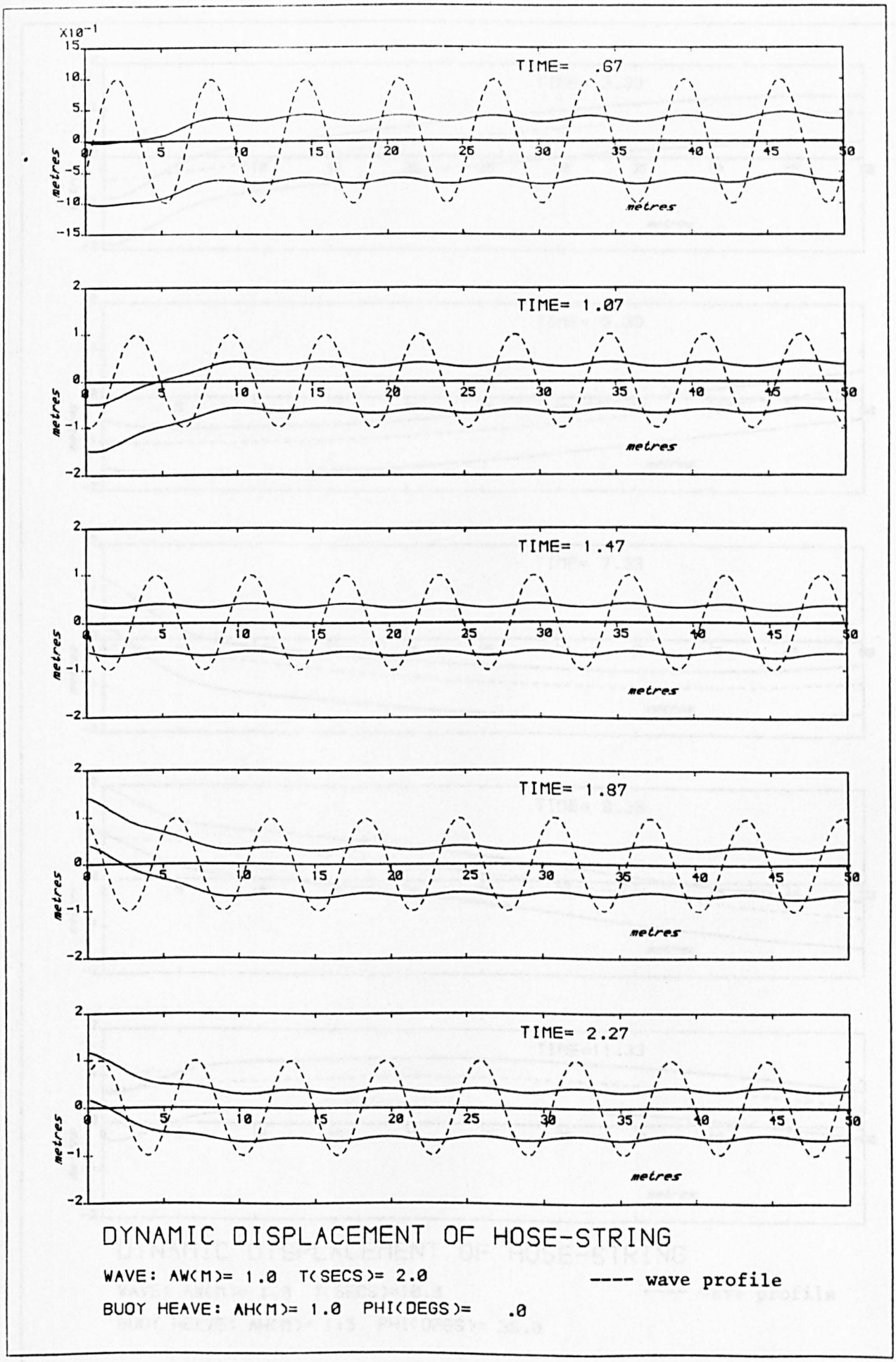

Figure 7.14 Dynamic displacement of first 50m of a hose-string in 2sec waves. (The SBM heaves with the same amplitude as the waves and in phase with the waves.)

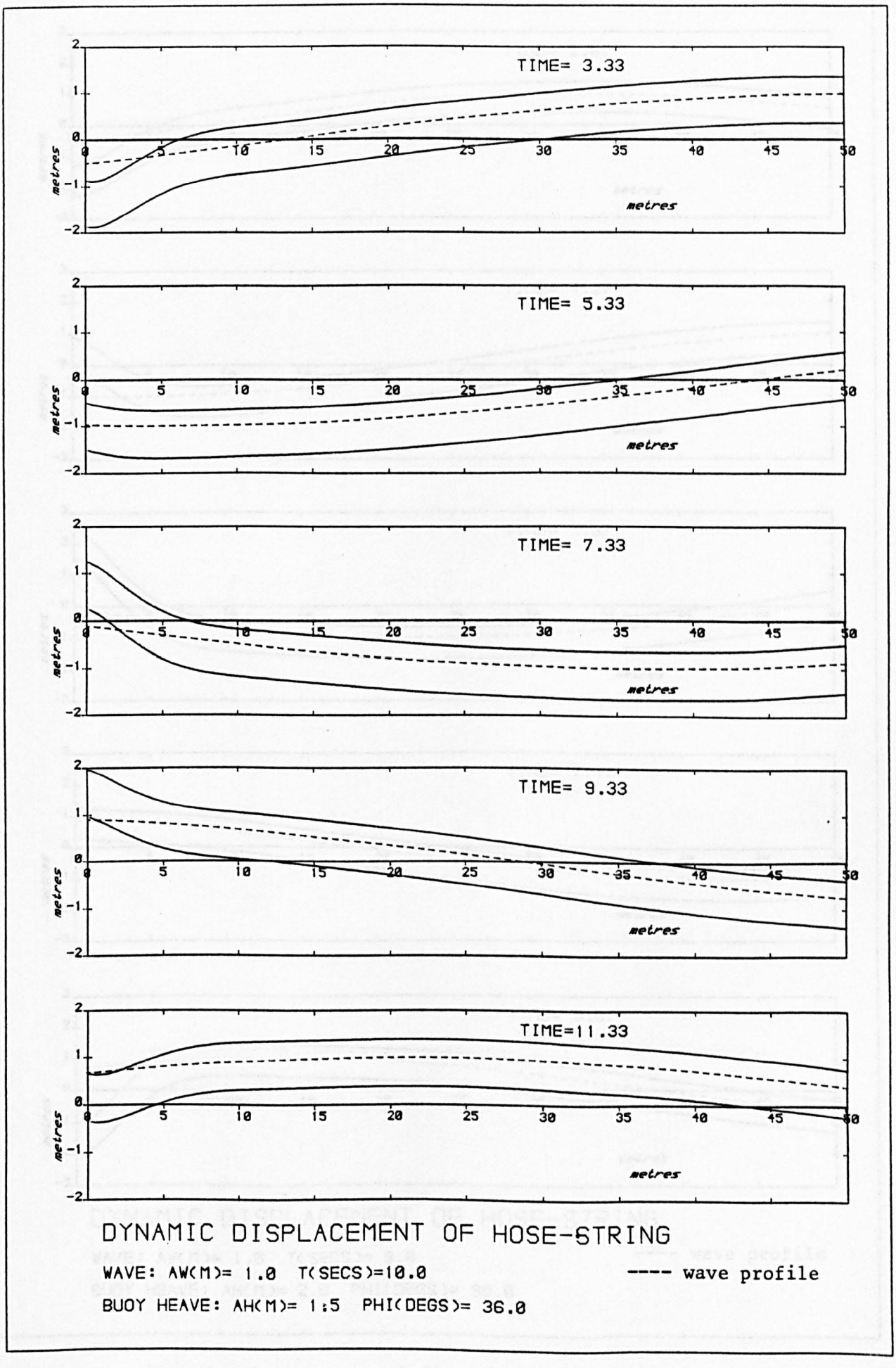

Figure 7.15 Dynamic displacement of first 50m of a hose-string in 10sec waves. (The SBM heave amplitude is not equal to the wave amplitude and the heave is not in phase with the waves.)

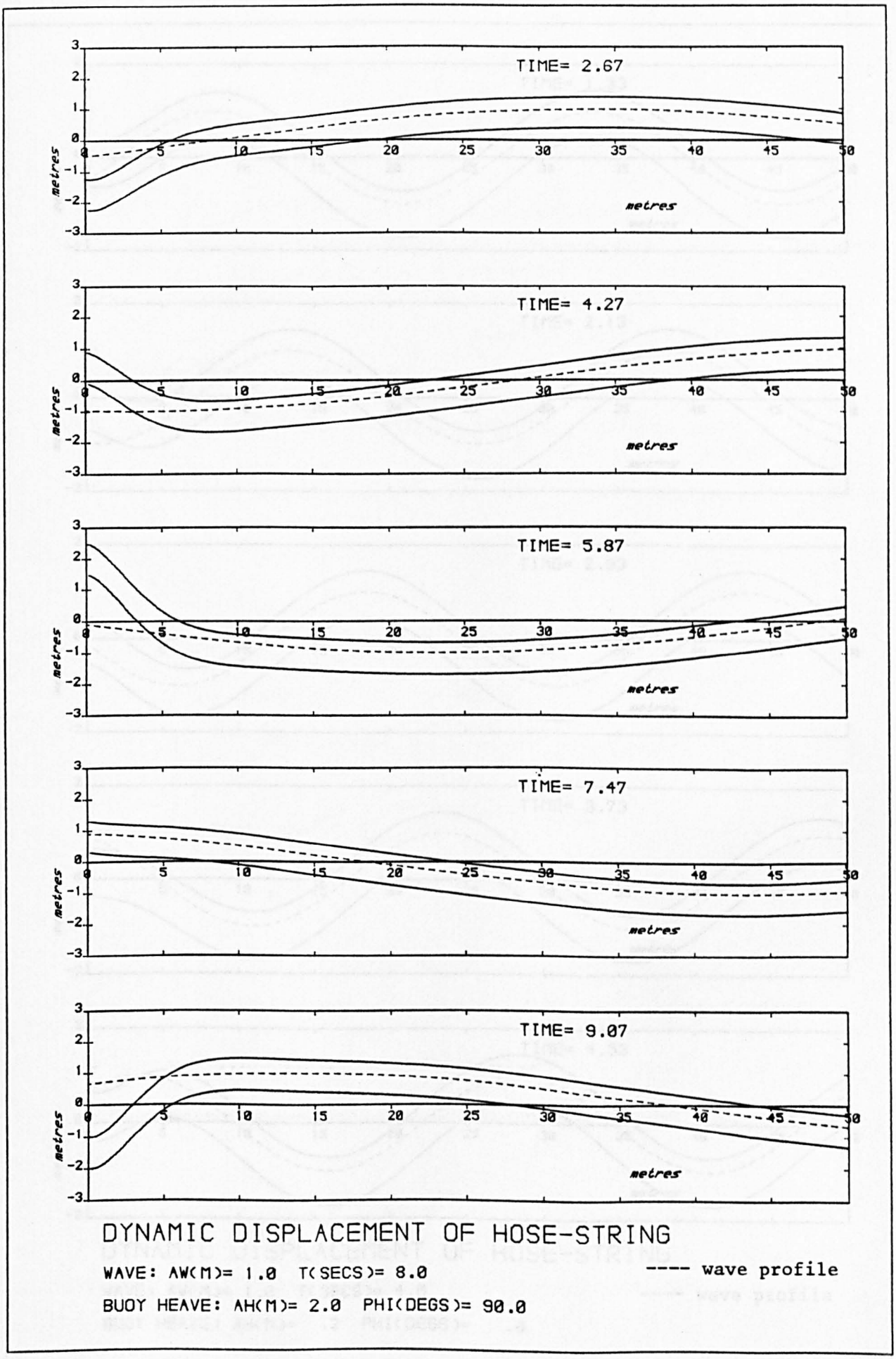

Figure 7.16 Dynamic displacement of first 50m of a hose-string in 8sec waves. (The SBM heave amplitude is not equal to the wave amplitude and the heave is not in phase with the waves.)

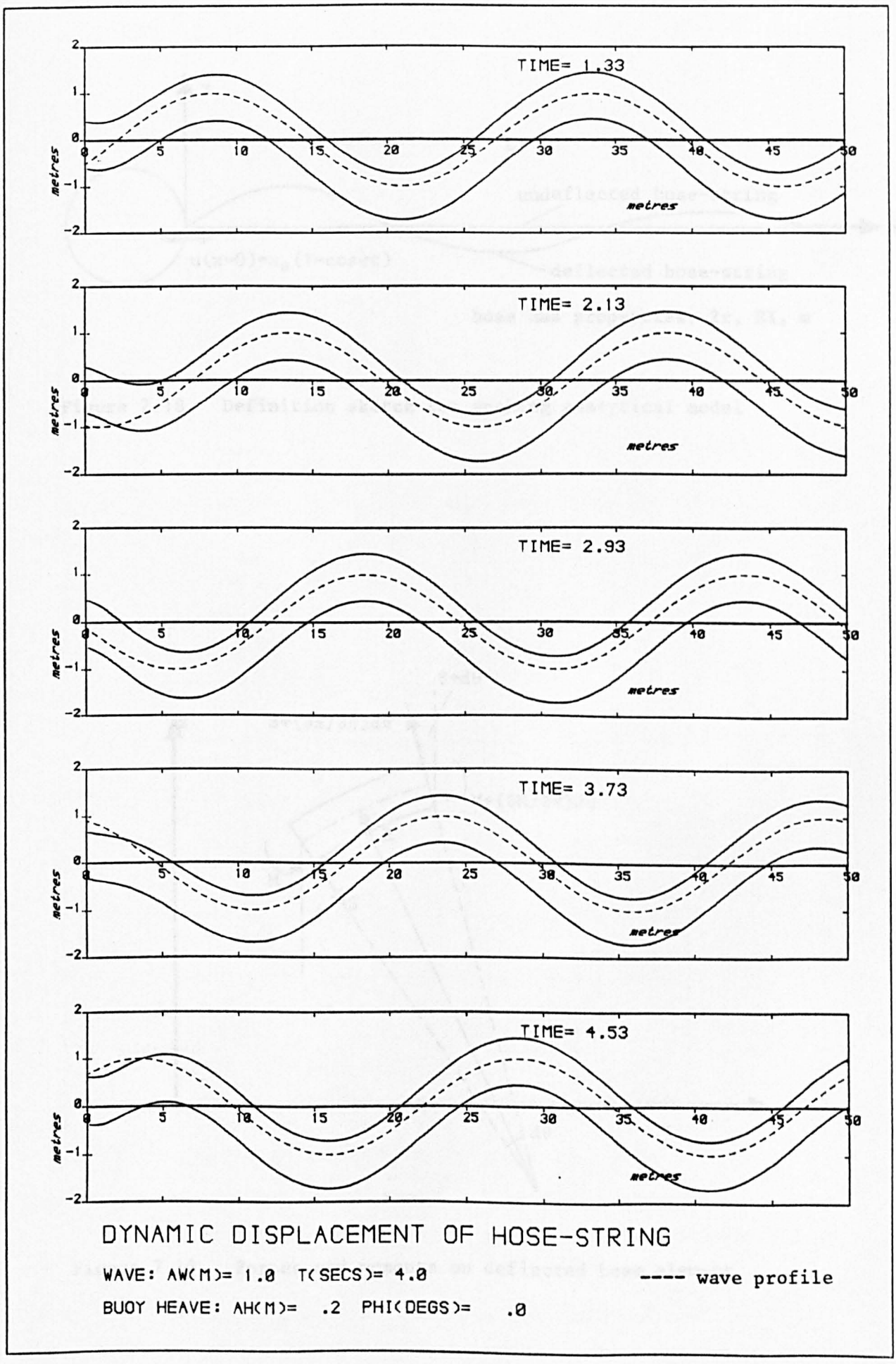

Figure 7.17 Dynamic displacement of first 50m of a hose-string in 2sec waves. (The SBM heave amplitude is not equal to the wave amplitude.)

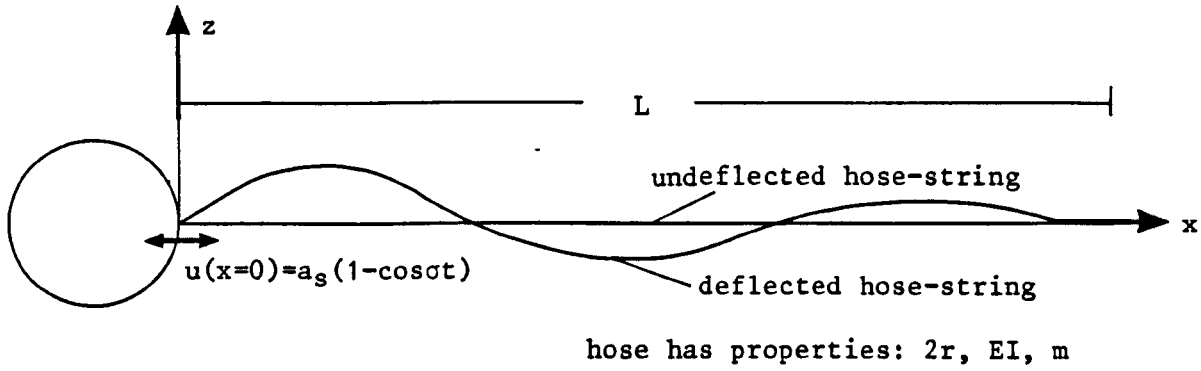

Figure 7.18 Definition sketch for snaking analytical model

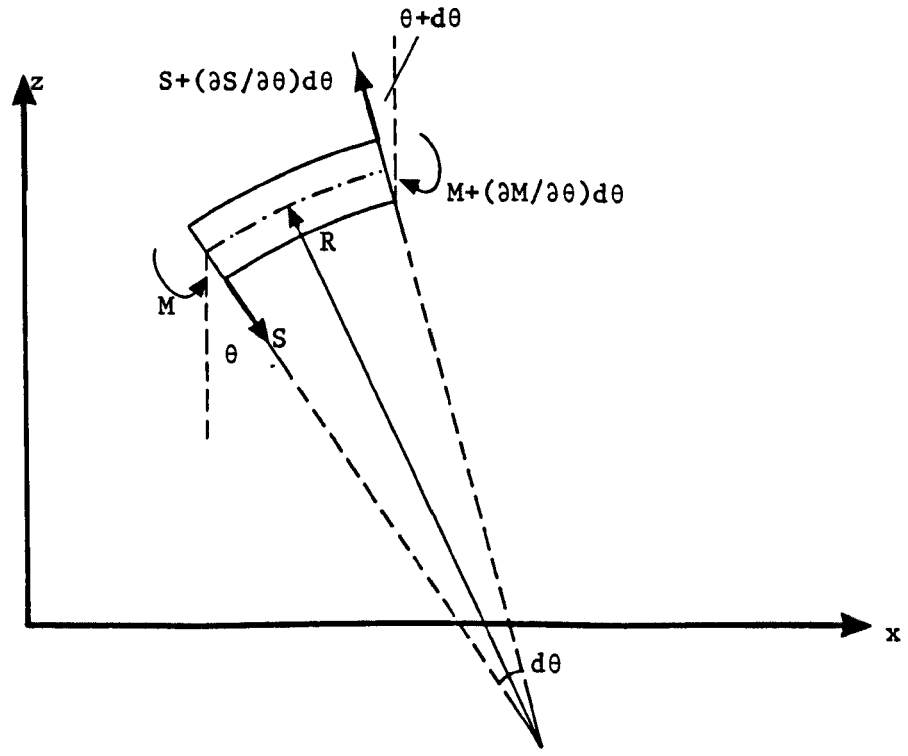

Figure 7.19 Forces and moments on deflected beam element

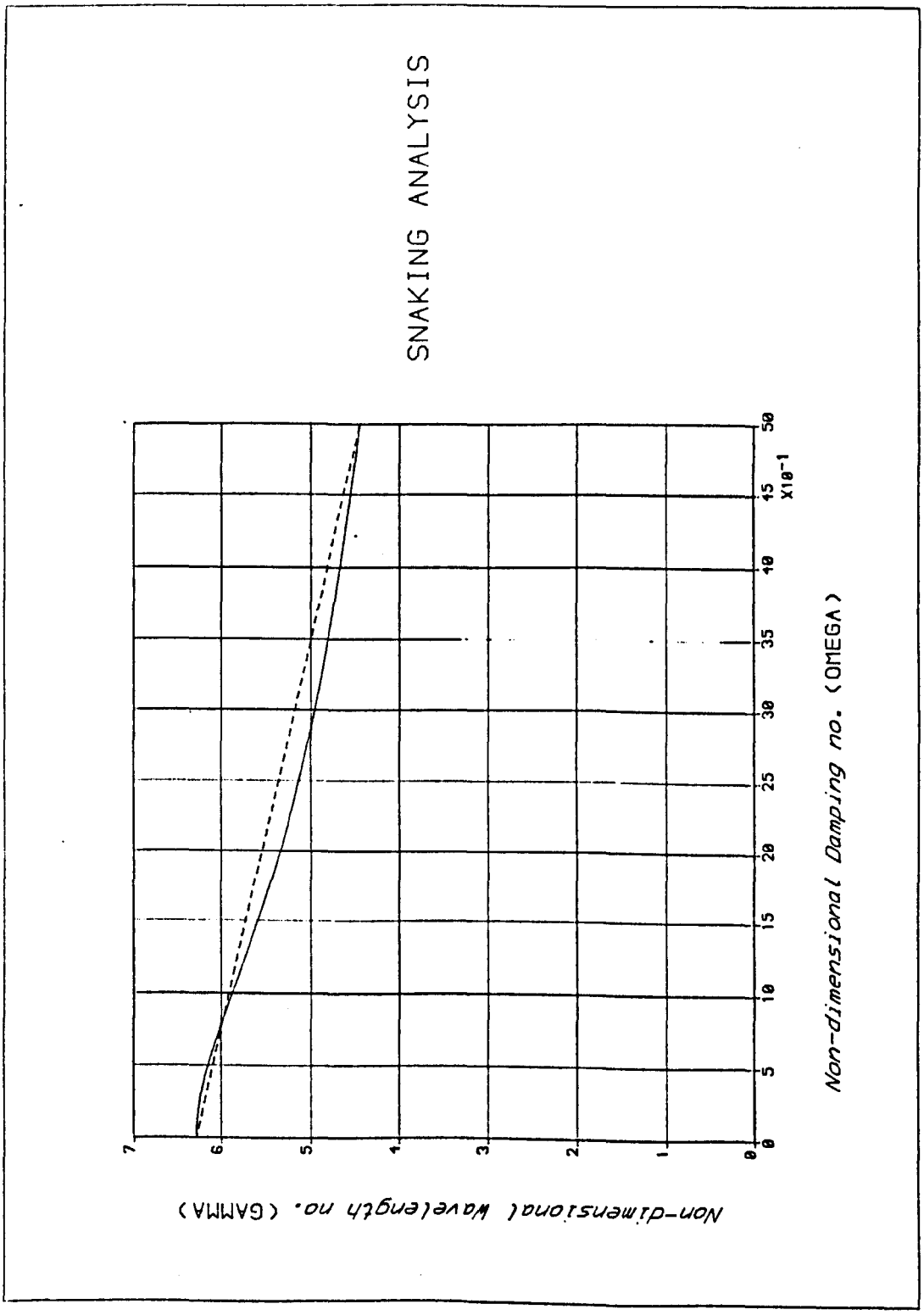

Figure 7.20 Non-dimensional no. γ versus non-dimensional no. Ω

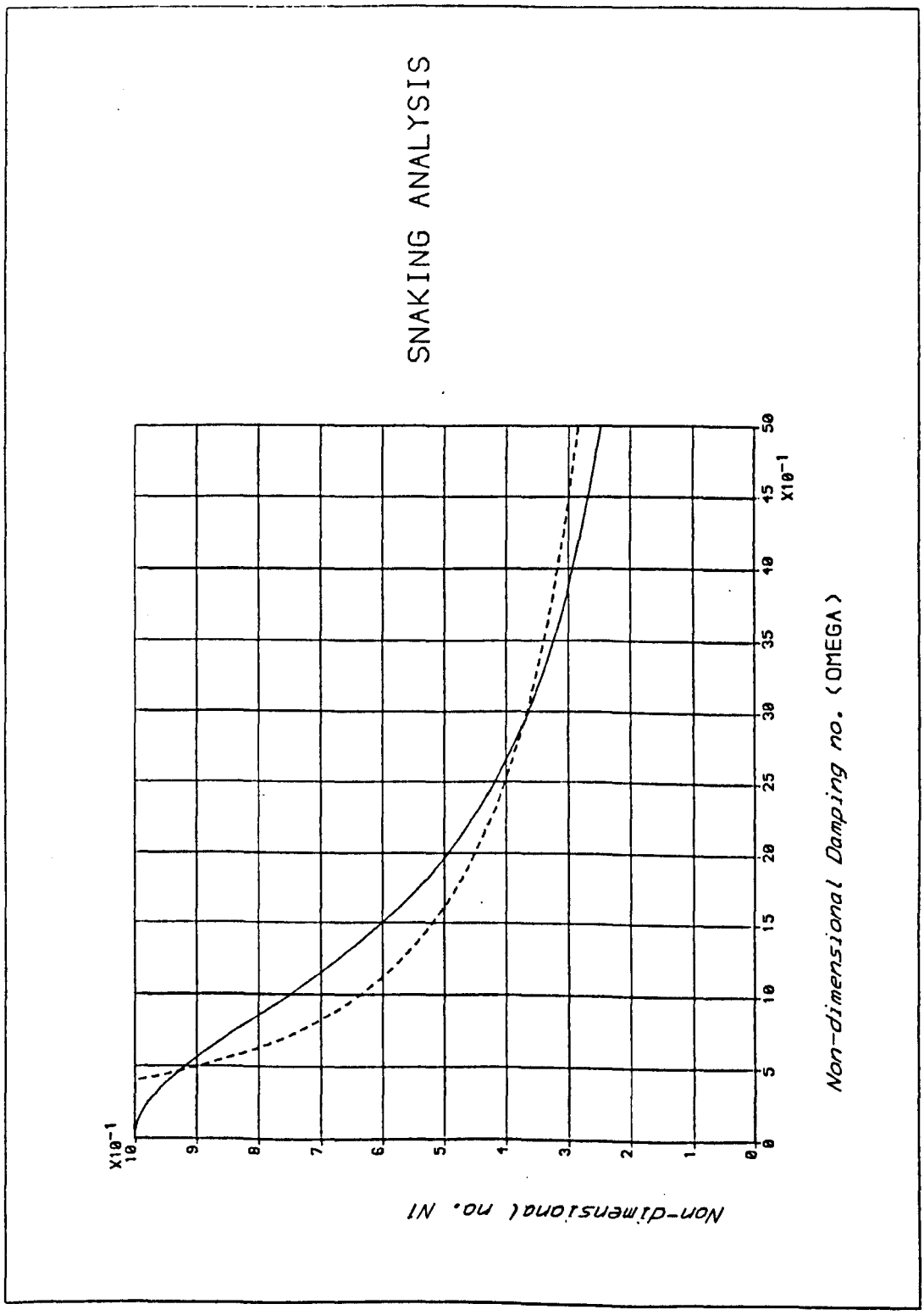

Figure 7.21 Non-dimensional no. N1 versus non-dimensional no. Ω

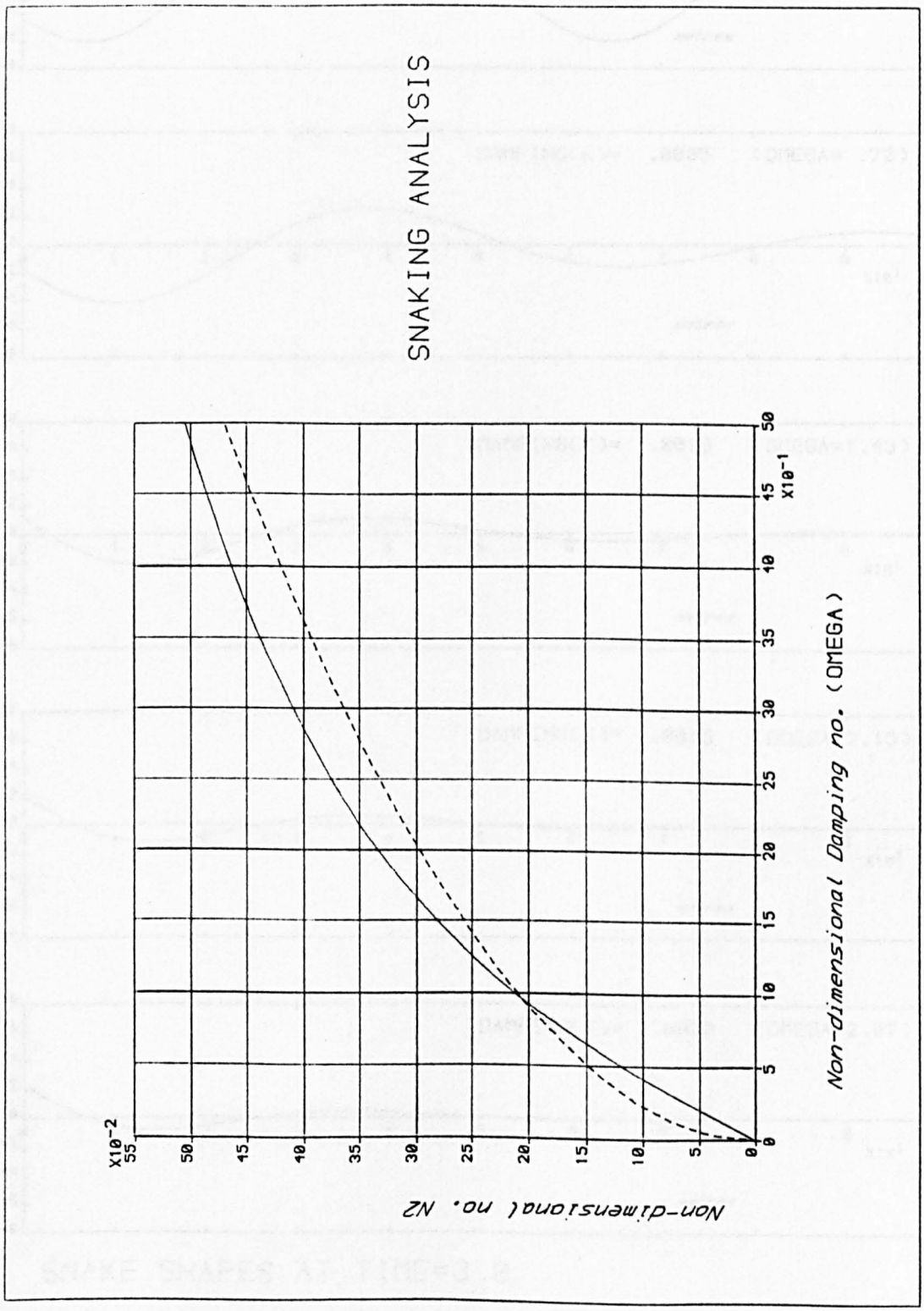

Figure 7.22 Non-dimensional no. N2 versus non-dimensional no. Ω

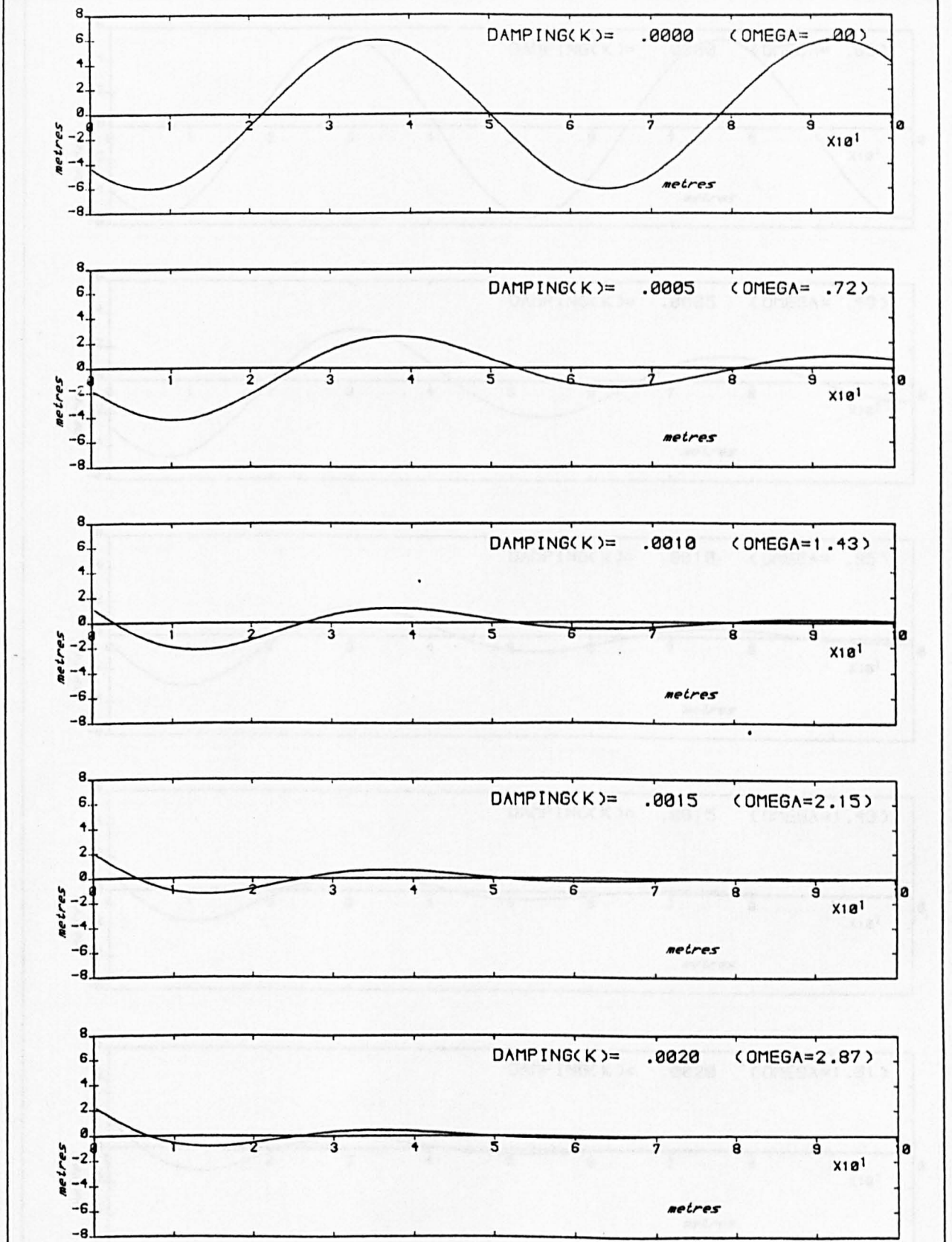

Figure 7.23 The effect of damping on snake shape for surge frequency = 0.067Hz

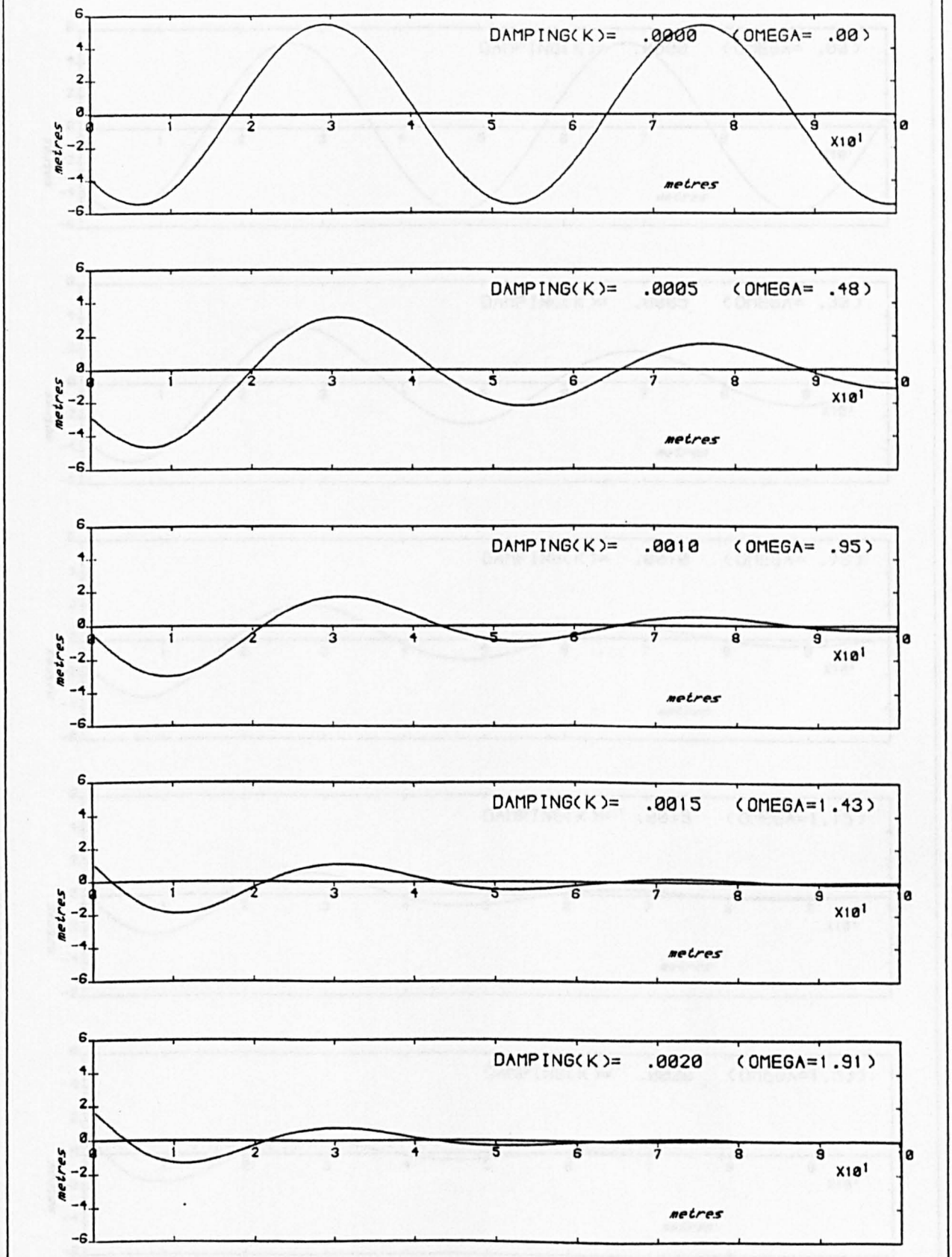

Figure 7.24 The effect of damping on snake shape for surge frequency = 0.1Hz

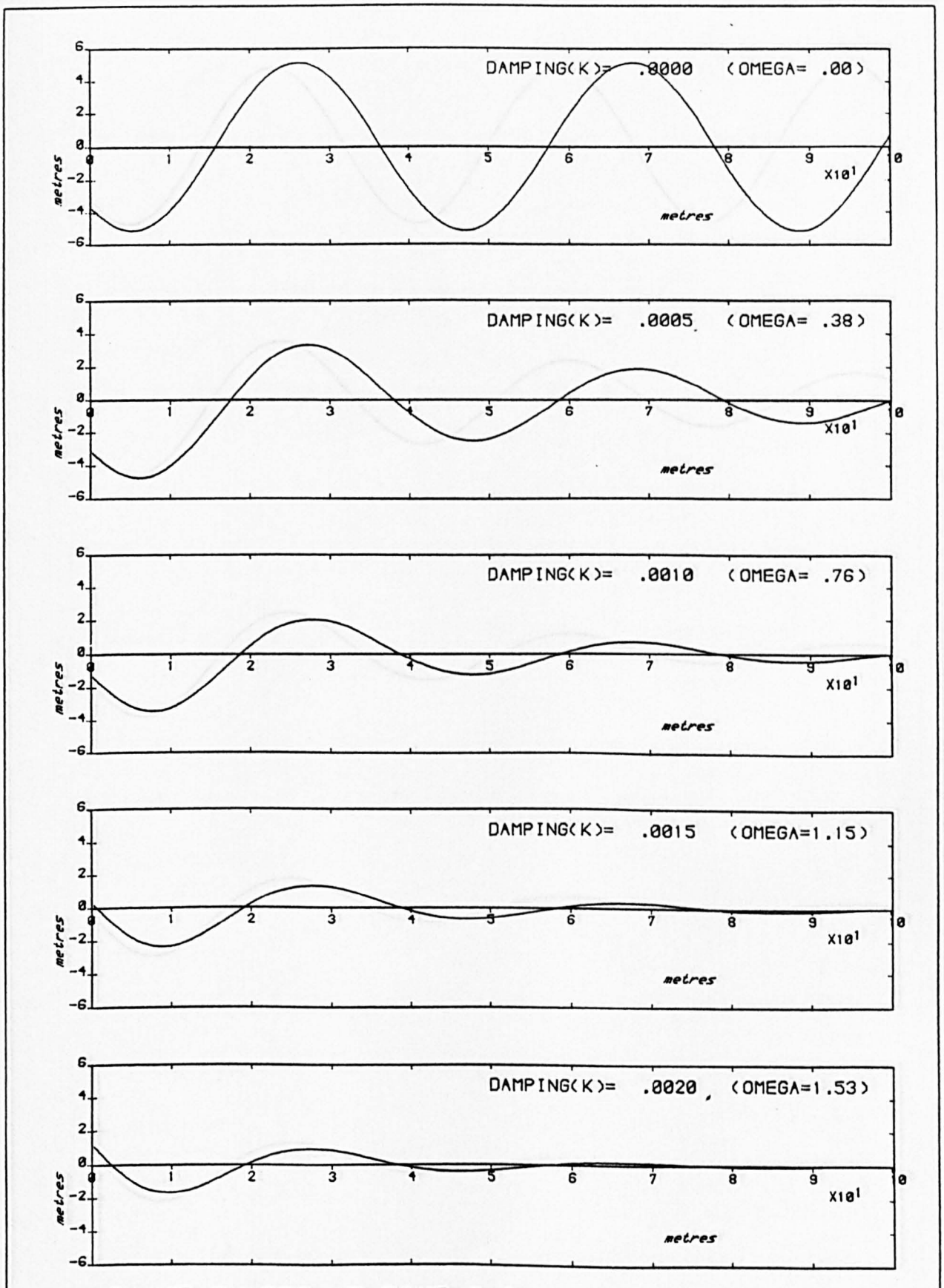

Figure 7.25 The effect of damping on snake shape for surge frequency = 0.125Hz

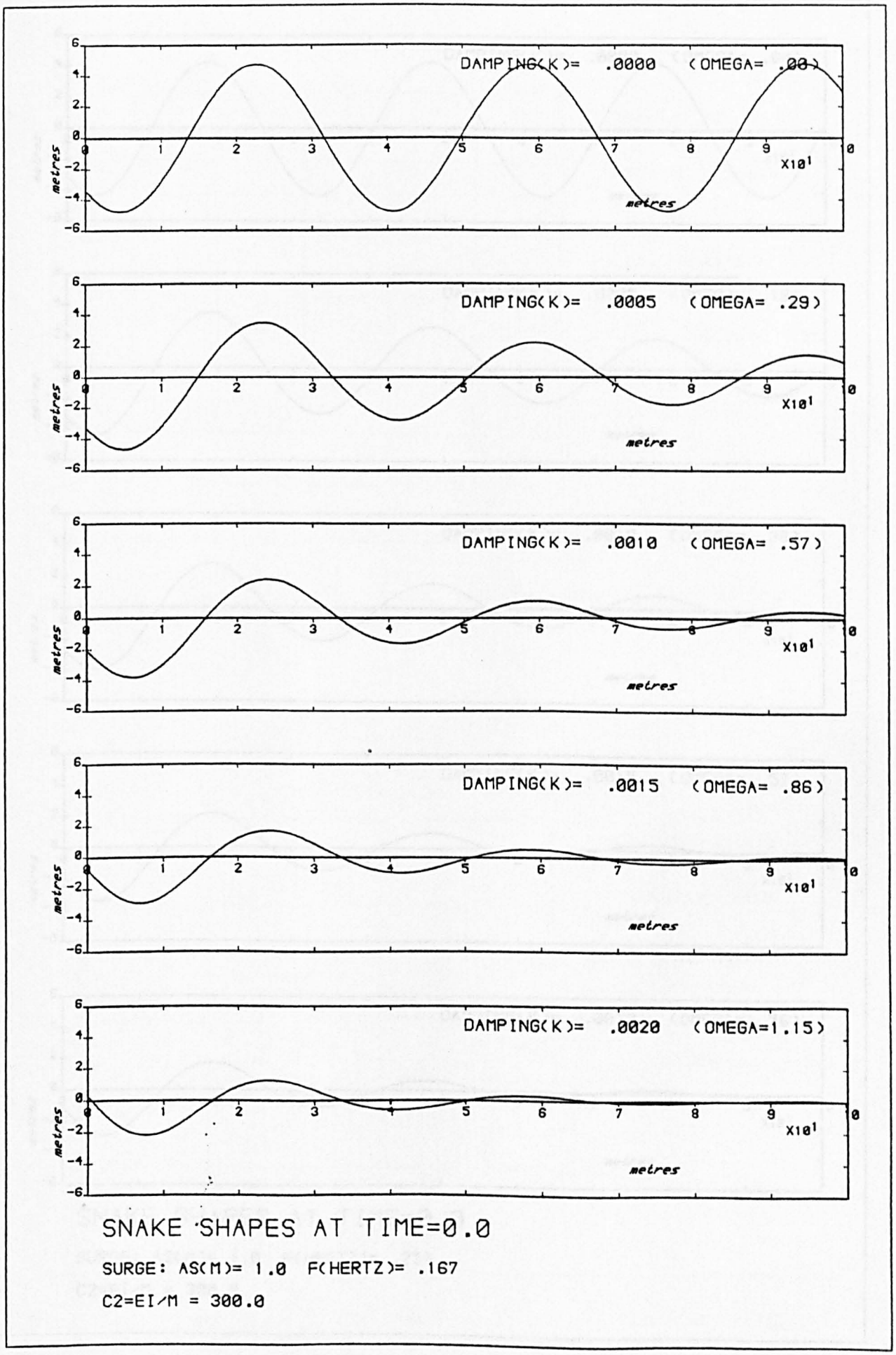

Figure 7.26 The effect of damping on snake shape for surge frequency = 0.167Hz

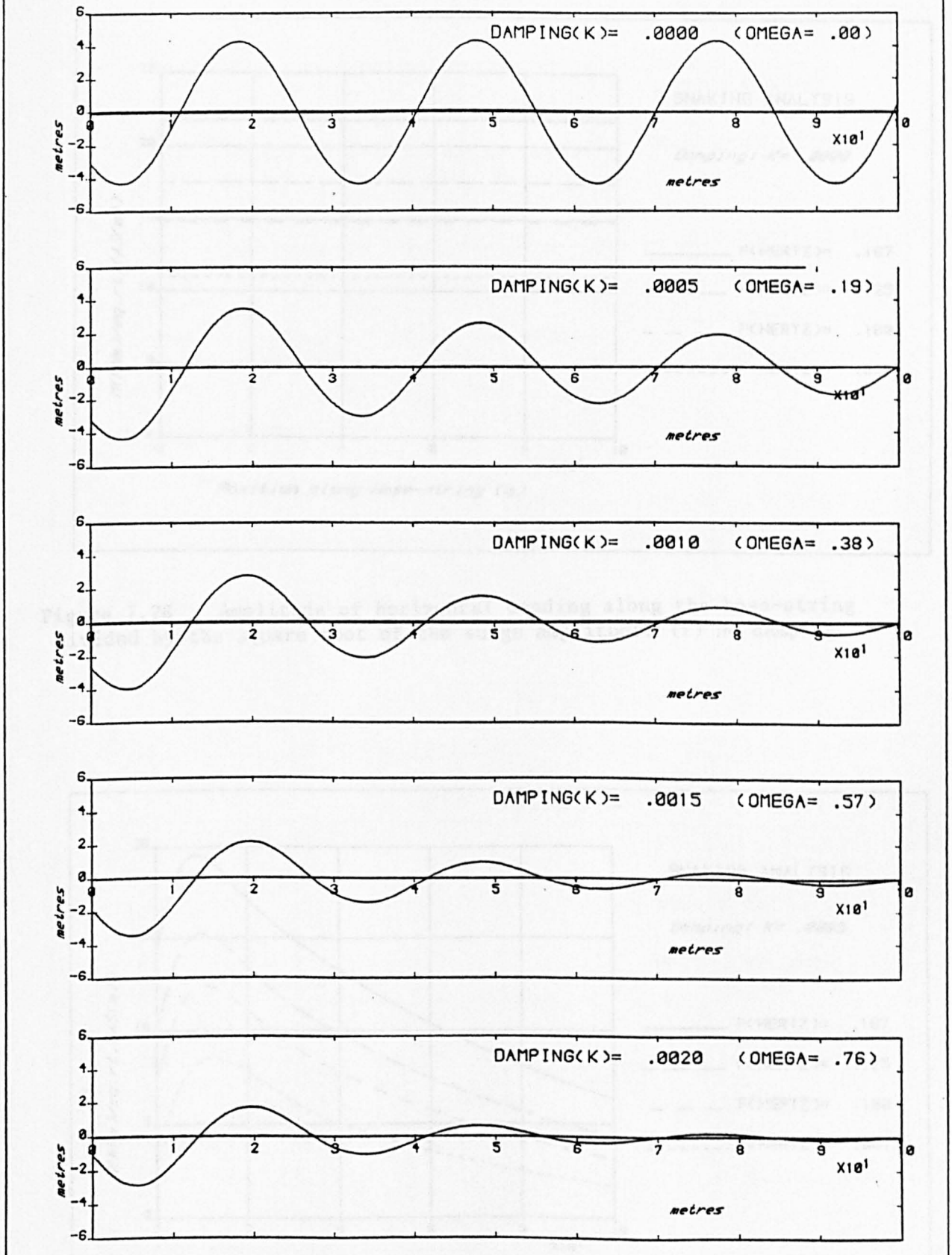

Figure 7.27 The effect of damping on snake shape for surge frequency = 0.25Hz

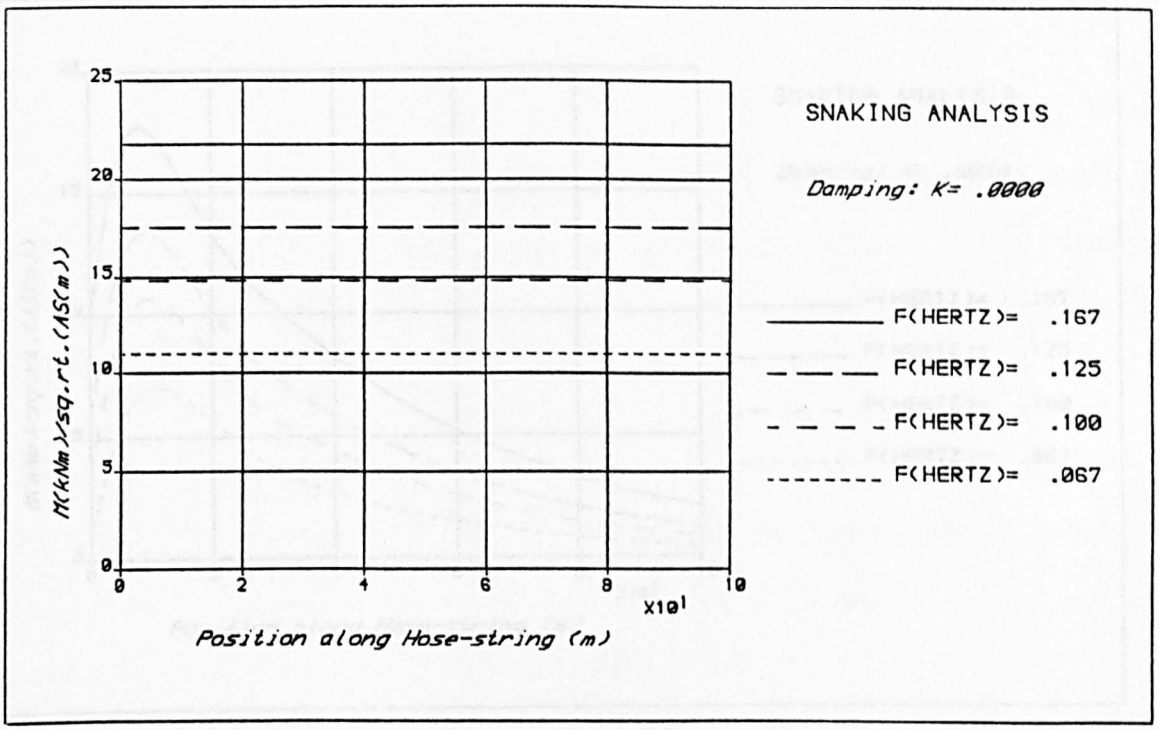

Figure 7.28 Amplitude of horizontal bending along the hose-string divided by the square root of the surge amplitude. (i) No damping

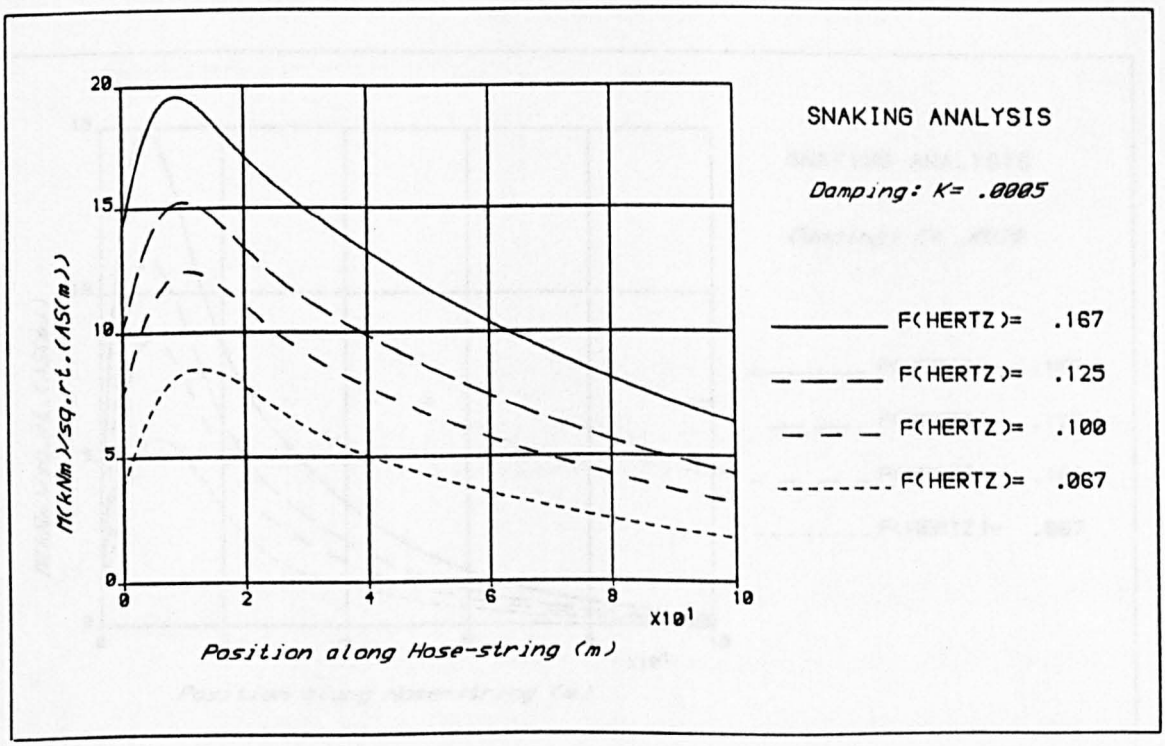

Figure 7.29 Amplitude of horizontal bending along the hose-string divided by the square root of the surge amplitude. (ii) Damping K = 0.0005

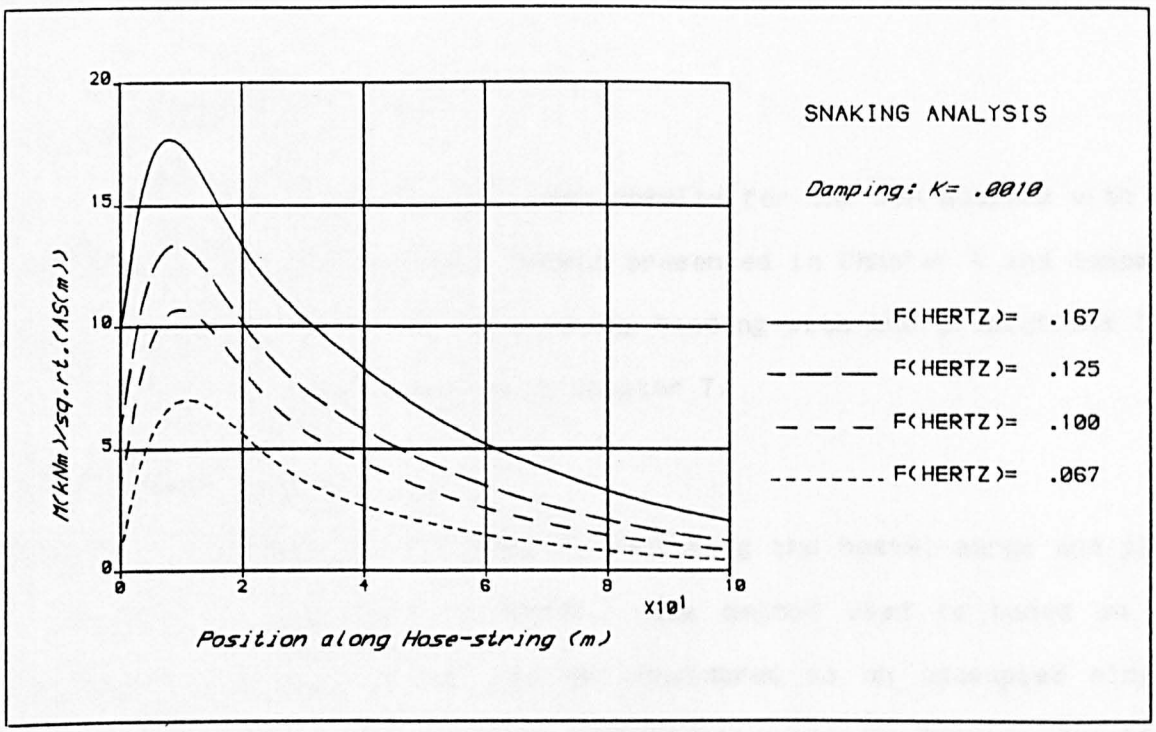

Figure 7.30 Amplitude of horizontal bending along the hose-string divided by the square root of the surge amplitude. (iii) Damping K = 0.001

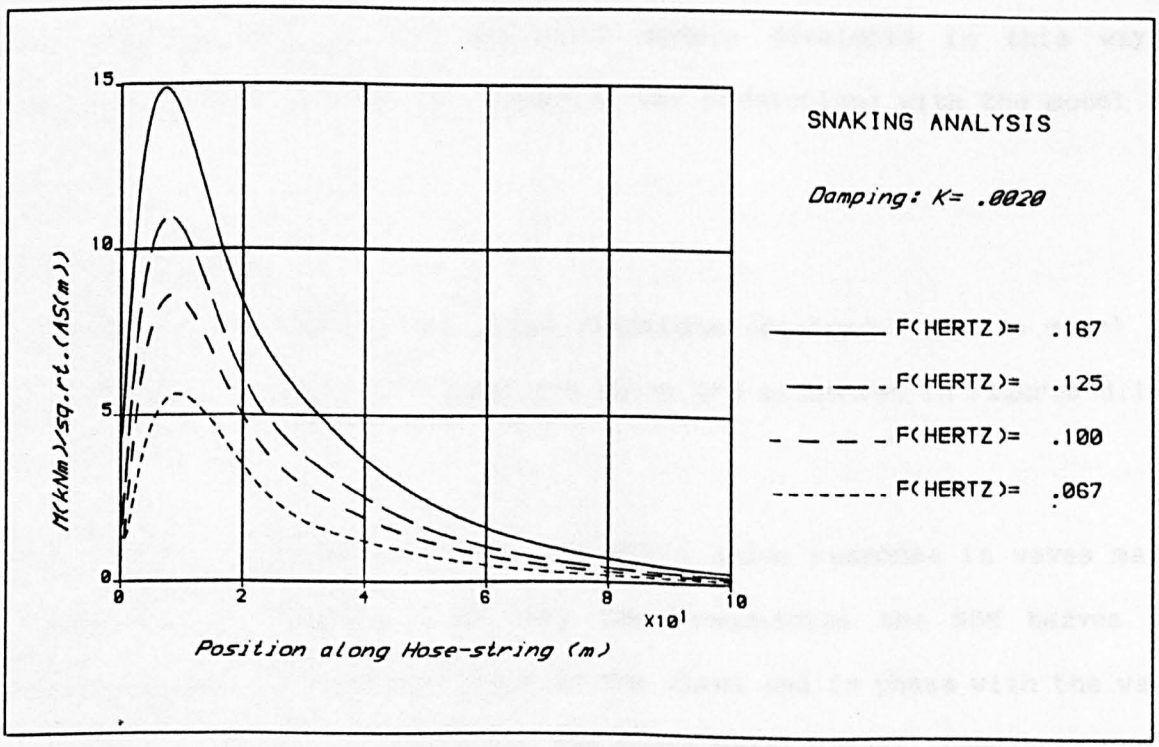

Figure 7.31 Amplitude of horizontal bending along the hose-string divided by the square root of the surge amplitude. (iv) Damping K = 0.002

8. COMPARISON OF RESULTS

This chapter compares the model test results for the SBM motions with the predictions from the empirical models presented in Chapter 6 and compares the model test results for hose-string bending with the predictions from the analytical models presented in Chapter 7.

8.1 SBM Motions

Chapter 6 addressed the problem of predicting the heave, surge and pitch response of a CALM buoy in waves. The method used is based on the assumption that each motion can be considered as an uncoupled single-degree-of-freedom system with a harmonically-varying forcing function. The hydrodynamically-dependent excitation forces and moments are obtained by approximating the buoy as a vertical circular cylinder; the added mass and damping terms for heave and pitch have been established from the heave and pitch free- and forced-motion tests; the surge added mass and damping is obtained from the results for the cylinder approximation of the buoy. The effectiveness of the empirical models developed in this way is assessed in what follows by comparing the predictions with the model test results.

8.1.1 SBM Heave

The SBM heave transfer and phase functions obtained from the model test results and the empirical model for heave are presented in Figures 8.1 and 8.2.

The general characteristics of the SBM's heave response in waves may be summarised as follows: at very low frequencies the SBM heaves with approximately the same amplitude as the waves and in phase with the waves; as the wave frequency approaches the SBM's heave natural frequency the

heave amplitude and phase lag increase; the heave response rapidly approaches a near-zero value for frequencies greater than the heave natural frequency.

The transfer and phase functions obtained from the model tests and the empirical model follow the general characteristics described above but there are two notable differences in detail.

Firstly, the peak in the empirical transfer function occurs at 0.13Hz, corresponding to the heave natural frequency measured in the heave free-motion tests. The peak in the model test results, however, occurs between 0.11Hz and 0.12Hz, its magnitude is less than the empirical result and its energy is more widely spread around the peak value. It is expected that these differences are due mainly to the smoothing process applied to the spectral estimates which results in a spreading of energy around the spectral peak with a consequent lowering of the peak value and a possible shift in its position.

Secondly, for frequencies less than 0.1Hz the heave transfer function obtained from the model tests is up to twice that of the empirical model. The results imply that the empirical model under-estimates the heave excitation force and/or over-estimates the heave added mass at low frequencies. The excitation force has been obtained from the results for the cylinder approximation of the buoy with radius $r = 8.65m$ (Figure 6.5). If the radius taken is that corresponding to the outer radius on the underside of the buoy, i.e. $r = 10.65m$, then the magnitude of the force and response will increase by about 50%, bringing the empirical results closer to the model test results. The heave added mass has been obtained from the heave free-motion tests and, based on the results for a circular

cylinder, has been assumed constant with frequency. It may be, however, that the added mass decreases at the lower frequencies resulting in a greater heave response than predicted by the empirical model with the added mass assumed constant.

8.1.2 SBM Surge

The SBM surge transfer and phase functions obtained from the model tests and the empirical model for surge are presented in Figures 8.3 and 8.4.

It is clear from the very good agreement between the irregular and regular wave test results that the SBM surge transfer function and, to a lesser extent, the surge phase function are well defined by the model test results: the transfer function increases as the frequency decreases; at high frequencies, greater than 0.2Hz, the buoy tends to surge in phase with the wave crest; for frequencies less than 0.2Hz the buoy surge is approximately in phase with the positive slope of the wave. The tendency for the transfer function to level off between 0.1 and 0.05Hz, coupled with the rapid phase shift between these frequencies, indicates that the surge natural frequency of the SBM is between 0.1 and 0.05Hz.

The surge transfer and phase functions predicted by the empirical model are, in general, in good agreement with the model test results. The only notable difference between the model test results and the empirical prediction is that the empirical model does not evaluate the surge natural frequency between 0.1 and 0.05Hz as indicated by no change in phase in the empirical prediction within this frequency range. This arises from an over-estimate of the surge added mass at low frequencies.

It is noted that the surge excitation, added mass and damping terms used in the surge equation of motion have been obtained from the results for

the circular cylinder approximation of the buoy. The above results show that the cylinder approximation is valid for the surge motion of the buoy.

8.1.3 SBM Pitch

The SBM pitch transfer and phase functions obtained from the model test results and the empirical model for pitch are presented in Figures 8.5 and 8.6.

The pitch transfer function for the SBM is well defined by the regular and irregular wave test results. The pitch of the SBM is low, the maximum pitch amplitude occurs at the pitch natural frequency of 0.1Hz and is about 7^{o} per metre wave amplitude. The wide scatter in the phase function estimates reflects the difficulties involved in calculating the phase of very low responses.

The peak in the empirical pitch transfer function and the rapid phase shift at 0.1Hz corresponds to the pitch natural frequency of the SBM. This is as should be since the pitch added mass coefficient of 2.1 used in the empirical model was obtained from the measure of the pitch natural frequency obtained from the pitch free-motion tests.

The pitch response predicted by the empirical model does not agree with the model test results in terms of magnitude. The empirical result is always greater than the model test result; close to the natural frequency the empirical result is of the order of 10 times the model test result. There are two possible reasons for the main part of the error in the response predicted by the empirical model:

i The pitch excitation moment used in the empirical model is that obtained from the results of Garrett (1971) (Figure 6.6(c)) for the

cylinder approximation of the buoy. However Yeung (1981) reports that when the draft to radius ratio (h/r) is about 0.5 (as is the case for the buoy studied here) the pitch excitation moment is small and is zero at certain frequencies, a result that is in apparent disagreement with the results of Garrett (Section 6.3.2). There is some doubt therefore as to the value of the pitch excitation moment. The moment may be over-estimated in the empirical model by using the results of Garrett, resulting in over-estimates of the pitch response.

ii The pitch motion is over-simplified by the empirical model by considering pitch as an uncoupled single-degree-of-freedom system. It is suggested that the large heave and surge responses of the SBM (the amplitudes of the heave and surge responses at 0.1Hz are 3.0m and 2.0m per metre wave amplitude respectively) suppress the pitch response.

Of the empirical models developed in Chapter 6 for the prediction of the SBM's heave, surge and pitch in waves, only the results obtained from the surge model are in good agreement with the model test results. The hydrodynamic forces acting on the buoy in surge are approximately equal to those acting on a circular cylinder with the same radius and draft as the buoy.

In general, the poor results obtained from the heave and pitch empirical models are due to errors in quantifying the hydrodynamic forces acting on the buoy in these modes of motion. The assumption that the motions can be considered uncoupled can also lead to errors in the predicted responses.

The details in shape of a buoy can play an important part in determining

the hydrodynamic forces acting on the buoy. (There is a factor of two difference between the heave added mass coefficient for the buoy studied here and the heave added mass coefficient for the cylinder with the same radius and draft as the buoy.) It is concluded that the shape details should be incorporated in any numerical scheme or model test program carried out to determine the response characteristics of a buoy.

8.2 Hose-String Vertical Bending

8.2.1 Vertical Bending at Positions Far Away From the Buoy

The model test results have shown that the vertical bending of the hose-string at positions greater than about three hose lengths away from the buoy is independent of the buoy motions and depends only on the waves (Figure 5.1). Estimates of the wave-vertical bending transfer function at these positions have been obtained from the model tests as presented in Figure 5.5. The analytical prediction of the transfer function may be obtained for the hose-string used in the model tests from equation (7.41), using values of EI = 150kNm^2, m = 500kg/m and r = 0.5m. The analytical and model test results are presented for comparison in Figure 8.7. A second analytical result, with EI = 100kNm^2, is also presented in Figure 8.7.

The difficulties inherent in the measurement of vertical bending along the hose-string, discussed in Chapter 5, need to be restated here. The accuracy of the measurement of vertical bending depends on the accuracy of the alignment of the bending transducer. At the lower wave frequencies, when the vertical bending is small because of the low wave steepness and hose curvature, and snaking is large because of the greater surge displacements of the buoy, the horizontal bending induced on the hose-string is very much greater than the vertical bending. In such cases,

since the transducer cannot be aligned perfectly it will respond to a component of the large horizontal bending resulting in a recorded bending moment measurement that is greater than the actual vertical bending moment. At high frequencies, when little or no snaking occurs and the waves are steep, vertical bending predominates. In these latter cases an error in the transducer alignment will result in a recorded bending moment that is less than the actual vertical bending moment.

If engineer's bending theory can be applied to the hose-string then the vertical displacement of the hose-string as a function of wave frequency can be inferred from the model test results for the wave-vertical bending transfer function as follows.

The vertical displacement of the hose-string is given by

$$y(x,t) = a\cos(\sigma t - kx) \qquad (8.1)$$

where σ = wave circular frequency

k = wave number = σ^2/g

a = amplitude of hose displacement.

The hose displacement amplitude is a multiple of the wave amplitude, i.e.

$$a = ha_w \qquad (8.2)$$

where h depends on the mass, stiffness and radius of the hose and on the wave frequency (equation 7.37 and Figure 7.6). If engineer's bending theory can be applied then the amplitude of vertical bending $\bar{M}$ divided by the wave amplitude, that is the transfer function for wave-vertical bending, is

$$\bar{M}/a_w = EIk^2h$$

$$= 16.2EIhf^4 \qquad (8.3)$$

where f = wave linear frequency.

Therefore, from a measure of the wave-vertical bending transfer function at f, the value of h at f can be inferred. Equation (8.3) was used to calculate values of h from the model test transfer function estimates presented in Figure 8.7. For each frequency considered two estimates were obtained, corresponding to a "maximum" and "minimum" result at that frequency. The results are tabulated in Table 8.1 together with the theoretical values of h.

Frequency f (Hz)	Transfer Function estimates from model tests $\overline{M}/a_w$ (kNm/m)		h inferred from model test results (equation 8.3)		Theoretical h (Figure 7.6)
	max.	min.	max.	min.	
0.15	2.6	1.3	2.1	1.0	1.05
0.175	3.4	1.9	1.0	0.8	1.075
0.2	4.1	2.6	1.0	0.7	1.09
0.225	5.1	3.4	0.8	0.5	1.10
0.25	6.3	4.4	0.6	0.5	1.09
0.275	7.9	5.4	0.6	0.4	1.03
0.3	9.5	6.5	0.5	0.3	0.9

Table 8.1

A comparison of the values of h = (amplitude of hose-string vertical displacement/amplitude of wave) obtained from the model test results and predicted by the analytical model

Figure 8.7 shows that for wave frequencies less than about 0.175Hz the bending moment measured in the model tests is greater than the theoretical vertical bending with the difference between the results increasing as the frequency decreases. The implication is that the displacement of the hose-string in the model tests is greater than the theoretical displacement at these frequencies. For example, Table 8.1 shows that the implication of the model test results at 0.15Hz is that the hose-string displacement at this frequency may be up to 2.0 times the wave amplitude. It is known that this cannot be the case and that the hose-string more or less follows the wave profile in these relatively low frequency waves as predicted by the theoretical model. Following the arguments relating to the accuracy of vertical bending measurement presented above, it is concluded that the higher than theoretical values of the wave-vertical bending moment transfer function obtained from the model tests at frequencies less than 0.175Hz results from a corruption of the vertical bending measurements by snake-induced horizontal bending of the hose-string. (It is worth noting that at 0.15Hz those transfer function estimates obtained from the model tests which are close to the theoretical value were obtained from measurements recorded at position 10 on the hose-string where the snaking amplitude is small; the model test results which are about twice the theoretical result were obtained from measurements at positions 3 and 4 where the snaking amplitude is large (see Figure 5.5).)

Figure 8.7 shows that for wave frequencies greater than about 0.175Hz the theoretical vertical bending is greater than the bending measured in the model tests. The implication of the bending moment results are seen in Table 8.1: the theoretical model predicts that the hose-string more or less follows the wave profile (h approximately equal to 1.0) whereas the

model test results imply that the hose vertical displacement amplitude becomes increasingly less than the wave amplitude as the wave frequency increases.

It was stated above that an error in the alignment of the bending transducers leads to bending moment measurements that are less than the actual vertical bending moment at high frequencies. While the model test results in Figure 8.7 are affected by some error in transducer alignment (it is impossible to achieve perfect alignment) this fact alone cannot account for the factor of two difference between the theoretical and model test results at the high frequencies. It is concluded that the analytical model over-estimates the magnitude of the vertical bending at the higher frequencies. There are a number of reasons which may contribute to this being the case, including:

1. The analytical model takes no account of axial load along the hose-string. The axial loads caused by the surge motion of the buoy will reduce the vertical displacement of the hose-string. The effects will be greater as the curvature of the hose increases with increasing wave frequency.
2. The complex nature of the hose construction, comprising rubber built onto a wire helix, may cause the hose bending stiffness to be dynamically dependent. The bending stiffness may decrease with increasing curvature resulting in lower bending moments than if the stiffness remained constant at $150kNm^2$. The result from the analytical model with EI = $100kNm^2$ has been presented in Figure 8.7 to illustrate the effect of lower bending stiffness.

8.2.2 Vertical Bending at the Hose-Buoy Manifold

The transfer function between incident waves and the vertical bending at the hose-buoy manifold has been obtained from the irregular and regular wave model test results. The dynamic vertical bending at the buoy depends on the buoy's motions. The discussion of the results has explained that the separate effects of heave, surge and pitch on the vertical bending cannot be separated from the test results.

The analytical model developed in Chapter 7 predicts the vertical bending at the hose-buoy manifold for known buoy heave and wave conditions. The real situation has therefore been simplified by assuming that heave is the main buoy motion affecting the vertical bending at the buoy. The usefulness of the model is tested in what follows by comparing its results with those of the model tests.

If the heave amplitude and phase of the buoy in waves of amplitude a_w and frequency σ are a_h and ϕ respectively, then the amplitude of the dynamic vertical bending at the buoy, predicted by the analytical model, is (equation 7.47)

$$\bar{M} = EI(M_1^2 + M_2^2)^{1/2} \qquad (8.4)$$

where

$$M_1 = 2R^2(a_h\cos\phi - ha_w) + ha_w(\sigma^2/g)^2$$

$$M_2 = -2R^2[a_h\sin\phi + ha_w\sigma^2/(gR)]$$

$$4R^4 = \pi r^2\rho g/2rEI - \sigma^2/c^2$$

and h is the dynamic amplification factor given by equation (7.37).

The first 5m of the first-off-the-buoy hose used in the model tests has radius 0.35m. The bending stiffness and mass per unit length of the first-off-the-buoy hose used in the model tests are the same as for the rest of the hose-string. For the analytical results presented in what follows therefore r = 0.35m, EI = 150kNm^2 and m = 500kg/m. (In practice the first-off-the-buoy hose is very much stiffer than the other hoses in the string.)

The values of the heave amplitude and phase of the buoy to be used in the analytical model are obtained from the heave transfer and phase functions established from the model tests (Figures 8.1 and 8.2). The heave data is presented in the first three columns of Table 8.2. There is some doubt as to the heave amplitude and phase at 0.15Hz, the values taken being 1.5 and -50° respectively. The phase value for frequencies greater than 0.15Hz is taken as zero, the actual value not being important since the heave amplitude is close to zero.

With the heave data obtained from the model tests as input, the value of $\bar{M}$ per unit wave amplitude has been obtained for a range of wave frequencies using equation (8.4). The results are tabulated in the fourth column of Table 8.2 and are presented in Figure 8.8 together with the model test results.

The major difficulty in applying the analytical model at the buoy is that the hose must remain partially submerged for the linear load approximation inherent in the analysis to be valid. When the hose becomes totally exposed or submerged, which can occur when the heave amplitude is not equal to the wave amplitude and/or the heave is out of phase with the waves, the linear load approximation over-estimates the loading as has

Wave Frequency (Hz)	Buoy Heave Data a_h/a_w	ϕ^o	$\bar{M}$(kNm/m) eq(8.4)	ψ eq(8.6)	$\bar{M}_H$(kNm/m) eq(8.5)	α eq(8.13)	$\bar{M}_L$(kNm/m) eq(8.9)
0.05	1.76	21	25.8	0.9	25.6	1.6	16.0
0.057	1.98	16	30.2	1.1	30.1	2.0	17.3
0.065	2.21	11	35.1	1.24	35.3	2.5	18.7
0.072	2.4	5.5	39.6	1.4	40.2	3.0	20.0
0.08	2.6	0	44.4	1.6	45.5	3.6	21.3
0.09	2.8	-14.5	50.4	1.8	52.6	4.3	22.9
0.10	3.0	- 29	59.8	2.2	63.4	5.4	25.1
0.112	3.15	- 42	66.0	2.5	71.0	6.1	26.6
0.115	3.3	- 55	75.3	2.8	80.8	7.1	28.4
0.122	3.1	- 67	74.9	2.9	81.4	7.2	28.5
0.13	2.9	- 80	75.5	2.9	82.5	7.3	28.5
0.135	2.5	- 71	60.2	2.4	67.4	5.8	25.9
0.14	2.1	- 63	45.9	1.9	53.3	4.35	23.0
0.145	1.8	-56.5	35.2	1.5	42.7	3.3	20.6
0.15	1.5	- 50	25.1	1.2	32.7	1.4	15.4
0.157	0.83	- 25	8.1	0.43	12.2	0.23	11.0
0.165	0.16	0	24.8	0.8	23.8	1.2	14.9
0.172	0.13	0	25.5	0.87	24.7	1.5	15.7
0.18	0.1	0	26.2	0.9	25.6	1.6	15.9
0.19	0.09	0	26.3	0.9	25.9	1.6	16.0
0.2	0.08	0	26.3	0.92	26.2	1.6	16.1
0.205	0.06	0	26.4	0.93	26.6	1.7	16.3
0.21	0.05	0	26.6	0.95	27.0	1.7	16.4
0.217	0.02	0	26.8	0.97	27.7	1.8	16.6
0.225	0.0	0	26.9	1.0	28.4	1.9	16.8
0.25	0.0	0	24.7	1.0	28.4	1.9	16.8

Hose data: r = 0.35m ; EI = 150kNm^2 ; m = 500kg/m

Table 8.2

SBM heave data from model test results and corresponding predicted estimates of vertical bending at the hose-buoy manifold

been described in Section 7.2.2. For such cases the effect of the higher loading on the resulting bending moments must be quantified in some way. The approach used here is to use a second linear load approximation to the loading which under-estimates the loading when the hose does not remain partially submerged. The end result is two values of bending moment between which the actual value must lie.

An approximation to the analytical result given by equation (8.4) has been given in Chapter 7 (equation 7.48) and is

$$\bar{M}_H = a_w s^{1/2} EI^{1/2} \psi \qquad (8.5)$$

where $s = \pi r^2 \rho g / 2r$ is the slope of the linear load approximation and ψ depends on the heave amplitude and phase (Figure 7.10) and is given by

$$\psi = [(a_h/a_w)^2 + 1.0 - 2(a_h/a_w)\cos\phi]^{1/2} \qquad (8.6)$$

Subscript 'H' in equation (8.5) refers to the over-estimate of the bending moment. The values of ψ for the heave data in Table 8.2 and the corresponding values of $\bar{M}_H$ obtained from equation (8.5) are tabulated in columns five and six of Table 8.2. Note that the difference between the values of $\bar{M}$ obtained using equations (8.4) and (8.5) is generally less than 10%.

Consider the case when the wave-buoy relative displacement is such that the base of the hose clears the water surface by αr (α positive) at the maximum of its upward movement and lies $(2+\alpha)r$ below the water surface at the maximum of its downward movement as illustrated in Figure 8.9. The actual vertical loading as the hose moves between these two limits and two linear approximations to the loading are illustrated in Figure 8.10. The solid line in Figure 8.10 represents the linear load approximation which

over-estimates the loading (approximation #1); the chained line represents a second linear load approximation which under-estimates the loading (approximation #2). The slope of approximation #2 is

$$s_L = s/(1+\alpha) \tag{8.7}$$

where subscript 'L' refers to an under-estimate.

Following equation (8.5) the under-estimate of the bending moment is

$$\bar{M}_L = a_w[s/(1+\alpha)]^{1/2}EI^{1/2}\psi \tag{8.8}$$

or

$$\bar{M}_L = (1+\alpha)^{-1/2}\bar{M}_H \tag{8.9}$$

For the buoy with heave amplitude a_h and phase ϕ in waves of amplitude a_w and frequency σ the value of α is obtained as follows. The distance between the hose axis and the water level at any instant in time is

$$\xi = |a_h\cos(\sigma t+\phi) - a_w\cos\sigma t| \tag{8.10}$$

ξ is a maximum when $d\xi/dt = 0$, i.e. when

$$\sigma t = \gamma = \tan^{-1}[\sin\phi/(a_w/a_h - \cos\phi)] \tag{8.11}$$

The maximum value of ξ is then

$$\xi_{max} = |a_h\cos(\gamma+\phi) - a_w\cos\gamma| \tag{8.12}$$

If $\xi_{max} \leq r$, where r is the hose radius, then the hose remains partially submerged and $\alpha = 0$; if $\xi_{max} > r$ then α is given by

$$\alpha = (\xi_{max}-r)/r \quad , \text{ for } \xi_{max} > r \tag{8.13}$$

The values of α for the heave data in Table 8.2 and the corresponding

values of $\bar{M}_L$ obtained using equation (8.9) are tabulated in columns seven and eight of Table 8.2. The upper estimates $\bar{M}_H$ and the lower estimates $\bar{M}_L$ of the bending moment amplitude at the buoy are plotted with the model test results in Figure 8.11.

The analytical and model test results are seen to be in good agreement in Figure 8.11 in the sense that the model test results lie between the upper and lower limits obtained from the analytical model.

For frequencies greater than about 0.15Hz the amplitude of the hose vertical bending at the buoy remains fairly constant. This is due to the buoy remaining almost still in high frequency waves.

The dynamic vertical bending at the buoy is greatest at 0.13Hz, the heave natural frequency of the SBM. At this frequency the heave amplitude and phase is a maximum resulting in the value of ψ being a maximum. The analytical result is least certain at this frequency in that the ratio of the upper and lower estimates is greatest.

As the wave frequency tends to very low values the buoy tends to move in phase with the waves and with the same amplitude. The upper and lower estimates will tend to converge as the hose becomes less submerged and exposed resulting in a decrease in the value of α. In the limit, when $a_h = a_w$ and $\phi = 0$, both estimates will be zero since $\psi = 0$ as illustrated in Figure 7.10.

8.2.3 General Conclusion for Vertical Bending

There is general good agreement between the model test results and the predictions of the analytical model for vertical bending at the hose-buoy manifold. The results indicate that for the buoy with low pitch response, the vertical bending at the buoy can be considered as predominantly heave-

dependent and the surge motions can be neglected. The vertical bending at the buoy predicted by the analytical model detailed in Chapter 7 will yield conservative estimates of the actual vertical bending; this result follows from the linear load approximation inherent in the analysis. For design purposes, the amplitude of the dynamic vertical bending $\bar{M}$ at the buoy, for buoy heave amplitude a_h and phase ϕ in waves of amplitude a_w, will lie between the limits given by

$$(1+\alpha)^{-1/2} < \bar{M}/[a_w(s.EI)^{1/2}\psi] < 1.0 \qquad (8.14)$$

where $s = \pi r^2 \rho g/2r$

α is the maximum number of hose radii (Figure 8.9) that the hose at the buoy is submerged and clears the water surface throughout the wave cycle and depends on a_w, a_h and ϕ as given by equations (8.11) to (8.13)

ψ depends on the heave response as given by equation (8.6) (and illustrated in Figure 7.10).

Agreement between the model test results and the predictions of the analytical model for vertical bending at positions away from the buoy is not good. The differences between the results are due to difficulties inherent in the measurement of vertical bending away from the buoy as well as limitations inherent in the analytical model. For design purposes, conservative estimates of the amplitude of the dynamic vertical bending at these positions in waves of amplitude a_w and circular frequency σ, are obtained from the simple analytical result

$$\bar{M} = a_w EI(\sigma^2/g)^2 h \qquad (8.15)$$

where h is given by equation (7.37) (and Figure 7.6) and is approximately

equal to 1.0. The estimate obtained at very high frequencies, i.e. at frequencies greater than about 0.25Hz, using equation (8.15) may be as high as twice the actual value at these frequencies.

8.3 Snaking and Horizontal Bending

8.3.1 Hydrodynamic Added Mass for the Snaking Hose-String

The snaking characteristics of the hose-string for a given surge frequency and amplitude depend on the stiffness and mass per unit length of the hose and on the hydrodynamic forces induced on the hose as it bends in the water surface. The component of the hydrodynamic force that is in phase with the velocity of the hose is the damping force; the component in phase with the acceleration of the hose is the added mass force. Account has been taken of the hydrodynamic damping in the governing equation of motion for snaking by the $Q\partial z/\partial t$ term in equation (7.61). The hydrodynamic added mass is added to the mass term in the equation of motion to give the total inertia term $m\partial^2 z/\partial t^2$ in equation (7.61). The governing equation of motion for snaking is more precisely given as

$$[EI]\partial^4 z/\partial x^4 + [Q]\partial z/\partial t + (1+C_a)m\partial^2 z/\partial t^2 = 0 \qquad (8.16)$$

or

$$\partial^4 z/\partial x^4 + [K]\partial z/\partial t + [1/c^2]\partial^2 z/\partial t^2 = 0 \qquad (8.17)$$

where C_a is the coefficient of added mass

$K = Q/EI$

$c^2 = EI/[(1+C_a)m]$.

However, because added mass must not be included in the boundary condition, introducing the effect of added mass to the snaking solution is more complicated than a direct substitution of $c^2 = EI/m$ by $c^2 =$

$EI/(1+C_a)m$. The boundary condition remains (equation 7.59)

$$EI\partial/\partial x(\partial^3 z/\partial x^3 . \partial z/\partial x) = m\partial^2 u/\partial t^2 \qquad (8.18)$$

where $u = a_s(1 - \cos\sigma t)$

a_s is the surge amplitude.

Using $c^2 = EI/(1+C_a)m$ the boundary condition may be written as

$$\partial/\partial x(\partial^3 z/\partial x^3 . \partial z/\partial x) = \frac{a_s}{(1+C_a)}(\sigma^2/c^2)\cos\sigma t \qquad (8.19)$$

Equation (8.19) is the same as equation (7.65) except that a_s is replaced by $a_s/(1+C_a)$. Therefore, introducing the added mass effects to the snaking solution given by equation (7.76) requires the value of c in equation (7.76) to be given by $c^2 = EI/(1+C_a)m$ and a_s to be replaced by $a_s/(1+C_a)$.

Vugts (1968) carried out experiments to measure the hydrodynamic added mass and damping forces on floating horizontal cylinders moving in the water surface. His results include a graph of the sway added mass coefficient for a semi-immersed circular cylinder against the non-dimensional frequency parameter $\chi = \omega(2r/2g)^{1/2}$, where ω is the circular frequency of the sway motion and r is the cylinder radius. The results show that for $\chi < 0.7$ the added mass coefficient is always greater than 1.0 and has a maximum value of 1.5. For the cylinder therefore with r = 0.5m, corresponding to the radius of the hose, Vugts' results imply that C_a is always greater than 1.0 for sway frequencies less than 0.5Hz.

Based on the results of Vugts (1968) and on physical reasoning (e.g. the hose radius is discontinuous due to the spaces between the floatation pieces along its length) the added mass coefficient for the hose-string

snaking in the water surface is considered to have some value between 1.0 and 2.0. Fortunately, the precise value of the added mass coefficient between 1.0 and 2.0 is not critical in determining the snaking characteristics, as the following analysis shows.

The zero-damping wavelength predicted by the analytical model is given by

$$\lambda_s|_{K=0} = 2\pi/(\sigma/2c)^{1/2} \qquad (8.20)$$

where $\sigma = 2\pi f$ = surge circular frequency

$c^2 = EI/[(1+C_a)m]$.

The dependence of the snake wavelength on the added mass coefficient is, therefore,

$$\lambda_s|_{K=0} \propto (1+C_a)^{-1/4} \qquad (8.21)$$

If, therefore, the snake wavelength estimate is $\bar{\lambda}_s$ corresponding to an added mass coefficient estimate $C_a = 1.5$, the actual snake wavelength will lie between $1.056\bar{\lambda}_s$ (if $C_a = 1.0$) and $0.99\bar{\lambda}_s$ (if $C_a = 2.0$); i.e. the possible error in the wavelength estimate $\bar{\lambda}$ is +5.6%, -1.0%.

Furthermore, by substituting for c and a_s in equation (7.79) it may be seen that

$$M \propto (1 + C_a)^{-1/8} \qquad (8.22)$$

There is therefore a weak dependence of bending moment on the added mass value: the possible error in the bending moment estimate using $C_a = 1.5$ is approximately ±3%.

In the context of this study, the possible errors in wavelength and bending moment associated with an added mass value $C_a = 1.5$ are considered

small.

8.3.2 Comparison of the Measured and Predicted General Snaking Characteristics

The general characteristics of the snaking behaviour predicted by the analytical model have been observed and measured in the model tests. These are:

i the snake frequency is half the surge frequency;

ii the snake amplitude increases as the surge amplitude increases;

iii the snake wavelength decreases as the surge (and snake) frequency increases; for equivalent surge amplitudes therefore, horizontal bending increases as the surge frequency increases;

iv the snake amplitude decays as it travels along the hose-string.

The analytical model developed for snaking assumes that the SBM surges with a single frequency value, resulting in a snake of single frequency being generated. The model cannot therefore predict the excitation of natural modes of vibration caused by the forcing having an associated frequency bandwidth. Accordingly the model cannot predict the beating phenomenon measured in the regular wave tests with f = 0.1Hz and the effects of the excited natural vibration modes on the decay of the bending moments along the hose-string (Section 5.2.1).

The results obtained in the regular wave tests with f = 0.125Hz indicate that no natural vibration modes are excited in these tests and the snaking produced has a single frequency value which depends on the frequency of the SBM's surge motion. Accordingly, the results from these tests are suitable for detailed comparison with the predictions of the analytical model.

8.3.3 Model Test Results and Analytical Predictions of Snaking in Regular Waves With f = 0.125Hz

(The equivalent prototype values of the bending stiffness and mass per unit length of the hose-string used in the model tests are EI = 150kNm^2 and m = 500kg/m respectively.)

For a surge frequency of 0.125Hz, the zero-damping snake wavelength is obtained using equation (8.18) and is 33.2m. The wavelength is calculated with C_a = 1.5 so the possible error in the wavelength estimate is (+1.8, -0.3)m. The snake wavelength obtained from the model tests is 32(±2)m. The model test result and analytical prediction are in good agreement indicating that the added mass coefficient is greater than 1.0 as expected (with C_a = 0.0 the wavelength is 41.7m). A more accurate prediction of the wavelength can be made once some estimate of the damping is known.

Figure 8.12 presents the analytical model prediction of horizontal bending moment along the hose-string for a surge frequency f = 0.125Hz and five different values of damping. The model test results are also shown.

There is generally good agreement between the model test results and the analytical prediction when the damping K is between 0.001 and 0.0015. The damping appropriate to the surge frequency of 0.125Hz is therefore of the order K = 0.001 to 0.0015.

8.3.4 Comparison of Measured and Predicted Snake Wavelengths

Based on the results for f = 0.125Hz, the snake wavelength for any surge frequency can now be calculated using C_a = 1.5 and K = 0.0012 (equation 7.87). (It is appreciated that both added mass and damping are frequency-dependent but since the precise value of C_a between 1.0 and 2.0 is not critical in determining wavelength and since damping has little effect on the wavelength the values C_a = 1.5 and K = 0.0012 can be used as first

estimates.) The analytical predictions of snake wavelength for surge frequencies f = 0.06, 0.09 and 0.125Hz are compared to the model test results in Table 8.3.

Surge Frequency (Hz)	Snake Wavelength From Model Tests (m)	Snake Wavelength From Analytical Model (m) C_a = 1.5, K = 0.0012
0.06	43 (±2)	46 (+2.5, -0.4)
0.09	37 (±2)	38 (+2.1, -0.4)
0.125	32 (±2)	33 (+1.8, -0.3)

Table 8.3

Comparison of snake wavelengths obtained from the model tests and predicted by the analytical model

Table 8.4 shows that there is general good agreement between the snake wavelengths obtained from the model tests and predicted by the analytical model.

8.3.5 Comparison of Measured and Predicted Values of Maximum Horizontal Bending Moment

It remains to assess the ability of the analytical model to predict the snake amplitude of the hose-string. This is done by comparing the analytical predictions of bending moments along the hose-string with the measured bending moments.

Bending moments along the hose-string have been measured in regular wave tests with f = 0.125Hz and f = 0.1Hz and in the irregular seas SEA2 and SEA3. The comparison between the measured and predicted bending along the hose-string with f = 0.125Hz has already been carried out (Figure 8.12). A similar comparison cannot be carried out for the regular wave test with

f = 0.1Hz or for the irregular wave tests, mainly because natural modes of vibration are excited in the model tests which cannot be predicted by the analytical model. However, comparisons can be made between the measured and predicted values of maximum bending since maximum bending depends on the amplitude and frequency of the SBM's surge and is independent of any excited natural vibration of the hose-string.

The maximum bending moments measured along the hose-string in the model tests occur at the end of the first-off-the-buoy hose. Table 8.4 presents the maximum bending moment M and maximum surge displacement a_s measured in each of the regular wave tests with f = 0.125Hz and f = 0.1Hz and in the irregular seas SEA2 and SEA3. The frequency signature for the surge response in the irregular seas SEA2 and SEA3 is given by the surge peak spectral frequency and is 0.11Hz and 0.07Hz respectively (Figure 4.7).

Figure 8.13 presents the analytical prediction of horizontal bending along the hose-string for surge frequencies 0.07, 0.1, 0.11 and 0.125Hz. The damping used is K = 0.0012 and the coefficient of added mass is $C_a = 1.5$. It is seen that the model predicts that maximum bending occurs at approximately x = 10m, i.e. at the end of the first-off-the-buoy hose. The values of $M/(a_s)^{1/2}$ are presented in Table 8.4 for comparison with the model test results.

Table 8.4 shows that the maximum bending predicted by the analytical model is always less than that measured in the model tests. For frequencies 0.125, 0.11 and 0.1Hz the analytical model predictions are between 20% and 30% less than the measured values. The prediction for f = 0.07Hz is 50% less than the measured value in SEA3; this very large difference is likely to be due in part to the maximum bending in SEA3 occurring when the

Regular Wave Test Results				Analytical Prediction
Surge freq. f (Hz)	Max. Surge a_s (m)	Max. Bend. M (kNm)	$M/(a_s)^{1/2}$	$C_a = 1.5$, $K = 0.0012$ $M/(a_s)^{1/2}$
0.125	0.37	11.6	19.1	13.5
0.1	0.5	10.5	14.8	11.0
Irregular Wave Test Results				
0.11 (SEA2)	2.44	26.0	16.6	12.1
0.07 (SEA3)	2.25	21.7	14.5	8.0

Table 8.4

Comparison of maximum horizontal bending moments measured in the model tests and predicted by the analytical model; maximum bending occurs at the end of the first-off-the-buoy hose

surge frequency is greater than the surge peak spectral frequency of 0.07Hz.

Concentrating on the results obtained for frequencies 0.125, 0.11 and 0.1Hz, it may be stated that the analytical model consistently predicts maximum bending moment values that are about 30% less than the actual values. This effectively means that the amplitude of the snake predicted by the model is 30% less than the actual amplitude. It is thought that this is due to the limited definition of the boundary condition at the buoy end of the hose-string in the analytical model: the boundary condition used specifies only that the end moves longitudinally with amplitude equal to the surge amplitude of the buoy; the boundary condition cannot specify whether the hose is built-into the buoy, pinned to the buoy or whether the buoy acts as a rotating or sliding end. These details in the end condition can play an important role in determining the amplitude of the lateral vibrations of the hose-string.

To quantify the role played by the end condition details in determining the amplitude of the vibration, a useful analogy may be made with a beam which is forced to vibrate by a sinusoidal lateral motion at one end, as shown in Figure 8.14. In Figure 8.14(a) the beam is built into the moving end and the amplitude of vibration at x along the beam is a_{bx}. In Figure 8.14(b) the beam is pinned to the moving end and the amplitude of the vibration at x is a_{px}. It is known that the ratio a_{bx}/a_{px} is $\sqrt{2}$. Therefore, the difference in detail at the end has resulted in a $\sqrt{2}$ factor of difference between the amplitudes of the vibrations (and, hence, bending moments) induced on the beam. It is clear that the limited definition of the boundary condition in the analytical model for snaking can lead to differences between the predicted and actual values of snake amplitude and horizontal bending. Based on the above analogy, it is concluded that the difference involved may be of the order of 40% and this may account for the difference between the analytical predictions and model test measurements presented in Table 8.4.

The general conclusion from the comparison between the snaking properties and horizontal bending predicted by the analytical model and measured in the model tests is that the analytical model accurately predicts the snake frequency and wavelength but under-estimates the snake amplitude and, hence, the bending amplitude by about 30%. The difference between the actual and predicted values of bending is thought to be due to the limited definition of the boundary condition in the snaking model.

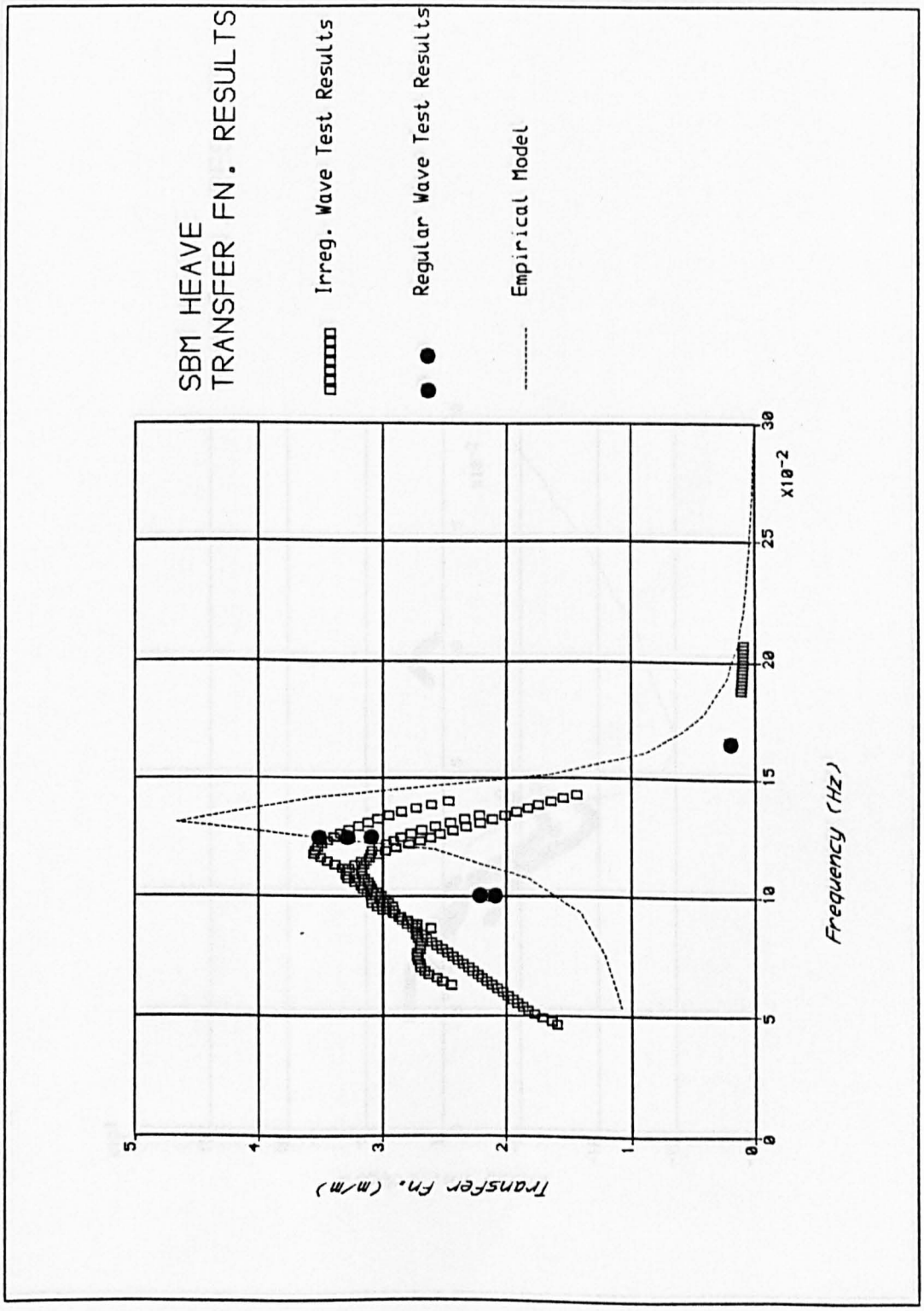

Figure 8.1 SBM heave transfer function from model tests and empirical model

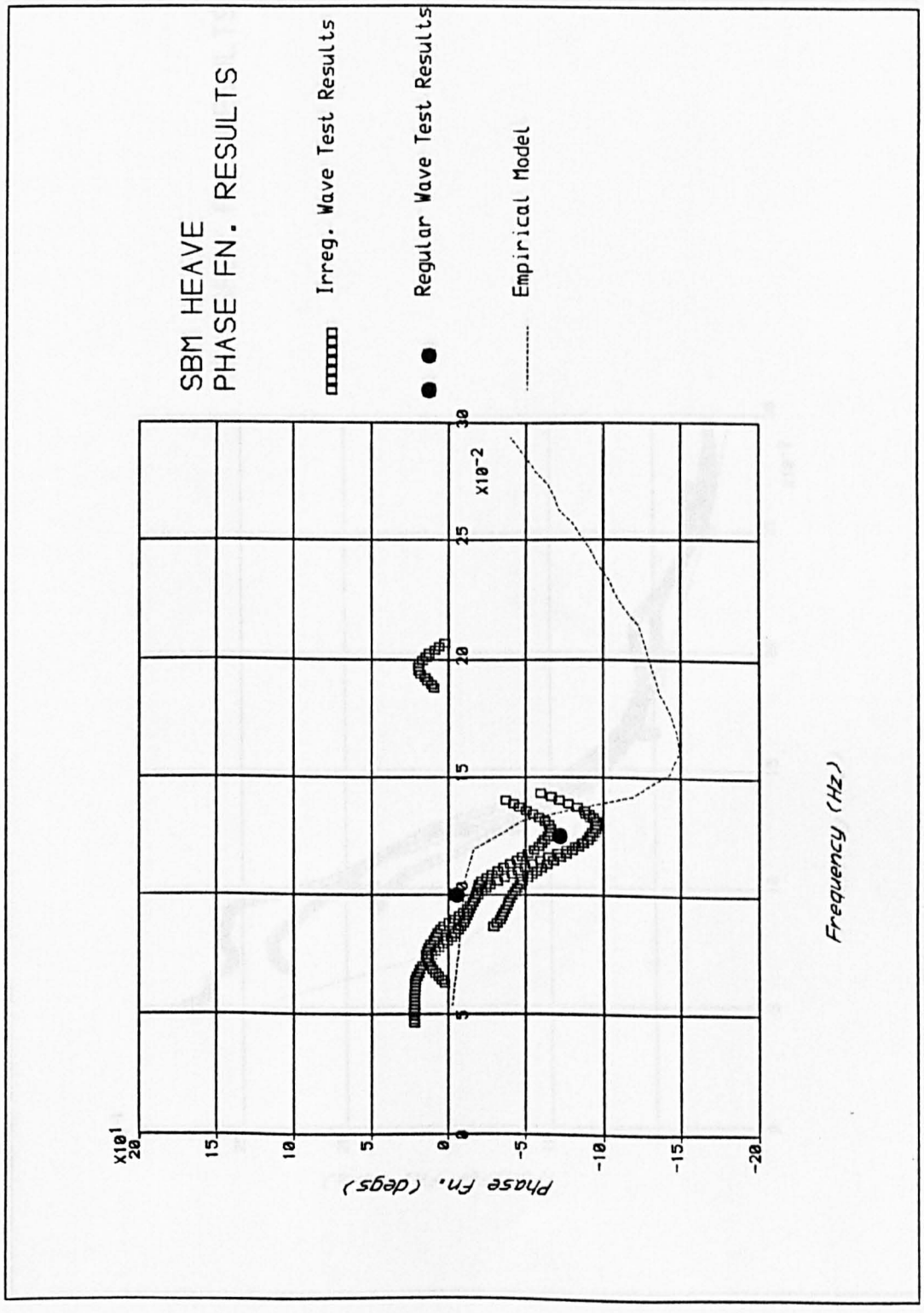

Figure 8.2 SBM heave phase function from model tests and empirical model

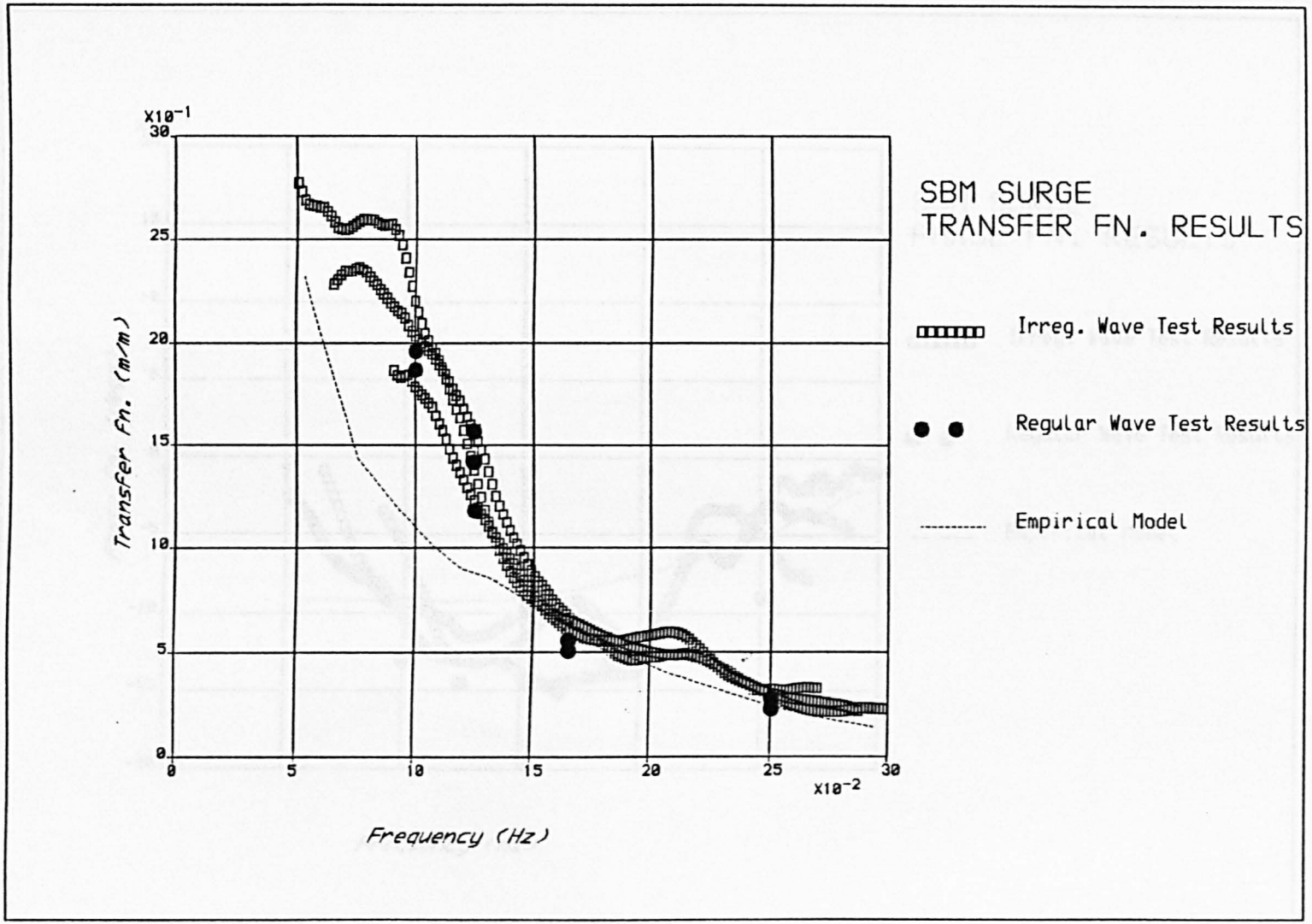

Figure 8.3 SBM surge transfer function from model tests and empirical model

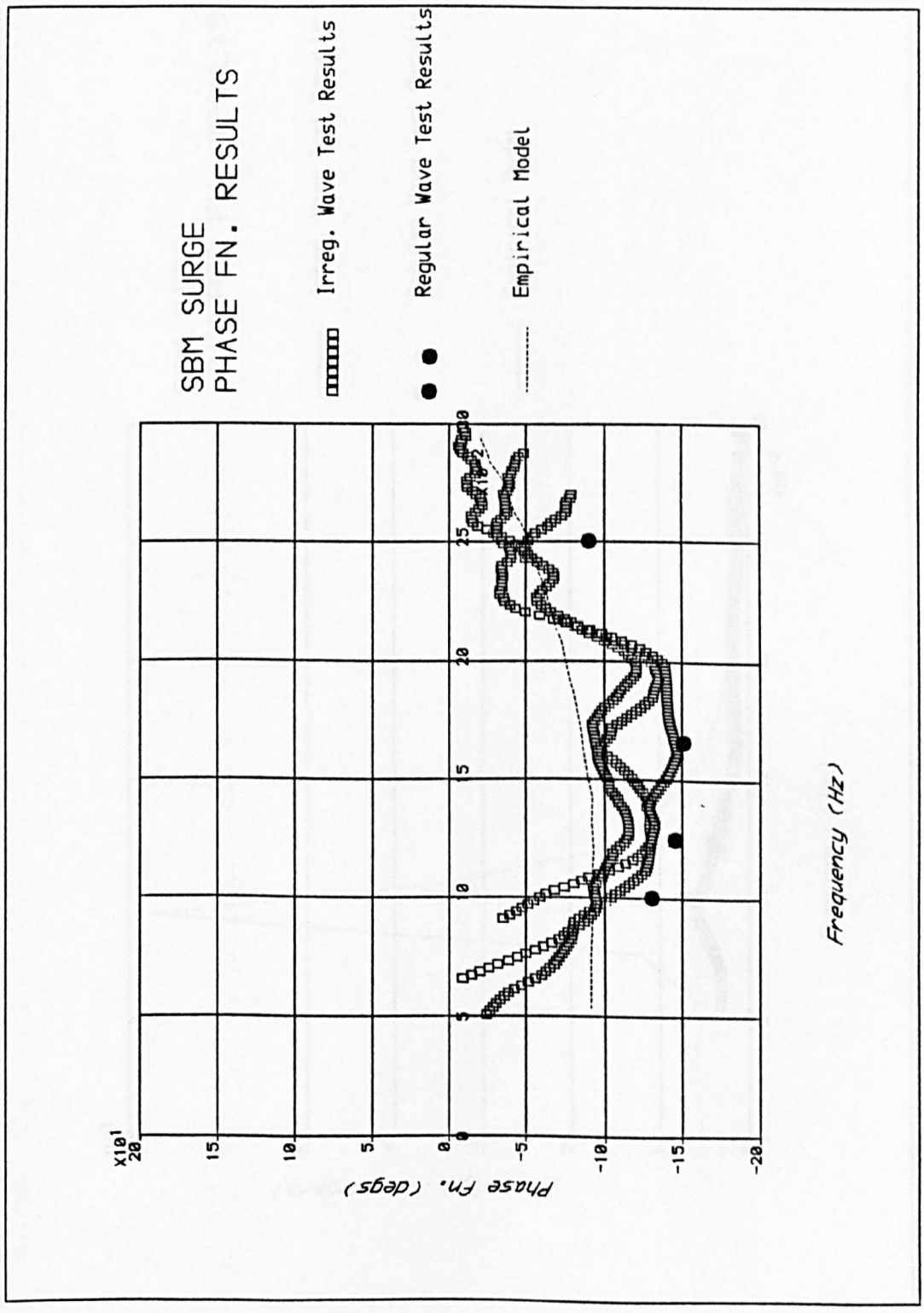

Figure 8.4 SBM surge phase function from model tests and empirical model

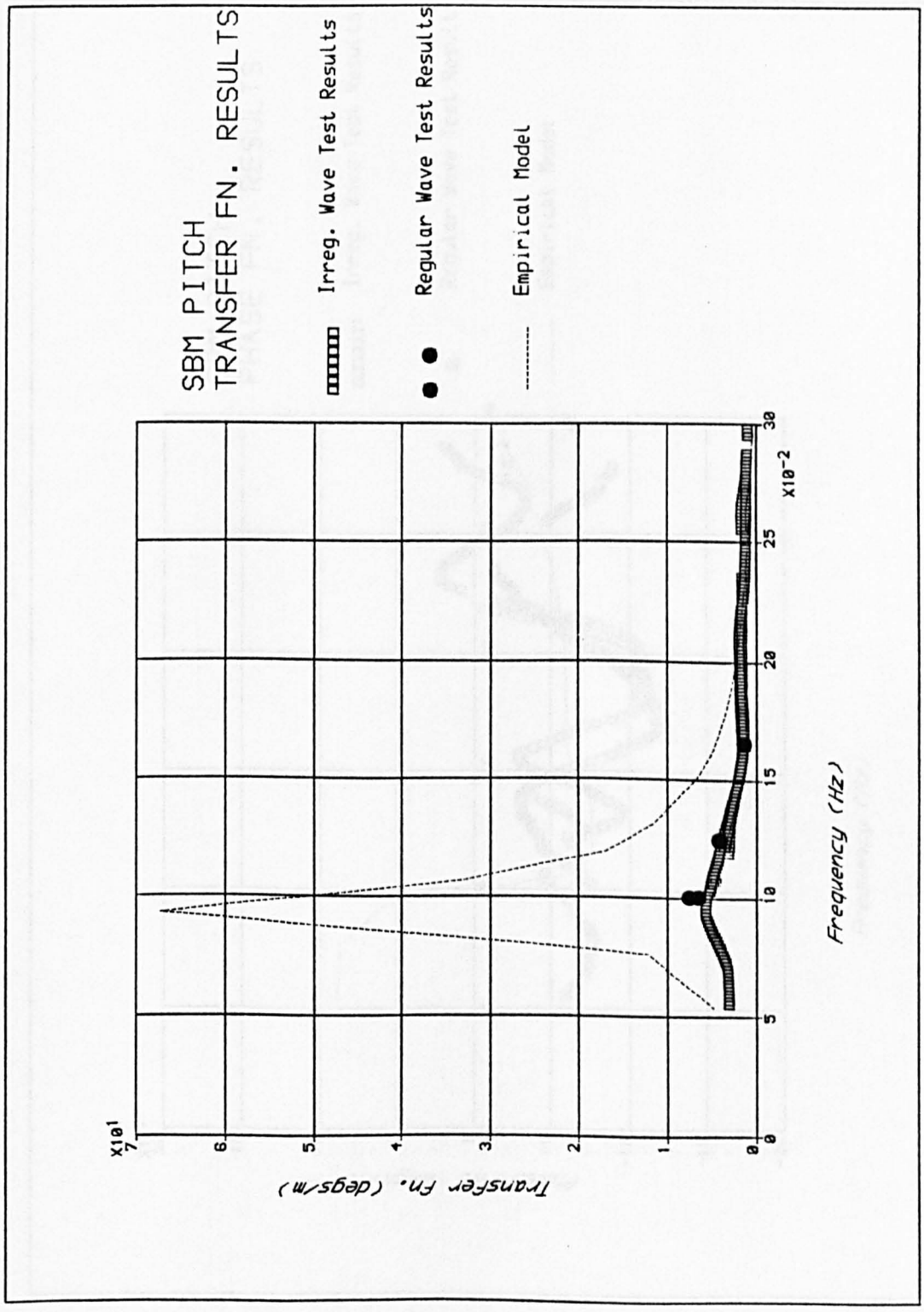

Figure 8.5 SBM pitch transfer function from model tests and empirical model

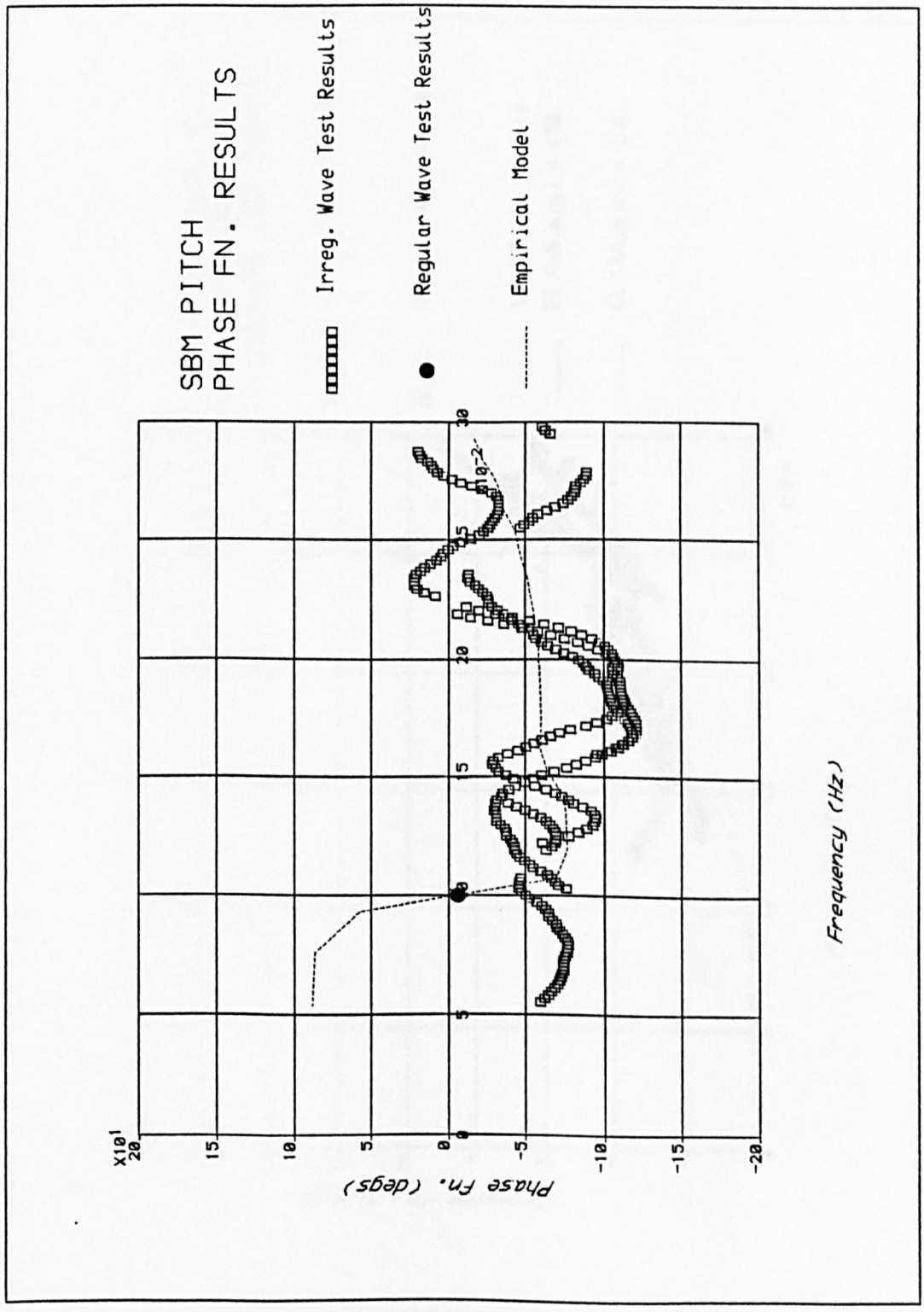

Figure 8.6 SBM pitch phase function from model tests and empirical model

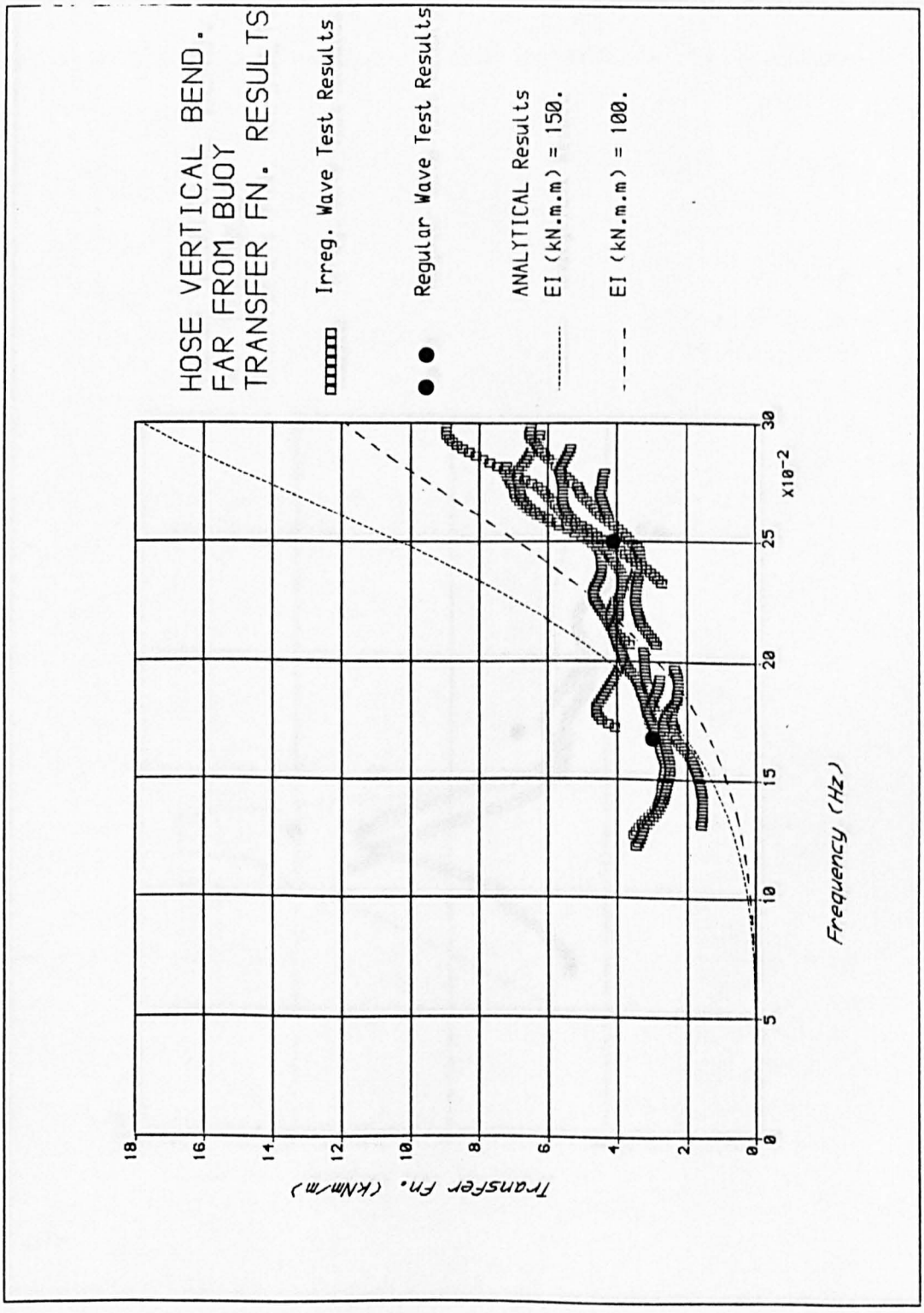

Figure 8.7 Transfer function for waves - vertical bending at positions away from the buoy obtained from the model tests and the analytical model

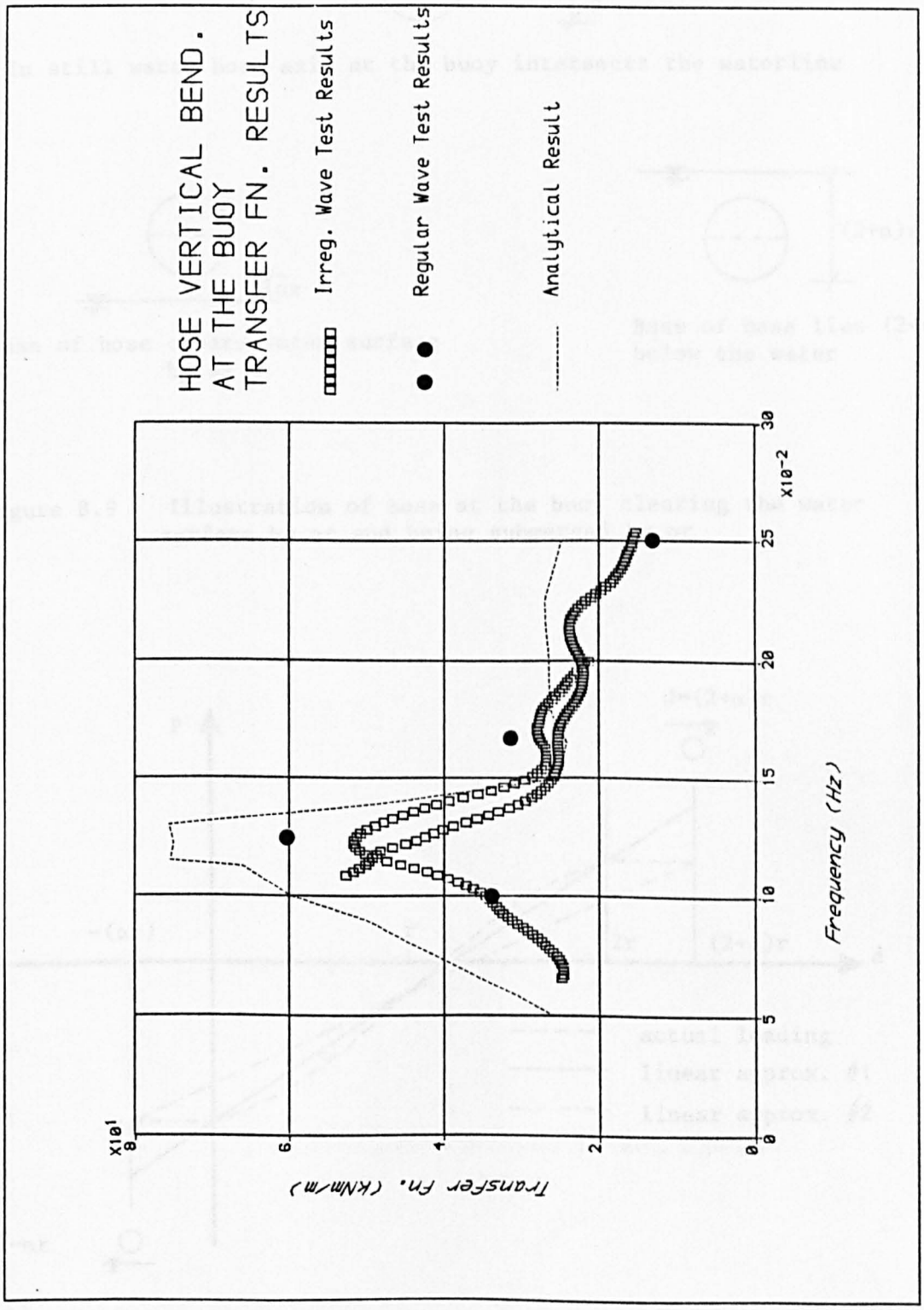

Figure 8.8 Transfer function for waves - vertical bending at the buoy obtained from the model tests and the analytical model

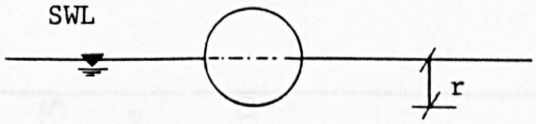

In still water hose axis at the buoy intersects the waterline

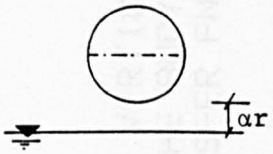

Base of hose clears water surface by αr

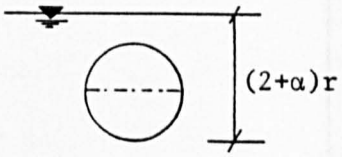

Base of hose lies (2+α)r below the water

Figure 8.9 Illustration of hose at the buoy clearing the water surface by αr and being submerged by αr

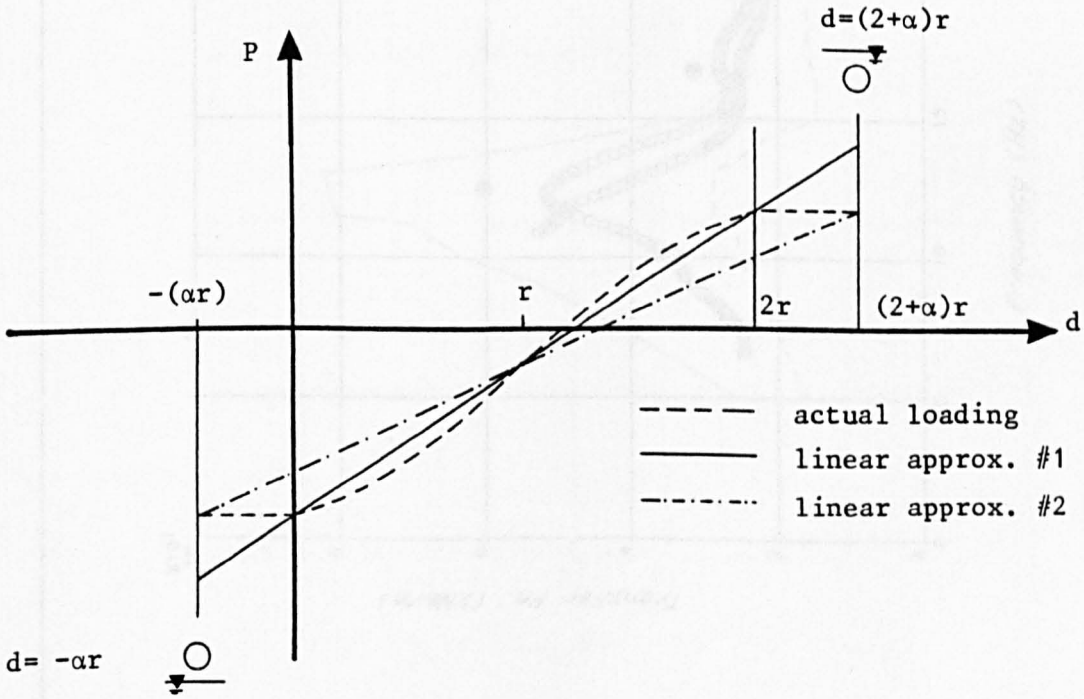

Figure 8.10 Loading on the hose at the buoy as the hose moves between the limits illustrated in Figure 8.9

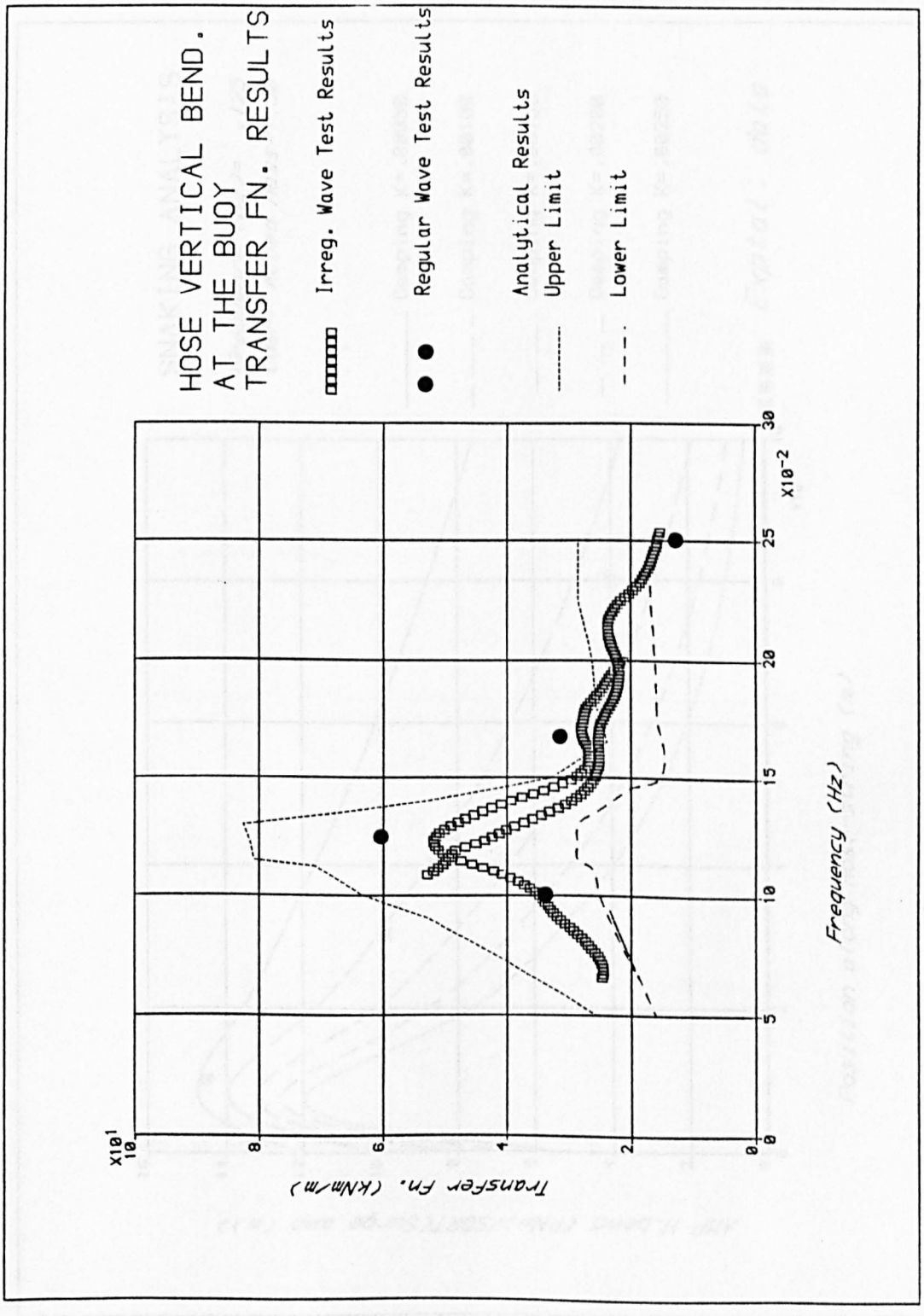

Figure 8.11 Transfer function for waves - vertical bending at the buoy obtained from the model tests and two estimates of the transfer function obtained from the analytical model

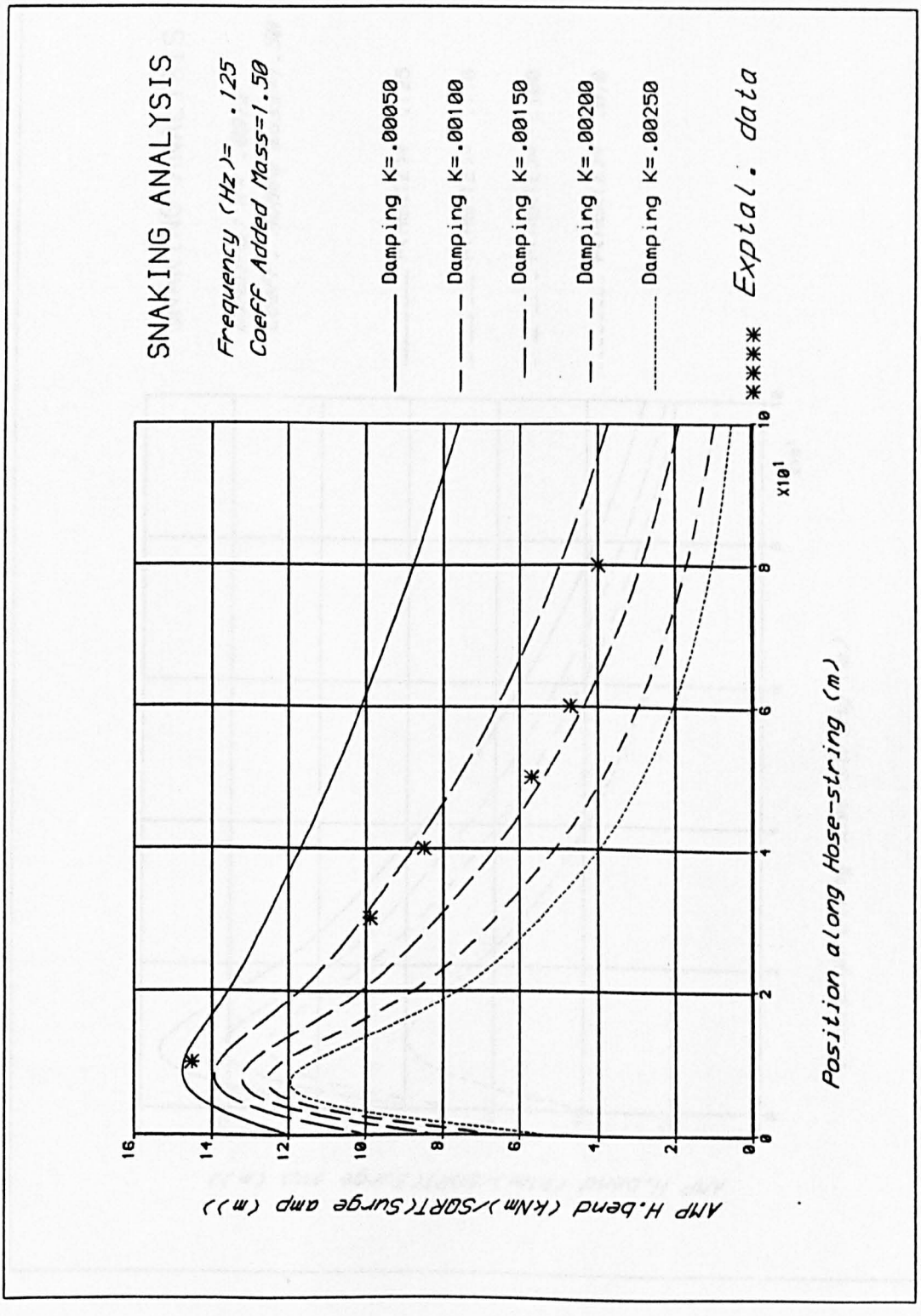

Figure 8.12 Horizontal bending along the hose-string for a surge frequency of 0.125Hz predicted by the analytical model and measured in the model tests

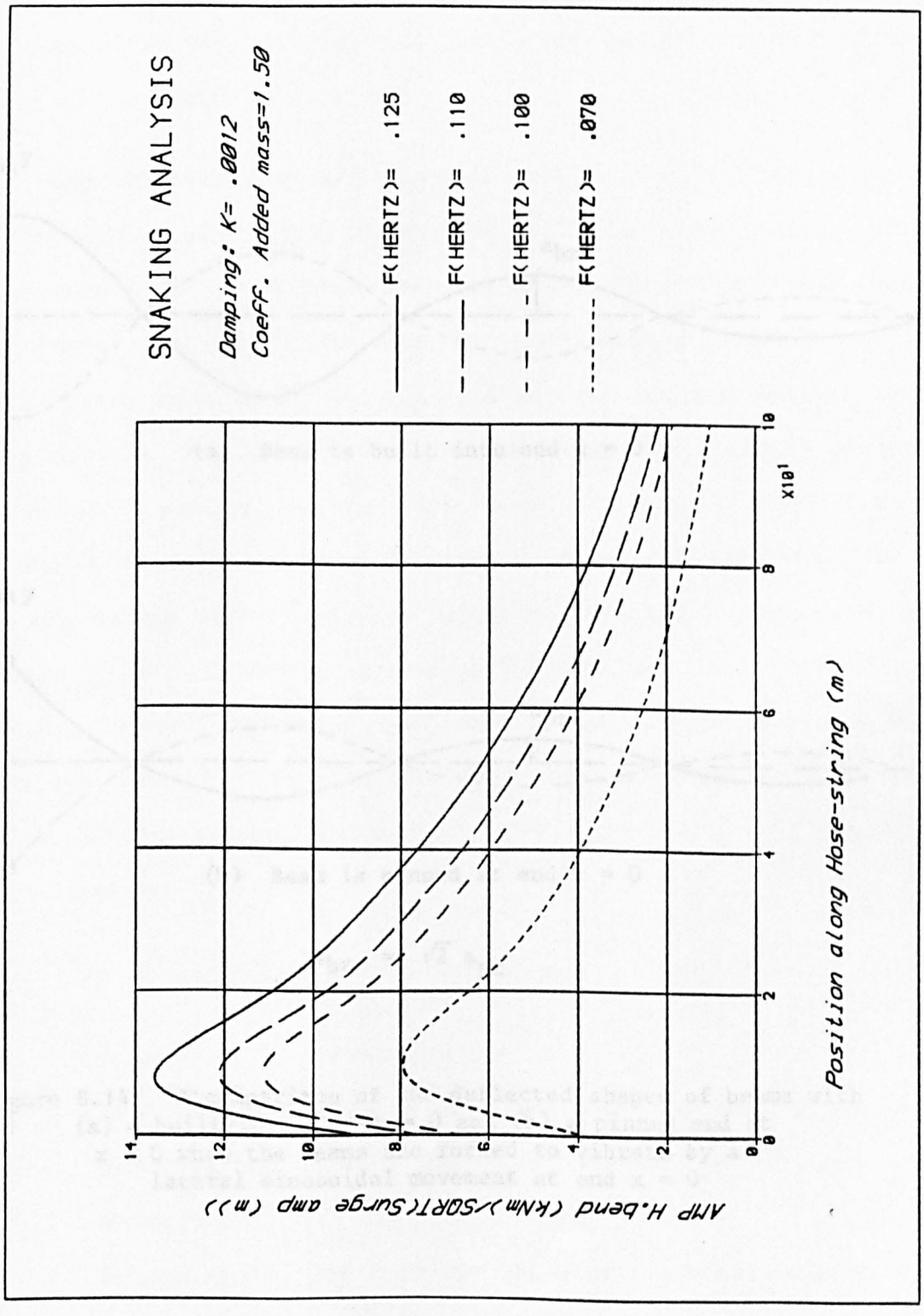

Figure 8.13 Analytical model prediction of horizontal bending along the hose-string for four different values of the surge frequency

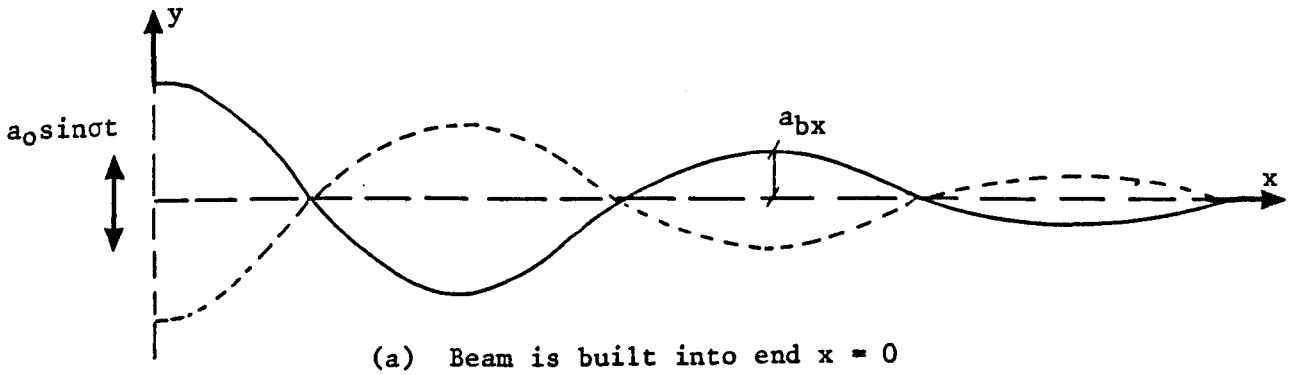

(a) Beam is built into end x = 0

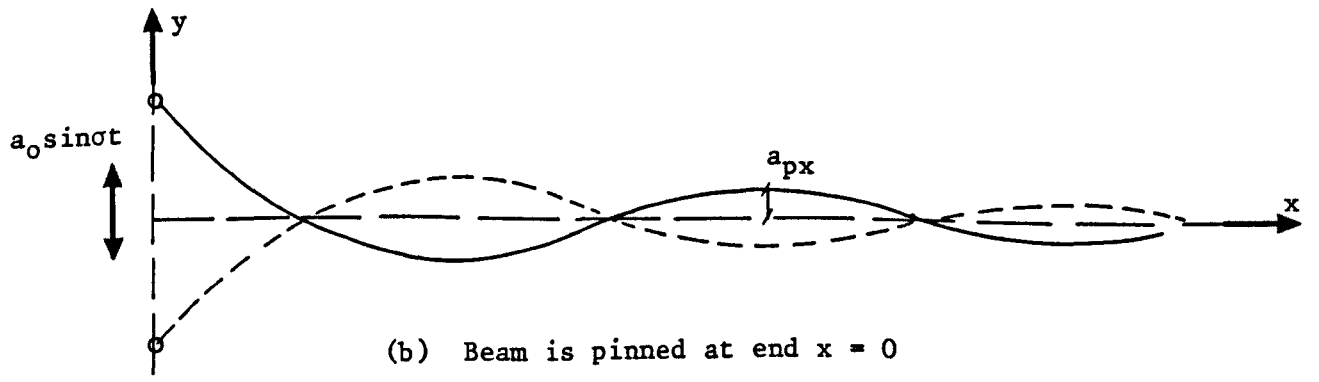

(b) Beam is pinned at end x = 0

$$a_{bx} = \sqrt{2}\, a_{px}$$

Figure 8.14 A comparison of the deflected shapes of beams with (a) a built-in end at x = 0 and (b) a pinned end at x = 0 when the beams are forced to vibrate by a lateral sinusoidal movement at end x = 0

9. CONCLUSION

This chapter serves to close the thesis by summarising the principal results of the study, as follows.

(i) Vertical Bending at the Buoy

The dynamic vertical bending of the hose at the hose-buoy manifold depends for the most part on the heave response of the SBM to the incident waves. The vertical bending at the buoy increases with increasing SBM heave amplitude and phase difference with the waves. Maximum vertical bending occurs at wave frequencies close to the SBM's heave natural frequency. The vertical bending at the buoy tends to zero at very low wave frequencies as the buoy tends to move in phase with and with the same amplitude as the waves; at high values of the wave frequency the heave response is low and bending depends on the wave amplitude. From the good agreement between the model test results and the predictions of the analytical model, it is concluded that the amplitude of the dynamic vertical bending at the buoy $\bar{M}$ in waves of amplitude a_w lies between the limits given by

$$(1+\alpha)^{-1/2} < \bar{M}/[a_w(s.EI)^{1/2}\psi] < 1.0 \qquad (9.1)$$

where $s = \pi r^2 \rho g/2r$, r is the hose radius

- α is the maximum number of hose radii that the hose at the buoy is submerged and clears the water surface in the wave period (equations 8.11 to 8.13)
- ψ depends on the amplitude and phase of the heave response of the SBM in the waves (Figure 7.10).

(ii) Vertical Bending Away From the Buoy

The dynamic vertical bending at positions on the hose-string which are two or more hose lengths away from the buoy is independent of the SBM's motions. At these positions the frequency of the vertical bending is the same as that of the waves and the bending amplitude increases as the wave frequency and, hence, the wave steepness increase. Conservative estimates of the amplitude of the dynamic vertical bending $\bar{M}$ at positions away from the buoy in waves of frequency σ rads/sec are obtained from the simple analytical result

$$\bar{M} = a_w EI(\sigma^2/g)^2 h \qquad (9.2)$$

where h is a dynamic amplification factor and is approximately equal to 1.0.

(iii) Horizontal Bending

The frequency and amplitude of the dynamic horizontal bending of the hose-string is determined by the frequency, amplitude and wavelength of the snake generated by the surge response of the SBM in waves. The general dependence of snaking and, hence, of horizontal bending on the surge response of the SBM is summarised as follows:

- the snake frequency is half the surge frequency;
- the snake wavelength is inversely proportional to the square root of the surge frequency; this implies that horizontal bending increases as the surge frequency increases;
- the snake amplitude is proportional to the square root of the surge amplitude.

Maximum horizontal bending occurs at the end of the first-off-the-buoy hose.

(iv) Axial Load

The dynamic axial loads on the hose-string are determined by the push-pull action exerted on the string by the surge motion of the SBM in waves. The frequency of dynamic axial load is the same as the surge frequency. The magnitude of the axial load at a position on the string depends on the length of string "ahead" of that position and on the frequency of the SBM's surge response. The analysis of the model test measurements has resulted in the following simple empirical model for estimating the amplitude of the dynamic axial load $\overline{F}_i$ (kN) at a position on the string that is L_i (m) from the free end:

$$\overline{F}_i = a_s L_i S \tag{9.3}$$

where a_s (m) is the surge amplitude and the value of S (kN/m^2) depends on the surge frequency (Figure 5.32) and increases approximately linearly as the surge frequency increases. (In irregular waves the surge amplitude a_s in equation (9.3) is replaced by the r.m.s. surge to give the r.m.s. axial load.)

(v) Empirical models for the prediction of the heave, surge and pitch of a CALM buoy in waves have been developed in the course of this study. Of these models, only the results obtained for surge are in good agreement with the model test results. In general, the poor results obtained for heave and pitch are due to errors in quantifying the hydrodynamic forces on the buoy. It is concluded that the shape details of a buoy can play an important role in determining the hydrodynamic forces acting on the buoy. The shape details should be incorporated in any numerical scheme or model test program carried out to determine the response characteristics of the buoy in waves.

The primary objective of this research study has been achieved: the dynamic bending moments and axial loads induced on a floating hose-string attached to a CALM buoy by the combined action of waves and buoy motions have been established. The results presented in this thesis may be used to help establish the design of floating hose-strings on a more scientific basis than heretofore.

APPENDIX A1

A technique for the design of an 8-chain CALM SBM model which accurately models the prototype's draft and mass-stiffness ratios in heave and surge. The model may be distorted with respect to water depth, cross-sectional area of the buoy, buoy mass, chain weight and chain pretension.

Notation:		
	scale	S
	water depth	d
	buoy mass	M
	buoy draft	h
	buoy mean submerged X-sectional area	A
	chain pretension angle	ϕ
	chain weight in water	ω
	sum of vertical components of chain tension at the fairlead at equilibrium	$\sum T_v^o$
	stiffness of 8 chains in heave	C_H
	stiffness of 8 chains in surge	C_s

Subscripts m and p refer to model and prototype respectively.

The following data is known for the prototype CALM SBM:

d_p, M_p, h_p, A_p, ϕ_p and ω_p

From a catenary analysis with d_p, ϕ_p and ω_p as input the following values are obtained: $(\sum T_v^o)_p$, $(C_H)_p$ and $(C_s)_p$.

The following is known for the CALM SBM model: A_m, d_m.

It is required to find M_m, ϕ_m and ω_m such that the model reproduces the prototype buoy's draft and the prototype heave and surge mass to stiffness

ratios of the SBM. If r is the ratio of mass to stiffness for the degree of freedom concerned then it is required that:

$$M_m = \rho A_m h_p / S - (\sum T_v{}^o)_m / g \qquad (A1.1)$$

$$(r_H)_m = (r_H)_p / S \qquad (A1.2)$$

and

$$(r_s)_m = (r_s)_p / S \qquad (A1.3)$$

Equations (A1.2) and (A1.3) follow from the Froude scaling laws since r has units of $(\text{seconds})^2$ and Froude scaling requires that $(\text{seconds})_m/(\text{seconds})_p = S^{-1/2}$.

The ratios r_H and r_s are given by:

$$r_H = M/(\rho g A + C_H) \qquad (A1.4)$$

and

$$r_s = M/C_s \qquad (A1.5)$$

Substitution for r_H and r_s in equations (A1.2) and (A1.3) gives

$$M_m = c_1 - (\sum T_v{}^o)_m / g \qquad (A1.6)$$

$$M_m = c_2 (C_H)_m + c_3 \qquad (A1.7)$$

$$M_m = c_4 (C_s)_m \qquad (A1.8)$$

where c_1, c_2, c_3 and c_4 are constants which depend on the known values for the prototype SBM, on A_m and the on scale S. The values of c_1, c_2, c_3 and c_4 are given by

$$c_1 = \rho A_m h_p / S \qquad (A1.9)$$

$$c_2 = M_p/S[\rho g A_p + (C_H)_p] \tag{A1.10}$$

$$c_3 = M_p \rho g A_m/S[\rho g A_p + (C_H)_p] \tag{A1.11}$$

$$c_4 = M_p/S(C_s)_p \tag{A1.12}$$

It may be shown from catenary analysis that C_{H_m} and C_{s_m} can be approximated as linear functions of $\sum T_v^o$ as follows:

$$(C_H)_m = c_5(\sum T_v^o)_m \tag{A1.13}$$

and

$$(C_s)_m = c_6(\sum T_v^o)_m \tag{A1.14}$$

The constants c_5 and c_6 depend on the water depth and the chain pretension angles but are independent of the chain weight.

Substituting for $(C_H)_m$ and $(C_s)_m$ in equations (A1.7) and (A1.8) gives

$$M_m = c_2c_5(\sum T_v^o)_m + c_3 \tag{A1.15}$$

and

$$M_m = c_4c_6(\sum T_v^o)_m \tag{A1.16}$$

It may be shown from simple algebra that, for the simultaneous equations (A1.6), (A1.15) and (A1.16) to have a solution, then c_6 and c_5 are related as follows:

$$c_6 = \{c_1c_2/(c_1c_4-c_3c_4)\}c_5 + \{c_3/g(c_1c_4-c_3c_4)\} \tag{A1.17}$$

or, more simply,

$$c_6 = c_7c_5 + c_8 \tag{A1.18}$$

Therefore, we require to find ϕ_m for the catenary chains in water of depth (d_m-h_m) such that equation (A1.17) is satisfied. Once ϕ_m and hence c_5 and c_6 have been obtained, equations (A1.6), (A1.15) and (A1.16) reduce to three equations with only two unknowns, M_m and $(\sum T_v^o)_m$. The required weight of chain, ω_m, is then obtained from $(\sum T_v^o)_m$ using the results of the catenary analysis.

Example. It is required to model the Shell UK Oil Anglesey SBM in the wave basin using the buoy constructed for the floating hose study. The buoy models the general configuration of the Anglesey prototype on a 43 scale. However the mean submerged cross-sectional area of the buoy model is greater than the corresponding scaled value of the prototype by about 40%. Moreover the water depth in the wave basin does not correspond exactly with the water depth at Anglesey though the discrepancy is only about 2%.

The prototype data is summarised as follows:

d_p = 39.5m

h_p = 4.5m

A_p = 162m^2

M_p = 600,000kg

ϕ_p = 60^o

ω_p = 2.57 x 10^{3}N/m

From catenary analysis: $(C_H)_p$ = 68,125.0N/m

$(C_s)_p$ = 65,439.0N/m

$(\sum T_v^o)_p$ = 1.246 x 10^{6}N

The model scale is S = 43

For the SBM model d_m = 0.9 and A_m = 0.123m^2

From equations (A1.9) to (A1.12):

$c_1 = 12.872,\ c_2 = 0.00842,\ c_3 = 10.16,\ c_4 = 0.213$

From equation (A1.17):

$c_7 = 0.1876,\ c_8 = 1.793$

The chains of the SBM model lie in a water depth of (0.9-4.5/43) = 0.795m.

Table A1.1 presents the results of catenary analysis for a chain depth of 0.795m and chain weight 1.0N/m. It is required to find the pretension angle, ϕ_m, from Table A1.1 such that the following equation is satisfied:

$$c_6 = 0.1876c_5 + 1.793 \qquad \text{(A1.19)}$$

The best result is $\phi_m = 60^o$ with $c_5 = 2.41$ and $c_6 = 2.21$.

The required buoy mass and total vertical chain tension are obtained by solving the following pair of simultaneous equations:

$$M_m = 0.00842 \times 2.4063(\sum T_v^o)_m + 10.16$$
$$M_m = 0.213 \times 2.21(\sum T_v^o)_m \qquad \text{(A1.20)}$$

These give $M_m = 10.62$kg and $(\sum T_v^o)_m = 22.55$N. The required chain weight is then (using the result for $\sum T_v^o$ in Table A1.1)

$$\omega_m = 22.55(1.0/11.01) = 2.047\text{N/m} \qquad \text{(A1.21)}$$

Table A1.2 summarises the results obtained using the above procedure. The percentage difference between the properties of the distorted model and those of an exact model of the SBM are presented. The results show that the 40% distortion of the mean submerged cross-sectional area has necessitated an equivalent distortion of the buoy's mass in order that the

heave mass to stiffness ratio and the buoy's draft are reproduced in the model. The increase in the buoy mass has in turn necessitated the 47% increase in the chain weight in order that the surge mass to stiffness ratio is reproduced.

The results for a second example in which the same prototype SBM is modelled in a water depth that is about 50% less than that required by an exact model but the buoy model used has a mean submerged sectional area that is geometrically similar to the prototype's, are summarised below. The percentage given in brackets is the difference in value between an exact model and the distorted model.

d_m = 0.5m (-46%)

A_m = 0.0876m^2 (0%)

M_m = 7.77kg (+2.9%)

ϕ_m = 70° (+16.6%)

ω_m = 3.046N/m (+119%)

In this example there is little effect on the mass of the buoy but the chain weight has more than doubled and the pretension angle has increased from 60° to 70°.

Catenary Analysis

Water depth = 0.795m

Chain weight in water = 1.0N/m

Pretension Angle (degs)	$8T_V^o$ (N)	C_5 (1/m)	C_6 (1/m)
72.5	8.67	2.26	1.16
70.0	9.08	2.3	1.34
67.5	9.52	2.33	1.53
65.0	9.98	2.36	1.74
62.5	10.48	2.38	1.96
60.0	11.01	2.41	2.21
57.5	11.59	2.43	2.47
55.0	12.22	2.44	2.73

Table A1.1

Computations carried out to seek the pretension angle for which the relationship $c_6 = 0.1876c_5 + 1.793$ is satisfied. The best result is 60°.

Property	Exact Model	Distorted Model	% Difference
water depth (m)	0.92	0.9	-2.0
X-sectional area (m^2)	0.088	0.123	+ 40
SBM mass (kg)	7.55	10.62	+ 40
chain weight (N/m)	1.39	2.05	+ 47
pretension angle (degs)	60	60	0

Table A1.2

APPENDIX A2

MEASUREMENT OF 6 DEGREES OF FREEDOM OF BUOY MOTIONS USING A 2 CAMERA/4 LED SELSPOT SYSTEM

A2.1 Test Set-Up

The two SELSPOT cameras and four LEDs are set up as shown in Figure A2.1.

The LEDs lie on the same horizontal plane in the stationary position and the centre of the LED system lies above the centre of gravity of the buoy. Both cameras are at the same level. The cameras are positioned such that LEDs 1 and 3 lie on the camera Y-axis and LEDs 2 and 4 lie on the camera X-axis.

A2.2 Camera Calibration

The voltages from each LED are represented as shown in Table A2.1 in the discussion which follows. For example, the x-axis voltage measured from LED2 by camera 1 is V_3.

	CAMERA 1								CAMERA 2							
LED	1		2		3		4		1		2		3		4	
axis	X	Y	X	Y	X	Y	X	Y	X	Y	X	Y	X	Y	X	Y
Voltage	V_1	V_2	V_3	V_4	V_5	V_6	V_7	V_8	V_9	V_{10}	V_{11}	V_{12}	V_{13}	V_{14}	V_{15}	V_{16}

Table A2.1

Measured LED Voltages

The camera calibration factors, relating the voltage to the position of the LED, are obtained from the voltages recorded at the stationary condition as follows.

With reference to Figure A2.2(a) the x-axis calibration factor for camera 1, kx_1, is defined by

$$\tan\phi_2 = kx_1 V_3 = (x - D_{24})/D_1$$

and (A2.1)

$$\tan\phi_4 = kx_1 V_7 = x/D_1$$

Solving these equations for kx_1 gives

$$kx_1 = D_{24}/D_1[V_7 - V_3] \quad (A2.2)$$

Since V_3 is negative when the cameras and LEDs are set up correctly then

$$kx_1 = D_{24}/D_1[|V_7| + |V_3|] \quad (A2.3)$$

The x-axis calibration factor for camera 2, kx_2, is defined by (Figure A2.2(b))

$$\tan\phi_2 = kx_2 V_{11}$$

and (A2.4)

$$\tan\phi_4 = kx_2 V_{15}$$

In a similar way to kx_1, kx_2 may be shown to be

$$kx_2 = D_{24}/D_2[|V_{11}| + |V_{15}|] \quad (A2.5)$$

The y-axis calibration factor for camera 1, ky_1, is (Figure A2.2(c)) defined by

$$\tan\phi_3 = ky_1 V_6 = [D_{13}\sin\alpha_1/2]/[D_1 + D_{13}\cos\alpha_1/2]$$

and

$$\tan\phi_1 = ky_1 V_2 = [D_{13}\sin\alpha_1/2]/[D_1 - D_{13}\cos\alpha_1/2] \qquad \text{(A2.6)}$$

where

$$\sin\alpha_1 = V/D_1$$

$$\cos\alpha_1 = H_1/D_1$$

These equations may be solved simultaneously to give

$$ky_1 = \frac{D_{13}V}{4D_1^2}\left[\frac{V_2 + V_6}{V_6 V_2}\right] \qquad \text{(A2.7)}$$

V_2 is negative and V_6 is positive when correctly set up. Therefore

$$ky_1 = D_{13}V/4D_1^2\left[\frac{|V_2| - |V_6|}{|V_2||V_6|}\right] \qquad \text{(A2.8)}$$

It may be similarly shown for camera 2 that

$$ky_2 = D_{13}V/4D_1^2\left[\frac{|V_{14}| - |V_{10}|}{|V_{14}||V_{10}|}\right] \qquad \text{(A2.9)}$$

The camera calibration factors kx_1, kx_2, ky_1 and ky_2 are therefore obtained from the LED voltages measured at stationary conditions using equations (A2.3), (A2.5), (A2.8) and (A2.9) respectively.

A2.3 Coordinates of LED in Non-Stationary Position

Once the camera calibration factors have been established the position of each LED at any instant during a model test may be obtained from the voltages measured at that instant as follows.

In Figure A2.3 the instantaneous position of the LED is represented by P. We seek to establish the coordinates of P relative to the axes shown, i.e. x, y, z. The projections of P onto the X-Y plane, the Y-Z plane and X-Z plane are shown by P_{xy}, P_{yz} and P_{xz} respectively. If the y voltage measured at camera 1 is V_{y_1} and the y-axis calibration factor for camera 1 is ky_1 then with reference to Figure A2.3, β_1 can be obtained from

$$\beta_1 = \tan^{-1}(ky_1 Vy_1) \qquad (A2.10)$$

But $\beta_1 = \theta_1 - \alpha_1$ where $\theta_1 = \tan^{-1}V/H_1$, and so

$$\alpha_1 = \tan^{-1}V/H_1 - \tan^{-1}(ky_1 Vy_1) \qquad (A2.11)$$

Now

$$\tan\alpha_1 = y/(H_1 + x) \qquad (A2.12)$$

or

$$y = H_1\tan\alpha_1 + x\tan\alpha_1 \qquad (A2.13)$$

Consider the y voltage measured at camera 2. Let this be Vy_2 and let the calibration factor be ky_2, then

$$\beta_2 = \tan^{-1}(ky_2 Vy_2) \qquad (A2.14)$$

and

$$\alpha_2 = -(\pi - \tan^{-1}V/H_2) - \tan^{-1}(ky_2 Vy_2) \qquad (A2.15)$$

Now

$$\tan\alpha_2 = -(y/H_2 - x) \qquad (A2.16)$$

or

$$y = -H_2\tan\alpha_2 + x\tan\alpha_2 \qquad \text{(A2.17)}$$

Equations (A2.13) and (A2.17) are a pair of simultaneous equations with two unknowns x and y. Solving yields

$$x = (H_1\tan\alpha_1 + H_2\tan\alpha_2)/\tan\alpha_2 - \tan\alpha_1 \qquad \text{(A2.18)}$$

and

$$y = ((H_1 + H_2)\tan\alpha_1\tan\alpha_2)/\tan\alpha_2 - \tan\alpha_1 \qquad \text{(A2.19)}$$

The z-coordinate of the instantaneous LED position P is obtained using Figure A2.4 as follows.

If Vx_1 is the x voltage measured at camera 1 and kx_1 is the x-axis calibration factor for camera 1 then

$$\beta_1 = \tan^{-1}(kx_1Vx_1) \qquad \text{(A2.20)}$$

Now

$$\tan\beta_1 = z/AD \qquad \text{(A2.21)}$$

where z is the z-coordinate that is sought and AD is the distance shown in Figure A2.4.

Also

$$\cos(\theta_1 - \alpha_1) = AD/AC \qquad \text{(A2.22)}$$

and

$$\cos\alpha_1 = (H_1 + x)/AC \qquad \text{(A2.23)}$$

Therefore

$$AC = (H_1 + x)/\cos\alpha_1 \qquad (A2.24)$$

$$AD = (H_1 + x)\cos(\theta_1 - \alpha_1)/\cos\alpha_1 \qquad (A2.25)$$

and

$$z = (H_1 + x)\cos(\theta_1 - \alpha_1)\tan\beta_1/\cos\alpha_1 \qquad (A2.26)$$

(H_1+x), $\cos\alpha_1$ and $\cos(\theta_1-\alpha_1)$ are positive. $\tan\beta_1$ is negative. Since it is required that z is positive according to the coordinate system shown then

$$z = -(H_1 + x)\frac{\cos(\theta_1 - \alpha_1)}{\cos\alpha_1}\tan\beta_1 \qquad (A2.27)$$

If Vx_2 is the x voltage measured at camera 2 and kx_2 is the x-axis calibration factor for camera 2 then

$$\beta_2 = \tan^{-1}(kx_2Vx_2) \qquad (A2.28)$$

Following the procedure used for camera 1 it may be shown that the z-coordinate may also be obtained from the x voltage measured at camera 2 and is

$$z = (x - H_2)\frac{\cos(\alpha - \theta_2)}{\cos\alpha_2}\tan\beta_2 \qquad (A2.29)$$

In practice the two estimates of z obtained from equations (A2.27) and (A2.29) are never exactly equal and so the average value is used.

To summarise, equations (A2.18), (A2.19), (A2.27) and (A2.28) are used to obtain the x, y, z coordinates of the instantaneous position of the LED. The angles α and β in these equations are obtained from the instantaneous x and y voltages measured at the two cameras.

A2.4 Buoy Motions From LED Positions

Let the coordinates of the LEDs 1, 2, 3, 4 at any instant be (x_1, y_1, z_1), (x_2, y_2, z_2), (x_3, y_3, z_3) and (x_4, y_4, z_4). From Figure A2.5 the direction numbers of the line perpendicular to the LED plane are calculated from

$$\underline{n} = \underline{a} \times \underline{b} = \underline{d} \times \underline{c} \tag{A2.30}$$

where

$$\underline{a} = [(x_2-x_1), (y_2-y_1), (z_2-z_1)] = (x_{21},y_{21},z_{21})$$

$$\underline{b} = [(x_4-x_1), (y_4-y_1), (z_4-z_1)] = (x_{41},y_{41},z_{41})$$

$$\underline{c} = [(x_2-x_3), (y_2-y_3), (z_2-z_3)] = (x_{23},y_{23},z_{23})$$

and

$$\underline{d} = [(x_4-x_3), (y_4-y_3), (z_4-z_3)] = (x_{43},y_{43},z_{43})$$

Calculating $\underline{n}$ from $\underline{a} \times \underline{b}$ gives

$$\underline{n}_1 = [(y_{21}z_{41}-y_{41}z_{21}), (x_{41}z_{21}-x_{21}z_{41}), (x_{21}y_{41}-x_{41}z_{21})]$$

$$= (a_1,b_1,c_1) \tag{A2.31}$$

Calculating $\underline{n}$ from $\underline{d} \times \underline{c}$ gives

$$\underline{n}_2 = [(y_{43}z_{23}-y_{23}z_{43}), (x_{23}z_{43}-x_{43}z_{23}), (x_{43}y_{23}-x_{23}y_{43})]$$

$$= (a_2,b_2,c_2) \tag{A2.32}$$

$\underline{n}_1$ and $\underline{n}_2$ will not be exactly equal because of measurement and computational errors inherent in the system. To reduce these errors the normal vector is obtained from the average of $\underline{n}_1$ and $\underline{n}_2$, i.e.

$$\underline{n} = \frac{1}{2}\{\underline{n}_1 + \underline{n}_2\} = (a,b,c) \tag{A2.33}$$

The magnitude of $\underline{n}$ is $(a^2 + b^2 + c^2)^{1/2}$ and so the direction cosines of $\underline{n}$ are

$$\begin{aligned} da &= a/(a^2 + b^2 + c^2)^{1/2} \\ db &= b/(a^2 + b^2 + c^2)^{1/2} \\ dc &= c/(a^2 + b^2 + c^2)^{1/2} \end{aligned} \qquad \text{(A2.34)}$$

The coordinates of the centre of the LED plane are x_L, y_L, z_L where

$$\begin{aligned} x_L &= (x_1 + x_2 + x_3 + x_4)/4 \\ y_L &= (y_1 + y_2 + y_3 + y_4)/4 \\ z_L &= (z_1 + z_2 + z_3 + z_4)/4 \end{aligned} \qquad \text{(A2.35)}$$

If H is the vertical distance of the buoy's centre of gravity below the LED plane then the coordinates of the buoy's centre of gravity, x_G, y_G, z_G, are obtained from the product of the direction cosines and H added to x_L, y_L and z_L, i.e.

$$\begin{aligned} x_G &= x_L + d_a H \\ y_G &= y_L + d_b H \\ z_G &= z_L + d_c H \end{aligned} \qquad \text{(A2.36)}$$

Figure A2.5 shows the convention adopted for buoy motions. The buoy translations are obtained directly from the coordinates of the centre of gravity:

$$\begin{aligned} \text{surge} &= -z_G \\ \text{sway} &= x_G \\ \text{heave} &= -(y_G - V) \end{aligned} \qquad \text{(A2.37)}$$

The top rotation of the buoy is given by

$$\theta_{\text{top rotation}} = \tan^{-1} z_{31}/x_{31} \tag{A2.38}$$

But

$$x_{31} = (D_{13}^2 - y_{13}^2 - z_{31}^2)^{1/2} \tag{A2.39}$$

so

$$\theta_{\text{top rotation}} = \tan^{-1}[z_{31}/(D_{13}^2 - y_{13}^2 - z_{31}^2)^{1/2}] \tag{A2.40}$$

The buoy's pitch is

$$\theta_{\text{pitch}} = -\tan^{-1}[y_{24}/(D_{24}^2 - y_{24}^2)^{1/2}] \tag{A2.41}$$

and the buoy's roll is

$$\theta_{\text{roll}} = \tan^{-1}[y_{13}/(D_{13}^2 - y_{13}^2)^{1/2}] \tag{A2.42}$$

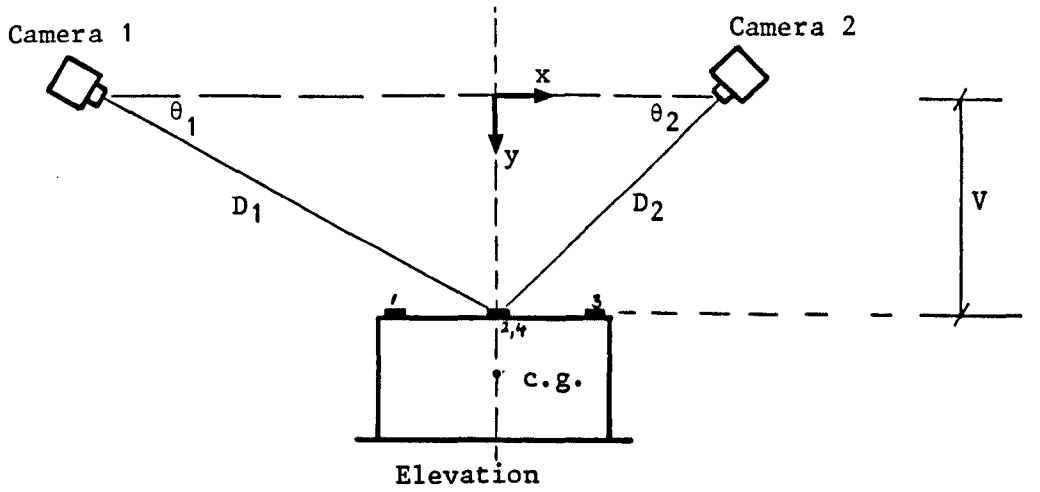

Elevation

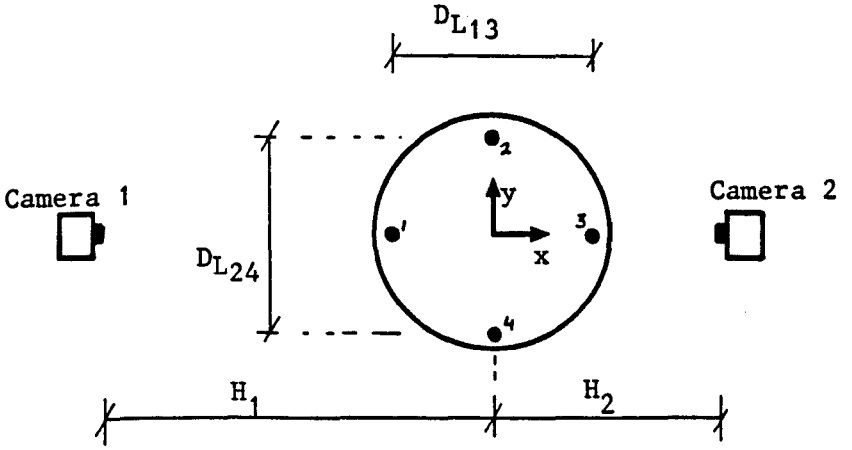

Plan

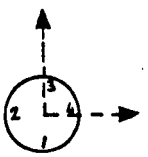

View of LEDs
from camera 1

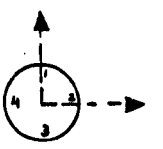

View of LEDs
from camera 2

Figure A2.1 2 camera/4 LEDs set-up for measurement of 6 dof of buoy motion

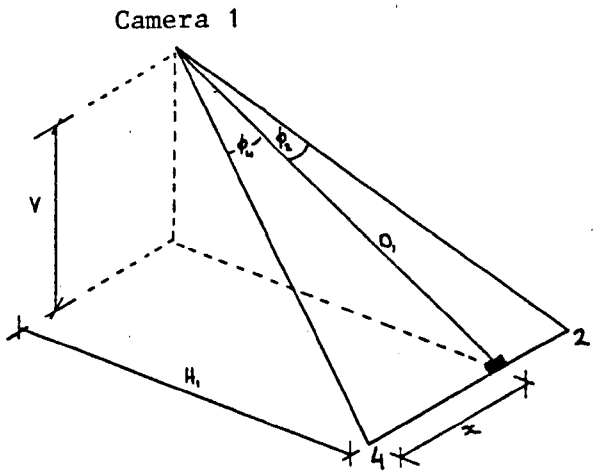

Figure A2.2(a) Camera scaling factor: X-factor, camera 1

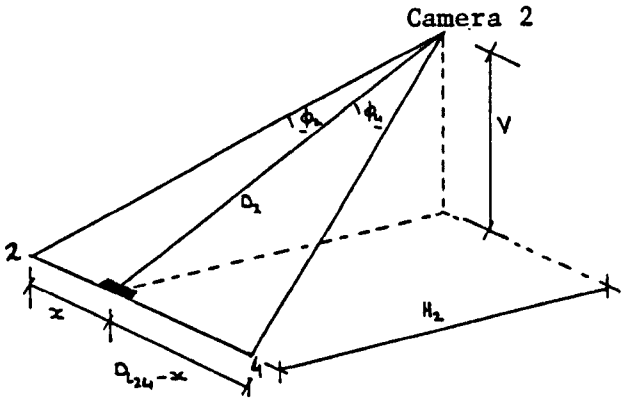

Figure A2.2(b) Camera scaling factor: X-factor, camera 2

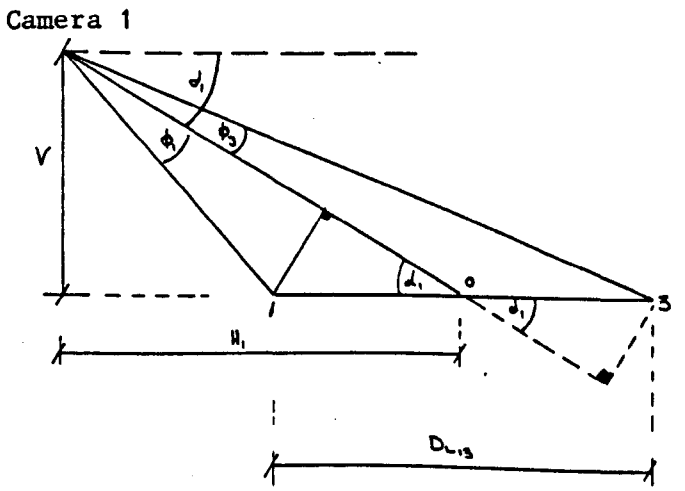

Figure A2.2(c) Camera scaling factor: Y-factor, camera 1

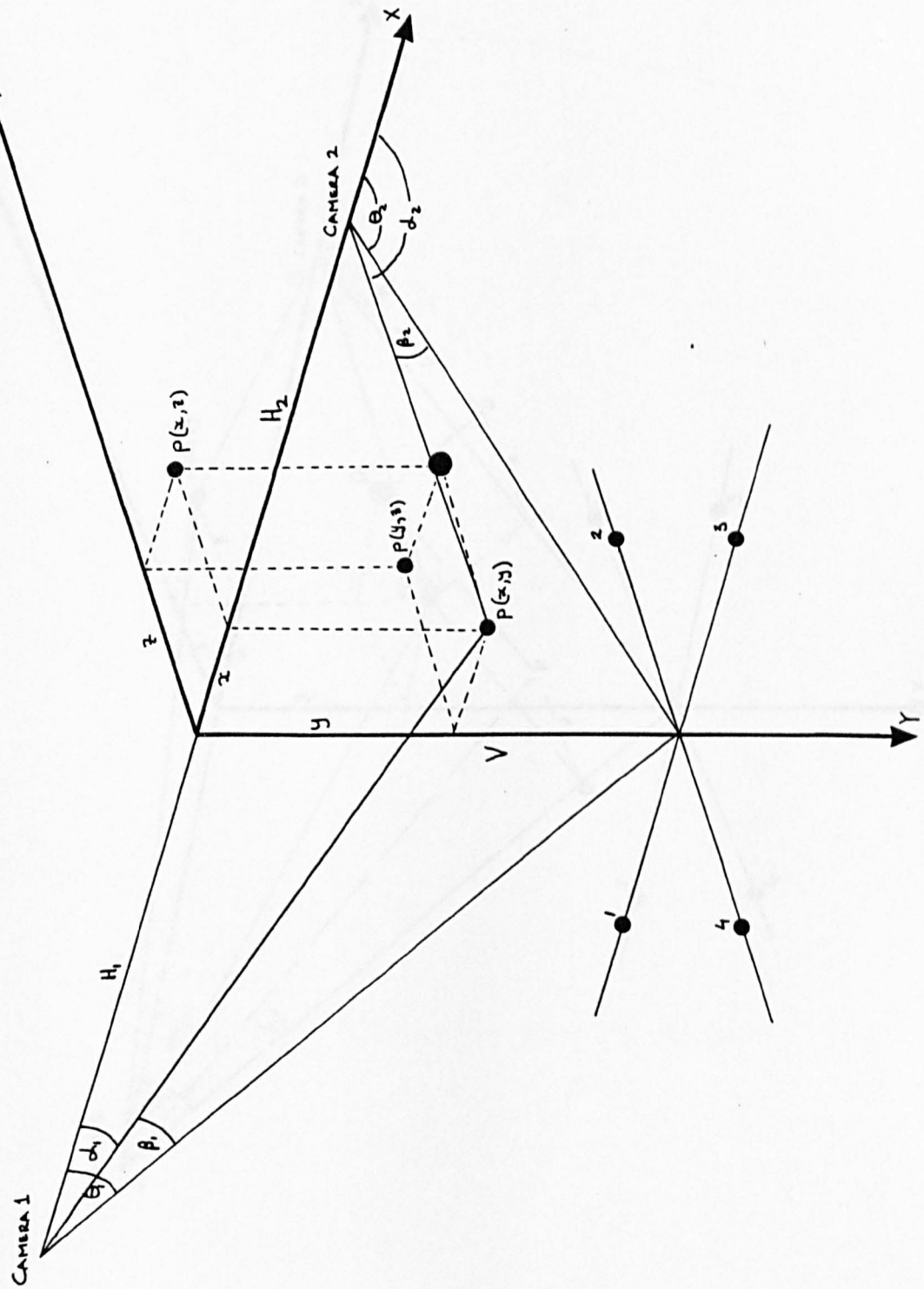

Figure A2.3 Sketch for x and y coordinates

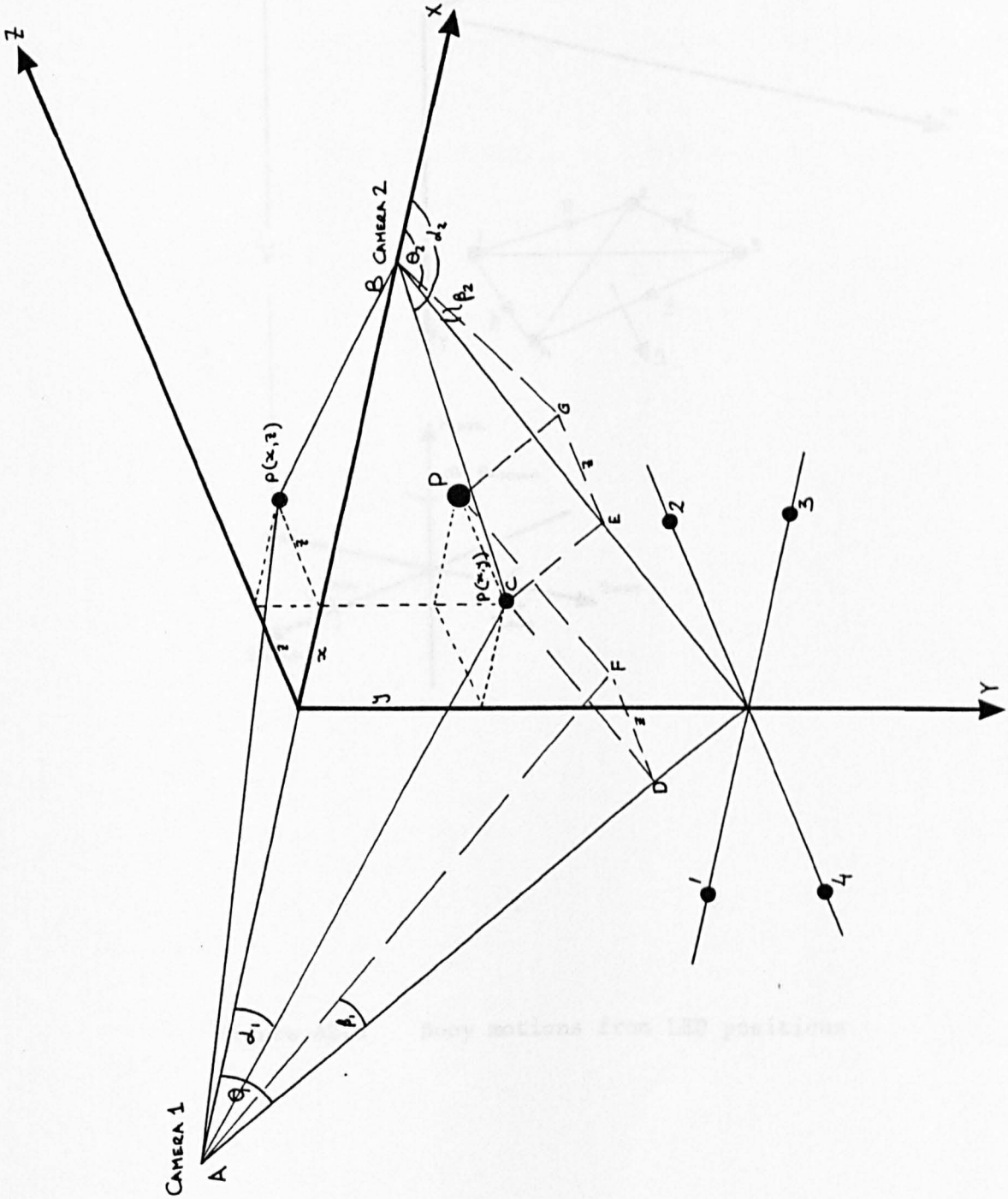

Figure A2.4 Sketch for z coordinate

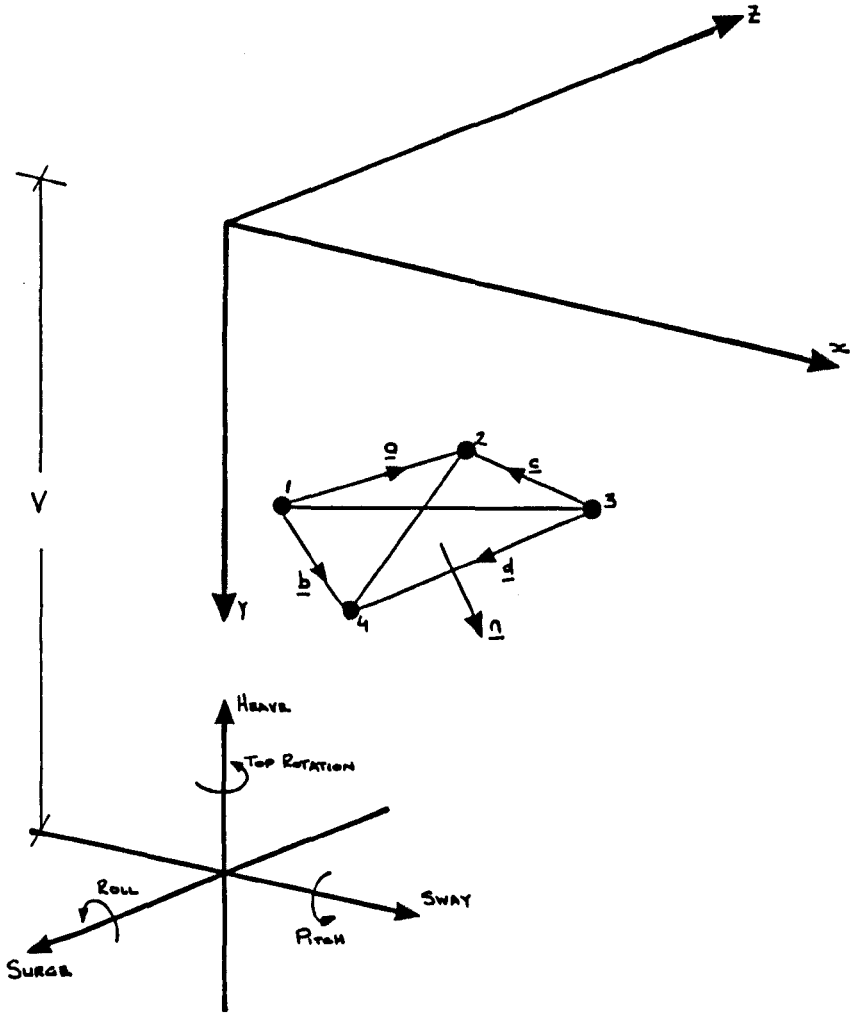

Figure A2.5 Buoy motions from LED positions

A3.1 Examples of Vertical Bending Measurements and their Spectra

Figure A3.1.1 Vertical bending at position 1 in SEA1

Figure A3.1.2 Vertical bending at position 2 in SEA1

Figure A3.1.3 Vertical bending at position 3 in SEA1

Figure A3.1.4 Vertical bending at position 1 in regular waves with f = 0.25Hz

Figure A3.1.5 Vertical bending at position 2 in regular waves with f = 0.25Hz

Figure A3.1.6 Vertical bending at position 3 in regular waves with f = 0.25Hz

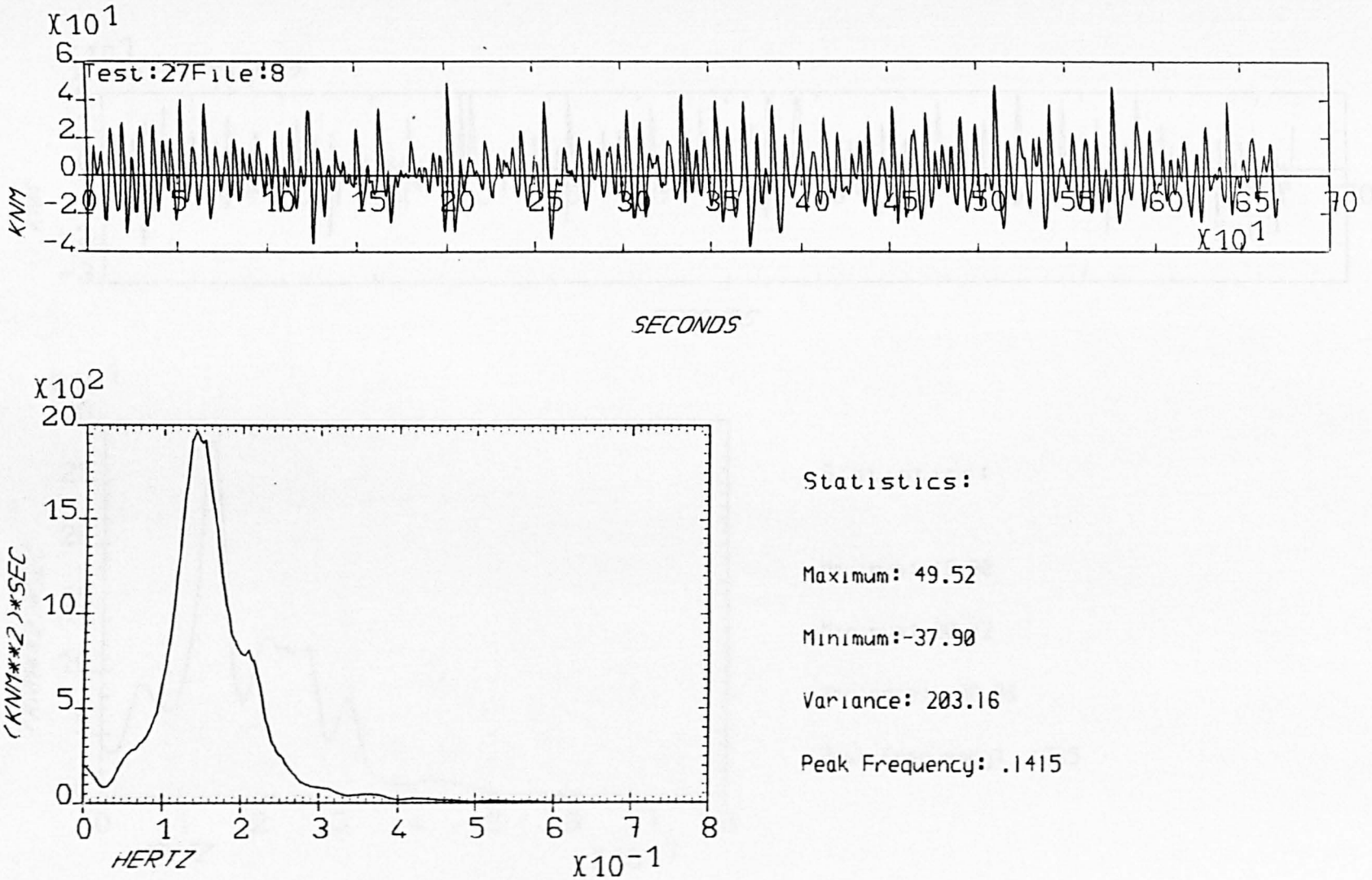
X10^1
Test:27File:8
KNM
SECONDS
X10^1
X10^2
(KNM**2)*SEC
HERTZ
X10^-1
Statistics:
Maximum: 49.52
Minimum:-37.90
Variance: 203.16
Peak Frequency: .1415
VTBEND. AT POSITION 1 WITH 1 HOSES IN A 2.1M SEA

Figure A3.1.1

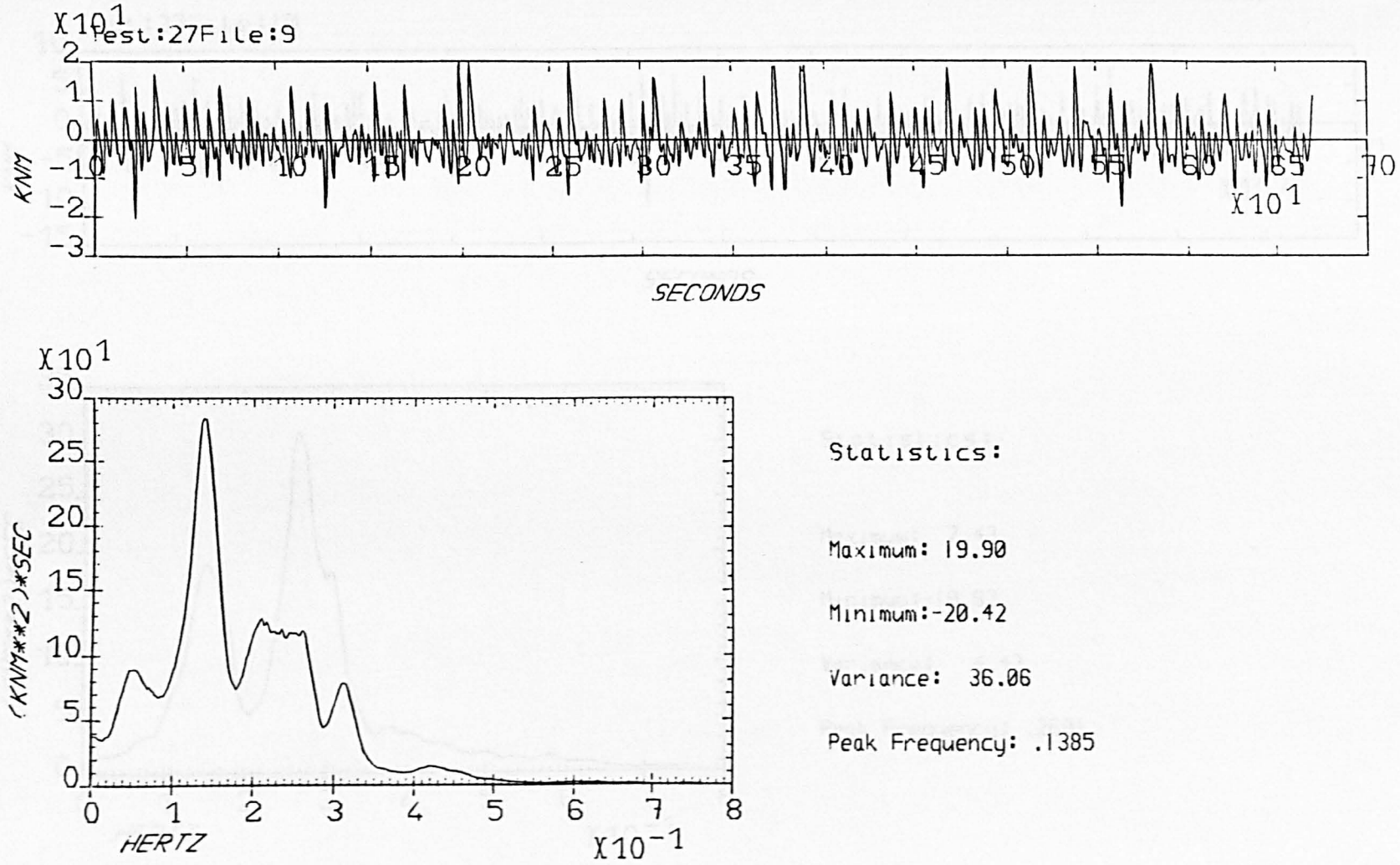
X10 1
Test:27File:9
KNM
SECONDS
X10 1
X10 1
(KNM**2)*SEC
HERTZ
X10 -1
Statistics:
Maximum: 19.90
Minimum:-20.42
Variance: 36.06
Peak Frequency: .1385
VTBEND. AT POSITION 2 WITH 1 HOSES IN A 2.1M SEA

Figure A3.1.2

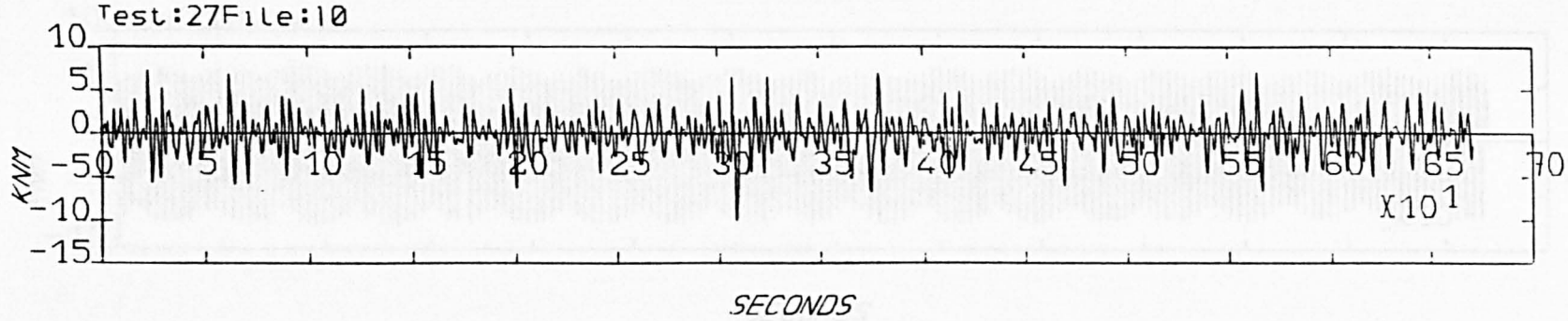

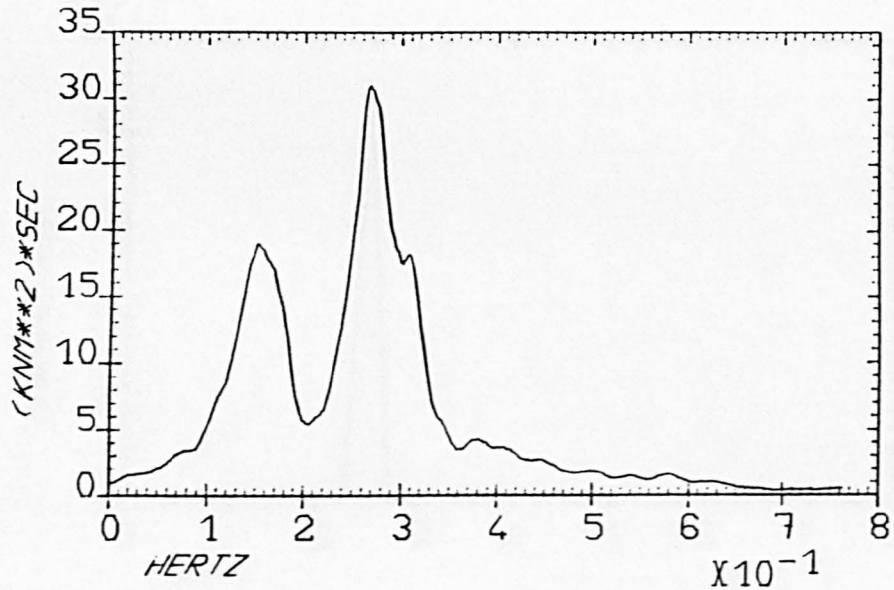

Statistics:

Maximum: 7.43

Minimum:-10.02

Variance: 4.42

Peak Frequency: .2681

VTBEND. AT POSITION 3 WITH 1 HOSES IN A 2.1M SEA

Figure A3.1.3

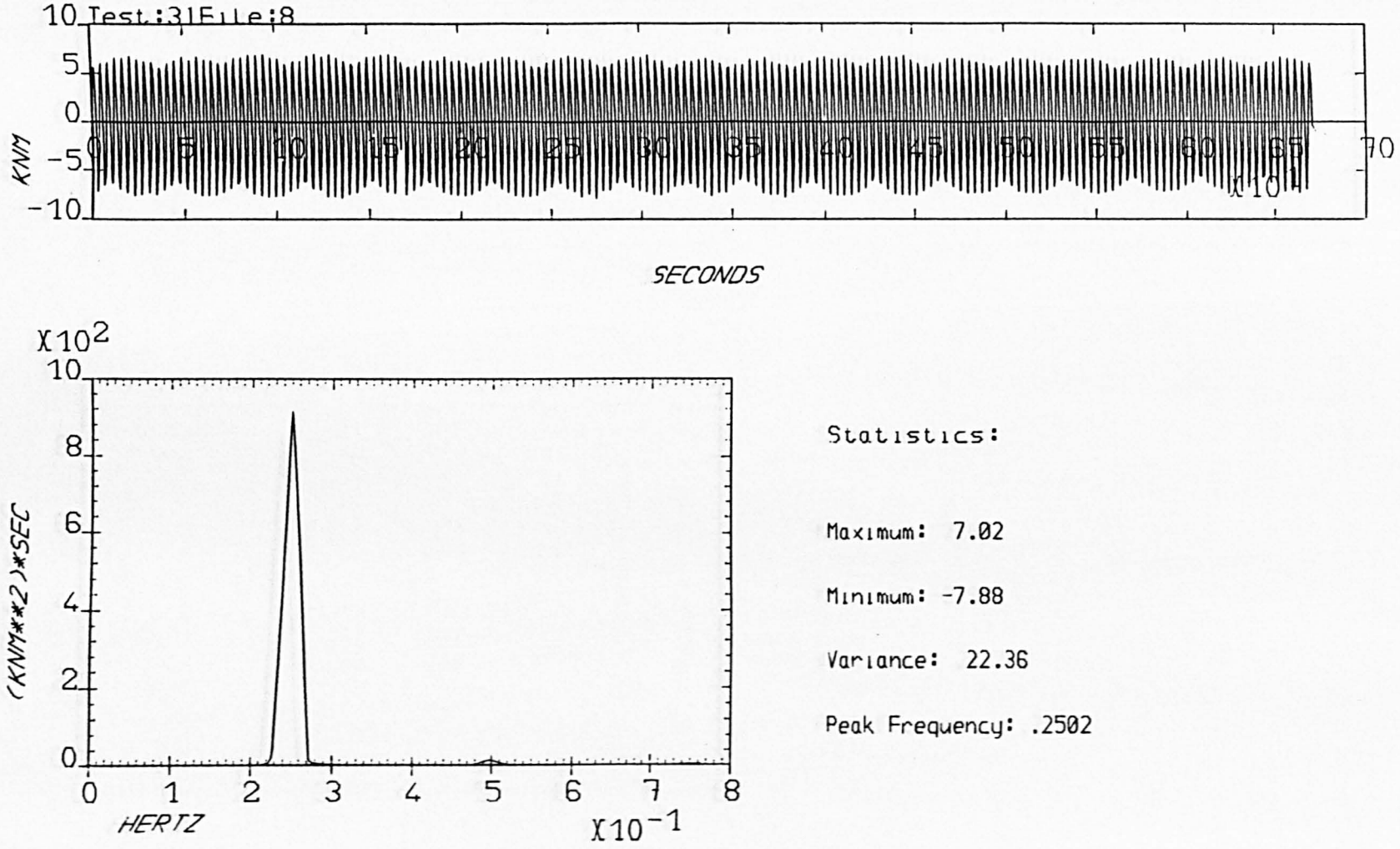
Test:3 File:8
10
5
0
-5
-10
KNM
0
5
10
15
20
25
30
35
40
45
50
55
60
65
70
X10
SECONDS
X10^2
10
8
6
4
2
0
(KNM**2)*SEC
0
1
2
3
4
5
6
7
8
HERTZ
X10^-1
Statistics:
Maximum: 7.02
Minimum: -7.88
Variance: 22.36
Peak Frequency: .2502
VTBEND. AT POSITION 1 WITH 1 HOSES IN REGULAR WAVES F(HZ)= .250 H(M)= 1.01

Figure A3.1.4

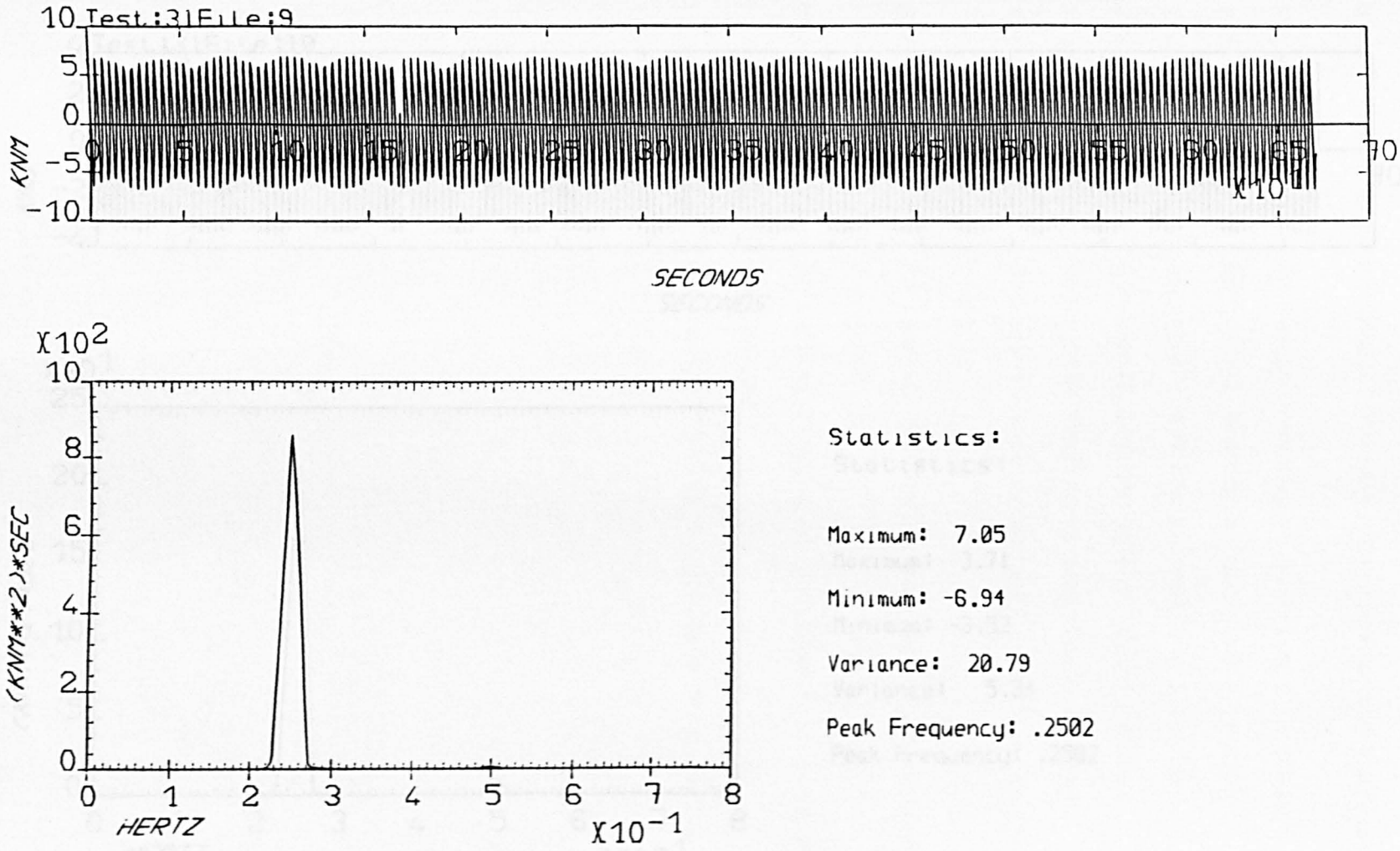
Test:3 File:9
10
5
0
-5
-10
KNM
0
5
10
15
20
25
30
35
40
45
50
55
60
65
70
X10
SECONDS
X10^2
10
8
6
4
2
0
(KNM**2)*SEC
0
1
2
3
4
5
6
7
8
HERTZ
X10^-1
Statistics:
Maximum: 7.05
Minimum: -6.94
Variance: 20.79
Peak Frequency: .2502
VTBEND. AT POSITION 2 WITH 1 HOSES IN REGULAR WAVES F(HZ)= .250 H(M)= 1.01

Figure A3.1.5

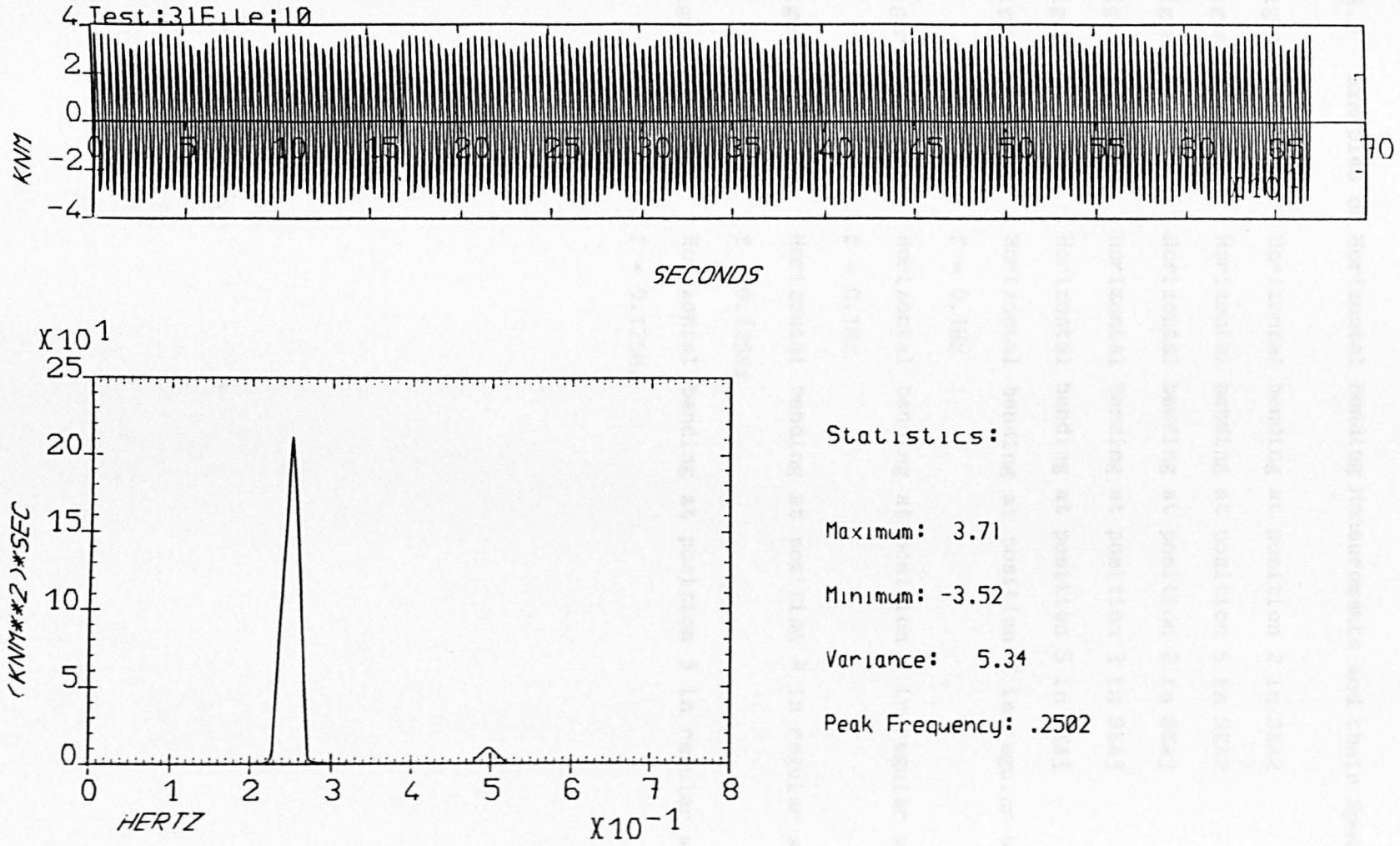
4 Test:3 File:10
2
0
-2
-4
KN/M
0
5
10
15
20
25
30
35
40
45
50
55
60
65
70
X10^1
SECONDS
X10^1
25
20
15
10
5
0
(KN/M**2)*SEC
0
1
2
3
4
5
6
7
8
HERTZ
X10^-1
Statistics:
Maximum: 3.71
Minimum: -3.52
Variance: 5.34
Peak Frequency: .2502
VTBEND. AT POSITION 3 WITH 1 HOSES IN REGULAR WAVES F(HZ)= .250 H(M)= 1.01

Figure A3.1.6

A3.2 Examples of Horizontal Bending Measurements and their Spectra

Figure A3.2.1 Horizontal bending at position 2 in SEA2

Figure A3.2.2 Horizontal bending at position 5 in SEA2

Figure A3.2.3 Horizontal bending at position 2 in SEA3

Figure A3.2.4 Horizontal bending at position 3 in SEA3

Figure A3.2.5 Horizontal bending at position 5 in SEA3

Figure A3.2.6 Horizontal bending at position 2 in regular waves with f = 0.1Hz

Figure A3.2.7 Horizontal bending at position 4 in regular waves with f = 0.1Hz

Figure A3.2.8 Horizontal bending at position 4 in regular waves with f = 0.125Hz

Figure A3.2.9 Horizontal bending at position 5 in regular waves with f = 0.125Hz

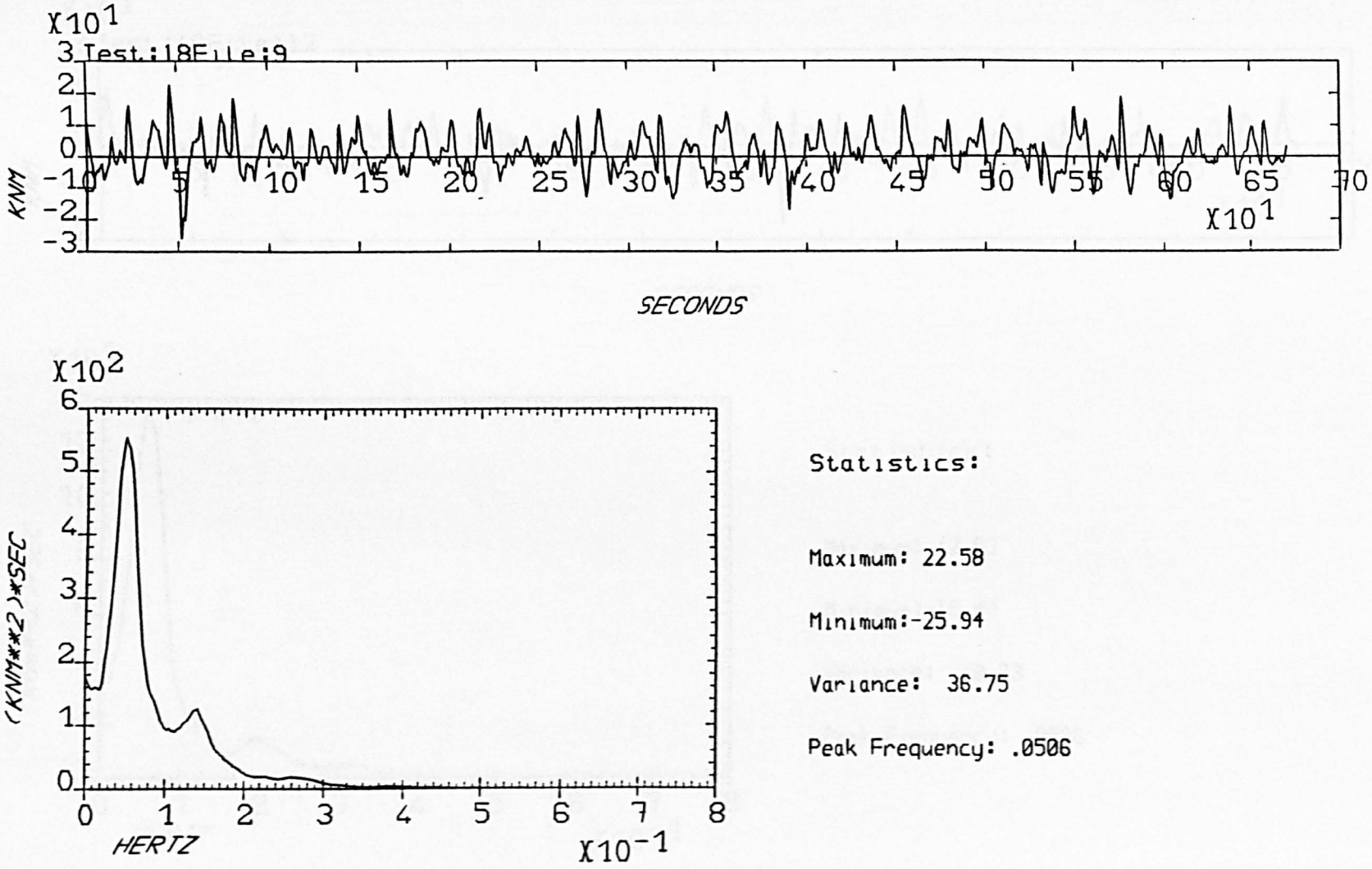
X10^1
Test:18File:9
KNM
SECONDS
X10^1
X10^2
(KNM**2)*SEC
HERTZ
X10^-1
Statistics:
Maximum: 22.58
Minimum:-25.94
Variance: 36.75
Peak Frequency: .0506
HZBEND. AT POSITION 2 WITH 1 HOSES IN A 1.8M SEA

Figure A3.2.1

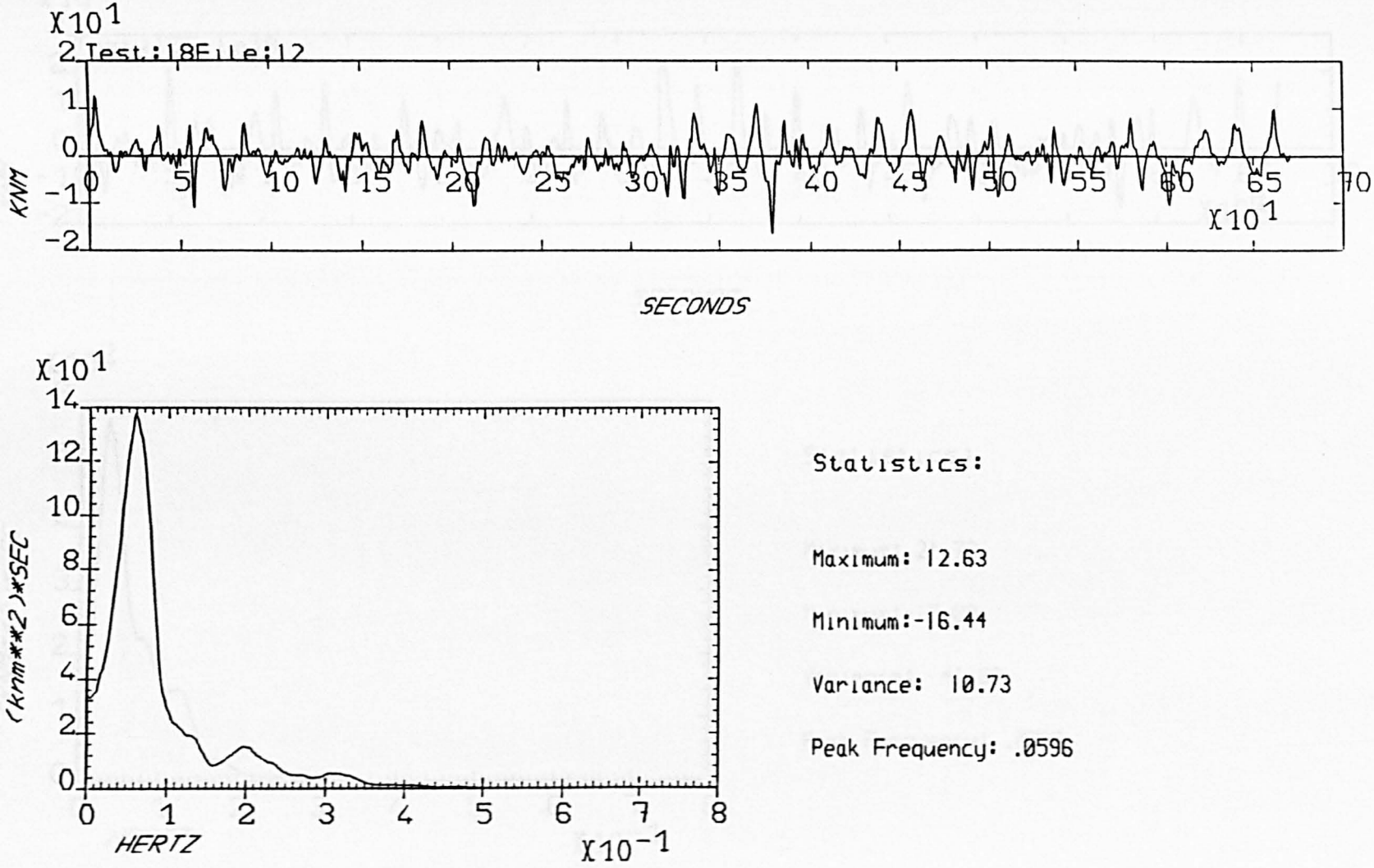
X10 1
Test:18File:12
KNM
SECONDS
X10 1
X10 1
(KNM**2)*SEC
HERTZ
X10 -1
Statistics:
Maximum: 12.63
Minimum:-16.44
Variance: 10.73
Peak Frequency: .0596
HZBEND. AT POSITION 5 WITH 1 HOSES IN A 1.8M SEA

Figure A3.2.2

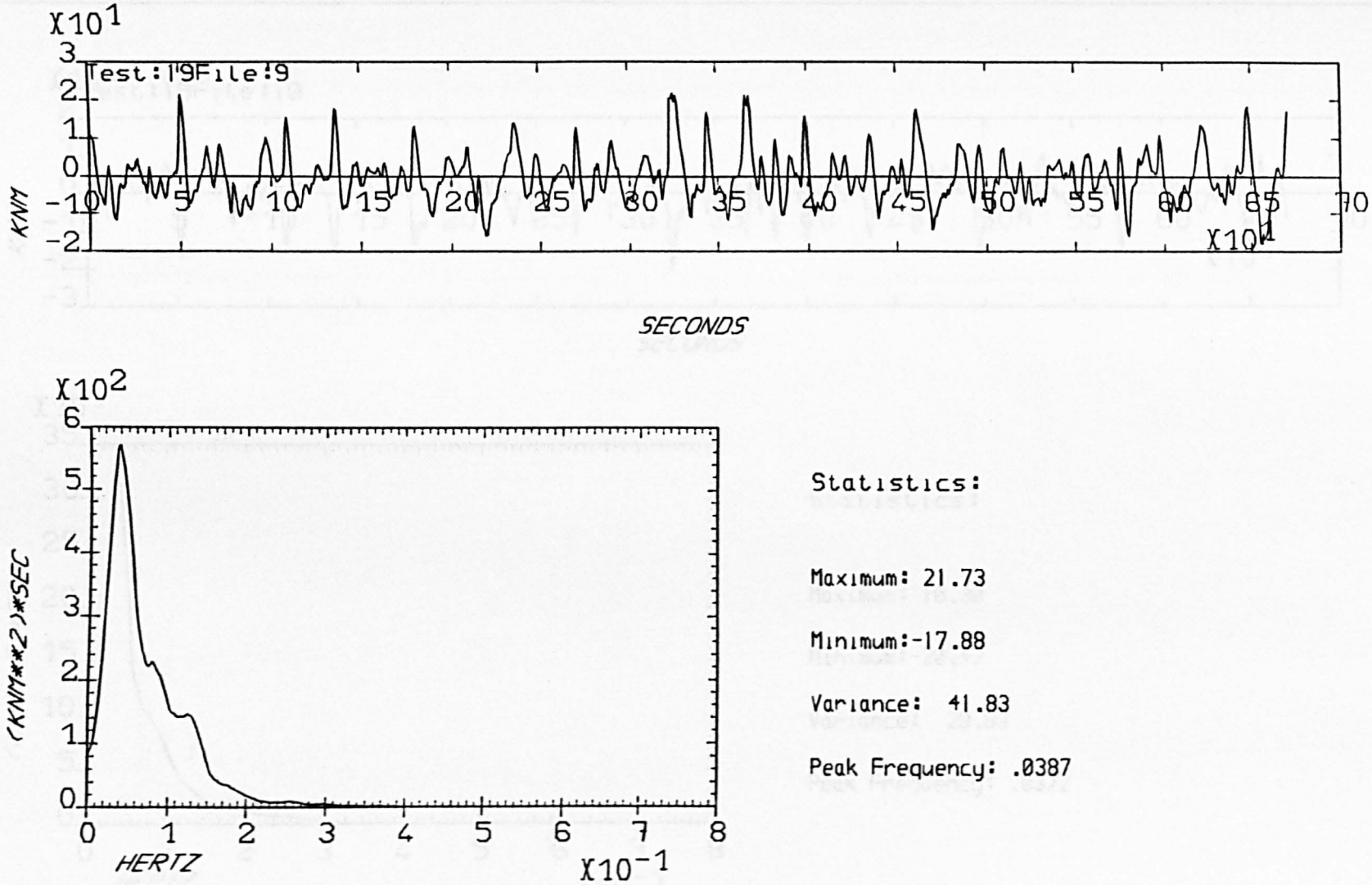
X10^1
Test:19File:9
KNM
SECONDS
X10^2
(KNM**2)*SEC
HERTZ
X10^-1
Statistics:
Maximum: 21.73
Minimum:-17.88
Variance: 41.83
Peak Frequency: .0387
HZBEND. AT POSITION 2 WITH 1 HOSES IN A 1.4M SEA

Figure A3.2.3

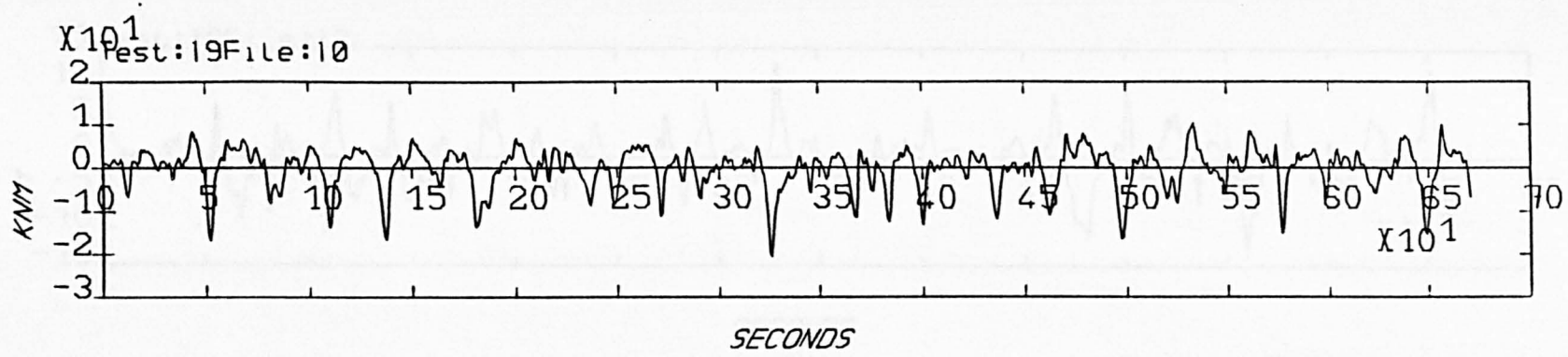

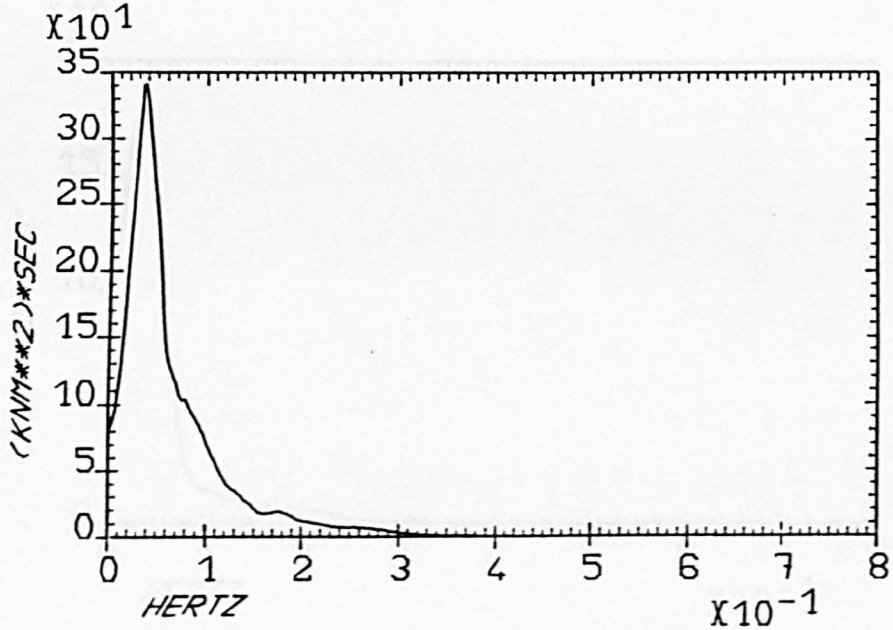

Statistics:

Maximum: 10.30

Minimum:-20.47

Variance: 20.83

Peak Frequency: .0372

HZBEND. AT POSITION 3 WITH 1 HOSES IN A 1.4M SEA

Figure A3.2.4

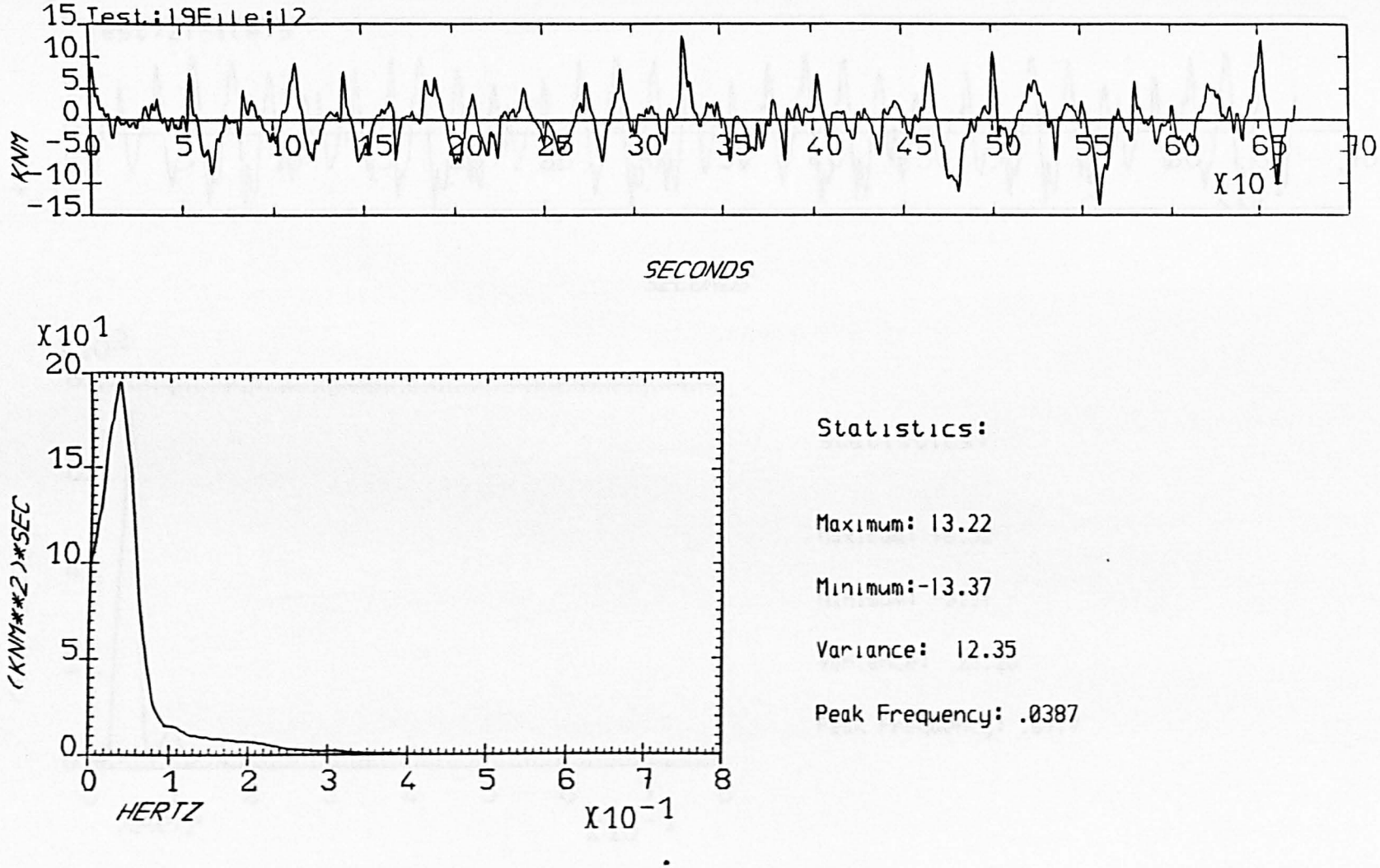
Test:19File:12
15
10
5
0
-5
-10
-15
KNM
5
10
15
20
25
30
35
40
45
50
55
60
65
70
X10 1
SECONDS
X10 1
20
15
10
5
0
(KNM**2)*SEC
0
1
2
3
4
5
6
7
8
HERTZ
X10 -1
Statistics:
Maximum: 13.22
Minimum:-13.37
Variance: 12.35
Peak Frequency: .0387
HZBEND. AT POSITION 5 WITH 1 HOSES IN A 1.4M SEA

Figure A3.2.5

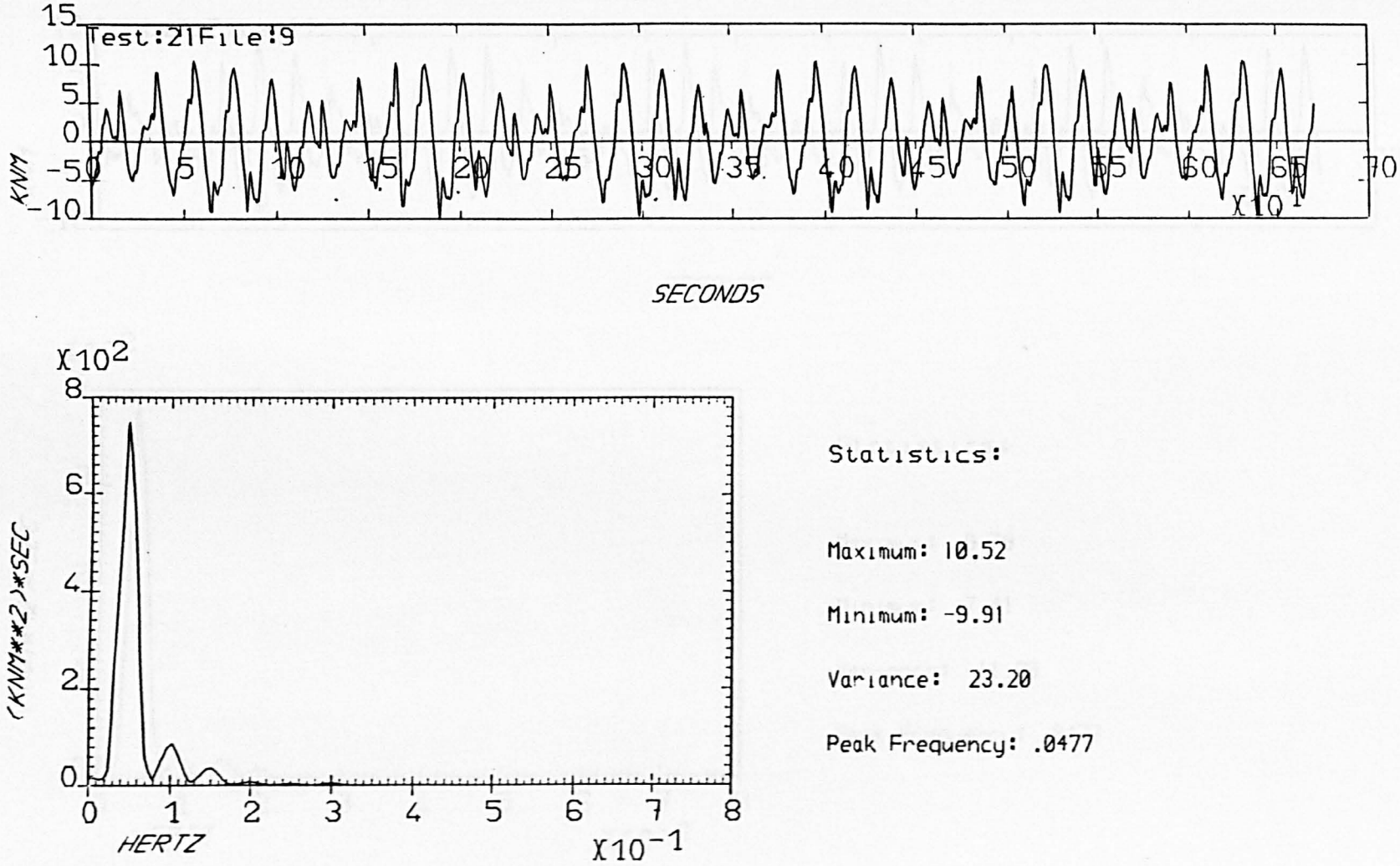
Test:21File:9
KNM
SECONDS
X10^1
X10^2
(KNM**2)*SEC
HERTZ
X10^-1
Statistics:
Maximum: 10.52
Minimum: -9.91
Variance: 23.20
Peak Frequency: .0477
HZBEND. AT POSITION 2 WITH 1 HOSES IN REGULAR WAVES F(HZ)= .100 H(M)= .60

Figure A3.2.6

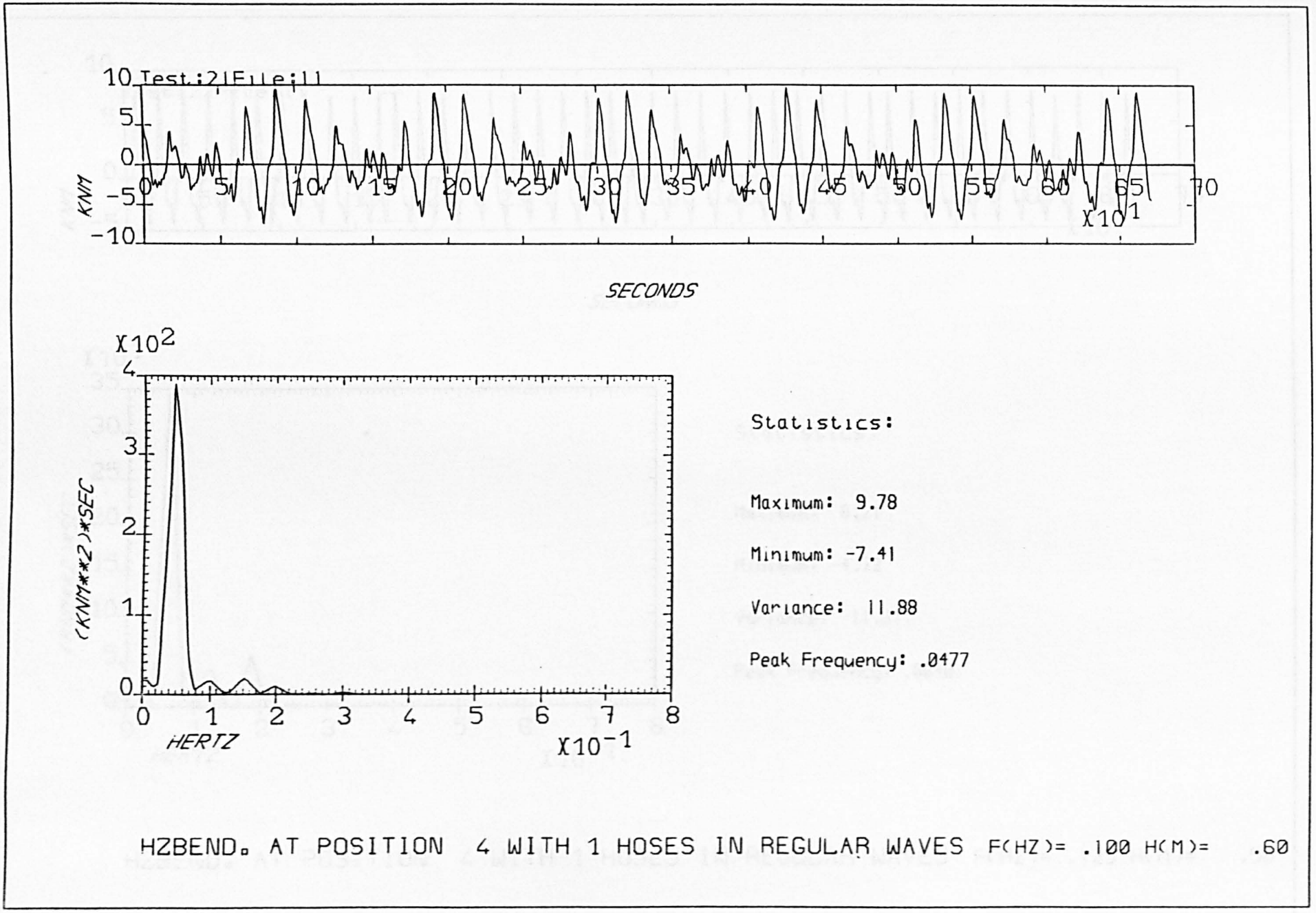
Test:2|File:11
KNM
10
5
0
-5
-10
0
5
10
15
20
25
30
35
40
45
50
55
60
65
70
X10^1
SECONDS
X10^2
(KNM**2)*SEC
4
3
2
1
0
0
1
2
3
4
5
6
7
8
HERTZ
X10^-1
Statistics:
Maximum: 9.78
Minimum: -7.41
Variance: 11.88
Peak Frequency: .0477
HZBEND. AT POSITION 4 WITH 1 HOSES IN REGULAR WAVES F(HZ)= .100 H(M)= .60

Figure A3.2.7

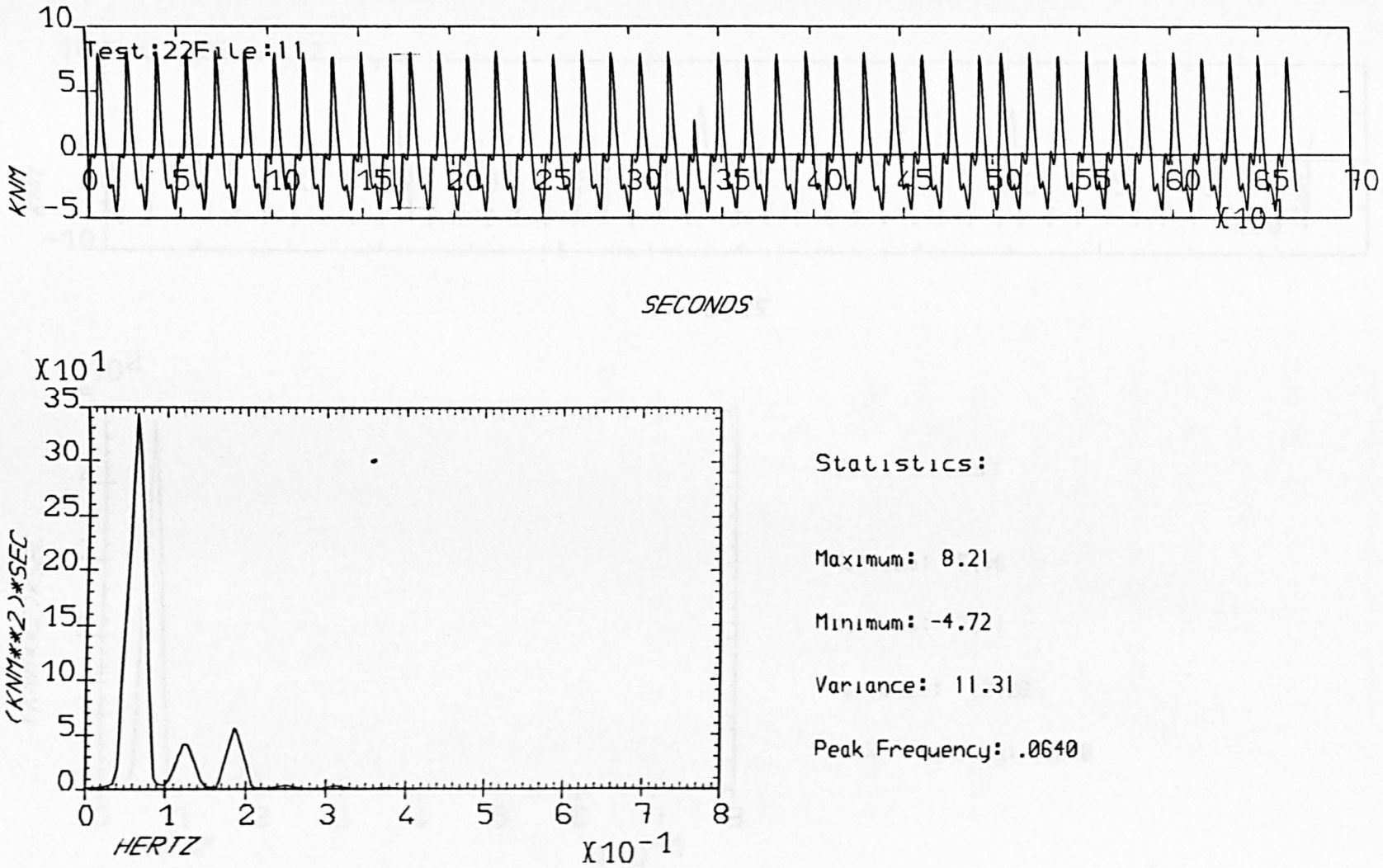
Test:22File:11
10
5
0
-5
KN/M
0 5 10 15 20 25 30 35 40 45 50 55 60 65 70
X10^1
SECONDS
X10^1
35
30
25
20
15
10
5
0
(KN/M**2)**2*SEC
0 1 2 3 4 5 6 7 8
HERTZ
X10^-1
Statistics:
Maximum: 8.21
Minimum: -4.72
Variance: 11.31
Peak Frequency: .0640
HZBEND. AT POSITION 4 WITH 1 HOSES IN REGULAR WAVES F(HZ)= .125 H(M)= .58

Figure A3.2.8

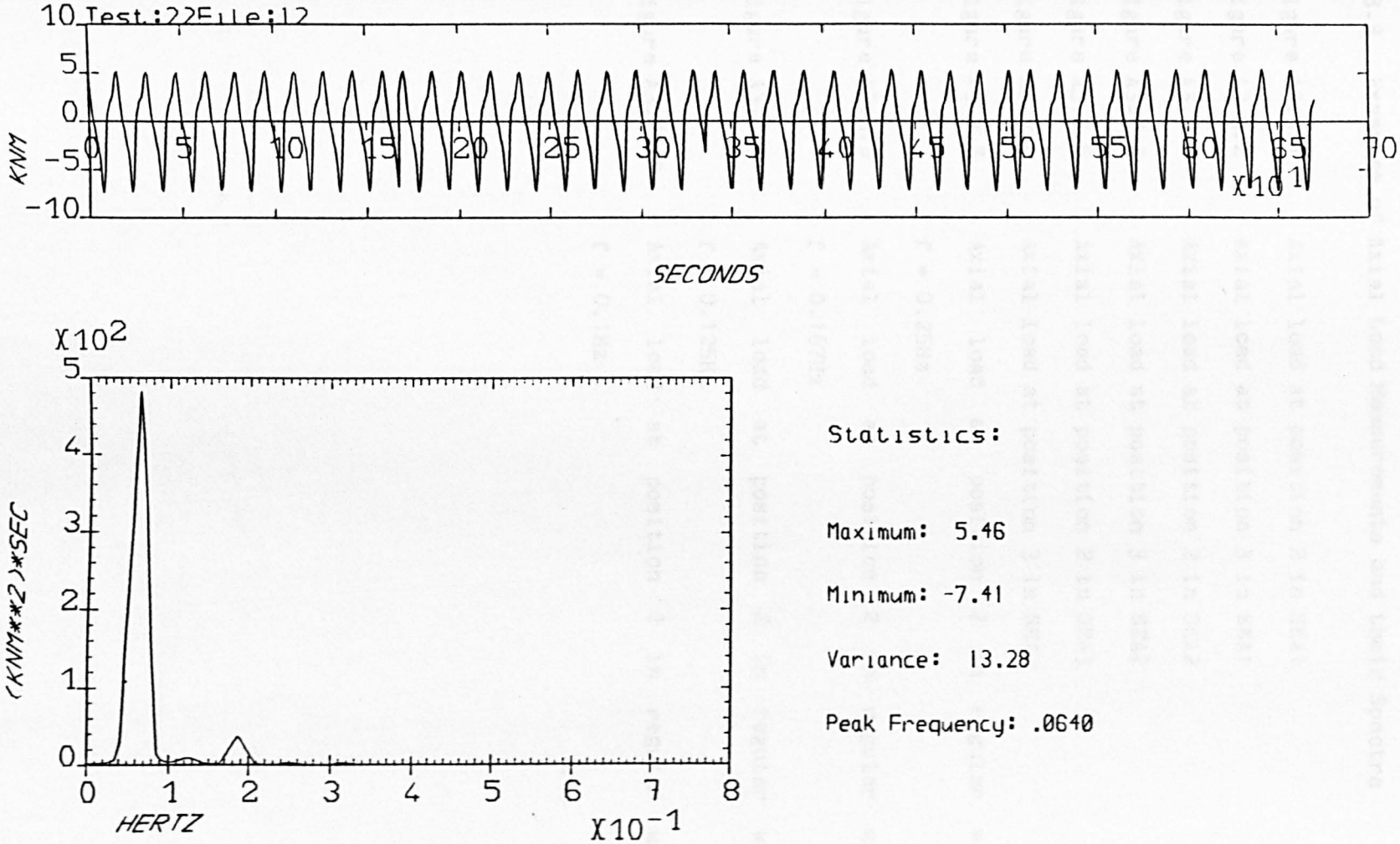
Test:22File:12
10
5
0
-5
-10
KNM
0
5
10
15
20
25
30
35
40
45
50
55
60
65
70
X10^1
SECONDS
X10^2
5
4
3
2
1
0
(KNM**2)*SEC
0
1
2
3
4
5
6
7
8
HERTZ
X10^-1
Statistics:
Maximum: 5.46
Minimum: -7.41
Variance: 13.28
Peak Frequency: .0640
HZBEND. AT POSITION 5 WITH 1 HOSES IN REGULAR WAVES F(HZ)= .125 H(M)= .58

Figure A3.2.9

A3.3 Examples of Axial Load Measurements and their Spectra

Figure A3.3.1 Axial load at position 2 in SEA1

Figure A3.3.2 Axial load at position 3 in SEA1

Figure A3.3.3 Axial load at position 2 in SEA2

Figure A3.3.4 Axial load at position 3 in SEA2

Figure A3.3.5 Axial load at position 2 in SEA3

Figure A3.3.6 Axial load at position 3 in SEA3

Figure A3.3.7 Axial load at position 2 in regular waves with f = 0.25Hz

Figure A3.3.8 Axial load at position 2 in regular waves with f = 0.167Hz

Figure A3.3.9 Axial load at position 2 in regular waves with f = 0.125Hz

Figure A3.3.10 Axial load at position 2 in regular waves with f = 0.1Hz

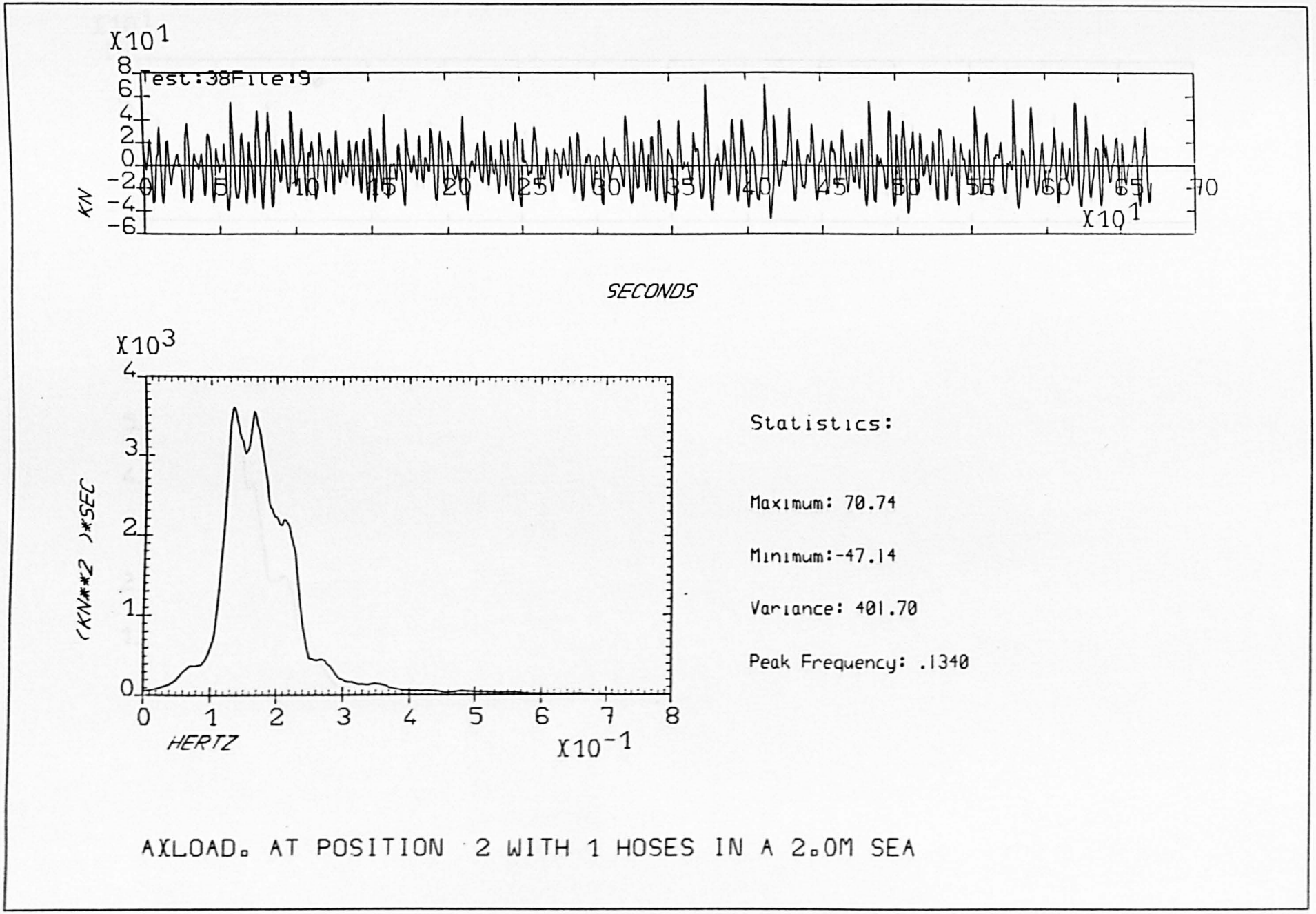
X10 1
Test:38File:9
KN
SECONDS
X10 1
X10 3
(KN**2)*SEC
HERTZ
X10 -1
Statistics:
Maximum: 70.74
Minimum:-47.14
Variance: 401.70
Peak Frequency: .1340
AXLOAD. AT POSITION 2 WITH 1 HOSES IN A 2.0M SEA

Figure A3.3.1

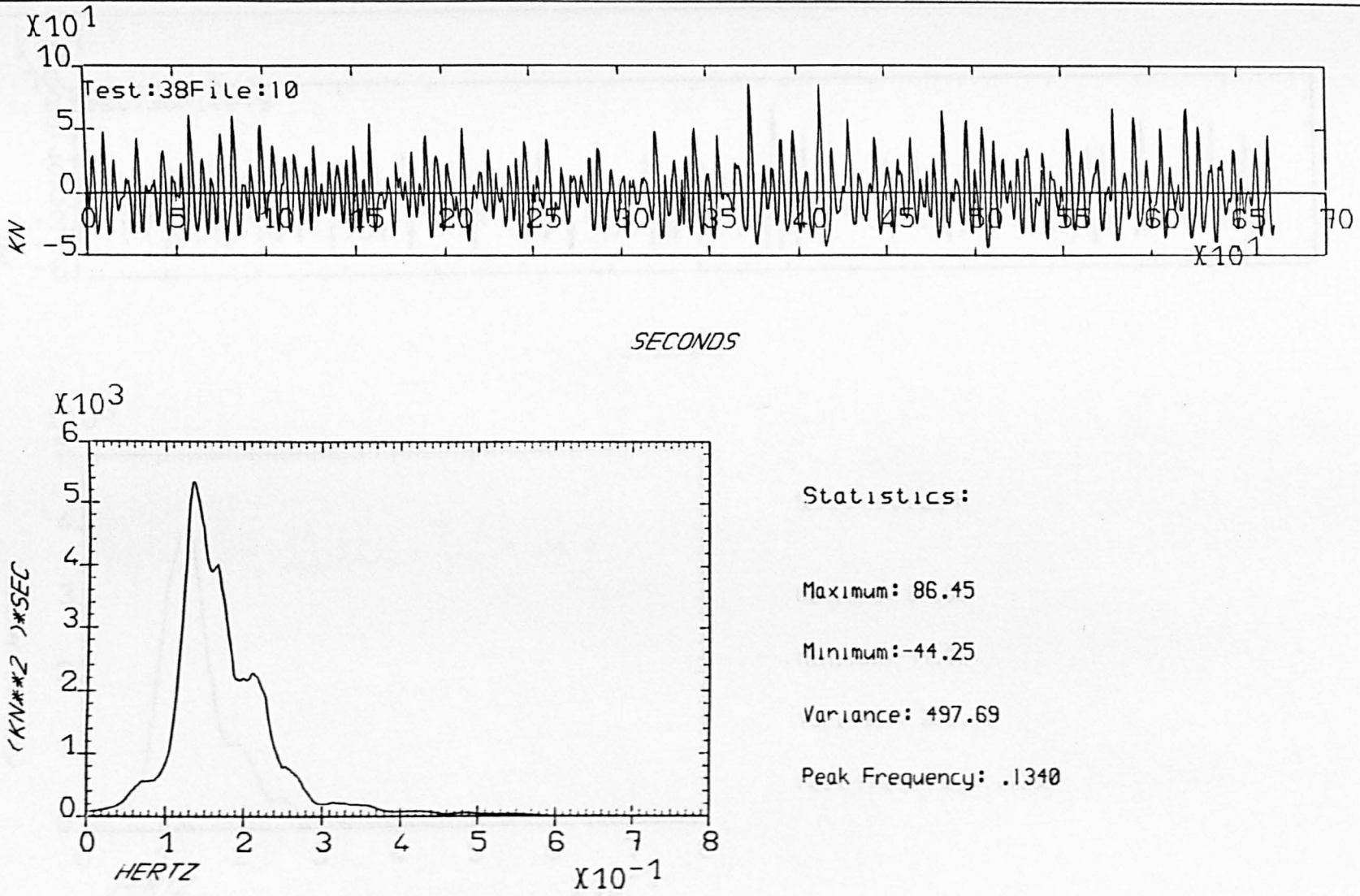
X10 1
10
5
0
-5
KN
Test:38File:10
0 5 10 15 20 25 30 35 40 45 50 55 60 65 70
X10 1
SECONDS
X10 3
6
5
4
3
2
1
0
(KN**2)*SEC
0 1 2 3 4 5 6 7 8
HERTZ
X10 -1
Statistics:
Maximum: 86.45
Minimum:-44.25
Variance: 497.69
Peak Frequency: .1340
AXLOAD. AT POSITION 3 WITH 1 HOSES IN A 2.0M SEA

Figure A3.3.2

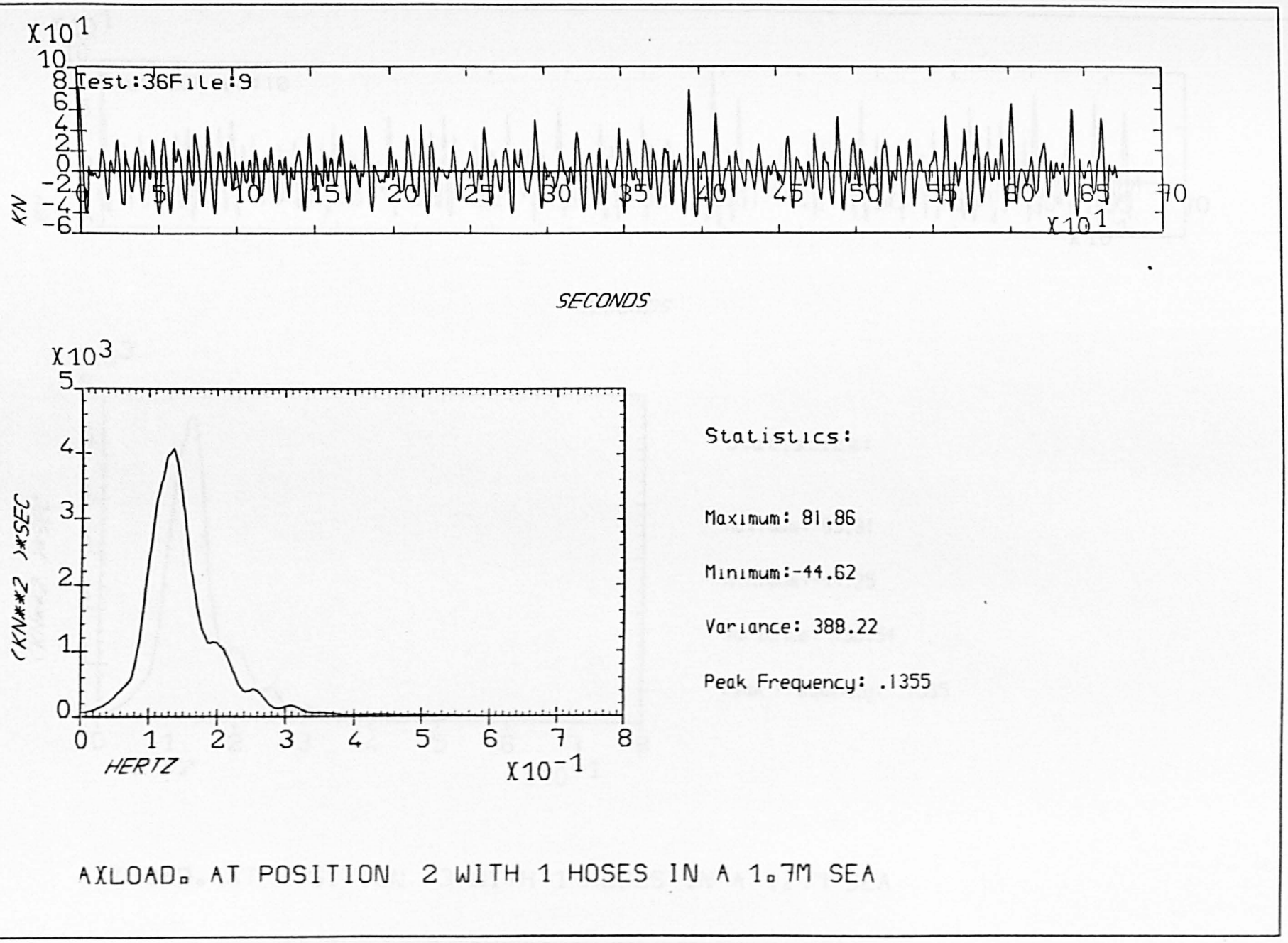
X10^1
Test:36File:9
KN
SECONDS
X10^1
X10^3
(KN**2)*SEC
HERTZ
X10^-1
Statistics:
Maximum: 81.86
Minimum:-44.62
Variance: 388.22
Peak Frequency: .1355
AXLOAD. AT POSITION 2 WITH 1 HOSES IN A 1.7M SEA

Figure A3.3.3

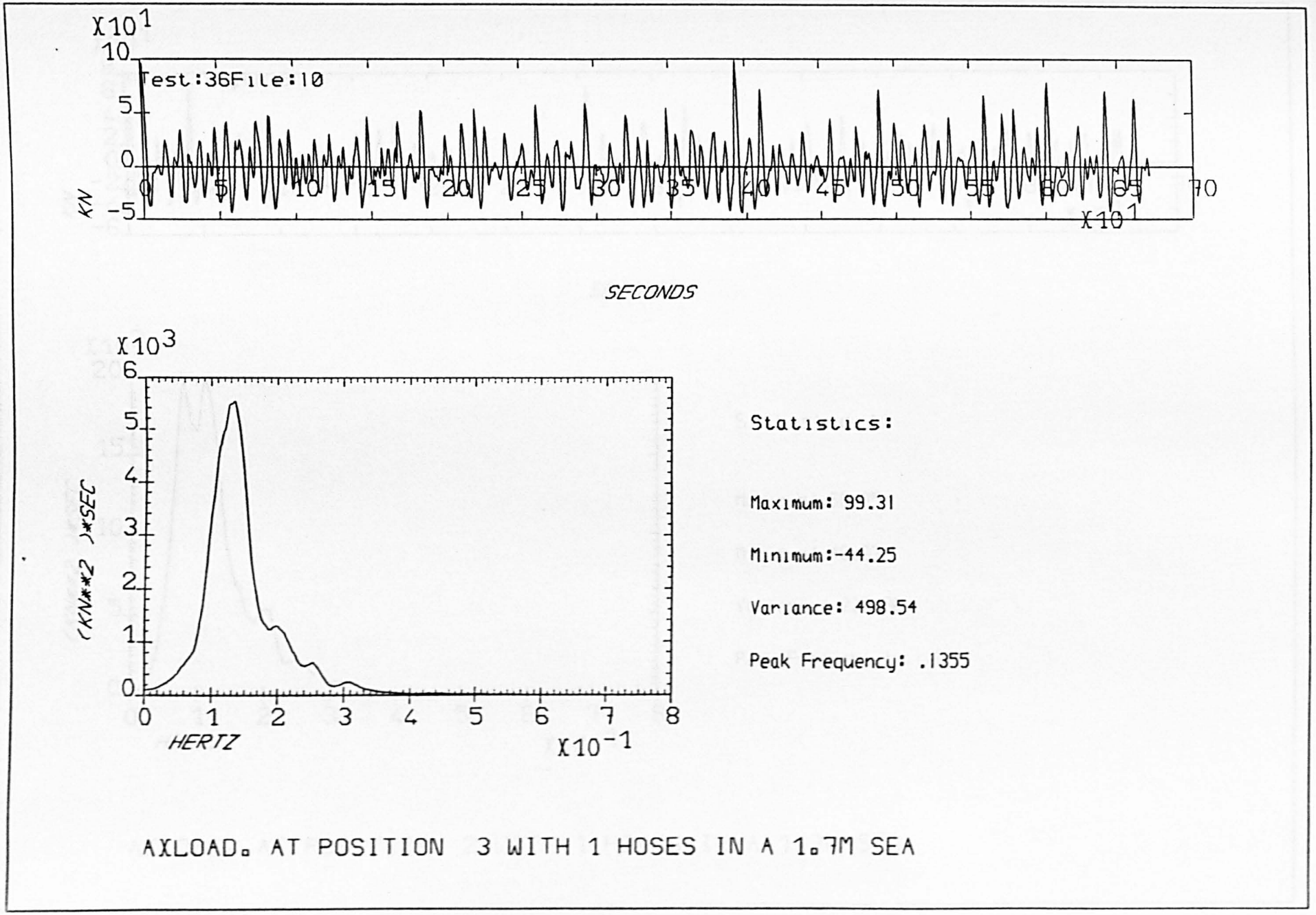
X10^1
Test:36File:10
KN
SECONDS
X10^-1
X10^3
(KN**2)*SEC
HERTZ
X10^-1
Statistics:
Maximum: 99.31
Minimum:-44.25
Variance: 498.54
Peak Frequency: .1355
AXLOAD. AT POSITION 3 WITH 1 HOSES IN A 1.7M SEA

Figure A3.3.4

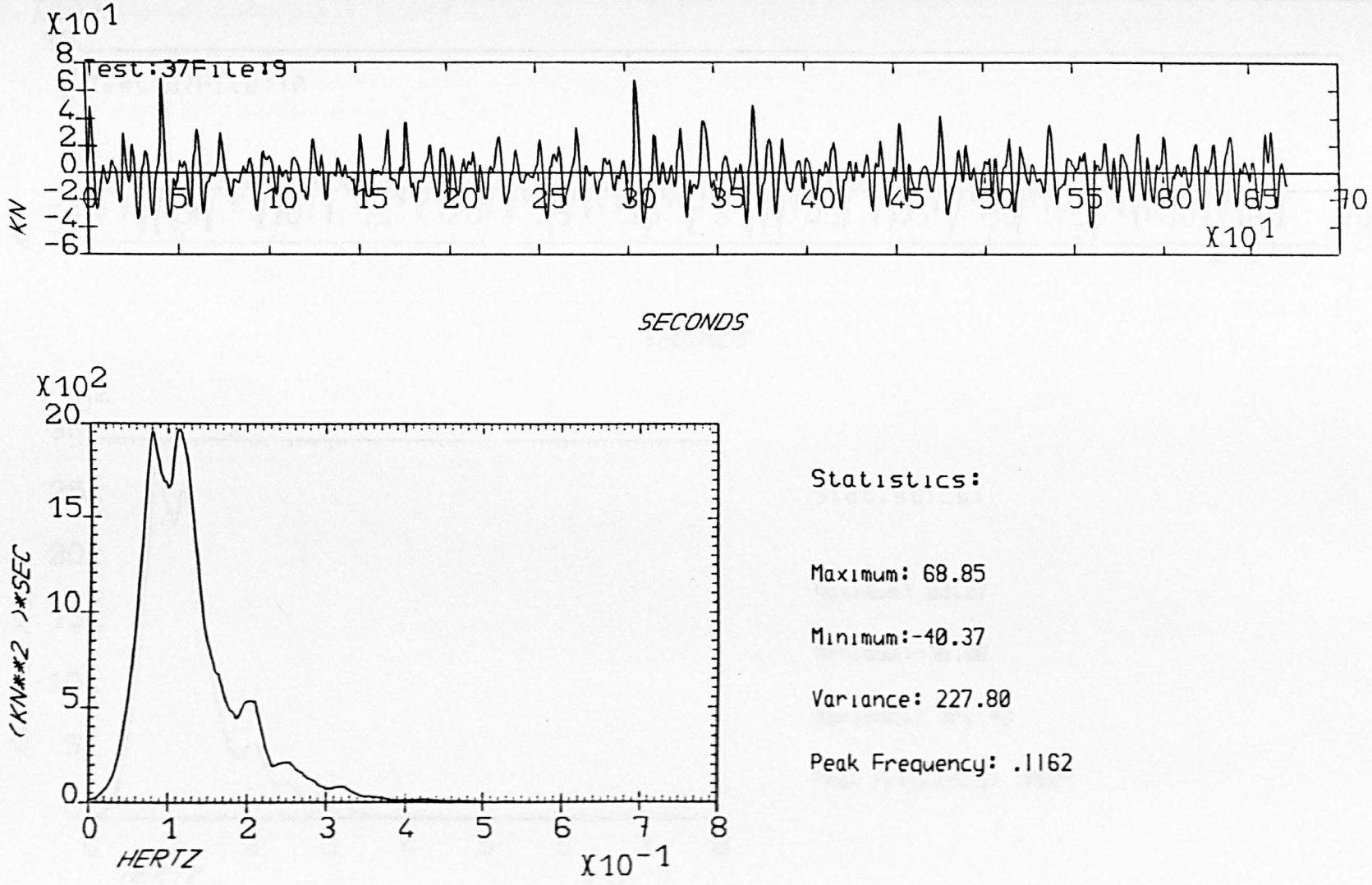
X10^1
Test:37File:9
KN
SECONDS
X10^1
X10^2
(KN**2)*SEC
HERTZ
X10^-1
Statistics:
Maximum: 68.85
Minimum:-40.37
Variance: 227.80
Peak Frequency: .1162
AXLOAD. AT POSITION 2 WITH 1 HOSES IN A 1.3M SEA

Figure A3.3.5

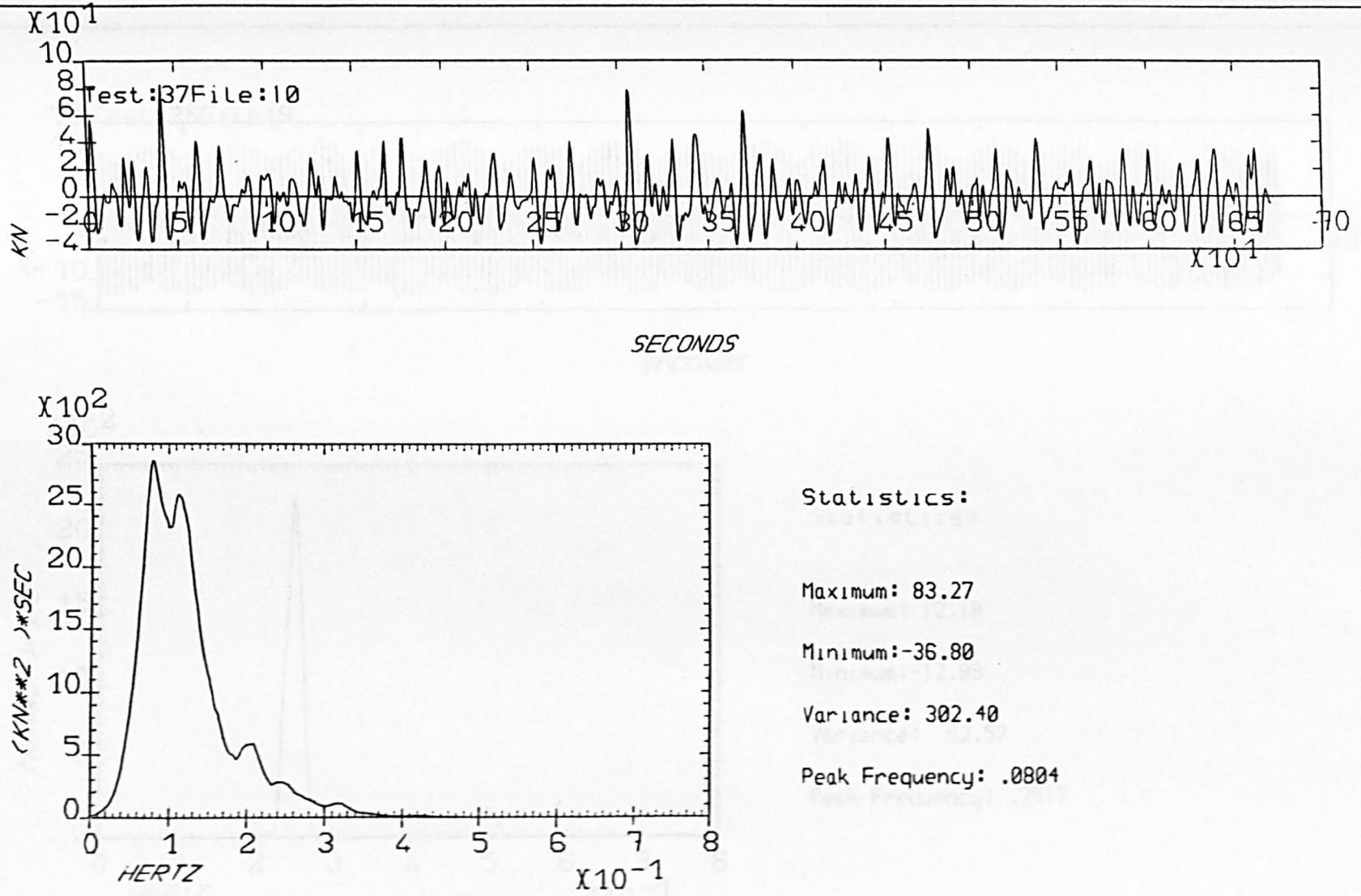
X10 1
10
8
6
4
2
0
-2
-4
Test:37File:10
KN
0 5 10 15 20 25 30 35 40 45 50 55 60 65 70
X10 1
SECONDS
X10 2
30
25
20
15
10
5
0
(KN**2)*SEC
0 1 2 3 4 5 6 7 8
HERTZ
X10 -1
Statistics:
Maximum: 83.27
Minimum:-36.80
Variance: 302.40
Peak Frequency: .0804
AXLOAD. AT POSITION 3 WITH 1 HOSES IN A 1.3M SEA

Figure A3.3.6

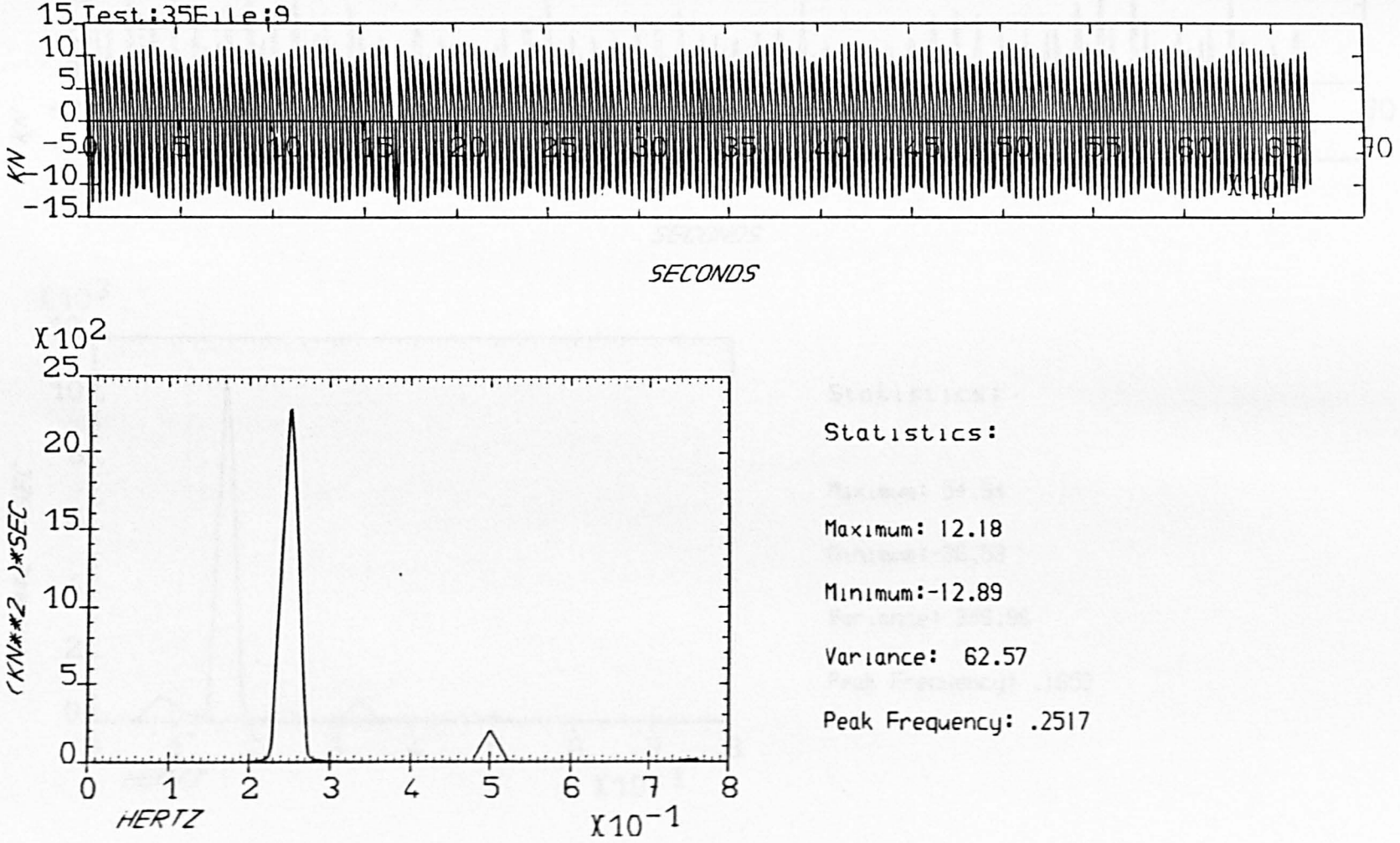
Test:35File:9
15
10
5
0
-5
-10
-15
KN
0
5
10
15
20
25
30
35
40
45
50
55
60
65
70
X10
SECONDS
X10^2
25
20
15
10
5
0
(KN**2)*SEC
0
1
2
3
4
5
6
7
8
HERTZ
X10^-1
Statistics:
Maximum: 12.18
Minimum:-12.89
Variance: 62.57
Peak Frequency: .2517
AXLOAD. AT POSITION 2 WITH 1 HOSES IN REGULAR WAVES F(HZ)= .250 H(M)= .88

Figure A3.3.7

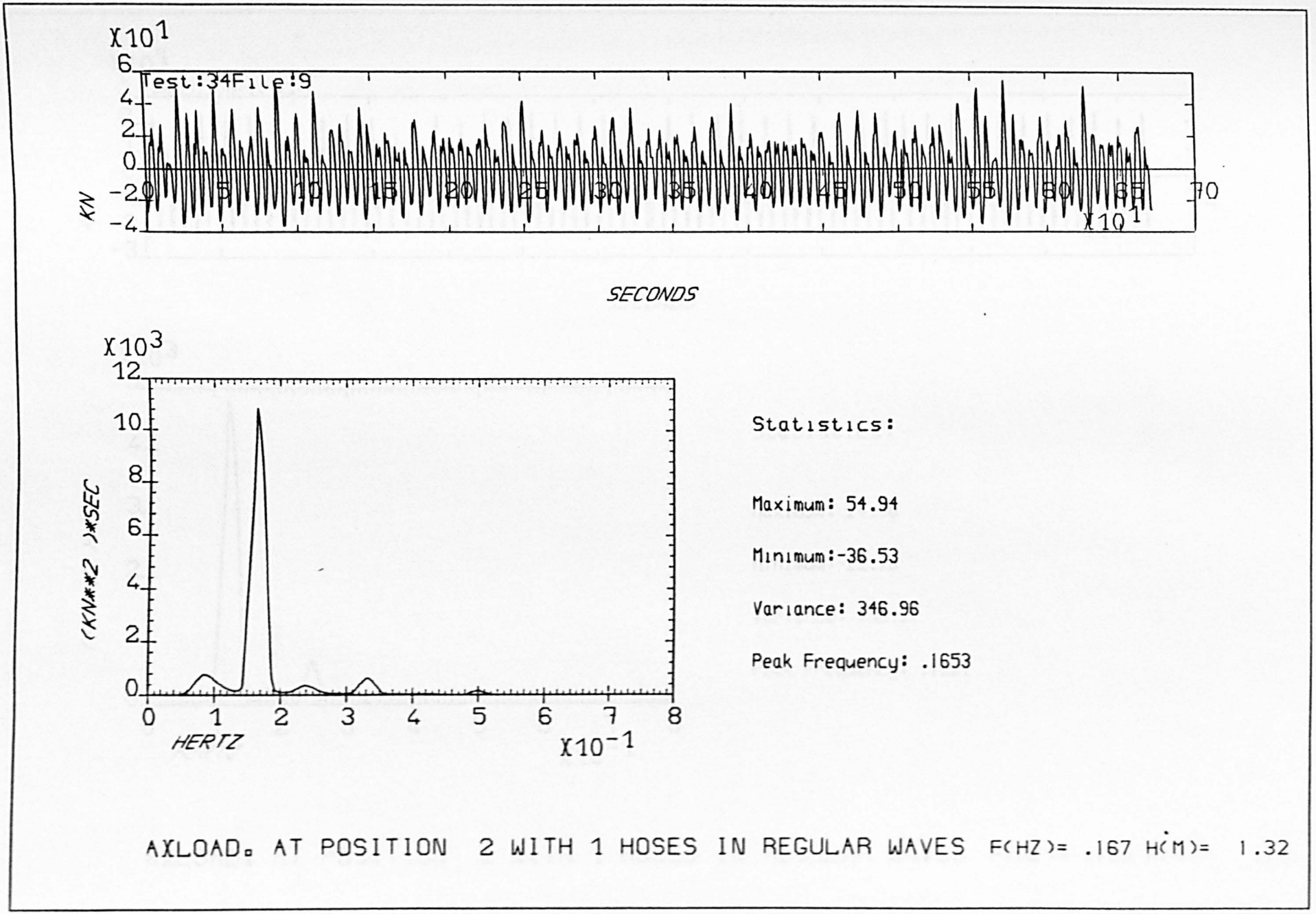
X10^1
Test:34File:9
KN
SECONDS
X10^3
(KN**2)*SEC
HERTZ
X10^-1
Statistics:
Maximum: 54.94
Minimum:-36.53
Variance: 346.96
Peak Frequency: .1653
AXLOAD. AT POSITION 2 WITH 1 HOSES IN REGULAR WAVES F(HZ)= .167 H(M)= 1.32

Figure A3.3.8

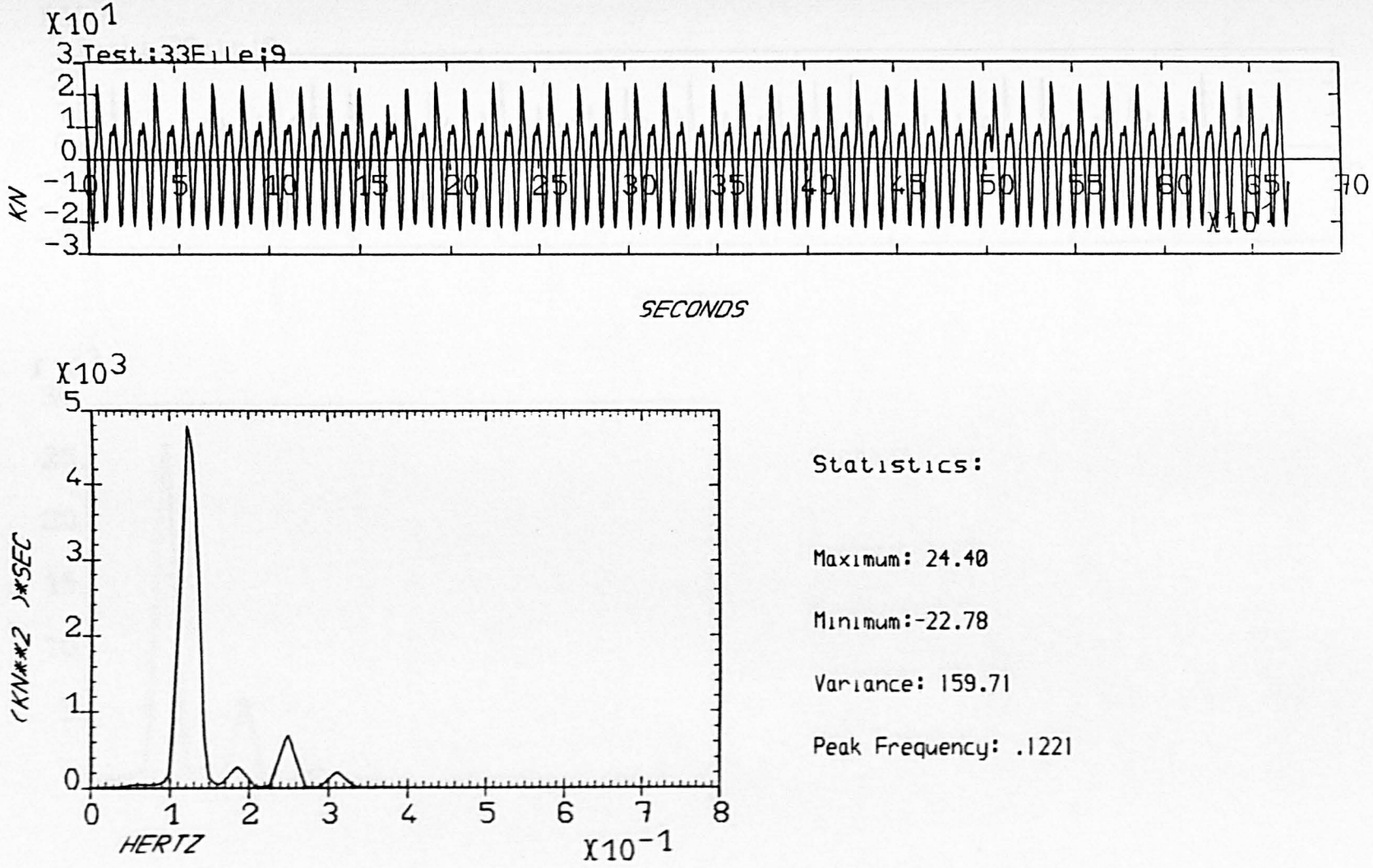
X10 1
3 Test:33File:9
2
1
0
-1
-2
-3
KN
0 5 10 15 20 25 30 35 40 45 50 55 60 65 70
X10 1
SECONDS
X10 3
5
4
3
2
1
0
(KN**2)*SEC
0 1 2 3 4 5 6 7 8
HERTZ
X10 -1
Statistics:
Maximum: 24.40
Minimum:-22.78
Variance: 159.71
Peak Frequency: .1221
AXLOAD. AT POSITION 2 WITH 1 HOSES IN REGULAR WAVES F(HZ)= .125 H(M)= .70

Figure A3.3.9

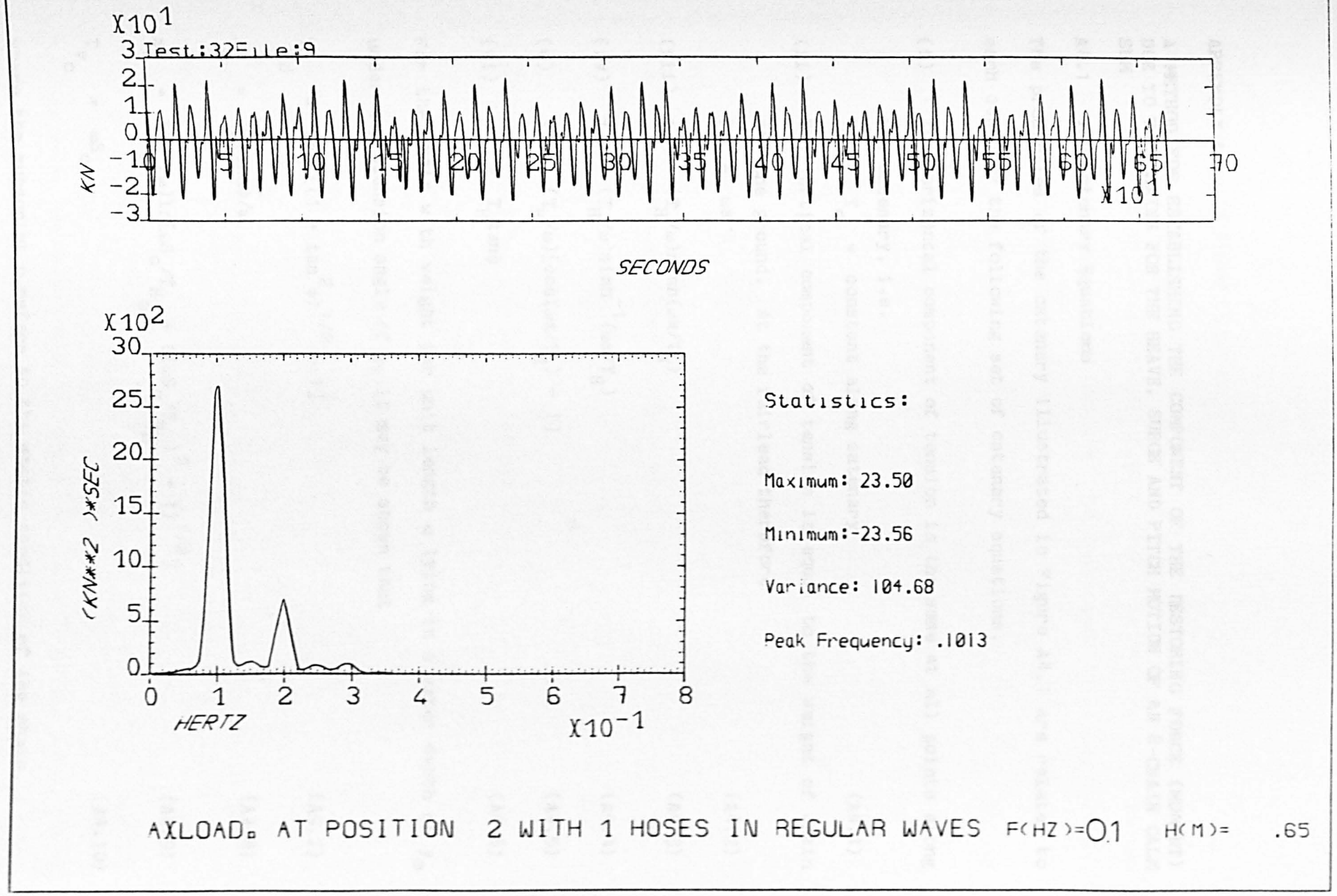

Figure A3.3.10

APPENDIX A4

A METHOD FOR ESTABLISHING THE COMPONENT OF THE RESTORING FORCE (MOMENT) DUE TO THE CHAINS FOR THE HEAVE, SURGE AND PITCH MOTION OF AN 8-CHAIN CALM SBM

A4.1 The Catenary Equations

The properties of the catenary illustrated in Figure A4.1 are related to each other by the following set of catenary equations.

(i) The horizontal component of tension is the same at all points along the catenary, i.e.

$$T_H = T_c = \text{constant along catenary} \qquad (A4.1)$$

(ii) The vertical component of tension is equal to the weight of chain off the ground. At the fairlead therefore

$$T_V = \omega s \qquad (A4.2)$$

(iii) $$s = (T_H/\omega)\sinh(\omega x/T_H) \qquad (A4.3)$$

(iv) $$x = (T_H/\omega)\sinh^{-1}(\omega s/T_H) \qquad (A4.4)$$

(v) $$y = (T_H/\omega)[\cos(\omega x/T_H) - 1] \qquad (A4.5)$$

(vi) $$\omega s = T_H \tan\phi \qquad (A4.6)$$

For the chain with weight per unit length ω lying in a water depth of y_o under a pretension angle of ϕ, it may be shown that

$$T_{H_o} = \omega y_o/[(1 + \tan^2\phi)^{1/2} - 1] \qquad (A4.7)$$

$$S_o = T_{H_o} \tan\phi/\omega \qquad (A4.8)$$

$$x_o = (T_{H_o}/\omega)\ln[\omega S_o/T_{H_o} + ((\omega S_o/T_{H_o})^2 + 1)^{1/2}] \qquad (A4.9)$$

$$T_{V_o} = \omega S_o \qquad (A4.10)$$

where the subscript o refers to the static condition of the chain.

A4.2 Restoring Force in Heave

Consider the vertical (heave) displacement y of a catenary chain from its static position as illustrated in Figure A4.2. We require to establish the increase in the vertical component of chain tension at the fairlead due to the displacement y. From geometry

$$S_1 = S_o + (x_1 - x_o) \tag{A4.11}$$

where subscript 1 refers to the displaced condition. Therefore

$$x_1 = S_1 - S_o + x_o \tag{A4.12}$$

From equation (A4.4)

$$x_1 = (T_{H_1}/\omega)\sinh^{-1}(\omega S_1/T_{H_1}) \tag{A4.13}$$

From the catenary equations it may be shown that

$$T_{H_1} = (T_{V_1}^2 - \omega y_1^2)/2\omega y_1 \tag{A4.14}$$

Substitution for T_{H_1} in equation (A4.13) gives

$$x_1 = [(S_1^2 - y_1^2)/2y_1]\sinh^{-1}(2S_1y_1/(S_1^2 - y_1^2)) \tag{A4.15}$$

Substitution for x_1 in equation (A4.11) gives

$$S_1 - S_o + x_o = (1/2y_1)(S_1^2 - y_1^2)\sinh^{-1}(2S_1y_1/(S_1^2 - y_1^2)) \tag{A4.16}$$

By defining $r_1 = S_1/y_o$, $r_o = S_o/y_o$ and $r_y = y_1/y_o$, equation (A4.16) can be rewritten as

$$f(r_1) = r_1 - r_o + x_o/y_o - (1/2r_y)(r_1^2 - r_y^2)\sinh^{-1}(2r_1r_y/(r_1^2 - r_y^2)) = 0 \tag{A4.17}$$

For the given heave displacement y, equation (A4.17) may be solved for r_1 using the Newton-Raphson method. Once r_1 is known then the vertical

component of tension T_{v_1} is obtained from

$$T_{v_1} = \omega S_1 = \omega r_1 y_o \qquad (A4.18)$$

The heave restoring force due to 8 such chains is

$$R_H = 8(T_{v_1} - T_{v_o}) \qquad (A4.19)$$

(as given by equation (6.8) in the main text).

A4.3 Restoring Force in Surge

Figure A4.3 shows the layout of the mooring chains in relation to the direction of surge motion. We require to establish the change in the horizontal component of tension at the fairlead for each chain due to a surge displacement x.

(a) Chain #1

The surge displacement of chain #1 is illustrated in Figure A4.4. From geometry,

$$x_1 - (x + x_o) = S_1 - S_o \qquad (A4.20)$$

i.e.

$$S_1 - S_o + x + x_o = x_1 \qquad (A4.21)$$

From equation (A4.4)

$$x_1 = (T_{H_1}/\omega)\sinh^{-1}(\omega S_1/T_{H_1}) \qquad (A4.22)$$

Also

$$T_{H_1} = [(\omega S_1)^2 - (\omega y_o)^2]/2\omega y_o \qquad (A4.22)$$

Substitution in equation (A4.21) gives

$$S_1 - S_o + x + x_o = [(S_1^2 - y_o^2)/2y_o]\sinh^{-1}[2S_1y_o/(S_1^2 - y_o^2)] \quad (A4.23)$$

Defining $r_1 = S_1/y_o$ and $r_o = S_o/y_o$, equation (A4.23) can be rewritten as

$$f(r_1) = r_1 - r_o + x/y_o + x_o/y_o - \frac{1}{2}(r_1^2-1)\sinh^{-1}[2r_1/(r_1^2-1)] = 0 \quad (A4.24)$$

The values of r_o, x_o and y_o are all constants which are determined by the static conditions. For a given surge displacement x, equation (A4.24) can be solved for r_1 using the Newton-Raphson method. The horizontal component of tension at the fairlead of chain #1 is given by the catenary equation

$$T_{H_1} = \frac{1}{2}\omega y_o(r_1^2-1) \quad (A4.25)$$

The surge restoring force due to chain #1 is then

$$R_1 = T_{H_1}^{\ 1} - T_{H_o} \quad (A4.26)$$

where superscript 1 refers to chain #1.

(b) Chain #2

The surge displacement of chain #2 is illustrated in Figure A4.5. From geometry

$$x_o - (x_1+x) = S_o - S_1 \quad (A4.27)$$

i.e.

$$S_1 - S_o - x + x_o = x_1 \quad (A4.28)$$

In the same way as for chain #1 we get

$$f(r_1) = r_1 - r_o - x/y_o + x_o/y_o - \frac{1}{2}(r_1^2-1)\sinh^{-1}(2r_1/(r_1^2-1)] = 0 \quad (A4.29)$$

Equation (A4.29) can be solved to give r_1; the horizontal component of tension T_{H_1} is obtained using equation (A4.25); the surge restoring force due to chain #2 is then

$$R_2 = -(T_{H_1}^{\ 2} - T_{H_o}) \qquad (A4.30)$$

where superscript 2 refers to chain #2.

(c) Chain #3

For a surge displacement of x, chains #3 undergo an effective displacement of $x\cos45^o$ in the direction of their lines of action. The solution for the displaced condition is then obtained from

$$f(r_1) = r_1 - r_o + x\cos45^o/y_o + x_o/y_o - \frac{1}{2}(r_1^{\ 2}-1)\sinh^{-1}[2r_1/(r_1^{\ 2}-1)] = 0 \qquad (A4.31)$$

Solving equation (A4.31) using the Newton-Raphson method yields the value of $r_1 = S_1/y_o$. The 'horizontal' component of tension T_{H_1} is obtained from equation (A4.25) and the total surge restoring force due to the chains #3 is

$$R_3 = 2(T_{H_1}^{\ 3}\cos\alpha_3 - T_{H_o}\cos45^o) \qquad (A4.32)$$

where α_3 (Figure A4.6) is given by

$$\alpha_3 = 45^o - \sin^{-1}(x\cos45^o/x_1) \qquad (A4.33)$$

where x_1 is obtained using equation (A4.4).

(d) Chain #4

For a surge displacement x, the effective displacement of chains #4 is $-x\cos45^o$ and equation (A4.31) becomes

$$f(r_1) = r_1 - r_o - x\cos45^o/y_o + x_o/y_o - \frac{1}{2}(r_1^{\ 2}-1)\sinh^{-1}[2r_1/(r_1^{\ 2}-1)] = 0 \qquad (A4.34)$$

Equation (A4.34) may be solved for r_1; T_{H_1} is then obtained using (A4.25). The surge restoring force due to chains #4 is

$$R_H = -2(T_{H_1}{}^4 \cos\alpha_4 - T_{H_o} \cos 45^o) \qquad (A4.35)$$

where α_4 (Figure A4.7) is given by

$$\alpha_4 = 45^o + \sin^{-1}(x\cos 45^o / x_1) \qquad (A4.36)$$

where x_1 is obtained using equation (A4.4).

Assuming that the surge restoring forces due to chains #5 are negligible then the total surge restoring force due to the chains is

$$R_s = R_1 + R_2 + R_3 + R_4 \qquad (A4.37)$$

$$= (T_{H_1}{}^1 - T_{H_o}) - (T_{H_1}{}^2 - T_{H_o}) + 2(T_{H_1}{}^3 \cos\alpha_3 - T_{H_o} \cos 45^o)$$

$$- 2(T_{H_1}{}^4 \cos\alpha_4 - T_{H_o} \cos 45^o)$$

$$R_s = T_{H_1}{}^1 - T_{H_1}{}^2 + 2T_{H_1}{}^3 \cos\alpha_3 - 2T_{H_1}{}^4 \cos\alpha_4 \qquad (A4.38)$$

where superscripts 1, 2, 3, 4 refer to the chain numbers in Figure A4.3. (Equation (A4.38) is the same as equation (6.13) in the main text.)

A4.4 Restoring Moment in Pitch

Figure A4.8 shows the SBM and the layout of the mooring chains. It is required to establish the restoring moment due to the chains when the buoy pitches through angle θ.

Consider first the restoring moment due to chains #1 and #2 when the pitch displacement is θ, as shown in Figure A4.9. If the buoy pitches about the

axis through c then the restoring moment about c due to chains #1 and #2 is

$$M_{1+2} = T_{V_1}(\frac{b}{2} + s_1) - T_{H_1}(d-h_1) - T_{V_2}(\frac{b}{2} - s_2) + T_{H_2}(d+h_2) \qquad (A4.39)$$

where T_V and T_H are the horizontal and vertical components of chain tension; s_1, h_1, s_2 and h_2 are the distances shown in Figure A4.9.

From geometry:

$$\begin{aligned} h_1 &= \frac{b}{2}\sin\theta + d(1-\cos\theta) \\ s_1 &= \frac{b}{2}(\cos\theta-1) + d\sin\theta \\ h_2 &= \frac{b}{2}\sin\theta - d(1-\cos\theta) \\ s_2 &= \frac{b}{2}(1-\cos\theta) + d\sin\theta \end{aligned} \qquad (A4.40)$$

Therefore

$$\begin{aligned} \frac{b}{2} + s_1 &= d\sin\theta + \frac{b}{2}\cos\theta \\ d - h_1 &= d\cos\theta - \frac{b}{2}\sin\theta \\ \frac{b}{2} - s_2 &= \frac{b}{2}\cos\theta - d\sin\theta \\ d + h_2 &= d\cos\theta + \frac{b}{2}\sin\theta \end{aligned} \qquad (A4.41)$$

Substitution in equation (A4.39) gives

$$M_{1+2} = T_{V_1}(d\sin\theta + \frac{b}{2}\cos\theta) - T_{H_1}(d\cos\theta - \frac{b}{2}\sin\theta)$$

$$- T_{V_2}(\frac{b}{2}\cos\theta - d\sin\theta) + T_{H_2}(d\cos\theta + \frac{b}{2}\sin\theta)$$

If the pitch angle is small so that the horizontal and vertical components

of tension in the chains in the displaced condition are approximately equal to the horizontal and vertical components of tension in the chains when the SBM is in equilibrium, then

$$T_{H_1} = T_{H_2} = T_{H_o}$$

and (A4.43)

$$T_{V_1} = T_{V_2} = T_{V_o}$$

Equation (A4.42) becomes

$$M_{1+2} = (T_{H_o} b + 2T_{V_o} d)\sin\theta \quad \text{(A4.44)}$$

Consider now the restoring moment due to chains #3 and #4, Figure A4.10. The restoring moment (moment about c) due to chains #3 and #4 is

$$M_{3+4} = T_{V_3}(\tfrac{b}{2}\sin 45^o + s_3) - T_{H_3}\cos 45^o(d - h_3)$$
$$- T_{V_4}(\tfrac{b}{2}\sin 45^o - s_4) + T_{H_4}\cos 45^o(d + h_4) \quad \text{(A4.45)}$$

From geometry:

$$h_3 = \tfrac{b}{2}\sin 45^o\sin\theta + d(1-\cos\theta)$$
$$s_3 = \tfrac{b}{2}\sin 45^o(\cos\theta-1) + d\sin\theta$$
$$h_4 = \tfrac{b}{2}\sin 45^o\sin\theta - d(1-\cos\theta) \quad \text{(A4.46)}$$
$$s_4 = \tfrac{b}{2}\sin 45^o(1-\cos\theta) + d\sin\theta$$

Therefore

$$\frac{b}{2}\sin45^{o} + s_3 = \frac{b}{2}\sin45^{o}\cos\theta + d\sin\theta$$

$$d - h_3 = -\frac{b}{2}\sin45^{o}\cos\theta + d\cos\theta$$

$$\frac{b}{2}\sin45^{o} - s_4 = \frac{b}{2}\sin45^{o}\cos\theta - d\sin\theta \qquad \text{(A4.47)}$$

$$d + h_4 = \frac{b}{2}\sin45^{o}\sin\theta + d\cos\theta$$

Substitution in equation (A4.45) and letting

$$T_{v_3} = T_{v_4} = T_{v_o}$$

$$T_{H_3} = T_{H_4} = T_{H_o} \qquad \text{(A4.48)}$$

gives

$$M_{3+4} = 2T_{v_o} d\sin\theta + T_{H_o}\cos45^{o} b\sin45^{o}\sin\theta$$

$$= 2T_{v_o} d\sin\theta + T_{H_o}\frac{b}{2}\sin\theta \qquad \text{(A4.49)}$$

Since chains #5 provide no restoring moment in pitch, the total restoring moment due to the 8 chains is

$$M = M_{1+2} + 2(M_{1+3}) \qquad \text{(A4.50)}$$

Substitution for M_{1+2} and M_{1+3} gives

$$M = (2T_{H_o} b + 6T_{v_o} d)\sin\theta \qquad \text{(A4.51)}$$

For small angles of pitch $\sin\theta \approx \theta$ and so

$$M = (2T_{H_o} b + 6T_{v_o} d)\theta \qquad \text{(A4.52)}$$

(as given by equation (6.15) in the main text).

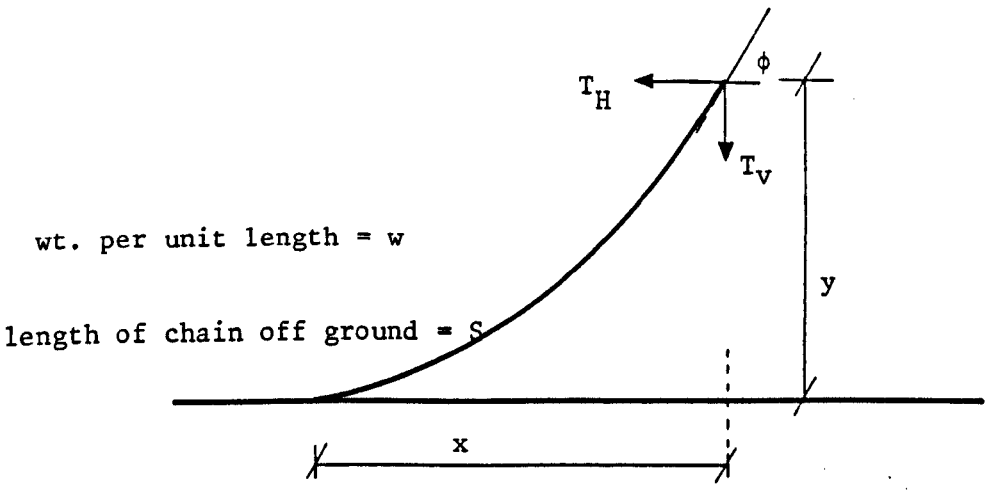

Figure A4.1 Definition sketch for catenary

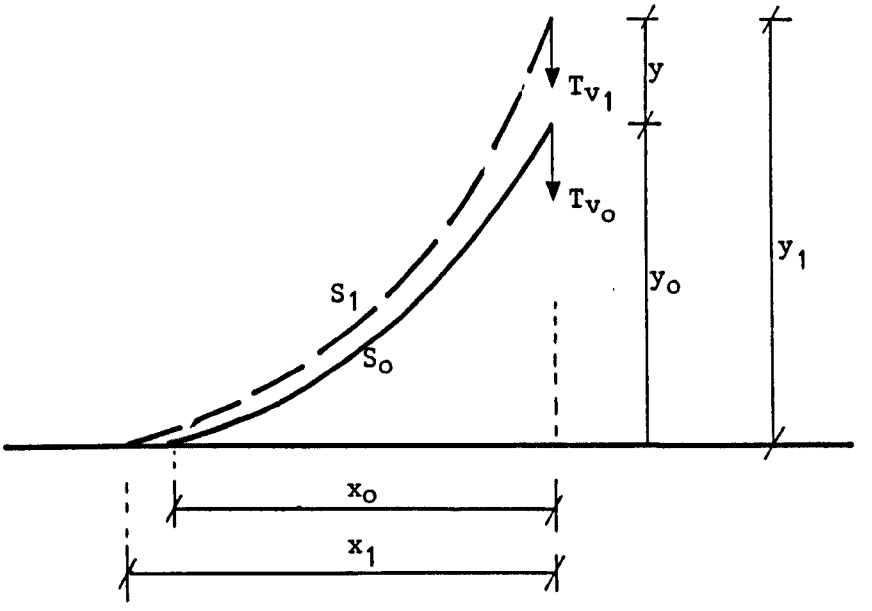

Figure A4.2 Heave displacement of catenary chain

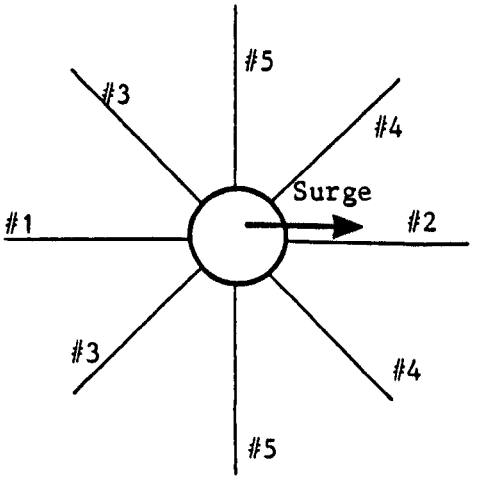

Figure A4.3 Chain layout relative to surge

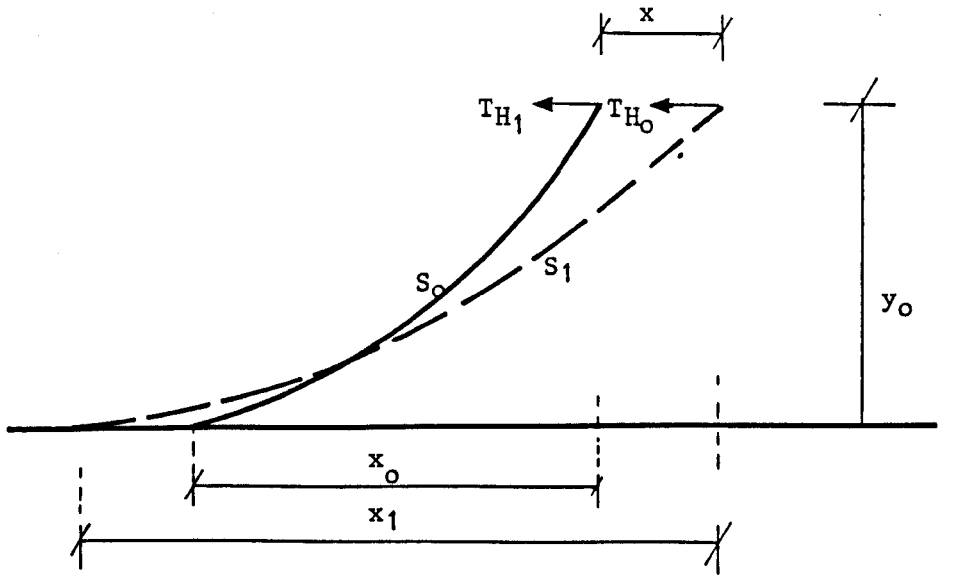

Figure A4.4 Surge displacement of chain #1

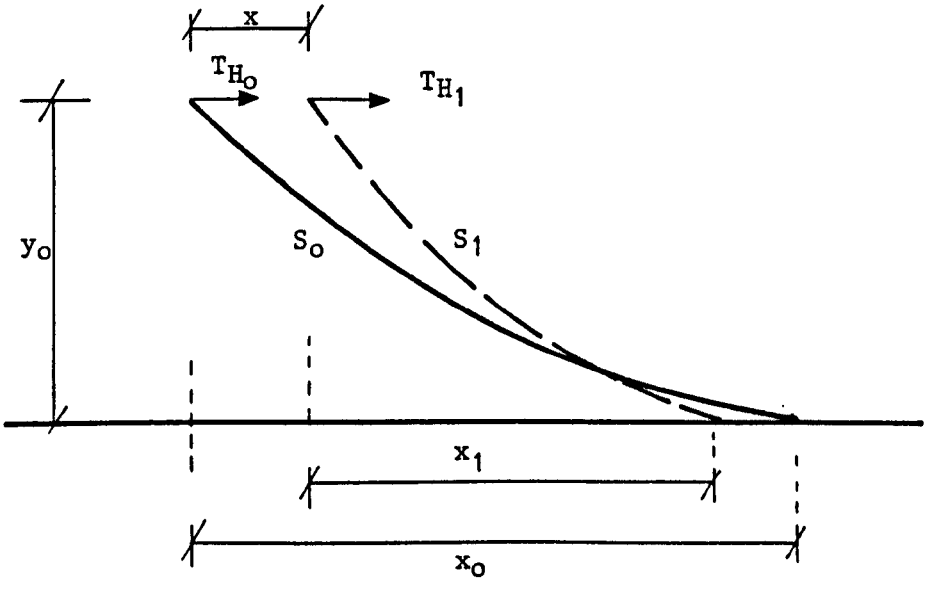

Figure A4.5 Surge displacement of chain #2

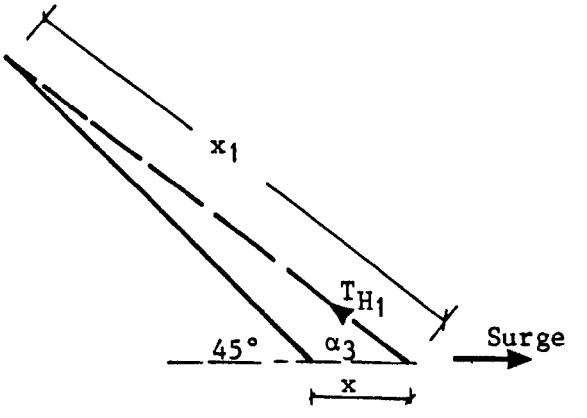

Figure A4.6 Line of action of chain #3

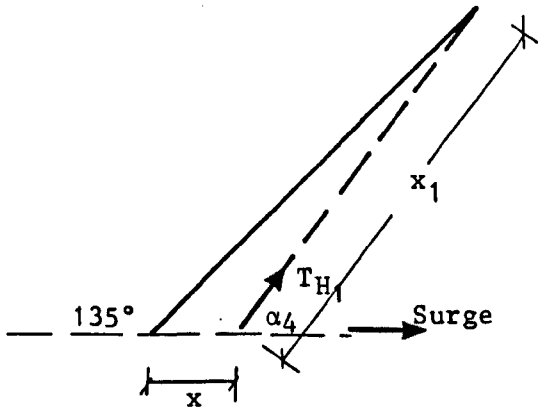

Figure A4.7 Line of action of chain #4

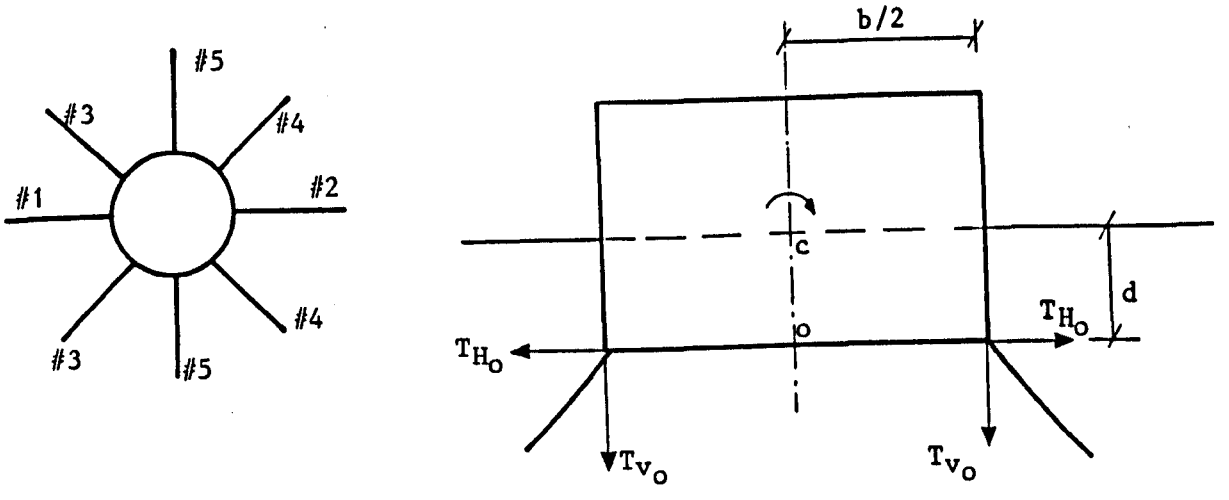

Figure A4.8 Equilibrium condition of SBM and layout of chains

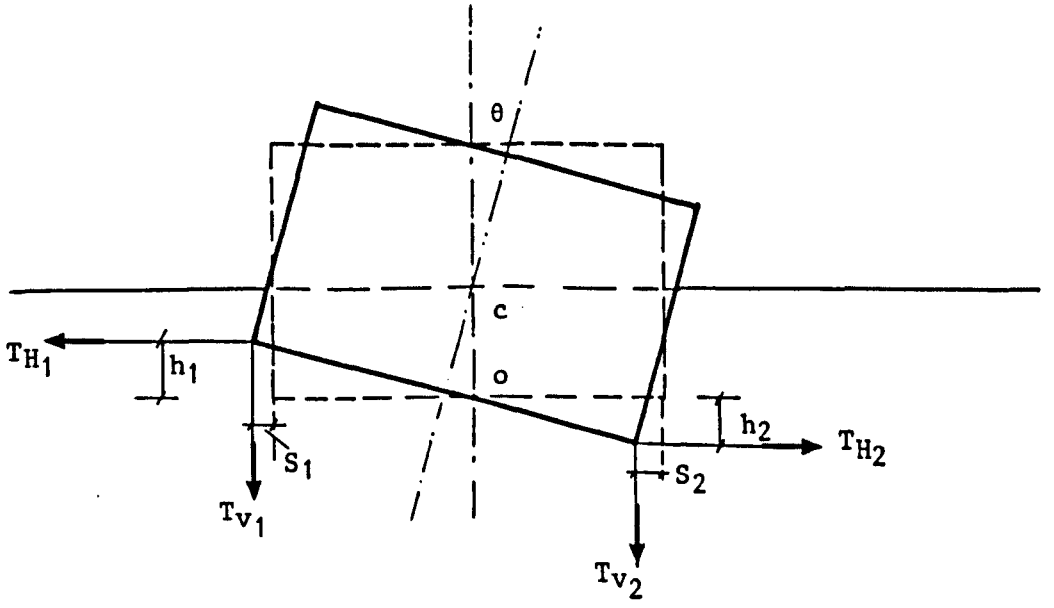

Figure A4.9 SBM pitch displacement = θ: sketch for calculating the restoring moment due to chains #1 and #2

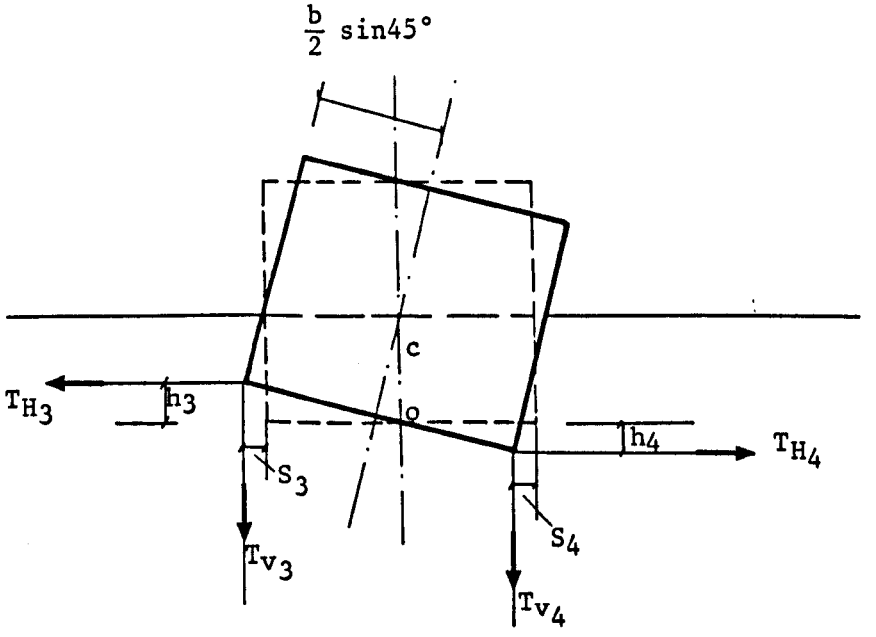

Figure A4.10 Sketch for calculating the restoring moment due to chains #3 and #4

APPENDIX A5

SOLUTION OF EQUATION OF MOTION FOR SNAKING

(The solution of the snaking problem has been carried out in collaboration with Mr J Bree, Department of Mathematics, Heriot-Watt University.)

The snaking problem requires the solution of

$$\partial^4 z/\partial x^4 + K\partial z/\partial t + (1/c^2)\partial^2 z/\partial t^2 = 0 \qquad \text{(A5.1)}$$

subject to the boundary condition

$$[\partial/\partial x(\partial^3 z/\partial x^3 . \partial z/\partial x)]_{x=0} = a_s(\sigma^2/c^2)\cos\sigma t \qquad \text{(A5.2)}$$

The solution takes the form of a travelling wave

$$z(x,t) = Ae^{i(kx-\omega t)} \qquad \text{(A5.3)}$$

Substituting for $\partial^4 z/\partial x^4$, $\partial z/\partial t$ and $\partial^2 z/\partial t^2$ in equation (A5.1) gives

$$k^4 - i\omega K - \omega^2/c^2 = 0 \qquad \text{(A5.4)}$$

Therefore

$$k^4 = (\omega^2/c^2) + i\omega K = Re^{i\theta} = Re^{i(\theta+2n\pi)} \qquad \text{(A5.5)}$$

where

$$R = (\omega^2/c^2 + \omega^2 K^2)^{1/2}$$

$$\theta = \tan^{-1}(Kc^2/\omega)$$

Therefore

$$k = R^{1/4} e^{i(\theta/4+n\pi/2)} \quad , \quad n = 0,1,2,3$$

When

$n = 0: \quad k = R^{1/4}(\cos\theta/4 + i\sin\theta/4)$

$n = 1: \quad k = R^{1/4}(-\sin\theta/4 + i\cos\theta/4)$

$n = 2: \quad k = R^{1/4}(-\cos\theta/4 - i\sin\theta/4)$

$n = 3: \quad k = R^{1/4}(\sin\theta/4 - i\cos\theta/4)$

Letting $R^{1/4}\cos\theta/4 = \alpha$ and $R^{1/4}\sin\theta/4 = \beta$ then the solution of the fourth order d.e. (equation A5.1) is the sum of four independent solutions and is given by

$$z(x,t) = A_1\exp[i\{(\alpha+i\beta)x-\omega t\}] + A_2\exp[i\{(-\beta+i\alpha)x-\omega t\}]$$
$$+ A_3\exp[i\{(-\alpha-i\beta)x-\omega t\}] + A_4\exp[i\{(\beta-i\alpha)x-\omega t\}]$$

or

$$z(x,t) = A_1e^{-\beta x}e^{i(\alpha x-\omega t)} + A_2e^{-\alpha x}e^{i(-\beta x-\omega t)}$$
$$+ A_3e^{\beta x}e^{i(-\alpha x-\omega t)} + A_4e^{\alpha x}e^{i(\beta x-\omega t)} \qquad (A5.6)$$

For a finite solution at $x = \infty$

$$z(x,t) = A_1e^{-\beta x}e^{i(\alpha x-\omega t)} + A_2e^{-\alpha x}e^{i(-\beta x-\omega t)} \qquad (A5.7)$$

Letting $A_1 = Ee^{i\gamma}$ and $A_2 = Fe^{i\delta}$ then

$$z(x,t) = Ee^{-\beta x}e^{i(\alpha x-\omega t+\gamma)} + Fe^{-\alpha x}e^{i(-\beta x-\omega t+\delta)} \qquad (A5.8)$$

$$[\partial z/\partial x] = E(-\beta+i\alpha)e^{-\beta x}e^{i(\alpha x-\omega t+\gamma)} + F(-\alpha-i\beta)e^{-\alpha x}e^{i(-\beta x-\omega t+\delta)}$$

But

$$(-\beta+i\alpha) = R^{1/4}e^{i(\theta/4+\pi/2)}$$

and

$$(-\alpha-i\beta) = R^{1/4}e^{i(\theta/4+\pi)}$$

Therefore

$$[\partial z/\partial x]_{x=0} = ER^{1/4}e^{i(-\omega t+\gamma+\theta/4+\pi/2)} + FR^{1/4}e^{i(-\omega t+\delta+\theta/4+\pi)} \quad (A5.9)$$

Also

$$[\partial^2 z/\partial x^2]_{x=0} = ER^{1/2}e^{i(-\omega t+\gamma+\theta/2+\pi)} + FR^{1/2}e^{i(-\omega t+\delta+\theta/2+2\pi)} \quad (A5.10)$$

$$[\partial^3 z/\partial x^3]_{x=0} = ER^{3/4}e^{i(-\omega t+\gamma+3\theta/4+3\pi/2)} + FR^{3/4}e^{i(-\omega t+\delta+3\theta/4+3\pi)} \quad (A5.11)$$

$$[\partial^4 z/\partial x^4]_{x=0} = ERe^{i(-\omega t+\gamma+\theta+2\pi)} + FRe^{i(-\omega t+\delta+\theta+4\pi)} \quad (A5.12)$$

Taking real parts:

$$[\partial z/\partial x]_{x=0} = ER^{1/4}\sin(\omega t-\theta/4-\gamma) - FR^{1/4}\cos(\omega t-\theta/4-\delta) \quad (A5.13)$$

$$[\partial^2 z/\partial x^2]_{x=0} = -ER^{1/2}\cos(\omega t-\theta/2-\gamma) + FR^{1/2}\cos(\omega t-\theta/2-\delta) \quad (A5.14)$$

$$[\partial^3 z/\partial x^3]_{x=0} = -ER^{3/4}\sin(\omega t-3\theta/4-\gamma) - FR^{3/4}\cos(\omega t-3\theta/4-\delta) \quad (A5.15)$$

$$[\partial^4 z/\partial x^4]_{x=0} = ER\cos(\omega t-\theta-\gamma) + FR\cos(\omega t-\theta-\delta) \quad (A5.16)$$

The boundary condition (equation A5.2) can be written as

$$[\partial^3 z/\partial x^3.\partial^2 z/\partial x^2 + \partial^4 z/\partial x^4.\partial z/\partial x)_{x=0} = a_s(\sigma^2/c^2)\cos\sigma t \quad (A5.17)$$

Substituting for the terms in the l.h.s. of equation (A5.17) gives:

$$\begin{aligned}\tfrac{1}{2}R^{5/4}[&E^2\sin(2\omega t-5\theta/4-2\gamma) - E^2\sin\theta/4 - EF\sin(2\omega t-5\theta/4-\gamma-\delta)\\ &+ EF\sin(\theta/4-\gamma-\delta) + EF\cos(2\omega t-5\theta/4-\gamma-\delta) + EF\cos(\theta/4-\gamma+\delta)\\ &- F^2\cos(2\omega t-5\theta/4-2\delta) - F^2\cos\theta/4 + E^2\sin(2\omega t-5\theta/4-2\gamma)\\ &+ E^2\sin 3\theta/4 - EF\cos(2\omega t-5\theta/4-\gamma-\delta) - EF\cos(3\theta/4-\delta+\gamma)\\ &+ EF\sin(2\omega t-5\theta/4-\gamma-\delta) + EF\sin(3\theta/4-\gamma+\delta)\\ &-F^2\cos(2\omega t-5\theta/4-2\delta) - F^2\cos 3\theta/4] = a_s(\sigma^2/c^2)\cos\omega t \quad (A5.18)\end{aligned}$$

For equation (A5.18) to be satisfied we require

$$\delta = \gamma \tag{A5.19}$$

and

$$(EF-E^2)\sin\theta/4 + (EF-F^2)\cos\theta/4 + (E^2+EF)\sin3\theta/4 - (EF+F^2)\cos3\theta/4 = 0$$

Putting $\lambda = F/E$, this gives on dividing by E^2

$$(\lambda-1)\sin\theta/4 + (\lambda-\lambda^2)\cos\theta/4 + (1+\lambda)\sin3\theta/4 - (\lambda+\lambda^2)\cos3\theta/4 = 0$$

That is, λ is the positive root of the quadratic

$$(\cos\theta/4+\cos3\theta/4)\lambda^2 - (\sin\theta/4+\cos\theta/4+\sin3\theta/4-\cos3\theta/4)\lambda$$
$$- (\sin3\theta/4-\sin\theta/4) = 0 \tag{A5.20}$$

Equation (A5.18) then becomes

$$E^2R^{5/4}[\sin(2\omega t-5\theta/4-2\gamma) - \lambda^2\cos(2\omega t-5\theta/4-2\gamma)] = a(\sigma^2/c^2)\cos\sigma t$$

or

$$E^2R^{5/4}(1+\lambda^4)^{1/2}\cos(2\omega t-5\theta/4-2\gamma+\phi) = a(\sigma^2/c^2)\cos\sigma t \tag{A5.21}$$

where $\phi = \tan^{-1}(1/\lambda^2)$ and is in the third quadrant.

Equation (A5.21) implies that

$$\gamma = \phi/2 - 5\theta/8 \tag{A5.22}$$

$$\omega = \sigma/2 \tag{A5.23}$$

$$E^2R^{5/4}(1+\lambda^4)^{1/2} = a(\sigma^2/c^2) \tag{A5.24}$$

(The solution is summarised in the main text, Section 7.3.3.)

REFERENCES

Brady I, Williams S and Golby P

"A study of the forces acting on hoses at a monobuoy due to environmental conditions"

OTC 2136, 6th Annual Offshore Technology Conference, Houston, 1974.

Bridgestone

"Study of causes of kinking in floating hoses at Petrobras/Tefran terminal"

Bridgestone Tyre Co of Japan

Report 6YMT-0011, 1976.

Brown M J

"Mathematical model of a marine hose-string at a buoy"

7th POLYMODEL Conf, Sunderland Polytechnic, May 1984

(pub Springer-Verlag).

Byrne D J

"UNITERM: The terminal emulator for the BBC microcomputer"

COMMPAK DATA, 1985.

Cooley J W and Tukey J W

"An algorithm for the machine computation of complex Fourier series"

Math Comput 19, 1965, pp297-301.

Dunlop Oil and Marine Division

"A study of the forces acting on hoses at a monobuoy"

Dunlop Oil and Marine, Grimsby, England

1973.

Dunlop Oil and Marine Division

"Offshore Hose Manual"

Dunlop Oil and Marine, Grimsby, England

1971.

Dean R G and Dalrymple R A

"Water Wave Mechanics for engineers and scientists"

pub Prentice-Hall, 1984.

Funke E R

"Random wave signal generation by minicomputer"

Proc 14th Coastal Eng Conf

Copenhagen, 1974.

Furness R L

"A dynamic program for improving SPM hose technology"

Oilweek, Vol 32, Part 27, pp126-130, 1981.

Garrett C J R

"Wave forces on a circular dock"

Jour Fluid Mech, Vol 46, Part 1, pp129-139, 1971.

Garrison C J

"Dynamic response of floating bodies"

OTC 2067, 6th Annual Offshore Technology Conference, Houston, 1974.

Graham H

"Newcastle model hose tests"

Report for Dunlop Oil and Marine, Grimsby, England, 1982.

Gruy R H

"Marginal Field (Early production): Options for offshore loading"

2nd Offshore Mechanics and Arctic Engineering Conf, Houston, 1982.

Lancaster University

"User Guide for BBC Kermit"

Computing Department, Lancaster University, England, April 1985.

Langley R S

"Some aspects of slack catenary moorings"

A short course at Cranfield Institute of Technology

Section 11, April 1982.

Loach M J

"Kermit-40 for GEC OS4000 (RAL), Version 1.1"

Science and Engineering Research Council, Rutherford Appleton Laboratory, Informatics Division, OS4000 USer Note 105, April 1985.

Lindner J T

"Single point mooring - an old idea receives new enthusiasm"

Noroil, Vol 7, No11, November 1979.

Newland D E

"An introduction to random vibrations and spectral analysis"

2nd edition, pub Longman, 1984.

Saito H, Mochizuki T, Fukai T and Okui K

"Actual measurements of external forces on marine hoses for SPM"

OTC 3803, 12th Annual Offshore Technology Conference, Houston, 1980.

Salmon J and Smith D

"Offshore loading: a review of improvements to CALM tanker terminals with particular reference to the North Sea"

2nd Offshore Mechanics and Arctic Engineering Conference, Houston, 1982.

Sarpkaya T and Isaacson M

"Mechanics of wave forces on offshore structures"

pub Van Nostrand Reinhold Co, 1981.

Selective Electronic Co

"The SELSPOT system"

Sweden, 1976.

Tschoepe E C

"SPM hose test program"

OTC 4105, 13th Offshore Technology Conference, Houston, 1981.

Vugts J H

"The hydrodynamic coefficients for swaying, heaving and rolling cylinders in a free surface"

International Shipbuilding Progress, Vol 15, Part 167, 1968.

Yeung R W

"Added mass and damping of a vertical cylinder in finite depth waters"

Applied Ocean Research, Vol 3, No3, July 1981.

Young R A, Brogren E E and Chakrabarti S K

"Behaviour of loading hose models in laboratory waves and currents"

OTC 3842, 12th Annual Offshore Technology Conference, Houston, 1980.

Ziccardi J J

"Selection of hose systems for SPM tanker terminals"

OTC 1152, 2nd Annual Offshore Technology Conference, Houston, 1970.

LIST OF TEXTBOOKS

The following lists the main textbooks used in the course of the study.

"Mechanics of Wave Forces on Offshore Structures"

by T Sarpkaya and M Isaacson

Van Nostrand Reinhold, 1981.

"Dynamics of Marine Structures"

by H G Hallam, N J Heaf and L R Wootton

CIRIA Underwater Engineering Group, 1978.

"Water wave mechanics for engineers and scientists"

by R G Dean and R A Dalrymple

Prentice Hall, 1984.

"An Introduction to Random Vibrations and Spectral Analysis"

by D E Newland

Longman Group, 1984.

"Engineering applications of correlation and spectral analysis"

by J S Bendat and A G Piersol

John Wiley, 1976.

"The Mechanics of Vibration"

by R E D Bishop and D C Johnson

Cambridge University Press, 1960.

"Fundamentals of Mechanical Vibrations"

by M Hussey

The MacMillan Press, 1983.

"Programming in Standard Fortran 77"

by A Balfour and D H Marwick

Heinemann, 1979.

"Computer Applications of Numerical Methods"

by S S Kuo

Addison-Wesley Publishing Co, 1972.